

Bars morphodynamics in trained rivers with heterogeneous sediment

Florian Cordier

▶ **To cite this version:**

Florian Cordier. Bars morphodynamics in trained rivers with heterogeneous sediment. Fluids mechanics [physics.class-ph]. Université Paris-Est, 2018. English. ⟨NNT : 2018PESC1149⟩. ⟨tel-02279316v2⟩

HAL Id: tel-02279316

https://pastel.hal.science/tel-02279316v2

Submitted on 24 Sep 2019

HAL is a multi-disciplinary open access archive for the deposit and dissemination of scientific research documents, whether they are published or not. The documents may come from teaching and research institutions in France or abroad, or from public or private research centers.

L'archive ouverte pluridisciplinaire **HAL**, est destinée au dépôt et à la diffusion de documents scientifiques de niveau recherche, publiés ou non, émanant des établissements d'enseignement et de recherche français ou étrangers, des laboratoires publics ou privés.



HAL Authorization

ÉCOLE DOCTORALE UNIVERSITÉ PARIS-EST
Sciences, Ingénierie et Environnement

LABORATOIRE D'HYDRAULIQUE SAINT-VENANT

EDF R&D

THÈSE DE L'UNIVERSITÉ DE PARIS-EST

Délivrée par

L'ÉCOLE DOCTORALE SIE

SPÉCIALITÉ : MÉCANIQUE DES FLUIDES

DIPLÔME DE DOCTORAT

(arrêté du 25 mai 2016)

Soutenue publiquement le 22 novembre, 2018 par

FLORIAN CORDIER

MORPHODYNAMIQUE DES BANCS DANS DES RIVIÈRES AMÉNAGÉES À GRANULOMÉTRIE ÉTENDUE

Convention CIFRE n° 2015-1055

Préparée au laboratoire d'Hydraulique Saint-Venant et EDF R&D LNHE, Chatou

Jury :

Rapporteurs :	M. Stefano Lanzoni	Professeur	Università di Padova
	M. Benoit Camenen	Dir. de recherche	Irstea Lyon
Examinateurs :	M. Annunziato Siviglia	Docteur	ETH Zürich
	M. Peter A. Nelson	Prof. ass.	Colorado State University
Directeur de thèse :	M. Damien Pham Van Bang	Professeur	ETE-INRS Québec
Encadrant :	M. Pablo Tassi	Docteur	EDF R&D LNHE/LHSV
Co-encadrant :	M. Nicolas Claude	Docteur	EDF R&D LNHE
Invités :	Mme Alessandra Crosato	Prof. ass.	IHE Delft
	M. Stéphane Rodrigues	Professeur	EPU Tours/CNRS
	M. Philippe Belleudy	Professeur	LTHE/UGA-IGE
	M. Pierre-Yves Lagrée	Dir. de recherche	UMPC

École doctorale Sciences, Ingénierie et Environnement
Université Paris-Est
Spécialité mécanique des fluides
6 & 8 avenue Blaise-Pascal - Cité Descartes - Champs sur Marne - 77455 MARNE-LA-VALLÉE, France
Tél. +33(0)1 60 95 75 00 – ed-sie@univ-paris-est.fr – www.univ-paris-est.fr

ÉCOLE DOCTORALE UNIVERSITÉ PARIS-EST
Sciences, Ingénierie et Environnement

LABORATOIRE D'HYDRAULIQUE SAINT-VENANT

EDF R&D

PH.D. THESIS OF PARIS-EST UNIVERSITY

delivered by

L'ÉCOLE DOCTORALE SIE

SPECIALITY: FLUID MECHANICS

PH.D. DIPLOMA

(arrêté du 25 mai 2016)

Defended publicly on November 22nd, 2018 by

FLORIAN CORDIER

BARS MORPHODYNAMICS IN TRAINED RIVERS WITH HETEROGENEOUS SEDIMENT

CIFRE convention n° 2015-1055

Prepared at the Saint-Venant Laboratory for Hydraulics et EDF R&D LNHE, Chatou

Jury :

Rapporteurs:	Mr. Stefano Lanzoni	Professor	Università di Padova
	Mr. Benoit Camenen	Research dir.	Irstea Lyon
Examiners:	Mr. Annunziato Siviglia	Doctor	ETH Zürich
	Mr. Peter A. Nelson	Ass. prof.	Colorado State University
Thesis director:	Mr. Damien Pham Van Bang	Professor	ETE-INRS Québec
Supervisor:	Mr. Pablo Tassi	Doctor	EDF R&D LNHE/LHSV
Co-supervisor:	Mr. Nicolas Claude	Doctor	EDF R&D LNHE
Guests:	Mrs Alessandra Crosato	Ass. Prof.	IHE Delft
	Mr. Stéphane Rodrigues	Professor	EPU Tours/CNRS
	Mr. Philippe Belleudy	Professor	LTHE/UGA-IGE
	Mr. Pierre-Yves Lagrée	Research dir.	UMPC/CNRS

École doctorale Sciences, Ingénierie et Environnement
Université Paris-Est
Spécialité mécanique des fluides
6 & 8 avenue Blaise-Pascal - Cité Descartes - Champs sur Marne - 77455 MARNE-LA-VALLÉE, France
Tél. +33(0)1 60 95 75 00 – ed-sie@univ-paris-est.fr – www.univ-paris-est.fr

Résumé

Morphodynamique des bancs dans des rivières aménagées à granulométrie étendue

Les rivières présentent généralement un lit ondulé causé par la présence de bancs, qui correspondent à des larges dépôts sédimentaires alternant avec des zones profondes (mouilles). Des travaux d'ingénierie importants et répétés modifiant la géométrie du cours d'eau, le régime hydraulique et l'apport sédimentaire peuvent à terme modifier la dynamique des bancs à l'échelle de la rivière. Une meilleure compréhension des processus liés aux bancs est importante pour les gestionnaires des rivières, car les bancs contrôlent activement la morphologie du lit et érodent les berges, impactant la navigation, les prises d'eaux, les ouvrages et la qualité des habitats. Même si les mécanismes régissant la formation et le développement des bancs sont bien connus, la compréhension de la morphodynamique des bancs en milieu fluvial reste limitée, en raison de la non-linéarité induite par la combinaison de facteurs naturels en atrophiques. La non-uniformité des sédiments est une caractéristique inhérente des rivières, mais son impact sur la propriété des bancs, même dans des cas simplifiés, reste obscure. Ce travail de thèse vise à étudier l'impact de l'hétérogénéité granulométrique sur des bancs dans des chenaux endigués, via l'utilisation d'un modèle morphodynamique bi-dimensionnel implémenté dans le système Telemac-Mascaret. Un certain nombre de développements numériques nécessaires (nouvelle formule de transport solide dédiée aux sédiments non-uniformes, tri granulométrique vertical) sont apportés afin d'être en accord avec l'état de l'art sur la modélisation de bancs avec un sédiment-non-uniforme. En premier lieu, le modèle numérique est utilisé pour reproduire la morphodynamique de bancs périodiques alternés avec un sédiment uniforme et non-uniforme dans un chenal à géométrie idéalisée et des conditions aux limites bien contrôlées. Par la suite, le modèle est appliqué à un tronçon sablo-graveleux de la Loire moyenne, présentant une configuration géométrique plus complexe et une combinaison de multiples forçages internes et externes, tels que des variations longitudinale de largeur de chenal ainsi qu'une hydrologie variable. Les résultats numériques montrent que des bancs périodiques de différents types (libres/hybrides) et différents motifs (mode faible/élevé) sont associés à des motifs de tri granulométrique distincts. Alors que le tri granulométrique spatial ne modifie pas les caractéristiques moyennées des bancs qui migrent, ce tri affecte de manière significative la géométrie des bancs stabilisés en les aplatissant et en les allongeant, ce qui tend à augmenter la mobilité des bancs situés plus à l'aval. De plus, une granulométrie plus étendue est suivie d'une augmentation du degré de tri granulométrique spatial, qui de ce fait joue sur les dimensions et la mobilité des bancs, comme mentionné précédemment. Les résultats permettent de valider l'approche de modélisation, démontrent la portabilité de celle-ci pour d'autres études, dans le but de les aider à mieux modéliser et prédire l'évolution des bancs dans les tronçons aménagés avant de proposer des solutions de gestion efficaces.

Mots-clés : Morphodynamique fluviale, transport sédimentaire, banc alluvial, sédiment non-uniforme, modélisation numérique, ingénierie fluviale.

Abstract

Bars morphodynamics in trained rivers with heterogeneous sediment

Rivers often present a wavy bed topography due to the presence of bars, corresponding to large sediment deposits alternating with deeper areas (pools). Intense and continual river engineering works altering the river geometry, flow regime and sediment supply can impact bar morphodynamics at the reach scale. A deep knowledge of bar processes is important for river managers, because bars actively control the river bed topography and influence bank erosion, with consequences for navigation, water intakes, infrastructure and the quality of their habitats. Although the origin of bar formation and propagation is well understood, the understanding of bar morphodynamics in rivers remains limited due to the non-linearity of a complex combination of variables of control. Sediment non-uniformity is an inherent characteristic of rivers, but its impact on bar properties, even considering simple configurations, is still unclear. This Ph.D. thesis aims at investigating the impact of sediment size heterogeneity on bars in rivers with non-erodible banks, using a two-dimensional morphodynamic model implemented in the Telemac-Mascaret system. Several key improvements of the model (new sediment transport formula dedicated to non-uniform material, vertical sediment sorting) have been proposed to reach the state of the art in modelling the influence of heterogeneous sediment on river bar morphodynamics. Firstly, the numerical model is applied to reproduce periodic bar morphodynamics with uniform and non-uniform sediment distribution in an idealized channel geometry and well controlled boundary conditions. Secondly, the morphodynamic model is applied to a sandy-gravel reach of the middle Loire river, presenting a combination of multiple internal and external forcing parameters, such as longitudinal variations of the channel width and variable hydrology. Numerical results show that periodic bars of different types (free/hybrid) and patterns (low/high bar mode) exhibit distinct sediment sorting patterns. Spatial sediment sorting is showed to not affect the averaged migrating bars characteristics, while it impacts significantly steady bar characteristics such as elongation and damping, which in turn increases further downstream bars mobility. Furthermore, a larger sediment size heterogeneity is showed to increase the degree of sediment sorting, with consequences on the dimensions and mobility of bars as explained previously. General outcomes of this thesis show the validity of the modelling approach, demonstrate its applicability for other study cases, and propose diverse recommendations for river engineers to model and predict bar morphodynamics processes before designing effective river management solutions.

Key words: Fluvial morphodynamics, sediment transport, alluvial bar, heterogeneous sediment, numerical modelling, fluvial engineering.

Acknowledgements

I would like to acknowledge EDF for funding this CIFRE Ph.D. through the projects CIGALE, VERONA and PHE; the Laboratory for Hydraulics of Saint-Venant and Université SIE Paris-EST; the members of my thesis jury committee for their deep interest to my work and carefully evaluating my dissertation and the oral presentation; my supervisors Pablo Tassi, Nicolas Claude, Alessandra Crosato, Stéphane Rodrigues and Damien Pham Van Bang, who shared their enthusiasm, knowledge and passion on the research on the discipline of morphodynamics; the members of my monitoring committee, Philippe Belleudy, Pierre-Yves Lagrée and Eric Valette; Kamal El-Kadi Abderrezzak and Olivier Delestre, for their kind advices; my interns Chenyu Liu and Jiaze Li, who contributed to this work; my co-workers Sébastien Barthélémy and Romain Leroux, for their creativeness, sense of humor and unquestionable joy of life; my family, my friends and my fiancée for their continuing support.

Contents

Page

Résumé **i**

Abstract **iii**

Acknowledgements **v**

List of figures **xv**

List of tables **xvii**

List of abbreviations **xix**

Glossary **xxi**

1 Introduction **1**
1.1 Global scientific context . . . 3
1.1.1 Rivers sinuosity and planform channel geometry . . . 3
1.1.2 Bars in alluvial rivers and classification . . . 4
1.1.3 Parameters influencing bar morphodynamics . . . 6
1.2 Main objectives and research questions . . . 14
1.2.1 Research questions . . . 14
1.2.2 Objectives . . . 14
1.3 Numerical modelling of fluvial bar processes . . . 15
1.3.1 State of the art on the numerical modelling of bar morphodynamics . . . 15
1.3.2 Improvement of the Telemac-Mascaret modelling system . . . 16
1.4 Methodology and plan of the manuscript . . . 17
1.5 Perimeter of the current framework . . . 17
□ Synthèse générale sur l'introduction . . . 19

I First Part. Numerical model set-up and activities of implementation and improvements **21**

2 Numerical model and developments **23**
▷ Motivations and objectives of this activity . . . 24
2.1 Mathematical and numerical model . . . 25
2.1.1 Hydrodynamic model . . . 25
2.1.2 Morphodynamic model . . . 25
2.1.3 Numerical scheme . . . 27
2.2 Numerical developments: motivation and practical use in this work . . . 28
2.2.1 Implementation of Wilcock and Crowe [2003]'s formula to assess bedload transport . . . 28
2.2.2 Implementation of the bookkeeping active layer model for vertical sediment sorting . . . 34

2.2.3 Implementation of sediment recirculation . . . 45
Nomenclature . . . 47
▷ Insights on numerical modelling of free bars . . . 49
□ Synthèse générale sur le choix, le développement et la validation du modèle numérique 50

II Second Part. Alternate bars morphodynamics with non-uniform sediment considering simplified configurations 51

3 Influence of numerical and physical parameters on the modelling of free bar morphodynamics 53
▷ Motivations and objectives of this study . . . 54
3.1 Introduction . . . 55
3.2 Materials and methods . . . 57
3.2.1 Mathematical and numerical model . . . 57
3.2.2 Study case . . . 59
3.2.3 Numerical model scenarios . . . 59
3.2.4 Model parameters . . . 60
3.3 Numerical results with uniform sediment . . . 61
3.3.1 Influence of numerical parameters . . . 61
3.3.2 Influence of physical parameters . . . 62
3.4 Numerical simulations with non-uniform sediment . . . 67
3.4.1 Influence of physical parameters . . . 67
3.4.2 Discussion on numerical behaviour of the front bar propagation . . . 70
3.5 General Outcomes . . . 72
Acknowledgment . . . 73
Nomenclature . . . 73
References . . . 74
▷ Insights on numerical modelling of free bars . . . 78
□ Synthèse générale sur l'influence des paramètres physiques et numériques sur la modélisation des bancs libres . . . 79

4 Numerical study of alternate bars in alluvial channels with non-uniform sediment 81
▷ Motivations and objectives of this study . . . 82
4.1 Introduction . . . 83
4.2 Materials and methods . . . 85
4.2.1 Mathematical and numerical model . . . 85
4.2.2 Study case . . . 89
4.2.3 Numerical model setup . . . 89
4.2.4 Numerical model simulations . . . 90
4.2.5 Analysis methods . . . 91
4.2.6 Bar mode prediction and concept of resonance . . . 92
4.3 Numerical results . . . 93
4.3.1 Scenarios without obstacle . . . 93
4.3.2 Scenarios with an obstacle . . . 101
4.3.3 Effects of sediment size heterogeneity . . . 103
4.3.4 Effects of spatial sediment sorting . . . 106
4.4 Discussion . . . 107

4.4.1 Considerations on channel bed sediment sorting . . . 107
4.4.2 Comparison of free and hybrid bars morphodynamics . . . 108
4.4.3 Influence of spatial sediment sorting on periodic bars morphodynamics . 109
4.4.4 Influence of sediment size heterogeneity on periodic bars morphodynamics 111
4.5 Conclusions . . . 112
Acknowledgments . . . 113
Nomenclature . . . 114
References . . . 115
▷ Considerations on periodic bar morphodynamics with non-uniform sediment . . . 123
□ Synthèse générale sur l'influence de l'hétérogénéité sédimentaire sur la morphodynamique des bancs . . . 124

III Third Part. Bars morphodynamics with non-uniform sediment under complex configurations 125

5 Bar pattern and sediment sorting in a channel contraction/expansion: application to a sandy-gravel river reach (Middle Loire, France) 127
▷ Motivations and objectives of this study . . . 128
5.1 Introduction . . . 129
5.2 Materials and methods . . . 132
5.2.1 Study case . . . 132
5.2.2 Mathematical and numerical model . . . 134
5.2.3 Numerical model setup . . . 136
5.2.4 Numerical model scenarios . . . 137
5.2.5 Analysis methods . . . 137
5.3 Numerical model calibration and validation . . . 139
5.3.1 Hydrodynamic model calibration . . . 139
5.3.2 Morphodynamic model calibration and validation . . . 139
5.4 Morphodynamic results . . . 140
5.4.1 Bed evolution with variable discharge and sediment sorting . . . 140
5.4.2 Bed evolution with variable discharge without sediment sorting . . . 144
5.4.3 Bed evolution with constant inflow . . . 144
5.4.4 Bar mode . . . 146
5.4.5 Sediment transport . . . 146
5.4.6 Sediment sorting . . . 151
5.5 Discussion . . . 152
5.5.1 Bar pattern and water discharge . . . 152
5.5.2 Sediment sorting processes . . . 155
5.5.3 Consequences on the estimation of grain size distribution . . . 156
5.5.4 Limitations and perspectives . . . 157
5.6 Conclusions . . . 158
Acknowledgments . . . 159
Nomenclature . . . 160
▷ Insights on numerical modelling of free bars . . . 162
□ Synthèse générale sur la morphodynamique des bancs à sédiment non-uniforme en configuration complexe . . . 163

IV Last Part. Conclusions and Perspectives **165**

6 Conclusions and Perspectives **167**
6.1 Relation between bar morphology and sediment sorting pattern 168
6.1.1 Major contributions on the understanding of bar processes 168
6.1.2 Implications for river managers 168
6.2 Influence of sediment sorting on bars 170
6.2.1 Major contributions on the understanding of bar processes 170
6.2.2 Implications for river managers 171
6.3 Influence of sediment size heterogeneity on bars 171
6.3.1 Major contributions on the understanding of bar processes 171
6.3.2 Implications for river managers 171
6.4 Considerations on the numerical model applicability 172
6.4.1 Performance of the model in this work 172
6.4.2 Model applications for other studies 172
6.4.3 Consequences of numerical and physical parameterization on simulated bar morphodynamics 172
6.5 Limitations and Perspectives 173
6.6 Publications and Deliverables 175
6.6.1 Scientific publications 175
6.6.2 Strategic deliverables 176
□ Synthèse générale sur la conclusion et les perspectives 177

References **178**

Appendices **195**

A Numerical modelling of the secondary current and the influence of hydrology on morphodynamics of bars in a channel expansion/contraction, Loire River, France **197**

B Mathematical analysis of the formula of Wilcock and Crowe (2003) **263**

C Implementation of WC-2003 in Sisyphe V7P3 **279**

D Review of the active layer model implemented in the Telemac-Mascaret System by De Linares (Sisyphe V7P2) **287**

E Active layer model implemented in the Telemac-Mascaret System in this work (Sisyphe V7P3) **299**

F Implementation of the sediment recirculation in Sisyphe V7P3 **307**

G Architecture and main characteristics of the HPC used in this work **311**

List of figures

1.1 Example of a) meandering river, Purus River (Brazil) [Parker et al., 2011], b) braided river, Rakaia River (South Island, New Zealand) [Below and Jol, 2005], c) weakly meandering river with forced bars, Allier River (Avermes, France) and d) straight river with migrating free alternate bars (Landquart, Switzerland). 2

1.2 a) Gradual variation of equilibrium channel patterns with channel-forming water discharge, valley slope and sediment size [Bridge, 2003] and b) scheme of main configurations of the river bed according to Schumm [1981]. 4

1.3 Scheme of the classification of bars according to Duró et al. [2016] 6

1.4 Idealized bed and flow deformations induced by the presence of periodic bars: (left) first bar mode (alternate bars) and (right) second bar mode (central bars) [Crosato and Mosselman, 2009]. 7

1.5 Example of asymmetrical bed configuration leading to the formation of a transverse bar. 7

1.6 Impact of channel width variations on the configuration of combined free and forced bars. Addition of the a) component corresponding to forced transverse bars (W02 and W04) or lateral bars (W06 and W06) with the b) component corresponding to free (alternate) bars lead to c) mixed bars patterns. Source: [Wu et al., 2011], later modified by [Claude, 2012] and re-modified here. 8

1.7 Idealized channel geometry for a simple channel pattern and equivalent alternate bar pattern in a straight channel (upper diagram) used for comparison, where the solid and dashed lines with arrows represent the location of maximum flow velocity for the high-flow and low-flow stage, respectively. Dashed lines in cross sections represent the low-flow-stage geometry [Bridge, 2003]. 10

1.8 a) Planform sediment sorting over a gravel bar in the Isère river illustrating the strong spatial variability of sediment (Fréterive, July 2015) and b) vertical sorting of sediment in a secondary channel of the middle Loire river showing the bed armor (Bréhemont, November 2016). 12

2.1 Scheme of application of the sediment transport model of WC-2003. Parameters in blue boxes are input parameters, those in white boxes are intermediary variables computed to estimate the transport rate of the i^{th} size fraction in the black box. . 30

2.2 Fluxes of sediment crossing the upstream and downstream model boundaries considering the numerical run based on [Lanzoni, 2000b]'s P2009 experiment. This figure illustrates that the averaged transport rate simulated with the formula of WC-2003 computes satisfactory transport rates with respect to the laboratory observations and the new algorithm for sediment recirculation is well implemented in Sisyphe. 32

2.3 Longitudinal profile of bed evolution and vertical sediment sorting at 20 cm from the left sidewall obtained with the numerical model reproducing the experiment P2009 of Lanzoni. 33

2.4 Sediment transport rates measured at Bréhémont (middle Loire river) and computed with the numerical model using the formula of WC-2003, validating the implementation and the choice of this formula for this work. 34

2.5 Discretization of the vertical bed structure into the active layer and substrate according to the mathematical concept of Hirano [1972], and discretization of the substrate into multiple sub-layers following the bookkeeping layer concept [Blom, 2008; Viparelli et al., 2010]. 36
2.7 Flowchart of the new algorithm based on the bookkeeping active layer model of Hirano [Hirano, 1971] developed in the purpose of this work in TMS V7P3. . . . 43
2.8 Computation of the sediment balance at a) $t = 10$ s and b) $t = 40,000$ s, with the scenario used to test transitions between erodible and rigid bed, showing that sediment recirculation and the new algorithm for vertical sediment sorting are well implemented in the TMS. 44
2.9 Computation of the sediment balance at $t = 40,000$ s with the scenario used to test transitions between erodible and rigid bed, showing that sediment recirculation and the new algorithm for vertical sediment sorting are well implemented in the TMS. 45
2.10 Scheme of the method used to recirculate the sediment in the model channel. . . 46

3.1 Planform evolution of the bed at $t = 28$ h with using computational time-steps in the range of [0.02-0.16] s with the morphodynamic (a-d) equilibrium boundary and (e-h) sediment recirculation boundary 62
3.2 Planform evolution of the bed at $t = 28$ h with using computational mesh sizes in the range of [0.046875-0.375] m with the morphodynamic (a-d) equilibrium boundary and (e-h) sediment recirculation boundary 63
3.3 Planform evolution of the riverbed at $t = 28$ h using a regular and an irregular computational mesh 63
3.4 Time-series of the bed evolution at (X=114 m;Y=0.375 m) with using the equilibrium and recirculation upstream morphodynamic boundary conditions 64
3.5 Longitudinal profiles of bed evolution at 0.55 m from the left sidewall obtained with various coefficients for the correction of bedload a) magnitude β_1 and b) direction β_2 65
3.6 Impact of the bedload deviation on planform bar morphology and cross-stream bedload transport rates at $t = 28$ h with $\beta_2 = 1$ and $\beta_2 = 2.5$ 66
3.7 Longitudinal profiles ($y = 0.55$ m) of the bed evolution plotted with different values of $\alpha_{k,s}$ at $t = 28$ h 66
3.8 Time-series of bed evolution at (X=102 m;Y=0.415 m) with using the equilibrium and recirculation upstream morphodynamic boundary conditions 67
3.9 Longitudinal stratigraphic profiles at t=280.000 s obtained with the formula of WC-2003 with a) L_a =5 mm, b) L_a =1 cm, c) L_a =2 cm and d) L_a=100 m. 68
3.10 Longitudinal stratigraphic profiles at t=25.600 s obtained with the formula of MPM with a) L_a =5 mm and b) L_a =2 cm. 69
3.11 Longitudinal stratigraphic profiles at t=25.600 s obtained with the formula of MPM-E with L_a =5 mm. 70
3.12 Longitudinal profiles of bed evolution at t=280.000 s obtained with the reference scenario with (a) $\nu_t = 0$ m^2/s and (b) $\nu_t = 10^{-6}$ m^2/s. 70
3.13 Longitudinal stratigraphic profiles at t=280.000 s obtained with the reference scenario with (a) $\nu_t = 0$ m^2/s and (b) $\nu_t = 10^{-6}$ m^2/s. 71
4.1 Illustration of the terminology and nomenclature used to describe bars. 92

4.2 Comparison of a) bed evolution along the left longitudinal profile and b) difference of bed elevation between the left and right longitudinal profiles at t =3 h, obtained with the calibrated numerical model (run P2009-1) and measured by Lanzoni [2000b]. 94
4.3 Bed evolution from $t = 0$ s to $t = 280\,000$ s at (x=102 m;y=0.55 m) for the scenarios considered in this study. 95
4.4 Planform evolution of bed topography, shear stress and surface sediment sorting without obstacle for the (a) reference and (b) extended sediments scenarios at $t = 280\,000$ s. 96
4.5 Longitudinal profiles of bed evolution and vertical sediment sorting without obstacle for the (a) reference and (b) extended sediments scenarios at $t = 280\,000$ s. 96
4.6 Bed evolution and surface sediment sorting at $t = 3$ h from $x = 40$ m to $x = 80$ m obtained with the reference scenario (run P2009-1). 97
4.7 Spatially averaged solid discharges with and without sediment sorting for (a) the reference sediment (run P2009-1) and (b) the extended sediment (run P2009-6) scenarios. $\bar{Q}_b$ is the averaged volume of sediment crossing the downstream boundary during the 280 000 s of simulation; $\bar{Q}_{b,1}$ (resp. $\bar{Q}_{b,2}$) is the averaged volume of fine (resp. coarse) sediment crossing the downstream boundary during the 280 000 s of simulation. 98
4.8 Planform surface sorting of sediment at $t = 2\,000$ s with the reference scenario showing the sedimentation wave front at $x \approx 23$ m (run P2009-1). 98
4.9 Time evolution of the spatially averaged fractional volume contents of fine sediment in each storage layer denoted $\bar{F}_{k,1}$ in the (a) first ($x \in [0;60]$ m) and (b) second half ($x \in [60;120]$ m) parts of the channel with the reference scenario (run P2009-1). 98
4.10 Longitudinal profiles of bed evolution and bed shear stress with the reference sediment at $t = 200\,000$ s a) without obstacle with sediment sorting (run P2009-1), b) with the obstacle with sediment sorting (run P2009-3) and c) with the obstacle without sediment sorting (run P2009-4). 99
4.11 Longitudinal profiles of bed evolution and total bedload transport rate with the reference sediment at $t = 200\,000$ s a) without obstacle with sediment sorting (run P2009-1), b) with the obstacle with sediment sorting (run P2009-3) and c) with the obstacle without sediment sorting (run P2009-4). 100
4.12 Planform distribution of the a) bed evolution, b) total volumetric bedload magnitude and c) component of the total volumetric bedload magnitude per unit of width without pores projected along y-axis at $t = 280\,000$ s for the reference scenario (run P2009-1). 100
4.13 Planform distribution of the bed evolution and total bedload magnitude at $t =$ 200 000 s using the obstacle and the reference sediment, with a) sediment sorting (run P2009-3) and b) without sediment sorting (run P2009-4). P denotes the measurement point located at (x=102 m;y=0.55 m). 101
4.14 Bed evolution from $t = 0$ s to $t = 100\,000$ s at point P (x=102 m;y=0.55 m) with reference sediment without (P2009-1) and with (P2009-3) the transverse obstacle. 101
4.15 Planform evolution of bed topography, shear stress and surface sediment sorting with the obstacle for the reference sediment scenario at $t = 280\,000$ s. 102
4.16 Longitudinal profiles of bed evolution and vertical sediment sorting with the obstacle with the (a) reference and (b) extended sediments scenarios at $t = 280\,000$ s.103

4.17 Cross-stream bed evolution of (a) free bars and (b) hybrid bars at bars front locations for the uniform, reference and extended sediments scenarios (different vertical scales are used). 104
4.18 Longitudinal profiles of bed evolution at $t = 200\,000$ s with the obstacle for the uniform (P2009-8), reference (P2009-3) and extended (P2009-9) sediments scenarios. 105
4.19 Planform bed evolution with an upstream transverse obstacle with the reference sediment at different times of the simulation showing the process of free bar detachment and formation (run P2009-3). 107
4.20 Longitudinal profiles of bed evolution at $t = 200\,000$ s with the reference sediment with sediment sorting (run P2009-3) and without sediment sorting (run P2009-4). 107

5.1 a) Map of France showing the location of the study reach in the Loire river watershed (credits for color-map: Shuttle Radar Topography Mission - NASA; river network = Global River Database [Andreadis et al., 2013]), b) medium scale aerial view of the study site took in September 2005, showing the presence of migrating bars in the main channel and secondary channels and c) small scale aerial view of the area of interest with the position of the main field measurements of Claude et al. [2012, 2014] and the presence of geometrical forcings. 133
5.2 Example of (a) longitudinal profile of the relative error on the water free surface (gray dashed lines correspond to a relative error of $\pm 5\%$) and (b) cross-sectional flow velocity magnitude profile used to calibrate the hydrodynamic model, computed for the scenario of December 19^{th}, 2010 with Q_w =701 m^3/s, see Figure 5.1 for location. 139
5.3 Power function obtained between the calibrated value of $\alpha_{k,s}$ obtained for each considered scenario and the associated flowrates Q_w. 140
5.4 Macro-scale planview of the bed topography computed with the calibrated morphodynamic model on September 15^{th} 2010 and November 20^{th} 2010, showing the upstream bars having an influence on downstream bar dynamics which are located in the area of interest. The color-scale is different from Figure 5.5 in order to better visualize the smaller bars forming at each sides of the central/transverse bar. 141
5.5 Planview of the bed topography and bed evolution measured in the field and computed with the calibrated morphodynamic model from March 15^{th} 2010 to March 15^{th} 2011. 143
5.6 Time-series of the RMSE and BSS computed on bed topography with accounting for sediment sorting (scenario A) from March 15^{th} 2010 to January 3^{rd} 2011. . . . 144
5.7 Planview of a) the bed topography computed without accounting for sediment sorting (scenario B) and b) difference of computed bed topography at this same date between the scenario accounting for sediment sorting (A) and the scenario without sediment sorting (B). The black squares correspond to twelve points distributed close to the left bank, the right bank and the center of the channel along P80, P87, P90 and P95 cross-sections, which are used to compare results from runs A and B. 145
5.8 Planview of the bed topography computed with the morphodynamic model after a period of 300 days with a constant inflow representative of a) the low-flow period (run C), b) mean annual flow (run D) and c) two year peak flood (run E). . 145

5.9 Time-series of the theoretical and numerical bar modes obtained with the scenario of reference (scenario A) from March 15^{th} 2010 to January 3^{rd} 2011. 146
5.10 Planview of the bed shear stress and bedload magnitude computed with scenario A with the transverse bar configuration on June 22^{th} 2010, which display both a similar spatial distribution. 147
5.11 Planview of the ratio between bedload magnitude and spatially averaged bedload magnitude computed with scenario A considering the configuration of a) central bar (September 15^{th} 2010), b) a transverse bar (June 19^{th} 2010) and c) alternate bars (January 3^{rd} 2011). 147
5.12 Time-series of the spatially averaged sediment transport rate and ratio between spatially averaged transport rates of the finest class of sediment over the total bedload, in the study area computed with scenario A from March 15^{th} 2010 to March 15^{th} 2011. 148
5.13 Planview of the angle of bedload deviation, computed with scenario A with a) the transverse bar on June 22^{th} 2010, b) alternate bars on January 3^{rd} 2011, c) central bar on September 15^{th} 2010, d) central/transverse bar November 8^{th} 2010, and e) the transverse bar on June 19^{th} 2010. The arrow below the color-scale indicates the direction of the deviation angle, where negative values are directed toward the right riverbank and positive values toward the left riverbank. 149
5.14 Planview of the angle between the bedload transport directions computed with scenario A with the transverse bar on June 22^{nd} 2010 and alternate bars on January 3^{rd} 2011. Negative (resp. positive) angle values depicted in purple (resp. in green) signify that the bedload vector computed with the transverse bar is more directed toward the left (resp. right) bank with respect to the bedload vector computed with alternate bars. 150
5.15 Planview of the mean sediment diameter at the bed surface computed with the with scenario A considering the configurations of a) transverse bar (June 22^{nd} 2010), b) central bar (September, 15^{th} 2010), c) central/transverse bar (November 8^{th} 2010) and d) alternate bars (January 3^{rd}, 2011). 152
5.16 Longitudinal (L2) and cross-sectional (P90) stratigraphic profiles computed with scenario A with the configuration of a) transverse bar (June 22^{th} 2010, $Q_w = 1030$ m^3/s), b) alternate bars (January 3^{rd} 2011, $Q_w = 882$ m^3/s) and c) central/transverse bar (November 8^{th} 2010, $Q_w = 434$ m^3/s). See Figure 5.1 for location of L2 and P90. 153
5.17 Time-series of a) the hydrogram of 2010-2011, b) spatially averaged mean sediment diameter in each sediment layer and c) ratio between the 9^{th} and 1^{st} fractiles used to estimate the degree of spatial sediment sorting with the reference scenario and the three scenarios with constant water discharges. 154

List of tables

3.1 Computational time obtained for the different scenarios assuming a constant CFL=0.2 64
4.1 Scenarios studied. 91
4.2 Sediment transport and observed bar characteristics for the studied scenarios. . . 93
4.3 Free bar characteristics at $t = 3$ h. 93
4.4 Values of the representative hydraulic parameters obtained at $t = 280\,000$ s for the numerical runs using various GSDs and sediment layer thicknesses. 104

5.1 Bar characteristics computed at different stages of the simulation with accounting for sediment sorting (scenario A). 142

List of abbreviations

1D / 2D / 3D:	One / Two / Three dimensional.
2D-H:	2D depth-averaged model.
CPU:	Central Processing Unit.
DREAL:	Direction régionale de l'environnement, de l'aménagement et du logement.
EDF:	Electricité De France.
GSD:	Grain Size Distribution.
IHE-Delft:	Unesco Institute for Water Education.
INRS-ETE:	Institut national de la recherche scientifique - Eau Terre Environnement Research Centre.
LNHE:	Laboratoire National de l'Hydraulique et Environnement.
LHSV:	Laboratoire d'Hydraulique de Saint-Venant.
MPI:	Message Passing Interface.
MPM:	Meyer-Peter-Müller.
MPM-E:	Meyer-Peter-Müller-Egiazaroff.
R&D:	Research and development.
RANS:	Reynolds-Averaged-Navier-Stokes equations.
SWE:	Shallow Water Equations.
TMS:	Telemac-Mascaret Modelling System.
WC-2003:	Wilcock and Crowe [2003].

Glossary

Alluvial bar: Large sediment deposit alterning with pools, which are either forced or periodic.

Bar characteristics/properties: Correspond to the bar geometry in terms of bar wavelength and amplitude and mobility (i.e. migration celerity).

Bar front: Corresponds to the migration front of a bar, generally defined by a steep negative slope.

Bar mode: Number of bar wavelengths contained in two channel widths.

Bar top: Also referred to bar head, bar tops are defined by the highest bed elevation of the bar and are located immediately upstream the bar fronts.

Bed aggradation/degradation: Increase (resp. decrease) of bed elevation and longitudinal bed slope following increased (resp. decreased) upstream sediment supply.

Bedload: Sediment transport process involving near-bed sediment motion.

Dam flusing: Operation useful to release the sediments trapped by the dams and to restore the river sediment continuity.

Embankment: Engineering structures constraining the water course by means of longitudinal dykes.

Flood: Natural overflowing of water onto land that is normally dry.

Fluvial morphodynamics: Analysis of the morphodynamic behavior of inland bodies, such as rivers, channels, bifurcations, *etc.*

Free bar: Periodic bar forming due to only inherent morphodynamic instabilities of the riverbed.

Forced bar: Local bar forming due to the presence of a geometrical forcing which permanently deviates the flow and sediment transport.

Grain size distribution/granulometry: Probability density function used to describe the composition of the non-cohesive bed material.

Hiding-exposure effects: Interaction between grains of different shape and size which tends to counterbalance the gravity effects on the bedload transport.

Hybrid bar: Periodic bar forming due to the inherent morphodynamic instabilities of the riverbed and remains steady due to the presence of an upstream forcing parameter.

Lee side: Transition between the bar front and the pool and has a negative slope.

Mesh convergency: Analysis performed to estimate the optimal (between the time and quality) resolution of a mesh to carry out computations.

Model calibration: Process of adjustment of the model parameters within the margins of the uncertainties to obtain a model representation of the processes of interest that satisfies pre-agreed criteria (see `http://www.coastalwiki.org/wiki/Model_calibration`).

Model validation: Formal confirmation of the model quality criteria achieved in model calibration. For model validation a set of independent data is used and the model parameters are fixed (see `http://www.coastalwiki.org/wiki/Model_calibration`).

Morphodynamics: Study of the interaction and adjustment of the topography and fluid hydrodynamic processes (rivers, lakes, estuaries, coastal, *etc*).

Non-uniform sediment: Alluvial material ideally composed of multiple particle size diameters.

Numerical modelling: Non-linear approach based on the numerical resolution of equations, using the discretization over the time and space.

Periodic bar: Corresponds to a bar forming due to the inherent instabilities of the riverbed.

Pool: Deepest area located immediately downstream of the bar top.

Secondary currents: Three dimensional effects corresponding to the helical flows produced by the gradient of pressure forming in channel curvatures.

Sediment transport: Physical process involving the motion of particles subjected to the energy of the water flows, at the origin of the river morphological evolution.

Sediment size heterogeneity: Also referred to as sediment non-uniformity, it corresponds to the spreading of the grain size distribution, which it is an inherent characteristic of sandy-gravel and gravel bed rivers.

Sediment sorting: Corresponds to the planform and vertical spatialization of the sediment sizes, leading to the formation of sediment sorting patterns.

Sensitivity analysis: Is used to test the model behavior and potential limits that could arise by studying the influence of parameters within the margins of the uncertainties.

(Bed) Slope effect: Physical phenomenon of increase of transport rate in the downslope direction and decrease in the upslope direction.

Stoss side: Transition between the pool and the next further downstream bar front.

Thalweg: Line of lowest bed elevation within a watercourse. In this work, we always dissociate the pools from the *thalweg*.

Uniform sediment: Alluvial material ideally composed of a single particle size diameter.

CHAPTER 1

INTRODUCTION

This Ph.D. thesis is related to the field of sediment transport and more specifically the discipline of fluvial morphodynamics. This work is part of some recent studies regarding the influence of the sediment size composing alluvial riverbeds on the dynamic evolution of sandy-gravel bars. Bars correspond to large sediment deposits alternating with deeper areas and are a common feature of rivers (Figure 1.1). Emphasis is placed on bars because they actively control the areas of erosion and deposition, govern the riverbed topography and influence bank erosion, and by extension the morphodynamics trajectories of rivers.

In the context of rivers subject to intense operational engineering works, later called "trained rivers", it is widely recognized that intense human works such as channelization, meander cutting, continual water withdrawal or sediment extraction, or dam construction can alter significantly bars morphodynamics at the reach scale. Consequences of such alteration can be manifested in various ways. For example, bars can be harmful for the stability of engineering infrastructures such as embankments and bridge piers. In gravel bed rivers, gravel bars dynamics can be reduced or even stopped because bars are subject to vegetation growth and further bar stabilization. This is the case of the Isère and Durance rivers, where colonization by vegetation is showed to reduce significantly bars mobility, decrease biodiversity and consequently increase the flooding risk. In sandy-gravel bed rivers, intense bar morphodynamics can usually be observed. In the middle Loire river, fast migrating bars are located close to the CNPE's (Centrale Nucléaire de Production d'Electricité), which in turn threatens the safety of the nuclear power-plants, because of risks of water intake clogging and increasing flooding hazards in the vicinity of the plants. The problems described above constitute an important issue for river managers such as EDF (Electricité de France), DREAL (Directions Régionales de l'Environnement, de l'Aménamegement et du Logement) or Agence de l'Eau to optimize river restoration works and maintenance activities such as dredging, grubbing, modification of hydroelectric dam management, etc., which have to be done within the respect of the environment and river ecosystems.

While the actual literature on alluvial bar processes outlines the importance of non-uniform sediment processes on bar morphodynamics, a gap still subsists on the real relationship between non-uniform sediment and bars. Where the success of training works and restoration projects depends on the proper management of river bars, it is has been judged necessary not only to better understand the processes involved between bars and heterogeneous sediment, but also provide a method to predict relevantly bar evolution which can be declined to diverse applications. To further this goal, the numerical modelling approach is brought forward in this work.

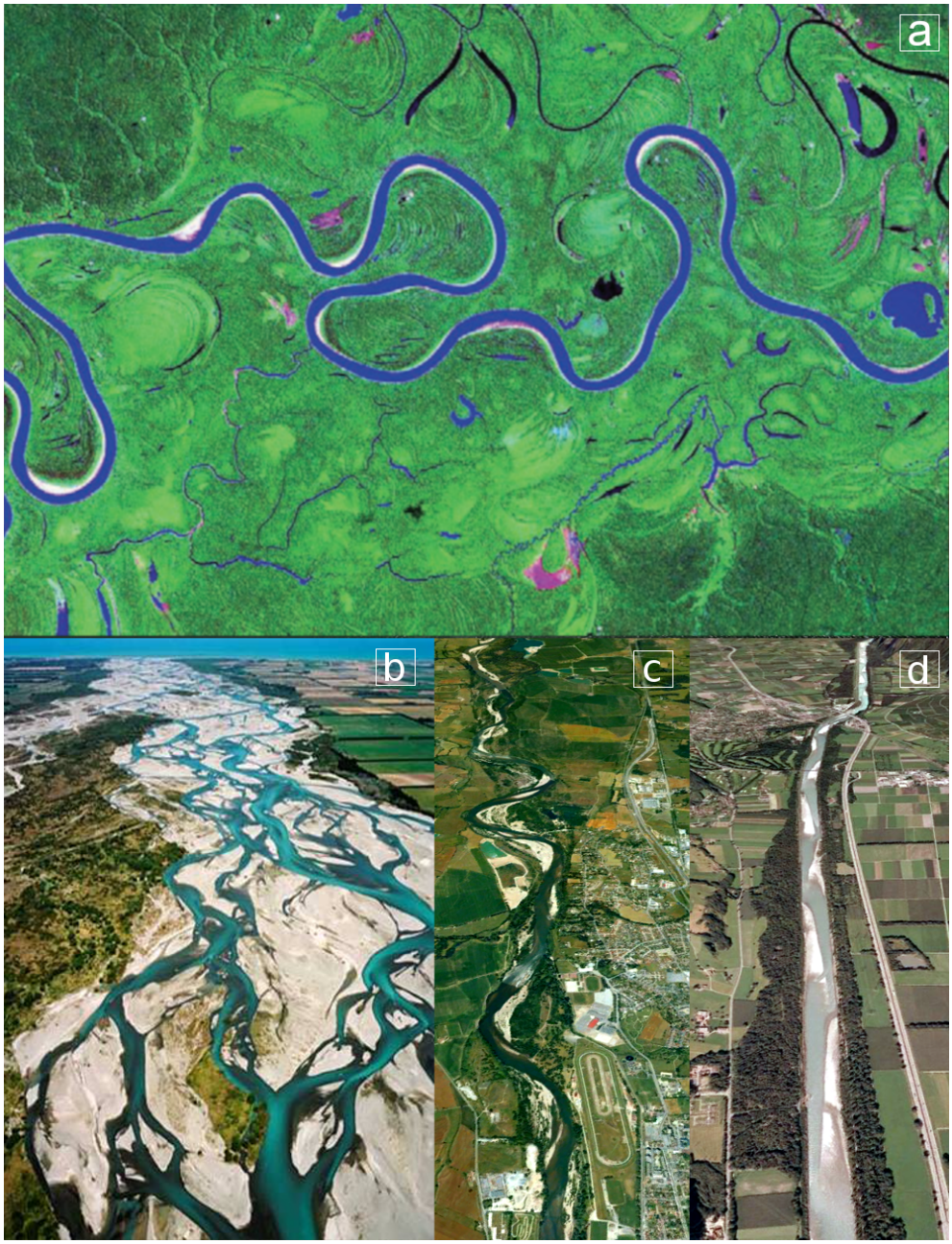


Figure 1.1: Example of a) meandering river, Purus River (Brazil) [Parker et al., 2011], b) braided river, Rakaia River (South Island, New Zealand) [Below and Jol, 2005], c) weakly meandering river with forced bars, Allier River (Avermes, France) and d) straight river with migrating free alternate bars (Landquart, Switzerland).

1.1 Global scientific context

This section presents a synthesis of river bar morphodynamics concepts and the mechanisms governing bars characteristics in alluvial rivers. Several concepts are introduced, from the distinction of the variety of river patterns found in the nature to the classification of bars in rivers.

1.1.1 Rivers sinuosity and planform channel geometry

1.1.1.1 Physical balance

The diversity of river patterns has been for a long time a point of interest for the scientist community, which proposed several classifications to tentatively describe stream and river reaches. Since most of the channels show a predominant pattern for meandering or a sinuous course, planform riverbed evolution has been firstly explained by the concept of minimization of energy expenditure [Leopold and Langbein, 1962]. This property of channels to meander is a natural depiction of a balance between several physical laws. A channel can be conceptualized as an open thermodynamic system, where the stability is approached with a compromise of two principles: the principle of least action and the uniform energy utilization. The potential energy of the water due to its elevation is converted in kinetic energy, implying erosion and loss in flow energy due to turbulence and friction. This compromise is based on the minimization of variance, which is statistically known as the equilibrium state and is clearly exhibited by sinuous channels. As the open boundaries of the system can fluctuate (flow, sediment supply, etc.), this equilibrium is never really reached and the system can only show a series of unstable equilibrium states, approximating a steady state [Bridge and Demicco, 2008]. This equilibrium can be defined mathematically by a sine-generated curve [Leopold and Langbein, 1962].

1.1.1.2 Classification of rivers planform geometry

Planform channel geometries forming in alluvial rivers, as known as patterns, have been originally distinguished by the geomorphologist community as straight, meandering and braided patterns [Leopold and Wolman, 1957] (Figure 1.1). According to this classification, meandering channels can be importantly sinuous and keep a periodical wavelength, whereas straight channels show a sinuous course where the occurrence of bends is not periodical. Eventually, braided channels are compounded of a network of multiple streams, separated by bars or islands and can be connected by secondary channels, which are regularly activated during floods. On the basis of this terminology, another classification dividing single (straight and meandering) channels of various degrees of sinuosity and multiple channels of various degrees of sinuosity has been proposed later.

1.1.1.3 Origins of rivers planform geometry

Conceptual models have been originally proposed to put into relation the flow discharge and other parameters such as the channel slope or sediment mobility to the resulting channel pattern (Figure 1.2). The generalizations presented above have been criticized, because contradictions can be found in the nature. For example, the discharge variability is not a major controlling factor on the existence of the plural channel patterns, as well as the sediment transport mode (suspended, bedload or both). The diversity of channel patterns also depends on other factors such as the stability of the riverbanks enhanced by the vegetation and sediment cohesion [Tal

and Paola, 2010]. To describe more relevantly river patterns and their trajectory, another method consists on the study of the planform distribution of alluvial bars and their evolution over time.

a) b)

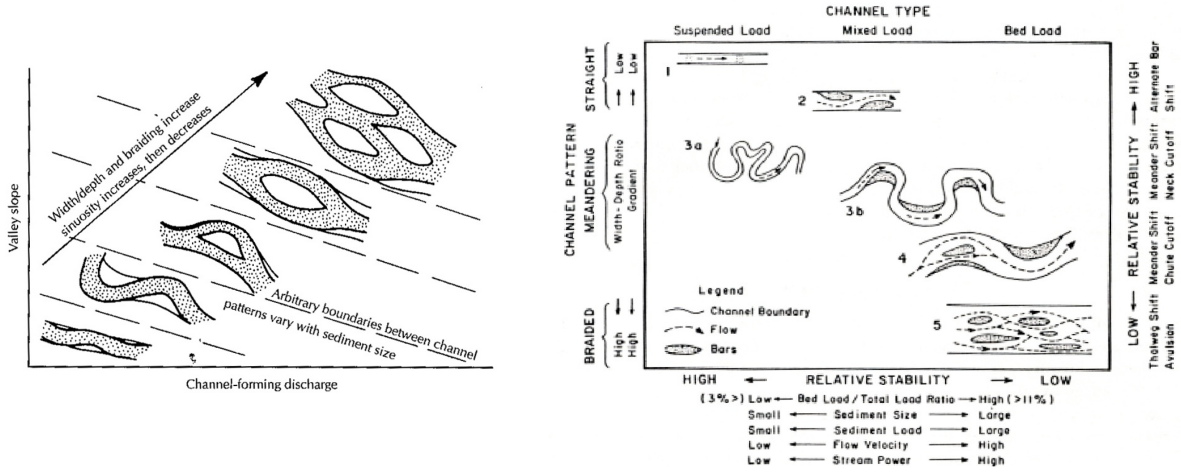


Figure 1.2: a) Gradual variation of equilibrium channel patterns with channel-forming water discharge, valley slope and sediment size [Bridge, 2003] and b) scheme of main configurations of the river bed according to Schumm [1981].

1.1.2 Bars in alluvial rivers and classification

Rivers often present a wavy bed topography due to the presence of periodic bars [Bridge and Demicco, 2008], corresponding to large sediment deposits alternating with deeper areas referred to as pools 1.2. These wavy patterns arise from an instability phenomenon of the alluvial bed [Engelund, 1970; Crosato and Mosselman, 2009]. Bars can be either migrating or steady, and alternate bars are often considered to initiate the incipient channel meandering if the banks are erodible.

Derived from the framework of linear stability analysis, the concept of resonance is commonly used to distinct three types of channels systems, namely "super-resonant" systems corresponding to shallower and wider channels with respect to "sub-resonant" channels, and "resonant" systems in between [Blondeaux and Seminara, 1985; Crosato and Mosselman, 2009; Siviglia et al., 2013]. Most of the time, steady bars originate from the forcing geometry induced by local channel curvatures, where steady bars form only downstream to the curvature if the system is sub-resonant, or also form upstream if the system is super-resonant [Siviglia et al., 2013]. The resonance property also determines if steady bars persist everywhere downstream in the channel in the case of super-resonance, or only persist only for a few bar wavelengths in the case of sub-resonance also referred to as spatially damped steady bars. But steady bars can also appear at resonant conditions of the system without forcing [Tubino et al., 1999; Lanzoni, 2000a] or even arise on the absence of local perturbations and under non-resonant conditions in narrower channels as showed experimentally by Crosato et al. [2011]. The diversity of bar patterns and the fact that bars can arise under several conditions has motivated for the emergence of multiple theories which are available in the literature [Struiksma et al., 1985; Colombini et al., 1987; Tubino and Seminara, 1990; Tubino et al., 1999; Crosato and Mosselman, 2009]. Accordingly, diverse terminologies to classify bars have been proposed. Here, emphasis is

placed on theories based on the linear stability of a growing perturbation, where the solution defines the river planform style, which corresponds to the so called "bar mode" (see Section 1.1.2.3). Other theories such as the ones based on the horizontal eddies and horizontal coherent structures are not considered in this work [Yalin, 2017].

1.1.2.1 The old terminology and limits

Bars have been commonly divided into *free* and *forced* bars [Tubino and Seminara, 1990], where the migrating bars are known as "free" bars and immobile bars are referred to as "forced" bars [Bridge, 2003]. Even if steady bars are often present due to forcing factors such as bends, they also can be free and due to an intrinsic response of the alluvial bed. Therefore, last structures are also considered as non-migrating bars. In the last four decades, scientists debated on the origin of the mechanism triggering steady bar development, giving a multitude of theoretical attempts [Blondeaux and Seminara, 1985]. Several experiments and non-linear analysis have been carried out to support the last theories [Mosselman, 2010]. The most accepted opinion was that steady bars arise either in the unstable range (primarily governed by the channel width-to-depth ratio) or due to forcing geometries (e.g. bends, bifurcations, etc.). Recent experiments of Crosato and Desta [2009] using a straight channel with non-erodible banks showed that steady bars can arise on the absence of local perturbations and under non-resonant conditions. Therefore, steady bars can arise from an intrinsic instability of the alluvial channel bed.

1.1.2.2 Terminology used in this work

The paradigm brought up above caused problematic ambiguity and vagueness, because it did not distinguish between forcing over the full length of a bar, as in the case of point bars that cannot be described by linear stability analysis, and forcing in a single cross-section, leading to a dynamic response of non-migrating bars that can be described using linear stability analysis. Eekhout et al. [2013] and Rodrigues et al. [2015] discussed this ambiguity of using the term “forced bars” for two types of bars, albeit without proposing a new terminology. The old ambiguity was resolved by introducing the term “hybrid bars”, which was then gratefully adopted by Duró et al. [2016] and Le et al. [2018a,b]. Other eminent researchers in bar theory recognized the improvement and quickly embraced the new terminology (e.g. [Scorpio et al., 2018]).

Consequently, according to Duró et al. [2016], two groups of bars can be distinguished: forced bars, and periodic bars of which two types exist corresponding to free and hybrid bars (Figure 1.3). While forced bars arise from a permanent flow deformation induced by an external factor (forcing), such as a channel geometry change, periodic bars arise from the inherent morphodynamic instability of the riverbed. Free bars originate purely from morphodynamic instability, while hybrid bars form on morphodynamically unstable riverbeds, like free bars, but require the presence of a permanent forcing which fixes their location [Crosato et al., 2011; Rodrigues et al., 2015; Duró et al., 2016; Cordier et al., 2019; Le et al., 2018a,b].

1.1.2.3 The bar mode

The approach used in this work to define the river plan geometry is based on the degree of the channel splitting with focus on the occurrence of alluvial bars. The term "bar mode" is introduced here to quantify how many transverse bar wavelength are contained in two channel widths. According to this, the periodical sequence of erosion holes and depositional fronts present in

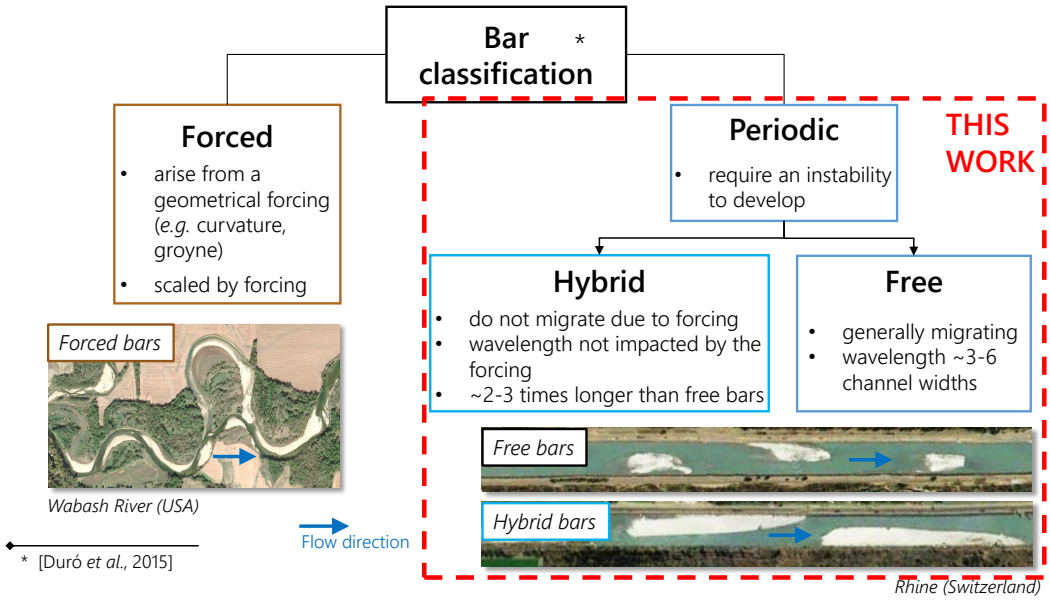


Figure 1.3: Scheme of the classification of bars according to Duró et al. [2016]

straight channels commonly organized in the typical pattern of alternate bars is associated to a mode equal to 1. Larger aspect ratio reaches can show more complex configurations, such as central bars with mode equal to 2 or multiple row bars with higher modes (Figure 1.4) [Crosato and Mosselman, 2009].

1.1.2.4 Asymmetrical bar configurations

In the illustrations presented above, because the channel geometry, the boundary flow and sedimentary conditions are all symmetrical, periodic bars are symmetrical too. In the presence of a local geometrical forcing or asymmetrical boundary condition, bars can exhibit an asymmetrical shape, which is commonly found in the nature. Consequently, another terms can be proposed to call these asymmetrical bars. In this work, we call a "transverse bar" (which is asymmetric, Figure 1.4) the equivalent of a central bar (which is symmetric, Figure 1.5) in terms of "bar mode", i.e. $m = 2$.

1.1.3 Parameters influencing bar morphodynamics

Numerous authors [Engelund, 1970; Colombini et al., 1987; Lanzoni and Tubino, 1999; Crosato and Mosselman, 2009] have showed that the formation and the pattern of bars are primarily governed by the width-to-depth ratio of the flow. The width-to-depth ratio of the flow and consequently bars dynamics are conditioned by a multitude of other physical parameters, which interact in a non-linear way with each others:

1. Geometrical (internal) forcings, which are induced by channel width variations, curvatures, non-erodible substratum or obstacles such as groynes and weirs;

2. Upstream (external) boundary forcings, which correspond to water discharge fluctuations and sediment supply variability;

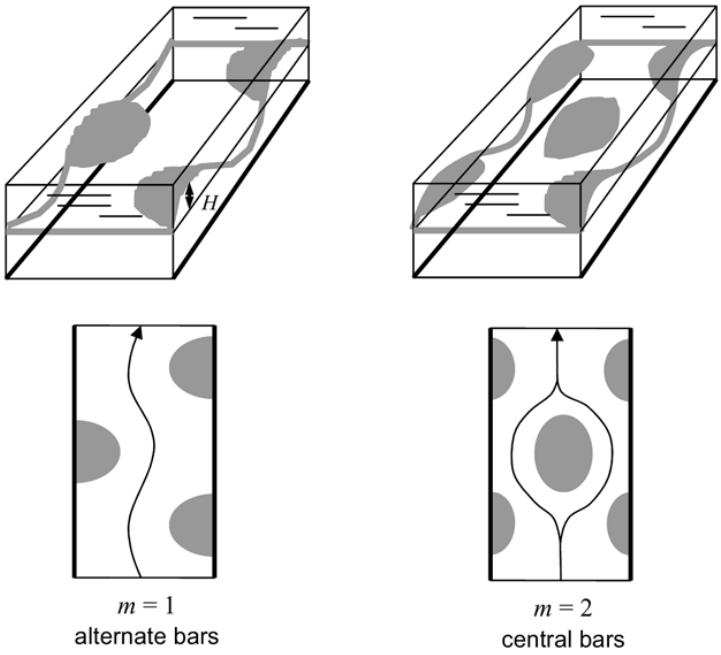


Figure 1.4: Idealized bed and flow deformations induced by the presence of periodic bars: (left) first bar mode (alternate bars) and (right) second bar mode (central bars) [Crosato and Mosselman, 2009].



Figure 1.5: Example of asymmetrical bed configuration leading to the formation of a transverse bar.

3. Sediment characteristics;

4. Vegetation recruitment and development.

1.1.3.1 Geometrical forcing

Considering medium spatial and time scales (i.e. between the duration of a flood and the decade), variations of the width-to-depth ratio induced by the hydro-sedimentary dynamics and bank stability impact the channel width, which in turn can vary importantly longitudinally. Geometrical changes in channels induce local areas of erosion or deposition [Bridge and Demicco, 2008], which can trigger the development of forced bars, or hybrid bars under unstable conditions. Forcing effects due to longitudinal width variations as well as formation of bars driven by channels curvature has been documented with the theory [Tubino et al., 1999; Repetto et al., 2002; Crosato, 2008; Zen et al., 2014], laboratory experiments [Ashmore, 1982; Struiksma

et al., 1985; Bertoldi et al., 2002; Wu and Yeh, 2005] field investigations [Luchi et al., 2010; Claude et al., 2014] and numerical modelling [Crosato, 2008; Duró et al., 2016].

Generally, local channel widening is associated to trigger bar formation, while local channel narrowing is followed by bar suppression [Nelson, 1990; Repetto et al., 2002; Wu and Yeh, 2005; Crosato and Mosselman, 2009; Duró et al., 2016]. Experimental [García and Niño, 1993; Whiting and Dietrich, 1993] and numerical [Wu et al., 2011] investigations showed that bars slow down with the longitudinal decrease of the aspect ratio, i.e. at the channel widening location.

Rodrigues et al. [2015] showed in a sandy-gravel bed river that the persistent geometrical forcing played by chutes located in the main channel could lead to the formation of steady bars, which are showed to continually develop and split in two shorter structures. While the upstream structure in the vicinity of the obstacle remains immobile, the second structure is released and migrates downstream. Duró et al. [2016] showed that free bars of different modes can coexist in the downstream straight segment of a channel due to upstream width variations, which is in agreement with the linear theory for steady bars of Struiksma et al. [1985] which allows incipient bars to vary longitudinally in amplitude. In the latter case, bar mode interactions generate more irregular and complex bar patterns. Moreover, Duró et al. [2016] showed numerically that imposing a perfectly symmetric water and sediment inflow could suppress alternate bar formation for certain distance, which needs to be tested experimentally or in the nature to assess its feasibility.

Theoretical and experimental works put in evidence that a local channel expansion can promote the settlement of a forced transverse bar or lateral and symmetrical forced bars [Bittner et al., 1995; Repetto et al., 2002; Wu and Yeh, 2005]. Wu et al. [2011] showed numerically that free alternate migrating bars can co-exist with forced transverse or lateral bars, giving rise to *mixed bars*. Depending on the migration of free bars, these mixed bars are either in alternate or transverse configurations. In this configuration, free bars amplitude and wavelength are invariably decreased, and as a function of the degree of channel sinuosity, migration of free bars can be increased or decreased. Mixed bars can show various configurations depending on the interactions between free and forced bars, and can be compared to alternate or transverse bar configurations (Figure 1.6). Deeper analysis on the flow structure over the transverse and alternate bar configurations has been later carried out in a channel contraction/expansion of the Loire river by Claude et al. [2014], where the bar configuration was showed to promote the spatial non-uniformity of flows induced by the bank curvature and encouraged the transition from alternate bars to a transverse bar configuration and reversely.

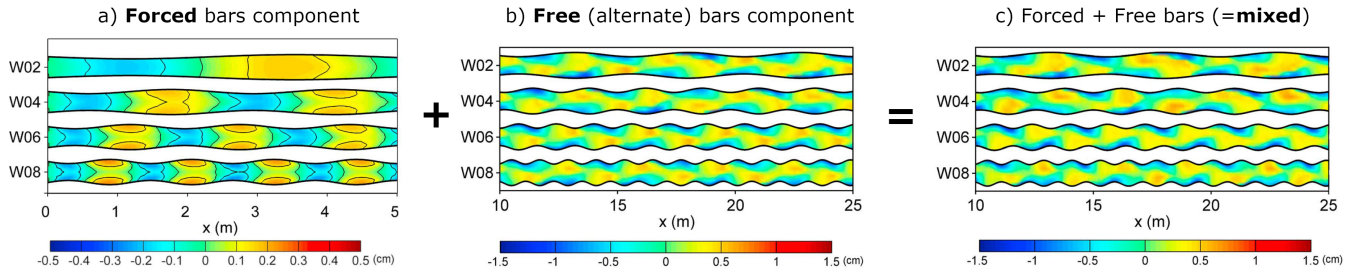


Figure 1.6: Impact of channel width variations on the configuration of combined free and forced bars. Addition of the a) component corresponding to forced transverse bars (W02 and W04) or lateral bars (W06 and W06) with the b) component corresponding to free (alternate) bars lead to c) mixed bars patterns. Source: [Wu et al., 2011], later modified by [Claude, 2012] and re-modified here.

1.1.3.2 Hydrological regime

Over the years, stability analyses have been proposed to study the initiation conditions for free alternate bars in straight channels under uniform flows [Callander, 1969; Colombini et al., 1987; Schielen, 1995; Federici and Seminara, 2003] and non-uniform flows [Tubino, 1991; Hall, 2004]. These theories all show that periodic bars are primarily controlled by the width-to-depth ratio of the flow, which is a crucial parameter to define the threshold between stability and instability. Because the latter is function of the water depth and consequently the hydrology, the water discharge is showed to be a crucial parameter which determines bar stability and dominant bar modes.

Considering two distinct sinusoidal water inflows periods, Miwa et al. [2003] observed experimentally that the wave period of the flow influences strongly the process of bar evolution, where short-waves have more impact than long-waves. This result is also illustrated with the hysteresis of water discharge/bar wavelength and water discharge/bar height, which are well pronounced in the case of short-waves and become smaller in the case of long-waves, and the response-lag of alternate bars to the discharge change becomes shorter with the long-waves. The comparison between constant water discharge and triangular hydrograms showed that unsteady flows were preliminary followed by changes in bar amplitude and was followed by a slower migration of bars, in comparison with uniform flow [Nelson and Morgan, 2018].

Increasing or decreasing flow discharge has been observed to be followed by a modification of the *thalweg* course (Figure 1.7). Consequently, with falling-flow stage, sediment is preferentially deposited in the *thalweg* and bars eroded, with respect to the rising-flow stage where the opposite happens, with scouring of the *thalweg* and deposition on bars [Bridge, 2003; Wintenberger et al., 2015].

1.1.3.3 Sediment supply

The sediment supply variability not only depends on the amount of sediment delivered from upstream (e.g. tributaries, dams, watershed, etc.) but also on the amount of available sediment in the riverbed (i.e. the thickness of alluvial sediment layer above the non-erodible substratum). Sediment supply changes affect strongly rivers morphodynamics at different time-scales and space-scales [Pierson et al., 2011; Buffington, 2012].

At the reach-scale, sediment waves propagate in response to a major sediment delivery/scarcity event (flood, volcanic eruption, dam construction or removal, etc.) and generate channel aggradation-degradation episodes [Gilbert, 1917; Madej et al., 2009; Allan James, 2010; Korup et al., 2010; East et al., 2015]. Many authors studied the behavior and the evolution of sediment waves in natural and anthropized rivers, especially with consideration of sediment pulses [Lisle et al., 1997; Sutherland et al., 2002; Cui et al., 2003b; Miwa and Parker, 2012; Venditti et al., 2010]. Sediment waves have been shown to translate and disperse in the downstream direction [Lisle et al., 1997; Cui et al., 2003b; Venditti et al., 2010; Humphries et al., 2012], and the phenomenon of dispersion is believed to be enhanced by to the presence of bedforms and bars. Increase of sediment supply is followed by a channel slope increase together with a global raising of the riverbed referred to as aggradation event [Mossa, 2016]. Conversely, decrease of sediment supply leads to a general deepening (i.e. incision) of the riverbed and decreased longitudinal bed slope, commonly known as river degradation.

Sediment supply, which can vary significantly in time in rivers [Mossa, 2016], is also found to play a significant role on bar morphodynamics [Madej et al., 2009; Podolak and Wilcock, 2013; Dhont and Ancey, 2018], which is enhanced by the sediment size heterogeneity composing the

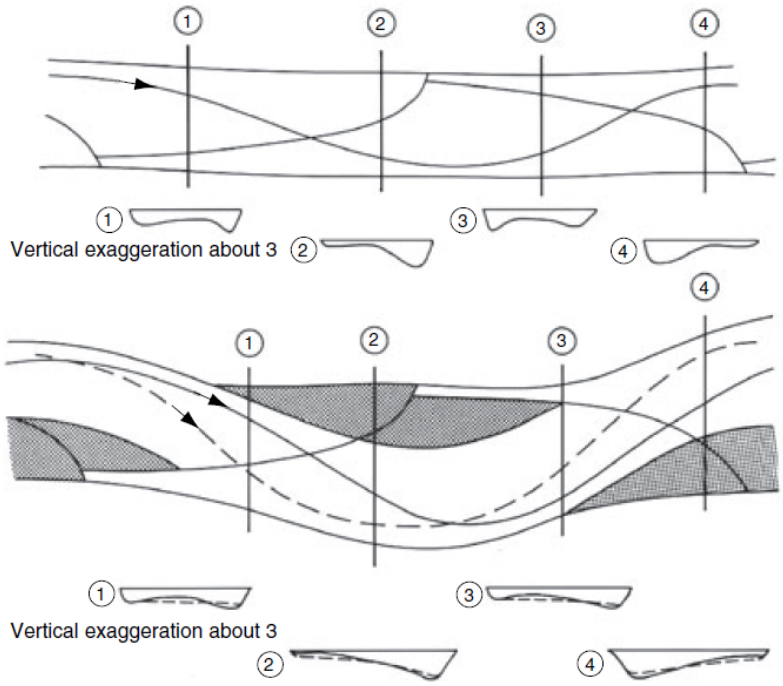


Figure 1.7: Idealized channel geometry for a simple channel pattern and equivalent alternate bar pattern in a straight channel (upper diagram) used for comparison, where the solid and dashed lines with arrows represent the location of maximum flow velocity for the high-flow and low-flow stage, respectively. Dashed lines in cross sections represent the low-flow-stage geometry [Bridge, 2003].

riverbed. A multitude of field investigations [Nelson and Dubé, 2015], experimental studies [Venditti et al., 2012; Podolak and Wilcock, 2013; Bankert and Nelson, 2018] and numerical works [Cui, 2007] explored the effects of sediment supply variation on relatively low mode bar morphodynamics considering non-uniform sediment. Increase in sediment supply is followed by increased transport rates, and is observed to fill the pools so that the flow is widen and bar amplitude is decreased. Consequently, the armoring effects are reduced and increased bar mobility and higher modes are generally observed. The opposite behavior is observed after sediment supply reduction: a decrease of the transport rate and consequently general deepening of pools, where the flow is lateraly confined and bar amplitude is increased. As a result, an increased armoring and coarsening of the riverbed are obtained, the bar stability is increased and decreased bar modes are generally observed.

After generating steady gravel bars in a straight flume, Bankert and Nelson [2018] show that bars only start migrating if a sufficient sediment supply increase is imposed. Moreover, the non-uniform bed stratigraphy obtained after sediment supply increases is showed to retroactively control the channel evolution during bed degradation, and explains why under given situations bars do not always retrieve the same pattern as before the bed aggradation-degradation event (i.e. reversibility cannot be achieved due to vertical sediment sorting processes). This point outlines the importance of non-uniform sediment and subsequent vertical sediment sorting, for which special attention is devoted below.

1.1.3.4 Sediment characteristics

Rivers often show a large spectrum of bed particle sizes, often referred as sediment non-uniformity, following either a unimodal or bimodal distribution of non-cohesive particles (i.e. sands, gravels, pebbles) and cohesive particles (i.e. silts and clays, Figure 1.8a). Due to their properties, cohesive sediments often confer a strong resistance against flows, enhance bank stability and tend to stabilize structures such as bars by colmatation, development of system biota and growth of vegetation. The strong porosity of clays (generally estimated twice as gravels) give them the ability to easily adsorb molecular chains such as pollutants, and provide a suitable environment for microbial development [Shaw et al., 2013]. Sediment mobility (represented by the Shields number) is crucial for bar morphodynamics and it depends on particle size and grain size distribution (GSD) of non-cohesive sediment forming the river bed [Lanzoni, 2000b; Nelson et al., 2015b; Singh et al., 2017].

A consequence of (non-cohesive) sediment size heterogeneity in rivers corresponds to surface armoring/paving (Figure 1.8b). Surface armoring is the result of *i*) an inherent tendency for small grains to settle between larger ones during the transport of all particle sizes [Parker et al., 1982], and *ii*) a selective erosion or trapping of fine bed material when the coarse material is generally immobile [Milhous, 1973; Sutherland, 1987; Powell, 1998]. The coarse surface granulometry of an emerged bar is the consequence of the last hydrological event, where finer sediments were removed either during the subsiding of floodwater or during weaker events able to mobilize only fine particles. The armor also shows an important spatial variability, due to local flow conditions and also deposits originated from single or plural flood events. A distinction is made in the case where the coarse surface layer is relatively mobile over the year or mainly immobile. If the latter is mostly immobile, it is referred to as armor. In the other case, it is preferentially referred to as paving.

At the bedload sheet scale, the interaction between grains of different shape and size, referred to as hiding-exposure effects, is showed to impact significantly sediment mobility [Einstein, 1950; Whiting et al., 1988; Parker, 1990; Wilcock and Crowe, 2003]. These last effects are manifested by the nature of coarse grains to hide finer grains in their interstices. While the gravitational effects make the larger particles harder to move, the hiding-exposure effects tend to counterbalance this phenomenon by increasing coarse grain mobility and decreasing the mobility of fine grains. At the bar scale, sediment size heterogeneity is also showed to affect bars morphodynamics. Considering a straight channel with fixed sidewalls, Lisle et al. [1991] concluded that poorly-sorted sediment enhanced bar stabilization. This outcome was later supported by the linear stability analysis of Lanzoni and Tubino [1999] and the experiments of Miwa et al. [2005], where the stabilizing effects have been attributed to the armoring effects observed over bars [Lisle and Madej, 1992]. As a result, gravel bed rivers have a much greater capacity than sand bed channels to control the mobility of the bed surface [Lisle et al., 1993], because of increased hiding-exposure effects. This means that gravel bedded rivers are more favorable to the stabilization of bars due to the effect of armoring. Based on this concept, techniques of sediment replenishment -also referred to as sediment nourishment- have been developed, consisting on injecting fine (non-cohesive) sediment downstream dams to reestablish sediment continuity and enhance bed mobility. Addition of finer fractions in gravel bed rivers showed an important increase of sediment transport rate and allowed in certain cases the mobilization of bars [Miwa and Parker, 2012].

The differences in sediment mobility found between grains of different sizes is responsible for the vertical sorting of sediment (Figure 1.8b), which is depicted by the riverbed stratigraphy and is controlled dynamically by the hydrology and the sediment supply. The thickness of

each horizontal sediment layer (also known as stratum), the sediment distribution and the shape formed by the deposited sediment can be used to keep track of the riverbed evolution overtime and draw the historical evolution of a reach following episodes of bed aggradation or degradation [Rodrigues et al., 2012].

a) b)



Figure 1.8: a) Planform sediment sorting over a gravel bar in the Isère river illustrating the strong spatial variability of sediment (Fréterive, July 2015) and b) vertical sorting of sediment in a secondary channel of the middle Loire river showing the bed armor (Bréhemont, November 2016).

Analytical studies [Lanzoni and Tubino, 1999], field and laboratory observations [Lisle and Madej, 1992; Powell, 1998; Lanzoni, 2000b; Lisle et al., 2000; Miwa et al., 2003], as well as numerical simulations [Hoey and Ferguson, 1994; Mosselman et al., 1999; Wu, 2004; Tritthart et al., 2011a,b; Mosselman, 2012; Nelson et al., 2015a,b; Juez et al., 2016; Qian et al., 2016; Singh et al., 2017] have showed that bars are affected by both size and heterogeneity of bed sediment. Lanzoni and Tubino [1999] as well as Takebayashi and Egashira [2001] state that sediment heterogeneity leads to the diminishing of free migrating bar amplitude and wavelength. Opposite results were obtained by Lanzoni [2000a,b] and Lisle et al. [1991] who find that, while free migrating bar amplitude is decreased, the trend exhibited by the wavelength is less clear. The effects of sediment heterogeneity on steady (resonant) free bars and hybrid bars, however, seem different. Using a numerical model, Nelson et al. [2015b] found a decrease of the steady (resonant) free bars and hybrid bars amplitude, confirming the findings on free migrating bars, but at the same time found an increase instead of a decrease of bar wavelength. Knowing that free migrating bars display a different topography with respect to resonant free and hybrid bars, the observation of Nelson et al. [2015b] highlights that sediment heterogeneity can affect steady periodic bars and free migrating bars in a different way.

Hoey and Ferguson [1994], Seal et al. [1997] and Toro-Escobar et al. [2000] observed that heterogeneous sediment tends to form a pattern of downstream fining during aggradational scenarios in sediment feeding flumes, whether alluvial bars formed or not. They linked this

process to the mechanism of selective sediment transport, because fine sediment moves faster than coarse sediment, resulting in the pattern of coarser sediment upstream and finer sediment downstream. The authors also observed that surface sediment is always coarser than subsurface sediment. The pattern of sediment sorting over bars can either display coarse sediment over bar crests and finer sediment in pools [Lisle et al., 1991; Lisle and Madej, 1992; Diplas, 1994; Lanzoni, 2000b; Nelson et al., 2015a] or the opposite, i.e. fine sediment over bar crests and coarser sediment in pools [Takebayashi and Egashira, 2001]. Nelson et al. [2015a,b] attribute the occurrence of coarser bar tops to the decrease of local flow velocity and increase of lateral flow, explaining that longer bars grow faster than shorter bars when the roughness is variable over space, with respect to a spatially constant roughness. In their numerical model, the authors used a single sediment storage layer, but outlined the importance of considering the effects of vertical sorting of sediments in future research works. Transversally, alternate bars often show a general coarsening by moving closer to the *thalweg*, limiting the main channel riverbed erosion [Anderson et al., 1975; Bluck, 1982; Diplas, 1994]. In the case of higher bars modes, in braided rivers, the sorting pattern consists on coarse in pools and fine sediment over bar heads, provided that the partial sediment mobility condition is reached [Singh et al., 2017]. In the case of full sediment mobility, Singh et al. [2017] showed that no consistent pattern could be observed, apart from coarse sediment in some parts of the deeper channels.

Recently, [Wintenberger et al., 2015, 2017] observed that sediment size heterogenity can also affect the survival and the development of colonizing riparian vegetation, and by extension river biomorphodynamic trajectories, which is presented hereafter.

1.1.3.5 Vegetation

The development of vegetation is associated with an accelerated fixation of bars and to be the implicit condition for river meandering or braiding [Ikeda et al., 1981; Blondeaux and Seminara, 1985; Tubino and Seminara, 1990; Crosato and Desta, 2009], by increasing local roughness, providing cohesion and enhancing riverbanks stability [Temmerman et al., 2005; Camporeale and Ridolfi, 2006; Bal et al., 2011]. The complex interactions between morphodynamics and vegetation can lead to dynamical changes of channels patterns and more complicated processes such as meander cut-off, channel bifurcation or bar mode reduction. Many observations in natural rivers and laboratory experiments showed that fluvial islands may arise from the vegetalization of central bars [Bertoldi et al., 2002; Wintenberger et al., 2015]. Therefore, vegetated banks and bars would offer a sufficient resistance for meandering development, whereas in the absence of vegetation the initial meandering channel evolves toward a braided pattern [Iwasaki et al., 2015]. In the other hand, it is shown that the original braided river could involve into a meandering channel due to the colonization of riparian vegetation [Tal and Paola, 2010]. The numerical study of the impacts of riparian vegetation recruitment and growth on the bio-morphodynamic trajectories of a straight gravel bed channel under the consideration of a variety of flooding hydrograms has showed two possible equilibrium bio-morphodynamic behaviors: stationary vegetated bars, or free migrating bars in the case of frequent vegetation removal during floods Jourdain et al. [2018]. Caponi and Siviglia [2018] observed numerically considering a vegetated patch that the competing influence of the potential flow erosion versus uprooting depth governs the plant-root controls on the gravel bed river morphodynamics. Moreover, vegetation is often showed to trap fine sediment whereas coarser sediment is found in the surrounding channels [Wintenberger et al., 2015], and consequently increases planform sediment sorting. Vegetation plays an important role in the river morphology, and is crucial in creating habitats [Paetzold et al., 2005] and covering ecosystems affecting water quality

[Marzadri et al., 2010].

1.1.3.6 Synthesis

The points presented above show that sediment size heterogeneity has strong implications on river bar morphodynamics and involves processes which are complex to understand. Despite of the multitude of theoretical, experimental, field and numerical analyses available in the literature, a number of points still have to be examined or clarified, namely:

- The contradictory findings that continue to spark debate over the relationship between non-uniform sediment and periodic bar characteristics;
- The link between the periodic bar pattern and the (vertical and planform) sorting of sediment;
- The limitations of the actual knowledge on the impact of combining non-uniform sediment with other internal and external forcing parameters, such as complex hydrology or channel geometry, on bar morphodynamics.

The work presented here will aim to better understand the relationship between periodic bars and non-uniform sediment.

1.2 Main objectives and research questions

1.2.1 Research questions

Subsequently, to meet the objectives defined here-after, the two following unanswered/open research questions have been identified:

I. **How does sediment size heterogeneity affect bar morphodynamics?** This question arises because sediment size heterogeneity (i.e. sediment non-uniformity) is an inherent characteristic of sandy-gravel bed rivers and gravel bed rivers, such as the rivers of interest for river managers and EDF (see Section 1.3), and because sediment size heterogeneity has already been showed to affect the bar dynamics [Lanzoni, 2000b; Nelson et al., 2015b] (see Section 1.1.3).

II. **How the bar pattern and non-uniform sediment co-evolve under the consideration of multiple internal and external forcing parameters?** This question is considered because rivers generally exhibit a combination of internal (i.e. geometry) and external (i.e. hydrology, sediment supply) forcing parameters, together with inherent sediment size heterogeneity [Bridge and Demicco, 2008]. This is particularly the case in the rivers subject to training works and of interest for river managers and EDF.

The thesis development will concentrate on these two major research questions which define the perimeter for this study.

1.2.2 Objectives

The final goal of this work aims at providing recommendations to hydroelectric dams and nuclear power-plants such as EDF and river managers (e.g. DREAL = Directions Régionales de l'Environnement, de l'Aménagement et du Logement, Agence de l'Eau, etc.) on flow

regulation and local adaptations of the river configuration to manage river bars in alluvial systems corresponding to sand-gravel bed rivers and gravel bed rivers.

In sandy-gravel bed rivers, the relatively high sediment mobility is often followed by intense bar morphodynamics and riverbed reworking. For example, in the middle Loire river [Claude et al., 2014], fastly migrating sandy-gravel bars are located close to the CNPE's (Centrale Nucléaire de Production d'Electricité), which in turn threatens the safety of the nuclear power-plants, because of water intake clogging and increasing flooding hazards in the vicinity of the plants. A better understanding and prediction of bars dynamics and subsequent clogging could help to anticipate and optimize the operations of sediment dredging, which are expensive.

Problems linked to alluvial bars can be manifested differently in gravel bed trained rivers subject to narrowing, sediment extraction or sediment discontinuity, where gravel bars dynamics is generally reduced or even stopped. After stabilization, bars are often subject to colonization by vegetation, which enhances bar stability such as in the Isère and Durance rivers [Scorpio et al., 2018; Serlet et al., 2018]. In these two rivers, an issue to increase bars dynamics and avoid the colonization of vegetation can consist on the management of bar formation either by altering the flow regime based on hydraulic dam management or by changing locally the river channel configuration. Because bars also affect the hydraulic and sedimentary conditions of the system, and so the quality of their ecological habitats, the management of hydraulic dams (e.g. restitution, sediment flush and emptying) has to be done within the respect of the environment and river ecosystems.

1.3 Numerical modelling of fluvial bar processes

1.3.1 State of the art on the numerical modelling of bar morphodynamics

Nowadays, the increasing confidence given on the numerical modelling approach is explained by the continuous development of knowledge and computer technology, which allows to investigate physical problems with increasing the level of detail as well as the spatial extent and time scales Mosselman [2012]. As a result, numerical morphodynamic models are widely used for different purposes, from the basic morphodynamic research to dealing with complex river engineering problems [Siviglia and Crosato, 2016]. However, numerical modelling of fluvial morphodynamics, which includes the processes bar formation and propagation, is far from being a solved issue and still involves many challenges [Siviglia and Crosato, 2016].

Defina [2003] outlined the importance of devoting more efforts to the numerical modelling of free bars to further better understanding the role of non-linear processes on bar morphodynamics. To further this goal, the author used a two-dimensional fully non-linear morphodynamic model to reproduce a laboratory experiment of free bar formation with uniform sediment [Lanzoni, 2000a], with paying a special attention to the influence of the initial bed perturbation on bar inception. Satisfying and physically relevant model calibration showed that the formation and evolution of free bars with uniform sediment can be captured using this modelling approach. The last study motivated other modelers to study bar formation and propagation with uniform sediment using various numerical solvers [Tassi et al., 2013]. Numerical models meant to study the interaction between free bars and steady bars with uniform sediment have been then used and showed consistence with the linear stability analysis [Vanzo et al., 2011; Siviglia et al., 2013].

Discussions on the consideration of non-uniform sediment processes on bar morphodynamics using numerical models has been initiated by Mosselman et al. [1999], who suggested that under certain circumstances, the use of constant grain size and constant bed roughness

can be successful if the effect of spatial sediment sorting is counterbalanced by the effect of spatial variations in bed roughness. Conversely, if this condition is not reached, including a physically-based sub-model for non-uniform sediment is mandatory, otherwise the modelling has to be cautiously if sediment sorting is not based on an appropriate model [Mosselman et al., 2003; Sloff et al., 2003].

The numerical modelling of bar formation and propagation with accounting for non-uniform sediment processes on the basis of appropriate sub-models to reproduce sediment sorting and induced spatially variable roughness effects has been undertaken only recently. On the basis of straight flume laboratory experiments, Nelson et al. [2015a,b] developed a numerical model accounting for the vertical sorting of sediment and specific formulations to account for the grain size induced roughness. The authors successfully reproduced the steady and slowly migrating bar patterns as well as the surface sediment sorting observed in the experiments by using only a unique layer and an underneath substrate. Numerical modelling of alternate bar stratigraphy has been initiated by Qian et al. [2016], on the basis of an experiment of free bar formation with non-uniform sediment [Lanzoni, 2000b]. The authors focused on the formation of bars using an upstream bump as initial bed perturbation, and investigated the sediment sorting patterns during the early stages of bar development.

1.3.2 Improvement of the Telemac-Mascaret modelling system

To respond to basic research questions and operational needs, the National Laboratory of Hydraulics and Environment (LNHE) often relies on the development and the use of numerical models, in particular the Telemac-Mascaret modelling system (TMS). Previous studies have showed the ability of the sediment transport and bed evolution module of TMS (module called Sisyphe) [Tassi et al., 2015] to compute the formation and development of bars in straight channels [Tassi et al., 2013] and high-amplitude meandering channels [Wang et al., 2014; Langendoen et al., 2015], under the consideration of different spatial and temporal scales. Despite being promising, these works are limited to simple configurations. The use of numerical models to compute the dynamic evolution of bars in natural configurations is a necessary step before a transfer to the operational unity of EDF.

The numerical model used in this work is based on the TMS, and has to be defined in compliance with the main objectives of this work, i.e. to answer to the research questions addressed in Section 1.2. To study relevantly fluvial bar morphodynamics with non-uniform sediment, under simple and later with more complex combinations of internal and external forcing parameters, the model requires further developments, namely:

- A formulation to compute physically relevant bedload transport rates with non-uniform sediment composed of a mixture of sand and gravel;
- A vertical sediment sorting model, which offers the possibility of reproducing the bed stratigraphy with supporting (in terms of robustness) the transition between erodible and non-erodible areas and offers a simple management of the sediment layer thicknesses;
- Adequates upstream morphodynamic boundary conditions to be able to study the long-term channel morphodynamics with respect to the reproduced laboratory experiments or field study cases.

1.4 Methodology and plan of the manuscript

To answer to the research questions defined in compliance with the operational requirements, the methodology presented below is adopted in this work. This methodology allows to organize the present thesis manuscript into chapters, where some chapters are in the format of publications. Because the articles are kept in their entirety to improve readability and guarantee self-standing, the content presented in the articles can be in part found to be replicated with other parts of the thesis manuscript.

Part I consists on the activity of setting-up the numerical model and bringing the developments which are required to model relevantly bar morphodynamics with non-uniform sediment processes (see Section 1.3), and is presented in Chapter 2.

Part II of this research work is based on the study of bar morphodynamics in idealized channels with non-uniform sediment. In Chapter 3, the morphodynamic model including new implementations is firstly subject to various tests to demonstrate the feasibility of predicting and studying bar development and migration under relatively simple and well controlled configurations. Chapter 4 consists on investigating the influence of sediment size heterogeneity on periodic alternate bars to answer to the research question I (see Section 1.2). The numerical results will be useful to better understand the sediment sorting processes and bar characteristics under simple, idealized bar configurations.

Part III aims at studying bar morphodynamics in real rivers with non-uniform sediment, and to answer to research question II defined in Section 1.2. In other words, the research activities consist on better understanding bar morphodynamics with non-uniform sediment under more complex configurations, with respect to the previous investigations conducted in Part II. Outcomes of this analysis is expected to shed light on bar dynamics in the study site, in the middle Loire river and more generally in sand-gravel bed rivers presenting similar characteristics.

Part IV stands for the conclusions and perspectives, with the feedback from the investigations carried out in Parts II and III. This part aims to step back from the partial discussions and conclusions expressed at each step of this project, and formulate a synthetic reasoning which -under the configurations considered- respond to the research questions defined in Section 1.2. In this last part, based on previous conclusions, a discussion including recommendations will be provided to respond to the main motivation of the study, which is the prediction of bar morphodynamics and the management of bars in sand-gravel and gravel bed trained rivers.

1.5 Perimeter of the current framework

A number of assumptions leading to well formulated model closure hypotheses are considered to define the present framework. The choice of these assumptions is further explained through the present manuscript. The essential motivation for limiting the number of modelled physical processes lies in the fact that it decreases the degree of complexity of the non-linear system, hence it facilitates for isolating the process of interest (e.g. hydrology, sediment size heterogeneity) and understanding its relative influence on the morphodynamic system. Emphasis is placed on the processes and criteria that are not accounted for numerical modelling:

1. Regarding the objectives aimed by the current work, the considered channels geometry leading essentially to 2D flows or limiting the development of 3D flow structures, and for a question of computational time efficiency, the hydrodynamic model is based on the solution of the Barré-de-Saint-Venant equations also called two-dimensional shallow water

equations (SWE) [de Saint-Venant, 1871; Weiyan, 1992; Nezu et al., 1994; Vreugdenhil, 2013]. This choices is indeed advantageous to multiply the scenarios and configurations to conduct sensitivity analyses and calibrate the morphodynamic model;

2. Because bedload has often been considered to be at the origin of bedforms development, the suspended load is not accounted in this work [Naqshband et al., 2014; Meles, 2015];
3. In the morphodynamic model, the grain size distribution is discretized into a finite number of size fractions, and then the modelled sediment probability density function (PDF) is discontinuous;
4. The bedload equations are based on the principle of capacity transport;
5. Vertical sorting of sediment is based on the active layer model of Hirano [1971] which is discrete, so continuous vertical sorting models (CVSM) are not used;
6. Processes of vegetation growth and colonization which are considered to enhance bar stabilization are not accounted in this work, because this study focuses essentially on bar formation, development and on the factors governing their evolution;
7. Similarly to vegetation processes, cohesive sediment processes are not accounted for this work;
8. Bank erosion processes are not considered in this work, because rivers of interest correspond to embanked channels with relatively fix banks, and the timescales considered in this work (i.e. from years to the decade) are relatively short in comparison with the evolution at the reach scale (i.e. from several decades to centuries).

These voluntary model limitations/restrictions also outline the possible perspectives of future research works meant to continually improve the modelling and the understanding of fluvial bar (bio-)morphodynamics.

□ Synthèse générale sur l'introduction

Ce travail de thèse s'inscrit dans la thématique du transport sédimentaire et plus spécifiquement le domaine de la morphodynamique fluviale, et porte sur l'étude de l'influence de l'hétérogénéité granulométrique des lits alluviaux sur l'évolution des bancs sablo-graveleux. Ces derniers correspondent à de vastes dépôts sédimentaires alternant avec des zones plus profondes -dites mouilles-, et qui sont caractéristiques des milieux fluviaux. Un profond intérêt est accordé aux bancs, car ils contrôlent activement les zones d'érosion et de dépôt sédimentaires, gouvernent la topographie du lit alluvial et influencent l'érosion des berges, et par conséquent la trajectoire morphodynamiques des rivières.

Il est couramment admis que des opérations de gestion de grande ampleur tels que la canalisation, la construction de forçages géométriques permanents comme des épis, la diminution du régime hydraulique, les continuels dragages sédimentaires ou la construction de barrage peut altérer de manière significative la morphodynamique des bancs à l'échelle du tronçon. Dans la mesure où de plus en plus de rivières -dites aménagées- sont sujettes à ces intenses modifications qui peut les dévier fortement de leur régime naturel, il est crucial de pouvoir mieux anticiper l'impact à court, moyen et à long termes de ces changements sur la morphologie des cours d'eau.

Les réponses à ces divers changements peuvent se manifester de manières bien distinctes. Par exemple, les bancs peuvent mettre en danger la stabilité des ouvrages fluviaux tels que les digues et les berges, mais aussi les piles de pont. Dans les rivières à gravier, la dynamique des bancs peut se voir ralentie ou bien même stoppée, car dans certains cas les bancs peuvent être sujets à une végétalisation et une stabilisation rapide. Le scenario dépeint précédemment est typique de l'Isère et de la Durance, où la colonisation végétale réduit fortement la mobilité des bancs, diminue la biodiversité et accroit le risque inondation. Un schéma différent est souvent observé en ce qui concerne les rivières sablo-greveleuses, où les bancs sont généralement soumis à une dynamique plus intense. Par exemple, en Loire moyenne, les bancs peuvent se rapprocher des prises d'eau des CNPE (Centrale Nucléaire de Production d'Electricité), entraîner un risque de colmatage de la source froide et mettre en péril les installations du parc nucléaire. Les problèmes présentés ci-dessus constituent un enjeu réel pour les gestionnaires des rivières tels qu'EDF (Electricité de France), les DREAL (Directions Régionales de l'Environnement, de l'Aménamegement et du Logement) ou l'Agence de l'Eau, qui se chargent de l'optimisation des travaux de maintenance et des activités liées à la restauration tels que les dragages, les essartements, la modification de la gestion des barrages hydrauliques, qui doivent être réalisés dans le respect de l'environnement et des écosystèmes fluviaux. Alors que la littérature actuelle souligne l'importance des processus liés à la non-uniformité sédimentaire sur la morphodynamique des bancs alluviaux, diverses lacunes subsistent encore sur la véritable relation entre les sédiments non-uniformes et les bancs.

Du fait que le succès des travaux d'aménagements et des projets de restauration des rivières dépendent de la bonne gestion des bancs, il est jugé à la fois primordial de mieux comprendre la morphodynamique des bancs en présence de granulométries non-uniformes et de proposer une méthode pour prédire plus pertinemment et efficacement l'évolution des bancs, avant de décliner l'approche à des fins opérationnelles. Dans l'optique d'apporter des éléments de réponse aux objectifs présentés ci-dessus, deux questions de recherche ont été identifiées :

I. **Comment la non-uniformité des sédiments affecte la morphodynamique des bancs ?**

II. **Comment le motif des bancs et un sédiment non-uniforme co-évoluent sous des condi-**

tions de multiples forçages internes et externes ?

L'approche numérique est mise en avant pour répondre à ces besoins, et le modèle numérique développé dans cette étude est implémenté dans le système de modélisation Telemac-Mascaret (TMS). L'état de l'art en matière de modélisation numérique des processus liés aux sédiments non-uniformes montre que plusieurs développements et mises à niveau sont nécessaires dans le TMS avant de pouvoir modéliser la morphodynamique de bancs dans des systèmes simples ou plus complexes sujets à la combinaison de forçages internes et externes :

- Une formulation pour estimer de manière plus pertinente le charriage d'un mélange de particules sableuses et graveleuses ;
- Un modèle de tri granulométrique vertical, offrant la possibilité de reproduire la stratigraphie et compatible avec les transitions entre un substrat non-érodable et lit alluvial érodable ;
- Des conditions limites sédimentaires amont adéquates, afin d'être capable de reproduire fidèlement les évolutions morphodynamiques à long-terme sur la base des expériences de laboratoire ou des observations de terrain.

La méthodologie adoptée dans ici permet de scinder le présent manuscrit en chapitres, où certains de ces derniers prennent le format de publications scientifiques. Dans le but de garantir l'intégrité de ces articles pour satisfaire leur caractère autoporteur, il est possible de retrouver du contenu partiellement répliqué d'un chapitre à un autre.

La première partie (Partie I) de ce travail se résume à la mise en place du modèle numérique et des divers développements nécessaires pour bien prendre en compte les processus liés aux sédiments non-uniformes et les bancs, et sont présentés dans le second chapitre (Chapitre 2).

La deuxième partie (Partie II) de ce travail de recherche est basée sur l'étude de la morphodynamique de bancs dans des configurations simples. Dans le Chapitre 3, le modèle morphodynamique est premièrement soumis à divers tests pour démontrer la faisabilité de prédire et d'étudier la formation et la migration de bancs dans des conditions simples et bien contrôlées. Le Chapitre 4 consiste à étudier plus en détail l'influence des sédiments non-uniformes sur les bancs périodiques alternés, afin de répondre à la première question de recherche. Les résultats numériques permettront d'alimenter la compréhension actuelle entre les processus de tri granulométriques et les bancs dans des configurations idéalisées.

En troisième partie (Partie III), l'attention est portée sur la dynamique des bancs dans des configurations de rivières dites « plus classiques » que dans le cas précédent, c'est-à-dire des systèmes morphodynamiques soumis à divers forçages internes et externes en présence de sédiments non-uniformes. Pour cela, le modèle numérique est utilisé pour reproduire la dynamique de bancs dans un tronçon de la Loire moyenne. Les résultats issus de l'étude présentée dans le Chapitre 5 permettront d'apporter des réponses à la deuxième question de recherche et mieux comprendre la dynamique des bancs dans la zone d'étude, dans la Loire moyenne et plus généralement dans les rivières sablo-graveleuses présentant des caractéristiques similaires.

La dernière partie (Partie IV) permet de conclure et de présenter les perspectives, via retour d'expérience sur les études menées au cours de ce travail de thèse. Diverses réponses aux questions de recherche et recommandations seront aussi exposées afin de mieux prédire et gérer les bancs dans des rivières sablo-graveleuses et graveleuses.

PART I

NUMERICAL MODEL SET-UP AND ACTIVITIES OF IMPLEMENTATION AND IMPROVEMENTS

CHAPTER 2

NUMERICAL MODEL AND DEVELOPMENTS

▷ Motivations and objectives of this activity

The research investigations undertaken in the present work rely on the use of a two dimensional numerical morphodynamic model, which is based on the Telemac-Mascaret modelling system (TMS). The literature review presented in Section 1.1.3 and preliminary revision of the morphodynamic module of TMS support the idea that multiple numerical model improvements are necessary before attempting to reproduce and investigate with the TMS bar morphodynamics processes associated to non-uniform sediment, and respond to the research questions expressed in Section 1.2. The modelling choices and further numerical developments are presented in the following chapter.

Implementation of appropriate formulas to estimate the bedload transport of non-uniform sediment is required in the sediment transport module of the software. For diverse reasons expressed later in this Chapter (notably in terms of physical relevance and range of validity), the formula of Wilcock and Crowe [2003] has been considered for the present research works and has been implemented in the numerical model. In the same way, the modelling of riverbed evolution with non-uniform sediment and vertical sediment sorting is based on mathematical models dedicated to this purpose, including specific numerical treatments to ensure computational efficiency as well as model robustness. Because appropriate formulations are mandatory in numerical models to reproduce relevantly fluvial bar processes, revision of the existing code and implementation of new features is carried out accordingly, based on the mathematical model of Hirano [1971, 1972]. A new module is then implemented in the morphodynamic model to account for the vertical sorting of sediment in the framework of modelling alluvial bars in rivers. Other aspects, such as the implementation of boundary conditions will be also addressed in this chapter.

2.1 Mathematical and numerical model

The two-dimensional morphodynamic model used in this work presents two components: a hydrodynamic module and a morphodynamic module.

2.1.1 Hydrodynamic model

The hydrodynamic module is based on the solution of the shallow-water equations (SWE) [de Saint-Venant, 1871; Weiyan, 1992; Nezu et al., 1994; Vreugdenhil, 2013]:

$$\begin{cases} \partial_t h + \vec{u} \cdot \nabla(h) + h\nabla \cdot (\vec{u}) = 0 \\ \partial_t u + \vec{u} \cdot \nabla(u) = -g\partial_x z_f - gS_{f,x} + h^{-1}\nabla \cdot (h\nu_t \nabla u) \\ \partial_t v + \vec{u} \cdot \nabla(v) = -g\partial_y z_f - gS_{f,y} + h^{-1}\nabla \cdot (h\nu_t \nabla v) \end{cases} , \tag{2.1}$$

where t [s] is the time, $\partial_t = \partial/\partial_t$, $\nabla = (\partial_x, \partial_y)$ is the gradient vector field, g= 9.81 m/s^2 is the acceleration due to gravity, h [m] is the water depth, z_b [m] is the elevation of the bed topography, $z_f = z_b + h$ [m] is the free surface elevation, $\vec{u} = (u, v)$ [m/s] is the depth-averaged flow velocity vector with u and v [m/s] the component along the longitudinal x-axis and transversal y-axis direction respectively, with $|\vec{u}|$ [m/s] the module of $\vec{u}$, and ν_t [m^2/s] is the turbulent eddy viscosity term that models the so-called Reynold stresses and the differential dispersion terms originated from the lack of vertical uniformity of the horizontal velocity field. The friction law $\vec{S_f}$ [-] of Chézy is given as follow:

$$\vec{S_f} = (S_{f,x}, S_{f,y}) = \frac{\vec{u}|\vec{u}|}{C^2 h} , \tag{2.2}$$

where $S_{f,x}$ and $S_{f,y}$ correspond to the components of the friction law $\vec{S_f}$ [-] along the longitudinal $x-$axis and transversal $y-$axis direction respectively and C [m$^{1/2}$/s] corresponds to the Chézy friction coefficient. The formula of Nikuradse [1950] is used to calculate the equivalent friction coefficient of Chézy denoted $C_f = g/C^2$ [-] as a function of the equivalent roughness height of the bed denoted with k_s [m]:

$$C_f = 2\left[\log\left(\frac{30h}{ek_s}\right)/\kappa\right]^{-2} , \tag{2.3}$$

where κ is the von Kármán coefficient (= 0.40 for clear waters) and e is the base of the natural logarithm.

2.1.2 Morphodynamic model

The morphodynamic module is based on the Exner equation [Exner, 1920; García, 2008]. In case of non-uniform sediment, the Exner equation is applied to every size fraction of sediment in which the mixture is subdivided. The following procedure is adopted: *i*) the sediment mixture is discretized into sediment fractions, and for each fraction the representative sediment diameter is given, *ii*) the bedload transport capacity equation and the mass conservation formula are applied for each separate fraction of sediment.

2.1.2.1 Sediment mass continuity and vertical sorting

The solution for sediment mass conservation is based on the mathematical concept proposed by Hirano [1971, 1972], who developed a continuity model for the vertical sorting of sediment. More details on the formulation of the active layer concept, the implementation and validation in the numerical code are given in the 2.2.2.

2.1.2.2 Bedload transport with uniform sediment

The bedload transport capacity of uniform sediment denoted as q_{b0} [m^2/s] is determined with the formula of Meyer-Peter and Müller [1948] (MPM):

$$\frac{q_{b,0}}{\sqrt{g\Delta_s d^3}} = \alpha_b \left(\tau_b^* - \tau_c^*\right)^\gamma, \text{ with } \alpha_b = 8, \gamma = \frac{3}{2} \ , \tag{2.4}$$

where d denotes the sediment diameter [m], $\Delta_s = \rho_s/\rho - 1$ is the relative submerged sediment density, $\tau_b^* = \tau_b/(g(\rho_s - \rho)d)$ the dimensionless bed shear stress also known as Shields parameter where τ_b [Pa] corresponds to the bed shear stress and d [m] the representative grain diameter of the uniform sediment distribution, and τ_c^* ($= 0.047$) the critical Shields parameter [Shields, 1936].

2.1.2.3 Bedload transport with non-uniform sediment

The bedload transport capacity of a given fraction of the non-sediment, later referred to as *fractional transport rate* and denoted as $q_{b0,i}$ [m^2/s] is determined with the formula of Wilcock and Crowe [2003] (WC-2003). More details on the formulation of the active layer concept, the implementation and validation in the numerical code are given in the 2.2.1.

2.1.2.4 Bed slope effects

Sediment transport capacity formulas are generally fitted against experimental data under the assumption of a flat bed (neglecting the gravitational effects). Natural riverbeds may show milder or steeper slopes due to the presence of dunes, ripples, steps, or pools in the longitudinal direction and curves in the transverse direction. As a result, gravity effects increase the bedload transport in downslope sections and lessen the movement of particles in upslope directions. Several formulas have been proposed to take into account the bed slope effect on *i*) the magnitude [Koch and Flokstra, 1980; Soulsby, 1997] and *ii*) the direction of bedload transport [Koch and Flokstra, 1980; Talmon et al., 1995]. The correction of bedload magnitude is modelled with the formula proposed by Koch and Flokstra [1980], where the fractional transport rate $q_{b0,i}$ is modified as a function of the bed slope degree with respect to the current direction:

$$q_{b,i} = q_{b0,i}\left(1 - \beta_1 \partial_s z_b\right) = q_{b0,i}\left[1 - \beta_1 \left(\partial_x z_b \cos\delta + \partial_y z_b \sin\delta\right)\right] \ , \tag{2.5}$$

where β_1 is an empirical coefficient accounting for the stream-wise bed slope effect, δ is the angle between the current and the x-axis direction, and s the coordinate along the current direction. The bedslope effect is similar to a diffusion term in the bed evolution equation [Van der Meer et al., 2011] and may smooth the bed topography and prevent from numerical instabilities [Zolezzi and Seminara, 2001; Cabrit, 2009; Kleinhans and van den Berg, 2011]. The correction of bedload direction is given by the relation of Bendegom [1947]:

$$\tan\alpha_i = \frac{q_{b,i,n}}{q_{b,i,s}} = \frac{\sin\delta - T_i \partial_y z_b}{\cos\delta - T_i \partial_x z_b} \ , \tag{2.6}$$

where α_i is the angle between the sediment transport vector of the i^{th} size fraction of sediment and x-axis direction which will deviate from the bed shear stress vector due to gravity effects, $q_{b,i,n}$ and $q_{b,i,s}$ correspond to the bedload magnitudes along the normal to the current direction

and the stream-wise direction, respectively, and where the coefficient T_i is calculated as follows [Talmon et al., 1995]:

$$T_i = \frac{1}{\beta_2 \sqrt{\tau^*_{b,i}}} \ , \tag{2.7}$$

where $\tau^*_{b,i}$ is the bed shear stress adimensionnalized by the diameter representative of the i^{th} size fraction of sediment and scales the gravity effects as a function of the grain diameter of the i^{th} size fraction, and β_2 is an empirical coefficient used as a calibration parameter.

2.1.2.5 Bed shear stress

The total shear stress τ [Pa] is calculated from the depth averaged flow velocity field, where $\tau = 0.5\rho C_f(u^2 + v^2)$ and C_f is equal to the sum of skin friction and bedform drag, plus other forms of macro-roughness induced by rip-raps, vegetation, etc. In this study, the bed shear stress is determined as a function of the total shear stress:

$$\tau_b = \mu\tau \ , \tag{2.8}$$

where $\mu = C'_f/C_f$ is the friction factor and C'_f [-] is the equivalent Chézy coefficient only due to skin friction and is the only component acting on bedload [Mendoza et al., 2016]. C'_f is calculated assuming a flat bed by using the Nikuradse's formula (Equation 2.3), where the roughness height k'_s [m] is a function of the mean sediment diameter at the bed surface with:

$$k'_s = \alpha_{k_s} \times d_{s,m} \ , \tag{2.9}$$

with α_{k_s} a calibration parameter. García [2008] summarized different values of α_{k_s} measured in the field and in the laboratory ranging from 1 to 6.6. More recently, it has been showed that the typical values of α_{k_s} for the total flow resistance produced by 2D laboratory dunes can increase of several orders of magnitude, which vary between 10 and 1,000 in the experiments of Huthoff [2012]. The friction induced by ripples and dunes is modelled through the coefficient α_{k_s} and the geometry of these smaller scale bedforms is not represented in the numerical model.

2.1.3 Numerical scheme

The numerical solution of Equations 2.1 is based on the finite element method P_1, where the advective terms are computed with the method of the characteristics. The numerical solution of the sediment transport continuity equation (Equation 2.14) is performed by a procedure that combines an implicit finite element scheme and an edge-based explicit upwind advection scheme. This procedure assures mass-conservation at machine accuracy, monotonicity of tracers, copes with dry zones and is easily applicable to domain decomposition [Hervouet et al., 2011].

2.2 Numerical developments: motivation and practical use in this work

Numerical modelling of non-uniform sediment processes in rivers is challenging [Siviglia and Crosato, 2016], and only few numerical studies have considered the sediment non-uniformity in the presence of bars [Mosselman et al., 1999; Cui et al., 2003a; Nelson, 2010; Nelson et al., 2015b]. Before starting any research investigation, many efforts have been devoted to ensure the robustness and the validity of the numerical model used in this work to model non-uniform sediment processes. According to the literature review (Section 1.1.3), the two main challenges which seem necessary to model bars with non-uniform sediment correspond to *i*) a physically relevant estimation of the sediment transport capacity at the interface between the flow and the riverbed topography and *ii*) an accurate modelling of the vertical sorting of sediment resulting from the erosion and deposition of heterogeneous sediment [Blom, 2008]. A review of the numerical code has been useful to detect the morphodynamic model limitations and lacks of robustness present in the TMS. This section aims to justify the different choices of reviewing the actual code or bringing new developments for this work, and explains in which context these developments will be used. The increasing number of scenarios to conduct sensitivity and calibration tests will for the use of high performance computing (HPC) clusters (see Appendix G) and for the parallelization of the code (using the MPI library).

2.2.1 Implementation of Wilcock and Crowe [2003]'s formula to assess bedload transport

2.2.1.1 Motivations for implementing the formula of Wilcock and Crowe [2003]

So far, two types of model have been proposed in the literature to estimate the sediment transport capacity of sediment mixtures: stochastic models and deterministic models.

Stochastic models for the transport of heterogeneous non-cohesive sediment are based on the computation of fractional mobility of sediment by using the concept of continuous-time Markov process [Sun and Donahue, 2000; Wu and Yang, 2004]. Stochastic models remained quite limited, as the model parameters such as particles velocity have to be determined from exhaustive field compaigns or experiments. Moreover, stochastics model still require improvement, for instance to account for the spatial and temporal variation of bed shear stress and sand content [Wu and Yang, 2004].

Deterministic models have been originally proposed to estimate the transport capacity of uniform sediment [Meyer-Peter and Müller, 1948; Engelund and Hansen, 1967]. Because sandy-gravel and gravel bed rivers often show an important degree of sediment size heterogeneity, the application of classical bedload equations usually fails in reproducing relevant transport rates [Recking, 2010]. This failure occurs mostly because the hiding-exposure effects are not represented (see Section 1.1.3.4). Simplest models proposed the calculation of a hiding-exposure coefficient for each separate sediment size fraction, to be replaced in the classical sediment transport capacity formula for uniform sediment to compute the transport rate of each sediment fraction [Parker et al., 1982]. These formulas are often used in numerical modelling of non-uniform sediment processes [Singh et al., 2017].

However, neither of these last formulations are based on data sampled in heterogeneous sediment beds, and there is no justification for assuming that either equation can be simply be applied with the Shields parameter based on d_i (the grain size of the i^{th} size fraction of sediment of bed surface) multiplied by $F_{a,i}$ (the volume fraction of the i^{th} size fraction of sediment in

the surface layer) [Wilcock and Crowe, 2003]. If a fractional transport procedure has to be used, it should be preferentially done with one of the formulations derived for that purpose [Recking et al., 2015]. These more sophisticated models account for the hiding-exposure effect, by calculating a fractional-based bedload transport based on a similarity analysis between the bedload transport rate of size fraction i denoted $q_{b,i}$ and the skin friction relative to the same size fraction denoted $\tau_{r,i}$ [Proffitt and Sutherland, 1983; Parker, 1990; Wilcock and Crowe, 2003; de Linares and Belleudy, 2007]. This similarity analysis is commonly known as the similarity collapse of the data and aims to determine a similarity collapse function f that is independent of grain size [García, 2008].

Finally, it is important to keep in mind that every deterministic models have a certain range of validity, because they have been calibrated on a specific range of sediment diameters and under specific flow conditions. Therefore, the choice of the sediment transport formula has to be done in respect to the given problem to solve.

It is of key interest to accurately estimate the sediment transport in natural rivers, since bed evolution (i.e. armor formation and break-up) and later bar morphodynamics depend on the estimation of fractional transport rates [Parker, 1990; Orrú et al., 2016; Powell et al., 2016] (see also Section 1.1.3.4). Therefore, the authors proposed to use the model of Wilcock and Crowe [2003] (WC-2003), which is interesting in the way that *i*) it is based on bed surface investigations carried out experimentally, and is particularly adapted for the prediction of transient conditions of bed armoring and scenarios of bed aggradation/degradation, *ii*) it considers the full size distribution of the bed surface (from finest sands to coarsest gravels), *iii*) it was calibrated under a wide range of water discharges and sediment mixtures, *iv*) the hiding-exposure function has been designed to resolve discrepancies observed from previous experiments [Proffitt and Sutherland, 1983; Parker, 1990] including the hiding-exposure effect of sand content on gravel transport for weak to high values of sand contents in the bulk, and *v*) it has already showed efficiency when applied for morphodynamics modelling [An et al., 2017].

2.2.1.2 Mathematical model of Wilcock and Crowe [2003]

For each i^{th} size fraction, the magnitude of the fractional transport rate without gravitational effects $q_{b0,i} = |\vec{q_{b0,i}}|$ [m^2/s] is estimated using the bedload capacity formula of Wilcock and Crowe [2003]:

$$W_i^* = f(\tau_b/\tau_{r,i}) = \frac{\Delta_s g q_{b0,i}}{F_{a,i} u_*^3} \quad , \tag{2.10}$$

where W_i^* [-] corresponds to the dimensionless transport rate for the i^{th} size fraction of sediment, $\Delta_s = \frac{\rho_s}{\rho} - 1$ [-] is the relative submerged sediment density, with ρ [kg/m^3] the water density and ρ_s the sediment density [kg/m^3], τ_b [Pa] is the bed shear stress, $\tau_{r,i}$ [Pa] the reference shear stress of the i^{th} size fraction defined as the value of τ_b at which $W_i^* = 0.002$ and $u_* = \sqrt{\tau_b/\rho}$ [m/s] the shear velocity (also called friction velocity), and $F_{a,i}$ the volume fraction content of the i^{th} size fraction of sediment at the bed surface (later referred to as active layer, see 2.2.2). The transport function of WC-2003 is defined as follows:

$$W_i^* = \begin{cases} 0.002\Phi_i^{7.5} & \text{for } \Phi_i < 1.35 \\ 14\left(1 - \frac{0.894}{\Phi_i^{0.5}}\right)^{4.5} & \text{for } \Phi_i \geq 1.35 \end{cases} \quad , \tag{2.11}$$

where the ratio $\Phi_i = \tau_b/\tau_{r,i}$ is incorrectly referred to as Φ in the literature [Wilcock and Crowe, 2003; Recking et al., 2015].

A hiding-exposure function is defined to estimate $\tau_{r,i}$ so that the sediment transport rates are lowered for finer fractions (i.e. increase of $\tau_{r,i}$) and increased for coarser material (i.e. decrease of $\tau_{r,i}$). This is accounted in the model as follows:

$$\frac{\tau_{r,i}}{\tau_{r,m}} = \left(\frac{d_i}{d_{s,m}}\right)^{b_i} \quad \text{with} \quad b_i = \frac{0.67}{1 + \exp\left(1.5 - \frac{d_i}{d_{s,m}}\right)}, \tag{2.12}$$

where d_i [m] corresponds to the sediment diameter of the i^{th} size fraction, $d_{s,m}$ [m] is the mean sediment diameter of surface, $\tau_{r,m}$ [Pa] is the reference shear stress of the mean sediment diameter of surface and b_i is the power-coefficient of the hiding-exposure function which is incorrectly referred to as b in the literature. $\tau_{r,m}$ is computed as a function of the dimensionless median reference shear stress of bed surface $\tau^*{}_{r,m}$ such that $\tau^*{}_{r,m} = \frac{\tau_{r,m}}{\Delta_s \rho g d_{s,m}}$ where $\tau^*{}_{r,m} = 0.021 + 0.015\exp[-20F_s]$, with F_s the fraction volume content of sand at the bed surface [-].

By using independent sediment transport measurements, several authors [e.g. Recking et al., 2015; An et al., 2017] have showed that the performance of the formula of WC-2003 could be improved by modifying one or several parameters. In this work, the authors proposed to calibrate the sediment transport formula by estimating the fractional transport rates of sediment with multiplying W_i^* by a dimensionless coefficient called α_b.

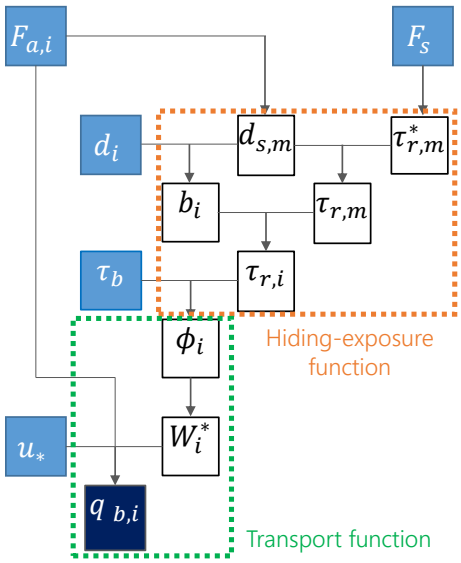


Figure 2.1: Scheme of application of the sediment transport model of WC-2003. Parameters in blue boxes are input parameters, those in white boxes are intermediary variables computed to estimate the transport rate of the i^{th} size fraction in the black box.

A mathematical analysis of the formula of WC-2003 presented in Appendix B has been performed to better understand the behavior of the model, to detect any limits when it is applied using one, two or a greater number of size fractions and eventual issues of robustness when the model is implemented numerically. Although the model offers many advantages, the following limitations have been found during the analysis: i) a small discontinuity in the dimensionless transport rate formula (Equation 2.11), and ii) when an unsuitable method for decomposing

the grain size distribution is chosen, the critical shear stress calculated for the sand fraction can vary importantly, which in turn might affect importantly the value of the computed sediment transport rates. To overcome the latter limitation, a proper discretization of the grain size distribution could consist on separating the sand (i.e. from which diameter is lesser than 2 mm) from the gravel (i.e. from which diameter is greater or equal to 2 mm). With this method, the whole portion of sand would be represented by a single size fraction and gravel would be represented through one or multiple size fractions.

2.2.1.3 Implementation of Wilcock and Crowe [2003]

Variables used in the model

`NSICLA`	▷ Number of size fractions/classes of sediment
`NPOIN`	▷ Number of computational nodes

The `Fortran` code is available in Appendix C. The pseudo code used in the new algorithm is presented below:

for `i=1,NSICLA` **do** ▷ Loop on the number of sediment size fractions

  $\alpha_b = 1.0$ ▷ User defined coefficient of calibration, by default equal to 1.0

  for `j=1,NPOIN` **do** ▷ Loop on the computational nodes `j`

    $\tau_{r,m} = (0.021 + 0.015\exp[-20F_s]) * (\Delta_s \rho g d_{s,m})$

    $b_i = \frac{0.67}{1+\exp\left(1.5-\frac{d_i}{d_{s,m}}\right)}$

    $\tau_{r,i} = \tau_{r,m}\left(\frac{d_i}{d_{s,m}}\right)^{b_i}$

    $\Phi_i = \tau_b / \tau_{r,i}$

    if $\boxed{\Phi_i < 1.35}$ **then** ▷ **Transport function (Equation 2.11)**

      $W_i^* = 0.002\Phi_i^{7.5}$

    else

      $W_i^* = 14\left(1 - \frac{0.894}{\Phi_i^{0.5}}\right)^{4.5}$

    end if

    $q_{b,i} = \alpha_b W_i^* F_{a,i} \frac{(\tau_b \mu/\rho)^{1.5}}{g\Delta_s}$ ▷ **Bedload of size fraction `i` at point `j` (Equation 2.10)**

    if $\boxed{q_{b,i} < 10^{-12}}$ **then**

      $q_{b,i} = 0$ ▷ **If very low transport impose $q_{b,i}$ = 0 (to avoid numerical artifacts)**

    end if

  end for

end for

2.2.1.4 Validation and practical use of the code

The implementation of the WC-2003 formula has been firstly tested with running a model which reproduces two of the experiments of Wilcock and Crowe [2003], namely BOMC2 and BOMC4, and comparing the computed fractional transport rates of sediment with the ones computed analytically. BOMC2 and BOMC4 experiments are selected, because they are characterized by very low and moderate sediment transport rates, respectively, and assume sub-critical flows. The fractional transport rates are computed numerically with scenarios considering distinct numbers of sediment size fractions (one, two, five and ten size fractions of sediment respectively). The comparison between the fractional and total transport rates of sediment obtained analytically and numerically shows that the model of WC-2003 is well implemented in the TMS (see Table 2.1).

Table 2.1: Comparison between the total and fractional transport rates obtained analytically and numerically on the basis of BOMC4 experiment, showing that the formula of WC-2003 is well implemented in the TMS.

Bedload [m^2/s]	Analytical	Numerical
(Total) q_{b0}^*	$6.77 \cdot 10^{-6}$	$6.78 \cdot 10^{-6}$
$q_{b0,1}^*$	$3.02 \cdot 10^{-6}$	$3.02 \cdot 10^{-6}$
$q_{b0,2}^*$	$2.02 \cdot 10^{-6}$	$2.02 \cdot 10^{-6}$
$q_{b0,3}^*$	$1.19 \cdot 10^{-6}$	$1.19 \cdot 10^{-6}$
$q_{b0,4}^*$	$5.38 \cdot 10^{-7}$	$5.41 \cdot 10^{-7}$
$q_{b0,5}^*$	$7.35 \cdot 10^{-9}$	$7.48 \cdot 10^{-9}$

Validation of the formula and comparison with other sediment transport formulas (MPM and MPM-Egiazaroff) is made in a second step [Cordier et al., 2016a], and help to validate the modelling approach under simple configurations, i.e. by considering one-dimensional flows and no bedforms. More details on this work can be found in Cordier et al. [2016a].

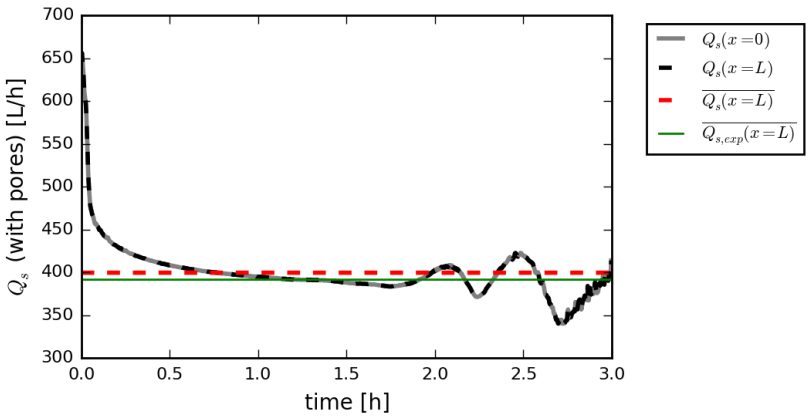


Figure 2.2: Fluxes of sediment crossing the upstream and downstream model boundaries considering the numerical run based on [Lanzoni, 2000b]'s P2009 experiment. This figure illustrates that the averaged transport rate simulated with the formula of WC-2003 computes satisfactory transport rates with respect to the laboratory observations and the new algorithm for sediment recirculation is well implemented in Sisyphe.

Thirdly, the bedload capacity formula of Wilcock and Crowe [2003] has been used in this work (see Chapter 3 and 4) to simulate the formation and migration of non-uniform sediment

bars composed of a mixture of sand and gravel under simple geometrical and well controlled boundary conditions [Lanzoni, 2000b]. Given this configuration, after calibration, the formula computes satisfactory values of sediment transport rates (Figure 2.2) as well as relevant sediment sorting patterns (Figure 2.3), with respect with the ones measured by Lanzoni [2000b]. Variations in sediment discharges observed in the last figure are explained by the continual downstream bar migration, which induces the periodical variation of the sediment flux across the boundaries. Although Lanzoni did not measured the fractional transport rates of sediment during his experiment, the sediment sorting pattern observed over the bars (Figure 2.3) indicates that the sediment transport formula of WC-2003 and the hiding-exposure function of this formula can produce physically relevant results and does not lead to numerical problems such as numerical instability. Hence, the sediment transport formula of WC-2003 is showed to compute physically relevant results and is numerically robust. This code will be available in the next version of Sisyphe (V8P0).

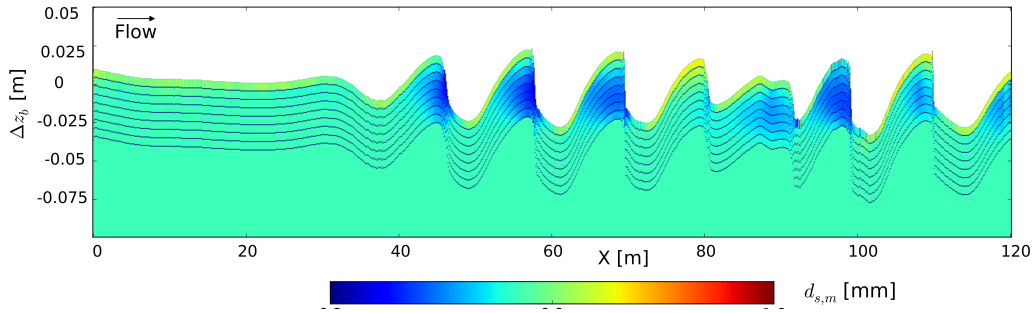


Figure 2.3: Longitudinal profile of bed evolution and vertical sediment sorting at 20 cm from the left sidewall obtained with the numerical model reproducing the experiment P2009 of Lanzoni.

Eventually, the formula is used to estimate the sediment transport in a selected reach of the middle Loire river, which is subjected to a multitude of non-linear forcing effects (Chapter 5). Once again, assuming a physically relevant calibration of the roughness effects induced by the grain roughness and bedforms on the estimation of bed shear stress (Chapter 5), the formula of WC-2003 is showed to be efficient and is numerically stable (Figure 2.4).

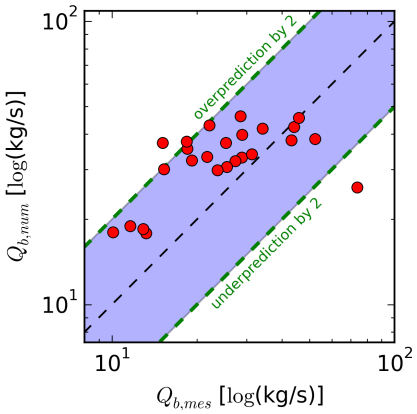


Figure 2.4: Sediment transport rates measured at Bréhémont (middle Loire river) and computed with the numerical model using the formula of WC-2003, validating the implementation and the choice of this formula for this work.

2.2.2 Implementation of the bookkeeping active layer model for vertical sediment sorting

2.2.2.1 Motivations for implementing a new active layer algorithm

Numerical modelling of vertical sediment sorting can rely on two types of models [Blom, 2008], namely the models based on the so-called three-layer concept (bedload, active and substract layers) originally proposed by Hirano [1971]; and the Continuum Vertical Sorting Models (CVSM) [Parker et al., 2000; Blom et al., 2003, 2008; Blom, 2008]. Multi-layers models based on the concept of Hirano [1971] are designed for the storage of sediment fractions in discrete layers and use sediment transfer functions to estimate the GSD changes in each layer after erosion or deposition of sediment, whereas CVSMs are based on the solution of a probabilistic sediment continuity equation [Parker et al., 2000]. Under non-equilibrium conditions, the CSVM is reduced to a sorting evolution model which solves the bedload transport composition and the vertical sorting profile from the initial sorting profile, the bedload transport rate and the probability function of bedforms elevation [García, 2008; Blom et al., 2003, 2008; Blom, 2008]. CSVMs are computationally expensive as *i*) they require information on the probability density function of bedform elevations, which can be provided by an external sub-model [Van der Mark and Blom, 2007] that requires first field/experimental measurements and *ii*) their application is cumbersome as it requires a relatively small numerical time step. Furthermore, no large-scale field application has yet been conceivable as it asks for the development of a new bed layer-type model [Blom, 2008]. Therefore, the present work is based on Hirano [1971]'s framework, notwithstanding the shortcomings of this method summed-up by Blom et al. [2008]; Siviglia et al. [2017]; Viparelli et al. [2017] (mainly the limits found in the formulation for the transfer of sediment between the sediment layers), the difficulties involved in the definition and the parameterization of the active layer thickness [Church and Haschenburger, 2017] and the recently exposed limitations of this model [Stecca et al., 2016; Chavarrias et al., 2018].

The first bookkeeping active layer model implemented in the TMS (version 6.2) was originally developed by De Linares [2007] to study sediment transport and bar morphodynamics in the Loire and the Arc rivers (France). This model has been continuously modified by the TMS user community for the purpose of other study cases. Under some circumstances, the algorithm used

in the last model shows lacks of robustness, even leading to simulation stopping [Reisenbüchler et al., 2016]. Numerical treatment of aggradation processes is limited in the actual version of this algorithm because no stratigraphy reconstruction (i.e. no new underlying layer creation) is made possible during scenarios of aggradation. This is resulting in a loss of information on the composition of the deposited sediment, which tends to be averaged when the first top substrate thickness continuously increases through time during scenarios of intense bed aggradation. The model also showed difficulties to ensure mass continuity in the case of transition between erodible and non-erodible areas. A more exhaustive review of this algorithm is presented in Appendix D. These problems, the difficulties encountered in the complete understanding of the algorithm and discussions with Reisenbüchler et al. [2016] motivated the authors to implement another algorithm to account for the vertical sorting of sediment in the TMS. By developing a new algorithm based on the bookkeeping active layer model, we wish to offer a simpler and more robust code in the TMS, ensuring both sediment mass continuity and numerical model stability, on the consideration of modelling alluvial bars in rivers.

2.2.2.2 Mathematical model of Hirano [1971]

The method is based on the decomposition of the bed into a homogeneous top layer, called *active layer*, and an unchanging homogeneous *substrate* [Church and Haschenburger, 2017; Ashmore et al., 2018] (Figure 2.5). The active layer is a fully mixed layer, defined as the layer where all the bed fluctuations are concentrated [Blanpain, 2009; Stecca et al., 2016]. Following Hirano [1971]'s concept, the bed is discretized in the vertical direction as follows:

$$z_b = \eta_{a:1} + L_a \ , \tag{2.13}$$

where $\eta_{a:1}$ [m] denotes the absolute elevation of the interface between the active layer and the substrate, and L_a [m] corresponds to the active layer thickness. The sediment mass continuity equation is given as follows [e.g. Parker et al., 2007]:

$$L_a \partial_t F_{a,i} + \left[F_{a,i} - \mathcal{F}_{a:1,i}\right] \underbrace{\partial_t L_a}_{=0} = \frac{1}{\epsilon_0}\left[\mathcal{F}_{a:1,i} \nabla \cdot \vec{q_b} - \nabla \cdot \vec{q_{b,i}}\right] \ , \tag{2.14}$$

where $\partial_t L_a = 0$ because the active layer thickness is assumed to be constant during the whole simulation, $F_{a,i}$ is the volume fraction content of the i^{th} size fraction in the active layer and $\mathcal{F}_{a:1,i}$ is the volume fraction content of the i^{th} size fraction in the interface separating the active layer and the substrate, $\vec{q_b} = (q_{b,x}, q_{b,y}) = q_b(\cos\alpha, \sin\alpha)$ [m^2/s] corresponds to the total volumetric bedload solid discharge per unit of width without pores, with components $q_{b,x}$ and $q_{b,y}$ along the $x-$ and $y-$ axis directions respectively, $\vec{q_{b,i}} = (q_{b,i,x}, q_{b,i,y}) = q_{b,i}(\cos\alpha_i, \sin\alpha_i)$ [m^2/s] corresponds to the fractional volumetric bedload solid discharge per unit of width without pores of the i^{th} size fraction, $\epsilon_0 = (1 - P_0)$ with P_0 the bed porosity, α is the angle between the bedload and the x-axis direction and α_i the angle between the transport rate of the i^{th} size fraction and the x-axis direction. In the current model, the vertical sorting of sediment is made possible by discretizing the substrate into several sublayers [Blom, 2008], where the fraction volume content of i^{th} size fraction of sediment in the k^{th} sublayer is denoted $F_{k,i}$. The implementation of the above equation requires the specification of the active layer and the sublayer thicknesses, the interfacial exchange fractions and the number of sublayers [Viparelli et al., 2017]. Vertical fluxes of sediment are computed following the formulation of Hirano [1971]:

$$\mathcal{F}_{a:1,i} = \begin{cases} F_{a,i} & \text{if } \partial_t z_b > 0 \\ F_{1,i} & \text{if } \partial_t z_b < 0 \end{cases} \ , \tag{2.15}$$

where $F_{1,i}$ corresponds to the fraction volume content of i^{th} size fraction of sediment in the first sublayer.

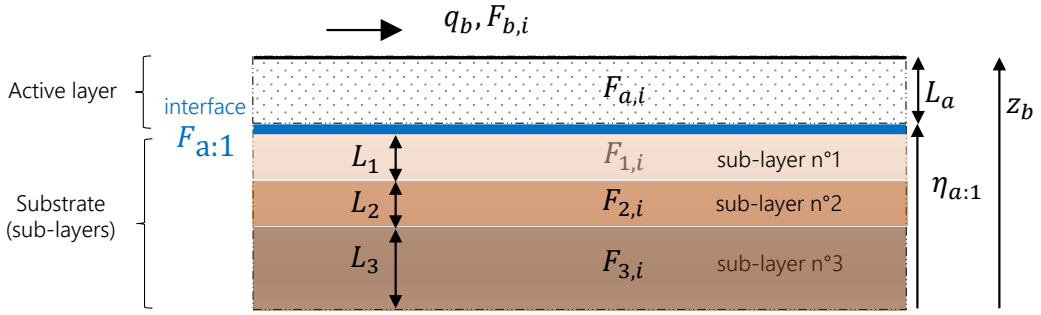


Figure 2.5: Discretization of the vertical bed structure into the active layer and substrate according to the mathematical concept of Hirano [1972], and discretization of the substrate into multiple sub-layers following the bookkeeping layer concept [Blom, 2008; Viparelli et al., 2010].

2.2.2.3 Implementation of the bookkeeping active layer model

The new algorithm developed in this work provides several advantages (simplicity, robustness) to simulate the vertical sorting of sediment, with respect to the one existing in the TMS originally developed by De Linares [2007]. The most significant difference between this new algorithm and the one already available in the TMS is based on the management of the sediment layer thicknesses. The model of De Linares [2007] assumes that the *active* layer and the *second* (or first substrate) layer thicknesses are variable in time, while only the *deepest* layer thicknesses is dynamic in the new algorithm (Figures D.1 and 2.6). In this model, if the sediment column is thick enough, the thickness of the various layers is voluntarily kept fixed, and the all layer structure is translated up in the case of aggradation, or down in the case of degradation (Figure 2.6). In this case, the volume fraction content of sediment in each layer is updated at each time-step of the numerical computation. The new module is also developed to solve the previous stability problems encountered with the one of De Linares [2007] at transitions between erodible and rigid beds addressed by Reisenbüchler et al. [2016].

Numerical procedure

At each computational node in the domain, computation of sediment layer thicknesses and transfer of sediment mass trough these layers is performed numerically as follows:

1. Initialization of variables (accounting for user parameterization):
   (a) Two variables denoted N_{fill} and N_{newlay} are defined and initialized. N_{fill} corresponds to the number of layers which contain sediment at time $t + \Delta t$. N_{newlay} corresponds to the difference of number of layers filled with sediment between time $t + \Delta t$ and t, respectively.
   (b) The layer thicknesses at the previous computational time-step denoted t are stored in the variable `ES_OLD` (vector type which dimension depends on the number of layers used for the simulation and is initially defined by the user).

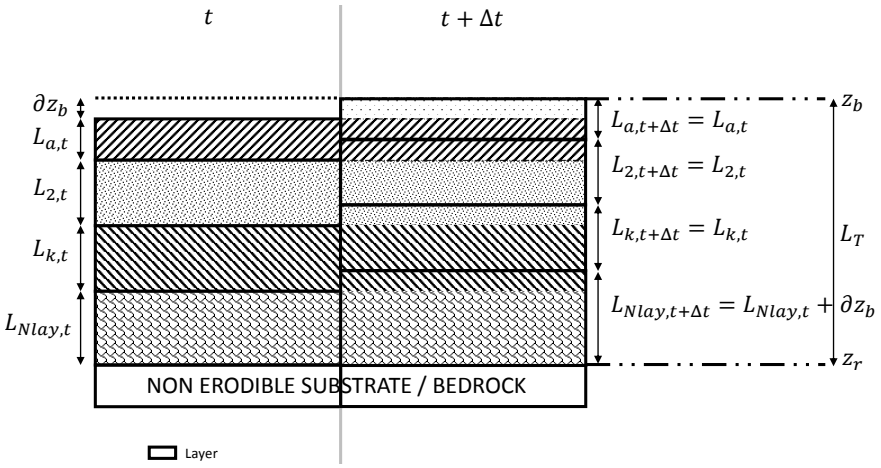


Figure 2.6: Illustrations of variables used in the case of deposition, according to the new model where L_a is always constant excepted from the case where it corresponds to the only layer containing sediment.

(c) The active layer thickness $L_{a,t+\Delta t}$ and sub-layer thicknesses are set as constant during all the simulation.

2. Computation of sediment column at $t + \Delta t$, update of the number and the thickness of sediment layers and computation of N_{fill} and N_{newlay}.

3. Computation of sediment fractions at $t + \Delta t$:

   (a) Calculation of bed evolution, the code stops if changes are larger than the user defined active layer thickness to ensure numerical stability.

   (b) The fractions are computed for bed aggradation (deposition). The update is made firstly for the deepest filled layer, then for the layers above the deepest filled layer. Errors of truncation are avoided in lines 82→85.

   (c) The fractions are computed for bed degradation (erosion). The update is made only if there is still sediment at time $t + \Delta t$. The volume fraction content of sediment in the active layer is firstly computed. Then, the volume fraction contents are updated for the underneath layers. Errors of truncation are avoided in lines 107→110.

   (d) If there is no erosion or no deposition, the fractions remain unchanged.

4. The sediment mass is computed for each size fraction of sediment.

Variables used in the model

$d_{s,m}$	▷ Median (mean) grain diameter (also referred to as d_{50}) at time $t + \Delta t$ [m]
Δt	▷ Time step duration [s]
$F_{a,i,t}$	▷ Fraction volume content of i-*th* sediment class in the active layer
$F_{k,i,t}$	▷ Fraction volume content of i-*th* sediment class in the k-*th* layer
L_a	▷ Active layer maximal thickness at time $t + \Delta t$ [m]
$L_{a,t}$	▷ Active layer thickness at previous time step [m]
$L_{a,t+\Delta t}$	▷ New active layer thickness [m]
L_k	▷ Maximal thickness of the k-*th* layer [m]
$L_{k,t}$	▷ k-*th* substrate layer thickness at previous time step [m]
$L_{k,t+\Delta t}$	▷ New k-*th* substrate layer thickness [m]
L_T	▷ Erodible thickness of sediments equal to $z_b - z_r$ [m]
N_{lay}	▷ Number of layers used for the computation (= remain constant)
N_{fill}	▷ Number of layers containing sediment at time $t + \Delta t$
N_{newlay}	▷ =-1 if a layer is deleted; =0 if same number of layers containing sediment; =1 if a new layer is used
∂z_b	▷ Evolution of the riverbed during Δt [m]
$\partial z_{b,i}$	▷ Evolution of the riverbed during Δt for i-*th* size class of sediment [m]
z_b	▷ Absolute elevation of the riverbed topography at time $t + \Delta t$ [m]
z_r	▷ Absolute elevation of the non-erodible layer at time $t + \Delta t$ [m]
`ES_OLD`	▷ Layers thickness at previous time step
`FRACT`	▷ Variable used to compute the thickness of exchanged sediment during aggradation from above to the layer of interest
`NSICLA`	▷ Number of size classes of sediment
`NPOIN`	▷ Number of computational nodes
`PLANTE`	▷ Bad termination of computation
`REST`	▷ Variable used to compute layers thicknesses
`THICK`	▷ Variable used to compute the thickness of exchanged sediment during aggradation from the layer of interest to a deeper layer
`ZERO`	▷ Definition of a numerical zero

The `Fortran` code is available in Appendix E. The pseudo code used in the new algorithm is presented below:

Pseudo-code of the new algorithm in Sisyphe V7P3 (1/4)

▷ **I Initialization of variables and user parameterization**

▷ **I.1 Data Initialization**

`ZERO = 0.D0` ▷ Zero machine

$N_{fill} = 0$ ▷ Initialization number of layers containing sediment

$N_{newlay} = 0$ ▷ Initialization number of layers created/suppressed from Δt to $\Delta t + \Delta t$

for `j=1,NPOIN` **do** ▷ Note: All variables below are dependent of the node `j`

  $N_{fill} = 0$ ▷ Re-initialization number of layers filled with sediment

  $N_{newlay} = 0$ ▷ Re-initialization number of layers created/suppressed from Δt to $\Delta t + \Delta t$

▷ **I.2 Storage of previous layers thicknesses**

  for `k=1,`N_{lay} **do**

    `ES_OLD(k)=`$L_{k,t}$ ▷ Thickness of the layer k at previous time-step

    if ES_OLD(k)>ZERO **then**

      $N_{newlay} = N_{newlay} - 1$ ▷ If kth layer contains sediment, decrement of N_{newlay}

    end if

  end for

▷ **I.3 User defined maximal thicknesses of sediment layers**

  L_a =`ELAY0` ▷ Maximal active layer thickness (user defined)

  for `k=2,`N_{lay} **do**

    $L_k = 1 \cdot$`ELAY0` ▷ Maximal kth layer thickness (user defined)

  end for

▷ **II Update the number and the thickness of sediment layers**

  $L_T = z_b - z_r$ ▷ Thickness of the sediment column

  if $N_{lay} = 1$ **then** ▷ If only one layer used in the model

    $L_{a,t+\Delta t} = \max(0, L_T)$

  else ▷ If two or more layers used in the model

    $L_{a,t+\Delta t} = \min(L_a, \max(0, L_T))$

    `REST=`$L_T - L_{a,t+\Delta t}$ ▷ Sediment column thickness below the active layer

    for `k=2,`$N_{lay} - 1$ **do**

      $L_{k,t+\Delta t} = \min(L_k, \max(0,$ `REST`$))$ ▷ Computation of kth layer thickness

      `REST=`$\max(0,$ `REST-`$L_{k,t+\Delta t})$ ▷ Sediment column thickness below the kth layer

    end for

    $L_{N_{lay},t+\Delta t} = \max(0,$ `REST`$)$ ▷ Thickness of the deepest layer

  end if

Pseudo-code of the new algorithm in Sisyphe V7P3 (2/4)

for k=1 , N_{lay} **do**
  if $L_{k,t+\Delta t}$ >ZERO **then** ▷ If kth layer contains sediment
    $N_{newlay} = N_{newlay} + 1$ ▷ Increment the number of layers containing sediment
    $N_{fill} = N_{fill} + 1$ ▷ Increment the number of layers created/suppressed from Δt to $\Delta t + \Delta t$
  end if
end for
▷ Note: Between t and $t + \Delta t$: $N_{fill} = 0$ if same number of layers, $N_{fill} = 1$ if a new layer receives sediment, $N_{fill} = -1$ if a layer becomes empty

▷ **III Update of sediment fractions**

▷ **III.1 Temporal bed elevation change**
$\partial z_b = 0$
for I=1,NSICLA **do** ▷ Total bed evolution during Δt
  $\partial z_b = \partial z_b + \partial z_{b,i}$
end for

if $|\partial z_b| > L_a$ **then** ▷ Plante if evolution greater than L_a for numerical stability
  PLANTE
end if

if $t \neq 0$ s **then** ▷ Fractions are not updated for the first time-step of simulation

▷ **III.2 Update of fractions for aggradation (deposition)**
  if $\partial z_b > 0$ **then** ▷ If aggradation
    for I=1,NSICLA **do** ▷ Update of fractions for each size fraction

▷ **III.2.1 Deepest filled layer**
      if $N_{fill} \leq 1$ **then** ▷ If aggradation
        FRACT=$\partial z_{b,i}$ ▷ If there is only the active layer at $t + \Delta t$
      else
        FRACT=$F_{N_{fill}-1,i} * \partial z_b$ ▷ If there is at least two layers at $t + \Delta t$
      end if
      if $N_{newlay} = 0$ **then** ▷ If same number of filled layers between t and $t + \Delta t$
        $F_{N_{fill},i,t+\Delta t} = \frac{(L_{N_{fill},t} * F_{N_{fill},t} + \texttt{FRACT})}{L_{N_{fill},t+\Delta t}}$
      else ▷ If a new layer is filled between t and $t + \Delta t$
        $F_{N_{fill},i,t+\Delta t} = \frac{\texttt{FRACT}}{\partial z_b}$
      end if

Pseudo-code of the new algorithm in Sisyphe V7P3 (3/4)

▷ **III.2.2 Layers above the deepest filled layer**
if $N_{fill} > 1$ **then** ▷ If 2 or more layers
if $N_{newlay} = 0$ **then** ▷ If same number of filled layers between t and $t + \Delta t$
THICK=$L_{N_{fill-1},t} - \partial z_b$
else ▷ If a new layer is filled between t and $t + \Delta t$
THICK=$L_{N_{fill-1},t} - L_{N_{fill},t+\Delta t}$
end if
for k=NFILL-1,1,-1 **do**
if k=1 **then** ▷ If it is the active layer
FRACT=$\partial z_{b,i}$
else ▷ If it is a sub-layer
FRACT=$F_{k-1,i,t} * \partial z_b$
end if
$F_{k,i,t+\Delta t} = \frac{\text{THICK}*F_{k,i,t}+\text{FRAC}}{L_{k,t}}$
end for
end if
for k=1,N_{lay} **do** ▷ Truncation of volume fractions of sediment
$F_{k,i,t+\Delta t} = \max(F_{k,i,t+\Delta t}, \text{ZERO})$
$F_{k,i,t+\Delta t} = \min(F_{k,i,t+\Delta t}, 1 - \text{ZERO})$
end for
end for

▷ **III.3 Update if fractions for degradation (erosion)**
else if $\partial z_b < 0$ **then** ▷ If degradation
for I=1,NSICLA **do** ▷ Update of fractions for each size fraction

if $N_{fill} > 0$ **then** ▷ **If there is still sediment at time** $t + \Delta t$

if $N_{fill} = 1$ **then** ▷ **III.3.1.a If only the active layer is filled at time** $t + \Delta t$

if $N_{newlay} = 0$ **then** ▷ If same number of filled layers between t and $t + \Delta t$
$F_{a,i,t+\Delta t} = \frac{F_{a,i,t}*L_{a,t}+\partial z_{b,i}}{L_{a,t+\Delta t}}$
else ▷ If a new layer is filled between t and $t + \Delta t$
$F_{a,i,t+\Delta t} = \frac{F_{a,i,t}*L_{a,t}+F_{2,i,t}*L_{2,t}+\partial z_{b,i}}{L_{a,t+\Delta t}}$
end if
else ▷ **III.3.1.b If two or more layers are filled at time** $t + \Delta t$
$F_{a,i,t+\Delta t} = \frac{F_{a,i,t}*L_{a,t}-F_{2,i,t}*\partial z_b+\partial z_{b,i}}{L_{a,t+\Delta t}}$
end if

Pseudo-code of the new algorithm in Sisyphe V7P3 (4/4)

99: **if** $\boxed{N_{fill} > 2}$ **then** ▷ **III.3.2 If more than 2 layers filled at time $t + \Delta t$**
100: **for** k=2 , $N_{fill} - 1$ **do** ▷ Layers between the active and deepest filled layer
101: $F_{k,i,t+\Delta t} = \frac{F_{k,i,t} * (L_{k,t} + \partial z_b) - F_{k+1,i,t} * \partial z_b}{L_{k,t+\Delta t}}$
102: **end for**
103: **end if**
104: $F_{N_{fill},i,t+\Delta t} = F_{N_{fill},i,t}$ ▷ Fraction in the deepest filled layer
105: **end if**
106: **for** k=1 , N_{lay} **do** ▷ Truncation of volume fractions of sediment
107: $F_{k,i,t+\Delta t} = \max(F_{k,i,t+\Delta t}, \texttt{ZERO})$
108: $F_{k,i,t+\Delta t} = \min(F_{k,i,t+\Delta t}, 1 - \texttt{ZERO})$
109: **end for**
110: **end for**
111: ▷ **III.4 No update of fractions if no evolution**
112: **else**
113: ▷ Nothing is done
114: **end if**
115: ▷ **III.5 Fractions of sediment set to 0 if no sediment at time $t + \Delta t$**
116: **if** $\boxed{L_{N_{lay}} \leq 0}$ **then** ▷ If the deepest layer is empty
117: **for** k=$N_{fill} + 1, N_{lay}$ **do**
118: **for** I=1 , NSICLA **do** ▷ For each size fraction
119: $F_{k,i,t+\Delta t} = 0$
120: **end for**
121: **end for**
122: **end if**
123: **end if** ▷ end if $\boxed{t = 0\,\text{s}}$
124: **end for** ▷ end loop on computational nodes
125: ▷ **IV. Computation of the total volume of sediments in the domain**
126: Other operations ▷ Computation of the total volume of sediment in the domain

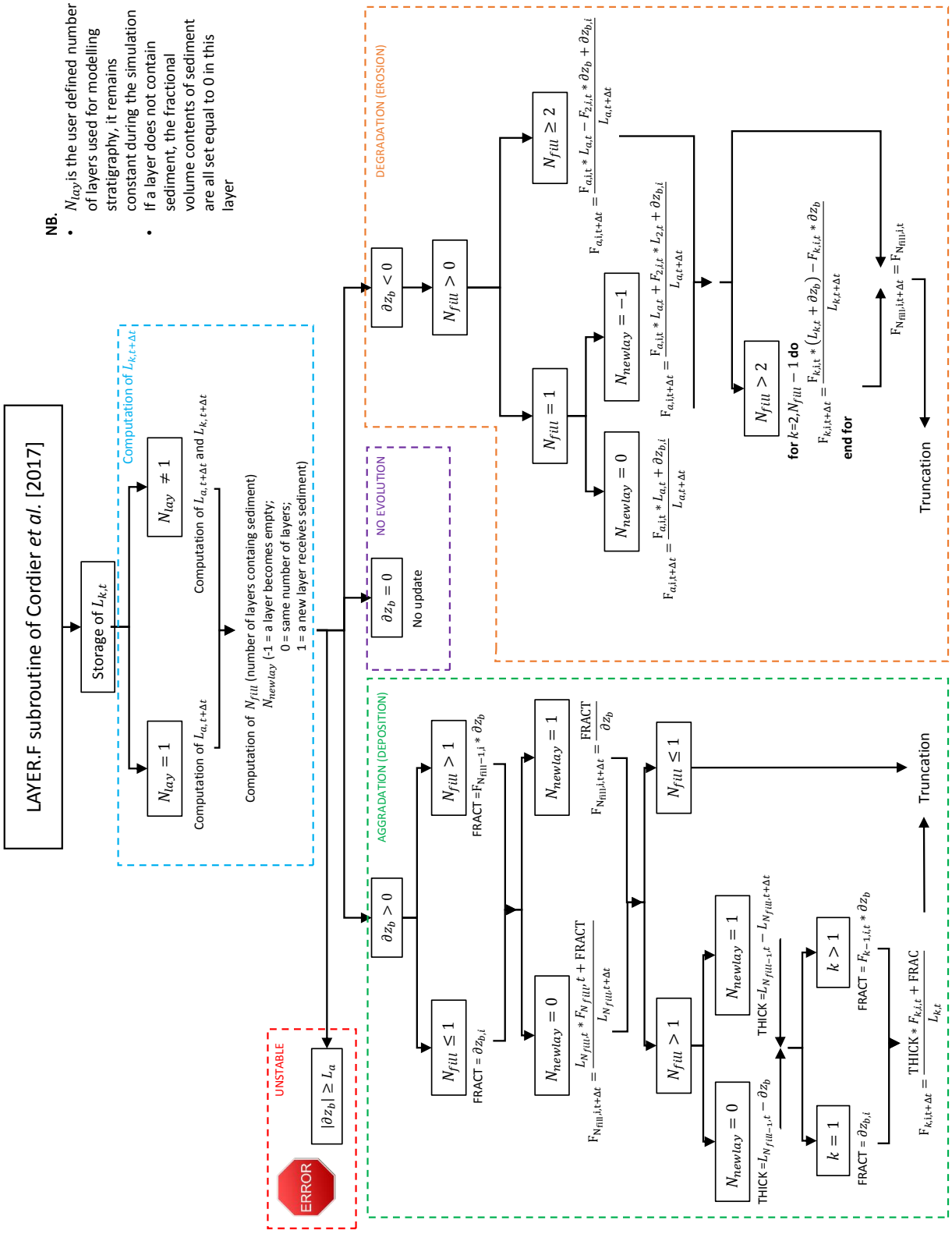


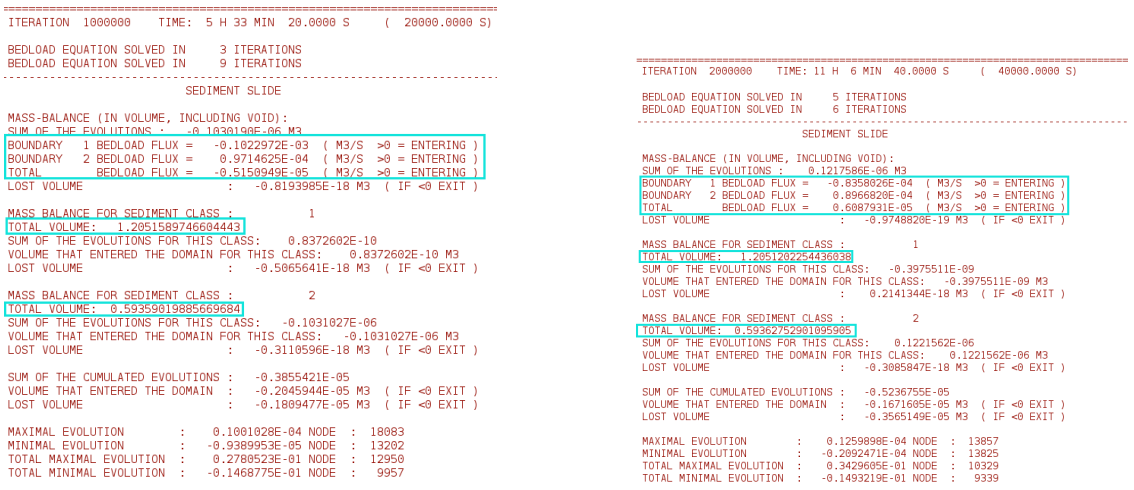
Figure 2.7: Flowchart of the new algorithm based on the bookkeeping active layer model of Hirano [Hirano, 1971] developed in the purpose of this work in TMS V7P3.

2.2.2.4 Validation and practical use of the code

The new algorithm developed in this work has been firstly subject to a multitude of basic numerical tests using one to ten sediment layers, to ensure the model robustness and the property of sediment mass conservation. These basic tests are not presented here because they can be easily replicated and are not necessary for the discussion.

Secondly, the implemented model is tested and validated on the basis of the experiment of Lanzoni [2000b]. Figure 2.3 shows that bed evolution and spatial sorting of sediment is well reproduced with this new algorithm, with respect the ones obtained in P2009 laboratory experiment. This illustrates that the bookkeeping active layer model and the numerical algorithm implemented in the morphodynamic module of TMS can reproduce accurately spatial and vertical sorting of non-uniform sediment, at least under the configurations of interest.

In order to test the model robustness at local transitions between an erodible and a rigid bed, a numerical scenario derived from the reference scenario (where the later is referred to as run P2009-1 in Chapter 4) is considered, where the initial sediment column is reduced to 1 cm everywhere in the channel. The simulation is ran from $t = 0$ to $t = 20,000$ s, then it is ran again from $t = 20,000$ s until $t = 40,000$ s in order to verify that the new algorithm is compatible with the continuation of a previous morphodynamic simulation. The total and fractional sediment balances are checked at the end of the simulation (i.e. at $t = 40,000$ s) with the the command-line interface (Figure 2.8) and with computing the volume of bed evolution from the binary results file generated by the TMS (Figure 2.9).



(a) (b)

Figure 2.8: Computation of the sediment balance at a) $t = 10$ s and b) $t = 40,000$ s, with the scenario used to test transitions between erodible and rigid bed, showing that sediment recirculation and the new algorithm for vertical sediment sorting are well implemented in the TMS.

In comparison with the original algorithm developed in TMS [De Linares, 2007], the algorithm developed in this work provides a simpler management of the sediment layers thicknesses, and a simpler method to update the fractional volume contents of sediment at each time-step. This algorithm is particularly robust as it can be used under various situations of bed aggradation and degradation, allowing for transitions between an erodible bed and a rigid bed, under simple and more complex configurations. The actual version of this algorithm is compatible

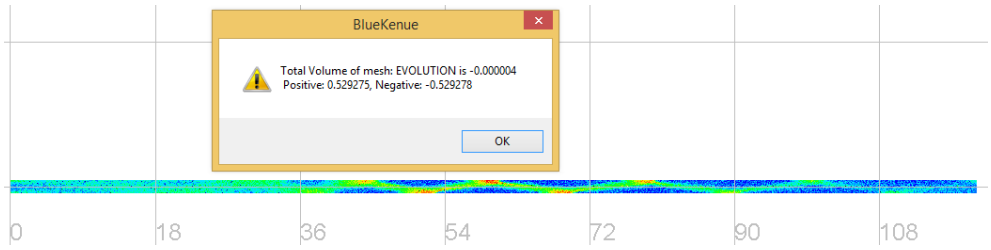


Figure 2.9: Computation of the sediment balance at $t = 40,000$ s with the scenario used to test transitions between erodible and rigid bed, showing that sediment recirculation and the new algorithm for vertical sediment sorting are well implemented in the TMS.

with a constant (over time) user-defined active layer thickness and sub-layer thicknesses.

2.2.3 Implementation of sediment recirculation

2.2.3.1 Motivations for implementing sediment recirculation

Laboratory experiments of sediment transport measurement [e.g. Parker and Wilcock, 1993; Wilcock and McArdell, 1993; Wilcock and Crowe, 2003] and channel morphodynamics with dunes and bars [e.g. Lanzoni, 2000a,b; Kleinhans, 2004; Crosato et al., 2012] often rely on the use of sediment recirculating straight flumes. In laboratory, different arrangements can be used for recirculating the water and the sediment [Southard, 2006]. The upstream water discharge, the downstream water depth and the initial longitudinal bed slope are specified and uniform flow can be maintained [Kleinhans, 2004]. In a sediment recirculating flume, the boundary condition for sediment supply is periodical, so that the recirculating flume has an additional degree of freedom in the system [Kleinhans, 2004]. Using a recirculating flume instead of a feeding flume generally lead to a distinct morphodynamic equilibrium when graded sediment is used [Parker and Wilcock, 1993; Wilcock and McArdell, 1993; Wilcock and Crowe, 2003; Kleinhans, 2004]. Indeed, in the beginning of the experiments with a feeding flume presenting a mild slopping bed, fine sediment is more mobilized than coarser sediment, leading to deposition of coarse sediment upstream and progressive increase of fine sediment content downstream, called downstream fining [Hoey and Ferguson, 1994; Seal et al., 1997; Toro-Escobar et al., 2000]. At equilibrium, the sediment feeding flume is forced to transport the same rate of coarse sediment than the input rate to follow the equal mobility condition. This equilibrium condition can be only reached by an adjustment of the longitudinal bed slope, which increases in order to increase bed shear stress and mobilize the coarsest sediment. On the other hand, the results can be strongly different with using a sediment recirculating flume with the same initial conditions and hydraulic boundaries. In the beginning of the experiments, only the fine fraction of sediment is mobilized and migrates out of the flume, before being re-injected upstream. In this case, the coarse sediment can form an immobile layer referred to as lag deposit [Kleinhans, 2004]. As a result, this condition deviates strongly from the hypothesis of equal mobility, with respect to the sediment feeding experiment. The longitudinal equilibrium bed slope is found less modified in comparison with the sediment feeding experiment and the bed shear stress is averagely lower.

Accounting for sediment recirculation is necessary in this work because the laboratory experiments of Lanzoni [2000a,b] were all conducted in a sediment recirculating flume and observations made on the equilibrium morphodynamic response of the channel bed.

2.2.3.2 Implementation of sediment recirculation

The procedure consists on computing the solid transport rates exiting the downstream boundary at the previous time step of computation for each size fraction of sediment (Figure 2.10), and redistributing the same volume of sediment at each upstream computational node, i.e. uniformly/equally along the upstream boundary. As a result, given this boundary condition, the bed topography varies depending on the amount of injected sediment. Because the algorithm modifications are obvious, the Fortran code is directly given in Appendix F.

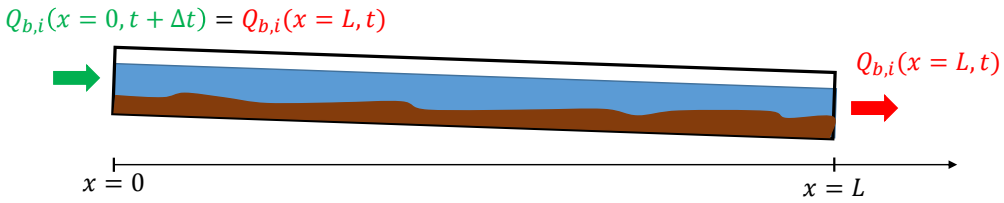


Figure 2.10: Scheme of the method used to recirculate the sediment in the model channel.

2.2.3.3 Validation and practical use of the code

Implementation of sediment recirculation in the TMS was originally performed by Mendoza et al. [2016] in the version 6.2 and was compatible with the transport of uniform sediment (i.e. compatible for a single sediment size fraction only). In the purpose of this work, recirculation of sediment has been integrated in the version 7.3 of the TMS in order to reproduce Lanzoni's laboratory experiments. The code has been updated to support parallelization to be used on HPC clusters (Appendix G) and to account for the recirculation of non-uniform sediment. The code has been validated using the reference cases based on the uniform and non-uniform sediment experiments of Lanzoni (Chapters 3 and 4), and is showed to be compatible with the other code implementations developed in this study where the sediment mass continuity is ensured in the system (Figure 2.2, 2.8 and 2.9).

Nomenclature

b_i Power coefficient of the hiding-exposure function of i^{th} size fraction [-]
C Chézy coefficient [$m^{1/2}/s$]
C_f Equivalent Chézy coefficient due to form drag and skin friction [-]
C'_f Equivalent Chézy coefficient due to skin friction only [-]
d_i Representative diameter of the i^{th} size fraction [m]
$d_{s,m}$ Median sediment diameter of surface [m]
d_X X^{th} centile of the GSD [m]
f Similarity collapse function independent of grain size
$\mathcal{F}_{a:1,i}$ Fraction volume content of i^{th} size fraction in the interface [-]
$F_{k,i}$ Fraction volume content of i^{th} size fraction in layer k [-]
F_s Fraction volume content of sand at the bed surface [-]
g Acceleration due to gravity (=9.81) [m/s^2]
h Water depth [m]
k_s Bed roughness height [m]
L_a Active layer thickness [m]
P_0 Bed porosity [-]
q_b Magnitude of bedload transport rate [m^2/s]
$\vec{q_b} = (q_{b,x}, q_{b,y})$ Vector of bedload transport rate [m^2/s]
q_{b0} Magnitude of bedload transport rate without gravitational effects [m^2/s]
$\vec{q_{b0}}$ Vector of bedload transport rate without gravitational effects [m^2/s]
$q_{b,i}$ Magnitude of fractional transport rate of i^{th} size fraction [m^2/s]
$\vec{q_{b,i}} = (q_{b,i,x}, q_{b,i,y})$ Vector of fractional transport rate of i^{th} size fraction [m^2/s]
$q_{b,i,n}$ Magnitude of normal fractional transport rate of i^{th} size fraction [m^2/s]
$q_{b,i,s}$ Magnitude of stream-wise fractional transport rate of i^{th} size fraction [m^2/s]
s Coordinate in the current direction [-]
$\vec{u} = (u, v)$ Flow velocity vector [m/s]
u, v Depth averaged velocity components along x- and y-axis [m/s]
s Coordinate in the current direction [-]
$\vec{S_f} = (S_{f,x}, S_{f,y})$ Friction law vector [-]
t Physical time [s]
α_b Coefficient used to calibrate the sediment transport capacity [-]
α_i Angle between the vector of fractional transport and x-axis [-]
$\alpha_{k,s}$ Calibration parameter [-]
β_1 Koch and Flosktra's empirical factor for bed slope effects magnitude [-]
β_2 Talmon's *et al.* empirical factor for bed slope effects deviation [-]
δ Angle between bottom shear stress and the flow direction [-]
Δ_s Relative submerged sediment density [-]
Δt Computational time-step [s]
Δz_b Evolution of the bed topography with respect to the initial bed elevation [m]
ϵ_0 Percentage of volumetric matter without voids [-]
$\eta_{a:1}$ Absolute elevation of the interface [m]
κ Constant of von Kármán (=0.40) [-]
μ Skin friction coefficient [-]

∇ Gradient vector field [1/m]
ν_t Turbulent eddy viscosity term [m^2/s]
$\partial_{x_2} x_1$ Partial derivative of the quantity x_1 in x_2 [x_2/x_1]
Φ_i Ratio of bed shear stress over reference shear stress of i^{th} size fraction [-]
ρ Water density [kg/m^3]
τ Total shear stress [Pa]
τ_b Bed shear stress [Pa]
$\tau^*_{b,i}$ Shear stress adimensionnalized by the i^{th} fraction [-]
$\tau_{r,i}$ Reference shear stress of the i^{th} size fraction [Pa]
$\tau_{r,m}$ Reference median shear stress of bed surface [Pa]

▷ Synthesis on the model set-up and numerical developments

A better understanding of the interactions between non-uniform sediment and bar morphodynamics in fluvial systems motivated for the numerical developments presented in this report. Up to now, the bedload formulations available in the TMS remained limited with respect to other formulas found in the literature, and the model of vertical sediment sorting available in the TMS suffered from a lack of consistency, robustness, and was even difficult to handle under certain situations. Several developments have been implemented here in order to reproduce in a more physical relevant way the phenomenons observed in flume experiments, and later for the purpose of modelling bar morphodynamics in real rivers.

Firstly, the formula of Wilcock and Crowe [2003] is implemented and validated by comparing the results obtained from the numerical model and from the analytical model. The formula is then considered for the estimation of sediment transport under the laboratory experiment P2009 of Lanzoni [2000b] and later in a study reach of the Loire river.

Secondly, the new algorithm developed in this work for the vertical sorting of sediment is tested and validated on the experiment P2009, and on a varied case of this experiment were we reduce the sediment column to 1 cm everywhere, in order to test the model robustness at transitions between an erodible and a rigid bed. The new algorithm reproduces well the bar characteristics and the sediment sorting pattern observed over bars with respect to laboratory observations. This code also provides a simpler management of the layers thicknesses and a more relevant method to compute the fractional volume contents of sediment with respect to the previous version available in the TMS. This algorithm is robust as it can be used under various situations of bed aggradation and degradation (at least under the configurations tested in this work), and allows for transitions between an erodible bed and a rigid bed. The current version of this algorithm works for constant (over time) user-defined active layer and sub-layer thicknesses, and do not allow for a dynamic evolution of the active layer thickness over time.

Finally, the recirculation of sediment is implemented and validated in the TMS with using the experiment of Lanzoni [2000b]. For each size fraction of sediment, the procedure redistributes the amount of sediment exiting the flume at time t on the upstream computational nodes at time $t + \Delta t$. The same volume of sediment is injected at each upstream node.

□ Synthèse générale sur le choix, le développement et la validation du modèle numérique

Les divers développements nécessaires à la bonne prise en compte des processus liés à la non-uniformité des sédiments ont pu être apportés dans le système de modélisation Telemac-Mascaret. L'implémentation d'une formule de transport solide pour le charriage d'un mélange de sables et de graviers, d'un modèle de tri granulométrique vertical basé sur le concept de la couche active et de conditions aux limites adéquates ont été testés et validés sur des cas de laboratoire et réels. Les cas de validation permettent notamment d'assurer la robustesse du code numérique, la compatibilité des modules implémentés avec le reste du code et la pertinence –sur le point de vue de la physique- des résultats numériques. Les résultats issus des travaux d'implémentation numérique présentés dans ce chapitre permettent de réconforter le choix des hypothèses de fermeture formulées au travers du modèle numérique, et démontrent par conséquent la possibilité d'utiliser ce modèle morphodynamique pour réaliser des activités de recherche sur la formation et de développement de bancs alluviaux en présence d'une granulométrie non-uniforme.

PART II

ALTERNATE BARS MORPHODYNAMICS WITH NON-UNIFORM SEDIMENT CONSIDERING SIMPLIFIED CONFIGURATIONS

CHAPTER 3

INFLUENCE OF NUMERICAL AND PHYSICAL PARAMETERS ON THE MODELLING OF FREE BAR MORPHODYNAMICS

A part of the work presented in this chapter is published in the
Book of proceedings of the XXVth TELEMAC-MASCARET User Conference, Norwich (UK)
entitled *Influence of numerical and physical parameters on the modelling of free bar morphodynamics*

by
Florian Cordier[1,2], Pablo Tassi[1,2] and Nicolas Claude[2]
[1]Laboratoire d'Hydraulique Saint-Venant (Chatou, France)
[2]EDF R&D LNHE - Laboratoire National d'Hydraulique et Environnement (Chatou, France)

Corresponding author: florian.cordier@edf.fr

▷ Motivations and objectives of this study

The work presented in this chapter aims to better understand the relative importance and the influence of the numerical and physical parameters on the numerical modelling of free bars morphodynamics.

To further this goal, the numerical model presented in Chapter 2 is firstly used to reproduce a laboratory experiment of free bar formation in a -idealized- straight channel with fixed sidewalls considering uniform sediment [Lanzoni, 2000a]. Systematical sensitivity analyses on numerical and physical parameters are conducted on the basis of the calibrated scenario used as reference, from which other scenarios are derived. These analyses are particularly useful to study not only the model behavior but also the potential model limitations that could exist.

Then, in a second time, the degree of complexity is increased where non-uniform sediment processes are accounted. A multitude of sensitivity analyses are considered, where the parameters of interest are specific to the modelling of non-uniform sediment processes such as the sediment layer thicknesses. The general outcomes from these analyses will be useful to validate and know the limits of the multiple assumptions (i.e. formula of WC-2003 and active layer model, see Chapter 2) chosen for the numerical modelling of bars with non-uniform sediment, considering simple geometry and well controlled boundary forcings.

Keypoints

- A thorough analysis is conducted on the influence of numerical and physical parameters on the modelling of free bar morphodynamics
- Results show that physical and numerical parameters have to be chosen carefully to model relevantly free bars
- Outcomes can be useful for modellers who are interested in management or restoration of straight/weakly-curved channels

Abstract

Periodic bars are a common feature of rivers and are large sediment deposits alternating with deeper areas (pools) that arise from an instability phenomenon of the alluvial bed. A deep knowledge of bar processes is important for river engineers and river managers, because bars strongly alter the river bed topography and influence bank erosion, with consequences for navigation, water intakes and infrastructure. This work aims at setting-up a 2D morphodynamic model able to reproduce laboratory experiments of free bar formation with uniform and non-uniform sediment. To reach this goal, we investigate the impact of the numerical solution and physical parameters on the computed bar morphology and characteristics. Numerical results show that the domain discretization influences the propagation of the perturbation at the origin of free bar formation, where a finer computational mesh reduces the perturbation growth. Model convergence is attained with CFL values less or equal to 0.2. The use of two distinct morphodynamic boundary conditions shows that boundaries influence the computed bar dynamics. Slope effects due to deviation are necessary to trigger free bar formation, and their parameterization impacts their properties. The formulation for skin friction correction also strongly modify free bars morphology. With non-uniform sediment, hiding-exposure effects are showed to be necessary to obtain a relevant sediment sorting over free bars. Results show that increasing sediment layers thicknesses slows down the process of sediment sorting with respect to bed evolution. Too thick layers lead to irrelevant computed sediment sorting pattern, for the same reason as mentioned before. Outcome of this study would help modellers to choose the correct set of numerical and physical parameters to model relevantly bars morphodynamics.

3.1 Introduction

Rivers often present a wavy bed due to the presence of periodic bars, which are large sediment deposits alternating with deeper areas (pools) that arise from an instability phenomenon of the alluvial bed. A deep knowledge of bar processes is important for river engineers and river managers, because bars strongly alter the river bed topography and influence bank erosion, with consequences for navigation, water intakes and infrastructure.

Numerous studies [Engelund, 1970; Colombini et al., 1987; Lanzoni and Tubino, 1999; Crosato and Mosselman, 2009] have shown that the formation and the geometry of bars in straight or weakly curved channels are primarily governed by the width-to-depth ratio of the flow, also known as "aspect ratio". At unstable conditions, starting from a flat bed, incipient bars tend to increase in size, eventually reaching a steady value of amplitude and wavelength [Fujita and Muramoto, 1985] which scales with the water depth and the channel width, respectively. The

commonly accepted definition for free bars is that they originate purely from morphodynamic instability, and migrate either in downstream or upstream direction, depending on river bar regime, with zero celerity at resonance conditions [Zolezzi and Seminara, 2001]. Free bar formation and propagation have been subject of extensive theoretical, experimental and numerical investigations in the past decades, with assuming uniform and later non-uniform grain size distributions [Siviglia et al., 2013; Cordier et al., 2019].

Nowadays, the increasing confidence given on the numerical modelling approach is explained by the continuous development of knowledge and computer technology, which allows to investigate physical problems with increasing the level of detail as well as the spatial extent and time scales Mosselman [2012]. As a result, numerical morphodynamic models are widely used for different purposes, from the basic morphodynamic research to dealing with complex river engineering problems [Siviglia and Crosato, 2016]. However, numerical modelling of fluvial morphodynamics, which includes the processes bar formation and propagation, is far from being a solved issue and still involves many challenges [Siviglia and Crosato, 2016].

Numerical and physical parameters can potentially control the computed free bar morphology and characteristics. The role of the computational domain discretization on the initiation of bed topographic perturbations and bar formation has been seldom explored. According to Schuurman and Kleinhans [2011], the large-scale characteristics of the bar pattern in a self-forming braided river are independent of the computational mesh resolution, where a finer mesh better describes the bar topography. Morphodynamic models often implement equilibrium boundary condition for sediment supply [Defina, 2003; Qian et al., 2016], but only few studies considered other boundary conditions such as sediment recirculation to study bar formation [Mendoza et al., 2016]. The influence of the bottom topographic perturbations set as initial conditions in numerical models on the initiation of free bars remains shortly understood [Defina, 2003]. The importance of accounting for gravity effects due to transverse bed slopes for computing bedload transport rates has been put in evidence in theoretical frameworks [Struiksma and Crosato, 1989; Crosato and Mosselman, 2009]. Nevertheless, parameterization of the slope effects on numerical models not only increases numerical diffusion and may smooths results [Siviglia et al., 2013], but also remains generally a work of calibration, where the interval chosen for calibrating the empirical values is not necessarily justified Schuurman and Kleinhans [2011]; Nelson et al. [2015a]; Cordier et al. [2016b]. For the same reasons, parameterization of the turbulence model could potentially play a role on the computed bar characteristics. Spatial roughness variations induced by the interactions between bed-forms of different origins and scale (i.e. grain roughness, ripples, dunes and bars) are often parameterized using a skin friction correction formulation [Mendoza et al., 2016]. The impact of using such formulation on free bar development deserves more attention.

The non-uniformity in sediment size, which is a common feature of sandy-gravel and gravel bed rivers, controls sediment mobility. Interactions between fine and coarse sediment correspond to the *hiding-exposure* effect, which is manifested by the nature of coarse grains to hide finer grains in their interstices [Parker and Klingeman, 1982]. While the gravitational effects make the larger particles harder to move, the hiding effects tends to counterbalance this phenomenon by increasing coarse grain mobility and decreasing the mobility of fine grains. Today, these formulations are commonly used in numerical modelling of non-uniform sediment processes [Singh et al., 2017], but the importance of accounting for hiding-exposure effects on the modelling of free bars has not been addressed yet. The modelling of vertical sediment sorting often relies on the active layer concept, which requires the specification of the active layer and sub-layers thicknesses [Viparelli et al., 2017; Church and Haschenburger, 2017]. Up to now, the

impact of changing the layers thicknesses on free bar dynamics and obtained sediment sorting remains unexplored.

The objective of this study is twofold. Firstly, this work aims at setting-up a numerical model able to reproduce accurately laboratory experiments of free bar formation and propagation with uniform sediment and non-uniform sediment [Lanzoni, 2000a,b]. Secondly, the authors investigate the impact of the numerical solution and physical parameters on the computed bar morphology and characteristics. The studied scenarios are organized in two major groups, according to the sediment distribution (uniform and non-uniform). For the first group, the influence of the sediment boundary conditions, bed slope effects, skin friction correction and initial bed perturbation is studied and discussed considering uniform sediment distribution. A convergence analysis is also performed to evaluate the impact of the space and time discretization on the numerical results. For the second group, the influence of physical and numerical parameters is investigated to assess the capabilities of the model, considering a non-uniform sediment distribution. To this goal, emphasis is put at analyzing the influence of the closure relationships used to compute the sediment fluxes as well as the vertical discretization of the bed structure, following the active layer concept of Hirano [1971]. The influence of the turbulent eddy viscosity on the numerical results is also presented and discussed. As the heterogeneity of sediment adds a degree of complexity in the numerical modelling of bars morphodynamics, analyses are firstly conducted with using a uniform sediment, and then with considering non-uniform sediment.

A description of the mathematical model (hydrodynamics and morphodynamics) and of the numerical treatment of physical processes is provided in Section 3.2, together with the study case from which numerical scenarios are derived. In Section 3.3, attention is given on the numerical results with uniform sediment. Numerical results obtained with non-uniform sediment are presented in Section 3.4. Outcome of this study presented in Section 3.5 would help modellers to choose the correct set of numerical and physical parameters to set-up (physically and numerically) relevant morphodynamic models in the context of fluvial free bars morphodynamics.

3.2 Materials and methods

3.2.1 Mathematical and numerical model

The two-dimensional morphodynamic model used in this work presents two components: a hydrodynamic module (TELEMAC 2D) and a morphodynamic module (Sisyphe). The hydrodynamic module is based on the solution of the 2-D depth-averaged shallow-water equations (SWE) de Saint-Venant [1871]; Weiyan [1992]; Nezu et al. [1994]; Vreugdenhil [2013], with a closure relationship for the turbulence based on a constant turbulent eddy viscosity ν_t [m^2/s], and the Nikuradse friction law to parameterize roughness effects. that models the so-called Reynold stresses and the differential dispersion terms originated from the lack of vertical uniformity of the horizontal velocity field.

The morphodynamic module is based on the Exner equation [Exner, 1920; García, 2008]. In case of non-uniform sediment, the Exner equation is applied to every size fraction of sediment in which the mixture is subdivided. The following procedure is adopted: *i*) the sediment mixture is discretized into sediment fractions, and for each fraction the representative sediment diameter is given, *ii*) the bedload transport capacity equation and the mass conservation formula are applied for each separate fraction of sediment. The solution for sediment mass conservation is based on

the mathematical concept proposed by Hirano [1971], who developed a continuity model for the vertical sorting of sediment. The method is based on the decomposition of the bed into a homogeneous top layer, called *active layer*, and an unchanging homogeneous *substrate* [Church and Haschenburger, 2017; Ashmore et al., 2018]. Following Hirano [1971]'s concept, the bed is discretized in the vertical direction where $z_b = \eta_{a:1} + L_a$, where $\eta_{a:1}$ [m] denotes the absolute elevation of the interface between the active layer and the substrate, and L_a [m] corresponds to the active layer thickness.

In this work, the sediment transport capacity of uniform sediment q_{b0} [m^2/s] is determined with the formula of Meyer-Peter and Müller (MPM) Meyer-Peter and Müller [1948]. With non-uniform sediment, the sediment transport capacity $q_{b0,i}$ [m^2/s] of the $i-th$ size fraction of sediment is determined with three different formulas, the first without hiding-exposure formulation using MPM, and the other ones with the hiding-exposure formulation of MPM-Egiazaroff [1965] (MPM-E) and of Wilcock and Crowe [2003] (WC-2003). The correction of bedload magnitude to account for the bed slope effects is modelled with the formula of Koch and Flokstra [1980], where the fractional transport rate $q_{b0,i}$ is modified as a function of the bed slope degree with respect to the current direction with $q_{b,i} = q_{b0,i}\left(1 - \beta_1 \partial_s z_b\right) = q_{b0,i}\Big[1 - \beta_1\left(\partial_x z_b \cos\delta + \partial_y z_b \sin\delta\right)\Big]$, where β_1 is an empirical coefficient accounting for the stream-wise bed slope effect, δ is the angle between the current and the x-axis direction, and s the coordinate along the current direction. The bedslope effect is similar to a diffusion term in the bed evolution equation [Van der Meer et al., 2011] and may smooth the bed topography and prevent from numerical instabilities [Zolezzi and Seminara, 2001; Cabrit, 2009]. The correction of bedload direction is given by the relation of Bendegom [1947] with $\tan\alpha_i = q_{b,i,n}/q_{b,i,s} = (\sin\delta - T_i\partial_y z_b)/(\cos\delta - T_i\partial_x z_b)$, where α_i is the angle between the sediment transport vector of the i^{th} size fraction of sediment and x-axis direction which will deviate from the bed shear stress vector due to gravity effects, $q_{b,i,n}$ and $q_{b,i,s}$ correspond to the bedload magnitudes along the normal to the current direction and the stream-wise direction, respectively, and where $T_i = 1/(\beta_2\sqrt{\tau^*_{b,i}})$ [Talmon et al., 1995], where $\tau^*_{b,i}$ is the bed shear stress adimensionnalized by the i^{th} size fraction of sediment also known as Shields parameter and scales the gravity effects as a function of the grain diameter of the i^{th} size fraction, and β_2 is an empirical coefficient used as a calibration parameter.

The total shear stress τ [Pa] is calculated from the depth averaged flow velocity field, where $\tau = 0.5\rho C_f(u^2 + v^2)$ and C_f is equal to the sum of skin friction and bedform drag. In this study, the bed shear stress is determined as a function of the total shear stress with $\tau_b = \mu\tau$, where $\mu = C'_f/C_f$ is the friction factor and C'_f [-] is the equivalent Chézy coefficient only due to skin friction and is the only component acting on bedload Mendoza et al. [2016]. C'_f is calculated assuming a flat bed by using the Nikuradse's formula, where the roughness height k'_s [m] is a function of the mean sediment diameter at the bed surface with $k'_s = \alpha_{k,s} \times d_{s,m}$ with $\alpha_{k,s}$ a calibration parameter.

The numerical solution of the SWE is based on the finite element method P_1, where the advective terms are computed with the method of the characteristics. The numerical solution of the sediment transport continuity equation is performed by a procedure that combines an implicit finite element scheme and an edge-based explicit upwind advection scheme. This procedure assures mass-conservation at machine accuracy, monotonicity of tracers, copes with dry zones and is easily applicable to domain decomposition Hervouet et al. [2011].

3.2.2 Study case

The numerical models are meant to reproduce two laboratory experiments carried out at Delft Hydraulics (The Netherlands) [Lanzoni, 2000a,b]. Lanzoni's experiments were performed in a water and sediment-recirculating rectangular 55 m long, 1.5 m wide and 1 m deep straight flume with rigid vertical sidewalls, with an initially flat bed. The imposed downstream free surface was adjusted so that the water surface profile was parallel to the longitudinal bed slope. Exiting sediment was continuously weighted to estimate sediment transport and then recirculated upstream Lanzoni [2000a]. According to Lanzoni, sediment was mainly transported as bedload.

Among the multitude of experiments of bar formation carried out with uniform sediment, test P1505 is selected here because bars formed relatively rapidly in this run, and other numerical studies successfully reproduced bar formation under this given configuration Mendoza et al. [2016]. This test was carried out with a constant flow discharge equal to $30 \cdot 10^{-3}$ m^3/s resulting in an average water depth equal to $\bar{h}$ =0.044 m, with an initial longitudinal bedslope equal to 0.00452. The width-to-depth ratio, denoted $\beta = B/\bar{h}$ [-] with B [m] the active width (i.e. at bankfull conditions), is equal to 34. The uniform sediment is composed of a mixture of well-sorted quartz sand with a geometric mean diameter of 0.48 mm, with $\rho_s = 2.65 \cdot 10^3$ kg/m^3. The averaged exiting discharge of sediment including pores was $2.63 \cdot 10^{-5}$ m^3/s.

Then, test P2009 is selected for the current study because sediment sorting was only measured and addressed for this experiment. The constant flow discharge was equal to $45 \cdot 10^{-3}$ m^3/s resulting in an average water depth equal to $\bar{h}$ =0.050 m, an initial longitudinal bedslope equal to 0.00525 and a width-to-depth ratio equal to 27. The bimodal grain size distribution (GSD) used by Lanzoni [2000b] was composed of a mixture of 67% of a well-sorted quartz sand with a geometric mean diameter of 0.19 mm and 33% of a well-sorted coarser sediment with a geometrical mean diameter of 2.0 mm, of same density than the uniform sediment. The averaged exiting discharge of sediment including pores was $1.09 \cdot 10^{-4}$ m^3/s. Due to the high shear stress, a condition of fully mobilized transport was observed during the experiment.

3.2.3 Numerical model scenarios

We investigate here the impact of the numerical solution and physical parameters on the computed bar morphology and characteristics. The studied scenarios are organized in two major groups, according to the sediment distribution (uniform and non-uniform). For the first group, the influence of the sediment boundary conditions, bed slope effects, skin friction correction and initial bed perturbation is studied and discussed considering uniform sediment distribution. A convergence analysis is also performed to evaluate the impact of the space and time discretization on the numerical results. For the second group, the influence of physical and numerical parameters is investigated to assess the capabilities of the model, considering a non-uniform sediment distribution. To this goal, emphasis is put at analyzing the influence of the closure relationships used to compute the sediment fluxes as well as the vertical discretization of the bed structure, following the active layer concept of Hirano [1971]. The influence of the turbulent eddy viscosity on the numerical results is also presented and discussed.

The model computations are performed as follows: *i*) the hydrodynamic model is run without bedforms (i.e. considering a flat bed) to obtain the mean hydraulic variables measured during the laboratory experiments, which are then used later as initial conditions for *ii*) the sediment transport and morphodynamic model where both the numerical averaged sediment transport and the bars characteristics are compared with experimental measurements. As the heterogeneity of sediment adds a degree of complexity in the numerical modelling of bars

morphodynamics, analyses are firstly conducted with using uniform sediment (i.e. P1505 run).

3.2.4 Model parameters

The numerical model of reference from which other models are derived uses an unstructured computational mesh composed triangles with typical length of approximately 0.093 m. In this model, the computational time step is set equal to $\Delta t = 0.04$ s in order to keep a Courant number (=CFL) approximately equal to 0.2, $\nu_t = 10^{-6}$ m^2/s and $\rho = 1000$ kg/m^3. As originally pointed out by Defina [2003] and observed later by other researchers Qian et al. [2016]; Mendoza et al. [2016], migrating bars could be observed in the numerical model only starting from approximately $x = 60$ m, which corresponds to the length of the laboratory flume. For this reason, the downstream boundary of this reference model has been extended to $x = 120$ m in order to observe the migration of fully developed bars in the system. No initial topographic perturbation is introduced in the reference model, i.e. the initial bed is flat. The boundary conditions of the hydrodynamic model correspond to an upstream constant flow discharge and a downstream constant free surface elevation, respectively. Sediment density and porosity are fixed to $\Delta_s = 1.65$ and $P_0 = 0.40$, respectively.

3.2.4.1 Uniform sediment

To carry out the sensitivity to the upstream morphodynamic boundary condition, two distinct formulations are imposed. The first boundary condition corresponds to the morphodynamic equilibrium (referred to -E), where the input solid discharge is determined from the bedload capacity formula such that the upstream topography remains constant overtime and the downstream boundary is let free. The second boundary condition corresponds to sediment recirculation (referred to -R), where the sediment exiting the flume is re-injected upstream at the next computational time-step. The sensitivity analysis to the temporal discretization is performed with using distinct computational time-steps $\Delta t \in [0.02 - 0.16]$ s, with considering both morphodynamic boundary conditions. The impact of domain discretization on computed bar formation and dynamics is investigated with the help of meshes composed of the same number of regular isosceles right triangles and irregular triangles. The reference coarsest mesh which is used (run P1505-E1/-R1) is composed of elements scaling 0.375 m. Three finer meshes are obtained by splitting the mesh of reference in 2 (run P1505-E2/-R2), 4 (run P1505-E3/-R3) and 8 (run P1505-E4/-R4). The low-resolution model (run P1505-E1/-R1) is run with a computational time step of $\Delta t = 0.16$ s, whilst the higher resolution models use a time-step equal to $\Delta t = 0.08$ s, $\Delta t = 0.04$ s and $\Delta t = 0.02$ s, respectively, in order to keep a Courant number around 0.2.

3.2.4.2 Non-uniform sediment

The same initial topographic perturbation in the range of [-5;5] mm is used in the numerical models with non-uniform sediment to fasten free bars formation. The roughness height of Nikuradse is set equal to 0.01 m in all scenarios. The non-uniform sediment consists of two size fractions having diameter $d_1 = 0.2$ mm (67%) and $d_2 = 2$ mm (33%), respectively. In order to model the vertical sorting of sediment, the bed is discretized into nine vertical sediment storage layers where the thickness of the sub-layers is equal to the active layer thickness, excepted from the deepest layer composing the substrate. Only boundary condition of sediment recirculation is considered with non-uniform sediment scenarios, and use the same computational mesh and time step as the reference numerical model.

3.3 Numerical results with uniform sediment

3.3.1 Influence of numerical parameters

3.3.1.1 Time discretization

Time-convergence analyses conducted under P1505 configuration show that the maximal CFL value for which the model remains stable is equal to 0.2. Above this value, the numerical model is unstable and compute physically irrelevant bed evolution. This result seems to be independent from the chosen morphodynamic boundary condition (i.e. equilibrium or recirculation, see Figure 3.1). The comparison between the numerical results computed with CFL=0.2 and CFL=0.1 shows that no major difference can be observed between both computed bed topographies. This suggests that using CFL values in this range do not affect the numerical solution which could have originated from diffusive effects. In this case, outcomes also suggest that model convergence is more related to the numerical scheme adopted for the solution, rather than a problem of numerical diffusion.

3.3.1.2 Spatial discretization

Outcomes from the mesh convergence analysis (Figure 3.2) show different trends depending on which morphodynamic boundary condition is used. When the mesh convergence analysis is carried out with the equilibrium boundary condition, free alternate bars always develop and migrate in the second part of the channel. Results show that bars generally form more downstream with decreasing mesh size, and suggests that perturbations at the origin of bar formation are reduced with finer computational meshes. When sediment recirculation is implemented, in the early stages of these runs, free alternate bars of similar characteristics can be observed from $x \approx 60$ m. During the late stages of these scenarios, the upstream stabilized bars produced by the coarse mesh trigger the formation of immediately downstream hybrid bars, which are originated from the growth and stabilization of free bars Duró et al. [2015]. The alternate bar dynamics turns out completely different when finer meshes are used (i.e runs P1505-R3 and P1505-R4), where a continual formation and propagation of free bars is observed. In the last case, the upstream boundary condition does not generate a geometrical forcing high enough which could induce hybrid bar formation. Obviously, these upstream topographic perturbations are not observed when the equilibrium boundary is used, because by definition the bed topography has to remain constant overtime.

According to Schuurman and Kleinhans [2011] the large-scale characteristics of the bar pattern in a self-forming braided river are independent of the computational mesh resolution, where a finer mesh better describes the bar topography rather than a coarser one. Results from the current analysis (Figure 3.2) partially support their conclusions, in the sense that convergence is not directly reached when sediment recirculation is considered (i.e. runs P1505-R1 and P1505-R2), where the formation of upstream topographic perturbations are larger enough -due to the large mesh size- to trigger the formation of upstream steady bars.

Comparison between the two scenarios using the irregular mesh (Run P1505-R3) and a regular mesh (Run P1505-R3b) shows that the irregular mesh enhances perturbation growth as free bars develop further upstream (Figure 3.3). Nevertheless, equilibrium bar characteristics remain unchanged, and the orientation of the mesh elements does not impact bar morphology.

The simulations were launched using the MPI library on Porthos cluster using 28 CPUs. Decreasing the computational time-step with keeping a constant CFL is showed to increase

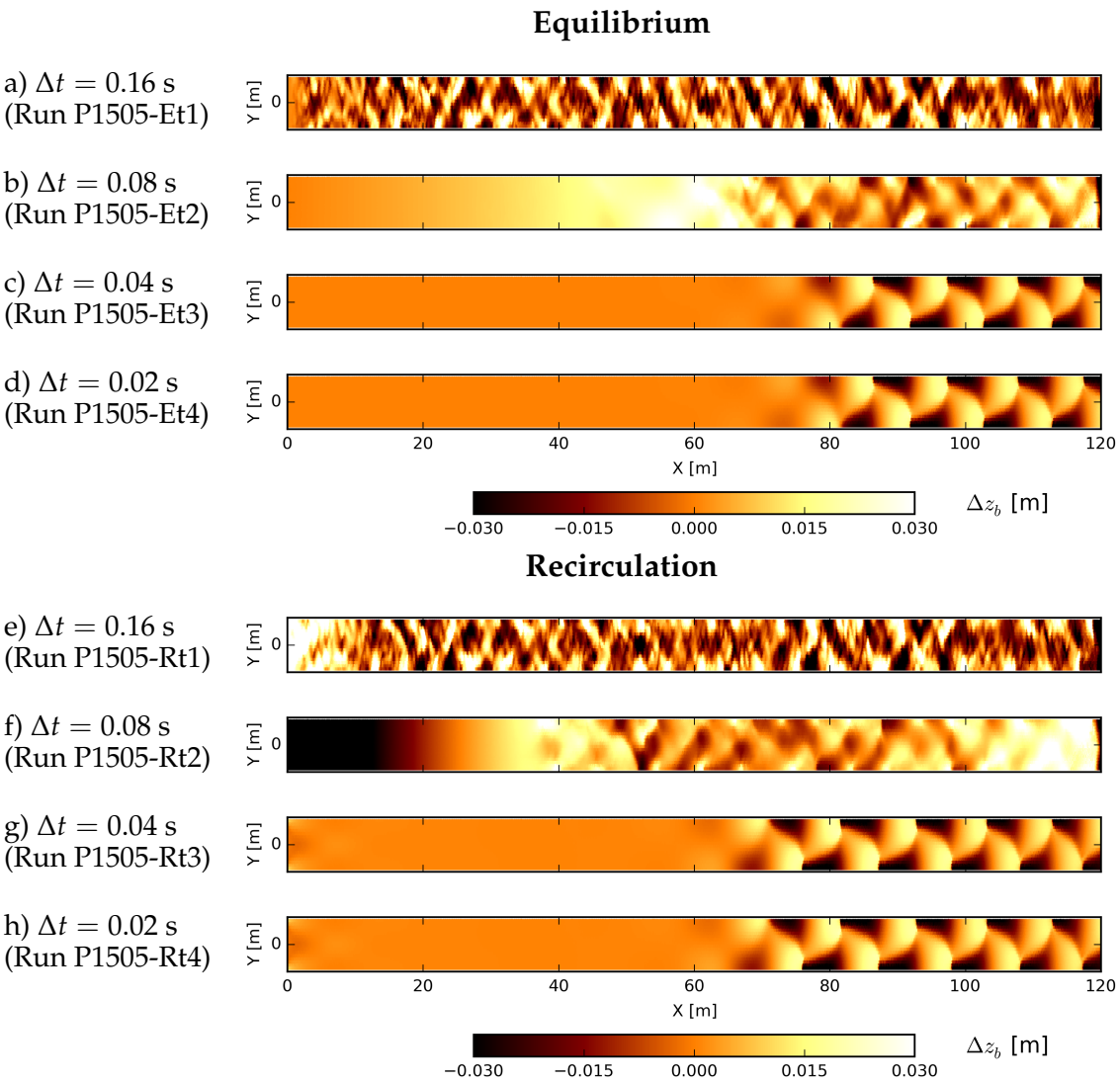


Figure 3.1: Planform evolution of the bed at $t = 28$ h with using computational time-steps in the range of [0.02-0.16] s with the morphodynamic (a-d) equilibrium boundary and (e-h) sediment recirculation boundary.

considerably the computational time, leading to cumbersome simulations when the time-step is equal to 0.02 s using both morphodynamic boundary conditions (Table 3.1). Consequently, using $\Delta t = 0.04$ s is showed to be a good compromise between the quality of the numerical results and computational time efficiency.

3.3.2 Influence of physical parameters

3.3.2.1 Sediment boundary condition

The comparison between numerical results obtained with the two different morphodynamic upstream boundary conditions measured over a period of 600.000 s shows that free bars are forming further upstream in the case of sediment recirculation (Figure 3.2c vs. g). The last observation suggests that the periodic condition of sediment recirculation enhances free bar

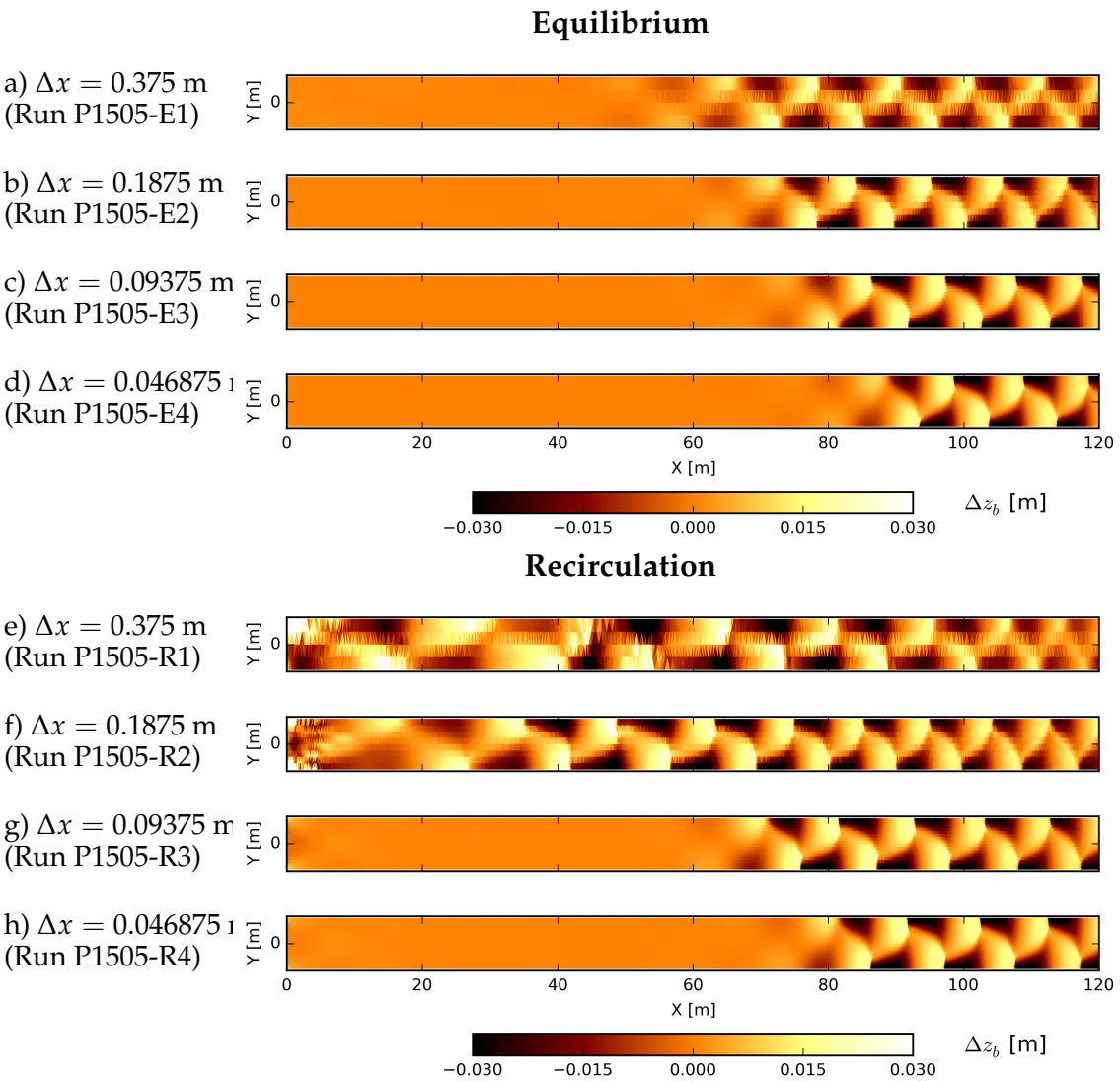


Figure 3.2: Planform evolution of the bed at $t = 28$ h with using computational mesh sizes in the range of [0.046875-0.375] m with the morphodynamic (a-d) equilibrium boundary and (e-h) sediment recirculation boundary.

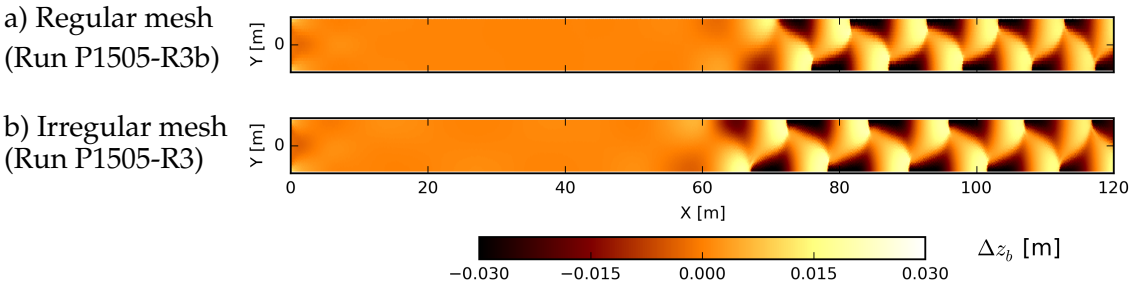


Figure 3.3: Planform evolution of the riverbed at $t = 28$ h using a regular and an irregular computational mesh.

Run	Δx [m]	Δt [t]	Run time [s]
P1505-E1	0.375	0.16	662
P1505-E2	0.1875	0.08	1911
P1505-E3	0.09375	0.04	8479
P1505-E4	0.046875	0.02	69215
P1505-R1	0.375	0.16	671
P1505-R2	0.1875	0.08	2011
P1505-R3	0.09375	0.04	8542
P1505-R4	0.046875	0.02	69520

Table 3.1: Computational time obtained for the different scenarios assuming a constant CFL=0.2.

dynamics with respect to the upstream equilibrium morphodynamic boundary condition. It is in agreement with the conclusions made by Mendoza et al. [2016], as they observed the complete decay of bars after a given time, even if small topographic perturbations continue to grow in the current runs, giving rise to smaller amplitude bars (Figure 3.4). As a result, free bar dynamics is not completely stopped as the system remains under the unstable condition for bar formation, but morphodynamic evolutions are importantly reduced and in the case where the flume would be longer, bars would continue to grow before eventually reaching their equilibrium characteristics.

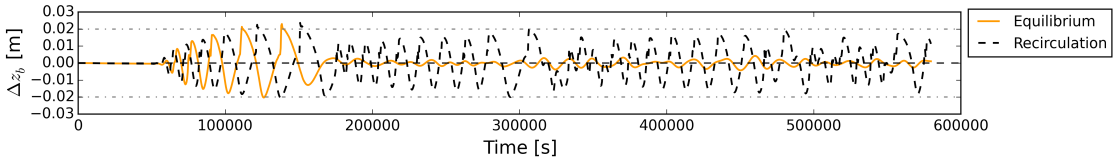


Figure 3.4: Time-series of the bed evolution at (X=114 m;Y=0.375 m) with using the equilibrium and recirculation upstream morphodynamic boundary conditions.

3.3.2.2 Bed slope effects

To quantify the influence of the bed slope effects on bar morphodynamics, a sensitivity analysis is carried out on the coefficients for the correction of bedload magnitude β_1 (=1.3 by default) and bedload deviation β_2 (=1.7 by default). Firstly, under the given configuration, numerical results show that bed slope effects affect very weakly the computed averaged sediment transport, where a difference between using $\beta_1 = 1.3$ and $\beta_1 = 2.5$ is less than 1%. While the formulation for bedload magnitude correction has no impact on bars properties because bar phase and dimensions are similar with various values of β_1 (Figure 3.5a), bedload deviation is showed to strongly impact bar morphodynamics (Figure 3.5b). In fact, increasing coefficients of deviation β_2 tend to increase bar amplitude by increasing the pool depth, resulting in a lateral constriction of the bedload transport over the lee side located at the opposite bank (Figure 3.5b and 3.6). Increase of β_2 is also followed by an earlier formation of bed perturbations and bars in the channel, that begins from around $x = 40$ m for $\beta_2 \geq 2$ (Figure 3.5). In terms of free bar morphology, the more β_2 increases, the more the longitudinal profile shows an irregular shape, with an abrupt transition between the bar top and the pool (i.e. lee side), which tends to form a terrace when $\beta_2 \geq 1.5$ (Figure 3.5b). When β_2 is decreased, bars display a smoother and more sinusoidal shape, resulting to a smaller bar amplitude. With $\beta_2 = 0.5$, bed perturbations are

completely smoothed-out and bar formation is not observed.

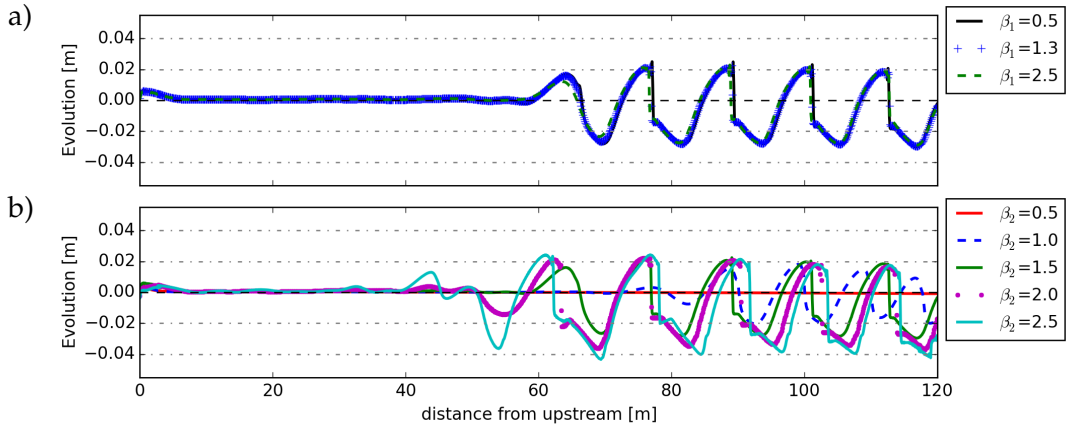


Figure 3.5: Longitudinal profiles of bed evolution at 0.55 m from the left sidewall obtained with various coefficients for the correction of bedload a) magnitude β_1 and b) direction β_2.

Increasing β_2 immediately increases the lateral transport rate as illustrated on Figure 3.6, where the sediment is steered from the bar toward the pool. The highest magnitude of lateral transport rates is located close to the steepest bedslopes, *i.e.* on the transition between a bar top and a pool, and the lowest lateral transport rates are found in the *thalweg* and along the two sidewalls. Finally, increased β_2 increase the bar wavelength (Figure 3.5b and 3.6) and decrease the bar celerity, which is approximately 1.1 m/h with $\beta_2 = 2.5$ and 1.7 m/h with $\beta_2 = 1$.

Bars could not be obtained with the current model without accounting for bed slope effects, leading to an unrealistic bed evolution. This result is in agreement with the fact that slope effects are necessary to obtain bars numerically. The last outcomes also coincide with Francalanci et al. [2009] who showed that including the effects of local high slopes in the numerical model can affect bar dynamics, and Nelson et al. [2015a] who showed that slope effects control actively the bars topography, where the bed displays steeper cross-stream slopes when the slope effects are increased.

3.3.2.3 Skin friction correction

In this work, the authors propose to compare two types of models: a model assuming that the bed shear stress is equal to the total shear stress (i.e. $\mu = 1$); models that recompute the bed shear stress accounting for the bed surface roughness. Four numerical scenarios are used to assess the role of skin friction correction on computed equilibrium bar characteristics. The same approach is systematically used for each run, where a weighting coefficient which multiplies the transport rate computed with the bedload formula is calibrated in order to keep the averaged volumetric discharge close to the value measured in the laboratory Lanzoni [2000a]. This approach has been chosen to only evaluate the influence of the skin friction correction on computed bars properties, with excluding the impact on the averaged transport of sediment.

The skin friction correction is showed to impact significantly the sediment transport distribution over space and resulting bars morphology (Figure 3.7). Indeed, any variations of the coefficient $\alpha_{k,s}$ modify the computed sediment transport rates and requires to calibrate the weighting coefficient of the bedload capacity formula α_b to compute relevant volumetric transport rates of sediment. Even if the same averaged sediment transport rate is computed for

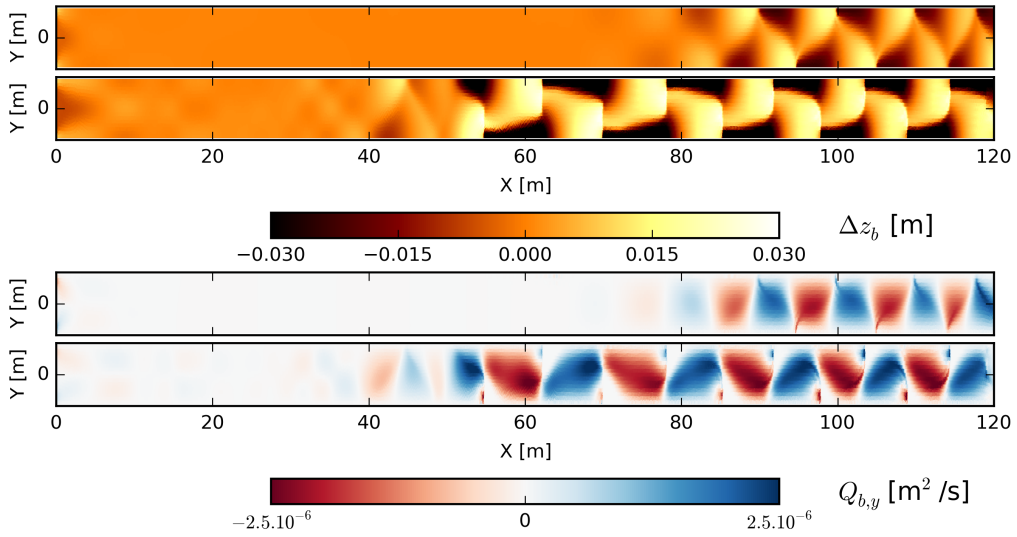


Figure 3.6: Impact of the bedload deviation on planform bar morphology and cross-stream bedload transport rates at $t = 28$ h with $\beta_2 = 1$ and $\beta_2 = 2.5$.

each scenario, the correction of skin friction impacts bar characteristics with damping the bar amplitude for increasing values of bed roughness (i.e. with increasing $\alpha_{k,s}$), showed in Figure 3.7. While the bar amplitude is decreased of 25% between experiments with $\mu = 0.5$ ($\alpha_{k,s} = 3.7$) and $\mu = 0.75$ ($\alpha_{k,s} = 10$), the bar wavelength is less affected with a small reduction of $\approx 5\%$, while the bar velocity is increased by $\approx 25\%$. In the case where the shear stress is equal to the total shear stress (i.e. $\mu = 1$), bar amplitudes are strongly decreased, and scale half the bar amplitude obtained with $\mu = 0.5$, which outlines that skin friction correction is a crucial physical parameter to compute free bar morphodynamics.

Results obtained using uniform sediment show that the parameterization of the friction correction plays an important role on the dimensions of bars (Figure 3.7). It suggests that, in presence of non-uniform sediment, this process should also have a strong influence on computed bars properties, because the planform spatialization of non-uniform sediment adds a degree of nonlinearity in the system with allowing for the variability of bed roughness and associated variability of $\alpha_{k,s}$.

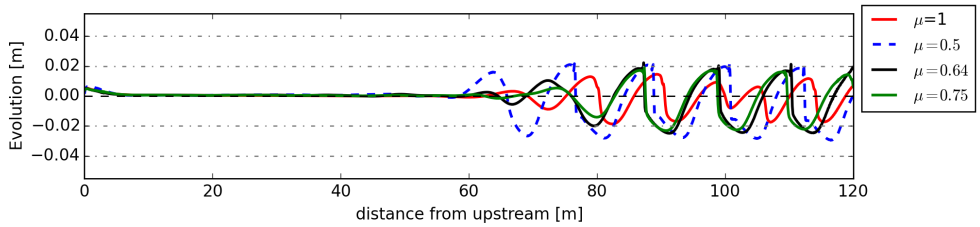


Figure 3.7: Longitudinal profiles ($y = 0.55$ m) of the bed evolution plotted with different values of $\alpha_{k,s}$ at $t = 28$ h.

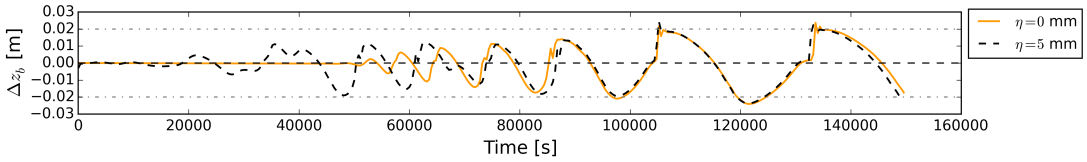


Figure 3.8: Time-series of bed evolution at (X=102 m;Y=0.415 m) with using the equilibrium and recirculation upstream morphodynamic boundary conditions.

3.3.2.4 Initial bed perturbation

Comparison between models without and with a uniformly distributed initial bed perturbation in the range [-5;5] mm shows that free bars formation is not necessarily due to the initial bed perturbation (Figure 3.8), but is rather due to the propagation of numerical disturbances Crosato et al. [2012]. Moreover, the formation of bed perturbations is clearly accelerated with introducing initial topographic perturbations (Figure 3.8). While bars are continually growing in amplitude and wavelength in the case where no initial topographic perturbation is used, the opposite phenomenon can be observed when using a randomly distributed initial perturbation. Finally, the initial random topographic perturbations used in this analysis seem not to affect significantly the long-term morphodynamics and equilibrium free bars characteristics.

3.4 Numerical simulations with non-uniform sediment

3.4.1 Influence of physical parameters

3.4.1.1 Sediment layers thicknesses

An analysis is conducted to evaluate the impact of choosing different storage layer thicknesses on the computed bar topography and sediment sorting. For that purpose, 3 scenarios implementing 9 sediment storage layers are simulated, where the active layer and sub-layer thicknesses (excepted from the deepest layer) are constant in space and time, and are equal to 5mm, 1 cm, 2cm and 100 m, respectively. The elevation of the non-erodible bed is set 100 meters above the initial bed topography so that sediment is always available, and the relative small bed evolution can be neglected with respect to the deepest layer thickness. In this last layer, the grain size distribution remains constant overtime. In this analysis, scenarios are run with using the bedload transport formula of WC-2003. Comparisons are performed at $t = 280.000$ s, i.e. when equilibrium free bars are dominant.

Results firstly suggest that using non-uniform sediment together with the active layer concept inevitably leads to the formation of topographic oscillations (Figure 3.9a,b,c). These oscillations are mainly observed immediately downstream bar fronts. The use of a thick active layer of L_a=100 m completely suppresses these oscillations. According to the scenario where L_a=5 mm, which is now defined as the scenario of reference, the sediment of surface becomes progressively coarser from the lee side until the next bar front (Figure 3.9a). The same tendency is generally observed in the underneath layers, where the difference is less pronounced the deeper the layer is. As a result, the pool surface is composed of the finest sediment, while the bar top surface is composed of the coarsest material. While the substrate becomes increasingly coarser underneath the pool, the opposite phenomenon is observed at the bar top location. Increased layer thicknesses from 5 mm to 2 cm is showed to strongly impact the computed

sediment sorting pattern (Figure 3.9a vs. c). Thinner the layers are, faster is the fluctuation of the fractional volume contents of sediment in the layers. The use of thicker layers increase the phase shift between the bed topography and the sorting sediment, where the sorting pattern is altered with coarser sediment on pools and fine over tops, because the fractional volumes contents of sediment vary slowly with respect to bed evolution. The use of intermediate layer thicknesses in [5-10] mm seem to produce consistent sorting patterns of sediment regarding the sorting observed in the laboratory experiment.

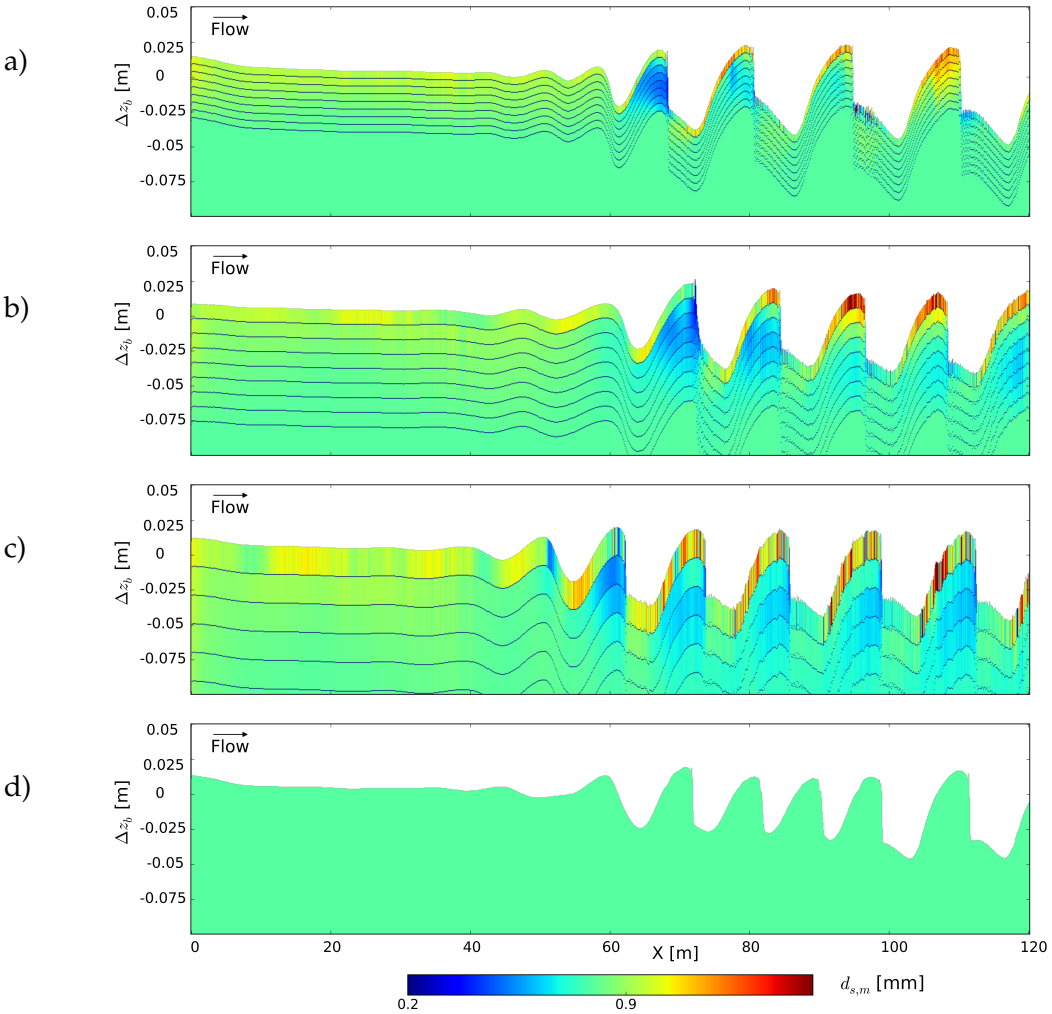


Figure 3.9: Longitudinal stratigraphic profiles at t=280.000 s obtained with the formula of WC-2003 with a) L_a =5 mm, b) L_a =1 cm, c) L_a =2 cm and d) L_a=100 m.

3.4.1.2 Influence of the hiding-exposure formula

To test the role of the hiding-exposure effects on computed bar properties and sediment sorting, two other models which derive from the model of reference defined in Section 3.4.1.1 are put into comparison. In the first model, the formula of MPM is used to compute the sediment transport rates, while the second model computes bedload transport with the formula of MPM-E, which includes the hiding-exposure relation of Egiazaroff [1965]. These two models are

calibrated independently on the coefficient multiplying the transport rate computed by the bedload formula, so that the same averaged sediment transport rates are computed as measured in the laboratory. This calibrated coefficient is equal to 11/8 for the model using MPM and 13/8 for the model using MPM-E. Comparisons are performed at $t = 25600$ s, i.e. when the first fully developed can bars be observed.

Results suggest that topographic oscillations are sharply pronounced in the case where the formula of MPM is used (Figure 3.10a), while they are damped when an hiding-exposure function is introduced in the sediment transport model (Figure 3.11), but can be still observed mainly immediately downstream of bar fronts. The same tendency was observed in Section 3.4.1.1 when the formula of WC-2003 is used (Figure 3.9). On the one hand, under the given configuration, the formula of MPM without hiding-exposure effects is showed to be incompatible with bar morphodynamics with non-uniform sediment. The use of a thick active layer results in a non evident sediment sorting pattern as it shows abrupt transitions and is very different that the one observed in laboratory (Figure 3.10b). The decrease of the layer thicknesses leads to a smooth variation of the bed and suggests a sediment sorting pattern with coarse over bar heads and coarse on pools, which is inconsistent with laboratory observations (Figure 3.10a). On the other hand, the sediment transport models including a hiding-exposure formulation are particularly robust as they display much less topographic undulations and smaller divergences of sediment fractions (Figure 3.9a and 3.11). By re-balancing sediment transport, the hiding-exposure function decreases the spatial divergence of fractional contents of sediment, which in turn tends to smooth the bed topography.

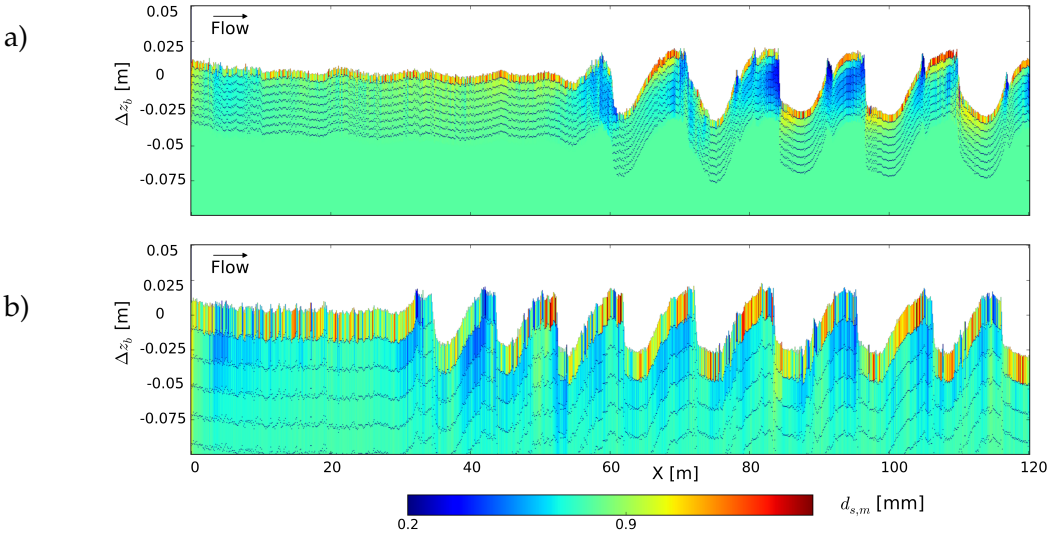


Figure 3.10: Longitudinal stratigraphic profiles at t=25.600 s obtained with the formula of MPM with a) L_a =5 mm and b) L_a =2 cm.

3.4.1.3 Influence of the turbulent eddy viscosity

The additional terms that arise as a consequence of the vertical non-uniformity of horizontal velocities are modeled using an eddy viscosity approach. In all of the last runs presented above, ν_t is already very low with imposing a constant value equal to $\nu_t = 10^{-6}$ m^2/s, corresponding to the kinematic viscosity of clean water at a temperature of 20°C. However, even a small value of

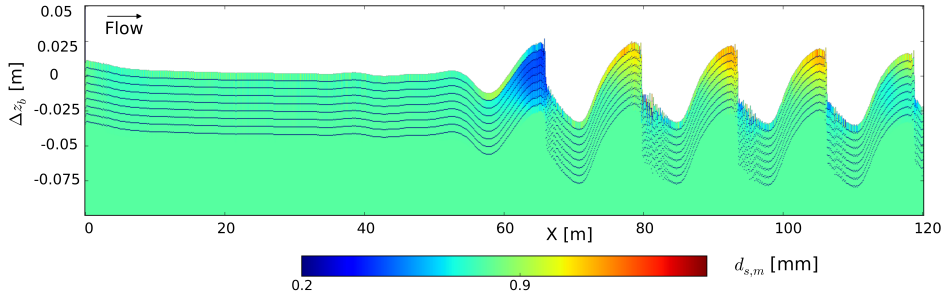


Figure 3.11: Longitudinal stratigraphic profiles at t=25.600 s obtained with the formula of MPM-E with L_a =5 mm.

ν_t could potentially impact bar properties due to numerical diffusion. Hence, another scenario derived from the one using the formula of WC-2003 and $L_a = 5$ mm is simulated, where $\nu_t = 0$ m^2/s.

The comparison between the scenario using $\nu_t = 10^{-6}$ m^2/s and $\nu_t = 0$ m^2/s (Figure 3.12 and 3.13) suggest that the dispersive stresses played by the parameterization of ν_t in the current scenarios are relatively low, and have a low impact on the simulated bed topography. The bed evolution in both simulations (Figure 3.12) shows that ν_t does not impact the results in the first 100.000 s of simulation, and then impact very weakly the averaged bar properties. As free bars arise from small perturbations due to numerical truncation, the change of ν_t explains the differences exhibited by the two scenarios. Moreover, these differences do not affect the numerical model stability, because the computed topography and sediment sorting are still physically relevant with neglecting the turbulent eddy viscosity.

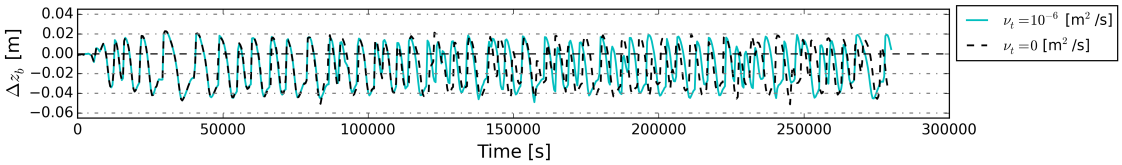


Figure 3.12: Longitudinal profiles of bed evolution at t=280.000 s obtained with the reference scenario with (a) $\nu_t = 0$ m^2/s and (b) $\nu_t = 10^{-6}$ m^2/s.

3.4.2 Discussion on numerical behaviour of the front bar propagation

High frequency fluctuations and an oscillating behaviour of the bed topography can be observed in every modeled scenario presented in this paper, and the authors tried to grant importance to this phenomenon. It seems that these fluctuations -which are well exaggerated due to the distortion of the vertical scale with respect to the longitudinal scale- are determined by several factors, are hypothetically related to a) the numerical solution of the Exner equation, b) the ill-posedness of the mathematical model of Hirano [1971] and the c) limitations on the wetting-dry algorithm when bars could emerge.

Firstly, some numerical results presented here effectively display small length fluctuations which are located at the extremity of the bar top, before the breaking slope separating the bar head and the pool, and in the pool, immediately downstream of the bar head. This issue seems to be independent from the sediment size heterogeneity, as it is also observed using a

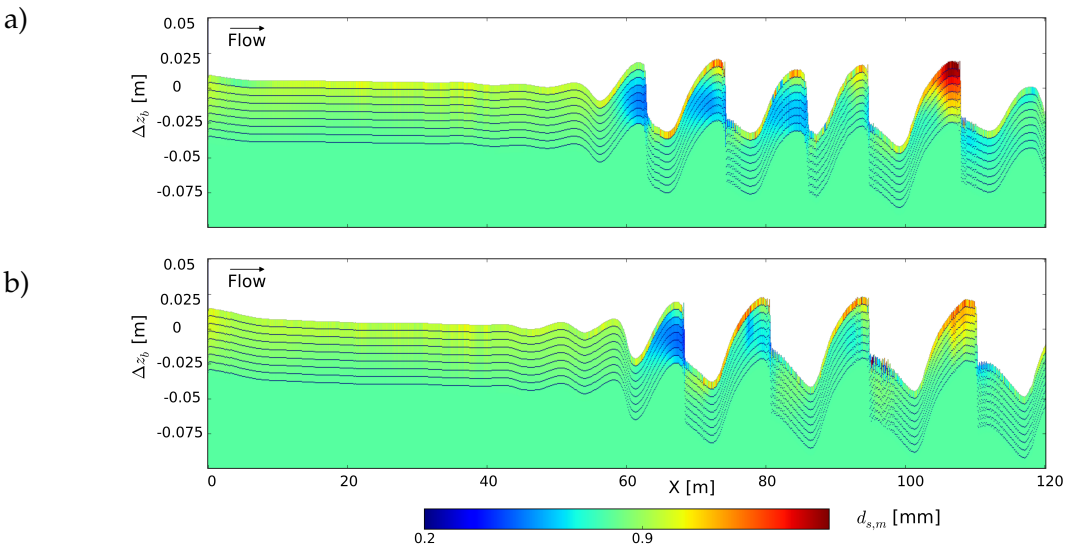


Figure 3.13: Longitudinal stratigraphic profiles at t=280.000 s obtained with the reference scenario with (a) $\nu_t = 0$ m^2/s and (b) $\nu_t = 10^{-6}$ m^2/s.

unique layer composed of single-size (uniform) sediment (scenario P1505, 3.5a). The averaged amplitude of these fluctuations is relatively low in comparison with free bar amplitude, and according to the results the presence of fluctuations seem to not modify bar morphodynamics (i.e. free bars migrate continuously, and their celerity is not impacted by the formation of upstream/downstream fluctuations). These fluctuations, also referred to as wiggles, correspond to unavoidable numerical perturbations generated in the system when a non-dissipative scheme is used. In order to dampen these numerical artefacts, it is possible to add artificial viscosity term to the discrete equations and in order to smooth very strong gradients [Cabrit, 2009]. Further analyses including a dissipation operator for the numerical scheme [Tassi et al., 2007] are planned for future research activities. In a second time, attention has been recently given on the ill-posedness of the mathematical model of Hirano [Stecca et al., 2014, 2016; Chavarrias et al., 2018], showing that the solution can be unstable to short-wave perturbations during phases of bed aggradation and degradation, and the amplitude of the oscillations depend on space discretization, leading to physically unrealistic results and even numerical simulations failures. Our model assumes (i) two sediment size fractions, (ii) steady flows, (iii) a constant active layer thickness and (iv) under aggradational scenarios the depositional flux of sediment to the substrate is entirely composed of active layer sediment. Although a hiding-exposure formulation is used and can lead to reverse sediment mobility, according to the conclusions given by [Chavarrias et al., 2018], the likelihood of the present active layer model to be ill-posed should be decreased due to the conditions assumed above. Although the formulation and conditions of use of the active layer model can lead to ill-posedness and unphysical fluctuations of bed topography and of sediment sorting in our model, which is today a very challenging topic, the last point developed below should give more confidence on the numerical results presented in this paper. In order to eliminate the role of the ill-posed formulation of Hirano on the computed bar topography, we can refer to as the computations in which all bed changes occur only in the active layer, i.e. the scenarios in which sediment sorting was not accounted with using an active layer thickness of 100 m. In the last case, small bed topography fluctuations can be observed over bar tops, at least when their amplitude is high enough so that water depth

is close to 0 above bar heads. The algorithm used to differ wet cells from dry cells also called tidal flats in our model is defined by a threshold value of 1 mm for the water depth. In the current model, no threshold condition has been set up to prevent from bedload in the case of small water depths. The relatively small amplitude of these fluctuations with respect to free bar amplitude and their specific location seem to play a minor role in comparison to the impact of the physical parameters on the simulated bar morphodynamics. Finally, with referring to already published numerical studies based on the simulation of bars with heterogeneous sediment, other authors observed the same behavior using a finite-difference numerical scheme [Nelson et al., 2015b].

3.5 General Outcomes

In this work, a 2D morphodynamic model has been set-up and is able to reproduce laboratory experiments of free bar formation with uniform sediment and non-uniform sediment. Before that, it has been necessary to investigate the impact of the numerical solution and physical parameters on the computed bar morphology and characteristics. Numerical results from this comprehensive numerical analysis firstly show that the domain discretization influences the propagation of the perturbation at the origin of free bar formation, where a finer computational mesh reduces the perturbation growth. This result particularly illustrates that the numerical truncation errors at the origin of these perturbations become more important when the computational mesh becomes coarser, and also explains why bars require a longer distance to form in comparison to the laboratory experiment. This analysis also shows that using approximately 15 to 20 cross stream computational nodes is enough to observe the bar features correctly, with a computational time which remains acceptable. Model convergence is attained with CFL values less or equal to 0.2. The use of two distinct morphodynamic boundary conditions shows that boundaries influence the computed bar dynamics. Sediment recirculation enhances free bar dynamics with respect to the equilibrium morphodynamic boundary condition. Disturbances triggered by the numerical solution and the origin of bar formation in the numerical model is a topic that deserves further investigation. Numerical results are in agreement with the theory, which shows that gravity effects are necessary to trigger free bar formation, and also suggest that only the correction of bedload deviation determine whether bars should form or not. The formulation for skin friction correction is also showed to strongly modify free bars morphology, hence a careful parameterization is required to compute physically relevant bar dynamics. The comparisons presented thereabove justify the use of the bookkeeping active layer concept combined with the use of a sediment transport model that includes a hiding-exposure function to reproduce the sediment sorting patterns observed in the laboratory. The active layer (and underneath sub-layers) thickness plays a crucial role on the vertical and planform sorting of sediment. The definition of the active layer (and underneath sub-layers), which is subject to calibration, is showed to play a crucial role on the computed sediment sorting pattern. Results show that increasing of layers thicknesses tends to slow down the process of sediment sorting with respect to bed evolution. Using thicker layers, the computed sediment sorting pattern becomes irrelevant as the variation of fractional volume contents of sediment is too slow in comparison to bed evolution. The diffusion effects associated to low values of Reynolds stress do not play a fundamental role in the case of bar formation and migration with heterogeneous sediment, at least under the given configuration. Outcome of this study can provide guidance to modellers for choosing the correct set of numerical and physical parameters to model relevantly free bars morphodynamics in straight or weakly-curved channels.

Acknowledgments

We would like to kindly acknowledge S. Lanzoni for sharing his experimental data. The authors gratefully acknowledge the support of Electricité de France (EDF).

Nomenclature

B Channel width [m]
b Degree of nonlinearity in the dependence of sediment transport on the flow velocity [-]
C Chézy coefficient [$m^{1/2}/s$]
C_f Equivalent Chézy coefficient due to form drag and skin friction [-]
C'_f Equivalent Chézy coefficient due to skin friction only [-]
d_i Representative diameter of the i^{th} size fraction [m]
$d_{s,m}$ Median sediment diameter of surface [m]
g Acceleration due to gravity (=9.81) [m/s^2]
h Water depth [m]
$\bar{h}$ Spatially averaged water depth [m]
i_0 Longitudinal bed slope at $t = 0$ s [-]
k_s Bed roughness height [m]
L_a Active layer thickness [m]
P_0 Bed porosity [-]
q_b Magnitude of bedload transport rate [m^2/s]
$\vec{q_b} = (q_{b,x}, q_{b,y})$ Vector of bedload transport rate [m^2/s]
q_{b0} Magnitude of bedload transport rate without gravitational effects [m^2/s]
$\vec{q_{b0}}$ Vector of bedload transport rate without gravitational effects [m^2/s]
$q_{b,i}$ Magnitude of fractional transport rate of i^{th} size fraction [m^2/s]
$\vec{q_{b,i}} = (q_{b,i,x}, q_{b,i,y})$ Vector of fractional transport rate of i^{th} size fraction [m^2/s]
$q_{b,i,n}$ Magnitude of normal fractional transport rate of i^{th} size fraction [m^2/s]
$q_{b,i,s}$ Magnitude of stream-wise fractional transport rate of i^{th} size fraction [m^2/s]
s Coordinate in the current direction [-]
$\vec{u} = (u, v)$ Flow velocity vector [m/s]
$\bar{u}$ Spatially averaged flow velocity [m/s]
u, v Depth averaged velocity components along x- and y-axis [m/s]
s Coordinate in the current direction [-]
$\vec{S_f} = (S_{f,x}, S_{f,y})$ Friction law vector [-]
t Physical time [s]
T_i Coefficient of deviation for the i^{th} size fraction [-]
u_* Shear velocity [m/s] $x-, y-, z-$ Axis notation of the Coordinate Cartesian system [-]
z_b Bed elevation [m]
α_b Coefficient used to calibrate the sediment transport capacity [-]
α_i Angle between the vector of fractional transport and x-axis [-]
$\alpha_{k,s}$ Calibration parameter [-]
β Width-to-depth ratio [-]
β_1 Koch and Flosktra's empirical factor for bed slope effects magnitude [-]
β_2 Talmon's *et al.* empirical factor for bed slope effects deviation [-]
δ Angle between bottom shear stress and the flow direction [-]
Δ_s Relative submerged sediment density [-]

Δt Computational time-step [s]
Δz_b Evolution of the bed topography with respect to the initial bed elevation [m]
ϵ_0 Percentage of volumetric matter without voids [-]
$\eta_{a:1}$ Absolute elevation of the interface [m]
κ Constant of von Kármán (=0.40) [-]
μ Skin friction coefficient [-]
∇ Gradient vector field [1/m]
ν_t Turbulent eddy viscosity term [m^2/s]
$\partial_{x_2} x_1$ Partial derivative of the quantity x_1 in x_2 [x_2/x_1]
ρ Water density [kg/m^3]
τ Total shear stress [Pa]
τ_b Bed shear stress [Pa]
$\tau^*_{b,i}$ Shear stress adimensionnalized by the i^{th} fraction [-]

References

Ashmore, P., Peirce, S., and Leduc, P. (2018). Expanding the Active Layer: Discussion of Church and Haschenburger (2017) What is the Active Layer? Water Resources Research 53, 510, Doi:10.1002/2016WR019675. *Water Resources Research*, 54(3):1425–1427. 35, 58, 86, 135

Bendegom, L. V. (1947). Some considerations on river morphology and river improvement, De Ingenieur vol. 59–4, pp. B1–11. *Dutch. English translation: Nat. Res. Council of Canada, Technical Translation*, 1054:1963. 26, 58, 88, 135

Cabrit, O. (2009). *Modélisation des flux pariétaux sur les tuyères des moteurs à propergol solide*. PhD thesis, Montpellier 2. 26, 58, 71, 88, 135

Church, M. and Haschenburger, J. K. (2017). What is the active layer? *Water Resources Research*, 53(1):5–10. 34, 35, 56, 58, 86, 97, 135, 288

Colombini, M., Seminara, G., and Tubino, M. (1987). Finite-amplitude alternate bars. *Journal of Fluid Mechanics*, 181:213–232. 4, 6, 9, 55, 84

Cordier, F., Tassi, P., Claude, N., Crosato, A., Rodrigues, S., and Pham Van Bang, D. (2017). Influence of sediment size heterogeneity on free and hybrid alternate bar morphodynamics. *Water Resources Research*, submitted:1–30. 5, 56, 130, 134, 135, 137, 155, 156, 157, 175

Cordier, F., Tassi, P., Jodeau, M., and Camenen, B. (2016). Large-scale morphodynamics structures in the Arc en Maurienne River (France). *River Flow 2016*, 1:n/a – n/a. 56

Crosato, A. and Mosselman, E. (2009). Simple physics-based predictor for the number of river bars and the transition between meandering and braiding. *Water Resources Research*, 45(3):1–12. xi, 4, 6, 7, 8, 55, 56, 84, 92, 130, 131, 137, 146, 152, 153, 154, 157

de Saint-Venant, A. B. (1871). Théorie du mouvement non permanent des eaux, avec application aux crues des rivières et à l'introduction des marées dans leurs lits. *Comptes Rendus des séances de l'Académie des Sciences*, 73:237–240. 18, 25, 57, 85, 134

Defina, A. (2003). Numerical experiments on bar growth. *Water Resources Research*, 39(4):1–12. 15, 56, 60, 90

Egiazaroff, I. (1965). Calculation of nonuniform sediment concentrations. *Journal of the Hydraulics Division*, 91(4):225–247. 58, 68

Engelund, F. (1970). Instability of erodible beds. *Journal of Fluid Mechanics*, 42(2):225–244. 4, 6, 55, 83, 84, 130

Exner, F. M. (1920). *Zur physik der dünen*. Hölder. 25, 57, 86, 135

Fujita, Y. and Muramoto, Y. (1985). Studies on the process of development of alternate bars. *Bulletin of the Disaster Prevention Research Institute*, 35:1 – 33. 55, 84

García, M. H. (2008). Sedimentation engineering. *Processes, Measurements, Modeling, and Practice. ASCE Manuals and Reports on Engineering Practice*, 110:1–1132. 25, 27, 29, 34, 57, 86, 89, 97, 136

Hervouet, J., Razafindrakoto, E., and Villaret, C. (2011). Dealing with dry zones in free surface flows: a new class of advection schemes. In Barton, A., editor, *Proceedings of the 34th World Congress of the International Association for Hydro-Environment Research and Engineering: 33rd Hydrology and Water Resources Symposium and 10th Conference on Hydraulics in Water Engineering*, pages 4103–411. Australia. 27, 58, 89, 136

Hirano, M. (1971). *River bed degradation with armoring*. PhD thesis, Japanese Society of Civil Engineering. xii, 18, 24, 25, 34, 35, 43, 57, 58, 70, 85, 86, 135, 158, 167, 173, 174, 288, 300

Koch, F. and Flokstra, C. (1980). *Bed Level Computations for Curved Alluvial Channels: Prepared for the 19th IAHR Congress, New Delhi, India, February 1981*. Waterloopkundig Laboratorium. 26, 58, 88, 135, 139

Lanzoni, S. (2000a). Experiments on bar formation in a straight flume 1. Uniform sediment. *Water Resources Research*, 36(11):3337–3349. 4, 12, 15, 45, 54, 57, 59, 65, 84, 89, 111, 174

Lanzoni, S. (2000b). Experiments on bar formation in a straight flume: 2. Graded sediment. *Water Resources Research*, 36(11):3351–3363. xi, xiii, 11, 12, 13, 14, 16, 32, 33, 44, 45, 49, 57, 59, 84, 85, 89, 90, 93, 94, 97, 107, 109, 111, 112, 130, 155, 162, 173, 174

Lanzoni, S. and Tubino, M. (1999). Grain sorting and bar instability. *Journal of Fluid Mechanics*, 393:149–174. 6, 11, 12, 55, 84

Mendoza, A., Abad, J. D., Langendoen, E. J., Wang, D., Tassi, P., and Abderrezzak, K. E. K. (2016). Effect of Sediment Transport Boundary Conditions on the Numerical Modeling of Bed Morphodynamics. *Journal of Hydraulic Engineering*, 143(4): . 27, 46, 56, 58, 59, 60, 64, 88, 90, 136, 158, 174

Meyer-Peter, E. and Müller, R. (1948). Formulas for bed-load transport. In *International Association for Hydraulic Structures Research*. IAHR. 26, 28, 58, 134, 155

Mosselman, E. (2012). Modelling Sediment Transport and Morphodynamics of Gravel-Bed Rivers. *Gravel-Bed Rivers: Processes, Tools, Environments*, 1:101–115. 12, 15, 56, 84

Nelson, P. A., McDonald, R. R., Nelson, J. M., and Dietrich, W. E. (2015). Coevolution of bed surface patchiness and channel morphology: 1. Mechanisms of forced patch formation. *Journal of Geophysical Research: Earth Surface*, 120(9):1687–1707. 12, 13, 16, 56, 65, 84, 91, 107, 109, 130, 137, 155

Nezu, I., Nakagawa, H., and Jirka, G. H. (1994). Turbulence in open-channel flows. *Journal of Hydraulic Engineering*, 120(10):1235–1237. 18, 25, 57, 85, 134

Parker, G. and Klingeman, P. C. (1982). On why gravel bed streams are paved. *Water Resources Research*, 18(5):1409–1423. 56

Qian, H., Cao, Z., Liu, H., and Pender, G. (2016). Numerical modelling of alternate bar formation, development and sediment sorting in straight channels. *Earth Surface Processes and Landforms*, 607:613–622. ESP-15-0409.R2. 12, 16, 56, 60, 84, 90

Schuurman, F. and Kleinhans, M. (2011). Self-formed braid bars in a numerical model. In *AGU Fall Meeting Abstracts*. 56, 61

Singh, U., Crosato, A., Giri, S., and Hicks, M. (2017). Sediment heterogeneity and mobility in the morphodynamic modelling of gravel-bed braided rivers. *Advances in Water Resources*, 104:127–144. 11, 12, 13, 28, 56, 84, 130, 155, 158, 174

Siviglia, A. and Crosato, A. (2016). Numerical modelling of river morphodynamics: latest developments and remaining challenges. *Advances in Water Resources*, 90:1–9. 15, 28, 56, 84

Siviglia, A., Stecca, G., Vanzo, D., Zolezzi, G., Toro, E. F., and Tubino, M. (2013). Numerical modelling of two-dimensional morphodynamics with applications to river bars and bifurcations. *Advances in Water Resources*, 52:243–260. 4, 15, 56, 110

Struiksma, N. and Crosato, A. (1989). *Analysis of a 2-D Bed Topography Model for Rivers*. Wiley Online Library. 56, 106

Talmon, A., Struiksma, N., and Van Mierlo, M. (1995). Laboratory measurements of the direction of sediment transport on transverse alluvial-bed slopes. *Journal of Hydraulic Research*, 33(4):495–517. 26, 27, 58, 88, 92, 135, 138, 139

Van der Meer, C., Mosselman, E., Sloff, K., Jagers, B., Zolezzi, G., and Tubino, M. (2011). *Numerical simulations of upstream and downstream overdeepening*. RCEM 2011, Proceedings of the 7th IAHR Symposium of River, Coastal and Estuarine Morphodynamics. 26, 58, 88, 135

Viparelli, E., Blom, A., and Moreira, R. R. H. (2017). *Modeling Stratigraphy-Based Gravel-Bed River Morphodynamics*, chapter Modeling Stratigraphy-Based Gravel-Bed River Morphodynamics, pages 609–637. John Wiley & Sons, Ltd. 34, 35, 56, 86, 97, 174

Vreugdenhil, C. B. (2013). *Numerical methods for shallow-water flow*, volume 13. Springer Science & Business Media. 18, 25, 57, 85, 134

Weiyan, T. (1992). *Shallow Water Hydrodynamics: Mathematical Theory and Numerical Solution for a Two-dimensional System of Shallow Water Equations*. Number vol. 55 in Elsevier oceanography series. Water & Power Press. 18, 25, 57, 85, 134

Wilcock, P. R. and Crowe, J. C. (2003). Surface-based transport model for mixed-size sediment. *Journal of Hydraulic Engineering*, 129(2):120–128. vii, 11, 24, 26, 28, 29, 31, 32, 45, 49, 58, 87, 103, 135, 158, 167, 173

Zolezzi, G. and Seminara, G. (2001). Downstream and upstream influence in river meandering. Part 1. General theory and application to overdeepening. *Journal of Fluid Mechanics*, 438:183–211.
26, 56, 58, 88, 135

▷ Insights on numerical modelling of free bars under simple configurations

Outcomes show that the morphodynamic model used in this work is not only able to reproduce accurately free bar morphodynamics with uniform sediment, but also with a non-uniform sediment, which asks for an increased degree of complexity in the numerical modelling to account for non-uniform sediment processes. The last point validates the modelling approach (at least for the configuration of the two experiments) and the set of assumptions that have been chosen in Chapter 2 to set-up the morphodynamic model. The main outcome of the present Chapter is that physical and numerical parameters can both play an important role on the prediction of periodic bar characteristics.

To a certain extent, computed bar properties can be importantly biased by the numerical model parameterization. For example, because free bars originate purely from intrinsic bed instability, which is propagated through errors of truncation in the numerical simulations, the spatial discretization (i.e. the computational mesh) is showed to influence the formation of free bars in the current model runs. As a result, depending on mesh size and orientation, bars start to develop at different locations along the longitudinal channel axis, and consequently the same observation is made for the location of the first fully developed free bars. Considering the case of a sediment recirculating channel, the mesh size is even showed to control the bar type: the use of a relatively coarse mesh induces an upstream geometrical forcing, promoting the formation of steady (hybrid) bars, which are by definition much more longer than free bars. By decreasing the mesh size, the result is totally different because only free bars form.

It is noteworthy that the physical parameters used for model calibration also control significantly bars characteristics. For example, the bed slope deviation effects are showed to impact strongly the bar height. The use of a formula which does not include any formulation for the hiding-exposure effects can lead to unrealistic bed evolution and sediment sorting patterns, and points out the physically irrelevance of the approach. A wrong parameterization of the sediment layer thicknesses can also conduct to the same issues as mentioned before.

Numerical studies of bar formation and development in straight embanked reaches should account for the last observations, because misunderstanding or lack of control on the numerical or physical parameterization may be equal to lose some of their relevance, and could later lead to a misinterpretation of bar morphodynamics processes. Calibration of physical parameters has to be done with respect to the values of reference found in the literature, and a special focus on the physical relevance of the numerical results.

Because model calibration has been successfully achieved with uniform and non-uniform sediment, the reference scenario with non-uniform sediment will be used in Chapter 4 to study the interaction between heterogeneous sediment and bar morphodynamics.

☐ Synthèse générale sur l'influence des paramètres physiques et numériques sur la modélisation des bancs libres

Les activités entreprises dans ce chapitre ont pour but de mieux comprendre l'influence et l'importance relative des paramètres physiques et numériques sur la modélisation de bancs libres. Pour cela, le modèle morphodynamique est utilisé pour reproduire des expériences de laboratoire consistant à générer la formation de bancs libres dans une configuration idéalisée, i.e. dans un chenal à géométrie rectiligne. Les critères de paramétrisation physique et numérique jugés les plus importants vis-à-vis des caractéristiques résultantes des bancs sont soumis à des tests de sensibilité, où les valeurs de ces paramètres sont choisies dans des intervalles couramment retrouvés dans la littérature. Dans un premier temps, le modèle est utilisé pour reproduire la formation de bancs libres avec un sédiment uniforme, et dans un second temps avec un sédiment non-uniforme. Les résultats montrent que les paramètres physiques et numériques jouent tous deux un rôle important sur la prédiction des propriétés des bancs. Une mauvaise paramétrisation de certains coefficients empiriques tels que les effets de pente peut jouer fortement sur la géométrie et la dynamique des bancs, ou un défaut de pertinence sur les processus physiques tel que la non prise en compte de l'effet de masquage-exposition peut se suivre d'une évolution irréaliste du lit et des motifs de répartition spatiale des sédiments. Les paramètres numériques ont aussi une forte influence sur la morphodynamique des bancs libres, où il est montré qu'une discrétisation spatiale suffisamment grossière peut générer un forçage permanent dans le chenal, entraînant la stabilisation des bancs dans le chenal et par conséquent présentant une géométrie bien distincte de celle des bancs libres. Les études numériques portées sur la formation de bancs dans des chenaux rectilignes devraient prendre en compte ces observations, car des mauvais choix peuvent se faire ressentir par un manque de pertinence sur les résultats numériques et conduire à des interprétations erronées des processus morphodynamiques prédits par le modèle.

CHAPTER 4

NUMERICAL STUDY OF ALTERNATE BARS IN ALLUVIAL CHANNELS WITH NON-UNIFORM SEDIMENT

The work presented in this chapter has been submitted to the *Water Resources Research* journal on December 13th, 2017 with reference 2017WR022420 entitled *Numerical study of alternate bars in alluvial channels with non-uniform sediment*

by
Florian Cordier[1,2], Pablo Tassi[1,2], Nicolas Claude[2], Alessandra Crosato[3], Stéphane Rodrigues[4] and Damien Pham Van Bang[5]
[1]Laboratoire d'Hydraulique Saint-Venant (Chatou, France)
[2]EDF R&D LNHE - Laboratoire National d'Hydraulique et Environnement (Chatou, France)
[3]IHE Delft (Delft, The Netherlands)
[4]Ecole Polytechnique Universitaire de Tours & UMR CNRS 7324 CITERES (France)
[5]INRS-ETE, LHE & Lab. CT-Scan (Québec, Canada)

Corresponding author: florian.cordier@edf.fr

▷ Motivations and objectives of this study

This chapter aims to answer to the research question I (see Section 1.2): *How does sediment size heterogeneity affect bar morphodynamics?*

In order to study the interaction between non-uniform sediment and periodic alternate bars, we present a clear distinction between free bars and hybrid bars. Nine numerical scenarios are developed, where a transverse obstacle is used to generate hybrid bars in four of these scenarios. To investigate the impact of the sediment size heterogeneity on bars, three grain size distributions having the same median sediment diameter but a different degree of size heterogeneity are considered. To estimate the impact of planform and vertical sediment sorting on free bars and hybrid bars, two types of scenarios are compared: scenarios for which sediment sorting is accounted and scenarios for which sediment sorting is not accounted.

Outcomes of this study are expected to enrich our actual understanding on the interactions between non-uniform sediment and bar characteristics under simple, idealized channel geometry and bar configurations. The distinction between free and hybrid bars could help to elucidate the different sorting patterns observed over periodic bars addressed in the literature (see Section 1.1.3). Highlights of this research activity will also help to better evaluate the importance of accounting for non-uniform sediment processes in numerical models when they are used for prediction of bar formation and migration in rivers with straight fixed banks, or possible undesirable consequences of not accounting for it.

Keypoints

- Free bars and hybrid bars show distinct topography, bed shear stress, sediment transport and sediment sorting patterns
- Increased sediment size heterogeneity induces longer free and hybrid bars,free bars of higher amplitudes but no general trend for the hybrid bar amplitude
- Sediment sorting does not impact the averaged free bar characteristics, while hybrid bars become longer and damped: a clear distinction between these two types of bars has to be considered for the further works

Abstract

Rivers typically present heterogeneus bed material, but the effects of sediment non-uniformity on river bar characteristics are still unclear. This work investigates the impact of sediment size heterogeneity on alternate bars with a morphodynamic numerical model. The model is firstly used to reproduce a laboratory experiment showing alternate bar formation with non-uniform bed material. Subsequently, the influence of sediment size heterogeneity on free and hybrid alternate bars is investigated considering the results of nine scenarios. In four of them, a transverse obstacle is used to generate hybrid bars. Three grain size distributions are considered. The computations are based on the Telemac-Mascaret modelling system, which solves the two-dimensional shallow water equations with a finite element approach. The bed evolution is based on a model accounting for vertical sediment sorting processes. The results show that sediment heterogeneity affects free migrating and hybrid bars in a different way. The difference lies in the presence/absence of a migration front, so that distinct relations between bed topography, bed shear stress and sediment sorting are obtained. Sediment sorting and associated planform redistribution of bed roughness only slightly modify free migrating bar morphodynamics, whereas hybrid bars are greatly impacted, with decreased amplitude and increased wavelength. Increased sediment size heterogeneity increases the degree of sediment sorting, while the sorting pattern remains the same for both free and hybrid bars. Moreover, it produces averagely higher, longer and faster free bars, while in the case of hybrid bars their wavelength is increased but no general trend can be determined for their amplitude.

4.1 Introduction

Rivers often present a wavy bed due to the presence of *periodic bars* [Bridge and Demicco, 2008], which are large sediment deposits alternating with deeper areas (pools) that arise from an instability phenomenon of the alluvial bed [Engelund, 1970]. The number of bars in river cross-sections can be used to characterize the river type. For instance, the sequence of sediment deposits on one bank and pool at the opposite bank, i.e. alternate bars, is typical of single thread rivers and meanders, while the presence of multiple bars in the cross-section characterize braided rivers [Engelund and Skovgaard, 1973]. A deep knowledge of bar processes is important for river engineers and river managers, because bars strongly alter the river bed topography and influence bank erosion, with consequences for navigation, water intakes and infrastructure [Bridge, 2003; Claude, 2012; Claude et al., 2014; Jaballah et al., 2015]. Bars also affect the hydraulic

and sedimentary conditions of river systems, and therefore the quality of their habitats [Tonina and Buffington, 2007; Wintenberger et al., 2015].

Numerous studies [e.g. Engelund, 1970; Colombini et al., 1987; Lanzoni and Tubino, 1999; Crosato and Mosselman, 2009] have shown that the formation and the geometry of bars are primarily governed by the width-to-depth ratio of the flow (or aspect ratio). At unstable conditions, starting from a flat bed, incipient bars tend to increase in size, eventually reaching a steady value of amplitude and wavelength [Fujita and Muramoto, 1985] which scales with the water depth and the channel width, respectively. Over time, multiple bars may tend to merge to form much larger bars [e.g. Enggrob and Tjerry, 1999]. Duró et al. [2016] distinguish two types of periodic bars: *free* and *hybrid* bars. Hybrid bars form on morphodynamically unstable river beds, like free bars, but their migration is inhibited by an external factor (forcing), *e.g.* a change in channel geometry, which permanently deform the flow field, fixing their location. For this reason, hybrid bars do not migrate and their wavelength is not influenced by the forcing itself, but corresponds to the one of resonant free bars, which is generally 2 to 3 times longer than the wavelength of free migrating bars [Crosato et al., 2011; Rodrigues et al., 2015; Duró et al., 2016]. A common earlier term for hybrid bars is "forced bars" [e.g. Blondeaux and Seminara, 1985; Tubino and Seminara, 1990; Seminara, 1998].

Sediment mobility, represented by the Shields number, is crucial for bar morphodynamics and it depends on particle size and grain size distribution (GSD) of the mixture forming the river bed. Analytical studies [e.g. Lanzoni and Tubino, 1999], field and laboratory observations [e.g. Lisle and Madej, 1992; Powell, 1998; Lanzoni, 2000b; Lisle et al., 2000], as well as numerical simulations [e.g. Hoey and Ferguson, 1994; Mosselman et al., 1999; Wu, 2004; Tritthart et al., 2011a,b; Mosselman, 2012; Nelson et al., 2015a,b; Juez et al., 2016; Qian et al., 2016; Siviglia and Crosato, 2016; Singh et al., 2017] have shown that bars are affected by both size and heterogeneity of bed sediment. Lanzoni and Tubino [1999] as well as Takebayashi and Egashira [2001] state that sediment heterogeneity leads to the diminishing of free migrating bar amplitude and wavelength. Opposite results were obtained by Lanzoni [2000a,b] and Lisle et al. [1991] who find that, while free migrating bar amplitude is decreased, the trend exhibited by the wavelength is less clear. The effects of sediment heterogeneity on resonant free bars and hybrid bars, however, seem different. Using a numerical model, Nelson et al. [2015b] found a decrease of the resonant free bars and hybrid bars amplitude, confirming the findings on free migrating bars, but at the same time found an increase instead of a decrease of bar wavelength. Knowing that free migrating bars display a different topography with respect to resonant free and hybrid bars, the observation of Nelson et al. [2015b] highlights that sediment heterogeneity can affect steady periodic bars and free migrating bars in a different way.

Hoey and Ferguson [1994], Seal et al. [1997] and Toro-Escobar et al. [2000] observed that heterogeneous sediment tends to form a pattern of downstream fining during aggradational scenarios in sediment feeding flumes, whether alluvial bars formed or not. They linked this process to the mechanism of selective sediment transport, because fine sediment moves faster than coarse sediment, resulting in the pattern of coarser sediment upstream and finer sediment downstream. The authors also observed that surface sediment is always coarser than subsurface sediment. The pattern of sediment sorting over bars can either display coarse sediment over bar crests and finer sediment in pools [Lisle et al., 1991; Lisle and Madej, 1992; Diplas, 1994; Lanzoni, 2000b; Nelson et al., 2015a] or the opposite, i.e. fine sediment over bar crests and coarser sediment in pools [Takebayashi and Egashira, 2001]. Nelson et al. [2015a,b] attribute the occurrence of coarser bar tops to the decrease of local flow velocity and increase of lateral flow, explaining that longer bars grow faster than shorter bars when the roughness is variable

over space, with respect to a spatially constant roughness. In their numerical model, the authors used a single sediment storage layer, but outlined the importance of considering the effects of vertical sorting of sediments in future research works.

The points presented above underline the limitations of the actual knowledge and also the contradictory findings that continue to spark debate over the relationship between non-uniform sediment and bar morphodynamics. The work presented here aims to better understand this relationship, by clearly distinguishing free migrating bars from hybrid bars. To this goal, a two-dimensional fully-nonlinear model is constructed to simulate a laboratory experiment carried out by Lanzoni [2000b]. Based on this model, nine scenarios are then simulated to study the effects of sediment sorting and sediment heterogeneity on bar characteristics, taking into account vertical sediment sorting. The numerical model is constructed using the Telemac-Mascaret Modelling System (TMS)[1] in which the bed evolution module is based on the active layer model formulated by Hirano [1971], where the vertical substrate is decomposed in several sediment storage layers (i.e. bookkeeping layer model) [Blom, 2008].

A thorough description of the materials and methods used for the study is given in Section 4.2, which includes the formulation of the mathematical and numerical model, details on the laboratory experiment used for the numerical model calibration and on the setting-up of this model, a presentation of the numerical scenarios and of the methods to analyse the computed bar characteristics. In Section 4.3, the numerical results of interest corresponding to the flow and sediment transport, bars properties and planform and vertical sorting of sediment are fully detailed for all the scenarios simulated. Then, on the basis of these results, a discussion is held in Section 4.4 on the influence of sediment size heterogeneity and sediment sorting on free and hybrid bars morphodynamics. The conclusions of this work are given in Section 4.5.

4.2 Materials and methods

4.2.1 Mathematical and numerical model

The two-dimensional morphodynamic model used in this work presents two components: a hydrodynamic module and a morphodynamic module. The hydrodynamic module is based on the solution of the shallow-water equations (SWE) [de Saint-Venant, 1871; Weiyan, 1992; Nezu et al., 1994; Vreugdenhil, 2013]:

$$\begin{cases} \partial_t h + \vec{u} \cdot \nabla(h) + h\nabla \cdot (\vec{u}) = 0 \\ \partial_t u + \vec{u} \cdot \nabla(u) = -g\partial_x z_f - gS_{f,x} + h^{-1}\nabla \cdot (h\nu_t \nabla u) \\ \partial_t v + \vec{u} \cdot \nabla(v) = -g\partial_y z_f - gS_{f,y} + h^{-1}\nabla \cdot (h\nu_t \nabla v) \end{cases} , \tag{4.1}$$

where t [s] is the time, $\partial_t = \partial/\partial_t$, $\nabla = (\partial_x, \partial_y)$ is the gradient vector field, g= 9.81 m/s^2 is the acceleration due to gravity, h [m] is the water depth, z_b [m] is the elevation of the bed topography, $z_f = z_b + h$ [m] is the free surface elevation, $\vec{u} = (u, v)$ [m/s] is the depth-averaged flow velocity vector with u and v [m/s] the component along the longitudinal x-axis and transversal y-axis direction respectively, with $|\vec{u}|$ [m/s] the module of $\vec{u}$, and ν_t [m^2/s] is the turbulent eddy viscosity term that models the so-called Reynold stresses and the differential dispersion terms originated from the lack of vertical uniformity of the horizontal velocity field. The friction law $\vec{S_f}$ [-] of Chézy is given as follow:

$$\vec{S_f} = (S_{f,x}, S_{f,y}) = \frac{\vec{u}|\vec{u}|}{C^2 h} , \tag{4.2}$$

[1] www.opentelemac.org

where $S_{f,x}$ and $S_{f,y}$ correspond to the components of the friction law $\vec{S_f}$ [-] along the longitudinal $x-$axis and transversal $y-$axis direction respectively and C [$m^{1/2}/s$] corresponds to the Chézy friction coefficient. The formula of Nikuradse [1950] is used to calculate the equivalent friction coefficient of Chézy denoted $C_f = g/C^2$ [-] as a function of the equivalent roughness height of the bed denoted with k_s [m]:

$$C_f = 2\Big[\log\Big(\frac{30h}{ek_s}\Big)/\kappa\Big]^{-2} \ , \tag{4.3}$$

where κ is the von Kármán coefficient (= 0.40 for clear waters) and e is the base of the natural logarithm.

The morphodynamic module is based on the Exner equation [Exner, 1920; García, 2008]. In case of non-uniform sediment, the Exner equation is applied to every size fraction of sediment in which the mixture is subdivided. The following procedure is adopted: *i*) the sediment mixture is discretized into sediment fractions, and for each fraction the representative sediment diameter is given, *ii*) the bedload transport capacity equation and the mass conservation formula are applied for each separate fraction of sediment.

The solution for sediment mass conservation is based on the mathematical concept proposed by Hirano [1971], who developed a continuity model for the vertical sorting of sediment. The method is based on the decomposition of the bed into a homogeneous top layer, called *active layer*, and an unchanging homogeneous *substrate* [Church and Haschenburger, 2017; Ashmore et al., 2018]. The active layer is a fully mixed layer, defined as the layer where all the bed fluctuations are concentrated [Blanpain, 2009; Stecca et al., 2016]. Following Hirano [1971]'s concept, the bed is discretized in the vertical direction as follows:

$$z_b = \eta_{a:1} + L_a \ , \tag{4.4}$$

where $\eta_{a:1}$ [m] denotes the absolute elevation of the interface between the active layer and the substrate, and L_a [m] corresponds to the active layer thickness. The sediment mass continuity equation is given as follows [e.g. Parker et al., 2007]:

$$L_a\partial_t F_{a,i} + \big[F_{a,i} - \mathcal{F}_{a:1,i}\big]\underbrace{\partial_t L_a}_{=0} = \frac{1}{\epsilon_0}\big[\mathcal{F}_{a:1,i}\nabla\cdot\vec{q_b} - \nabla\cdot\vec{q_{b,i}}\big] \ , \tag{4.5}$$

where $\partial_t L_a = 0$ because the active layer thickness is assumed to be constant during the whole simulation, $F_{a,i}$ is the volume fraction content of the i^{th} size fraction in the active layer and $\mathcal{F}_{a:1,i}$ is the volume fraction content of the i^{th} size fraction in the interface separating the active layer and the substrate, $\vec{q_b} = (q_{b,x}, q_{b,y}) = q_b(\cos\alpha, \sin\alpha)$ [m^2/s] corresponds to the total volumetric bedload solid discharge per unit of width without pores, with components $q_{b,x}$ and $q_{b,y}$ along the $x-$ and $y-$ axis directions respectively, $\vec{q_{b,i}} = (q_{b,i,x}, q_{b,i,y}) = q_{b,i}(\cos\alpha_i, \sin\alpha_i)$ [m^2/s] corresponds to the fractional volumetric bedload solid discharge per unit of width without pores of the i^{th} size fraction, $\epsilon_0 = (1 - P_0)$ with P_0 the bed porosity, α is the angle between the bedload and the x-axis direction and α_i the angle between the transport rate of the i^{th} size fraction and the x-axis direction. In the current model, the vertical sorting of sediment is made possible by discretizing the substrate into several sublayers [Blom, 2008], where the fraction volume content of i^{th} size fraction of sediment in the k^{th} sublayer is denoted $F_{k,i}$. The implementation of the above equation requires the specification of the active layer and the sublayer thicknesses, the interfacial exchange fractions and the number of sublayers [Viparelli et al., 2017]. Vertical fluxes of sediment are computed following the formulation of Hirano

[1971]:

$$\mathcal{F}_{a:1,i} = \begin{cases} F_{a,i} & \text{if } \partial_t z_b > 0 \\ F_{1,i} & \text{if } \partial_t z_b < 0 \end{cases} , \tag{4.6}$$

where $F_{1,i}$ corresponds to the fraction volume content of i^{th} size fraction of sediment in the first sublayer.

It is of key interest to accurately estimate the sediment transport in natural rivers, since bar evolution (*i.e.* armor formation and *break-up*) depends on fractional transport rates estimation [Parker, 1990; Orrú et al., 2016; Powell et al., 2016]. Therefore, the authors proposed to use the model of Wilcock and Crowe [2003] (WC-2003), which is interesting in the way that *i*) it is based on surface investigations and is particularly adapted for the prediction of transient conditions of bed armoring and scenarios of bed aggradation/degradation, *ii*) it considers the full size distribution of the bed surface (from finest sands to coarsest gravels), *iii*) it was calibrated under a wide range of water discharges and sediment mixtures, *iv*) the hiding function has been designed to resolve discrepancies observed from previous experiments [Proffitt and Sutherland, 1983; Parker, 1990] including the hiding-exposure effect of sand content on gravel transport for weak to high values of sand contents in the bulk, and *v*) it has already showed efficiency when applied for morphodynamics modelling [An et al., 2017]. For each i^{th} size fraction, the magnitude of the fractional transport rate without gravitational effects $q_{b0,i} = |\vec{q_{b0,i}}|$ [m^2/s] is estimated using the bedload capacity formula of Wilcock and Crowe [2003]:

$$W_i^* = f(\tau_b/\tau_{r,i}) = \frac{\Delta_s g q_{b0,i}}{F_{a,i} u_*^3} , \tag{4.7}$$

where W_i^* [-] corresponds to the dimensionless transport rate for the i^{th} size fraction of sediment, $\Delta_s = \frac{\rho_s}{\rho} - 1$ [-] is the relative submerged sediment density, with ρ [kg/m^3] the water density and ρ_s the sediment density [kg/m^3], τ_b [Pa] is the bed shear stress, $\tau_{r,i}$ [Pa] the reference shear stress of the i^{th} size fraction defined as the value of τ_b at which $W_i^* = 0.002$ and $u_* = \sqrt{\tau_b/\rho}$ [m/s] the shear velocity (also called friction velocity). The transport function of WC-2003 is defined as follows:

$$W_i^* = \begin{cases} 0.002\Phi_i^{7.5} & \text{for } \Phi_i < 1.35 \\ 14\left(1 - \frac{0.894}{\Phi_i^{0.5}}\right)^{4.5} & \text{for } \Phi_i \geq 1.35 \end{cases} , \tag{4.8}$$

where the ratio $\Phi_i = \tau_b/\tau_{r,i}$ is incorrectly referred to as Φ in the literature [Wilcock and Crowe, 2003; Recking et al., 2015].

A hiding-exposure function is defined to estimate $\tau_{r,i}$ so that the sediment transport rates are lowered for finer fractions (i.e. increase of $\tau_{r,i}$) and increased for coarser material (i.e. decrease of $\tau_{r,i}$). This is accounted in the model as follows:

$$\frac{\tau_{r,i}}{\tau_{r,m}} = \left(\frac{d_i}{d_{s,m}}\right)^{b_i} \quad \text{with} \quad b_i = \frac{0.67}{1 + \exp\left(1.5 - \frac{d_i}{d_{s,m}}\right)} , \tag{4.9}$$

where d_i [m] corresponds to the sediment diameter of the i^{th} size fraction, $d_{s,m}$ [m] is the mean sediment diameter of surface, $\tau_{r,m}$ [Pa] is the reference shear stress of the mean sediment diameter of surface and b_i is the power-coefficient of the hiding-exposure function which is incorrectly referred to as b in the literature. $\tau_{r,m}$ is computed as a function of the dimensionless median reference shear stress of bed surface $\tau^*{}_{r,m}$ such that $\tau^*{}_{r,m} = \frac{\tau_{r,m}}{\Delta_s \rho g d_{s,m}}$ where $\tau^*{}_{r,m} = 0.021 + 0.015\exp[-20F_s]$, with F_s the fraction volume content of sand at the bed surface [-].

By using independent sediment transport measurements, several authors [e.g. Recking et al., 2015; An et al., 2017] have showed that the performance of the formula of WC-2003 could be improved by modifying one or several parameters. In this work, the authors proposed to calibrate the sediment transport formula by estimating the fractional transport rates of sediment with multiplying W_i^* by a dimensionless coefficient called α_b.

Sediment transport capacity formulas are generally fitted against experimental data under the assumption of a flat bed (neglecting the gravitational effects). Natural riverbeds may show milder or steeper slopes due to the presence of dunes, ripples, steps, or pools in the longitudinal direction and curves in the transverse direction. As a result, gravity effects increase the bedload transport in downslope sections and lessen the movement of particles in upslope directions. Several formulas have been proposed to take into account the bed slope effect on *i*) the magnitude [Koch and Flokstra, 1980; Soulsby, 1997] and *ii*) the direction of bedload transport [Koch and Flokstra, 1980; Talmon et al., 1995]. The correction of bedload magnitude is modelled with the formula proposed by Koch and Flokstra [1980], where the fractional transport rate $q_{b0,i}$ is modified as a function of the bed slope degree with respect to the current direction:

$$q_{b,i} = q_{b0,i}\Big(1 - \beta_1 \partial_s z_b\Big) = q_{b0,i}\Big[1 - \beta_1\left(\partial_x z_b \cos\delta + \partial_y z_b \sin\delta\right)\Big] \ , \tag{4.10}$$

where β_1 is an empirical coefficient accounting for the streamwise bed slope effect, δ is the angle between the current and the x-axis direction, and s the coordinate along the current direction. The bedslope effect is similar to a diffusion term in the bed evolution equation [Van der Meer et al., 2011] and may smooth the bed topography and prevent from numerical instabilities [Zolezzi and Seminara, 2001; Cabrit, 2009]. The correction of bedload direction is given by the relation of Bendegom [1947]:

$$\tan\alpha_i = \frac{q_{b,i,n}}{q_{b,i,s}} = \frac{\sin\delta - T_i \partial_y z_b}{\cos\delta - T_i \partial_x z_b} \ , \tag{4.11}$$

where α_i is the angle between the sediment transport vector of the i^{th} size fraction of sediment and x-axis direction which will deviate from the bed shear stress vector due to gravity effects, $q_{b,i,n}$ and $q_{b,i,s}$ correspond to the bedload magnitudes along the normal to the current direction and the streamwise direction, respectively, and where the coefficient T_i is calculated as follows [Talmon et al., 1995]:

$$T_i = \frac{1}{\beta_2 \sqrt{\tau^*_{b,i}}} \ , \tag{4.12}$$

where $\tau^*_{b,i}$ is the bed shear stress adimensionnalized by the i^{th} size fraction of sediment also known as Shields parameter and scales the gravity effects as a function of the grain diameter of the i^{th} size fraction, and β_2 is an empirical coefficient used as a calibration parameter.

The total shear stress τ [Pa] is calculated from the depth averaged flow velocity field, where $\tau = 0.5\rho C_f(u^2 + v^2)$ and C_f is equal to the sum of skin friction and bedform drag. In this study, the bed shear stress is determined as a function of the total shear stress:

$$\tau_b = \mu\tau \ , \tag{4.13}$$

where $\mu = C'_f/C_f$ is the friction factor and C'_f [-] is the equivalent Chézy coefficient only due to skin friction and is the only component acting on bedload [Mendoza et al., 2016]. C'_f is calculated

assuming a flat bed by using the Nikuradse's formula (Equation 4.3), where the roughness height k_s' [m] is a function of the mean sediment diameter at the bed surface with:

$$k_s' = \alpha_{k,s} \times d_{s,m} \ , \tag{4.14}$$

with $\alpha_{k,s}$ a calibration parameter. García [2008] summarized different values of $\alpha_{k,s}$ measured in the field and in the laboratory ranging from 1 to 6.6.

The numerical solution of Equations 4.1 is based on the finite element method P_1, where the advective terms are computed with the method of the characteristics. The numerical solution of the sediment transport continuity equation (Equation 4.5) is performed by a procedure that combines an implicit finite element scheme and an edge-based explicit upwind advection scheme. This procedure assures mass-conservation at machine accuracy, monotonicity of tracers, copes with dry zones and is easily applicable to domain decomposition [Hervouet et al., 2011].

4.2.2 Study case

The reference numerical model is meant to reproduce one laboratory experiment carried out by Lanzoni [2000b] at Delft Hydraulics (The Netherlands). Lanzoni's experiments were performed in a water and sediment-recirculating rectangular straight flume of 55 m long, 1.5 m wide and 1 m deep with rigid vertical sidewalls, with an initially flat bed. The imposed downstream free surface was adjusted so that the water surface profile was parallel to the longitudinal bed slope. Exiting sediment was continuously weighted to estimate sediment transport and then recirculated upstream [Lanzoni, 2000a]. According to Lanzoni, sediment was mainly transported as bedload. The bimodal grain size distribution (GSD) used by Lanzoni [2000b] was composed of a mixture of 67% of a well-sorted quartz sand with a geometric mean diameter of 0.19 mm and 33% of a well-sorted coarser sediment with a geometrical mean diameter of 2.0 mm, with $\rho_s = 2.65 \cdot 10^3$ kg/m^3. Among the experiments performed by Lanzoni, test P2009 is selected for the current study because sediment sorting was only measured and adressed for this experiment.

Test P2009 was carried out with a constant flow discharge equal to $45 \cdot 10^{-3}$ m^3/s resulting in an average water depth equal to $\bar{h}$ =0.050 m, with an initial longitudinal bedslope equal to 0.00525. Under the conditions of this experiment, the width-to-depth ratio, denoted $\beta = B/\bar{h}$ [-] with B [m] the active width (i.e. at bankfull conditions), is equal to 27. The averaged exiting discharge of sediment including pores was $1.088 \cdot 10^{-4}$ m^3/s. Due to the high shear stress, a condition of fully mobilized transport was observed during the experiment. The longitudinal bar topography was measured at 20 cm from the sidewalls and on the center of the flume at $t = 3$ h when alternate migrating bars were well developed. During the experiments, non-uniform sediment was observed to strongly inhibit the formation of small-scale bedforms, such as ripples and dunes [Lanzoni, 2000b].

4.2.3 Numerical model setup

The numerical model from which all scenarios are derived uses an unstructured computational mesh composed triangles with typical length of approximately 0.093 m with a computational time step of $\Delta t = 0.04$ s in order to keep a Courant number approximately equal to 0.2. Mesh and time convergence analyses have been conducted in order to obtain a satisfying spatial representation of the bars and ensuring numerical stability of the model. For all simulations, the turbulent eddy viscosity is set equal to $\nu_t = 10^{-6}$ m^2/s and $\rho = 1\,000$ kg/m^3. The initial longitudinal bed slope is set equal to $i_0 = 0.00525$ and an initial random bed perturbation in the range [-5; 5] mm is used in order to fasten the formation of free bars. The sediment consists

of two size fractions having diameter $d_1 = 0.2$ mm (67%) and $d_2 = 2$ mm (33%), respectively, with $\Delta_s = 1.65$ and $P_0 = 0.40$. In order to model the vertical sorting of sediment, the bed is discretized into nine vertical sediment storage layers where the thickness of the sublayers is equal to the active layer thickness, excepted from the deepest one.

The boundary conditions of the hydrodynamic model correspond to an upstream constant flow discharge equal to $45 \cdot 10^{-3}$ m^3/s and a downstream constant free surface elevation. Recirculation of sediment is simulated in the numerical model, which consists of re-injecting the volume of sediment that exits the channel uniformly across the upstream boundary, so that sediment mass continuity is always ensured in the channel.

As pointed out by Defina [2003] and observed later by Qian et al. [2016] and Mendoza et al. [2016], free bars develop far from the upstream boundary. For this reason, the model flume has been extended from $x = 60$ m to $x = 120$ m.

4.2.4 Numerical model simulations

Calibration of the hydrodynamic model is performed based on the available hydraulic data (i.e. mean water depth, longitudinal slope of the water surface and flow velocity), where $k_s = 0.01$ m yields satisfactory values of averaged water depth and velocity. Calibration of the morphodynamic model is based on the available sediment transport volume and raw data of longitudinal bed evolution profiles measured in the laboratory. Satisfactory values of bar amplitude, wavelength and celerity are obtained with $\alpha_b = 3.2$, $\beta_1 = 1.3$, $\beta_2 = 1.6$, $\alpha_{k,s} = 5.5$ and $L_a = 5$ mm (*cf* 4.3.1). Before calibrating the model, a sensitivity analysis based on the active and subsurface layers thicknesses has been conducted. This analysis showed that the sediment sorting pattern tends to be identical using layer thicknesses in the range of [5-10] mm, even if the increasing of layers thicknesses tends to slow down the process of sediment sorting with respect to bed evolution. Using thicker layers, the computed sediment sorting pattern becomes irrelevant as the variation of fractional volume contents of sediment is too slow in comparison to bed evolution." This calibrated model is then used as a scenario of reference (run P2009-1) for the simulation runs presented thereafter.

Eight numerical scenarios (P2009-2 to -9) have been derived from the reference scenario (P2009-1). All scenarios have a duration of 280 000 s (≈83 h) in order to reach morphodynamic equilibrium. Four of these scenarios (P2009-3, -4, -8 and -9) have a transverse obstacle obstructing 2/3 of the channel width, which is inserted in the channel at $x = 10$ m on the right side wall to generate hybrid bars [e.g. Crosato et al., 2011].

The influence of sediment size heterogeneity on free and hybrid bars is analysed by comparing the results of scenarios with different sediment mixtures having the same median grain diameter, hence exhibiting different degrees of sediment size heterogeneity. Runs P2009-5 and -8 correspond to a uniform sediment of median diameter equal to $d_{50} = 0.48$ mm, which is equal to the median grain diameter of the non-uniform sediment used by Lanzoni [2000b], referred to as uniform sediment (Uni-GSD); runs P2009-1 and -3 correspond to the non-uniform sediment used by Lanzoni, referred to as reference sediment (Ref GSD); runs P2009-6 and -9 correspond to a GSD with $d_1 = 0.1$ mm (67%) and $d_2 = 4$ mm (33%), referred to as extended sediment (Ext-GSD).

The role of planform and vertical sediment sorting on free and hybrid bars is investigated by comparing the results of two types of scenarios: scenarios for which sediment sorting is accounted (runs P2009-1, -3 and -6) and scenarios for which sediment sorting is not accounted (runs P2009-2, -4 and -7). To avoid planform and vertical grain size sorting, these scenarios are characterized by a thick active layer of $L_a = 100$ m. Indeed, using the active layer approach

of Hirano, the volume fraction content of the i^{th} size fraction in the active layer $F_{a,i}(x,y,t)$ is assumed to be constant along the vertical (i.e. independent from z), but it is a function of the longitudinal, transversal coordinates (x,y) and time t. This dependence allows to describe the time evolution of the different volume fractions in the active layer. Assuming a thick active layer is equivalent to neglect mass exchange between the active layer and the substrate, where the volume fraction of the i^{th} size fraction in the substrate denoted as $F_{sub,i}(x,y,z,t)$ is also function of the vertical axes z (Equation 4.5). All scenarios are listed in Table 4.1.

Table 4.1: Scenarios studied.

Run	Scenario description *	Grain Size Distribution (GSD)	Obstacle (Y/N)	Sediment sorting (Y/N)	Bars at equilibrium F=Free H=Hybrid
P2009-1	Reference	Ref	No	Yes	F
P2009-2	Reference without sorting	Ref	No	No	F
P2009-3	Reference with obstacle	Ref	Yes	Yes	F & H
P2009-4	Reference with obstacle without sorting	Ref	Yes	No	H
P2009-5	Reference with uniform sediment	Uni	No	No	F
P2009-6	Reference with extended sediment	Ext	No	Yes	F
P2009-7	Reference with extended sediment without sorting	Ext	No	No	F
P2009-8	Reference with obstacle with uniform sediment	Uni	Yes	No	F & H
P2009-9	Reference with obstacle with extended sediment	Ext	Yes	Yes	F & H

∗ The duration of the numerical simulations is equal to 280 000 s for all the scenarios.

4.2.5 Analysis methods

In this work, H_b [cm] denotes bar amplitude and corresponds to the elevation between a maximum and a minimum of bed topography [Nelson et al., 2015a] between the longitudinal profiles extracted at 20 cm from the left and the right sidewalls (i.e. at $y = \pm 0.55$ m). The bar wavelength λ_b [m] denotes the distance between the two nearest bar tops separated by a pool. Averaged free bar characteristics obtained numerically are computed in the last 40 meters of the channel, i.e. 80-120 m, as here are assumed to be fully developed in this area. Similarly, the characteristics of hybrid bars are measured in the interval [35-70] m. The bar wavelength denoted by $\lambda_{b,max}$ [m] corresponds to the longest free bar wavelength observed during a given simulation, that is representative to the most fully developed free bar during the numerical run. The bar wavelength denoted by $\lambda_{b,s}$ [m] corresponds to the hybrid bar wavelength measured at the end of the simulation. The free bar celerity c_b [m/h] is measured as the distance of migration of a bar front during a given lapse of time, while the free bar rate c_r [bar/h] is defined as the number of bar fronts that intersect a given section during a given lapse of time. This lapse of time corresponds to the time between when the first fully developed free bars are observed in the channel and the end of the simulation. The bed evolution Δz_b [m] is computed as the difference between the channel bed elevation obtained at a given time and that from the initial time (i.e. $t = 0$ s). The raw longitudinal bed profiles measured in the laboratory experiment are analysed and compared to consider only fully developed bar characteristics. The morphodynamic equilibrium is assumed to be reached when all morphodynamics variables are time periodic for each point of the domain.

Bar *tops* or *crests* denote the highest topographic points of bars, while *pools* correspond to the lowest topographic points (Figure 4.1). For free bar migrating in downstream direction, as in the experiments of Lanzoni, the bar *fronts* are located downstream of the bar top, just before

the transition with the lee side. Originally defined for dunes, the *lee side* corresponds to the transition between the bar front and the pool and has a negative slope, while the *stoss side* is used for the transition between the pool and the next bar front (Figure 4.1). As for dunes, we compute the dimensionless ratio of bar amplitude over bar wavelength ($=\frac{H_b}{\lambda_b}$) to determine the lee and stoss sides slopes.

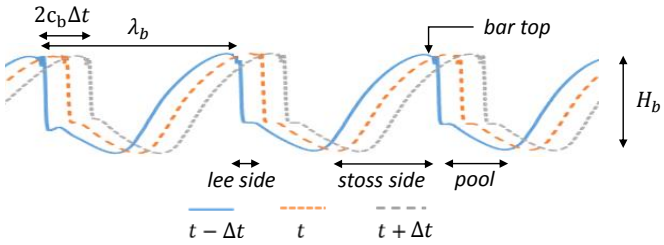


Figure 4.1: Illustration of the terminology and nomenclature used to describe bars.

4.2.6 Bar mode prediction and concept of resonance

The physics-based predictor for the number of river bars per cross-section of Crosato and Mosselman [2009] is used in the present study. The most likely number of bars per cross section, denoted m, is derived from the following equation:

$$m = \frac{\beta}{\pi}\sqrt{(b-3)f(\bar{\tau}^*)C_f}\ , \tag{4.15}$$

where b (here =5) [-] is the degree of nonlinearity in the dependence of sediment transport on the flow velocity, $\bar{\tau}^*$ [-] corresponds to the reach-averaged Shields number and $f(\bar{\tau}^*) = \frac{0.85}{E}\sqrt{\bar{\tau}^*}$ according to Talmon et al. [1995], where E is a coefficient of calibration, commonly set equal to 0.5. To remain consistent with the formulation for the correction of bedload direction used in the numerical model, E is set equal to 0.53 so that $\beta_2 = 1.6$ in Equation 4.12.

While the bar mode is defined as an integer number, when derived using Equation (15), it results as a real number. For this reason, we indicate "mode" the real result of Equation (15). In the case of $m = 1$, the system is at right resonant conditions for alternate bars. When $m < 1$, the system is at sub-resonant conditions, so that hybrid bars amplitude decreases longitudinally. When $m > 1$, the system is at super-resonant conditions, so that hybrid bars amplitude grows longitudinally. The resonant width-to-depth ratio for alternate bars, denoted β_r, is derived from Equation 4.15 by imposing the value $m = 1$.

4.3 Numerical results

In this section, the influence of sediment size heterogeneity and planform and vertical sorting of sediment on bar morphodynamics are studied for the scenarios with and without the presence of an upstream obstacle obstructing 2/3 of the channel width. The values of morphodynamic variables and the bar characteristics at equilibrium are summarized in Table 4.2 for all scenarios.

Table 4.2: Sediment transport and observed bar characteristics for the studied scenarios.

Run	$\bar{Q_b}$ 10^{-4}[m^3/s]	$\frac{\bar{Q_{b,1}}}{\bar{Q_{b,2}}}$	$F_{a,1}$	$F_{sub,1}$	$\lambda_{b,s}$ [m]	$H_{b,s}$ [cm]	$\lambda_{b,max}$ [m]	H_b [cm]	c_r [bar/h]
P2009-1	1.097	2.6	0.58	0.65	-	-	14.4	5.2	0.63
P2009-2	1.091	4.5	0.67	0.67	-	-	14.7	5.4	0.61
P2009-3	1.133	2.3	0.60	0.66	28.5	4.6	20.1	5.8	0.29
P2009-4	1.150	4.3	0.67	0.67	20.6	8.0	-	-	-
P2009-5	1.081	-	-	-	-	-	13.9	4.7	0.65
P2009-6	1.229	2.7	0.53	0.64	-	-	15.0	6.1	0.70
P2009-7	1.231	8.2	0.67	0.67	-	-	15.7	6.2	0.72
P2009-8	1.108	-	-	-	26.4	5.0	21.8	5.1	0.31
P2009-9	1.262	2.6	0.58	0.65	30.3	6.1	22.7	4.1	0.30

$\bar{Q_b}$ (resp. $\bar{Q_{b,1}}/\bar{Q_{b,2}}$) is the averaged solid discharge (resp. is the ratio between the averaged fractional solid discharges) crossing the downstream boundary during the 280 000 s of simulation; $F_{a,1}$ (resp. $F_{sub,1}$) is the spatially averaged fractional volume content of fine sediment in the active layer (resp. in the substrate excepted from the deepest layer); H_b (resp. $H_{b,s}$) denotes the averaged free bar (resp. hybrid bar) amplitude measured from t =20 000 s to t =280 000 s (resp. at t = 280 000 s); $\lambda_{b,s}$ denotes the hybrid bar wavelength measured at the end of the simulation; c_r is the bar rate and is measured from t =20 000 s to t =280 000 s.

4.3.1 Scenarios without obstacle

To describe the numerical results obtained in the runs without obstacle, attention is firstly given on the reference scenario (P2009-1). Bar amplitude, wavelength and celerity obtained with the reference scenario (Figure 4.2 and Table 4.3) are in good agreement with Lanzoni [2000b]'s observations. The averaged exiting volume of sediment from the beginning of the numerical experiment to t = 3 h is equal to 1.083 $\cdot 10^{-4}$ m^3/s, which is close to 1.088 $\cdot 10^{-4}$ m^3/s measured during the laboratory experiments performed by Lanzoni [2000b]. At t = 3 h, the computed bar wavelength range is 10.8$\pm$1.1 m and the bar amplitude range 3.5$\pm$0.9 cm (Figure 4.2), while Lanzoni [2000b] measured a value of 10.2 m and 3.4 cm, respectively. The computed bar velocity is underestimated compared to the values measured during the experiments (9.8 m/h against 11.0 m/h, respectively) (Table 4.3 and Figure 4.3a). Experimentally and numerically, free bars show very steep topographic gradients at the transition between bar heads and pools, and mild stoss sides.

Author	H_b [cm]	λ_b [m]	c_b [m/h]
This work	3.5	10.8	9.8
Lanzoni [2000b]	3.4	10.2	11.0

Table 4.3: Free bar characteristics at t = 3 h.

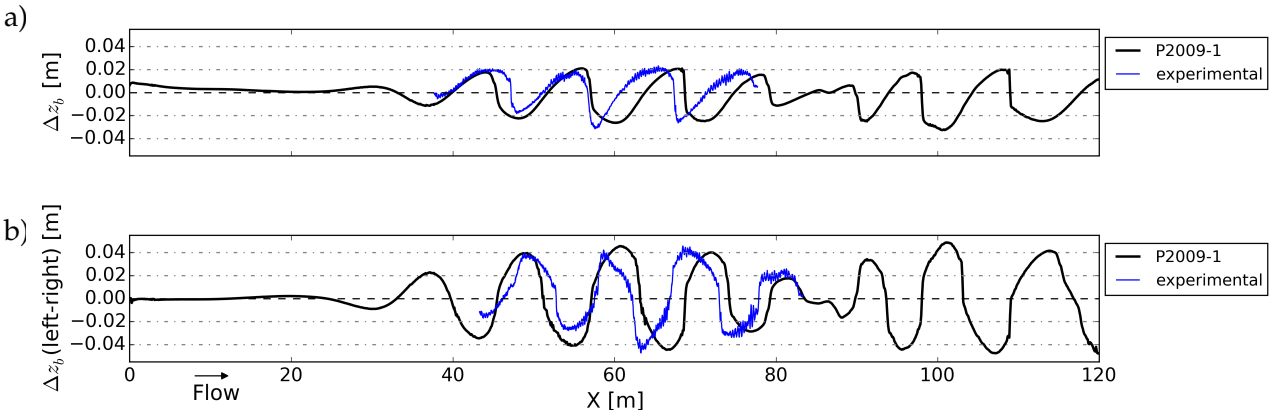
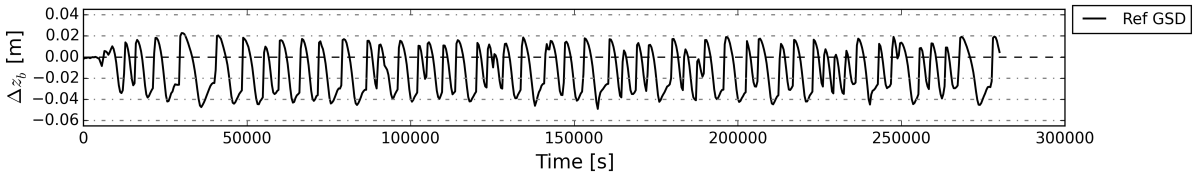
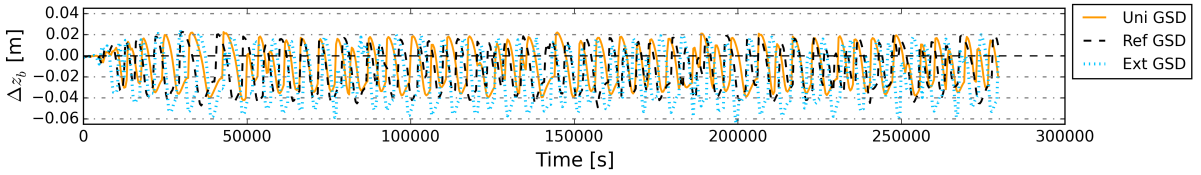


Figure 4.2: Comparison of a) bed evolution along the left longitudinal profile and b) difference of bed elevation between the left and right longitudinal profiles at t =3 h, obtained with the calibrated numerical model (run P2009-1) and measured by Lanzoni [2000b].

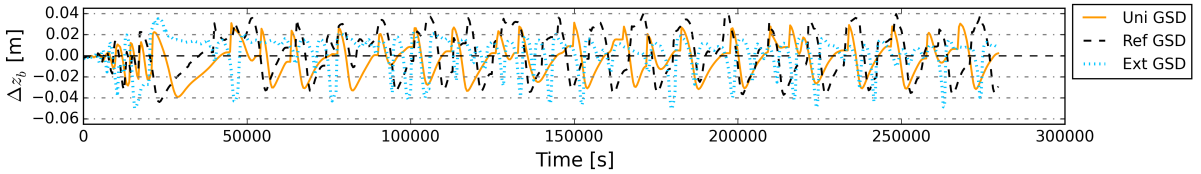
a) Reference scenario (run P2009-1)



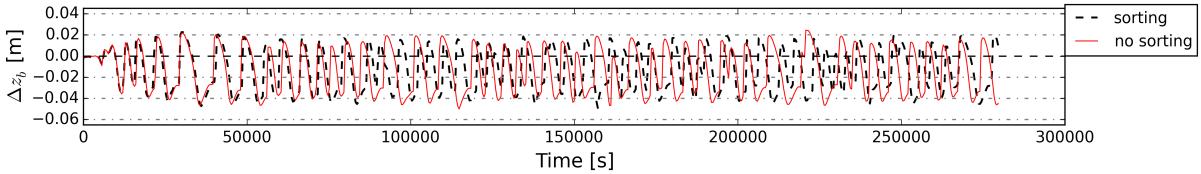
b) Influence of sediment size heterogeneity; without obstacle (runs P2009-1, -5 and -6)



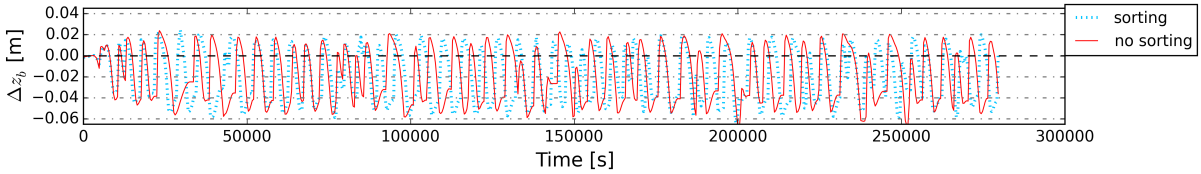
c) Influence of sediment size heterogeneity; with obstacle (runs P2009-3, -8 and -9)



d) Influence of sediment sorting; Ref GSD; without obstacle (runs P2009-1 and -2)



e) Influence of sediment sorting; Ext GSD; without obstacle (runs P2009-6 and -7)



f) Influence of sediment sorting; Ref GSD; with obstacle (runs P2009-3 and -4)

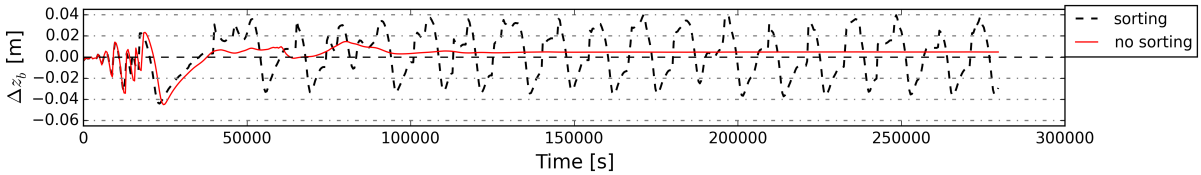


Figure 4.3: Bed evolution from $t = 0$ s to $t = 280\,000$ s at (x=102 m;y=0.55 m) for the scenarios considered in this study.

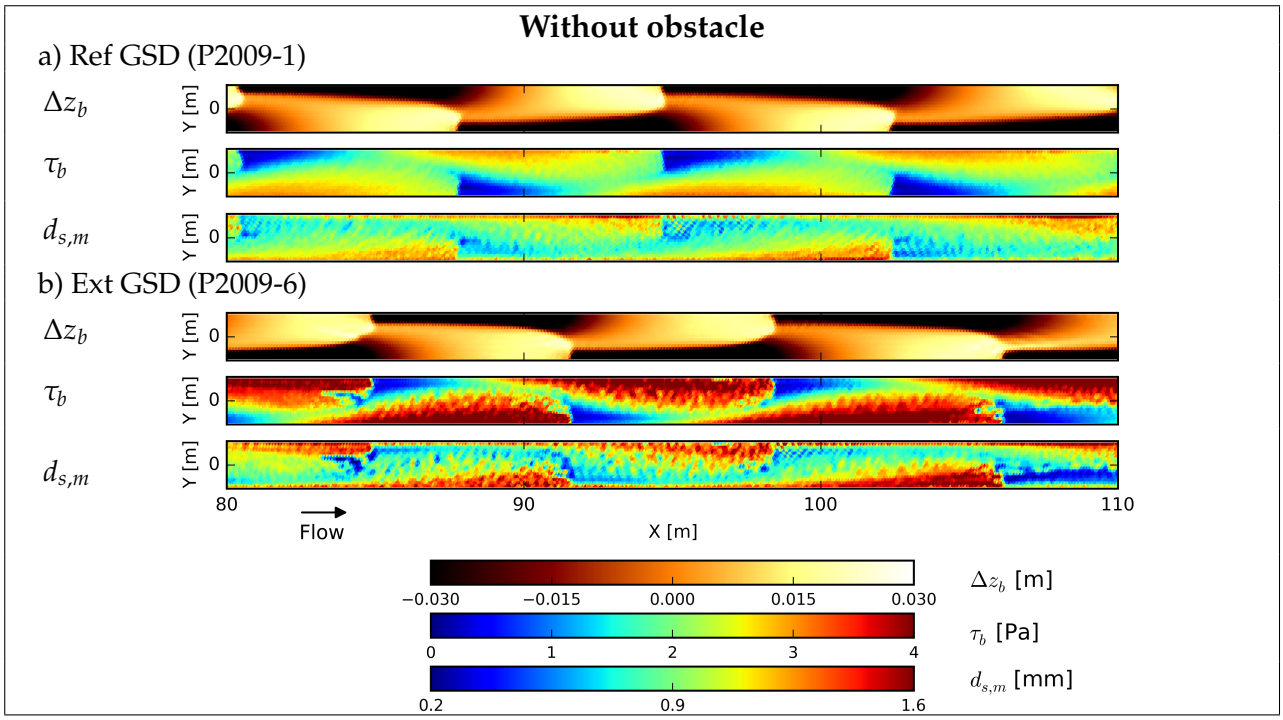


Figure 4.4: Planform evolution of bed topography, shear stress and surface sediment sorting without obstacle for the (a) reference and (b) extended sediments scenarios at $t = 280\,000$ s.

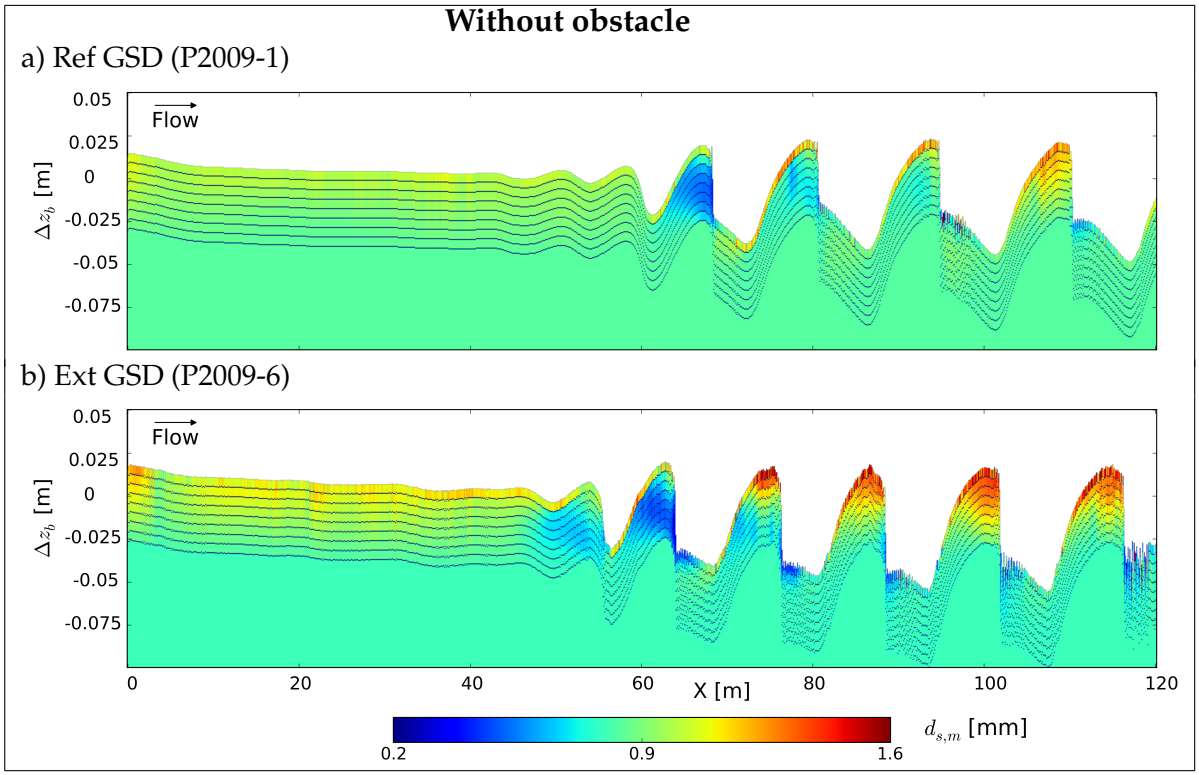


Figure 4.5: Longitudinal profiles of bed evolution and vertical sediment sorting without obstacle for the (a) reference and (b) extended sediments scenarios at $t = 280\,000$ s.

In the reference scenario, bars are similar to the ones observed experimentally by Lanzoni [2000b] as they continue to grow and elongate over time, before reaching a quasi-equilibrium state starting from $t \approx 20\,000$ s (≈ 5.6 h) wherein their amplitude and wavelength tend to vary moderately by oscillating toward an equilibrium value (Figure 4.3a). The last behavior is also observed when the uniform sediment (run P2009-5) and the extended sediment (run P2009-5) are used (Figure 4.3b). When non-uniform sediment is used (i.e. runs P2009-1 and -5), along the sidewalls, the material is increasingly coarser from the lee-side (transition between the bar front and the pool) until the next bar front (Figure 4.4, 4.5 and 4.6). While the bar top is covered by coarse material, where the coarsest material is located in the vicinity of the sidewall, the *thalweg* is found to be covered by fine material, where the finest material is found immediately downstream of the bar front. As a result, a pattern of coarse material on top and fine material in pools is found, and coincides with Lanzoni's observations at $t = 3$ h (Figure 4.6) in terms of spatial representation of sediment sorting. This is achieved when the active layer and subsurface layers thicknesses are set equal to $L_a = L_{k=1:7} = 2.5 \times d_{90}$ (= 5 mm), where d_{90} corresponds to the 90$^{\text{th}}$ centile of the GSD. The adopted layer thicknesses are found to lie in the range of the values mentioned in the literature, which is often of the same order of d_{90} [García, 2008; Church and Haschenburger, 2017; Viparelli et al., 2017].

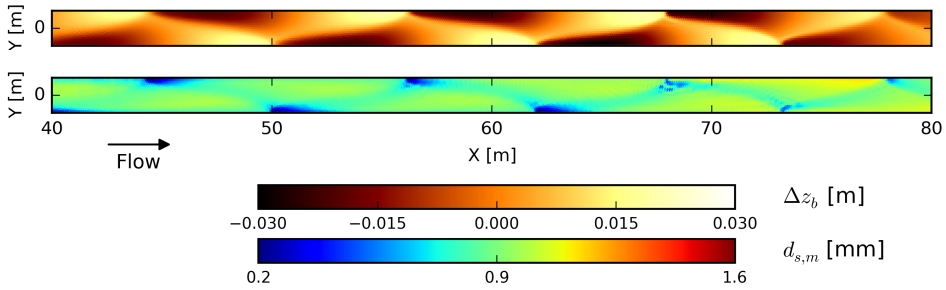


Figure 4.6: Bed evolution and surface sediment sorting at $t = 3$ h from $x = 40$ m to $x = 80$ m obtained with the reference scenario (run P2009-1).

At the early stages of the reference scenario ($t \leq 5\,000$ s), the transport rate of fine material is approximately 4 times higher than the coarse material rate (Figure 4.7a, solid lines), whereas the initial volume content of fine sediment is about twice the initial content of coarse sediment. In the upstream part of the flume, fine material is progressively removed and transported downstream as a sedimentation wave, illustrated by the wave front located at $x \approx 23$ m in Figure 4.8. This results in a decreasing of the fine material content in the upstream part of the flume and in an increasing of it in the downstream part in the active layer and it is even more pronounced in the sublayers (Table 4.2 and Figure 4.9a,b). Figure 4.9 shows that the fine material tends to be buried, as the upper layers gradually coarsen over time. A similar behavior has also been observed in the run with the extended sediment (Figure 4.7b), but is not detailed here.

In run P2009-1, even though the system remains highly dynamic and produces bars of different amplitudes, wavelengths and celerities (Figure 4.3a), and the averaged sediment transport rates oscillate around a constant value already after $t \approx 20\,000$ s (Figure 4.9), the morphodynamics equilibrium is assumed to be reached at around $t \approx 150\,000$ s when fractional transport rates of sediment and volume fractions content of sediment in the sediment storage layers are nearly constant (Figure 4.7a and 4.9). Depending on the longitudinal location in the flume, the bed displays different properties. A first zone is identified in the upstream part of the flume where bars do not form (Figure 4.10a). A distance is required to generate numerically a

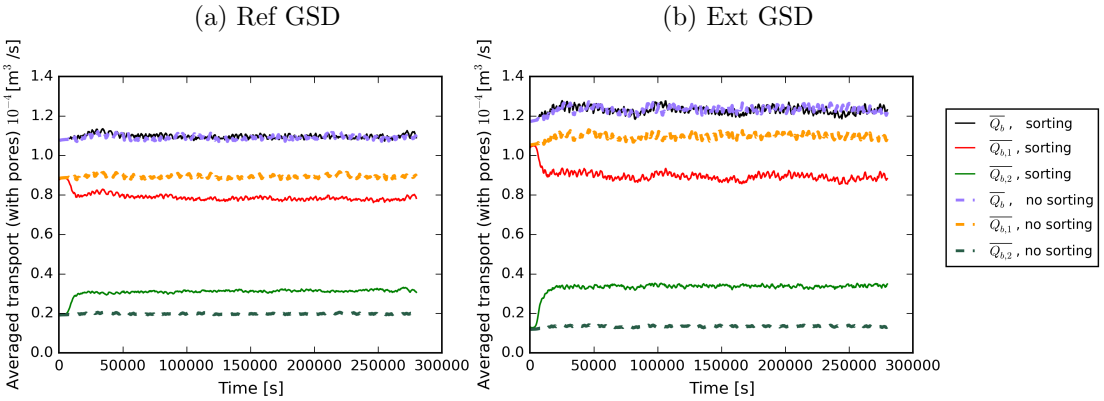


Figure 4.7: Spatially averaged solid discharges with and without sediment sorting for (a) the reference sediment (run P2009-1) and (b) the extended sediment (run P2009-6) scenarios. $\bar{Q}_b$ is the averaged volume of sediment crossing the downstream boundary during the 280 000 s of simulation; $\bar{Q_{b,1}}$ (resp. $\bar{Q_{b,2}}$) is the averaged volume of fine (resp. coarse) sediment crossing the downstream boundary during the 280 000 s of simulation.

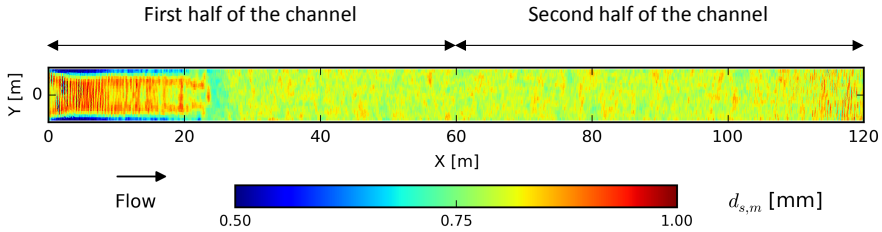


Figure 4.8: Planform surface sorting of sediment at $t = 2\,000$ s with the reference scenario showing the sedimentation wave front at $x \approx 23$ m (run P2009-1).

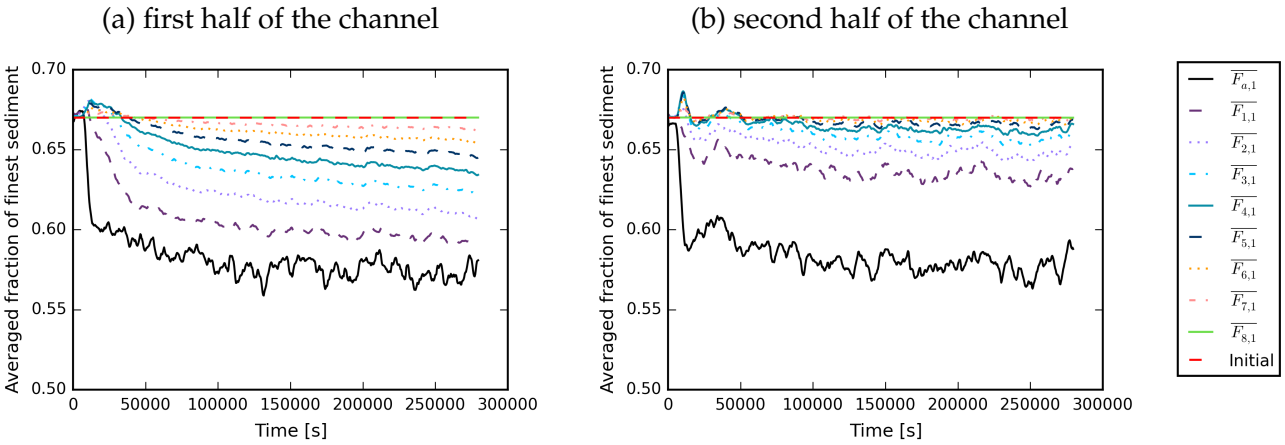
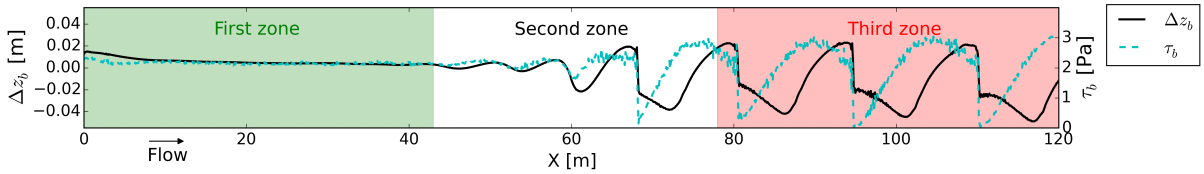


Figure 4.9: Time evolution of the spatially averaged fractional volume contents of fine sediment in each storage layer denoted $\bar{F}_{k,1}$ in the (a) first ($x \in [0; 60]$ m) and (b) second half ($x \in [60; 120]$ m) parts of the channel with the reference scenario (run P2009-1).

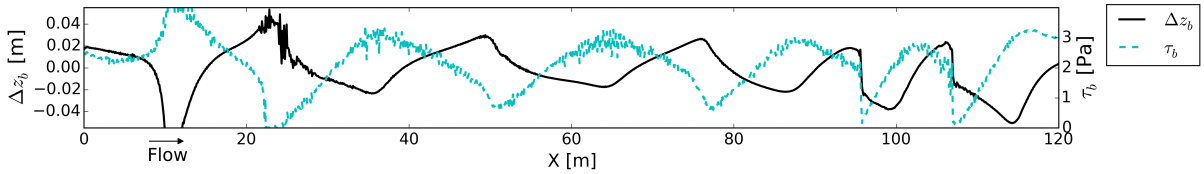
sufficient lateral bed deformation leading to the formation of bars [Crosato et al., 2012], and is approximately equal to $x = 40$ m in run P2009-1, corresponding to approximately $3.5 \times \lambda_b$. A second zone can be identified immediately downstream, where bars are forming, developing and merging (Figure 4.10a). In the conditions of the current numerical run, this area extends from $x \approx 50$ m to $x \approx 85$ m, corresponding to approximately from $4 \times \lambda_b$ to $7 \times \lambda_b$. The last identified area corresponds to a zone where bars are fully developed and propagate with a regular pattern (Figure 4.10a). These zones are also present when the uniform sediment (run P2009-5) and extended sediment (run P2009-6) are used, and have the same spatial extent that in the case where the reference sediment (run P2009-1) is used (e.g. Figure 4.4 and 4.5).

In such a configuration, the bed shear stress is the lowest immediately downstream of the bar fronts and progressively increases until approximately the middle of the stoss side, before decreasing progressively toward the bar front (Figure 4.10a). A sudden drop of bed shear stress is located downstream of the bar front, as the water depth immediately increases and the flow velocity decreases at this location. This leads to high sediment transport rates over the bar, which suddenly drops at the bar front (Figure 4.11a). Consequently, the free migrating bar topography, the distribution of bed shear stress and sediment transport display an asymmetrical longitudinal shape (Figure 4.10a, 4.11a and 4.12a,b). Small values of α indicate that the vector of the sediment transport slightly deviates from the flow direction (Figure 4.12). As a result, the gravitational forces exerted by the transverse slopes weakly contributes to the bedload transport (e.g. 9% in the case of the reference scenario, Figure 4.12c), where the remaining fraction of bedload follows the flow direction (Figure 4.12b).

a) Without obstacle with sorting



b) With obstacle with sorting



c) With obstacle without sorting

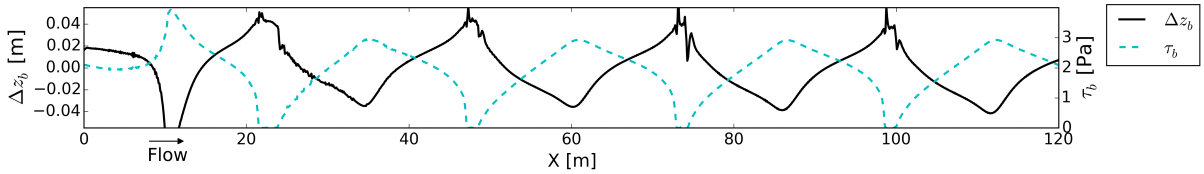


Figure 4.10: Longitudinal profiles of bed evolution and bed shear stress with the reference sediment at $t = 200\,000$ s a) without obstacle with sediment sorting (run P2009-1), b) with the obstacle with sediment sorting (run P2009-3) and c) with the obstacle without sediment sorting (run P2009-4).

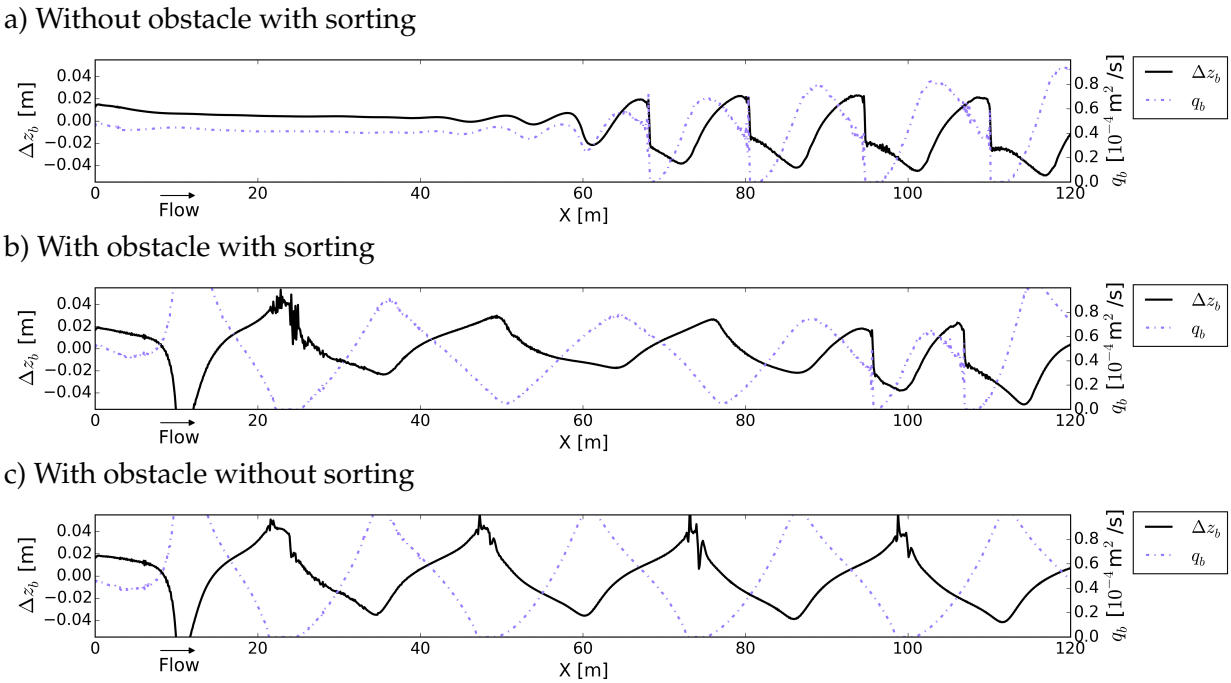


Figure 4.11: Longitudinal profiles of bed evolution and total bedload transport rate with the reference sediment at $t = 200\,000$ s a) without obstacle with sediment sorting (run P2009-1), b) with the obstacle with sediment sorting (run P2009-3) and c) with the obstacle without sediment sorting (run P2009-4).

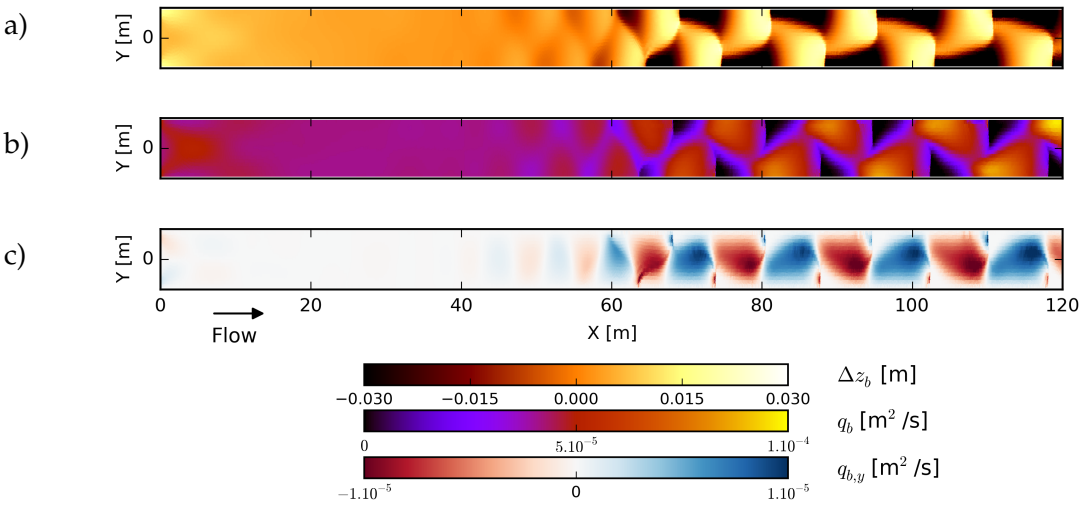
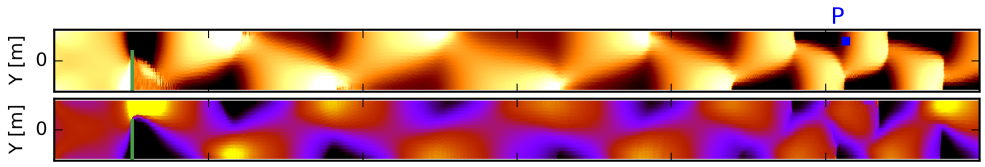


Figure 4.12: Planform distribution of the a) bed evolution, b) total volumetric bedload magnitude and c) component of the total volumetric bedload magnitude per unit of width without pores projected along y-axis at $t = 280\,000$ s for the reference scenario (run P2009-1).

4.3.2 Scenarios with an obstacle

The transverse obstacle set at $x = 10$ m and obstructing 2/3 of the flume width (Figure 4.13a,b) generates a forced bar immediately downstream in all the scenarios considered (runs P2009-3, -4, -8 and -9) [Crosato and Desta, 2009; Nelson et al., 2015b; Duró et al., 2016]. The first pool is located in front of the obstacle and is $\approx$ 8 cm deep. The forced bar located immediately downstream of the obstacle is $\approx$ 5 m long (Figure 4.13a,b). At $t = 0$, a train of free alternate bars progressively forms in the vicinity of the obstacle and migrates downstream. In all scenarios, bars located in the vicinity of the obstacle gradually slow down and stabilize in amplitude and wavelength, leading to the development of hybrid bars in this region (from $x \approx 30$ m to $x \approx 65$ m, Figure 4.13a,b).

a) With sorting



b) Without sorting

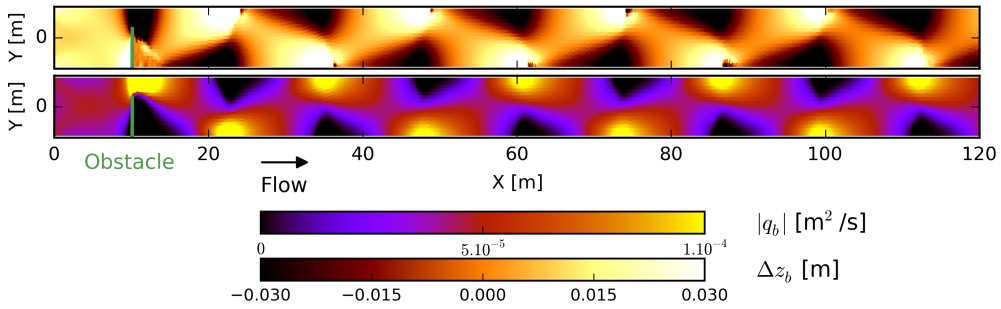


Figure 4.13: Planform distribution of the bed evolution and total bedload magnitude at $t = 200\,000$ s using the obstacle and the reference sediment, with a) sediment sorting (run P2009-3) and b) without sediment sorting (run P2009-4). P denotes the measurement point located at (x=102 m;y=0.55 m).

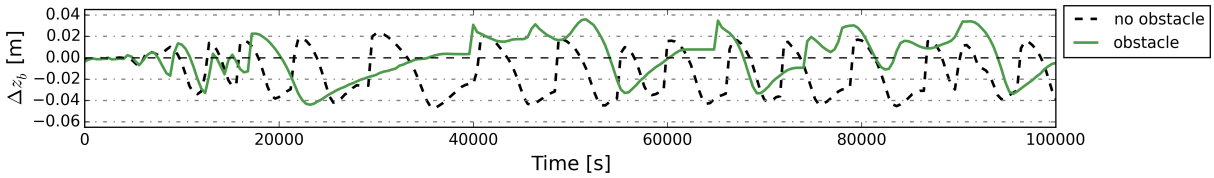


Figure 4.14: Bed evolution from $t = 0$ s to $t = 100\,000$ s at point P (x=102 m;y=0.55 m) with reference sediment without (P2009-1) and with (P2009-3) the transverse obstacle.

For $t < 25\,000$ s, the downstream free bars obtained without (run P2009-3) and with (run P2009-4) the transverse obstacle show distinct amplitudes, wavelengths and celerities (Figure 4.14), while the averaged free bar amplitude, maximal wavelength and migration rate are affected by less than 10%. From $t > 25\,000$ s, for scenarios P2009-3, -4, -8 and -9, the obstacle has an influence on the downstream free bars ($x > 85$ m), where their averaged characteristics

differ from the ones obtained without obstacle (Table 4.2). The presence of hybrid bars slows down free bar migration, increasing the free bar wavelength while the amplitude can either increase when uniform or reference sediments are used (runs P2009-1 vs. -3 and P2009-5 vs. -8) or decrease when the extended sediment is used (run P2009-6 vs. -9, Table 4.2 and Figure 4.3d,f). Free bars are present in the most downstream part of the flume i.e. for $x > 85$ m only if sediment sorting is accounted for or when the uniform sediment is used (runs P2009-3, -8 and -9, Figure 4.3f and 4.13a). Otherwise, free bars are completely replaced by hybrid bars, as showed by the steady time-series of the bed topography (run P2009-4, Figure 4.3f and 4.13b).

The longitudinal distribution of bed shear stress and total bedload transport rates over free bars obtained with and without an obstacle show a similar behaviour (Figure 4.10a,b and 4.11a,b). The variation of bed shear stress over hybrid bars (i.e. from $x \approx 30$ m to $x \approx 65$ m) is smoother than for free bars (i.e. $x > 85$ m), as well as the longitudinal topographic variations, where the lee side and the stoss side of hybrid bars display milder slopes (Figure 4.10b). In the case of hybrid bars, the maximum value of bed shear stress (≈ 3 Pa) is located in the pools, and the minimum of bed shear stress (≈ 0.6 Pa) is found above bar tops and is strictly positive. Moreover, as hybrid bars are longer than free bars, the decrease of bed shear stress from the middle of the stoss side to the front of hybrid bars is more pronounced than for free bars. Consequently, the sediment transport over hybrid bars is distributed differently than for free bars, where the variation of sediment transport is smoother than for free bars and is weakly increased in the *thalweg* and weakly decreased over bar tops (Figure 4.11a,b, 4.12a,b and 4.13). As a result, the hybrid bar topography, the bed shear stress and the sediment transport rates display a more symmetrical shape with respect to the ones obtained with free migrating bars.

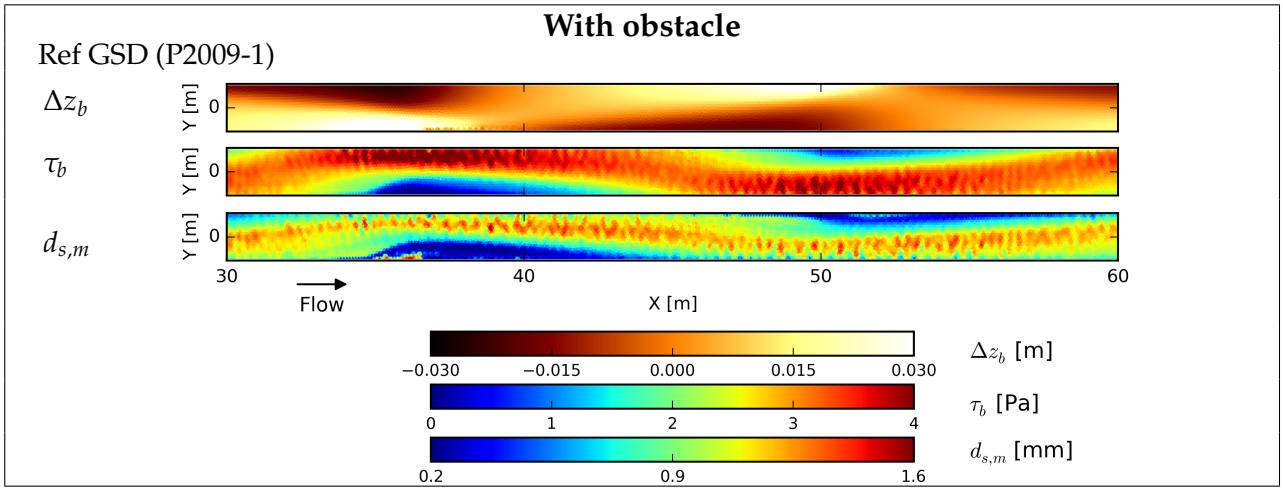


Figure 4.15: Planform evolution of bed topography, shear stress and surface sediment sorting with the obstacle for the reference sediment scenario at $t = 280\,000$ s.

According to Figures 4.15 and 4.16a,b, the finest sediment and the lowest shear stress are located at the downstream end of hybrid bar tops and at their fronts. Moreover, values of $d_{s,m}$ and τ_b tend to increase progressively until a point located between the pool and the first half of the stoss side, and then decrease progressively until the next bar top. On the opposite, the coarsest sediment tends to accumulate in the stoss side and in the *thalweg*, where the value of the bed shear stress is higher.

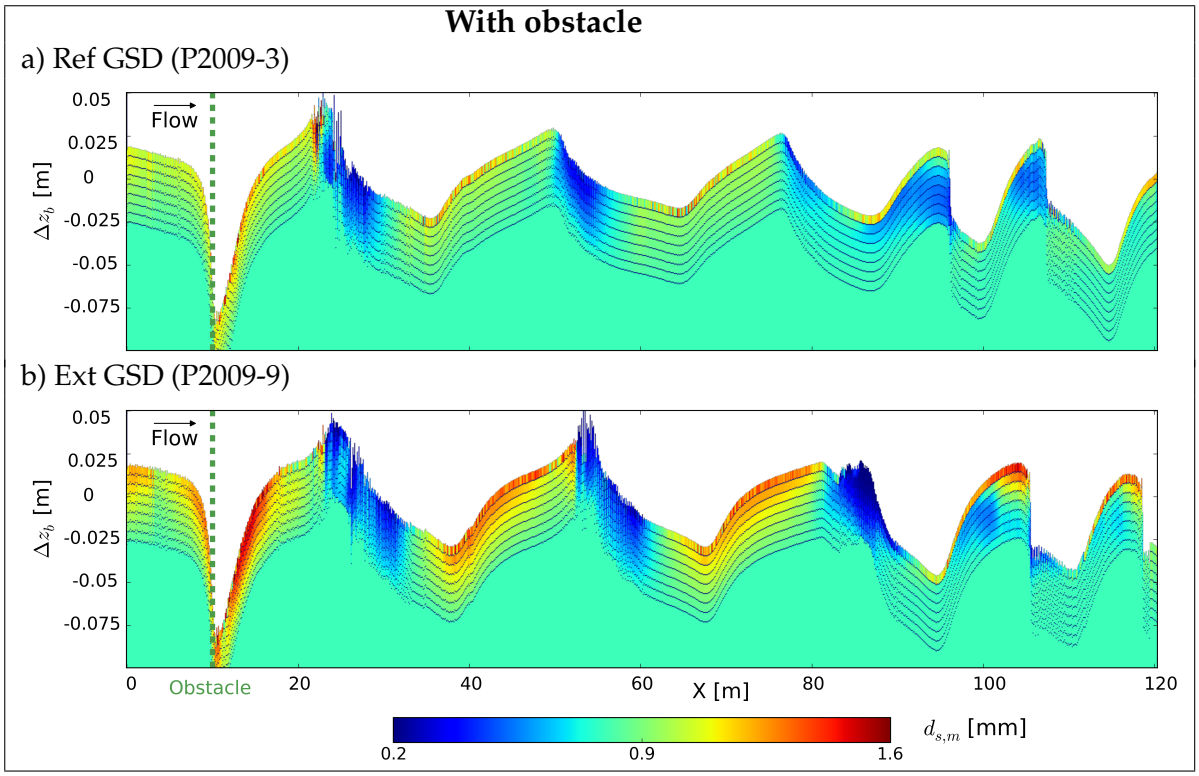


Figure 4.16: Longitudinal profiles of bed evolution and vertical sediment sorting with the obstacle with the (a) reference and (b) extended sediments scenarios at $t = 280\,000$ s.

4.3.3 Effects of sediment size heterogeneity

4.3.3.1 Free bars

The spatially averaged flow velocity, water depth, bed shear stress and equilibrium longitudinal slope obtained at the end of the numerical scenarios using various GSDs (runs P2009-1, -5 and -6) without the obstacle are summed-up in Table 4.4. The change of GSD does not affect the averaged flow depth and velocity, since the differences in flow velocity and water depth are less than 2%. On the other hand, in comparison with uniform sediment (run P2009-5), sediment size heterogeneity leads to a general increasing of bed shear stress and Shields numbers of around 31% with the reference sediment (run P2009-1) and 81% with the extended sediment (run P2009-6) (Table 4.4, Figure 4.4a,b). Similarly, the averaged total transport rate increases when a more heterogeneous sediment is considered, and the ratio of fine over coarse particles transport also increases slightly (Table 4.2 and Figure 4.7a vs. 4.7b). These results show that increased sediment size heterogeneity induces higher bedload transport rates, where the transport of fine sediment is significantly increased, while the transport of coarse sediment is only weakly increased (Tab. 4.4 and Figure 4.7a vs. 4.7b). This effect is associated to the hiding-exposure phenomenon [e.g. Wilcock and Crowe, 2003]. Consequently, the increasing of sediment transport rate is followed by a small, but not negligible, increasing of longitudinal reach slope denoted as i_∞ [-]. Indeed, at the end of the runs, the longitudinal slope obtained with uniform sediment is about 5.6‰,while it increases by 0.1‰ with the reference sediment and increases by 0.2‰ with the extended sediment (Table 4.4).

Table 4.4: Values of the representative hydraulic parameters obtained at $t = 280\,000$ s for the numerical runs using various GSDs and sediment layer thicknesses.

	Run	GSD	$\bar{u}$ [m/s]	$\bar{h}$ [m]	$\bar{\tau}_b$ [Pa]	$\bar{\tau}^*_{b,1}$ [-]	$\bar{\tau}^*_{b,2}$ [-]	i_∞ [-]	
	runs without obstacle								
Heterogeneity ↓	P2009-5	Uni	0.54	0.056	1.6	28	9	5.4 ‰	} sorting
	P2009-1	Ref	0.54	0.056	2.1	37	12	5.5 ‰	
	P2009-6	Ext	0.54	0.056	2.9	51	16	5.6 ‰	
Heterogeneity ↓	P2009-2	Ref	0.54	0.056	2.0	35	11	5.5 ‰	} no sorting
	P2009-7	Ext	0.54	0.056	2.5	44	14	5.6 ‰	
	runs with obstacle								
Heterogeneity ↓	P2009-8	Uni	0.53	0.055	1.6	28	9	5.5 ‰	} sorting
	P2009-3	Ref	0.53	0.056	2.0	35	11	5.6 ‰	
	P2009-9	Ext	0.53	0.055	2.6	46	14	5.6 ‰	

Heterogeneity ↓ = increase of sediment size heterogeneity

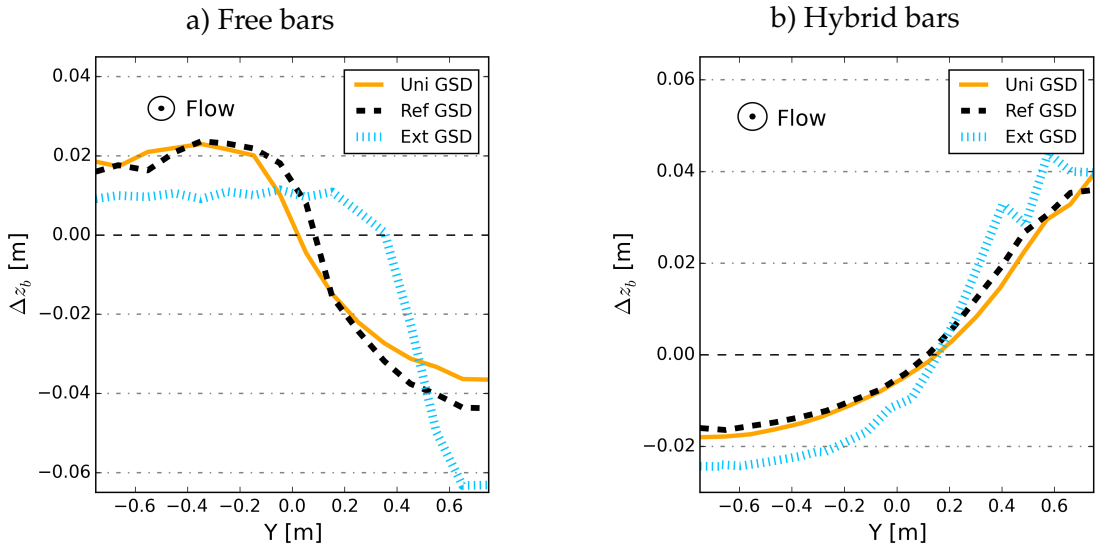


Figure 4.17: Cross-stream bed evolution of (a) free bars and (b) hybrid bars at bars front locations for the uniform, reference and extended sediments scenarios (different vertical scales are used).

Sediment size heterogeneity affects both free bar wavelength and amplitude (Figure 4.3b, 4.5a,b and 4.17a). The cross-stream profiles of the bar show that in comparison with uniform sediment, increasing sediment size heterogeneity tends to widen free bars by approximately 0.10 m ($\approx$ 15%) with the reference sediment and 0.30 m ($\approx$ 46%) for the extended sediment (Figure 4.17a). As a result, the flow is concentrated in the narrow pool, which tends to be deepen by approximately 0.8 cm ($\approx$ 13%) with the reference sediment and 2.4 cm ($\approx$ 40%) for the extended sediment. The change of GSD has a low impact on the elevation of the bar top (Figure 4.17a). Therefore, the free bar amplitude increases by approximately 11% in the case of the reference sediment with respect to the uniform sediment(Table 4.2 and Figure 4.3b and 4.5a vs. 4.5b). In the same way, the free bar amplitude increases by approximately 12% in the case of the extended sediment with respect to the reference sediment. In comparison with the uniform sediment, the time-averaged bar rate computed at (x=102 m;y=0.55 m) is weakly decreased by 3% with the

reference sediment, whereas the extended sediment tends to increase moderately by 11% the bar rate (Table 4.2). Consequently, as bars rate and wavelength are increased with increasing sediment size heterogeneity, bars celerity turns out to be higher too. When the obstacle is set-up (runs P2009-3, -8 and -9), in comparison with uniform sediment, increased sediment size heterogeneity tends to increase the free bar amplitude by 35% with the reference sediment and to decrease by 20% with the extended sediment (Table 4.2 and Figure 4.3c). In general, if the free bar amplitude increases, the maximal wavelength tends to decrease. The mean free bar velocities tend to follow the same trend as in the runs without obstacle, where bar velocity increases with the extended sediment.

Comparison between runs with the reference sediment and with the extended sediment (runs P2009-1 vs. P2009-6, P2009-3 vs. -9) indicates that planform and vertical sediment sorting become much more pronounced when a more heterogeneous sediment is used, whereas the surface sorting pattern remains identical considering a varying sediment size heterogeneity (Figure 4.4a,b and 4.5a,b). Moreover, the fully developed bars (from $x \approx 80$ m to $x \approx 120$ m) obtained in the reference and extended sediments scenarios generally show the same vertical sediment sorting pattern, which is defined by a progressive fining from the bar top surface until the deepest sediment layer and the opposite behaviour at the pool location.

4.3.3.2 Hybrid bars

Hybrid bars arise from the presence of a transverse obstacle as described in Section 4.3.2. With the obstacle, sediment size heterogeneity leads to a general increasing of bed shear stress of around 25% with the reference sediment (run P2009-3) and 62% with the extended sediment (run P2009-9), in comparison with uniform sediment (run P2009-8) (Table 4.4). The spatially averaged bedload transport rate slighty increases by 2.5% for the runs with an obstacle in comparison with scenarios without obstacle (Table 4.2). The decreasing of the ratio between the fine over the coarse fractional bedload transport rates shows that the obstacle tends to averagely coarsen the bedload, especially for the reference sediment. The averaged volume fractions for the fine material of surface and the sublayers (excepted from the deepest layer) present higher magnitudes (0.60 with the Ref GSD and 0.58 with the Ext GSD) in comparison with the experiments without channel obstacle (0.58 with the Ref GSD and 0.53 with the Ext GSD, Table 4.2).

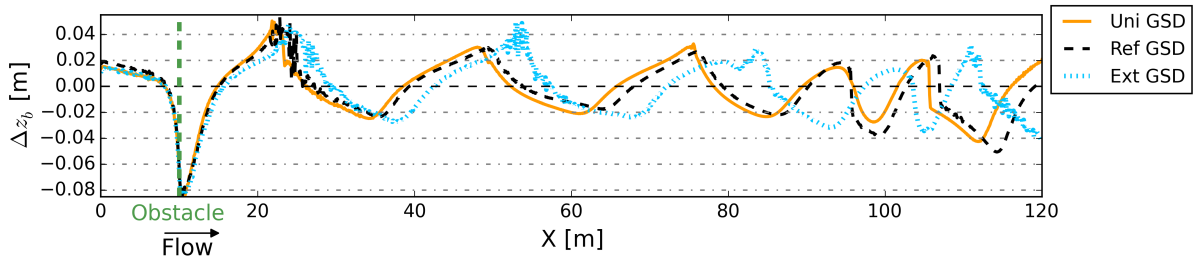


Figure 4.18: Longitudinal profiles of bed evolution at $t = 200\,000$ s with the obstacle for the uniform (P2009-8), reference (P2009-3) and extended (P2009-9) sediments scenarios.

Increasing of sediment size heterogeneity tend to decrease the hybrid bar amplitude and increase the wavelength by 8% with the reference sediment, and to increase importantly the hybrid bar amplitude by 22% and the wavelength by 15% with the extended size heterogeneity

(Table 4.2, Figure 4.3c and 4.18). The sediment sorting pattern obtained with the reference and extended sediments are similar, while the degree of sediment sorting increases if sediment size heterogeneity is increased (Figure 4.16a,b).

4.3.4 Effects of spatial sediment sorting

4.3.4.1 Free bars

While the spatially averaged water depth and scalar flow velocity are not significantly impacted by the sorting of sediment (Table 4.4) (run P2009-1 vs. P2009-2; run P2009-6 vs. P2009-7), the opposite phenomenon is observed for the bed shear stress. When the sorting of sediment is accounted for, indeed, the bed shear stress varies as a function of the local surface grain size (refer to Equation 4.13 and 4.14). In general, the averaged bed shear stress increases if sediment sorting is simulated (Table 4.4). Long-term simulations show that sediment sorting does not affect the longitudinal reach slope. Furthermore, for all the scenarios where sediment sorting is accounted, the surface sediment progressively coarsens whereas fine sediment tends to be buried (Figure 4.5a,b).

Comparison between runs in which sediment sorting is accounted (runs P2009-1 and -6) and in which sediment sorting is not accounted (runs P2009-2 and -7) show that planform and vertical sediment sorting has a negligible impact on the bed evolution during the earliest stages of free bar development (i.e. for $t < 80\,000$ s with the reference sediment and $t < 20\,000$ s with the extended sediment, Figure 4.3d,e). Later on, the sorting of sediment impacts the bed evolution, where bars shift in phase by slowing down (resp. accelerating), or alternatively increasing (resp. decreasing) their wavelength (Figure 4.3d,e). While sediment sorting decreases weakly the maximal bar wavelength by around 5%, it does not impact significantly the averaged free bar amplitude (Table 4.2), where bars tend to propagate at the same migration rate.

4.3.4.2 Hybrid bars

When sediment sorting is considered, at the late stage of run P2009-3, the formation of downstream free bars is controlled by a steady bar located at approximately $x = 70$ m, i.e. at a distance of approximately $2.5 \times \lambda_{b,s}$ downstream from the obstacle. Free bar and hybrid bar dynamics tend to follow a cyclic and repetitive pattern: the hybrid bar gradually elongates in amplitude (Figure 4.19a,b), until it reaches a maximum wavelength corresponding approximately to the wavelength of the steady bars formed more upstream (Figure 4.19b). Then, the last hybrid bar splits into two shorter bars (Figure 4.19c,d). The most upstream one remains steady, whereas the second one migrates downstream as a free bar (Figure 4.19d,e). This phenomenon of free bar formation is not observed when sediment sorting is not considered (run P2009-4), where hybrid bars develop from upstream and replace progressively all free bars (Figure 4.3f).

When sediment sorting is accounted for, the hybrid bar wavelength increases by 38% and the bar amplitude decreases by 74% (Table 4.2, Figure 4.13a,b and 4.20) with respect to the scenario without sediment sorting (run P2009-4). With sediment sorting, bars are damped in longitudinal direction [Struiksma and Crosato, 1989] and the bed shear stress is larger than zero over hybrid bar tops (Figure 4.10b). In the case without sediment sorting, the water depth over hybrid bars tops is close to zero, so that the bed shear stress and the sediment transport are equal to zero at bar front locations (Figure 4.10c 4.11c).

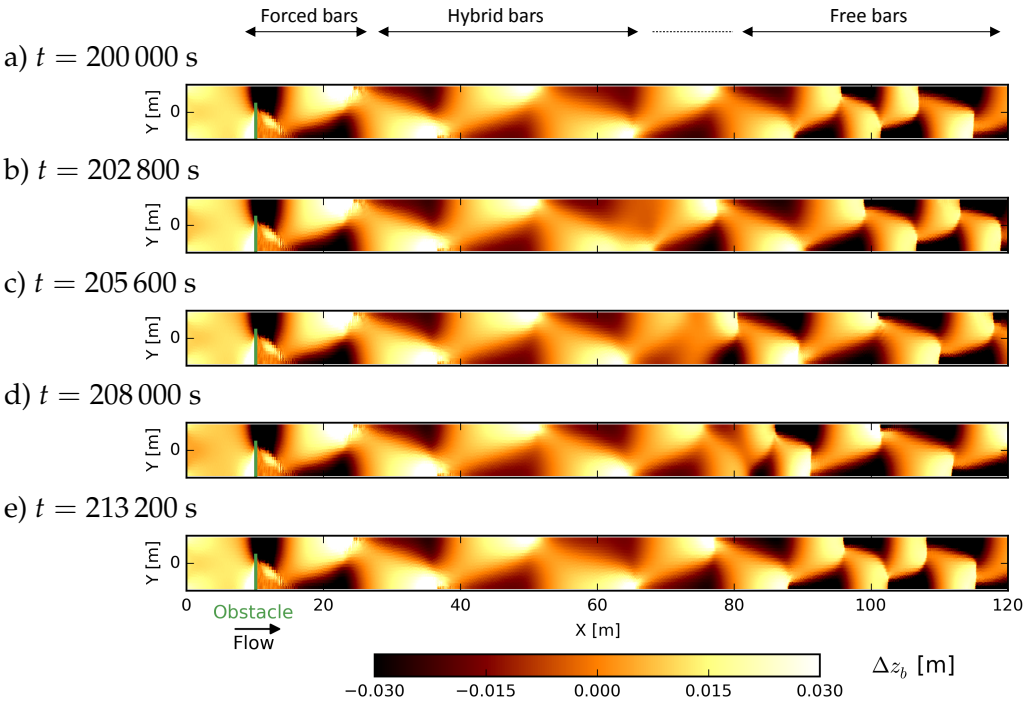


Figure 4.19: Planform bed evolution with an upstream transverse obstacle with the reference sediment at different times of the simulation showing the process of free bar detachment and formation (run P2009-3).

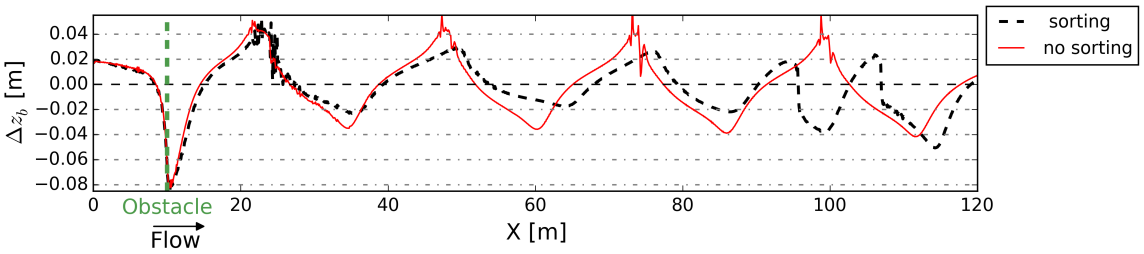


Figure 4.20: Longitudinal profiles of bed evolution at $t = 200\,000$ s with the reference sediment with sediment sorting (run P2009-3) and without sediment sorting (run P2009-4).

4.4 Discussion

4.4.1 Considerations on channel bed sediment sorting

According to the numerical results obtained with the model reproducing Lanzoni [2000b]'s experiment P2009 (run P2009-1), the sediment sorting pattern displays the expected sediment segregation resulting in coarse material over bar tops and finer sediment on the pools. In the model, the main mechanism controlling the sorting of sediment results from the interaction between the bed topography, the bed shear stress and the GSD used for the experiment. Fine material accumulates in areas characterized by low bed shear stresses. The increase of bed shear stress along the bar induces selective entrainment, so that grain size gradually coarsens along the bar, as also observed by Nelson et al. [2015a]. The pattern of coarse material on bar tops

and fine material on pools becomes more appreciable on the long-term than at the beginning of the experiments, showing that the degree of sediment sorting is amplified when bars are fully developed and that bed topography actively controls sediment sorting (Figure 4.4a). Numerical results also show that the sediment of surface and underneath layers coarsen progressively over time, while the sediment tends to be finer downstream than upstream (= downstream fining) and the bedload progressively coarsens during the simulation as observed experimentally by Hoey and Ferguson [1994], Seal et al. [1997] and Toro-Escobar et al. [2000] (Table 4.2 and Figure 4.7a and 4.9a,b). In the nature, this phenomenon should be depicted by a pattern of downstream fining, so that the fine sediment would be buried and the surface sediment would become coarser and less heterogeneous in size, and the fine sediment would be stored in areas of low constraints (i.e. downstream of bar fronts).

In the area where bars are forming, developing and merging (i.e. from $x \approx 50$ m to $x \approx 85$ m), free migrating bars display a sorting pattern with fine sediment in pools and coarse sediment on bar tops. The sediment at the surface of bars coarsens moderately, while the sediment of subsurface becomes finer (Figure 4.5a). By migrating downstream (i.e. for $x > 85$ m), free bars display the same sediment sorting pattern but with a higher degree of sorting (Figure 4.5a). This highlights the fact that the sorting of sediment does not adapt immediately to the topographic changes and hydraulic conditions, as the degree of sediment sorting is not the same in the area of bar formation and in the area of bar stabilization. In this case, sediment sorting rather requires a certain time or length (at approximately $6.5 \times \lambda_b$ from the channel inlet) to find a stable condition illustrated by the fully developed bars located at $x > 85$ m.

4.4.2 Comparison of free and hybrid bars morphodynamics

Free and hybrid bars show consistently a different bed topography (Table 4.2 and Figure 4.5a,b vs 4.16a,b, 4.19a-e and 4.20). Free bars are at least two times shorter than hybrid bars, which is in agreement with previous observations [Duró et al., 2016]. Free bar amplitude is of the same order than the amplitude of hybrid bars. As a result, the slope of the lee side and of the stoss side of free bars are steeper ($\frac{H_b}{\lambda_b} \approx 4 \cdot 10^{-3}$) than the ones of hybrid bars ($\frac{H_{b,s}}{\lambda_{b,s}} \approx 2.5 \cdot 10^{-3}$). The most striking difference is depicted at the bar front location: while free bars always show a very steep, almost vertical topographic gradient immediately downstream of their fronts, hybrid bars generally show a milder slope, which makes a smoother transition between their front and the lee side. Consequently, the distribution of bed shear stress and sediment transport along hybrid bars (Figure 4.10b and 4.11b,c) is different from the ones displayed by free bars (Figure 4.10a and 4.11a), where the longitudinal variations of bed shear stress and sediment transport are generally smoother over hybrid bars. With hybrid bars, the maximum values of bed shear stress are located in the pools and in the *thalweg*, while with free bars they are located closer to the middle of the stoss side. Moreover, the minimum of shear stress found immediately downstream of the bar front can be different from zero for hybrid bars, whereas it is always found to be equal to zero for free migrating bars. The averaged bed shear stress in the system is similar with and without the transverse obstacle (Table 4.4). However, it is relatively higher in the *thalweg* for hybrid bars in comparison with free bars, and to counterbalance this effect, the bed shear stress is lowered over hybrid bars tops (Figure 4.4a,b vs. 4.15). The same observation is made concerning the sediment transport rates (Figure 4.12a,b vs. 4.13a,b and 4.11a vs. b). The topography, the bed shear stress and the sediment transport rates measured over hybrid bars present a symmetrical shape, in contrast with free bars that show an asymmetrical shape, especially at the bar front location.

The difference observed between the distribution of bed shear stress over the hybrid and free bars explains how the hybrid bar topography enhances its stability by redistributing the bed shear stress over space, and consequently the sediment transport rates over bars. Indeed, in the case of free bars, the flow erodes the bar tops, so that the sediment is deposited in the pool found immediately downstream due to the sudden decrease of bed shear stress in this area (Figure 4.10a and 4.12a,b). This process may be at the origin of free bar migration, where bars progressively migrate by filling the pools and eroding their stoss side. In the case of hybrid bars, bar tops are characterized by low or zero bed shear stress, which prevents from bar top erosion or sedimentation because the divergence of sediment transport rates is equal to zero (Figure 4.10b,c and 4.13a,b).

Therefore, hybrid bars generate a permanent geometrical forcing which, by analogy with weak or middle amplitude meanders, deflect the flow toward the outer bend and concentrate the flow in the *thalweg* [Güneralp et al., 2012]. In the current numerical runs, the intensity the geometrical forcing is mainly controlled by the hybrid bar amplitude, which influences the stability of the downstream bars. When the hybrid bar amplitude is high, the geometrical forcing is high enough to sustain the development of hybrid bars everywhere in the channel (run P2009-4, Figure 4.10c and 4.13b). On the opposite, when the hybrid bar amplitude decreases, the geometrical forcing is not able to sustain the development of hybrid bars because the bed shear stress and sediment transport rates are increased over the bar tops, which in turn remobilize bars which become free (run P2009-3, Figure 4.10b and 4.13a). The origin of the difference of free bar and hybrid bar dominance in the simulations with and without sediment sorting is investigated more in detail in Section 4.4.3.

From the results presented in sections Section 4.3.1 and Section 4.3.2, it is found that hybrid bars and free bars exhibit different sediment sorting patterns (Figure 4.4 vs. 4.15 and 4.5 vs. 4.16). Fully developed free migrating bars always display fine sediment in pools and coarser sediment over their tops, which is in agreement with the observations of Lisle et al. [1991], Lisle and Madej [1992], Diplas [1994], Lanzoni [2000b] and Nelson et al. [2015a]. In the current numerical runs, free bars display a progressive coarsening from the lee side until the next bar front (Figure 4.4a,b and 4.5a,b). Hybrid bars display a high concentration of fine sediment at the beginning of the lee side (Figure 4.15 and 4.16), which smoothly decreases until the middle of the stoss side, and then progressively increases until the next bar top. In this case, the coarsest sediment tends to be concentrated in the *thalweg*, but it is also deposited over the stoss side due to the high shear stress and sediment transport in the *thalweg*. Hence, this study highlights that bars of different types can show different equilibrium conditions (bed topography, distribution of shear stress and sediment sorting pattern). These differences explain why sediment size heterogeneity and sediment sorting impact differently free migrating bars and hybrid bars.

4.4.3 Influence of spatial sediment sorting on periodic bars morphodynamics

The numerical results show that spatial sediment sorting induces higher bed shear stress, which correlates with a general coarsening of sediment at the surface and increased bed roughness (Table 4.2). The latter offers a larger resistance to the flow, which is taken into account by the model by computing the bed shear stress as a function of the bed roughness (Equation 4.3, 4.13 and 4.14). When free migrating bars are fully developed, the numerical results suggest that sediment sorting does not impact significantly the averaged free migrating bar properties.

The implementation of a lateral channel obstacle resulted in hybrid bar formation. The distribution of the bed shear stress over hybrid bars (Figure 4.10a) is comparable to the one obtained by Nelson et al. [2015b] over slowly migrating free bars (i.e. $c_b \approx 0$) and hybrid

bars. Comparison between runs with (run P2009-3) and without (run P2009-4) sediment sorting demonstrates that the latter has a strong impact on hybrid bars as it alters their characteristics and enhance the dynamics of free bars still present at the end of the model domain, as explained above (Figure 4.13a). The sediment sorting results in increased hybrid bar wavelength and reduced hybrid bar amplitude, which is in agreement with the observation of Nelson et al. [2015b]. Indeed, Nelson et al. [2015b] showed numerically that the spatially varying bottom roughness due to the spatialization of sediment size had a strong influence on equilibrium bar morphology. Bars were longer and damped when a variable bottom roughness was used because the roughness effects over bar tops (where the coarse sediment is concentrated) caused the local streamwise velocity to decrease and induced lateral flow in this region. In turn, it reduces the gradient of bed shear stress over bar tops, resulting in less deposition over the bar and explaining that longer and flatter bars are obtained when roughness is variable over space. As a result, the authors observed that the averaged bar wavelength increased by 39% whereas bar amplitude decreased by 22% if the bottom roughness was considered spatially variable. In their runs, bars tended to migrate slowly (i.e. $c_b \approx 0$) or slow down and stretch-out before reaching a quasi-equilibrium condition and became essentially fixed in place. This illustrates that the wavelength of these bars was equal to the ones of resonant free and hybrid bars [Crosato et al., 2011; Rodrigues et al., 2015; Duró et al., 2016], and explains why sediment sorting impacts in the same way the hybrid bars obtained in our model and the bars obtained by Nelson et al. [2015b].

From the theoretical perspective, the linear stability analysis (Equation 4.15) predicts $m = 1.02$ ($\beta_r = 26.5$) when sediment sorting is accounted (run P2009-3), while a higher bar "mode" equal to $m = 1.06$ ($\beta_r = 25.6$) is obtained when sorting is not accounted (run P2009-4). In both cases, the theory suggests that the system is close to resonance at super-resonant conditions as $m \approx 1$ (i.e. $\beta_r \approx 27$), suggesting that hybrid bars persist with the same characteristics from the obstacle until the channel outlet, see Siviglia et al. [2013]. While the theory is in agreement with the numerical results when sediment sorting is not accounted (run P2009-4), opposite behavior is obtained when sediment sorting is accounted (run P2009-3). In the numerical runs, hybrid bars persist only $2.5 \times \lambda_{b,s}$ downstream to the obstacle (in the same order of magnitude than Vanzo et al. [2011] who found approximately $3 \times \lambda_{b,s}$), and downstream to that area, the effect of the obstacle disappears and shorter free migrating bars appear. This difference may come from many reasons, such as the value chosen for b, or from the linear theory at the base of the formula and other simplifications, or even because the numerical solution includes truncation errors and numerical smoothing, which could explain that the theoretical bar regime is not fully represented in the simulations, where numerical smoothing is expected to increase damping in the longitudinal direction with respect to the theory. Taking these uncertainties into account, the fact that m is very close to 1 (i.e. close to the resonant conditions for alternate bars) explains the tendency of the system to switch easily from dominant free bars (run P2009-3) to dominant hybrid bars (run P2009-4). Eventually, in this context, both approaches suggest that sediment sorting invariably decreases the bar "mode" m.

The phenomenon of free bar detachment and formation, which has already been observed in a sandy-gravel-bed river on a hybrid bar located in a secondary channel [Rodrigues et al., 2012, 2015], is observed only if sediment sorting is simulated (run P2009-3, Figure 4.19). This process is not observed if sediment sorting is not accounted for, because the tops of hybrid bars are high enough - and generate a sufficient geometrical forcing - to prevent from erosion (Figure 4.10a), so that a train of hybrid bars progressively stabilizes and replaces the downstream free migrating bars. Sediment sorting is showed to impact bar characteristics, which in turn

control the distribution of the hydraulics variables over space resulting in modified sediment transport. Retroactively, it enhances bar mobility in the system. Therefore, under the conditions simulated, bar mobility and bed topography seem to be the primary factor controlling the sorting of sediment, which in turn impacts bar characteristics.

4.4.4 Influence of sediment size heterogeneity on periodic bars morphodynamics

In the current numerical runs, increasing sediment size heterogeneity increased the free bar amplitude and wavelength. The major differences found between the free bars obtained with using different GSDs can be mostly explained in terms of sediment mobility. The single increase of sediment size heterogeneity leads to higher bed shear stress because the Shields numbers $\bar{\tau}_1^*$ and $\bar{\tau}_2^*$ are dependent of the chosen GSD (Table 4.2). This leads to higher sediment transport rates (Table 4.2), inducing the formation of larger bars where flows concentrate along the opposite bank in the pools and increase bed shear stress there, resulting in higher pool erosion and resulting in higher bar amplitude (Figure 4.4a vs. 4.4b, 4.5a vs. 4.5b and 4.17a). In addition, as a result of increased size heterogeneity, a higher degree of sediment sorting is observed. By linking this observation with the findings of Nelson et al. [2015b] over resonant free and hybrid bars, this implies that due to the increasing of sediment size heterogeneity, the higher concentration of coarse sediment observed over the stoss side and the bar top (Figure 4.4a vs. 4.4b and 4.5a vs 4.5b) increases the local bed roughness, reducing the longitudinal flow velocity and increasing the lateral flow over bar tops, which enhances the steering of the flow exerted by the bed topography and explains that longer features grow faster than shorter ones. As a result, the free bar wavelength increases. Retroactively, as free bars are longer with increased sediment size heterogeneity, the flow shoals over the stoss side for a longer distance. For this reason, sediment transport becomes more size selective, which explains the increased degree of sediment sorting. Moreover, the increased degree of sediment sorting is also due to the fact that fine sediments are more mobile whereas coarse sediment tends to remain over bar tops when sediment size heterogeneity increases.

A linear stability analysis [Tubino et al., 1999] and flume experiments [Lisle et al., 1991] suggested that sediment heterogeneity leads to the reduction of free bar amplitude and wavelength. Lanzoni [2000a,b] also observed the reduction of free bar amplitude with respect to uniform sediment in his flume experiments, but did not clearly observe changes in averaged free bar wavelength. The main limitation of previous laboratory work is that despite the large number of experiments that have been carried out, data from using a uniform and a non-uniform sediment under the same experimental conditions (e.g. water discharge, longitudinal bed slope) is not available. For the numerical cases presented here, results show that increasing sediment heterogeneity generally results in increased free bar amplitude, wavelength and celerity. The discrepancy between the numerical results and results from the linear stability analysis of Tubino et al. [1999] could be explained by the fact that the models are based under different laws and assumptions (friction, bed slopes, bedload transport formula), or initial and boundary conditions (initial bottom perturbation, sediment boundary conditions), that have eventually a strong impact on the computed free bar properties.

The impact of increasing sediment size heterogeneity on hybrid bars is more complicated to understand and less documented in the literature. Nelson et al. [2015b] observed a decrease of 18% of bar amplitude and the increase of 35% of the wavelength with uniform sediment vs. non-uniform sediment. For the numerical cases presented here, hybrid bars tend to elongate when the degree of size heterogeneity increases (Figure 4.18), but no general trend can be observed concerning their amplitude, as the increase of sediment size heterogeneity induces both the

moderate decrease (run P2009-3) and the strong increase (run P2009-9) of their amplitude (Table 4.2 and Figure 4.17b). As for free bars, increasing sediment size heterogeneity leads to an increased degree of sediment sorting (Figure 4.16a,b).

The above discussion outlines the difficulty of understanding and establishing a relationship between the sediment size heterogeneity and bar characteristics, and more data of high resolution are therefore required. The use of different run conditions and combined approaches could help to better understand this phenomenon.

4.5 Conclusions

A fully non-linear physics-based morphodynamic model has been implemented to better understand the interaction between non-uniform sediment and free and hybrid bar morphodynamics. The model is based on the solution of the shallow-water equations, and is coupled with a morphodynamic module which takes into consideration the gravitational effects and the hiding-exposure effects on bedload transport, the planform and vertical sediment sorting and the feedback of varying bottom roughness on sediment transport due to planform sediment sorting. Nine scenarios are simulated starting from this numerical model based on the laboratory experiment of Lanzoni [2000b] with non-uniform sediment. A comprehensive analysis is conducted on the flow and sediment transport, bar properties and planform and vertical sorting of sediment for all the simulations.

The reference scenario shows consistency with the laboratory experiment as it is able to reproduce the process of bar development and spatial sediment sorting with using layers thicknesses in the same order than the coarsest grain diameter. Moreover, the degree of complexity of the model is showed to be necessary to reproduce the phenomena of interest and to give access to processes which are difficult to observe experimentally.

The numerical simulation reproducing Lanzoni [2000b]'s laboratory experiment shows that even under the conditions of morphodynamic equilibrium, the system remains highly dynamic and produces fully developed free migrating bars of sharp different amplitude, wavelength and celerity. In the simulation, the first mechanism controlling the sorting of sediment results from the interaction between bed topography, bed shear stress and the sediment used for the experiment. The bed shear stress over these bars is relatively high on the stoss side and over the bar top, while it suddenly decreases at the bar front location due to the high topographic gradient. A similar observation is made concerning the transport of sediment. This process is at the origin of free bar migration, where bars progressively migrate by filling the pools located immediately downstream. The sediment sorting pattern is characterized by the presence of fine sediment in pools and coarse particles over bar tops, which becomes more appreciable when free migrating bars are fully developed, and seems to be primarily controlled by the bed shear stress. Vertically, these bars display a sediment sorting pattern with coarse material over bar tops and finer sediment on the deepest sediment layer, while the opposite behaviour is observed at the pool location. In this context, the implementation of a bookkeeping active layer is particularly useful to conclude that the planform and vertical sediment sorting does not adapt immediately to the fast topographic and hydraulic changes, but requires a certain time and length to find a more stable condition. Moreover, the use of a bookkeeping active layer model allowed the formation of downstream fining but also a general coarsening of the bed surface over time.

Hybrid bars are obtained by setting-up a transverse obstacle upstream. The free migrating bars and hybrid bars obtained in the simulations show consistently a different bed topography: hybrid bars are generally more than two times longer than fully developed free bars, whereas

their amplitude is in the same order of magnitude than the ones of free bars. Consequently, hybrid bars are flatter than free migrating bars and display milder slopes so that the distributions of bed shear stress, sediment transport rates and sediment sorting are different for these two types of bars. In the case of hybrid bars, the bed topography, the bed shear stress and the sediment transport present a symmetrical shape while free migrating bars present an important asymmetry on their fronts. For this reason, hybrid bars display a sediment sorting pattern with the finest sediment at the beginning of the lee side which smoothly coarsens until the middle of the stoss side, and then becomes progressively finer until the next bar top. Moreover, the low (resp. zero) shear stress found above hybrid bar tops induce low (resp. zero) sediment transport in this area, so that bar tops are protected from erosion. Fixed hybrid bar tops can be seen as geometrical forcing, which have an influence on the downstream bar morphodynamics. The amplitude of hybrid bars is showed to primarily control the intensity of this geometrical forcing, which can sustain the development of hybrid bars everywhere in the reach if the forcing is high enough, or in the opposite trigger free bar detachment if the forcing becomes too low. These results are also supported by the linear analytical theory.

Planform and vertical sediment sorting are showed to only slightly modify free migrating bar morphodynamics whereas hybrid bars are greatly impacted. Under the conditions given by the experiment, hybrid bars tend to be longer and flatter if sediment sorting is accounted for. Their amplitude decreases in longitudinal direction so that they do not dominate the bed topography in the downstream end of the domain, where free migrating bars form and migrate downstream.

For free and hybrid bars, increased sediment size heterogeneity increases the degree of sediment sorting, while the sorting pattern remains the same for each type of bar. Free and hybrid bars are impacted and respond differently to changes of sediment size heterogeneity. The increasing of sediment size heterogeneity produces averagely higher, longer and faster free bars, while in the case of hybrid bars, the wavelength is increased and the amplitude is decreased only when a very heterogeneous sediment is used.

The last conclusions highlight that understanding the mechanisms involved behind non-uniform sediment and bars morphodynamics is not straightforward. Indeed, the numerical simulations show that non-uniform sediment has a different impact on bars depending on if they are free and migrating, if they are hybrid or free but do not migrate, or if different types coexist. The effects of planform and vertical sediment sorting and sediment size heterogeneity on free migrating bars and steady hybrid bars observed numerically could eventually explain the contradictory findings presented in the literature. The modelling of vertical sediment sorting and the clear distinction between the types of bars obtained numerically constitute a starting point for completing and improving the findings reported in the literature. This subject of debate is not closed, but the last conclusions stress the fact that a clear distinction between the types of bars has to be considered before investigating the influence of any physical parameter on bar morphodynamics.

Acknowledgments

We would like to kindly acknowledge S. Lanzoni for sharing his experimental data (DOI: 10.1029/2000WR900161). The authors gratefully acknowledge the support of Electricité de France (EDF). The authors are very grateful to Annunziato Siviglia and the two other reviewers for their careful and meticulous reading of the paper, whose suggestions helped improve and clarify the manuscript.

Nomenclature

B Channel width [m]
b Degree of nonlinearity in the dependence of sediment transport on the flow velocity [-]
C Chézy coefficient [$m^{1/2}/s$]
C_f Equivalent Chézy coefficient due to form drag and skin friction [-]
C'_f Equivalent Chézy coefficient due to skin friction only [-]
c_b Free migrating bar celerity [m/h]
c_r Free migrating bar rate [bar/h]
d_i Representative diameter of the i^{th} size fraction [m]
$d_{s,m}$ Median sediment diameter of surface [m]
d_X X^{th} centile of the GSD [m]
E Coefficient of calibration for the correction of bedload direction [-]
$\mathcal{F}_{a:1,i}$ Fraction volume content of i^{th} size fraction in the interface [-]
$F_{k,i}$ Fraction volume content of i^{th} size fraction in layer k [-]
$\bar{F_{k,i}}$ Spatially averaged fraction volume content of i^{th} size fraction in layer k [-]
F_s Fraction volume content of sand at the bed surface [-]
$F_{sub,i}$ Fraction volume content i^{th} size fraction in the substrate [-]
g Acceleration due to gravity (=9.81) [m/s^2]
h Water depth [m]
$\bar{h}$ Spatially averaged water depth [m]
H_b Time-averaged free bar height [m]
$H_{b,s}$ Hybrid bar height [m]
i_0 Longitudinal bed slope at $t = 0$ s [-]
i_∞ Longitudinal bed slope at the equilibrium [-]
k_s Bed roughness height [m]
L_a Active layer thickness [m]
m Bar "mode" (real number) [-]
P_0 Bed porosity [-]
q_b Magnitude of bedload transport rate [m^2/s]
$\vec{q_b} = (q_{b,x}, q_{b,y})$ Vector of bedload transport rate [m^2/s]
q_{b0} Magnitude of bedload transport rate without gravitational effects [m^2/s]
$\vec{q_{b0}}$ Vector of bedload transport rate without gravitational effects [m^2/s]
$q_{b,i}$ Magnitude of fractional transport rate of i^{th} size fraction [m^2/s]
$\vec{q_{b,i}} = (q_{b,i,x}, q_{b,i,y})$ Vector of fractional transport rate of i^{th} size fraction [m^2/s]
$q_{b,i,n}$ Magnitude of normal fractional transport rate of i^{th} size fraction [m^2/s]
$q_{b,i,s}$ Magnitude of stream-wise fractional transport rate of i^{th} size fraction [m^2/s]
$\bar{Q_{s,i}}$ Spatially averaged discharge of i^{th} size fraction [m^3/s]
s Coordinate in the current direction [-]
$\vec{u} = (u, v)$ Flow velocity vector [m/s]
$\bar{u}$ Spatially averaged flow velocity [m/s]
u, v Depth averaged velocity components along x- and y-axis [m/s]
s Coordinate in the current direction [-]
$\vec{S_f} = (S_{f,x}, S_{f,y})$ Friction law vector [-]
t Physical time [s]

α_b Coefficient used to calibrate the sediment transport capacity [-]
α_i Angle between the vector of fractional transport and x-axis [-]
$\alpha_{k,s}$ Calibration parameter [-]
β Width-to-depth ratio [-]
β_r Resonant width-to-depth ratio [-]
β_1 Koch and Flosktra's empirical factor for bed slope effects magnitude [-]
β_2 Talmon's *et al.* empirical factor for bed slope effects deviation [-]
δ Angle between bottom shear stress and the flow direction [-]
Δ_s Relative submerged sediment density [-]
Δt Computational time-step [s]
Δz_b Evolution of the bed topography with respect to the initial bed elevation [m]
ϵ_0 Percentage of volumetric matter without voids [-]
$\eta_{a:1}$ Absolute elevation of the interface [m]
κ Constant of von Kármán (=0.40) [-]
$\lambda_{b,max}$ Maximal free bar wavelength [m]
$\lambda_{b,s}$ Hybrid bar wavelength [m]
μ Skin friction coefficient [-]
∇ Gradient vector field [1/m]
ν_t Turbulent eddy viscosity term [m^2/s]
$\partial_{x_2} x_1$ Partial derivative of the quantity x_1 in x_2 [x_2/x_1]
Φ_i Ratio of bed shear stress over reference shear stress of i^{th} size fraction [-]
ρ Water density [kg/m^3]
τ Total shear stress [Pa]
$\bar{\tau^*}$ Spatially averaged Shields number [-]
τ_b Bed shear stress [Pa]
$\tau^*_{b,i}$ Shear stress adimensionnalized by the i^{th} fraction [-]
$\bar{\tau^*_{b,i}}$ Spatially averaged shear stress adimensionnalized by the i^{th} fraction [-]
$\tau_{r,i}$ Reference shear stress of the i^{th} size fraction [Pa]
$\tau_{r,m}$ Reference median shear stress of bed surface [Pa]

REFERENCES

An, C., Cui, Y., Fu, X., and Parker, G. (2017). Gravel-bed River Evolution in Earthquake-Prone Regions Subject to Cycled Hydrographs and Repeated Sediment Pulses. *Earth Surface Processes and Landforms*, 42(15):2503–2696. 29, 30, 87, 88

Ashmore, P., Peirce, S., and Leduc, P. (2018). Expanding the Active Layer: Discussion of Church and Haschenburger (2017) What is the Active Layer? Water Resources Research 53, 510, Doi:10.1002/2016WR019675. *Water Resources Research*, 54(3):1425–1427. 35, 58, 86, 135

Bendegom, L. V. (1947). Some considerations on river morphology and river improvement, De Ingenieur vol. 59–4, pp. B1–11. *Dutch. English translation: Nat. Res. Council of Canada, Technical Translation*, 1054:1963. 26, 58, 88, 135

Blanpain, O. (2009). *Dynamique sédimentaire multiclasse: de l'étude des processus à la modélisation en Manche*. PhD thesis, Université de Rouen. 35, 86, 288

Blom, A. (2008). Different approaches to handling vertical and streamwise sorting in modeling river morphodynamics. *Water resources research*, 44(3):1 – 17. xii, 28, 34, 35, 36, 85, 86, 174, 288

Blondeaux, P. and Seminara, G. (1985). A unified bar-bend theory of river meanders. *Journal of Fluid Mechanics*, 157:449–470. 4, 5, 13, 84

Bridge, J. and Demicco, R. (2008). *Earth surface processes, landforms and sediment deposits*. Cambridge University Press. 3, 4, 7, 14, 83, 129, 131

Bridge, J. S. (2003). *Rivers and floodplains: forms, processes, and sedimentary record*. John Wiley & Sons. xi, 4, 5, 9, 10, 83, 130, 131, 155

Cabrit, O. (2009). *Modélisation des flux pariétaux sur les tuyères des moteurs à propergol solide*. PhD thesis, Montpellier 2. 26, 58, 71, 88, 135

Church, M. and Haschenburger, J. K. (2017). What is the active layer? *Water Resources Research*, 53(1):5–10. 34, 35, 56, 58, 86, 97, 135, 288

Claude, N., Rodrigues, S., Bustillo, V., Bréhéret, J.-G., Tassi, P., and Jugé, P. (2014). Interactions between flow structure and morphodynamic of bars in a channel expansion/contraction, Loire River, France. *Water Resources Research*, 50(4):2850–2873. xiv, 8, 15, 83, 128, 129, 131, 133, 134, 137, 140, 141, 142, 144, 147, 153, 154, 157, 158, 174, 175

Colombini, M., Seminara, G., and Tubino, M. (1987). Finite-amplitude alternate bars. *Journal of Fluid Mechanics*, 181:213–232. 4, 6, 9, 55, 84

Crosato, A. and Desta, F. (2009). Intrinsic steady alternate bars in alluvial channels. Part 1: experimental observations and numerical tests. In *Proc. of the 6th Symp. on River Coastal and Estuarine Morphodynamics (RCEM 2009), 21-25 Sept. 2009, Santa Fe, Argentina, RCEM 2009, Vol. 2, pp. 759-765.* Taylor & Francis Group. 5, 13, 101

Crosato, A., Desta, F. B., Cornelisse, J., Schuurman, F., and Uijttewaal, W. S. J. (2012). Experimental and numerical findings on the long-term evolution of migrating alternate bars in alluvial channels. *Water Resources Research*, 48(6):1–14. W06524. 45, 67, 99

Crosato, A. and Mosselman, E. (2009). Simple physics-based predictor for the number of river bars and the transition between meandering and braiding. *Water Resources Research*, 45(3):1–12. xi, 4, 6, 7, 8, 55, 56, 84, 92, 130, 131, 137, 146, 152, 153, 154, 157

Crosato, A., Mosselman, E., Beidmariam Desta, F., and Uijttewaal, W. S. J. (2011). Experimental and numerical evidence for intrinsic nonmigrating bars in alluvial channels. *Water Resources Research*, 47(3):1–14. W03511. 4, 5, 84, 90, 110, 130, 131

de Saint-Venant, A. B. (1871). Théorie du mouvement non permanent des eaux, avec application aux crues des rivières et à l'introduction des marées dans leurs lits. *Comptes Rendus des séances de l'Académie des Sciences*, 73:237–240. 18, 25, 57, 85, 134

Defina, A. (2003). Numerical experiments on bar growth. *Water Resources Research*, 39(4):1–12. 15, 56, 60, 90

Diplas, P. (1994). Modelling of fine and coarse sediment interaction over alternate bars. *Journal of Hydrology*, 159(1):335–351. 13, 84, 109

Duró, G., Crosato, A., and Tassi, P. (2016). Numerical study on river bar response to spatial variations of channel width. *Advances in Water Resources*, 93(Part A):21 – 38. xi, 5, 6, 8, 84, 101, 108, 110, 130, 131, 153

Engelund, F. (1970). Instability of erodible beds. *Journal of Fluid Mechanics*, 42(2):225–244. 4, 6, 55, 83, 84, 130

Engelund, F. and Skovgaard, O. (1973). On the origin of meandering and braiding in alluvial streams. *Journal of Fluid Mechanics*, 57(02):289–302. 83

Enggrob, H. and Tjerry, S. (1999). Simulation of morphological characteristics of a braided river. In *Proceedings of the IAHR Symposium on River, Coastal and Estuarine Morphodynamics, Genova*, volume I, pages 585–594. 84

Exner, F. M. (1920). *Zur physik der dünen*. Hölder. 25, 57, 86, 135

Fujita, Y. and Muramoto, Y. (1985). Studies on the process of development of alternate bars. *Bulletin of the Disaster Prevention Research Institute*, 35:1 – 33. 55, 84

García, M. H. (2008). Sedimentation engineering. *Processes, Measurements, Modeling, and Practice. ASCE Manuals and Reports on Engineering Practice*, 110:1–1132. 25, 27, 29, 34, 57, 86, 89, 97, 136

Güneralp, I., Abad, J. D., Zolezzi, G., and Hooke, J. (2012). Advances and challenges in meandering channels research. *Geomorphology*, 163-164(Supplement C):1 – 9. Meandering Channels. 109

Hervouet, J., Razafindrakoto, E., and Villaret, C. (2011). Dealing with dry zones in free surface flows: a new class of advection schemes. In Barton, A., editor, *Proceedings of the 34th World Congress of the International Association for Hydro-Environment Research and Engineering: 33rd Hydrology and Water Resources Symposium and 10th Conference on Hydraulics in Water Engineering*, pages 4103–411. Australia. 27, 58, 89, 136

Hirano, M. (1971). *River bed degradation with armoring*. PhD thesis, Japanese Society of Civil Engineering. xii, 18, 24, 25, 34, 35, 43, 57, 58, 70, 85, 86, 135, 158, 167, 173, 174, 288, 300

Hoey, T. B. and Ferguson, R. (1994). Numerical simulation of downstream fining by selective transport in gravel bed rivers: Model development and illustration. *Water Resources Research*, 30(7):2251–2260. 12, 45, 84, 108

Jaballah, M., Camenen, B., Pénard, L., and Paquier, A. (2015). Alternate bar development in an alpine river following engineering works. *Advances in Water Resources*, 81:103–113. Fluvial Eco-Hydraulics And Morphodynamics. 83

Juez, C., Ferrer-Boix, C., Murillo, J., Hassan, M., and García-Navarro, P. (2016). A model based on Hirano-Exner equations for two-dimensional transient flows over heterogeneous erodible beds. *Advances in Water Resources*, 87:1–18. 12, 84

Koch, F. and Flokstra, C. (1980). *Bed Level Computations for Curved Alluvial Channels: Prepared for the 19th IAHR Congress, New Delhi, India, February 1981*. Waterloopkundig Laboratorium. 26, 58, 88, 135, 139

Lanzoni, S. (2000a). Experiments on bar formation in a straight flume 1. Uniform sediment. *Water Resources Research*, 36(11):3337–3349. 4, 12, 15, 45, 54, 57, 59, 65, 84, 89, 111, 174

Lanzoni, S. (2000b). Experiments on bar formation in a straight flume: 2. Graded sediment. *Water Resources Research*, 36(11):3351–3363. xi, xiii, 11, 12, 13, 14, 16, 32, 33, 44, 45, 49, 57, 59, 84, 85, 89, 90, 93, 94, 97, 107, 109, 111, 112, 130, 155, 162, 173, 174

Lanzoni, S. and Tubino, M. (1999). Grain sorting and bar instability. *Journal of Fluid Mechanics*, 393:149–174. 6, 11, 12, 55, 84

Lisle, T. E., Ikeda, H., and Iseya, F. (1991). Formation of stationary alternate bars in a steep channel with mixed-size sediment: A flume experiment. *Earth Surface Processes and Landforms*, 16(5):463–469. 11, 12, 13, 84, 109, 111

Lisle, T. E. and Madej, M. (1992). Spatial variation in armouring in a channel with high sediment supply. *Dynamics of Gravel-bed Rivers*, 1:277–296. 11, 12, 13, 84, 109

Lisle, T. E., Nelson, J. M., Pitlick, J., Madej, M. A., and Barkett, B. L. (2000). Variability of bed mobility in natural, gravel-bed channels and adjustments to sediment load at local and reach scales. *Water Resources Research*, 36:3743–3755. 12, 84

Mendoza, A., Abad, J. D., Langendoen, E. J., Wang, D., Tassi, P., and Abderrezzak, K. E. K. (2016). Effect of Sediment Transport Boundary Conditions on the Numerical Modeling of Bed Morphodynamics. *Journal of Hydraulic Engineering*, 143(4): . 27, 46, 56, 58, 59, 60, 64, 88, 90, 136, 158, 174

Mosselman, E. (2012). Modelling Sediment Transport and Morphodynamics of Gravel-Bed Rivers. *Gravel-Bed Rivers: Processes, Tools, Environments*, 1:101–115. 12, 15, 56, 84

Mosselman, E., Sieben, A., Sloff, K., and Wolters, A. (1999). Effect of spatial grain size variations on two-dimensional river bed morphology. In *Proceedings of River, Coastal and Estuarine Morphodynamics, Genova*, volume 1, pages 499–507. 12, 15, 28, 84

Nelson, P. A., McDonald, R. R., Nelson, J. M., and Dietrich, W. E. (2015a). Coevolution of bed surface patchiness and channel morphology: 1. Mechanisms of forced patch formation. *Journal of Geophysical Research: Earth Surface*, 120(9):1687–1707. 12, 13, 16, 56, 65, 84, 91, 107, 109, 130, 137, 155

Nelson, P. A., McDonald, R. R., Nelson, J. M., and Dietrich, W. E. (2015b). Coevolution of bed surface patchiness and channel morphology: 2. Numerical experiments. *Journal of Geophysical Research: Earth Surface*, 120(9):1708–1723. 11, 12, 13, 14, 16, 28, 72, 84, 101, 109, 110, 111, 123, 130, 155, 157, 162

Nezu, I., Nakagawa, H., and Jirka, G. H. (1994). Turbulence in open-channel flows. *Journal of Hydraulic Engineering*, 120(10):1235–1237. 18, 25, 57, 85, 134

Nikuradse, J. (1950). *Laws of flow in rough pipes*. NACA. 25, 86, 135

Orrú, C., Blom, A., and Uijttewaal, W. S. (2016). Armor breakup and reformation in a degradational laboratory experiment. *Earth Surface Dynamics*, 4(2):461. 29, 87

Parker, G. (1990). Surface-based bedload transport relation for gravel rivers. *Journal of hydraulic research*, 28(4):417–436. 11, 29, 87

Parker, G., Hassan, M., and Wilcock, P. (2007). Adjustment of the bed surface size distribution of gravel-bed rivers in response to cycled hydrographs. *Developments in Earth Surface Processes*, 11:241–285. 35, 86

Powell, D. M. (1998). Patterns and processes of sediment sorting in gravel-bed rivers. *Progress in Physical Geography*, 22(1):1–32. 11, 12, 84

Powell, D. M., Ockelford, A., Rice, S. P., Hillier, J. K., Nguyen, T., Reid, I., Tate, N. J., and Ackerley, D. (2016). Structural properties of mobile armors formed at different flow strengths in gravel-bed rivers. *Journal of Geophysical Research: Earth Surface*, 121(8):1494–1515. 2015JF003794. 29, 87

Proffitt, G. and Sutherland, A. (1983). Transport of non-uniform sediments. *Journal of Hydraulic Research*, 21(1):33–43. 29, 87

Qian, H., Cao, Z., Liu, H., and Pender, G. (2016). Numerical modelling of alternate bar formation, development and sediment sorting in straight channels. *Earth Surface Processes and Landforms*, 607:613–622. ESP-15-0409.R2. 12, 16, 56, 60, 84, 90

Recking, A., Piton, G., Vazquez-Tarrio, D., and Parker, G. (2015). Quantifying the Morphological Print of Bedload Transport. *Earth Surface Processes and Landforms*, 41(6):809–822. 29, 30, 87, 88, 135

Rodrigues, S., Claude, N., Juge, P., and Breheret, J.-G. (2012). An opportunity to connect the morphodynamics of alternate bars with their sedimentary products. *Earth Surface Processes and Landforms*, 37(2):240–248. 12, 110, 153, 155

Rodrigues, S., Mosselman, E., Claude, N., Wintenberger, C. L., and Juge, P. (2015). Alternate bars in a sandy gravel bed river: generation, migration and interactions with superimposed dunes. *Earth Surface Processes and Landforms*, 40(5):610–628. 5, 8, 84, 110, 129, 130, 131, 153, 155

Seal, R., Paola, C., Parker, G., Southard, J. B., and Wilcock, P. R. (1997). Experiments on downstream fining of gravel: I. Narrow-channel runs. *Journal of Hydraulic Engineering*, 123(10):874–884. 12, 45, 84, 108

Seminara, G. (1998). Stability and morphodynamics. *Meccanica*, 33(1):59–99. 84, 130

Singh, U., Crosato, A., Giri, S., and Hicks, M. (2017). Sediment heterogeneity and mobility in the morphodynamic modelling of gravel-bed braided rivers. *Advances in Water Resources*, 104:127–144. 11, 12, 13, 28, 56, 84, 130, 155, 158, 174

Siviglia, A. and Crosato, A. (2016). Numerical modelling of river morphodynamics: latest developments and remaining challenges. *Advances in Water Resources*, 90:1–9. 15, 28, 56, 84

Siviglia, A., Stecca, G., Vanzo, D., Zolezzi, G., Toro, E. F., and Tubino, M. (2013). Numerical modelling of two-dimensional morphodynamics with applications to river bars and bifurcations. *Advances in Water Resources*, 52:243–260. 4, 15, 56, 110

Soulsby, R. (1997). *Dynamics of marine sands: a manual for practical applications*. Thomas Telford. 26, 88

Stecca, G., Siviglia, A., and Blom, A. (2016). An accurate numerical solution to the Saint-Venant-Hirano model for mixed-sediment morphodynamics in rivers. *Advances in Water Resources*, 93:39–61. 34, 35, 71, 86, 158, 173

Struiksma, N. and Crosato, A. (1989). *Analysis of a 2-D Bed Topography Model for Rivers*. Wiley Online Library. 56, 106

Takebayashi, H. and Egashira, S. (2001). Dynamic state of sand bar formed on non-uniform sediment bed. *Proceedings of Hydraulic Engineering*, 45:727–732. 12, 13, 84

Talmon, A., Struiksma, N., and Van Mierlo, M. (1995). Laboratory measurements of the direction of sediment transport on transverse alluvial-bed slopes. *Journal of Hydraulic Research*, 33(4):495–517. 26, 27, 58, 88, 92, 135, 138, 139

Tonina, D. and Buffington, J. M. (2007). Hyporheic exchange in gravel bed rivers with pool-riffle morphology: Laboratory experiments and three-dimensional modeling. *Water Resources Research*, 43(1):1–16. 84

Toro-Escobar, C. M., Paola, C., Parker, G., Wilcock, P. R., and Southard, J. B. (2000). Experiments on downstream fining of gravel. II: Wide and sandy runs. *Journal of Hydraulic Engineering*, 126(3):198–208. 12, 45, 84, 108

Tritthart, M., Liedermann, M., Schober, B., and Habersack, H. (2011a). Non-uniformity and layering in sediment transport modelling 2: river application. *Journal of Hydraulic Research*, 49(3):335–344. 12, 84

Tritthart, M., Schober, B., and Habersack, H. (2011b). Non-uniformity and layering in sediment transport modelling 1: flume simulations. *Journal of Hydraulic research*, 49(3):325–334. 12, 84

Tubino, M., Repetto, R., and Zolezzi, G. (1999). Free bars in rivers. *Journal of Hydraulic Research*, 37(6):759–775. 4, 7, 111

Tubino, M. and Seminara, G. (1990). Free-forced interactions in developing meanders and suppression of free bars. *Journal of Fluid Mechanics*, 214:131–159. 4, 5, 13, 84

Van der Meer, C., Mosselman, E., Sloff, K., Jagers, B., Zolezzi, G., and Tubino, M. (2011). *Numerical simulations of upstream and downstream overdeepening*. RCEM 2011, Proceedings of the 7th IAHR Symposium of River, Coastal and Estuarine Morphodynamics. 26, 58, 88, 135

Vanzo, D., Siviglia, A., Zolezzi, G., Stecca, G., and Tubino, M. (2011). Interaction between steady and migrating bars in straight channels. In *RCEM 2011*. 15, 110

Viparelli, E., Blom, A., and Moreira, R. R. H. (2017). *Modeling Stratigraphy-Based Gravel-Bed River Morphodynamics*, chapter Modeling Stratigraphy-Based Gravel-Bed River Morphodynamics, pages 609–637. John Wiley & Sons, Ltd. 34, 35, 56, 86, 97, 174

Vreugdenhil, C. B. (2013). *Numerical methods for shallow-water flow*, volume 13. Springer Science & Business Media. 18, 25, 57, 85, 134

Weiyan, T. (1992). *Shallow Water Hydrodynamics: Mathematical Theory and Numerical Solution for a Two-dimensional System of Shallow Water Equations*. Number vol. 55 in Elsevier oceanography series. Water & Power Press. 18, 25, 57, 85, 134

Wilcock, P. R. and Crowe, J. C. (2003). Surface-based transport model for mixed-size sediment. *Journal of Hydraulic Engineering*, 129(2):120–128. vii, 11, 24, 26, 28, 29, 31, 32, 45, 49, 58, 87, 103, 135, 158, 167, 173

Wintenberger, C. L., Rodrigues, S., Bréhéret, J.-G., and Villar, M. (2015). Fluvial islands: First stage of development from nonmigrating (forced) bars and woody-vegetation interactions. *Geomorphology*, 246:305–320. 9, 13, 84, 129, 131

Wu, W. (2004). Depth-averaged two-dimensional numerical modeling of unsteady flow and nonuniform sediment transport in open channels. *Journal of hydraulic engineering*, 130(10):1013–1024. 12, 84

Zolezzi, G. and Seminara, G. (2001). Downstream and upstream influence in river meandering. Part 1. General theory and application to overdeepening. *Journal of Fluid Mechanics*, 438:183–211. 26, 56, 58, 88, 135

▷ Considerations on periodic bar morphodynamics with non-uniform sediment

Numerical results firstly show that free bars and hybrid bars are characterized by a distinct sediment sorting pattern due to their different geometries, flow distribution and sediment transport patterns. Sediment size heterogeneity does not modify the sediment sorting patterns, but increases the degree of sediment sorting, where free bars respond differently to increasing size heterogeneity with respect to hybrid bars. Increased sediment size heterogeneity produces averagely higher, longer and faster free bars, while in the case of hybrid bars, the wavelength is increased and the amplitude is decreased only when a very heterogeneous sediment is used.

Secondly, numerical results show that averaged free bars characteristics are not impacted by the spatial sorting of sediment, while the sorting effects modify significantly hybrid bars characteristics. In agreement with results presented recently in the literature [Nelson et al., 2015b], steady (hybrid) bars are longer and flatter due to sediment sorting effects. As a result, hybrid bars only persist for a relatively short distance (i.e. a few hybrid bar lengths) downstream from the obstacle, because sediment sorting effects reduce their amplitude and by extension the geometrical forcing played by an hybrid bar on an immediately downstream bar. In this case, free bars continually form and migrate in the downstream part of the channel. Considering the same configuration, if sediment sorting is not accounted for, hybrid bars form everywhere in the downstream part of the channel.

The main outcomes from this study have implications on the understanding and the modelling of bar morphodynamics in trained rivers. Possible unwanted consequences of not accounting for the spatial sorting of sediment are illustrated below. Because averaged free bar properties are not impacted by the sorting of sediment in the current runs, this result could be extrapolated on the fast migrating free bars observed in sandy-gravel bed rivers (e.g. middle Loire river, see Section 1.2). In the case of fine (non-cohesive) sediment injections which tend to increase the degree of sediment size heterogeneity in the river reach, bars characteristics could be modified, with especially increased bar mobility. These results are in agreement with the increased bar mobility observed by Miwa and Parker [2012] after fine sediment injections (i.e. sand and fine gravel) conducted in sand-gravel bed rivers downstream dams. Results also suggest that in gravel bed rivers, the spatial sediment sorting could increase bar mobility and promote the dominance of free bars over hybrid bars. To model bars in gravel bed rivers presenting geometrical local forcing (e.g. Isère river), it is then recommended to account for the sediment sorting, otherwise the presence of hybrid bars could be over-predicted and free bars under-predicted. Accordingly, accounting for non-uniform sediment processes in numerical models can be crucial under certain situations, especially when they are used to predict bar patterns and dynamics for river management purposes. Finally, the distinct sediment sorting patterns observed between free bars and hybrid bars should be took into account before planning field sediment sampling campaigns over periodic, alternate bars. Future research work could consist on re-investigating the relationship between non-uniform sediment and bars morphodynamics using other numerical models available in the literature.

Because the above discussions and recommendations are drawn on the study of idealized channel configurations and relatively simple boundary conditions, another step is necessary in order to verify the previous assertions and demonstrate the real applicability of the developed approach under more complex, real situations. This task is undertaken in the next Part.

□ Synthèse générale sur l'influence de l'hétérogénéité sédimentaire sur la morphodynamique des bancs

Ce chapitre a permis d'analyser de manière détaillée les interactions entre des bancs périodiques et la non-uniformité sédimentaire. Pour cela, un scénario de formation de bancs libres en présence d'un sédiment non-uniforme est reproduit de manière fidèle avec le modèle morphodynamique présenté au second chapitre. Afin de mieux comprendre l'impact i) du degré de tri granulométrique du sédiment initial et ii) l'impact du tri granulométrique spatial (i.e. vertical et en plan) sur la morphodynamique des bancs périodiques, les résultats issus d'autres scenarios numériques dérivés du scenario calibré –dit de référence- sont analysés et confrontés. La création de bancs hybrides est rendue possible en plaçant un obstacle en partie amont du canal. La distinction entre les bancs libres et hybrides est nécessaire pour mieux comprendre la relation entre sédiments non-uniformes et bancs périodiques, et permet notamment de répondre aux contradictions rencontrées dans la littérature en matière des différents motifs de tri spatial observés. Les résultats ont des fortes implications dans la connaissance et la modélisation de la morphodynamique des bancs dans les rivières aménagées, et attestent de la véritable importance de la prise en compte de l'hétérogénéité granulométrique et du tri spatial des sédiments dans les modèles morphodynamiques censés reproduire et prédire le développement et la migration de bancs dans des configurations géométriques simples et des conditions aux limites bien contrôlées. Ces résultats avertissent d'ores et déjà les modélisateurs de rivières sur les possibles répercussions néfastes liées à une simplification trop importante de la représentation des systèmes morphodynamiques considérés pour les études opérationnelles.

PART III

BARS MORPHODYNAMICS WITH NON-UNIFORM SEDIMENT UNDER COMPLEX CONFIGURATIONS

CHAPTER 5

BAR PATTERN AND SEDIMENT SORTING IN A CHANNEL CONTRACTION/EXPANSION: APPLICATION TO A SANDY-GRAVEL RIVER REACH (MIDDLE LOIRE, FRANCE)

The work presented in this chapter is in preparation, entitled *Bar pattern and sediment sorting in a channel contraction/expansion: application to the Loire river at Bréhémont (France)*

by
Florian Cordier[1,2], Pablo Tassi[1,2], Nicolas Claude[2], Alessandra Crosato[3], Stéphane Rodrigues[4] and Damien Pham Van Bang[5]
[1]Laboratoire d'Hydraulique Saint-Venant (Chatou, France)
[2]EDF R&D LNHE - Laboratoire National d'Hydraulique et Environnement (Chatou, France)
[3]IHE Delft (Delft, The Netherlands)
[4]Ecole Polytechnique Universitaire de Tours & UMR CNRS 7324 CITERES (France)
[5]INRS-ETE, LHE & Lab. CT-Scan (Québec, Canada)

Corresponding author: florian.cordier@edf.fr

▷ Motivations and objectives of this study

The main objective of this part is to answer to research question II defined in Section 1.2: *How the bar pattern and non-uniform sediment co-evolve under the consideration of multiple internal and external forcing parameters?*

Hence, the research activities undertaken here consist on performing a numerical study which aims to investigate and better understand bar morphodynamics with non-uniform sediment under more complex configurations, with respect to the investigations conducted previously in Part II. The morphodynamic model developed in Chapter 2 and tested under simple configurations in Part II is then applied on a field study case in the middle Loire river at Bréhémont [Claude et al., 2014]. This case study has been selected because it presents not only a complex geometry defined by a curved channel contraction/expansion, secondary channels and showing complex hydrology and sediment supply variations, and the riverbed is composed by a mixture of sand and gravel. A large post-processed hydro-sedimentary dataset monitored during years 2010-2011 is available (water levels, flow discharge, flow velocity profiles, multi-beam echo-soundings, sediment transport, etc.), and the comprehension of bar morphodynamic processes in this area has been matter of previous field studies [Claude et al., 2014]. A preliminary numerical study presented in Appendix A has been necessary to assess the feasibility of reproducing the main hydraulic structures observed *in situ* using a two-dimensional hydrodynamic model.

Outcomes of this analysis are expected to shed light on bar dynamics in the study site, in the middle Loire river and more generally in sand-gravel bed rivers presenting similar characteristics. Comparison with the theoretical approach will help to enrich the discussion on bar morphodynamic processes under this configuration. The present study will be also useful to further validate the model closures and improvements implemented in Chapter 2 under a complex geometrical configuration and boundary conditions. Discussions will also provide additional information to modellers and river managers who are interested in understanding or predicting fluvial bar morphodynamics in sandy-gravel or gravel bed rivers.

Keypoints

- Competition between low and high bar modes originating from water discharge variations results in complex compound bars
- Sediment sorting patterns are different between unit and compound bar patterns
- Sediment sorting does not modify significantly the bar morphodynamics if the sediment mobility is high
- Floods decrease the sediment sorting degree

Abstract

Bars are large sediment deposits alternating with deeper areas that arise from an instability phenomenon of the alluvial river bed. The present study aims at investigating the impact of combined discharge variability, channel geometry and non-uniform sediment distribution on bar morphodynamics in natural or trained alluvial rivers. To this goal, a two-dimensional fully-nonlinear model is used to simulate the bed evolution of a 1 km long reach of the Loire River, corresponding to an area of contraction/expansion wherein complex bar dynamics have been observed. Comparisons with a comprehensive set of high-definition field data confirms that the model predicts satisfactorily the bar evolution, such as the transition from an alternate bar to a transverse bar system. In agreement with theory, varying discharge creates a competition between low and high bar modes. High flow rates induce bar mode reduction and lead to a pattern of coarse sediment over bar tops and fine in pools, whereas low-flow rates induce higher bar modes and the sorting pattern is inverted, with fine sediment over bar tops and coarser sediment in pools. Due to high sediment mobility and low grain roughness, sediment sorting does not significantly modify the bar dynamics. Bar dynamics appears strongly influenced by discharge variations in the channel contraction/expansion.

5.1 Introduction

Rivers often present a wavy bed topography due to the presence of periodic bars [Bridge and Demicco, 2008], which consist in large sediment deposits alternating with deeper areas (pools). In straight and weakly-curved channels, periodic bar development can enhance bank erosion, later resulting in longitudinal channel width variations, forming successions of channel expansion/contraction areas. Provided a certain degree of regularity in their occurrence, channel width variations constitute a typical characteristic of natural river planforms [Wu and Yeh, 2005], where bars of different types are co-existing as for instance in the Río Paraná (Argentina) [Nicholas, 2013], in the South Saskatchewan River (Canada) [Best et al., 2003] and in the Middle Loire River (France) [Rodrigues et al., 2015]. A better understanding of bar processes in expansion/contraction areas is important for river engineers and river managers, because bars actively control the riverbed topography and influence bank erosion, with potential harmful consequences for navigation, water intakes and infrastructures [Claude et al., 2014]. Bars also influence the hydraulics and the sedimentary conditions of river channels, and consequently habitat diversity, recruitment and succession of vegetal communities [Wintenberger et al., 2015].

According to Duró et al. [2016], two types of bars can be distinguished: forced bars, and periodic bars. While forced bars arise from a permanent flow deformation induced by an external forcing, such as a channel geometry change or a steady perturbation, periodic bars arise from morphodynamic instability of the riverbed. Periodic bars include free bars, which originate purely from morphodynamic instability, and hybrid bars, which form on morphodynamically unstable riverbeds, like free bars, but require the presence of a permanent forcing which fixes their location [Crosato et al., 2011; Rodrigues et al., 2015; Duró et al., 2016; Cordier et al., 2019]. Over the years, stability analyses have been proposed to study the initiation conditions for free alternate bars in straight channels under constant flows [e.g. Hansen, 1967; Engelund, 1970; Seminara, 1998] and variable flows [Hall, 2004]. Stability analyses were carried out also to study the conditions leading to the formation of hybrid bars [Struiksma et al., 1985]. These theories show that periodic bars are primarily governed by the width-to-depth ratio of the flow, which is a crucial parameter to define the threshold between stability and instability regimes as well as the bar "mode" a parameter that indicate the number of bars that form in the river cross-section [Engelund, 1970]. Mode equal to 1 indicates alternate bars, mode equal to 2 indicate central bars whereas larger values are associated to compound bar patters. Bars are influenced by water discharge, longitudinal channel width variations as well as sediment size and distribution.

Sediment size heterogeneity is an inherent characteristic of sandy-gravel and gravel-bed rivers. Grain Size Distribution (GSD) and sediment mobility are known to influence periodic bar morphodynamics [Lanzoni, 2000b; Nelson et al., 2015b; Singh et al., 2017; Cordier et al., 2019]. For instance, braiding is enhanced by conditions that are close to initiation of sediment motion, which are typical of gravel beds [Crosato and Mosselman, 2009]. Observed sediment sorting pattern on free alternate bars are characterized by fine sediment in pools and coarse sediment over the bar tops [Lanzoni, 2000b; Nelson et al., 2015a,b; Cordier et al., 2019]. Instead, in the case of multiple channels, such as in braiding rivers, the sorting pattern presents coarse particles in pools and fine sediment over bar tops for partial sediment mobility [Singh et al., 2017; Sun et al., 2015]. Singh et al. [2017] showed that no consistent sediment sorting pattern is present in case of full sediment mobility, apart from coarser sediment in the *thalweg*. The presence of coarser sediment might strengthen the resistance to erosion and play a key role on braiding [Sun et al., 2015]. Non-uniform sediment supply can modify the bar morphodynamics in a complex way. In a straight channel initially dominated by the presence of steady gravel bars, Bankert and Nelson [2018] observed an episode of bed aggradation due to increased gravel supply followed by an episode of bed degradation by reestablishing the initial sediment supply. However, the latter did not reestablish the bar pattern and characteristics observed initially. Reversibility of the system cannot be achieved due to vertical sediment sorting processes, and outlines the relative importance of non-uniform sediment and subsequent vertical sediment sorting on bar dynamics [Cordier et al., 2019].

Because the width-to-depth ratio is a function of water depth and thus of discharge, the latter is thus a crucial parameter for bar stability and bar mode. By considering two distinct sinusoidal water inflows periods, Miwa et al. [2003] observed experimentally that the wave period of the flow influences strongly periodic bar evolution, short-waves having more impact than long-waves. The comparison between constant water discharge and triangular hydrograms showed that unsteady flows were preliminary followed by changes in bar amplitude and bar celerity reduction, in comparison with constant flows [Nelson and Morgan, 2018]. Increasing or decreasing flow discharge has been observed to be followed by a modification of the *thalweg* course [Bridge, 2003]. Consequently, at falling-flow stages, sediment is preferentially deposited in the *thalweg* and bars tops are eroded, with respect to the rising-flow stage at which the opposite

happens, with scouring of the *thalweg* and deposition on bars [Bridge, 2003; Wintenberger et al., 2015].

Geometrical channel changes not only modify directly the width-to-depth ratio, but also induce local areas of erosion or deposition [Bridge and Demicco, 2008], which can trigger the development of forced bars under unstable conditions. Formation of bars driven by forced flow curvature has been documented with the theory [Zen et al., 2014; Crosato, 2008], laboratory experiments [Wu and Yeh, 2005; Struiksma et al., 1985], field investigations [Claude et al., 2014; Luchi et al., 2010] and numerical modelling [Duró et al., 2016; Nelson and Dubé, 2015; Crosato et al., 2011]. Sufficient channel widening allows for bar formation, while sufficient channel narrowing is followed by bar suppression [Nelson, 1990; Repetto et al., 2002; Wu and Yeh, 2005; Crosato and Mosselman, 2009; Duró et al., 2016]. Experimental [García and Niño, 1993; Whiting and Dietrich, 1993] and numerical [Wu et al., 2011] investigations showed that bars slow down with the longitudinal decrease of channel width. Rodrigues et al. [2015] showed in a sandy-gravel bed river that changing of riverbank direction causes forced bar formation. Duró et al. [2016] showed that free bars of different modes can coexist in the downstream straight segment of a channel due to upstream width variations, which is in agreement with the linear theory for steady bars of Struiksma et al. [1985] which allows incipient bars to vary longitudinally in amplitude. Moreover, Duró et al. [2016] showed numerically that imposing a perfectly symmetric water and sediment inflow could suppress alternate bar formation for a certain distance, which needs to be tested experimentally or in the nature to assess its feasibility.

The relationship between longitudinal channel width variations and the diversity of bar patterns has only been recently investigated in the literature [Bittner et al., 1995; Repetto et al., 2002]. Theoretical and experimental works put in evidence that a channel expansion/contraction can promote the settlement of a forced transverse bar or lateral and symmetrical forced bars [Bittner et al., 1995; Repetto et al., 2002; Wu and Yeh, 2005]. Wu et al. [2011] showed numerically that free alternate migrating bars can co-exist with forced transverse or lateral bars. Depending on the migration of free bars, these bars are either in alternate or transverse configurations. In this configuration, free bars amplitude and wavelength are invariably decreased, and as a function of the degree of channel sinuosity, migration of free bars can be increased or decreased. The superposition of free and forced bars can show various configurations depending on the interactions between free and forced bars, and can be compared to alternate or transverse bar configurations [Wu et al., 2011]. Deeper analysis on the flow structure over the transverse and alternate bar configurations has been later carried out in a channel contraction/expansion of the Middle Loire river by Claude et al. [2014], where the bar configuration was showed to promote the spatial non-uniformity of flows induced by the bank curvature and encouraged the transition from alternate bars to a transverse bar configuration and reversely.

Excepted from the study of Claude et al. [2014], the research works carried out in channel expansion/contraction areas always considered a constant upstream water inflow, reducing the diversity of the observed bar patterns. Moreover, to the best of our knowledge, the sediment sorting pattern over bars forming in a channel contraction/expansion remains poorly documented in the literature.

The present study is meant to better understand the diversity of *i)* bar patterns and *ii)* sediment sorting patterns forming in channels expansion/contraction areas, under the consideration of variable flows, which are representative of many natural and trained alluvial rivers reaches. To this goal, a two-dimensional fully-nonlinear model is used to simulate numerically the morphodynamics over a 1 km long reach of the Loire river at Bréhémont wherein free and forced bars coexist [Claude et al., 2014] using a 1 year hydrogram including low to high water

discharges. A comprehensive set of high-quality and high-resolution data is available, including *in situ* current measurements, bed topography and bedload [Claude, 2012]. The available dataset allows to study the river morphodynamics for a succession of medium, low and high flow periods including three flooding events. The morphodynamic numerical model is constructed using the Telemac-Mascaret Modelling System (TMS) (www.opentelemac.org). The numerical model is used to relax the uncertainty which was persistent on the upstream boundary conditions and processes involved in the entrance of bars in the channel contraction/expansion area.

In the first step, emphasis is placed on the role of hydrological conditions on the diversity of observed and computed bar patterns. Comparisons between the scenario of reference reproducing the hydrogram of 2010 and three distinct scenarios considering variable flow conditions will help to illustrate how the hydrology governs bar patterns in the study area. In the second step, the model is used to investigate processes of sediment sorting and the impact of sediment sorting on bars characteristics. To further this goal, the scenario of reference, in which sediment sorting is accounted for using a bookkeeping active layer model, is compared with another scenario in which sediment sorting is not accounted.

The mathematical and numerical models used in this work, together with the model set-up, simulations and analysis methods are presented in Section 5.2. The calibration and validation of the hydrodynamic and morphodynamic model are presented in Section 5.3. Section 5.4 is dedicated to the numerical results in terms of bed evolution, hydraulics, sediment transport and sediment sorting. Discussion on bar morphodynamics aspects, sediment sorting processes over bars, implications for data sampling and limitations and perspectives are presented in Section 5.5.

5.2 Materials and methods

5.2.1 Study case

The 1012-km long Loire river is the longest river in France, draining a catchment area of 117,500 km^2 [Tockner et al., 2008]. The study site (Figure 5.1) is located in the middle reach of the Loire river at 790 km downstream from the source, in the vicinity of the village of Bréhémont (47°17′43.31″N, 0°20′33.80″E). As many rivers in Europe, since the 19^{th} century, the middle Loire has been subject to considerable training works (*e.g.* embankment, groyne construction, sediment extraction) triggering the channelization and the incision of the riverbed, and resulting to a modification of the river morphology and development of vegetation in the most elevated parts of the riverbed. In this region, the Loire river presents a succession of single to multiple-channel patterns, depicted by the occurrence of alternate, transverse, central and more complex bar patterns in the main channel [Rodrigues et al., 2016]. The riverbed also presents secondary channels which are activated and islands (i.e. vegetated central or higher mode bars) which are partially submerged during flooding events [Rodrigues et al., 2006].

The study reach corresponds to a channel widening followed by a contraction area. The presence of permanent embankments on the right riverbank sustaining the main channel curvature, the submerged stretches of rip-rap corresponding to vestiges of ancient bank protection, the longitudinal channel widths variations (from 175 to 300 m) and the connection with a secondary channel (activated for discharges upper than 700 m^3/s at the gauging station of Langeais located 4.5 km upstream) generate permanent geometrical forcings of different amplitudes (Figure 5.1). The computed width-to-depth ratio β in the widening part of the reach (section P80, Figure 5.1) ranges between 56 (June 19^{th} 2010 with water discharge of $Q_w = 386$ m^3/s) and 159 (December

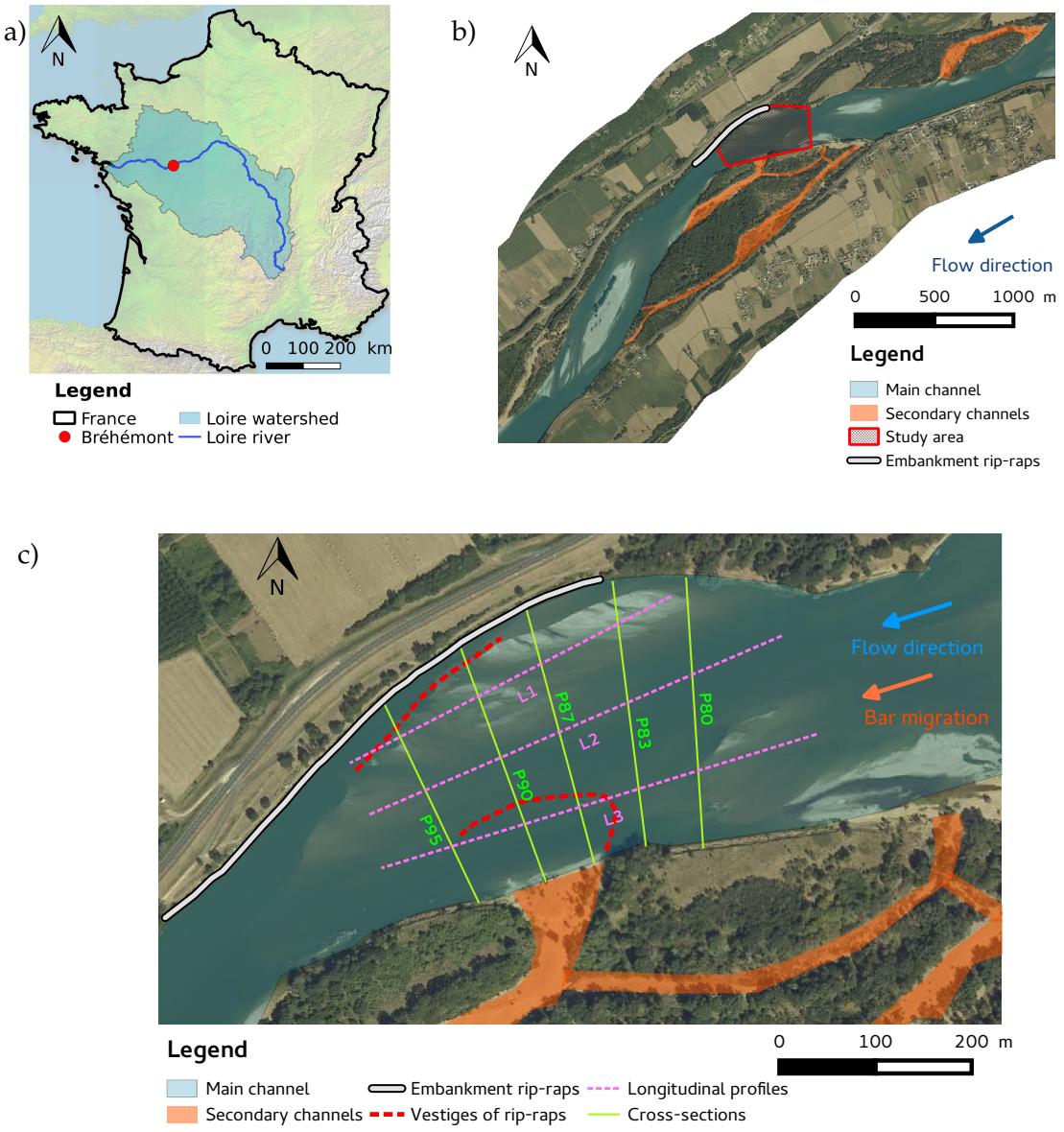


Figure 5.1: a) Map of France showing the location of the study reach in the Loire river watershed (credits for color-map: Shuttle Radar Topography Mission - NASA; river network = Global River Database [Andreadis et al., 2013]), b) medium scale aerial view of the study site took in September 2005, showing the presence of migrating bars in the main channel and secondary channels and c) small scale aerial view of the area of interest with the position of the main field measurements of Claude et al. [2012, 2014] and the presence of geometrical forcings.

11^{th} 2011 with $Q_w = 1950$ m^3/s), and the average longitudinal reach slope is equal to 0.3 m per km [Claude et al., 2012]. The bed material is mainly composed of a mixture of siliceous sand and gravel and is highly mobile, with a Shields number of approximately 0.10 when the flowrate is equal to 386 m^3/s, with respect to the mean inter-annual flowrate which is around 430 m^3/s. The sediment diameters d_{50} and d_{90} (corresponding to the 50^{th} and 90^{th} centile of the grain size

distribution [m]) are equal to 1.33 and 5.18 mm, respectively.

Nineteen field surveys corresponding to the daily monitoring of an annual flood that occurred in June 2010 (1030 m^3/s peak discharge) and two 2-year return period floods in December 2010 (1950 m^3/s and 1760 m^3/s peak discharge) are used for this study [Claude, 2012], together with measurements obtained punctually in March, April, May and November 2010. Daily riverbed topography records of 0.5 m resolution using multi-beam echo-soundings are available, as well as longitudinal water free surface profiles. The spatial distribution of velocities has been monitored on three cross-sections (namely P80, P90 and P95, Figure 5.1) using an ADCP (Acoustic Doppler Current Profiler). Claude et al. [2014] estimated bedload transport rates by means of a isokinetic sediment sampler (BTMA), from dunes celerity and geometrical properties (i.e. dune tracking) and using the Meyer-Peter and Müller [1948] and Van Rijn [1984] bedload transport capacity formulas. Upstream and downstream of the area of interest, the riverbed and secondary channels topography are obtained by linear interpolation of cross-sections measured in 2009 which are regularly spaced of 60 m along a distance of 2 km. Lidar data of 0.25 m resolution in plan from 2003 is used to reconstruct the floodplain and riverbanks. Supplementary information on the techniques used for data monitoring is provided by [Claude, 2012; Claude et al., 2012, 2014].

In the study area, considering a hydrological year, the bar migration celerity not only varies of several orders of magnitudes and can reach values up to one meter per day, but also complex morphodynamic processes have been observed with a succession of transverse bar and alternate bar configurations during a single hydrologic year in 2010 [Claude et al., 2014]. Claude et al. [2014] concluded that the bar configuration tended to evolve cyclically with a low dependence to the hydrological conditions in this expansion/contraction area. The authors suggest the following cycle: *i*) free alternate migrating bars cross the upstream channel expansion, *ii*) they progressively slow down and then stop migrating once they are located in the expansion area due to the forcing generated by the downstream channel narrowing, *iii*) the spatial non-uniformity of flows induce the lateral migration of bars leading to the formation of a transverse bars until they reach the opposite bank and *iv*) the migration of upstream free alternate bars re-balances the flow velocity field, inducing the lateral bar erosion and vanishing from the expansion area. More details can be found in Claude et al. [2014] and later in the present work (see Section 5.3). Dunes of [0.1-0.3] m height and [4-6.5] m length tend to be dominant [Claude et al., 2014]. The local channel curvature induced by the left-side island and the right-side dyke seems to induce only small amplitude secondary and vertical velocity structures, as concluded by Claude et al. [2014]. As observed by Claude et al. [2014], the flow deformation induced by this permanent geometrical forcing is not high enough to observe local forced bars as commonly found in meanders or bifurcations.

5.2.2 Mathematical and numerical model

The two-dimensional morphodynamic model used in this work presents two components: a hydrodynamic module and a morphodynamic module [Cordier et al., 2019]. The hydrodynamic module is based on the solution of the 2-D depth-averaged shallow-water equations (SWE) [de Saint-Venant, 1871; Weiyan, 1992; Nezu et al., 1994; Vreugdenhil, 2013], with a closure relationship for turbulence based on a constant turbulent eddy viscosity ν_t [m^2/s], where roughness effects are parameterized through the friction law $\vec{S_f}$ [-] of Chézy, given as follow:

$$\vec{S_f} = (S_{f,x}, S_{f,y}) = \frac{\vec{u}|\vec{u}|}{C^2 h} , \tag{5.1}$$

where $S_{f,x}$ and $S_{f,y}$ correspond to the components of the friction law $\vec{S_f}$ [-] along the longitudinal $x-$axis and transversal $y-$axis direction respectively, h [m] is the water depth, $\vec{u} = (u, v)$ [m/s] is the depth-averaged flow velocity vector with components u and v [m/s] the component along the longitudinal x-axis and transversal y-axis direction respectively, with $|\vec{u}|$ [m/s] the module of $\vec{u}$, and C [$m^{1/2}/s$] corresponds to the Chézy friction coefficient. The formula of Nikuradse [1950] is used to calculate the equivalent friction coefficient of Chézy denoted $C_f = g/C^2$ [-] as a function of the equivalent roughness height of the bed denoted with k_s [m]:

$$C_f = 2\left[\log\left(\frac{30h}{ek_s}\right)/\kappa\right]^{-2} , \tag{5.2}$$

where κ is the von Kármán coefficient (= 0.40 for clear waters) and e is the base of the natural logarithm.

The morphodynamic module is based on the solution of the Exner [1920] mass balance equation. In case of non-uniform sediment, the Exner equation is applied to every size fraction of sediment in which the mixture is subdivided. The following procedure is adopted: *i*) the sediment mixture is discretized into sediment fractions, and for each fraction the representative sediment diameter is given, *ii*) the bedload transport capacity equation and the mass conservation formula are applied for each separate fraction of sediment.

The solution for sediment mass conservation is based on the mathematical concept proposed by Hirano [1971], who developed a continuity model for vertical sediment sorting. The method is based on the decomposition of the bed into a homogeneous top layer, called *active layer*, and a *substrate* [Church and Haschenburger, 2017; Ashmore et al., 2018]. Further details on the specificity of this bookkeeping active layer model can be found in Cordier et al. [2019].

For each i^{th} size fraction of sediment, the sediment transport magnitude without gravitational effects $q_{b0,i} = |\vec{q_{b0,i}}|$ [m^2/s] is estimated using the bedload capacity formula of Wilcock and Crowe [2003] modified by Recking et al. [2015]. The correction of bedload magnitude to account for the gravitational effects (i.e. the bed slope effects) is modelled with the formula of Koch and Flokstra [1980], where the fractional transport rate $q_{b0,i}$ is modified as a function of the bed slope with respect to the current direction:

$$q_{b,i} = q_{b0,i}\left(1 - \beta_1 \partial_s z_b\right) = q_{b0,i}\left[1 - \beta_1\left(\partial_x z_b \cos\delta + \partial_y z_b \sin\delta\right)\right] , \tag{5.3}$$

where β_1 is an empirical coefficient accounting for the stream-wise bed slope effect, δ is the angle between the current and the x-axis direction, and s the coordinate along the current direction. The bed slope effect is similar to a diffusion term in the bed evolution equation [Van der Meer et al., 2011] and may smooth the bed topography and prevent from numerical instabilities [Zolezzi and Seminara, 2001; Cabrit, 2009]. The correction of bedload direction is given by the relation of Bendegom [1947]:

$$\tan\alpha_i = \frac{q_{b,i,n}}{q_{b,i,s}} = \frac{\sin\delta - T_i \partial_y z_b}{\cos\delta - T_i \partial_x z_b} , \tag{5.4}$$

where α_i is the angle between the sediment transport vector of the i^{th} size fraction of sediment and x-axis direction which will deviate from the bed shear stress vector due to gravity effects, $q_{b,i,n}$ and $q_{b,i,s}$ correspond to the bedload magnitudes along the normal to the current direction and the stream-wise direction, respectively, and where the coefficient T_i is calculated as $T_i = \frac{1}{\beta_2\sqrt{\tau^*_{b,i}}}$ [Talmon et al., 1995], where $\tau^*_{b,i}$ is the bed shear stress adimensionnalized by the i^{th} size

fraction of sediment also known as Shields parameter and scales the gravity effects as a function of the grain diameter of the i^{th} size fraction, and β_2 is an empirical coefficient and can be used as a calibration parameter.

The total shear stress τ [Pa] is calculated from the depth-averaged flow velocity field, where $\tau = 0.5\rho C_f(u^2 + v^2)$, $\rho = 1000$ kg/m^3 is the water density and C_f is equal to the sum of skin friction and bed form drag. In this study, the bed shear stress is determined as a function of the total shear stress with the relation:

$$\tau_b = \mu\tau \ , \tag{5.5}$$

where $\mu = C'_f/C_f$ is the friction factor and C'_f [-] is the equivalent Chézy coefficient only due to skin friction and is assumed to be the only component acting on bedload [Mendoza et al., 2016]. In this work, C'_f is calculated assuming a flat bed by using the Nikuradse's formula (Equation 5.2), where the roughness height k'_s [m] is a function of the mean sediment diameter at the bed surface with:

$$k'_s = \alpha_{k,s} \times d_{s,m} \ , \tag{5.6}$$

where $\alpha_{k,s}$ is used as a calibration parameter. García [2008] summarized different values of $\alpha_{k,s}$ induced by the grain size roughness measured in the field and in the laboratory ranging from 1 to 6.6, but according to Huthoff [2012] in the presence of dunes this coefficient is showed to increase of several orders of magnitude, i.e. between 10 and 1 000.

The numerical solution of the SWE is based on the finite element method P_1, where the advective terms are computed with the method of the characteristics. The numerical solution of the sediment transport continuity equation is performed by a procedure that combines an implicit finite element scheme and an edge-based explicit upwind advection scheme [Hervouet et al., 2011].

5.2.3 Numerical model setup

The boundary conditions of the hydrodynamic model correspond to an upstream flow discharge and a downstream free surface profile ranging in [97;1950] m^3/s and [31.8;35.2] m, respectively. The downstream free surface profile corresponds to the normal water depth obtained with the Chézy formula (Equation 5.1) for a rectangular open channel geometry, with $C = 35$ m$^{1/2}$/s corresponding to the averaged Chézy coefficient measured in the site Claude [2012]. A sediment-feed (equilibrium) upstream morphodynamic boundary condition is imposed at the upstream boundary, so that the bed topography along this boundary remains unchanged during the whole morphodynamic simulations. The morphodynamic downstream boundary is set as free.

The upstream and downstream model boundaries have been extended by 4 km upstream and 3 km downstream by means of straight reaches of regular slope equal to $i_0 = 3.10^{-4}$ corresponding to the averaged measured reach slope, in order to allow upstream flow stabilization and lessen the backwater effects in the study area. The cross-sectional profiles of the channel extensions correspond to the most upstream (or downstream) cross-section measured in 2009 (*cf.* 5.2.1).

The model uses an unstructured computational mesh composed of triangular elements, with typical length equal to 15 m in the upstream and downstream parts of the domain. Mesh density reduces progressively up to 5 m in the area of interest and in the secondary channels. The computational time step is fixed to $\Delta t = 0.5$ s in order to keep a Courant number below 0.25. Mesh and time convergence analyses are conducted to ensure numerical stability and to capture local sedimentary processes. For all simulations, $\rho = 1000$ kg/m^3, $\Delta_s = 1.65$, $P_0 = 0.40$ and $\nu_t = 0.05$ m^2/s. The last parameter has been subject to a sensitivity analysis using the

calibrated hydrodynamic model, performed with $\nu_t \in [10^{-6} - 10^{0}]$ m^2/s using the 1 year return flood event (i.e. $Q_{w,1y} = 1030$ m^3/s). Computed water depths and velocities are affected by less than 5% for the values of ν_t considered in this range. Hence, the value of $\nu_t = 0.05$ m^2/s is retained [Vionnet et al., 2004]. The GSD used in the numerical model corresponds to a mixture of $F_1 = 80\%$ of sand equal to $d_1 = 0.9$ mm and $F_2 = 20\%$ of gravel equal to $d_2 = 3.2$ mm. In order to model stratigraphic processes, the riverbed is discretized using nine vertical sediment storage layers of equal thickness, excepted from the deepest layer which is allowed to increase as long as deposition occurs. The submerged rip-raps presented in Section 5.2.1 and Figure 5.1 are set as non-erodible areas of the computational domain.

5.2.4 Numerical model scenarios

Based on the calibrated morphodynamic model presented in Section 5.3, five scenarios are proposed to investigate bar morphodynamics processes, with a special focus on the hydrological conditions and non-uniform sediment processes. To this goal, the first proposed scenario (run A) consists on reproducing numerically the bar evolution observed *in situ* by Claude et al. [2014] starting from March 15th 2010 and lasting for one year, using the hydrogram of 2010-2011.This scenario is also used to explore the sediment sorting processes (=vertical and planform) which can occur under real conditions, i.e. considering variable discharge, and is also referred to as "reference scenario". To better understand the role of sediment sorting on bar morphodynamics, a comparison is performed between the results of this previous scenario and another scenario in which sediment sorting is not accounted (run B). In the latter scenario, grain size sorting can be avoided numerically by using a thick active layer of $L_a = 100$ m. More details on this method can be found in Cordier et al. [2019]. The influence of the discharge on bar dynamics is investigated by comparing results from the reference scenario (i.e. run A) and three derived scenarios with constant water inflows (runs C, D and E), representing the low flow period (run C, Q_w =200 m^3/s), mean annual flow (run D, Q_w =500 m^3/s) and two-year flood peak (run E, Q_w =2000 m^3/s).

5.2.5 Analysis methods

5.2.5.1 Bar characteristics

Ideally, free migrating bars *fronts* are located downstream of the bar top, just before the transition with the lee side. Originally defined for dunes, the *lee side* corresponds to the transition between the bar front and the pool and has a negative slope, while the *stoss side* is used for the transition between the pool and the next bar front.

In this work, H_b [m] denotes bar amplitude, and corresponds to the elevation between the bar top and the pool [Nelson et al., 2015a]. The bar wavelength λ_b [m] denotes the longitudinal distance between the two nearest bar tops separated by a pool. The migrating bar celerity along the downstream-wise direction (respectively cross-sectional direction) denoted $c_{b,l}$ [m/d] (respectively $c_{b,t}$ [m/d]) is the displacement a bar front (respectively bar edge) during a given time lapse. The bed evolution Δz_b [m] is the difference between the channel bed elevation obtained at a given time and that from the initial time (i.e. $t = 0$ s).

The most likely number of bars per cross section, denoted m_{th}, is derived theoretically from the physics-based predictor of Crosato and Mosselman [2009]:

$$m_{th} = \frac{\beta}{\pi}\sqrt{(b-3)f(\bar{\tau}^*)C_f} \ , \tag{5.7}$$

where β [-] corresponds to the width-to-depth ratio of the flow, b [-] is the degree of non-linearity in the dependence of sediment transport on the flow velocity (here b=4), $\bar{\tau^*}$ [-] corresponds to the reach-averaged Shields number and $f(\bar{\tau^*}) = 1.7\sqrt{\bar{\tau^*}}$ according to Talmon et al. [1995]. While the bar mode is mathematically defined as an integer number, when derived using Equation 5.7 it will result as a real number.

5.2.5.2 Skill and accuracy assessment

The root-mean-square error (RMSE) is used to compute the error between field measurements and numerical results, and is obtained as follow:

$$RMSE = \sqrt{MSE} = \sqrt{\frac{1}{n}\sum_{k=1}^{n}(m_k - o_k)^2} \quad : (m_k, o_k) \in \mathbb{R}^n \times \mathbb{R}^n \quad , \tag{5.8}$$

where the MSE corresponds to the mean-square error, m and o are both vectors containing n scalar elements, m corresponding to numerical results and o to field observations, with k corresponding to the spatial index.

Error estimators such as the RMSE only inform how far numerical model predictions are from the observations, but do not inform on the physical relevance of the computed results. Estimation of morphodynamic models accuracy has been introduced recently using model skill scores [Sutherland et al., 2004; Bosboom et al., 2014; Baart et al., 2016; Dam et al., 2016]. In the current work, the Brier Skill Score (BSS) is applied to bed topographic changes:

$$BSS = 1 - \frac{MSE_{err}}{MSE_{sig}} = 1 - \frac{\frac{1}{n}\sum_{k=1}^{n}(m_k - o_k)^2}{\frac{1}{n}\sum_{k=1}^{n}(i_k - o_k)^2} \quad , \tag{5.9}$$

where i is a vector containing n scalar elements and corresponds to the initial topography, MSE_{err} is the error, which corresponds to the difference between model and observations, and MSE_{sig} is the signal, and corresponds to the changes of measured bed level since the beginning of the computation [Dam et al., 2016]. The sign of the skill score is determined by the difference between the reference data and the model prediction. $BSS < 0$ indicates that the reference initial topography is a better prediction than the model forecast. According to Sutherland et al. [2004] $BSS \in [0.1 - 0.3]$ indicates reasonably/fair predictions, $BSS \in [0.3 - 0.5]$ indicates good predictions and $BSS > 0.5$ mean excellent predictions.

5.2.5.3 Estimation of the degree of spatial sediment sorting

Analysis of the degree of spatial sediment sorting degree is performed through the calculation of the statistical distribution of the mean sediment diameter in the area of interest (Figure 5.1). The computed distribution allows to extract the particle size $\bar{d_{s,m_\chi}}$ corresponding to each given decile χ, for each day of the simulation. Determination of the ratio between two opposite deciles, i.e. $\bar{d_{s,m(50-\chi)}} / \bar{d_{s,m(50+\chi)}}$, can be used to observe the evolution of the degree of sediment sorting in the study area.

5.3 Numerical model calibration and validation

5.3.1 Hydrodynamic model calibration

The hydrodynamic model is calibrated on the basis of 9 permanent hydrological scenarios (3 events in June 2010, 5 in December 2010 and one in January 2011) using values of $k_s \in [0.05;0.50]$ m uniformly distributed in space, with updating the bed topography for each scenario and calibrating on longitudinal water levels (L_1-L_2-L_3) and cross-sectional velocity measurements (P80-P90-P95, Figure 5.1). These scenarios are run 30 000 s in order to reach the steady state. For each scenario, the best fitting value of k_s denoted $k_{s,cal}$ corresponds to the average value of k_s minimizing the RMSE of water depths and velocities computed along the profiles L_1, L_2, L_3, P80, P90 and P95. The calibrated roughness is generally lower $k_s = 0.11 \pm 0.04$ m in June compared to $k_s = 0.205 \pm 0.09$ m in December 2010, and could be hypothetically due to the bar configuration (i.e. transverse or alternate) and also dunes characteristics in the area of interest. Therefore, the roughness height used in the calibrated hydrodynamic model is set equal to the averaged value of the $k_{s,cal}$, i.e. $k_s = 0.178$ m. Using the last calibrated value, the averaged computed RMSE on water depths is ranging in $[0 - 0.25]$ m, highlighting a weak overestimation of water depths. Additionally, an analogous result is obtained for the flow velocity, where the averaged computed RMSE on flow velocity ranges in $[0 - 0.16]$ m/s, highlighting a weak overestimation of flow velocity (Figure 5.2). The present hydrodynamic model reproduces satisfactorily the spatial distribution of water depths and flow velocity in the area of interest for a given range of flow conditions from low to high flows and considering two distinct bar configurations.

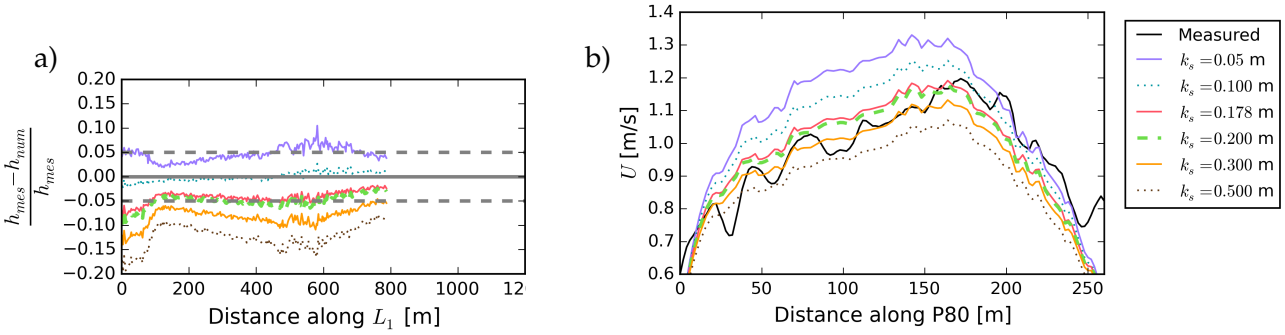


Figure 5.2: Example of (a) longitudinal profile of the relative error on the water free surface (gray dashed lines correspond to a relative error of ±5%) and (b) cross-sectional flow velocity magnitude profile used to calibrate the hydrodynamic model, computed for the scenario of December 19^{th}, 2010 with Q_w =701 m^3/s, see Figure 5.1 for location.

5.3.2 Morphodynamic model calibration and validation

The morphodynamic model calibration requires to compute not only relevant sediment transport rates but also a satisfactory riverbed evolution. In this work, the coefficients used for the bed slope effects are the same as found in the literature, so that $\beta_1 = 1.3$ and $\beta_2 = 1.7$ [Koch and Flokstra, 1980; Talmon et al., 1995]. The active layer and sub-layer thicknesses are set equal to 0.40 m, and the coefficient selected for calibration corresponds to $\alpha_{k,s}$. The morphodynamic model is calibrated on the same 9 scenarios (cf. 5.2.4) using averaged cross-sectional bedload

measurements (P83, Figure 5.1) and measured bed evolution. Calibration is performed by conducting short-term morphodynamic runs, in order to find the optimal value of $\alpha_{k,s}$ minimizing the difference between computed and measured transport rates for each of the 9 scenarios.

For each scenario, the morphodynamic simulation starts from the steady-state condition obtained with the calibrated hydrodynamic model using $k_s = 0.178$ m, and is run during 100 s to avoid bed topography changes. Bedload fluxes are computed at cross-section P83 (see Figure 5.1) using values of $\alpha_{k,s} \in [1;100]$. The best fitting value of $\alpha_{k,s}$ is then retained for each scenario. Figure 5.3 shows that the calibrated values of $\alpha_{k,s}$ vary as a power function of Q_w where $\alpha_{k,s} = f(Q_w) = 3.63 \times 10^6 \; {Q_w}^{-1.83}$. Because the above relation is obtained for values of $Q_w \in [386;1950]$ m^3/s, uncertainty on the predicted $\alpha_{k,s}$ increases greatly at low flowrates. To compensate for eventual over-prediction at low flowrates, a threshold value is introduced so that $\alpha_{k,s}$ remains constant for $Q_w < 300$ m^3/s (i.e. $\alpha_{k,s} = 106$).

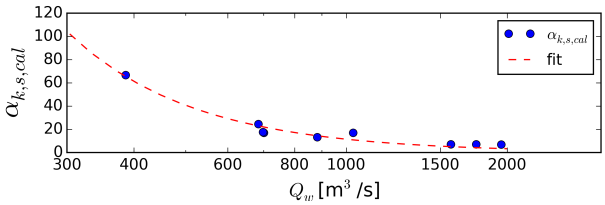


Figure 5.3: Power function obtained between the calibrated value of $\alpha_{k,s}$ obtained for each considered scenario and the associated flowrates Q_w.

The morphodynamic model is then validated by reproducing the one year morphodynamic event from March 15th 2010 to March 15th 2011, using the previously calibrated relation between $\alpha_{k,s}$ and Q_w. In the model, bars form further upstream of the area of contraction/expansion, and progressively migrate through this last area (Figure 5.4). The comparison between the sediment transport rates measured *in situ* and computed numerically show that the morphodynamic model computes satisfactory transport rates at distinct periods of the year, and by extension for different bar configurations and flowrates. A thorough comparison between the computed and measured bed topography in terms of *RMSE*, *BSS* and patterns of erosion/deposits is presented in Section 5.4.1 to show that the present morphodynamic model can be used for further investigations.

5.4 Morphodynamic results

5.4.1 Bed evolution with variable discharge and sediment sorting

Bed evolution in the scenario with variable hydrogram with sediment sorting (which is also used for the morphodnamic model validation) is obtained from a differential of bed topography between a given date and the initial time (Figure 5.5). The main computed bar characteristics corresponding to wavelength, amplitude, celerity and pattern are summarized in Table 5.1. On April 7th 2010, corresponding to the configuration of alternate bars, the upstream bar (left bank) and downstream bar (right bank) migrate downstream, following a mechanism of free bar front migration, as illustrated by the variable of bed evolution where the sediment is deposited on the lee sides and the eroded sediment from bars stoss sides. This result is consistent with Claude et al. [2014], who measured a downstream migration celerity of 2.2 m/d, against 2.5 m/d numerically (Table 5.1). According to field measurements, the alternate bar system progressively

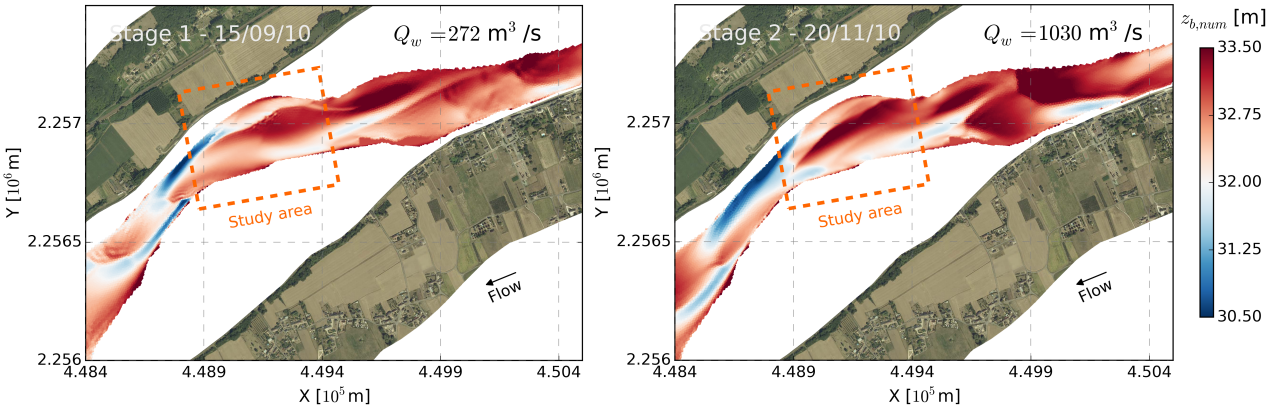


Figure 5.4: Macro-scale planview of the bed topography computed with the calibrated morphodynamic model on September 15th 2010 and November 20th 2010, showing the upstream bars having an influence on downstream bar dynamics which are located in the area of interest. The color-scale is different from Figure 5.5 in order to better visualize the smaller bars forming at each sides of the central/transverse bar.

evolves toward a difference bed configuration, with the presence of a transverse bar, as showed on June 22th 2010 (Figure 5.5). Numerical results also show the formation of a transverse bar front, this structure corresponds to a left side bar which not only migrates rapidly downstream at a celerity of 6.8 m/d, but also expands rapidly in the direction of the right bank at a celerity of 2.1 m/d, constraining the *thalweg* along the right bank in a narrow strip scaling from 1/3 to 1/4 local channel width. The migration front and the edge of this bar are characterized by high local bed slopes (Figure 5.5). In turn, this migrating structure induces not only the erosion of the right side bar, by deviating the flow towards the right bank and increasing local bed shear stress as observed by Claude et al. [2014], followed by the formation of an upstream left side channel. Given this configuration, numerical results show that upstream pools have progressively moved from the right to the left bank, while the opposite trend is observed downstream, indicating an inversion of the *thalweg* path in the study area. The behavior observed downstream is in agreement with field observations, while this comparison cannot be easily drawn upstream mostly because field data is not available immediately upstream of the study area.

From the end of June to November 2010, i.e. during the period of approximately four months of seasonal low flows, the riverbed topography has also experienced important changes as illustrated by the measurements and numerical results on November 8th 2010 (Figure 5.5). During this period, the transverse bar would move toward the right bank direction [Claude et al., 2014]. According to Figure 5.5, the upstream left side channel presented above, observable at its early stages of formation on June 22th 2010, tends to concentrate the flows along the left riverbank in a narrow strip scaling of approximately 1/3 local channel width. This leads to the alternate left-side bar erosion, and the development of a central bar in the area of interest, which stabilizes along the longitudinal direction as depicted by the migration celerity close to 0 in the longitudinal direction on September 15th 2010 (Figure 5.4a and Table 5.1). Under this configuration, the flow is concentrated in the *thalweg*, which is located at the left and right sides of the central bar, and trigger the formation and migration of shorter and smaller bars, as illustrated in Figures 5.5 and 5.4. Progressively, the central bar migrates toward the right

bank at a celerity approximately 1.2 m/d, which pattern corresponds to a transition between a transverse bar and a central bar, as showed on November 20^{th} 2010 (Figure 5.4b). Such a bar pattern could not be observed in the field but could have been missed due to a lack of field observations at this period of time [Claude, 2012].

The left-side alternate bar front visible on November 20^{th} 2010 (Figure 5.4b) and located immediately upstream of the study area migrates progressively downstream, before being visible (in the field and numerical model) in the study area on December 13^{th} 2010 (Figure 5.5). The left bar deviates the flow toward the right riverbank and re-inverts the *thalweg* path, which eventually follows the same pattern as on April 7^{th} 2010. As a result, the transverse bar tail migrates downstream at a celerity in the range of [5.1-9.5] m/d, and is pushed toward the right bank at [2.2-2.5] m/d, while the transverse bar front located in the channel contraction area remains immobile. This bar becomes eventually the right-side alternate bar observed on January 3^{rd} 2011 (Figure 5.5), where the bar lee side and edge are characterized by a steep slope which migrate toward the right bank (Figure 5.5).

Table 5.1: Bar characteristics computed at different stages of the simulation with accounting for sediment sorting (scenario A).

time ↓

Date [dd/mm/yyyy]	Q_w [m^3/s]	β [-]	λ_b [m]	H_b [m]	$c^*_{b,l}$ [m/day]	$c^*_{b,t}$ [m/day]	Bar pattern **	m^{***}_{th}	m^{***}_{num}
07/04/2010	846	95	1340	1.4	2.5	1.3	A	2	1.5
22/06/2010	1030	86	1510	1.3	6.8	2.1	T	2	2
15/09/2010	272	≈ 200	1440	1.3	≈ 0	1.2	C	3.5	2-2.5
08/11/2010	434	142	1180	1.3	≈ 0	≈ 0	C/T	3	3-3.5
20/11/2010	1030	82	1410	1.5	7.9	1.1	T	2	2.5
11/12/2010	1950	56	1410	1.9	9.5	2.5	A	1.5	2
03/01/2011	882	88	1260	2.0	5.1	2.2	A	2	1.5 - 2

* Bar celerity is measured over a period of 10 consecutive days, subscript l (respectively t) is used for the velocity component along longitudinal downstream (resp. cross-sectional right-side) direction
** Subscripts used to denote bar configuration: A=Alternate bars; C=Central bar; T= Transverse bar
*** m_{th} and m_{num} denote the bar modes computed theoretically with $b = 4$, $C_f = 0.008$, $B = 225$ m and $d_{s,m} = 1.36$ mm, and obtained numerically on P83 cross-section (see Figure 5.1), respectively.

These results suggest that the computed amount of erosion and deposition which is at the origin of the observed bar migration is in accordance with measurements [Claude et al., 2014]. This behavior is not only depicted by the planform distribution of bed topography and bed evolution (Figure 5.5), but also by the relatively low values of the $RMSE \leq 20$ cm computed between measured and computed bed topographies (Figure 5.6). It is found that $BSS \in [0.26 - 0.46]$, which seems reasonably good, considering the complexity of the morphodynamic processes taking place in the study area. The BSS increases progressively from March 15^{th} 2010 to June 25^{th} 2010, and then decreases progressively until January 3^{rd} 2011. This trend is explained by the fact that the reference bed topography used to compute the skill score is associated to an alternate bar configuration. Because of that, the lowest BSS's are generally reached when the model predicts an alternate bar pattern, and oppositely, highest BSS's are reached when the bar pattern is far from the initial configuration, i.e. when the bar is transverse, according to Figure 5.6.

No evident relationship between the flowrate and computed bar characteristics can be obtained (Table 5.1). On the whole, the computed bar amplitudes and wavelengths are of

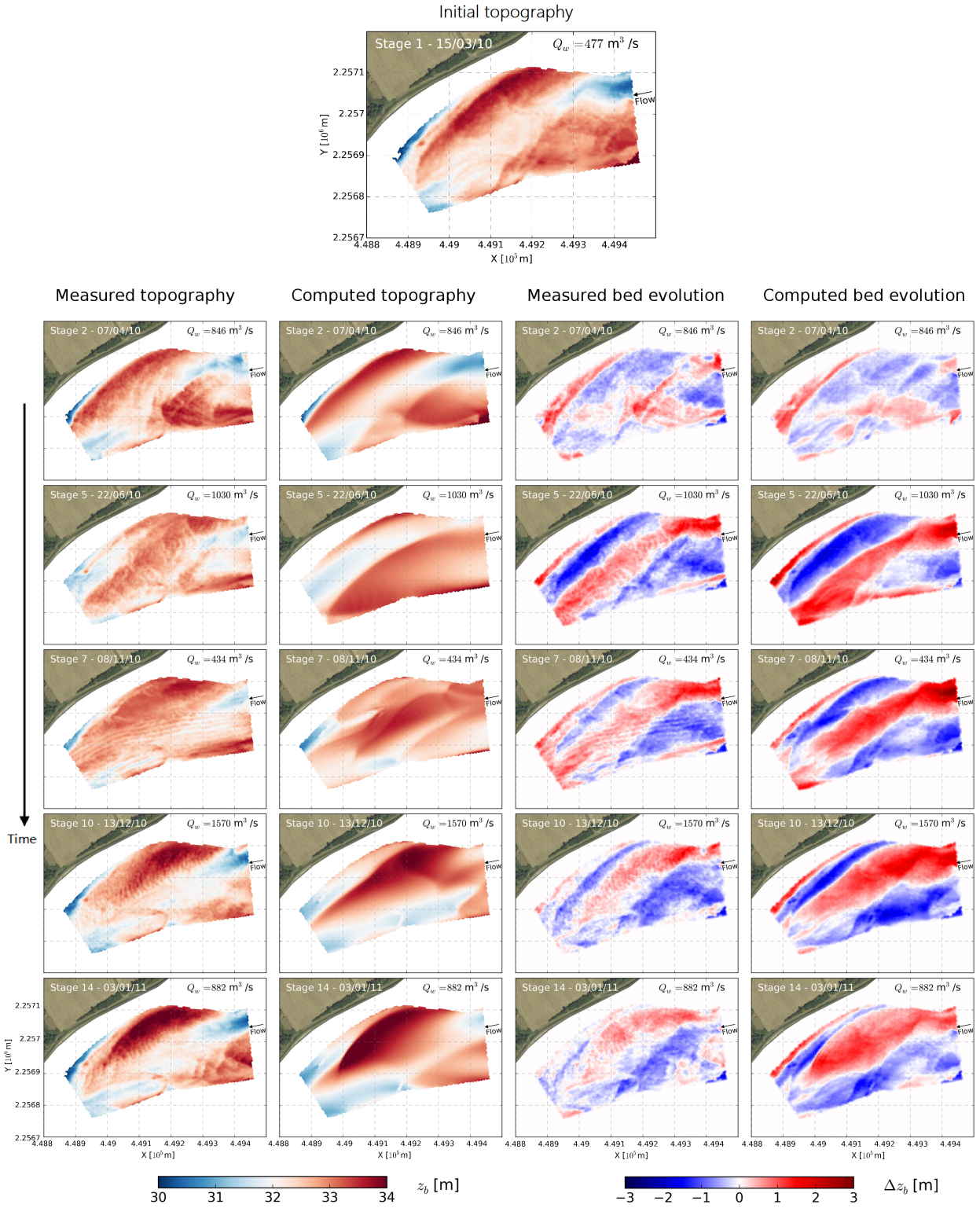


Figure 5.5: Planview of the bed topography and bed evolution measured in the field and computed with the calibrated morphodynamic model from March 15th 2010 to March 15th 2011.

the same order of magnitude than the values measured in the field, where computed bar wavelengths vary in [1180-1510] m vs. [1000-1140] m in the field, and computed bar amplitudes vary in [1.3-2.0] m vs. [1.29-2.20] m in the field [Claude et al., 2014]. The consistency observed between the bed topography measured in the field and the one computed numerically with the scenario of reference (Figure 5.5) shows that the morphodynamic model is able to reproduce the main processes of bar migration in the study area.

Largest differences are found in the magnitude of computed bed evolution, which is generally more intense than in the field (Figure 5.5). This difference could be attributed to several reasons. Firstly the spatial variation of dunes over bars observed in the field [Claude et al., 2014], which cannot be represented with the current modelling approach, and which are assumed to play also a role on the spatial non-uniformity of bed shear stress. Secondly the suspended sediment transport, which is not modelled but could increase diffusion and could decrease the intensity of bar topography [Meles, 2015] in the same way as observed for dunes [Naqshband et al., 2014].

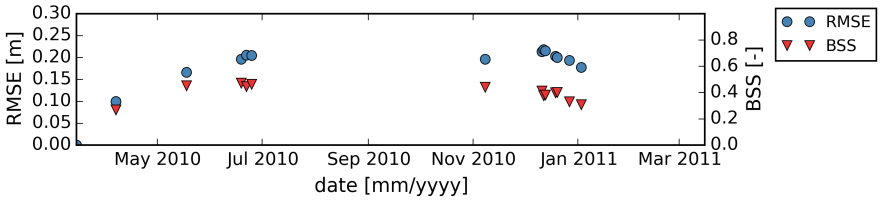


Figure 5.6: Time-series of the RMSE and BSS computed on bed topography with accounting for sediment sorting (scenario A) from March 15^{th} 2010 to January 3^{rd} 2011.

5.4.2 Bed evolution with variable discharge without sediment sorting

A thorough comparison is then performed on the bed topography and bed evolution computed accounting (scenario A) and not accounting (scenario B) for sediment sorting processes. A first approach consists on comparing the planform bed topography and bed evolution obtained at a given stage of the simulation with both scenarios. Two stages are used for this comparison, the first one corresponding to the end of the low flow period on November 8^{th} 2010, and the second corresponding to the end of the two-year flood event, on January 3^{th} 2011. Results from this comparison (Figure 5.5 vs. 5.7) suggest that the difference between computed topographies for the two scenarios is relatively small, with respect to the bed elevation changes occurring in each of these scenarios.

5.4.3 Bed evolution with constant inflow

Figure 5.8 illustrates the long-term response of the alluvial riverbed using three distinct constant water discharges in the expansion area, considering water discharges representative of the low-flow period (run C), mean annual flow (run D) and two year peak flood (run E). Results show that in every single scenario considering a constant flow rate, a dominant bar pattern is observed in the expansion area in the late stage of the simulations. In run C, the bed topography consists in a multiple channel pattern, where relatively short bars continually migrate downstream and rework the main channel riverbed. Conversely, in run E, the riverbed is characterized by the presence of alternate bars, which are particularly elongated and stop migrating. In run D, an intermediate state is obtained, where transverse bars and central bars patterns are alternating

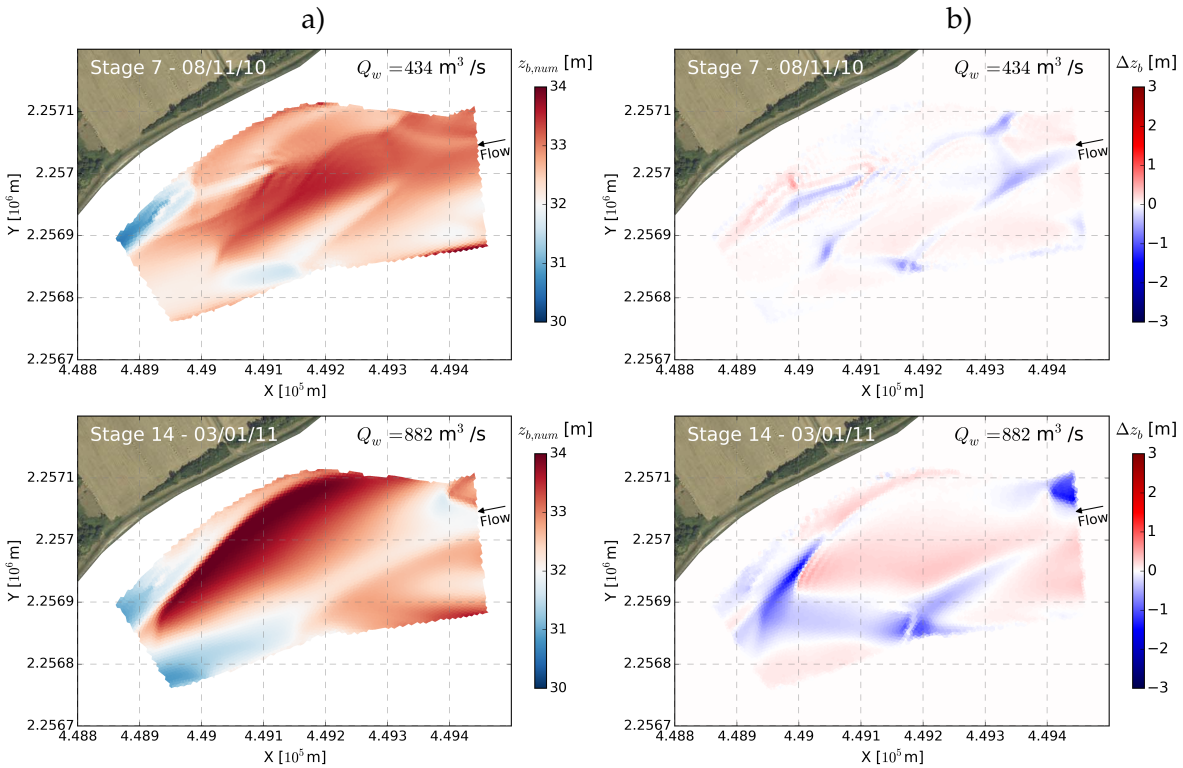


Figure 5.7: Planview of a) the bed topography computed without accounting for sediment sorting (scenario B) and b) difference of computed bed topography at this same date between the scenario accounting for sediment sorting (A) and the scenario without sediment sorting (B). The black squares correspond to twelve points distributed close to the left bank, the right bank and the center of the channel along P80, P87, P90 and P95 cross-sections, which are used to compare results from runs A and B.

over time, with moderate bar migration celerity. Comparison between these three runs shows that higher water discharges invariably decrease the long-term computed bar mode and induce simpler channel patterns.

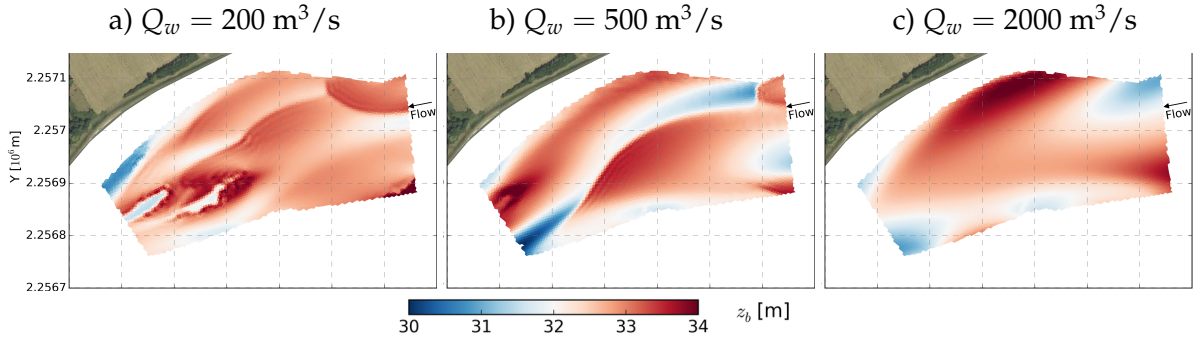


Figure 5.8: Planview of the bed topography computed with the morphodynamic model after a period of 300 days with a constant inflow representative of a) the low-flow period (run C), b) mean annual flow (run D) and c) two year peak flood (run E).

5.4.4 Bar mode

Computation of the most probable bar mode using the predictor of Crosato and Mosselman [2009] at different stages of the reference scenario (Table 5.1) and bar modes obtained from the numerical model (i.e. scenario A) suggest a strong variation of the bar pattern in the study area, varying between alternate bars ($m = 1$), central bars ($m = 2$) and a multi-channel -or braided- pattern ($m \geq 2.5$).

Theoretical bar modes suggest that alternate bars can only develop in the study area at relative high flowrates, i.e. during the 2-year flood peak of December 11^{th} 2010 (Figure 5.9), with $\beta \approx 50$ (Table 5.1). In the same way, the theory suggests that centrals bars (i.e. $m = 2$) are dominant at flowrates around the 1 year flood discharge of $Q_w \approx 1000$ m^3/s, corresponding to $\beta \approx 90$. These relatively simple bar patterns (i.e. alternate, central and transverse bars) are also computed numerically during periods of high flows. Moreover, the theory predicts higher bar modes at lower flowrates, with multi-channel bar patterns around the mean annual flowrate, i.e. for $\beta \approx 100$. Similarly, more complex bar patterns are obtained numerically during periods of low flows (Figure 5.9).

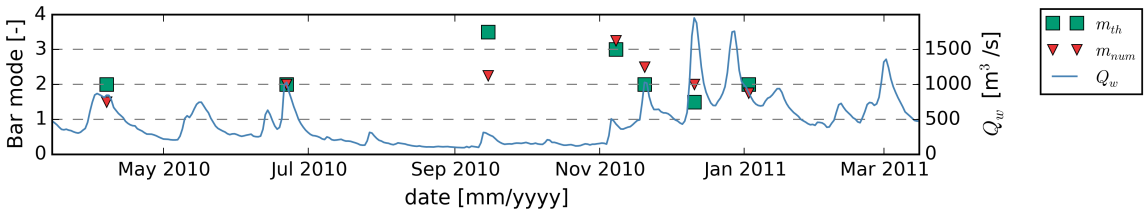


Figure 5.9: Time-series of the theoretical and numerical bar modes obtained with the scenario of reference (scenario A) from March 15^{th} 2010 to January 3^{rd} 2011.

5.4.5 Sediment transport

The spatial distribution of computed bed shear stress and bedload magnitude are similar, as depicted in Figure 5.10. This outcome is expectable in the sense that the computed sediment transport rate is primarily a power function of the bed shear stress, where the last is scaled by the total shear stress, which is a function of the depth-averaged flow velocity (see Equation 5.5). The high correlation found between the spatial distributions of flow velocity and bed shear stress suggest that the computation of bed shear stress from the total shear stress (see Equations 5.5 and 5.6) do not significantly impact the spatial redistribution of bed shear stress. Since shear stress and sediment transport are highly correlated, interest will be particularly given on the computed sediment transport in this section.

Figure 5.11 illustrates the patterns of normalized sediment transport (i.e. $q_b/\bar{q_b}$) obtained numerically with different bar configurations. The spatial distribution of sediment transport rates (and so bed shear stresses) is showed to be drastically different in the case where a transverse bar, alternate bars, or more complex bar patterns are present, i.e. is dependent of the bar configuration. Given the transverse bar configuration (Figure 5.11a), sediment transport is relatively high (i.e. $q_b/\bar{q_b} > 1.5$) over the bar head, while it drops to 0 in the immediately downstream adjacent pool visible on June 19^{th} 2010, and decreases importantly along the bed slope formed by the transverse bar edge (see Figure 5.5 for locating bar fronts). The bedload found in the *thalweg* close to the right bank tends to increase progressively in the downstream

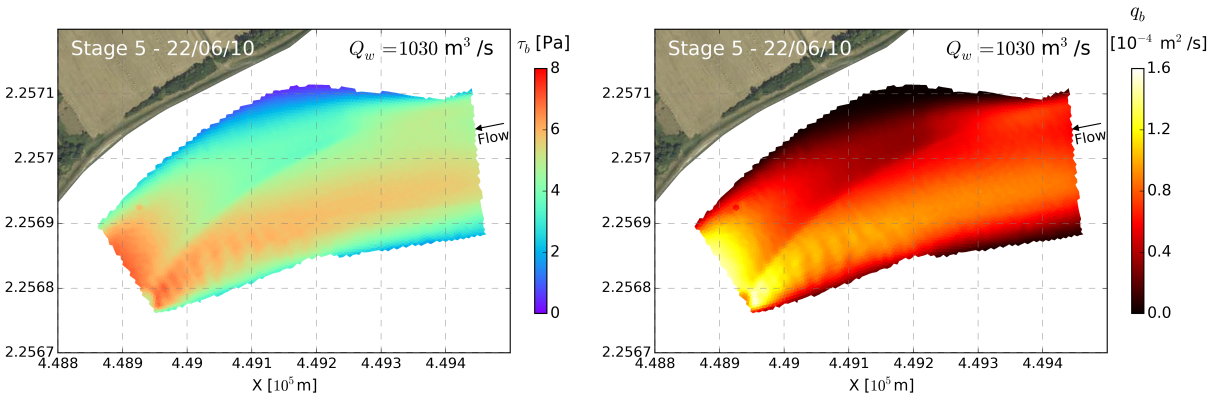


Figure 5.10: Planview of the bed shear stress and bedload magnitude computed with scenario A with the transverse bar configuration on June 22th 2010, which display both a similar spatial distribution.

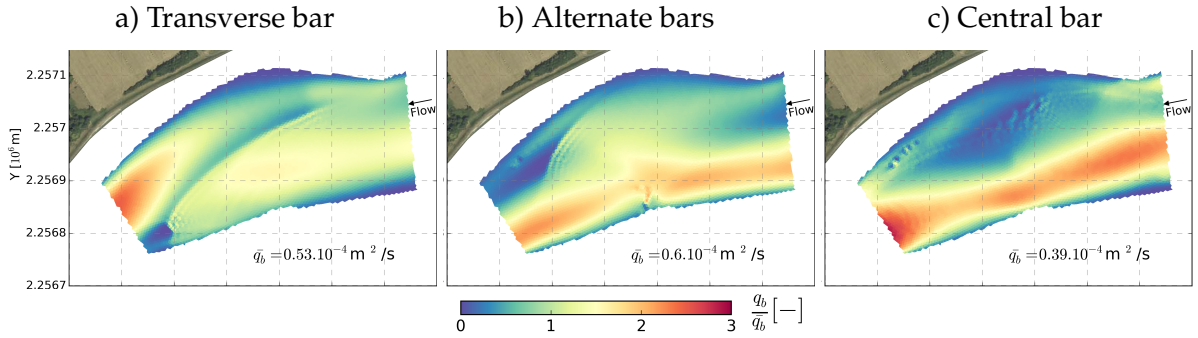


Figure 5.11: Planview of the ratio between bedload magnitude and spatially averaged bedload magnitude computed with scenario A considering the configuration of a) central bar (September 15th 2010), b) a transverse bar (June 19th 2010) and c) alternate bars (January 3rd 2011).

direction, and is found to be in the same order of magnitude than the bedload found over the transverse bar. Given the alternate bar configuration (Figure 5.11b), high sediment transport rates (i.e. $q_b/\bar{q}_b > 1.5$) are distributed along the left riverside, i.e. over the left migrating alternate bar and in the downstream adjacent pool, wherein the transition between the left bar/pool sequence is marked by a local and moderate longitudinal decrease of sediment transport. Along the right riverside, sediment transport increases longitudinally from the upstream pool until the downstream bar front, and drops to low values (i.e. $q_b/\bar{q}_b < 0.5$) in the immediate downstream pool (see Figure 5.5 for locating bar fronts). Given more complex bar configurations, i.e. with the presence of a central bar (Figure 5.11c), highest sediment transport concentrate in the left side of the channel, i.e. where the flow and high bed shear stress are concentrated. Moreover, the sediment transport over bar tops is found to be importantly decreased with respect to the alternate or transverse bar configurations, as the flow tends to concentrate in the narrow *thalweg*.

For all bar configurations, in the channel expansion area, sediment transport is very low in the proximity of the left and right riverbanks. This result may be explained by the high energy dissipation exerted by the water water motion on the river banks and sheltered areas induced by changes in bank direction, and coincides with the low flow velocities observed in these areas Claude et al. [2014]. In addition, the spatial distribution of bedload magnitude shows that

highest gradients are located at bar front and bar edge locations (Figures 5.4 and 5.5), which suggest that apart from these last areas, sediment transport rates tend to vary more smoothly. In general, the computed bedload is 3 to 5 times higher over submerged bars (i.e. excepted for the central/transverse bars which are not fully submerged) and in the deep channel than in the lee side and pools, and this difference is showed to increase for lower water discharges.

The temporal variation of the spatially averaged sediment transport rates in the study area (Figure 5.12) shows similarities with the hydrogram, especially during the period of low flows, although differences can be easily detected, such as in February 2011. This analysis suggests that sediment transport -in the study area- not only varies as a function of the hydrological conditions, but also depends on the local variability of sediment supply, which is due to the continuous migration of bars in the study area. The temporal variation of the ratio between the averaged transport rate of sand over total bedload suggest that sand participated to approximately 84% of bedload transport in the study area during the simulation, and varies very slightly in the interval [82-87]%. This result also shows that the portion of sand transport with respect to total transport decreases rapidly in the beginning of the simulation and tends to stabilize during the run.

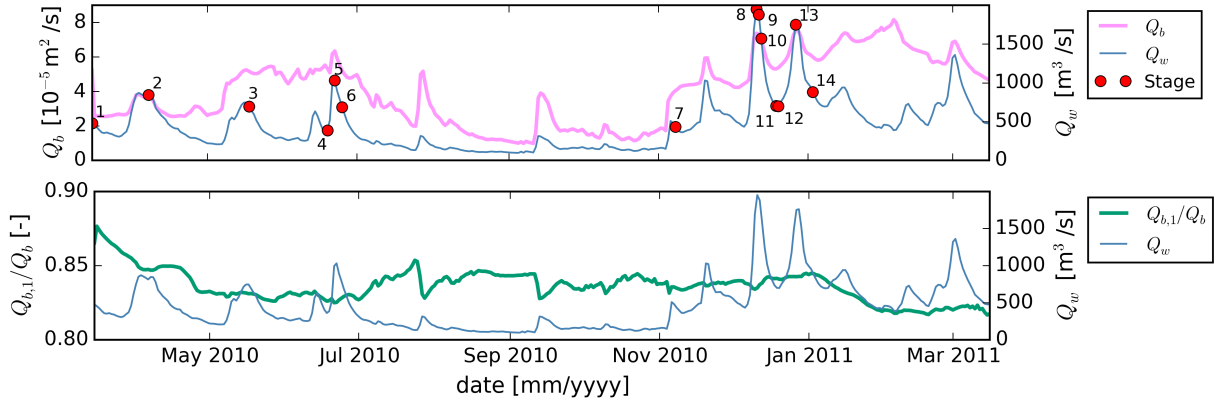


Figure 5.12: Time-series of the spatially averaged sediment transport rate and ratio between spatially averaged transport rates of the finest class of sediment over the total bedload, in the study area computed with scenario A from March 15th 2010 to March 15th 2011.

Figure 5.13 shows the planform distribution of the deviation angle between the bedload and the flow velocity vector fields for the transverse and alternate bar configurations. Sediment transport is always redirected toward the down-slope direction, as it is formulated in the model (Equation 5.4). As a consequence, highest angles of deviation are found at bar fronts and bar edge locations, and scale up to $\pm 5°$. The transverse bar and right alternate bar edges being oriented toward the right riverside (Figure 5.5), the sediment transport is then deviated toward the right bank direction (Figure 5.13), favoring the lateral migration of bars. In the case of the transverse bar configuration (Figure 5.13a), the remnant of the right side alternate bar deviates the sediment toward the *thalweg*, which is constrained along the right side of the transverse bar edge (Figure 5.5). Because the computed bedload is low along the right riverside, erosion of the remnant right side alternate bar is slow. While deviation angles are found to be generally low over the transverse bar (i.e. $|\alpha - \delta| < 1.5°$), the ones found over the right alternate bar head are higher (i.e. $|\alpha - \delta| > 1.5°$), where the sediment located over the bar head is moderately deviated toward the left bank direction, i.e. in the *thalweg*. As a result, under the given configuration of

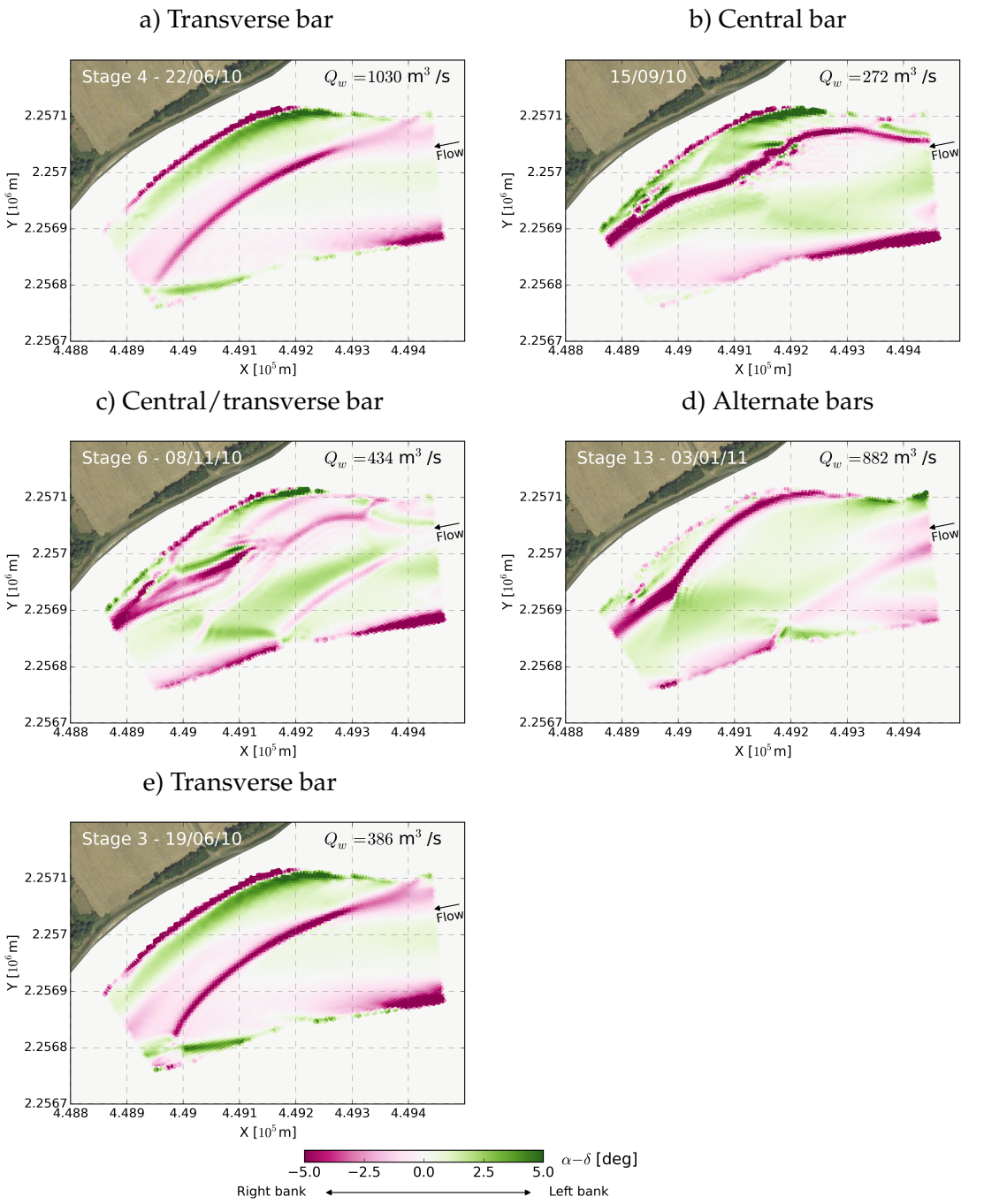


Figure 5.13: Planview of the angle of bedload deviation, computed with scenario A with a) the transverse bar on June 22th 2010, b) alternate bars on January 3rd 2011, c) central bar on September 15th 2010, d) central/transverse bar November 8th 2010, and e) the transverse bar on June 19th 2010. The arrow below the color-scale indicates the direction of the deviation angle, where negative values are directed toward the right riverbank and positive values toward the left riverbank.

alternate bars, the observed right bar not only migrates laterally, but also longitudinally.

The comparison between the directions of sediment transport obtained with the configura-

tion of the transverse bar and alternate bars is presented in Figure 5.14. In the case of a transverse bar configuration, the sediment transport along the right side of the channel is preferentially directed toward the left riverside, in comparison with alternate bars. The opposite behavior is observed in the center-left sides of the channel, where sediment transport is preferentially directed toward the right riverbank in the case of the transverse bar, in comparison to alternate bars. Highest absolute deviations angles are found at the exact location of alternate and transverse bar fronts and edges, and can reach values higher than 15°. This result is consistent with the previous outcomes (Figure 5.13), and illustrates that bedload deviation and bar geometry are strongly dependent on each other. It also shows that switching from a bar configuration to another tends to re-balance the bedload directions from the center-left side to the right side of the channel.

The sediment transport vector fields of June 19^{th} 2010 and June 22^{nd} 2010 are compared to estimate the influence of the water discharge on the direction of sediment transport (Figure 5.13a vs. 5.13e). These two events are selected because the computed bed topographies are similar for these two events, and are defined by weak ($Q_w = 386$ m^3/s) and relatively high ($Q_w = 1030$ m^3/s) water discharges, respectively. The higher color contrast exhibited in the case of low flows in comparison with high flows shows that decreasing water discharges are followed by an increased deviation of the bedload vector field toward the downslope direction. The last outcome agrees with the higher bedload deviations computed over the central bar and central/transverse bars at low water discharges in comparison with the alternate and transverse bars at relatively high flowrates (Figure 5.13b,c vs. 5.13a,d).

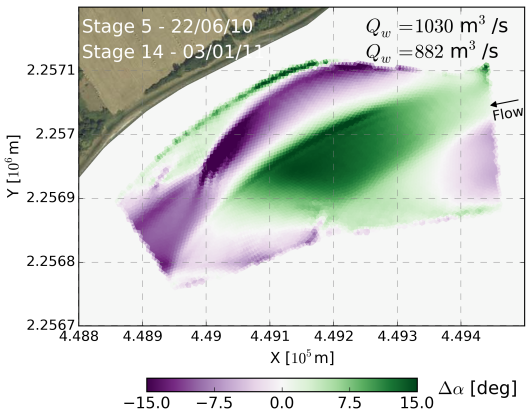


Figure 5.14: Planview of the angle between the bedload transport directions computed with scenario A with the transverse bar on June 22^{nd} 2010, and alternate bars on January 3^{rd} 2011. Negative (resp. positive) angle values depicted in purple (resp. in green) signify that the bedload vector computed with the transverse bar is more directed toward the left (resp. right) bank with respect to the bedload vector computed with alternate bars.

5.4.6 Sediment sorting

The planform distribution of the mean sediment diameter at the bed surface (i.e. in the active layer) offers a first information on processes of sediment sorting over bars (Figure 5.15). In the case of alternate or transverse bar configurations, coarse sediment is located over bars, but also in the *thalweg*, while fine sediment concentrates in pools which are located at the immediate down-slope of bar heads and edges (Figure 5.4 and 5.5). Hence, the same sediment sorting pattern is obtained with transverse and alternate bar configurations. Longitudinal and cross-sectional stratigraphic profiles obtained with the transverse and alternate bar configurations (Figure 5.16a,b) confirm the last outcome and also help to characterize the vertical sediment sorting in the bar-pool sequence. The computed bed stratigraphy always shows a coarser surface layer than the sub-layers over bar tops and stoss sides (e.g. Figure 5.16a along $L2$ from 200 m to 400 m and Figure 5.16b along $L2$ from 100 to 450 m), and in the *thalweg* (e.g. Figure 5.16a along $P90$ from 150 to 200 m and Figure 5.16b along $P90$ from 30 to 50 m). In contrast, the sub-layers located below pools and bar lee sides are generally composed of coarser sediment than the surface layer (e.g. Figure 5.16a from 80 m to 160 m along $L2$ and Figure 5.16b from 210 m to 240 m along $P90$). This results in coarse surface bars tops, which cover an important reserve of finer sediment in the sub-surface. Sediment sorting is found to be different in the case of the central/transverse bar configuration (Figure 5.4b). While the longitudinal sorting of sediment remains similar to the the one measured over previous bar configurations, the observed cross-sectional stratigraphy suggests another sediment sorting pattern (Figure 5.16c). The coarsest sediment is found to be located in the *thalweg* (from 0 m to 70 m along $L2$ and from 20 m to 70 m along $P90$), while $d_{s,m}$ decreases progressively transversally (i.e. perpendicular to the bar edge) to be the lowest over the bar top (from 70 to 140 m along $P90$). Under this configuration, the central/transverse bar surface is composed of fine sediment, which coarsens progressively in the deeper layers.

On the other side, the increasing color contrast observed in September 15^{th} and November 8^{th} 2010 (see Figure 5.15) suggests that the degree of sediment sorting is higher during this period of low flow periods, in comparison to periods of medium or higher flows.

The computation of the mean sediment diameter in the surface layer shows that it tends to increase rapidly in the early stages of the simulation, but also rapidly stabilizes before oscillating toward an equilibrium value of ≈ 1.42 mm (Figure 5.17b). On the opposite, in the sub-layers, the mean sediment diameter averagely decreases during the simulation (Figure 5.17b). High and fast mean sediment diameter fluctuations are observed in the first sub-layer, while fluctuations are progressively smoother and smaller in amplitude the deeper the sub-layer is. Starting from the 5^{th} sub-layer, the mean diameter decreases slowly over time. These outcomes suggest that most of sediment sorting changes occurs in the sediment layers close to the surface, and is consistent with obtained stratigraphic profiles (Figure 5.16).

According to the ratio $\bar{d_{s,m90}}/\bar{d_{s,m10}}$ (Figure 5.17c), in the first steps of the simulation, sediment sorting requires time to take place, as illustrated by the poor degree of sediment sorting in the sub-layers (Figure 5.17, Stage 1 to 2). In this period, the sorting degree jumps from 1 (i.e. homogeneous in space) to ≈ 1.2 (i.e. moderately heterogeneous in space). Later on, during the period of medium flows (Stage 2 to 6), the succession of three similar flooding events is associated to a stabilization and fluctuation of the sorting degree toward an equilibrium value of ≈ 1.25. The low flow period of approximately 4 months (Stage 6 to 7) is marked by the progressive increase of the sorting degree, which reaches 1.35 in November 2010. Eventually, the transition with the high flow period is followed by the progressive decrease of the sediment sorting degree, which attains values close to 1.20 shortly after the 2 year flood of December, 11^{th}

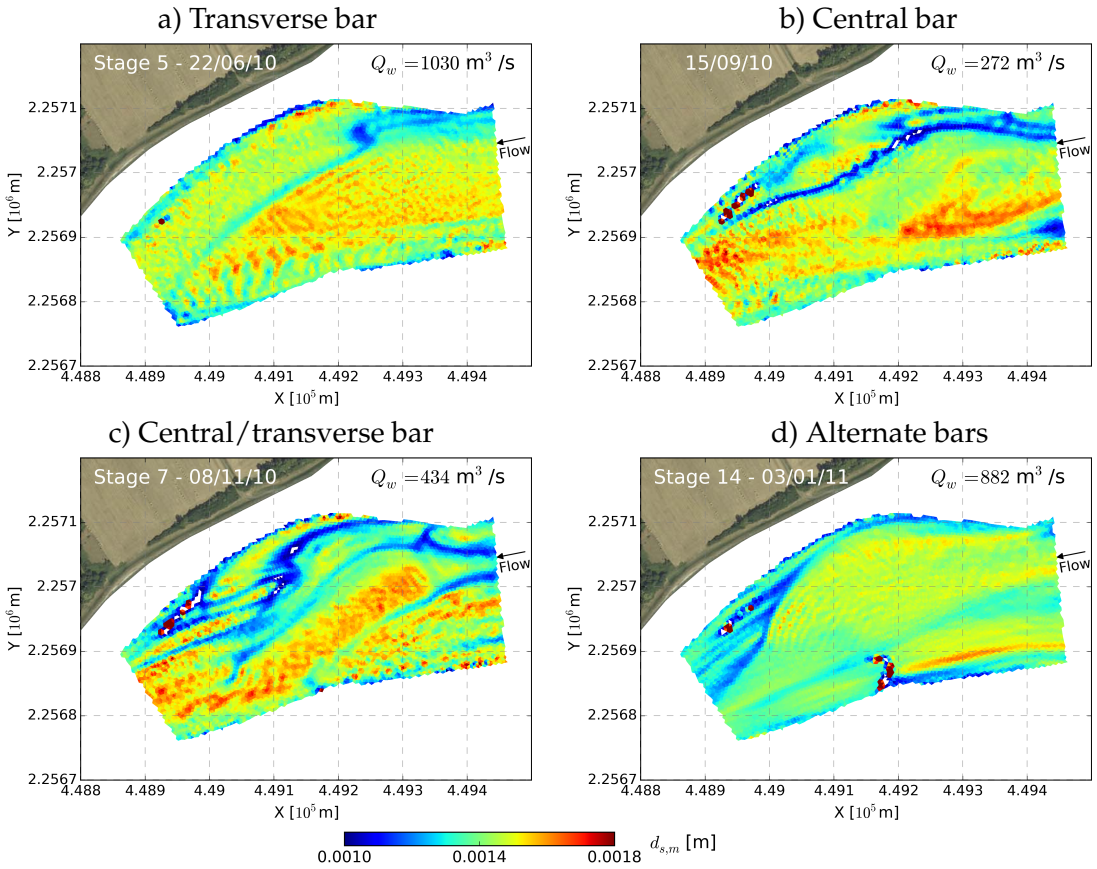


Figure 5.15: Planview of the mean sediment diameter at the bed surface computed with the with scenario A considering the configurations of a) transverse bar (June 22nd 2010), b) central bar (September, 15th 2010), c) central/transverse bar (November 8th 2010) and d) alternate bars (January 3rd, 2011).

2010, and later oscillate toward a similar equilibrium value than obtained in the medium flow period (February 2011 and later). In the late stages of the three simulations considering constant inflow, the sediment sorting degree depicted by $\bar{d_{s,m90}}/\bar{d_{s,m10}}$ tends to reach an equilibrium value (Figure 5.17c). This value is influenced by the flow rate, where higher values of water discharges invariably increase the spatially averaged surface sediment sorting degree.

5.5 Discussion

5.5.1 Bar pattern and water discharge

Bar modes obtained from the numerical results are showed to vary in the range [1.5-3.5], which is in the same range of bar modes estimated by the theory of Crosato and Mosselman [2009]. The competition between different width-to-depth ratios, illustrated by the different measured bar modes and wavelengths, results from the combination of varying water discharge and longitudinal channel width. At high flowrates, the model computes weak bar modes (i.e. alternate bars or transverse bar), while higher bar modes are computed at low flow conditions (i.e. central bars, multiple bars). This bar mode variability is consistent with the bar patterns

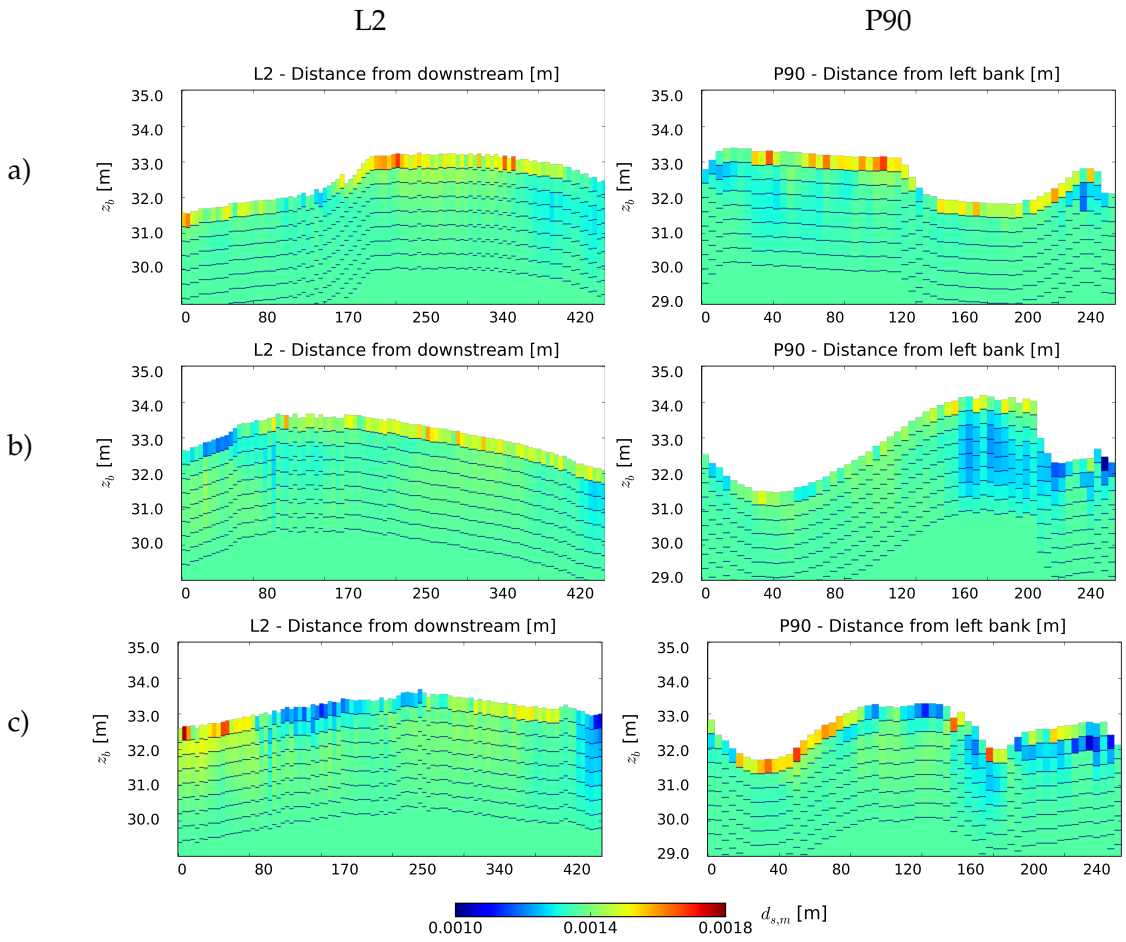


Figure 5.16: Longitudinal (L2) and cross-sectional (P90) stratigraphic profiles computed with scenario A with the configuration of a) transverse bar (June 22^{th} 2010, $Q_w = 1030$ m^3/s), b) alternate bars (January 3^{rd} 2011, $Q_w = 882$ m^3/s) and c) central/transverse bar (November 8^{th} 2010, $Q_w = 434$ m^3/s). See Figure 5.1 for location of L2 and P90.

observed in the Loire river [Claude et al., 2014; Rodrigues et al., 2012, 2015]. Due to changes in the longitudinal width-to-depth ratio, the bar mode is showed to increase in the area of expansion and to decrease in the area of contraction (Figure 5.5 and 5.4), which has been already observed numerically for low mode bars by Duró et al. [2016].

The temporal variation of the numerical bar modes generally show consistency with the theory, excepted on September 15^{th}, 2010 and on December 11^{th}, 2010 where the predicted bar modes are overestimated and underestimated, respectively. The last differences found between the two approaches can be due to several reasons. Firstly, the theory is based on the long-term response of the riverbed assuming a constant flowrate, while the water discharge is showed to vary importantly during the flooding event of December 11^{th} 2010. The peak flood of $Q_w = 1950$ m^3/s cannot trigger the formation of alternate bars in the numerical model, because of its too short duration. Secondly, according to Crosato and Mosselman [2009], the theory can deteriorate for $\beta > 100$, because the non-linear effects inducing bar merging (and consequently reduction of the bar mode) are not accounted into this simple predictive model. As a result, the theory is expected to overestimate bar modes at relatively high width-to-depth ratios, as it is observed

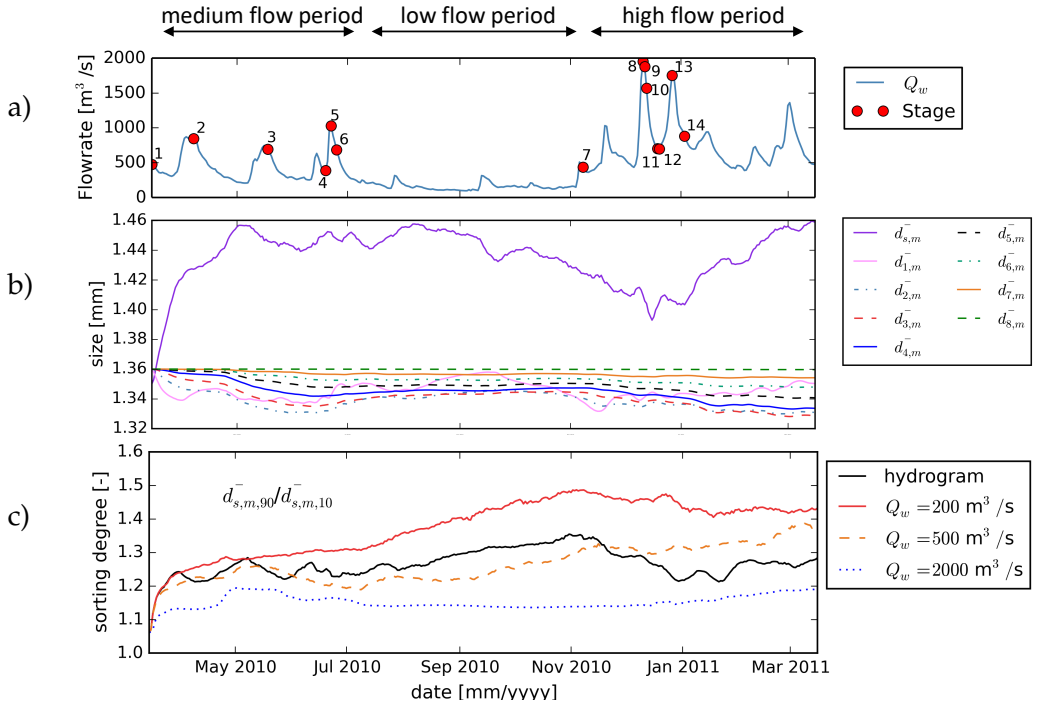


Figure 5.17: Time-series of a) the hydrogram of 2010-2011, b) spatially averaged mean sediment diameter in each sediment layer and c) ratio between the 9^{th} and 1^{st} fractiles used to estimate the degree of spatial sediment sorting with the reference scenario and the three scenarios with constant water discharges.

in September 15^{th} 2010. The last reasoning can be inferred from the visible time-lag between the evolution of the numerical bar mode and the flow regime (Figure 5.9). This configuration does not correspond to purely alternate bars, because the obtained alternating bars fronts are separated by a half bar length, instead of a full bar length in the case of ideal alternate bars (i.e. $m = 1$) or the presence of a bar on each riverside (i.e $m = 2$) [Crosato and Mosselman, 2009], which justify the use of $m = 1.5$. In this context, the bar mode predictor is showed to compute satisfactory bar modes even at relatively high width-to-depth ratios (i.e. $\beta > 100$). In this expansion area, bar mode variations are essentially governed by water discharge variations, as runs considering constant flows (runs C, D and E) all compute bar modes which do not vary significantly over time.

According to Claude et al. [2014], bar patterns evolve cyclically in the study area, where the hydrological conditions would be supposed to mostly control the frequency of these cycles. The last conclusion have been inferred from the spatial distribution of bed shear stress measured *in situ*, which was showed to not be modified by the water discharge, but mainly controlled by the bar configuration. However, the numerical outcomes suggest at the opposite that the hydrology plays an important role on the occurrence and diversity of bar patterns. Indeed, relatively low water discharges are showed to enhance the deviation of the bedload toward the downslope direction, and explain the latter increased degree of channel sinuosity, which is depicted by an increased bar mode and decreased bar wavelength (Figure 5.13a vs. 5.13e).

Numerical results show that the bed topography, i.e. more specifically the bar pattern, influences importantly the sediment transport directions and thus bar migration (Figure 5.13). In general, the computed bedload magnitude is more important (3 to 5 times) over bars (on the

condition that they are submerged) and in the *thalweg* than in pools and lee sides (Figure 5.11), which is also depicted by local high bedload gradients, and consequently bars advance by the migration of steep bar fronts or bar edges, in analogy with free bars. Bed slope deviation effects play an important role on the lateral migration of free bars, and their spatial distribution is also controlled by the bar configuration.

In the case of high bar modes configurations, bars forming in the side channels at each side of the central/transverse bar are shorter than typical wavelengths of low bar modes obtained at high flow conditions (Figure 5.5). This outcome is consistent with Singh et al. [2017]'s numerical findings in braided channels, who showed that increasing braiding indexes are followed by a decrease of bar wavelength. Moreover, numerical results show that increasing bar modes are generally followed by a decreased bar amplitude, which is due to lower bar tops (Table 5.1 and Figure 5.16), which is in also found to be consistent with Singh et al. [2017]. Eventually, even under relatively low flowrates, bars are showed to continue migrating in the study area. This last outcome suggests that bed reworking can occur almost every time in sandy gravel bed rivers, at least presenting characteristics similar to the Loire river in terms of sediment mobility. Therefore, numerical modelling of sandy-gravel river morphodynamics processes should be conducted carefully, in the sense that unlike for gravel bed rivers, even low water discharge could contribute to bar morphodynamics.

5.5.2 Sediment sorting processes

Numerical results show that vertical sediment sorting leading to stratigraphy occur over bars located in the main channel bed of the study area, which is in agreement with what is observed in sandy-gravel bed rivers [Bridge, 2003]. This result is consistent with the field observations by Rodrigues et al. [2012, 2015], who showed the presence of evident stratigraphy on free bars of a disconnected channel in the Loire river. The numerical approach allows to investigate in detail the processes of sediment sorting and to connect them to bar morphodynamics in the study area. In the area of expansion/contraction, bars display two distinct surface sediment sorting patterns: i) fine on pools and coarse over bar tops in the case of alternate or transverse bar configurations (i.e. low bar modes) and ii) coarse on pools and fine over bar tops in the case of transverse/central bar and multiple bar (i.e. higher bar modes) configuration. In every case, the *thalweg* surface -excepted from pools- is composed by relatively coarse sediment. The sorting pattern computed over the low bar modes (i.e. $m < 2$) is consistent with the ones obtained experimentally [Lanzoni, 2000b; Nelson et al., 2015a] and numerically [Nelson et al., 2015b; Cordier et al., 2019] over free alternate bars. As a rule, the presence of coarse sediment over bar tops and in the main channel (excepted pools) is due to the high constraints exerted by relatively high bed shear stress at these locations. Conversely, the presence of fine sediment in pools is due to the low constraints exerted by relatively low shear stress at pools location. The sorting pattern computed over the higher bar modes (i.e. $m > 2$) is consistent with the one obtained numerically by Singh et al. [2017], who observed the same sorting pattern provided that the partial sediment mobility condition is reached. In the case of full sediment mobility, Singh et al. [2017] showed that any consistent pattern could be detected, apart from coarse sediment in the *thalweg*. In this work, the important sand contribution to the total bedload transport ($\approx$ 80%) indicates that the system is averagely close to full transport, even at low flow and low transport conditions (Figure 5.12). Such difference could be due to the choice of the bedload formula, where Singh et al. [2017] showed that the use of Meyer-Peter and Müller [1948] closure relationship at high flowrates could fail at very high Shields numbers. At low flowrates, flow velocity, bed shear stress and consequently sediment transport are close to zero over bar tops, while the spatial

flow non-uniformity is increased and is followed by the concentration of the flow in a narrower *thalweg* (Figures 5.4b and 5.11c). Such a spatial re-balance of sediment transport is supposed to be at the origin of the distinct sediment sorting patterns observed in multi-channel patterns forming at relatively low water discharges (Figure 5.16c).

The degree of surface sediment sorting, like the bar mode, is also showed to be influenced by the hydrology of the river. Indeed, high water discharges induced by annual and two-year floods is followed by a decrease of sorting degree, while a long period of low-flows is followed by a progressive increase of spatial sediment heterogeneity (Figure 5.17c). This difference seems to be induced by the more homogeneous repartition of the sediment transport rates in the case of simple bar patterns (Figure 5.11b) in comparison to the more heterogeneous repartition of the sediment transport rates in the case of complex bar patterns (Figure 5.11c). As a result, low bar modes show a more homogeneous surface sediment sorting than high bar modes, i.e. lower degrees of surface sediment sorting (Figures 5.15 and 5.17c). The last deduction is also supported by the results obtained with considering constant inflows (run C, D and E). By considering constant water discharges, the degree of sediment sorting invariably diminishes with increasing flow rates. As a result, variations in degrees of sediment sorting in the reference scenario (run A) can be mainly attributed to the water discharges variations over time.

In the present study case, outcomes show that sediment sorting does not impact significantly bar morphodynamics. This result can be due to two main factors. The first could originate from the relatively low difference found between the two representative grain diameters, with a ratio equal to 3.6. The second may come from the fact that grain size roughness is small (order of millimeter) with respect to water depth (order of meters). This outcome is in agreement with [Cordier et al., 2019], who show that under conditions of full sediment mobility, sediment sorting modify weakly free bar morphodynamics, but not their time averaged characteristics. As a result, the computed sediment sorting only slightly modifies the computed bed shear stress (Equation 5.6), so that the impact on sediment transport and resulting bed topography is negligible. Bankert and Nelson [2018] show experimentally that in gravel-bed rivers heterogeneous stratigraphy can play an important role in determining whether bars persist or disappear after a sediment supply reduction. In the case of sandy-gravel bed rivers dominated by sand, i.e. in the present case, numerical results suggest that all the main channel sediment is mobile or easily moved, and even if sediment sorting is observed, bars and subsequent sediment sorting can vanish easily. This also suggest that armoring does not usually form in the main channel. As a result, in the last case, sediment sorting process can be considered as a "passive component" of the morphodynamic system as it neither retroactively alter the hydraulics, nor the bar properties.

5.5.3 Consequences on the estimation of grain size distribution

The last points of discussion suggest that in real rivers, the sediment sorting pattern and sorting degree are, like the bar mode, controlled by the variations of the channel width-to-depth ratio. This can have a consequence on the measurement of the grain size distribution during field campaigns. On the one hand, if the spatial variability of the sediment size of surface and sub-surface is not accounted during sediment sampling in the case of low mode bars, it can lead to an overestimation (resp. underestimation) of the surface sediment diameter if the sediment is only sampled over bar tops or only in the *thalweg* (resp. in pools); on the opposite an underestimation (resp. overestimation) of the sub-surface sediment diameter if the sediment is sampled only in the sub-surface of bars or only in the sub-surface of the *thalweg* (resp. of pools). In the case of higher bar modes, the opposite tendency will occur because the sediment sorting pattern is inverted between pools and bar tops, with respect to low bar modes. On the other hand,

if the time variability of the sediment sorting degree is not accounted for the granulometric samplings, the mean surface sediment diameter can be overestimated if it is sampled after a long period of low flows, and oppositely it can be underestimated if it is sampled after a period of high flows, in comparison with the mean annual sediment diameter of surface (Figure 5.16). Theoretical, numerical and experimental models meant to reproduce bar morphodynamics of a specific river reach generally rely on the estimation of the mean grain size distribution or the mean sediment diameter. The present numerical results highlight the strong sediment size variability in time and over space occurring over a single hydrological year in a local channel contraction/expansion area, which could actually occur in many engineered or natural rivers. Not taking into account this potential strong variability of sediment size before planning field campaigns measurements can affect the bar characteristics predicted with theory, experiments or numerically [Crosato and Mosselman, 2009; Nelson et al., 2015b; Cordier et al., 2019]. As a result, the minimal number of measurement points and their location to determine a relevant averaged grain size distribution in a river reach needs to be addressed in future research works.

5.5.4 Limitations and perspectives

The limitations arising from the modelling hypotheses and uncertainty on the data used for this study need to be addressed here i) to assess the pertinence of the numerical approach with regard to processes happening in the nature and then ii) consider the possible perspectives to continually improve the modelling and the understanding of fluvial bar processes.

The first type of limitation lies on the uncertainty of the initial conditions used for modelling. The initial sediment in the models used for calibration and for numerical investigations consists on a granulometry homogeneous over space, where sediment sorting requires at least one month before stabilization. Because sediment sorting governs the sediment transport, this can have consequences on the calibration of sediment transport. Moreover, at least during the first month of computation, numerical results should be interpreted cautiously in the reference scenario. The same issue has already been recently observed numerically with the formation of free alternate bars with non-uniform sediment in a straight channel, where the system requires a given lapse of time before reaching the morphodynamic equilibrium [Cordier et al., 2019]. Furthermore, the initial granulometry used in this work corresponds to the averaged grain size distribution measured in the middle Loire river, which depends on the time and location of granulometric measurements. The lack of field observations during the low flow period of year 2010 (i.e. from July to October) increases the uncertainty on the predicted bar patterns at this period of time, where complex bar patterns such as the one computed on November 20^{th} could not have been measured this year in the study site. The agreement with theoretical predictions during the low flow period and the consistency found between the bar patterns obtained *in situ* and numerically in the end of year 2010 increase the confidence placed on the morphodynamic model. Similarly, uncertainty is found on the bed topography located immediately upstream and downstream from the area of interest, which may have faced changes from the date of acquisition (i.e. year 2009) to the date of interest (i.e. year 2010). The last uncertainty can potentially impact the modelling of bars in the channel contraction/expansion area, as bars entering in the system (i.e. coming from upstream) are showed to migrate in the area of interest. Lastly, the persistent vestiges of rip-raps in the main channel put in evidence by Claude et al. [2014] play as geometrical forcing structures provided that the above sediment layer is fully eroded. The exact location and elevation of these rigid areas is also difficult to determine, and has been estimated from available topographic surveys.

The second type of limitation arise from the assumptions chosen for modelling. As bedload

has often been considered to be at the origin of bedforms development, the suspended load is not accounted here. Suspension could decrease dunes and bars amplitude due to smoothing effects [Meles, 2015; Naqshband et al., 2014]. In the numerical model, the sediment is discretized into two size fractions, and to comply with the bedload model of Wilcock and Crowe [2003], the first size fraction is composed of the portion of sand present in the mixture and the second size fraction corresponds to the portion of gravel. Not only the number of sediment fractions could be increased, but also other methods for decomposing the sediment mixture into size fractions could be used. Vertical sorting of sediment is based on the active layer model of Hirano [1971], while recent works conducted on the ill-posedness of this mathematical model [Stecca et al., 2014, 2016; Chavarrias et al., 2018] demonstrated that the solution can be ill-posed under certain situations. Following Chavarrias et al. [2018], the probability of the present active layer model to be ill-posed is reduced due to the conditions of use (only two sediment size fractions, constant sediment layer thicknesses and the use of Hirano [1971] formulation for the vertical transfer of sediment). Physically irrelevant fluctuations of bed topography and of sediment sorting are not observed here and the numerical model seems to be particularly robust. The current model assumes an equilibrium upstream morphodynamic condition, which could decrease bar initiation and dynamics in the upstream part of the model domain [Mendoza et al., 2016; Singh et al., 2017; Cordier et al., 2018a] with respect to the boundary of sediment recirculation, and in turn bar modify morphodynamics in the study area. The study domain has been extended by 4 km upstream from the study area (i.e. $\approx$ 14 times the channel width), which guarantees a sufficient distance for free bars to form here. Claude et al. [2014] observed the formation of two (small) secondary flow structures in the study area. Regarding the objectives of the present work and to optimize computational time, the use of a two-dimensional SWE model has been advantageous to multiply the scenarios and configurations to conduct sensitivity analyses and calibrate the morphodynamic model. Finally, the condition of uniformly distributed values of k_s and $\alpha_{k,s}$ over space could be relaxed in the future. Dunes are not represented in the model, so that the modelling of spatially variable dunes form drag could be improved through the use of an appropriate formulation found in the literature [Van Rijn, 1984, e.g.], but is out of the scope of the present work. Because the superimposition of dunes over bars was observed to enhance the spatial non-uniformity of the flows in the upstream channel expansion Claude et al. [2014], the non-linear interactions between bar and dunes is a topic which deserves more attention.

5.6 Conclusions

The numerical morphodynamic model developed in this work is able to predict satisfactorily the hydraulics and riverbed evolution in a study reach of the middle Loire river, and gives some general indications about the evolutionary tendencies of the investigated river reach. This information has been analyzed to better understand bar morphodynamics a channel expansion/contraction area, and to enrich the discussion of Claude et al. [2014]. The complex mechanism of bar migration where an upstream left migrating alternate bar progressively stops migrating longitudinally due to the forcing geometry of the downstream contraction, and then only migrates transversally which results in a transverse bar pattern, is captured relevantly with the numerical model. This last outcome illustrates that under complex geometrical configurations, transverse bar migration can become a dominant process with respect to longitudinal bar migration. Moreover, bars are found to migrate following the process of bar tops and bar edges erosion, where the bed slope effects are showed to contribute actively to the lateral migration of bars. Due to high sediment mobility and relatively low grain roughness with respect to water

depths, the general bed surface coarsening does not induce armoring. As a result, bars are found to migrate at averaged and even relatively low water discharges, while sediment sorting does not modify significantly bar morphodynamics in the study area. Frequent width-to-depth ratio changes induced by the varying water discharge promote a competition between low and high bar modes, i.e. from alternate bars to a multiple bar patterns. The theory supports the numerical results where bar modes predicted by the theory are in the same range than the ones obtained numerically. Low water discharges are showed to increase bed slopes deviation effects, which in turn increase the sinuosity of the riverbed topography by decreasing bar wavelength, and resulting to increased bar mode. Conversely, the bedload preferentially follows the flow direction (i.e. is less deviated) at higher water discharges, which yields into a less sinuous riverbed topography by increasing bar wavelength, and decreased bar mode. While reduced bar modes are associated to a pattern of coarse sediment over bar tops and fine in pools, the sorting pattern is inverted for higher bar modes with fine sediment over bar tops and coarser sediment in pools. Eventually, the sediment of surface is averagely coarser and the degree of sediment sorting is higher after periods of low flows, with respect to periods of high flows. This finding is supported by derived scenarios considering constant water inflows. These results could be generalized to alluvial rivers reaches presenting bars composed of a systematically mobile bed material. Future research activities could focus on the coexistence of dunes and bars and to better understand the effects of the spatially variable roughness induced by dunes on sediment sorting.

Acknowledgments

The authors gratefully acknowledge the support of Electricité de France (EDF).

Notations

B Channel width [m]
b Degree of non-linearity in the dependence of sediment transport on flow velocity [-]
C Chézy coefficient [$m^{1/2}/s$]
C_f Equivalent Chézy coefficient due to form drag and skin friction [-]
C'_f Equivalent Chézy coefficient due to skin friction only [-]
$c_{b,l}$ Downstream-wise migrating bar celerity [m/d]
$c_{b,t}$ Transverse migrating bar celerity [m/d]
d_i Representative diameter of the i^{th} size fraction [m]
$d_{s,m}$ Median sediment diameter of surface [m]
$d_{k,m}$ Median sediment diameter of in layer k [m]
$\bar{d_{s,m}}$ Spatially averaged median sediment diameter of surface [m]
$\bar{d_{k,m}}$ Spatially averaged median sediment diameter of in layer k [m]
$\bar{d_X}$ Spatially averaged X^{th} centile of the GSD [m]
d_{50+X}/d_{50-X} Ratio between opposite centiles or sediment sorting degree [-]
E Coefficient of calibration for the correction of bedload direction [-]
$\mathcal{F}_{a:1,i}$ Fraction volume content of i^{th} size fraction in the interface [-]
$F_{k,i}$ Fraction volume content of i^{th} size fraction in layer k [-]
F_s Fraction volume content of sand at the bed surface [-]
g Acceleration due to gravity (=9.81) [m/s^2]
h Water depth [m]
H_b Bar amplitude [m]
i_0 Longitudinal bed slope at $t = 0$ s [-]
k_s Bed roughness height [m]
L_a Active layer thickness [m]
m_{th} Theoretical bar mode [-]
m_{num} Numerical bar mode [-]
P_0 Bed porosity [-]
q_b Magnitude of bedload transport rate [m^2/s]
$\vec{q_b} = (q_{b,x}, q_{b,y})$ Vector of bedload transport rate [m^2/s]
q_{b0} Magnitude of bedload transport rate without gravitational effects [m^2/s]
$\vec{q_{b0}}$ Vector of bedload transport rate without gravitational effects [m^2/s]
$q_{b,i}$ Magnitude of fractional transport rate of i^{th} size fraction [m^2/s]
$\vec{q_{b,i}} = (q_{b,i,x}, q_{b,i,y})$ Vector of fractional transport rate of i^{th} size fraction [m^2/s]
$q_{b,i,n}$ Magnitude of normal fractional transport rate of i^{th} size fraction [m^2/s]
$q_{b,i,s}$ Magnitude of stream-wise fractional transport rate of i^{th} size fraction [m^2/s]
s Coordinate in the current direction [-]
$\vec{u} = (u, v)$ Flow velocity vector [m/s]
$\bar{u}$ Spatially averaged flow velocity [m/s]
u, v Depth-averaged velocity components along x- and y-axis [m/s]
s Coordinate in the current direction [-]
$\vec{S_f} = (S_{f,x}, S_{f,y})$ Friction law vector [-]
t Physical time [s]
T_i Coefficient of deviation for the i^{th} size fraction [-]
u_* Shear velocity [m/s]

$x-, y-, z-$ Axis notation of the Coordinate Cartesian system [-]
z_b Bed elevation [m]
z_f Free surface [m]
α_b Coefficient used to calibrate the sediment transport capacity [-]
α_i Angle between the vector of fractional transport and x-axis [-]
$\alpha_{k,s}$ Calibration parameter [-]
β Width-to-depth ratio [-]
β_1 Koch and Flosktra's empirical factor for bed slope effects magnitude [-]
β_2 Talmon's *et al.* empirical factor for bed slope effects deviation [-]
δ Angle between bottom shear stress and the flow direction [-]
Δ_s Relative submerged sediment density [-]
Δt Computational time-step [s]
Δz_b Evolution of the bed topography with respect to the initial bed elevation [m]
ϵ_0 Percentage of volumetric matter without voids [-]
$\eta_{a:1}$ Absolute elevation of the interface [m]
κ Constant of von Kármán (=0.40) [-]
λ_b Bar wavelength [m]
μ Skin friction coefficient [-]
∇ Gradient vector field [1/m]
ν_t Turbulent eddy viscosity term [m^2/s]
$\partial_{x_2} x_1$ Partial derivative of the quantity x_1 in x_2 [x_2/x_1]
ρ Water density [kg/m^3]
τ Total shear stress [Pa]
τ_b Bed shear stress [Pa]
$\tau^*_{b,i}$ Shear stress adimensionnalized by the i^{th} fraction [-]
χ Decile of the grain size distribution [-]

▷ Considerations on numerical modelling of bars under complex configurations

The agreement found between the numerical results and field observations demonstrate the capacity of the morphodynamic model developed in Chapter 2 to reproduce bar morphodynamics even considering a relatively complex system configuration, in terms of channel geometry and boundary conditions. In this context, the numerical approach allows to study the sediment sorting processes and bars morphodynamics with a relatively high accuracy, involving a large time scale, without intrusion, which could be difficult or even impossible using other approaches. Therefore, the present numerical model could be used as a predictive tool for engineering studies, river management or research purposes, even if we remind that it has to be confronted to other approaches (e.g. linear stability analysis, field observations, experiments) which all provide their own advantage.

In the current scenario, because of high sediment mobility, bars form and migrate at all considered water discharges. However, the spatial bedload non-uniformity induced by flows non-uniformity promotes the formation of simple bar patterns in the case of high flows (i.e. transverse and alternate bars, or low bar modes) and the development of inner shorter bars in the *thalweg* during periods of low flows, leading to the formation of more complex patterns (i.e. multiple channel pattern or high bar modes). These observations are also supported by other morphodynamic scenarios ran with assuming constant water discharges (see Appendix A). This result can be generalized to alluvial rivers reaches presenting a systematically mobile bed material.

Distinct sediment sorting patterns are found between low bar modes at high flow discharges and higher bar modes at low flows resulting from the distinct topographic patterns explained above. Furthermore, the sorting degree is showed to increase during the period of low flows, while it decreases during high flow periods (i.e. sediment homogenization). These last two findings suggest that not accounting for this spatial and time variability of sediment sorting can have a consequence on the estimation of the grain size distribution in sandy-gravel bed rivers but also in gravel bed rivers. Not accounting for this potential strong variability of sediment size before planning field campaigns might lead to a wrong estimation of the grain size distribution, which is generally used as input parameter of theoretical, numerical and experimental studies.

Eventually, even if the numerical results suggest that sediment sorting occurs in the main channel, the general bed surface coarsening does not induce armoring, because of the high sediment mobility. As a result, bars are found to migrate at averaged and even relatively low water discharges. The last outcome suggests that in sandy-gravel bed rivers characterized by fully mobile sediment, the sorting effects would not impact (or impact weakly) the sediment transport properties and consequently bar morphodynamics, which is also explained by the low grain roughness in comparison with the mean water depth. Conversely, these results suggest that surface armoring forming in gravel bed rivers and relatively high grain roughness in comparison to the mean water depth would severely increase the feedback of sediment sorting on hydraulics, sediment transport and bar morphodynamics. To conclude, numerical results support the idea that sediment sorting would be likely to not impact bar morphodynamics in the case of sandy-gravel bed rivers, with respect to the case of gravel bed rivers where the sorting of sediment would retroactively impact bar morphodynamics, as illustrated by Lanzoni [2000b], Nelson et al. [2015b] and results from Chapter 3. For river management purposes, accounting for sediment sorting processes in the numerical models predicting bar morphodynamics in reaches presenting similar characteristics as the middle Loire river could be not necessary.

□ Synthèse générale sur la morphodynamique des bancs à sédiment non-uniforme en configuration complexe

L'étude numérique présentée dans ce chapitre a permis de se concentrer plus en détail sur la relation entre les motifs des bancs et leur tri granulométrique lorsqu'ils sont soumis à divers forçages, qu'ils soient internes comme la géométrie ou externes comme l'hydrologie et l'apport sédimentaire. Pour y arriver, le modèle numérique a été utilisé pour reproduire l'évolution de bancs situés dans un tronçon d'1 km de la Loire moyenne, à Bréhémont (France), pour lequel un riche set de données de mesures est disponible sur l'échelle d'une année hydrologique et où la morphodynamique des bancs a déjà fait l'objet d'une analyse de terrain approfondie. Les résultats numériques mettent en évidence une compétition entre différents motifs de bancs qui sont dus d'une part à la géométrie complexe de la zone d'élargissement/rétrécissement du chenal, et d'autre part qui sont causés par la fluctuation du régime hydraulique du fleuve. Les résultats mettent en évidence la relation étroite entre les motifs des bancs et les motifs de tri granulométriques prédits, et permettent de resituer ces observations dans l'état de l'art actuel en matière de relation entre sédiments non-uniformes et bancs périodiques. Les résultats permettent également d'informer et mettre en garde les modélisateurs sur la relative importance de prendre en compte l'impact du tri granulométrique sur l'évolution des bancs et la géométrie de ceux-ci.

PART IV

CONCLUSIONS AND PERSPECTIVES

CHAPTER 6

CONCLUSIONS AND PERSPECTIVES

Alluvial bars are a common feature of fluvial systems, and actively control the river bed topography and influence bank erosion, with large consequences in trained rivers for navigation, water intakes and infrastructure. The actual literature on alluvial bar processes outlines the importance of non-uniform sediment processes on bar morphodynamics, while a gap still subsists on the real relationship between non-uniform sediment and bars.

In the framework of bar management in trained rivers, it is has been judged necessary not only to better understand the processes involved between bars and heterogeneous sediment, but also provide a method to predict relevantly bar evolution which can be declined to diverse applications.

The research investigations undertaken in the present work rely on the use of a two dimensional morphodynamic model, which is based on the Telemac-Mascaret modelling system (TMS). The model has been reviewed, adapted and improved in order to account for the processes linked to non-uniform sediment with the objective of reproducing and later predicting alluvial bars in trained rivers. The main numerical developments correspond to i) the implementation of a physics-based sediment transport capacity formula for mixtures of sand a gravel [Wilcock and Crowe, 2003], ii) the integration of a bookkeeping active layer model to account for vertical sediment sorting when solving the sediment mass continuity equation [Hirano, 1971], iii) and appropriate morphodynamic boundary conditions to reproduce the ones which are often used in laboratory experiments of bar formation.

The morphodynamic model has been then used firstly to reproduce bar morphodynamics with uniform and non-uniform sediment under the consideration of simple channel geometry and well controlled boundary conditions, and on the basis of this exercise, to conduct numerical research investigations in order to better understand the relationship between heterogeneous sediment and bar morphodynamics. A multitude of sensitivity analyses have been carried out in order to to better estimate the influence of the numerical and physical parameters on the computed bar properties and to test the limits of the model. In a second time, the morphodynamic model has been applied to a sandy-gravel reach presenting a combination of multiple internal and external forcing parameters, in order to better understand the relation between these forcing parameters, the sediment non-uniformity and bars morphodynamics.

The main outcomes from this study have implications on the understanding and the modelling of bar morphodynamics in trained rivers, which are addressed synthetically in the following conclusion.

6.1 Relation between bar morphology and sediment sorting pattern

6.1.1 Major contributions on the understanding of bar processes

The relation between the bar morphology and the sediment sorting pattern has been firstly investigated numerically under the consideration of uniform flows and idealized channel geometries dominated by the presence of straight alternate bars. Making a clear distinction between free bars and hybrid bars has been useful to demonstrate that the bar geometry is responsible for the different sediment sorting patterns observed in experiments, in river reaches and computed numerically. Indeed, hybrid bars are found to be at least two times longer than fully developed free bars, whereas both types of bars have a similar amplitude. Consequently, hybrid bars are flatter than free migrating bars, and present a symmetrical shape while free migrating bars always present an important asymmetry on their fronts. In the case of free bars, the sediment sorting pattern is characterized by the presence of fine sediment in pools and coarse particles over bar tops, which becomes more appreciable when free migrating bars are fully developed. In the case of hybrid bars, the sediment sorting pattern consists on the finest sediment at the beginning of the lee side, which smoothly coarsens until the middle of the stoss side and then becomes progressively finer until the next bar top. In every considered scenario, the bed surface coarsens over time.

In a second step, emphasis is placed on the relation between the bar morphology and the sediment sorting pattern given non-uniform flows and a complex channel geometry defined by a channel contraction/expansion area located in the middle Loire river, where a diversity of bar patterns can be observed during a single hydrological year. Because of high sediment mobility, bars of different characteristics form and migrate at all considered water discharges. In this context, simple bar patterns are obtained during periods of high flows (i.e. transverse and alternate bars, referred to as low mode bars). During periods of low flows, the flow is concentrated in the *thalweg*, and some parts of the bars are not exposed to the flows, enhancing the spatial flow non-uniformity in the study area. As a result, shorter bars develop in the *thalweg*, leading to the formation of more complex bar patterns (i.e. multiple channel pattern referred to as high mode bars). These differences explain the distinct sediment sorting patterns obtained over simple bar patterns and complex bar patterns, with i) fine on pools and coarse over bars in the case of simple bar configurations and ii) coarse on pools and fine over bar heads in the case of more complex configurations. The sorting pattern obtained over simple bar patterns is consistent with the one computed in the straight channel over free alternate bars, and the sorting pattern computed over complex bar patterns is consistent with numerical findings presented in the literature in braided rivers with partial sediment mobility. Moreover, the sediment of surface is showed to be more heterogeneous during the period of low flows (i.e. in the case of a multi-channel pattern), while it tends to homogenize during high flow periods (resp. in the case of simple bar pattern). This result can be generalized to alluvial rivers reaches presenting a highly mobile bed material with fixed and relatively straight banks.

6.1.2 Implications for river managers

Outcomes show that sediment transport and bar morphodynamic processes are well predicted by the numerical model developed in this work. This model reproduces accurately the bar characteristics which correspond namely to the bar height, length, celerity of migration, as well as relevant sediment sorting patterns. The predictability exhibited by this model can be advantageous to later investigate scenarios of river management for operational purposes,

provided a sufficient preliminary calibration based on available data:

- In rivers where bars are found to be highly dynamic due to high sediment mobility, i.e. preferentially in sandy-gravel bed rivers, such as in the middle Loire river where bars can migrate at a celerity close to one meter per day, the model used in this work can help to better understand -or even predict- the formation or migration of bars in hazardous areas, e.g. to avoid the clogging of heat sinks of the nuclear power-plants and optimize the operations of sediment dredging.

- In rivers where bars are found to be less dynamic due to partial sediment mobility, i.e. preferentially in gravel bed rivers, where bar mobility is restricted to seasonal high flows or dam flushes provided that bars are free of vegetation, the model used in this work can help to firstly better understand the processes of bar formation, development and stabilization in the river, secondly help to predict the locations of the areas which might be the most subject to bank erosion, and thirdly investigating the possibility of conducting dam flushes operations to re-mobilize steady periodic bars.

- Numerical results also indicate that in rivers characterized by continual longitudinal channel width variations delimited by stable banks, such as the middle Loire river, flooding events tend to straighten and confine the flows in a single thread channel. This result is made possible because the sediment mainly accumulates at each side of the expansion area, while severe erosion occurs in the contraction area. Long term repercussions can lead to severe bank weakening or even bank erosion, and is important for river managers such as DREAL in France (=Direction Régionale de l'Environnement, de l'Aménagement et du Logement) who are responsible for the maintenance of the longitudinal dykes.

- Because the model is able to compute relevant bar heights, it can also be used to determine the location of the areas which could be preferentially subject to erosion or deposition, and by extension could assess the potential risks exerted by bars on engineering structures such as riverbanks or bridge piers. Outcomes can be interesting for river engineers and managers who aim at protecting embankments to avoid inundations which are triggered by the deficit of sediment supply leading to river incision. To further this goal, in the middle Loire river, river trainers try to restore the sediment continuity through the river and are interested in the estimation of the sediment budget and the sediment mobility. Derived model applications could consist on the study of the impact of increased (resp. decreased) sediment supply induced by local sediment injection (resp. extraction) on bar morphology and dynamics, which is interesting for river managers who want to assess the impact of training works or to restore rivers and sediment continuity.

Numerical findings support the idea that not accounting for this spatial and time variability of sediment sorting can have strong implications on the estimation of the grain size distribution in sandy-gravel bed rivers but also in gravel bed rivers. Not considering this potential strong variability of sediment size before planning field campaigns measurements can lead to a wrong estimation of the grain size distribution, which is generally used as input parameter of theoretical, numerical and experimental studies. Therefore, the diversity of sediment sorting patterns exhibited by the different bar patterns should be took into account before planning field sediment sampling campaigns. Indeed, the estimation of the averaged grain size distribution representative of the river reach can be importantly biased by the location and the time of the granulometric measurements. As a rule, grain size samplings campaigns are planned

during periods of low/medium flows, because bars are not exposed to the flows and are easily accessible. On the opposite, measurements are avoided during flooding periods because bar are damped and difficultly accessible, and such conditions can threaten the safety of the field experimenters. Moreover, measurements are essentially made over the bars, and not everywhere in the channel such as deepest areas because of their difficult accessibility. In rivers where surface armoring enhances importantly bar stability, i.e. especially in gravel bed rivers, study of bar mobility should account for the spatial (vertical and planform) sediment sorting. For example, a possible consequence of overestimating the grain size distribution in the Isère river could lead to miscalculation of the bar dimensions but also their dynamics (i.e. mobility). The minimal number of measurement points and their location to determine a relevant averaged grain size distribution in a river reach needs to be addressed in future research works.

6.2 Influence of sediment sorting on bars

6.2.1 Major contributions on the understanding of bar processes

To estimate and better understand the effects induced by the spatial (i.e. planform an vertical) variations of the grain size distribution, referred to as sediment sorting in the present work, two types of scenarios have been systematically compared: scenarios for which sediment sorting is accounted and scenarios for which sediment sorting is not accounted.

In the idealized channel simulations, numerical results show that averaged free bars characteristics are not impacted by the spatial sorting of sediment, while the sorting effects modify significantly hybrid bars characteristics. This outcome outlines the importance of distinguishing free bars from hybrid bars in this work. In agreement with numerical findings recently addressed in the literature, steady (hybrid) bars are longer and flatter due to sediment sorting effects. As a result, hybrid bars only persist for a relatively short distance (i.e. a few hybrid bar lengths) downstream from the obstacle, because sediment sorting effects reduce the hybrid bar amplitude and by extension the geometrical forcing played by an hybrid bar on an immediately downstream bar. In this case, free bars continually form and migrate in the downstream part of the channel. Considering the same configuration, if sorting sediment sorting is not accounted for, hybrid bars form everywhere in the downstream part of the channel.

In the simulation based on the middle Loire river, even if sediment sorting occurs in the main channel, the general bed surface coarsening never induces armoring, because of the high sediment mobility. As a result, bars are found to migrate even at averaged or relatively low water discharges. The last outcome suggests that in sandy-gravel bed rivers characterized by fully mobile sediment, the sorting effects do not impact (or impact very weakly) the sediment transport properties and consequently bars morphodynamics, which is also explained by the low grain roughness in comparison with the mean water depth. On the opposite, these results suggest that surface armoring forming in gravel bed rivers and relatively high grain roughness in comparison to the mean water depth would severely increase the feedback of sediment sorting on hydraulics, sediment transport and bar morphodynamics. To conclude, numerical results support the idea that sediment sorting is likely to not impact bar morphodynamics in the case of sandy-gravel bed rivers, with respect to the case of gravel bed rivers where the sorting of sediment retroactively impacts bar morphodynamics.

6.2.2 Implications for river managers

The research works presented here illustrate the possible undesirable consequences of not considering the spatial sorting of sediment when the numerical modelling approach is used.

Outcomes suggests that sediment sorting could increase bar mobility and promote the dominance of free bars over hybrid bars on bars forming in gravel bed rivers. Not accounting for the sorting of sediment and the feedback played by grain roughness on flow and sediment transport can, in the later case, predict a different bar pattern than expected, by overestimating the bar height and stability, and underestimating the bar length. This lack of physical relevance could later lead to misinterpretations of the bed response to engineering works, such as the construction of a groyne or a bridge pier, for the reasons presented above. In this context, modellers are particularly warned in the case where they are interested in modelling scenarios where bars are initially present in the model channel. Indeed, uncertainty on the initial conditions in terms of sediment sorting can be interpreted as a lack of physical relevance. However, due to uncertainties on the grain size distribution and relative complexity to parametrize it as initial conditions in the numerical model, modellers often use the same granulometry everywhere in the model. In this condition, sediment sorting is showed to not adapt immediately to the fast topographic and hydraulic changes, but requires a certain time and distance from the upstream boundary to find a more stable condition. This property has to be considered by river modellers, because a certain time has to be respected to obtain relevant sorting patterns in the case where the initial sedimentary conditions are different from the one reproduced, and can lead to misinterpretation of morphodynamic processes during this "*buffering*" time.

For river management purposes, accounting for sediment sorting processes in the numerical models predicting bar morphodynamics in reaches of similar characteristics as the middle Loire river could be not always necessary.

6.3 Influence of sediment size heterogeneity on bars

6.3.1 Major contributions on the understanding of bar processes

The influence of sediment size heterogeneity on bar morphodynamics has been particularly investigated under the straight channel configuration. To further this goal, three grain size distributions having the same median sediment diameter but a different degree of size heterogeneity have been considered. For free and hybrid bars, increased sediment size heterogeneity increases the degree of sediment sorting, while the sorting pattern remains the same for each type of bar. Free and hybrid bars are impacted and respond differently to changes of sediment size heterogeneity. The increasing of sediment size heterogeneity produces averagely higher, longer and faster free bars, while in the case of hybrid bars, the wavelength is increased and the amplitude is decreased only when a highly heterogeneous sediment is used.

6.3.2 Implications for river managers

River managers could apply the present model to study the effects of sediment injection which alter the degree of sediment size heterogeneity in the river, and as a result modify bar morphodynamics to increase mobility. In the case of fine (non-cohesive) sediment injections which tend to increase the degree of sediment size heterogeneity in the river reach, results indicate that bars characteristics could be modified, with especially increased bar mobility.

6.4 Considerations on the numerical model applicability

6.4.1 Performance of the model in this work

Outcomes demonstrate the model performance to reproduce accurately periodic bar morphodynamics with uniform and non-uniform sediment under idealized geometrical and well controlled boundary conditions, but also under the consideration of a complex channel geometry and boundary conditions. In this context, the numerical approach allows to study the sediment sorting processes and bars morphodynamics with a relatively high accuracy, involving a large time scale, without intrusion, which could be difficult or even impossible using other approaches. The model is also showed to be particularly robust. This also validates the modelling approach and the set of assumptions that have been chosen to set-up the morphodynamic model. Increasing the model complexity with the inclusion of other processes such as vegetation development or bank erosion is possible. Therefore, the present numerical model can be used as a predictive tool for river management or for research purposes, even if we remind that it has to be confronted to other approaches (e.g. linear stability analysis, field observations, experiments) which all provide their own advantage.

6.4.2 Model applications for other studies

The model, the approach and the operating experience developed and acquired progressively along this work are currently used for other numerical studies for research and operational purposes. Firstly, the method has been used to study the formation and the development of migrating and steady bars in an idealized reach having similar characteristics that the Isère river at Fréterive (Combe de Savoie, France), with the aim of estimating the artificial flooding discharge which could re-mobilize bars in the study site. Secondly, the model developed in this work has been modified to include the processes of riparian vegetation recruitment and colonization [Jourdain et al., 2018]. The final objective of the latter work consists on simulating the diverse trajectories of river bars in a gravel bed channel having similar characteristics than the Isère river in Combe de Savoie, under the consideration of a variety of flooding hydrograms. Thirdly, the methodology has been replicated to develop a morphodynamic model based on a downstream reach of the Loire river located at Saint-Mathurin-sur-Loire. The objective of this study aims to better understand the interactions between bar and dunes morphodynamics, and preliminary results show that the model reproduced well bed evolution for a morphodynamic scenario of one month on the basis of field measurements.

6.4.3 Consequences of numerical and physical parameterization on simulated bar morphodynamics

Even if the model implementation and approach have been validated under different configurations, it has been of utmost importance to estimate the influence of the physical and numerical parameters on the formation and propagation of bars. In fact, these analyses can be re-used later to advise modelers for choosing the correct set of physical and numerical parameters to model relevantly bar morphodynamics, and prevent them from the risks induced a bad model setting-up.

Physical and numerical parameters can both play an important role on the prediction of periodic bar characteristics. To a certain extent, computed bar properties can be importantly biased by the numerical model parameterization. The spatial discretization is showed to

influence the formation of free bars in the straight channel runs, and is even showed to control the bar type when sediment recirculation is considered: hybrid bars are obtained with a coarse mesh, while only free bars form with a finer mesh. It is noteworthy that the physical parameters used for model calibration also control significantly bars characteristics, such as the bed slope deviation effects which impact severely the bar height. The use of a formula which does not account for the hiding-exposure effects can lead to unrealistic bed evolution and sediment sorting patterns, and points out the physically irrelevance of the approach. A wrong parameterization of the sediment layer thicknesses (i.e. too thin or too thick with respect to the bed evolution and grain size) can also conduct to the same issues as mentioned before.

Numerical studies of bar formation and development in straight embanked reaches should account for the last observations, because misunderstanding or lack of control on the numerical or physical parameterization may be equal to lose some of their relevance, and could later lead to a misinterpretation of bar morphodynamics processes.

6.5 Limitations and Perspectives

Although the closure hypotheses used for the analyses presented in this work are all justifiable, the limitations arising from these hypotheses need to be addressed here i) to assess the pertinence of the numerical approach with regard to processes happening in the nature and then ii) consider the possible perspectives to continually improve the modelling and the understanding of fluvial bar processes.

Several limitations consist on the uncertainty of the initial conditions used for modelling. In this work, the sediment used as initial condition in numerical models consists on a homogeneous granulometry over space, where sediment sorting requires several hours to stabilize toward an equilibrium pattern under the configuration of the experiment of Lanzoni [2000b] (Chapter 4), to at least one month under the configuration of the site of Bréhémont (Chapter 5). For example, the initial granulometry used to model bar morphodynamics in a study reach of the middle Loire river (see Chapter 5) corresponds to the averaged grain size distribution measured in the middle Loire river, which is showed to be dependent on the time and location of grain size measurements according to the numerical results. Consequently, at least during the first stages of the simulations carried out in this work, numerical results should be interpreted cautiously.

Other limitations arise from the assumptions chose for modelling, namely:

1. As bedload has often been considered to be at the origin of bedforms development, the suspended load is not accounted here. Suspension could decrease dunes and bars amplitude due to smoothing effects [Meles, 2015; Naqshband et al., 2014].

2. In the numerical model, the sediment is discretized into two size fractions, and to comply with the bedload model of Wilcock and Crowe [2003], the first size fraction is composed of the portion of sand present in the mixture and the second size fraction corresponds to the portion of gravel. A greater number of sediment size fractions could be considered, as well as other methods for decomposing the sediment mixture into size fractions could be used.

3. Vertical sorting of sediment is based on the active layer model of Hirano [1971], while recent works conducted on the ill-posedness of this mathematical model [Stecca et al., 2014, 2016; Siviglia et al., 2017; Chavarrias et al., 2018] demonstrated that the solution can be unstable to short-wave perturbations during phases of bed aggradation and degradation, and the amplitude of the oscillations depend on space discretization, leading to physically

unrealistic results and even numerical simulations failures. The model used in this work assumes i) two sediment size fractions, ii) a constant active layer thickness and iii) under aggradational scenarios the depositional flux of sediment to the substrate is entirely composed of the active layer sediment (Equation 2.15). According to Chavarrias et al. [2018], chances of the active layer model used in this work to be ill-posed should be decreased, due to the particular conditions of use mentioned above. Physically irrelevant fluctuations of bed topography and of sediment sorting are not observed here and the numerical model seems to be particularly robust.

4. According to [Siviglia et al., 2017] the existing active layer models based on the concept of Hirano [1971] oversimplify some physical processes which can be important, and in some cases may lead to unreliable numerical results, such as poor predictions of the development of bed stratigraphy, due to oversimplification of vertical mass fluxes formulated into transfer functions. The continuous vertical sediment models (CVSMs) offer the property of performing more accurately in this respect [Siviglia et al., 2017], but are known to be computationally expensive and no large-scale field application has yet been conceivable as it asks for the development of a new bed layer-type model [Blom, 2008]. Long-term and large-scale computations have been firstly carried out using one-dimensional models [Blom, 2008], but only recently using two-dimensional models [Viparelli et al., 2017] including the TMS [Merkel, 2011; Merkel and Kopmann, 2012; Merkel, 2017; Bleyel and Kopmann, 2018]. Future research work could consist on re-investigating the relationship between non-uniform sediment and bars morphodynamics with using other bookkeeping layer models available in the literature and CVSMs models.

5. The current morphodynamic models assume idealized upstream morphodynamic conditions corresponding to the equilibrium or sediment recirculation. The periodic property of the sediment recirculation is known to increase bar formation and dynamics in the upstream part of the model domain and by extension in the remaining part of the channel [Mendoza et al., 2016; Singh et al., 2017; Cordier et al., 2018a] with respect to the equilibrium boundary. For the site of Bréhémont, this point has been accounted and the study domain has been extended by 4 km upstream from the study area (i.e. $\approx$ 14 times the channel width) to guarantee a sufficient distance for free bars to form upstream of the study area, because the upstream morphodynamic condition is at equilibrium.

6. The present work focuses on straight or weakly curved channels, where it is assumed that secondary flows do not play a fundamental role on the equilibrium free bar characteristics. Not accounting for the secondary flows effects in the model meant to reproduce the experiments of Lanzoni [2000a,b] in a straight channel is showed to be successful and sufficient enough. The last point can be justified by the results of Iwasaki et al. [2016], showing that under steady discharge conditions, accounting for secondary flows gives similar equilibrium bar morphology. Considering the complex configuration of the channel area contraction/expansion located at Bréhémont, the comparison of a SWE model including a formulation for the secondary currents corrections and a three dimensional model solving the Navier-Stokes equations has been preliminary conducted to identify the existence and importance of secondary currents in the study site (Appendix A). This analysis showed that there secondary currents should not be important in the study site, which is in agreement with Claude et al. [2014] who observed only the formation of two small secondary structures. Regarding the objectives of the present work and to optimize computational time, the use of a two-dimensional SWE model has been advantageous to

multiply the scenarios and configurations to conduct sensitivity analyses and calibrate the morphodynamic model. Study of bar morphodynamics co-existing with three dimensional flow structures could be considered provided the implementation of an appropriate formulation for the secondary currents in the current model [Iwasaki et al., 2016] or solving the Navier-Stokes equations.

7. The current study mainly focus on bars morphodynamics in trained rivers which have been subject to channelization. Therefore, bank erosion processes are not been considered in this work. Moreover, the water discharges and the time-scales considered in this work are assumed to be not large enough to observe severe riverbank erosion.

8. Vegetation and cohesive sediment processes are not accounted for, because these processes are considered to enhance bar stabilization and this study focuses essentially on bar formation, development and on the factors governing bars evolution.

9. The present model is always perfectible. Indeed, the condition of uniformly distributed values of k_s and $\alpha_{k,s}$ over space could be relaxed in future research activities. Furthermore, because this work aims at investigating bar morphodynamics, dunes are not fully represented in the model, but their impact on flow and sediment transport are implicitly transcribed through the high values of k_s. Modelling of spatially variable dunes form drag could be improved through the use of an appropriate formulation found in the literature [e.g. Van Rijn, 1984], but is out of the scope of the present work. Because the superimposition of dunes over bars was observed to enhance the non-uniformity of the flow structure in the upstream channel expansion Claude et al. [2014], the non-linear interactions between bar and dunes constitute a research line which deserves more attention, meanwhile research works are actually conducted in a reach 60 km downstream from the site of Bréhémont [Le Guern, 2018].

10. Statistical approaches could be used in the future for different purposes. Uncertainty propagation (e.g. Monte-Carlo method) [Bakker, 2009; van Maren and Cronin, 2016; Leroux et al., 2018] could be used to better estimate the impact of the model input uncertainties (i.e. physical and numerical parameters) on the computed bed evolution and associated fluvial bar morphodynamics. Automatic calibration could be also used in the future to assess the relative importance of each parameter (e.g. bed slope effects, sediment layer thickness, skin friction) to continually improve the current fluvial morphodynamic model [Robins et al., 2018].

6.6 Publications and Deliverables

6.6.1 Scientific publications

A part of this work has been presented in European and International conferences such as the European Geoscience Union (EGU)[Cordier et al., 2017c], River Coastal and Estuarine Morphodynamics (RCEM)[Cordier et al., 2017b], River Flow [Cordier et al., 2018b], Transport solide et mesures dans les rivières (TSMR)[Cordier et al., 2017a] and the TELEMAC-Mascaret User Conference (TUC)[Cordier et al., 2016a, 2018a]. Chapters 4 and 5 are currently under review [Cordier et al., 2019] and in preparation, respectively, to be published in high impact factor scientific journals (Water Resources Research and Earth Surface Processes and Landforms, respectively).

6.6.2 Strategic deliverables

Strategically speaking, the numerical developments brought in this work will be embedded in the morphodynamic module of TMS, and validation benchmarks (e.g. reference test case with non-uniform sediment in a straight channel defined in Chapter 4) will also be released. A non-negligible part of this work consisted on the development of `Shell` scripts to launch sequential or parallel computations to perform sensitivity analysis and calibrate the hydrodynamic/morphodynamic model. In the same way, a variety of `Python` scripts have been especially developed for the post-treatment of the numerical results, to asses results quality (i.e. accuracy and skill), compute bar dimensions and characteristics (wavelength, amplitude and celerity), and visualize any variable of interest in terms of time evolution (i.e. time-series) and spatial distribution (cross-sectional and longitudinal profiles, planform and three dimensional views). Provided the generalization of these scripts, they could be later shared with the TMS user community in a dedicated repository.

□ Synthèse générale sur la conclusion et les perspectives

Tout d'abord, la consistance générale entre le modèle morphodynamique développé dans cette étude et les approches théoriques, expérimentales et de terrain montrent que les différents choix de modélisation numérique et des hypothèses de fermeture permettent de reproduire les principaux processus liés à l'évolution de bancs périodiques à la fois dans des chenaux à géométrie simple et soumis à des forçages externes bien contrôlés, mais aussi dans des configurations géométriques plus complexes et des forçages externes parfois très fluctuants qui sont typiques des rivières aménagées. Ces résultats démontrent aussi la portabilité de la méthode et des développements fournis dans le cadre de ce travail dans l'optique de reproduire ou bien même prédire les trajectoires morphodynamiques des bancs pour d'autres cas d'application.

Mises bout à bout, les discussions présentées lors de chaque étude permettent de fournir de nouveaux éléments de compréhension autour de la problématique liée aux interactions entre la non-uniformité sédimentaire et les bancs, mais permettent également d'apporter divers conseils et préconisations en matière de modélisation numérique via la conception du modèle et la paramétrisation de celui-ci. Les nouveautés scientifiques acquises lors de ce travail et les retours d'expérience en matière de modélisation numérique permettent de d'offrir un certain nombre de recommandations aux gestionnaires des rivières, dans le but de les aider à mieux modéliser et prédire l'évolution des bancs dans les tronçons aménagés avant de proposer des solutions de gestion efficaces.

Diverses perspectives peuvent être envisagées à la suite de ce travail. Il serait intéressant de pouvoir conduire, sur la base des cas d'études présentés lors ce travail, de nouvelles simulations numériques en déployant un modèle de tri granulométrique vertical de type continu. Une autre piste de recherche pourrait consister à étudier plus en détail la relation entre les bancs et la non-uniformité sédimentaire en prenant en compte les interactions avec les dunes. Une meilleure estimation de l'impact des paramètres d'entrée des modèles sur les propriétés des bancs et la morphodynamique fluviale pourrait être fournie grâce à la propagation d'incertitudes, et des méthodes de calibration automatique pourraient être déployées afin de quantifier l'importance de chaque paramètre et pour continuer à améliorer les modèles morphodynamiques fluviaux.

References

Allan James, L. (2010). Secular sediment waves, channel bed waves, and legacy sediment. *Geography Compass*, 4(6):576–598. 9

An, C., Cui, Y., Fu, X., and Parker, G. (2017). Gravel-bed River Evolution in Earthquake-Prone Regions Subject to Cycled Hydrographs and Repeated Sediment Pulses. *Earth Surface Processes and Landforms*, 42(15):2503–2696. 29, 30, 87, 88

Anderson, A. G., Parker, G., and Wood, A. (1975). The flow and stability characteristics of alluvial river channels. *University of Minnesota Digital Conservancy*, 1:1–116. 13

Andreadis, K. M., Schumann, G. J.-P., and Pavelsky, T. (2013). A simple global river bankfull width and depth database. *Water Resources Research*, 49(10):7164–7168. xiv, 133

Ashmore, P., Peirce, S., and Leduc, P. (2018). Expanding the Active Layer: Discussion of Church and Haschenburger (2017) What is the Active Layer? Water Resources Research 53, 510, Doi:10.1002/2016WR019675. *Water Resources Research*, 54(3):1425–1427. 35, 58, 86, 135

Ashmore, P. E. (1982). Laboratory modelling of gravel braided stream morphology. *Earth Surface Processes and Landforms*, 7(3):201–225. 7

Baart, F., van Ormondt, M., van Thiel de Vries, J., and van Koningsveld, M. (2016). Morphological Impact of a Storm Can Be Predicted Three Days Ahead. *Computational Geosciences*, 90(PB):17–23. 138

Bakker, S. A. (2009). Uncertainty analysis of the mud infill prediction of the olokola lng terminal. *Terra et Aqua*, 120:9–18. 175

Bal, K., Struyf, E., Vereecken, H., Viaene, P., De Doncker, L., de Deckere, E., Mostaert, F., and Meire, P. (2011). How do macrophyte distribution patterns affect hydraulic resistances? *Ecological Engineering*, 37(3):529–533. 13

Bankert, A. R. and Nelson, P. A. (2018). Alternate bar dynamics in response to increases and decreases of sediment supply. *Sedimentology*, 65(3):702–720. 10, 130, 156

Below, C. and Jol, H. (2005). Fluvial Processes of Braided Streams: Rakaia River, South Island New Zealand. xi, 2

Bendegom, L. V. (1947). Some considerations on river morphology and river improvement, De Ingenieur vol. 59–4, pp. B1–11. *Dutch. English translation: Nat. Res. Council of Canada, Technical Translation*, 1054:1963. 26, 58, 88, 135

Bertoldi, W., Tubino, M., and Zolezzi, G. (2002). Experimental observations of river bifurcations with uniform and graded sediments. *AIRH, editor. River Flow, Louvain la Neuve*, n/a:n/a—n/a. 8, 13

Best, J. L., Ashworth, P. J., Bristow, C. S., and Roden, J. (2003). Three-dimensional sedimentary architecture of a large, mid-channel sand braid bar, jamuna river, bangladesh. *Journal of Sedimentary Research*, 73(4):516–530. 129

Bittner, L. D., Nino, Y., and Garcia, M. H. (1995). River Bed Response to Channel Width Variation: Theory and Experiments. Technical report, University of Illinois, Urbana-Champaign. 8, 131

Blanpain, O. (2009). *Dynamique sédimentaire multiclasse: de l'étude des processus à la modélisation en Manche*. PhD thesis, Université de Rouen. 35, 86, 288

Bleyel, B. and Kopmann, R. (2018). Influence of the layer model (Hirano versus C-VSM) on a 2D sediment transport model. In *Proceedings TUC 2018*. 174

Blom, A. (2008). Different approaches to handling vertical and streamwise sorting in modeling river morphodynamics. *Water resources research*, 44(3):1 – 17. xii, 28, 34, 35, 36, 85, 86, 174, 288

Blom, A., De Vriend, H., Parker, G., and Ribberink, J. (2003). A Vertical Sorting Model for Rivers with Non-uniform Sediment and Dunes. Technical report, UT (University of Twente). 34

Blom, A., Ribberink, J. S., and Parker, G. (2008). Vertical sorting and the morphodynamics of bed form-dominated rivers: A sorting evolution model. *Journal of Geophysical Research: Earth Surface*, 113(F1):n/a–n/a. 34

Blondeaux, P. and Seminara, G. (1985). A unified bar-bend theory of river meanders. *Journal of Fluid Mechanics*, 157:449–470. 4, 5, 13, 84

Bluck, B. (1982). Texture of gravel bars in braided streams. *Gravel Bed Rivers. John Wiley and Sons, Chichester*, 1:339–355. 13

Bosboom, J., Reniers, A. J. H. M., and P, L. A. (2014). On the perception of morphodynamic model skill. *Coastal Engineering*, 94:112 – 125. 138

Bridge, J. and Demicco, R. (2008). *Earth surface processes, landforms and sediment deposits*. Cambridge University Press. 3, 4, 7, 14, 83, 129, 131

Bridge, J. S. (2003). *Rivers and floodplains: forms, processes, and sedimentary record*. John Wiley & Sons. xi, 4, 5, 9, 10, 83, 130, 131, 155

Buffington, J. M. (2012). Changes in channel morphology over human time scales [Chapter 32]. *Treesearch*, 1:435–463. 9

Cabrit, O. (2009). *Modélisation des flux pariétaux sur les tuyères des moteurs à propergol solide*. PhD thesis, Montpellier 2. 26, 58, 71, 88, 135

Callander, R. (1969). Instability and river channels. *Journal of Fluid Mechanics*, 36(03):465–480. 9

Camporeale, C. and Ridolfi, L. (2006). Riparian vegetation distribution induced by river flow variability: A stochastic approach. *Water Resources Research*, 42(10):n/a – n/a. 13

Caponi, F. and Siviglia, A. (2018). Numerical Modeling of Plant Root Controls on Gravel Bed River Morphodynamics. *Geophysical Research Letters*, n/a(0):n/a. 13

Chavarrias, V., Stecca, G., and Blom, A. (2018). Ill-posedness in modeling mixed sediment river morphodynamics. *Advances in Water Resources*, 114:219 – 235. 34, 71, 158, 173, 174

Church, M. and Haschenburger, J. K. (2017). What is the active layer? *Water Resources Research*, 53(1):5–10. 34, 35, 56, 58, 86, 97, 135, 288

Claude, N. (2012). *Processus et flux hydro-sédimentaires en rivière sablo-graveleuse: influence de la largeur de section et des bifurcations en Loire moyenne (France)*. PhD thesis, Tours. xi, 8, 83, 132, 134, 136, 142

Claude, N., Rodrigues, S., Bustillo, V., Bréhéret, J.-G., Macaire, J.-J., and Jugé, P. (2012). Estimating bedload transport in a large sand-gravel bed river from direct sampling, dune tracking and empirical formulas. *Geomorphology*, 179:40–57. xiv, 133, 134

Claude, N., Rodrigues, S., Bustillo, V., Bréhéret, J.-G., Tassi, P., and Jugé, P. (2014). Interactions between flow structure and morphodynamic of bars in a channel expansion/contraction, Loire River, France. *Water Resources Research*, 50(4):2850–2873. xiv, 8, 15, 83, 128, 129, 131, 133, 134, 137, 140, 141, 142, 144, 147, 153, 154, 157, 158, 174, 175

Colombini, M., Seminara, G., and Tubino, M. (1987). Finite-amplitude alternate bars. *Journal of Fluid Mechanics*, 181:213–232. 4, 6, 9, 55, 84

Cordier, F., Tassi, P., and Claude, N. (2018a). Influence of numerical and physical parameters on the modelling of free bar morphodynamics. In *XXVth TELEMAC-MASCARET User Conference Proceedings*. 158, 174, 175

Cordier, F., Tassi, P., Claude, N., Crosato, A., Rodrigues, S., and Pham Van Bang, D. (2016a). Numerical modelling of graded sediment transport based on the experiments of Wilcock and Crowe (2003). In *XXIIIrd TELEMAC-MASCARET User Conference Proceedings*. 32, 175

Cordier, F., Tassi, P., Claude, N., Crosato, A., Rodrigues, S., and Pham Van Bang, D. (2017a). Influence de l'étendue granulométrique sur la morphodynamique de barres alternées libres et hybrides. In *Transport Solide et Morphodynamique des Rivières 2017 (TSMR 2017)*. 175

Cordier, F., Tassi, P., Claude, N., Crosato, A., Rodrigues, S., and Pham Van Bang, D. (2017b). Influence of the graded sediment distribution and sediment supply on river bar patterns and dynamics. In *Book of proceedings RCEM 2017*. 175

Cordier, F., Tassi, P., Claude, N., Crosato, A., Rodrigues, S., and Pham Van Bang, D. (2017c). Morphodynamic modelling of alternate bars in channels with graded sediment. In *EGU 2017 - Book of abstracts*. 175

Cordier, F., Tassi, P., Claude, N., Crosato, A., Rodrigues, S., and Pham Van Bang, D. (2018b). Influence of hydrology, sediment supply and sediment gradation on river bar morphodynamics: application to the Loire River at Bréhémont (France). In *Book of Proceedings RiverFlow 2018 conference*. 175

Cordier, F., Tassi, P., Claude, N., Crosato, A., Rodrigues, S., and Pham Van Bang, D. (2019). Numerical study of alternate bars in alluvial channels with nonuniform sediment. *Water Resources Research*, 55(0):1–30. 5, 56, 130, 134, 135, 137, 155, 156, 157, 175

Cordier, F., Tassi, P., Jodeau, M., and Camenen, B. (2016b). Large-scale morphodynamics structures in the Arc en Maurienne River (France). *River Flow 2016*, 1:n/a – n/a. 56

Crosato, A. (2008). *Analysis and modelling of river meandering*. TU Delft, Delft University of Technology. 7, 8, 131

Crosato, A. and Desta, F. (2009). Intrinsic steady alternate bars in alluvial channels. Part 1: experimental observations and numerical tests. In *Proc. of the 6th Symp. on River Coastal and Estuarine Morphodynamics (RCEM 2009), 21-25 Sept. 2009, Santa Fe, Argentina, RCEM 2009, Vol. 2, pp. 759-765.* Taylor & Francis Group. 5, 13, 101

Crosato, A., Desta, F. B., Cornelisse, J., Schuurman, F., and Uijttewaal, W. S. J. (2012). Experimental and numerical findings on the long-term evolution of migrating alternate bars in alluvial channels. *Water Resources Research*, 48(6):1–14. W06524. 45, 67, 99

Crosato, A. and Mosselman, E. (2009). Simple physics-based predictor for the number of river bars and the transition between meandering and braiding. *Water Resources Research*, 45(3):1–12. xi, 4, 6, 7, 8, 55, 56, 84, 92, 130, 131, 137, 146, 152, 153, 154, 157

Crosato, A., Mosselman, E., Beidmariam Desta, F., and Uijttewaal, W. S. J. (2011). Experimental and numerical evidence for intrinsic nonmigrating bars in alluvial channels. *Water Resources Research*, 47(3):1–14. W03511. 4, 5, 84, 90, 110, 130, 131

Cui, Y. (2007). The Unified Gravel-Sand (TUGS) Model: Simulating Sediment Transport and Gravel/Sand Grain Size Distributions in Gravel-Bedded Rivers. *Water resources research*, 43(10):1 – 16. 10

Cui, Y., Parker, G., Lisle, T. E., Gott, J., Hansler-Ball, M. E., Pizzuto, J. E., Allmendinger, N. E., and Reed, J. M. (2003a). Sediment pulses in mountain rivers: 1. Experiments. *Water Resources Research*, 39(9):1–12. 28

Cui, Y., Parker, G., Pizzuto, J., and Lisle, T. E. (2003b). Sediment pulses in mountain rivers: 2. Comparison between experiments and numerical predictions. *Water Resources Research*, 39(9):1 – 11. 9

Dam, G., Wegen, M., Labeur, R. J., and Roelvink, D. (2016). Modeling centuries of estuarine morphodynamics in the Western Scheldt estuary. *Geophysical Research Letters*, 43(8):3839–3847. 138

De Linares, M. (2007). *Two-dimensional numerical modelling of bed load transport and fluvial morphology. Validation on two sites on the Loire river and on the Arc river.* Theses, Université Joseph-Fourier - Grenoble I. 34, 36, 44

de Linares, M. and Belleudy, P. (2007). Critical Shear Stress of Bimodal Sediment in Sand-Gravel Rivers. *Journal of Hydraulic Engineering*, 133(5):555–559. 29, 297

de Saint-Venant, A. B. (1871). Théorie du mouvement non permanent des eaux, avec application aux crues des rivières et à l'introduction des marées dans leurs lits. *Comptes Rendus des séances de l'Académie des Sciences*, 73:237–240. 18, 25, 57, 85, 134

Defina, A. (2003). Numerical experiments on bar growth. *Water Resources Research*, 39(4):1–12. 15, 56, 60, 90

Dhont, B. and Ancey, C. (2018). Are Bedload Transport Pulses in Gravel Bed Rivers Created by Bar Migration or Sediment Waves? *Geophysical Research Letters*, 45(11):5501–5508. 9

Diplas, P. (1994). Modelling of fine and coarse sediment interaction over alternate bars. *Journal of Hydrology*, 159(1):335–351. 13, 84, 109

Duró, G., Crosato, A., and Tassi, P. (2015). Numerical experiments to explore bar management by channel width variations. *E-proceedings of the 36-th IAHR World Congress*, 1:1–4. 61

Duró, G., Crosato, A., and Tassi, P. (2016). Numerical study on river bar response to spatial variations of channel width. *Advances in Water Resources*, 93(Part A):21 – 38. xi, 5, 6, 8, 84, 101, 108, 110, 130, 131, 153

East, A. E., Pess, G. R., Bountry, J. A., Magirl, C. S., Ritchie, A. C., Logan, J. B., Randle, T. J., Mastin, M. C., Minear, J. T., Duda, J. J., et al. (2015). Large-scale dam removal on the Elwha River, Washington, USA: River channel and floodplain geomorphic change. *Geomorphology*, 228:765–786. 9

Eekhout, J., Hoitink, A., and Mosselman, E. (2013). Field experiment on alternate bar development in a straight sand-bed stream. *Water Resources Research*, 49(12):8357–8369. 5

Egiazaroff, I. (1965). Calculation of nonuniform sediment concentrations. *Journal of the Hydraulics Division*, 91(4):225–247. 58, 68

Einstein, H. A. (1950). *The bed-load function for sediment transportation in open channel flows*. Number 1026. US Department of Agriculture. 11

Engelund, F. (1970). Instability of erodible beds. *Journal of Fluid Mechanics*, 42(2):225–244. 4, 6, 55, 83, 84, 130

Engelund, F. and Hansen, E. (1967). A monograph on sediment transport in alluvial streams. Technical report, Tekniskforlag Skelbrekgade 4 Copenhagen V, Denmark. 28

Engelund, F. and Skovgaard, O. (1973). On the origin of meandering and braiding in alluvial streams. *Journal of Fluid Mechanics*, 57(02):289–302. 83

Enggrob, H. and Tjerry, S. (1999). Simulation of morphological characteristics of a braided river. In *Proceedings of the IAHR Symposium on River, Coastal and Estuarine Morphodynamics, Genova*, volume I, pages 585–594. 84

Exner, F. M. (1920). *Zur physik der dünen*. Hölder. 25, 57, 86, 135

Federici, B. and Seminara, G. (2003). On the convective nature of bar instability. *Journal of Fluid Mechanics*, 487:125–145. 9

Francalanci, S., Solari, L., and Toffolon, M. (2009). Local high-slope effects on sediment transport and fluvial bed form dynamics. *Water Resources Research*, 45-5(5):1–15. 65

Fujita, Y. and Muramoto, Y. (1985). Studies on the process of development of alternate bars. *Bulletin of the Disaster Prevention Research Institute*, 35:1 – 33. 55, 84

García, M. and Niño, Y. (1993). Dynamics of sediment bars in straight and meandering channels: experiments on the resonance phenomenon. *Journal of Hydraulic Research*, 31(6):739–761. 8, 131

García, M. H. (2008). Sedimentation engineering. *Processes, Measurements, Modeling, and Practice. ASCE Manuals and Reports on Engineering Practice*, 110:1–1132. 25, 27, 29, 34, 57, 86, 89, 97, 136

Gilbert, G. K. (1917). *Hydraulic-mining debris in the Sierra Nevada*. US Government Printing Office. 9

Güneralp, I., Abad, J. D., Zolezzi, G., and Hooke, J. (2012). Advances and challenges in meandering channels research. *Geomorphology*, 163-164(Supplement C):1 – 9. Meandering Channels. 109

Hall, P. (2004). Alternating bar instabilities in unsteady channel flows over erodible beds. *Journal of Fluid mechanics*, 499:49–73. 9, 130

Hansen, E. (1967). On the formation of meanders as a stability problem. progress report 13, p.9. Technical report, Coastal engineering Lab., Technical Unviversity Denmark, Basis Research. 130

Hervouet, J., Razafindrakoto, E., and Villaret, C. (2011). Dealing with dry zones in free surface flows: a new class of advection schemes. In Barton, A., editor, *Proceedings of the 34th World Congress of the International Association for Hydro-Environment Research and Engineering: 33rd Hydrology and Water Resources Symposium and 10th Conference on Hydraulics in Water Engineering*, pages 4103–411. Australia. 27, 58, 89, 136

Hirano, M. (1971). *River bed degradation with armoring*. PhD thesis, Japanese Society of Civil Engineering. xii, 18, 24, 25, 34, 35, 43, 57, 58, 70, 85, 86, 135, 158, 167, 173, 174, 288, 300

Hirano, M. (1972). Studies on variation and equilibrium state of a river bed composed of nonuniform material. *Trans. Jpn. Soc. Civ. Eng*, 4:128–129. xii, 24, 25, 36

Hoey, T. B. and Ferguson, R. (1994). Numerical simulation of downstream fining by selective transport in gravel bed rivers: Model development and illustration. *Water Resources Research*, 30(7):2251–2260. 12, 45, 84, 108

Humphries, R., Venditti, J. G., Sklar, L. S., and Wooster, J. K. (2012). Experimental evidence for the effect of hydrographs on sediment pulse dynamics in gravel-bedded rivers. *Water Resources Research*, 48(1):1–10. 9

Huthoff, F. (2012). Theory for flow resistance caused by submerged roughness elements. *Journal of Hydraulic Research*, 50(1):10–17. 27, 136

Ikeda, S., Parker, G., and Sawai, K. (1981). Bend theory of river meanders. Part 1. Linear development. *Journal of Fluid Mechanics*, 112:363–377. 13

Iwasaki, T., Shimizu, Y., and Kimura, I. (2015). Numerical simulation of bar and bank erosion in a vegetated floodplain: A case study in the Otofuke River. *Advances in Water Resources*, n/a:1 – 17. 13

Iwasaki, T., Shimizu, Y., and Kimura, I. (2016). Sensitivity of free bar morphology in rivers to secondary flow modeling: Linear stability analysis and numerical simulation. *Advances in water resources*, 92:57–72. 174, 175

Jaballah, M., Camenen, B., Pénard, L., and Paquier, A. (2015). Alternate bar development in an alpine river following engineering works. *Advances in Water Resources*, 81:103–113. Fluvial Eco-Hydraulics And Morphodynamics. 83

Jourdain, C., Claude, N., Antoine, G., Tassi, P., and Cordier, F. (2018). Morphodynamics of alternate bars in the presence of riparian vegetation: insights from numerical modeling. *Earth Surface Processes and Landforms*, under review:n/a. 13, 172

Juez, C., Ferrer-Boix, C., Murillo, J., Hassan, M., and García-Navarro, P. (2016). A model based on Hirano-Exner equations for two-dimensional transient flows over heterogeneous erodible beds. *Advances in Water Resources*, 87:1–18. 12, 84

Kleinhans, M. (2004). Experimental dune trough scour in sediment mixtures. Marine Sandwave and RIver Dune Dynamics. 45

Kleinhans, M. G. and van den Berg, J. H. (2011). River channel and bar patterns explained and predicted by an empirical and a physics-based method. *Earth Surface Processes and Landforms*, 36(6):721–738. 26

Koch, F. and Flokstra, C. (1980). *Bed Level Computations for Curved Alluvial Channels: Prepared for the 19th IAHR Congress, New Delhi, India, February 1981*. Waterloopkundig Laboratorium. 26, 58, 88, 135, 139

Korup, O., Densmore, A. L., and Schlunegger, F. (2010). The role of landslides in mountain range evolution. *Geomorphology*, 120(1):77–90. 9

Langendoen, E. J., Mendoza, A., Abad, J. D., Tassi, P., Wang, D., Ata, R., kadi Abderrezzak, K. E., and Hervouet, J.-M. (2015). Improved numerical modeling of morphodynamics of rivers with steep banks. *Advances in Water Resources*, n/a:n/a – n/a. 16

Lanzoni, S. (2000a). Experiments on bar formation in a straight flume 1. Uniform sediment. *Water Resources Research*, 36(11):3337–3349. 4, 12, 15, 45, 54, 57, 59, 65, 84, 89, 111, 174

Lanzoni, S. (2000b). Experiments on bar formation in a straight flume: 2. Graded sediment. *Water Resources Research*, 36(11):3351–3363. xi, xiii, 11, 12, 13, 14, 16, 32, 33, 44, 45, 49, 57, 59, 84, 85, 89, 90, 93, 94, 97, 107, 109, 111, 112, 130, 155, 162, 173, 174

Lanzoni, S. and Tubino, M. (1999). Grain sorting and bar instability. *Journal of Fluid Mechanics*, 393:149–174. 6, 11, 12, 55, 84

Le, T., Crosato, A., Mosselman, E., and Uijttewaal, W. (2018a). On the stability of river bifurcations created by longitudinal training walls. Numerical investigation. *Advances in Water Resources*, 113:112–125. 5

Le, T., Crosato, A., and Uijttewaal, W. (2018b). Long-term morphological developments of river channels separated by a longitudinal training wall. *Advances in Water Resources*, 113:73–85. 5

Le Guern, J. (2018). *Morphodynamique et interactions des barres et des dunes dans un cours d'eau sablo-graveleux. Compréhension des processus et quantification des flux solides à l'entrée du bief esturarien de la Loire*. PhD thesis, Université de Tours. 175

Leopold, L. and Wolman, M. (1957). River channel patterns. *Fluv Geom: Geom Crit Conc Vol*, 1:3. 3

Leopold, L. B. and Langbein, W. B. (1962). *The concept of entropy in landscape evolution*. US Government Printing Office Washington, DC, USA. 3

Leroux, R., Goeury, C., Abderrezzak, K. E. K., and Tassi, P. (2018). Uncertainty Quantification in 2D Morphodynamic Model: Application to the Gironde Estuary. In Loggia, G. L., Freni, G., Puleo, V., and Marchis, M. D., editors, *HIC 2018. 13th International Conference on Hydroinformatics*, volume 3 of *EPiC Series in Engineering*, pages 1147–1154. EasyChair. 175

Lisle, T. E., Ikeda, H., and Iseya, F. (1991). Formation of stationary alternate bars in a steep channel with mixed-size sediment: A flume experiment. *Earth Surface Processes and Landforms*, 16(5):463–469. 11, 12, 13, 84, 109, 111

Lisle, T. E., Iseya, F., and Ikeda, H. (1993). Response of a channel with alternate bars to a decrease in supply of mixed-size bed load: A flume experiment. *Water Resources Research*, 29(11):3623–3629. 11

Lisle, T. E. and Madej, M. (1992). Spatial variation in armouring in a channel with high sediment supply. *Dynamics of Gravel-bed Rivers*, 1:277–296. 11, 12, 13, 84, 109

Lisle, T. E., Nelson, J. M., Pitlick, J., Madej, M. A., and Barkett, B. L. (2000). Variability of bed mobility in natural, gravel-bed channels and adjustments to sediment load at local and reach scales. *Water Resources Research*, 36:3743–3755. 12, 84

Lisle, T. E., Pizzuto, J. E., Ikeda, H., Iseya, F., and Kodama, Y. (1997). Evolution of a sediment wave in an experimental channel. *Water Resources Research*, 33(8):1971–1981. 9

Luchi, R., Hooke, J., Zolezzi, G., and Bertoldi, W. (2010). Width variations and mid-channel bar inception in meanders: River Bollin (UK). *Geomorphology*, 119(1):1–8. 8, 131

Madej, M. A., Sutherland, D. G., Lisle, T. E., and Pryor, B. (2009). Channel responses to varying sediment input: A flume experiment modeled after Redwood Creek, California. *Geomorphology*, 103(4):507–519. 9

Marzadri, A., Tonina, D., Bellin, A., Vignoli, G., and Tubino, M. (2010). Semianalytical analysis of hyporheic flow induced by alternate bars. *Water Resources Research*, 46(7):n/a – n/a. 14

Meles, S. T. (2015). Effects of suspended sediments on river bars. Master's thesis, Unesco IHE Delft. 18, 144, 158, 173

Mendoza, A., Abad, J. D., Langendoen, E. J., Wang, D., Tassi, P., and Abderrezzak, K. E. K. (2016). Effect of Sediment Transport Boundary Conditions on the Numerical Modeling of Bed Morphodynamics. *Journal of Hydraulic Engineering*, 143(4): . 27, 46, 56, 58, 59, 60, 64, 88, 90, 136, 158, 174

Merkel, U. (2011). A continuous sediment layer concept for Sisyphe. In *18th Telemac-Mascaret User Club*. 174

Merkel, U. (2017). C-VSM-II: Large Scale and Long Time Simulations with Sisyphe's Continuous Vertical Grain Sorting Model. In *Proceedings of the 24th Telemac-Mascaret User Conference*. 174

Merkel, U. and Kopmann, R. (2012). Continuous Vertical Grain Sorting for TELEMAC & SISYPHE v6p2. In *Proceedings XIXth TELEMAC-MASCARET User Conference*. 174

Meyer-Peter, E. and Müller, R. (1948). Formulas for bed-load transport. In *International Association for Hydraulic Structures Research*. IAHR. 26, 28, 58, 134, 155

Milhous, R. T. (1973). *Sediment transport in a gravel-bottomed stream*. PhD thesis, Oregon State University (USA). 11

Miwa, H., Daido, A., and Yokogawa, J. (2003). Growth and transformation of alternate bars under sinusoidal wave flood conditions. *Bulletin of Maizuru National College of Technology*, 38:81–88. 9, 12, 130

Miwa, H., Daido, A., and Yokogawa, J. (2005). Effects of sediment supply and grain sorting on low-watercourse formation in channel with alternate bars. *Proceedings of hydraulic engineering*, 49:949–954. 11

Miwa, H. and Parker, G. (2012). Numerical simulation of low-flow channel evolution due to sediment augmentation. *International Journal of Sediment Research*, 27:351–361. 9, 11, 123

Mossa, J. (2016). The changing geomorphology of the Atchafalaya River, Louisiana: A historical perspective. *Geomorphology*, 252:112 – 127. The Natural and Human Structuring of Rivers and other Geomorphic Systems: A Special Issue in Honor of William L. Graf. 9

Mosselman, E. (2010). Intrinsic steady alternate bars in alluvial channels. In *Proceedings of the international scientific and business conference: Waterways of Russia: engineering, operation and maintenance, management, part III, 2010*. 5

Mosselman, E. (2012). Modelling Sediment Transport and Morphodynamics of Gravel-Bed Rivers. *Gravel-Bed Rivers: Processes, Tools, Environments*, 1:101–115. 12, 15, 56, 84

Mosselman, E., Hassan, K. I., and Sieben, A. (2003). Effect of spatial grain size variations in two-dimensional morphological computations with uniform sediment. In *Proceedings IAHR Symposium River, Coastal and Estuarine Morphodynamics*, pages 236–246. Int. Assoc. for Hydro-Environ. Eng. and Res. Madrid. 16

Mosselman, E., Sieben, A., Sloff, K., and Wolters, A. (1999). Effect of spatial grain size variations on two-dimensional river bed morphology. In *Proceedings of River, Coastal and Estuarine Morphodynamics, Genova*, volume 1, pages 499–507. 12, 15, 28, 84

Naqshband, S., Ribberink, J., Hulscher, S., and Hurther, D. (2014). Sediment transport distribution along developing sand dunes. In Schleiss, A., De Cesare, G., Franca, M., and Pfister, M., editors, *River Flow 2014*, pages 1039–1044, United Kingdom. Taylor & Francis. 18, 144, 158, 173

Nelson, A. and Dubé, K. (2015). Channel response to an extreme flood and sediment pulse in a mixed bedrock and gravel-bed river. *Earth Surface Processes and Landforms*, 41:178–195. 10, 131

Nelson, J. M. (1990). The initial instability and finite-amplitude stability of alternate bars in straight channels. *Earth-Science Reviews*, 29(1):97 – 115. 8, 131

Nelson, P. A. (2010). *Bed surface patchiness in gravel-bed rivers*. University of California, Berkeley, Ph D. student. 28

Nelson, P. A., McDonald, R. R., Nelson, J. M., and Dietrich, W. E. (2015a). Coevolution of bed surface patchiness and channel morphology: 1. Mechanisms of forced patch formation. *Journal of Geophysical Research: Earth Surface*, 120(9):1687–1707. 12, 13, 16, 56, 65, 84, 91, 107, 109, 130, 137, 155

Nelson, P. A., McDonald, R. R., Nelson, J. M., and Dietrich, W. E. (2015b). Coevolution of bed surface patchiness and channel morphology: 2. Numerical experiments. *Journal of Geophysical Research: Earth Surface*, 120(9):1708–1723. 11, 12, 13, 14, 16, 28, 72, 84, 101, 109, 110, 111, 123, 130, 155, 157, 162

Nelson, P. A. and Morgan, J. A. (2018). Flume experiments on flow and sediment supply controls on gravel bedform dynamics. *Geomorphology*, n/a:n/a–n/a. 9, 130

Nezu, I., Nakagawa, H., and Jirka, G. H. (1994). Turbulence in open-channel flows. *Journal of Hydraulic Engineering*, 120(10):1235–1237. 18, 25, 57, 85, 134

Nicholas, A. P. (2013). Modelling the continuum of river channel patterns. *Earth Surface Processes and Landforms*, 38(10):1187–1196. 129

Nikuradse, J. (1950). *Laws of flow in rough pipes*. NACA. 25, 86, 135

Orrú, C., Blom, A., and Uijttewaal, W. S. (2016). Armor breakup and reformation in a degradational laboratory experiment. *Earth Surface Dynamics*, 4(2):461. 29, 87

Paetzold, A., Schubert, C. J., and Tockner, K. (2005). Aquatic terrestrial linkages along a braided-river: riparian arthropods feeding on aquatic insects. *Ecosystems*, 8(7):748–759. 13

Parker, G. (1990). Surface-based bedload transport relation for gravel rivers. *Journal of hydraulic research*, 28(4):417–436. 11, 29, 87

Parker, G., Hassan, M., and Wilcock, P. (2007). Adjustment of the bed surface size distribution of gravel-bed rivers in response to cycled hydrographs. *Developments in Earth Surface Processes*, 11:241–285. 35, 86

Parker, G. and Klingeman, P. C. (1982). On why gravel bed streams are paved. *Water Resources Research*, 18(5):1409–1423. 56

Parker, G., Klingeman, P. C., and McLean, D. G. (1982). Bedload and size distribution in paved gravel-bed streams. *Journal of the Hydraulics Division*, 108(4):544–571. 11, 28

Parker, G., Paola, C., and Leclair, S. (2000). Probabilistic Exner Sediment Continuity Equation for Mixtures with No Active Layer. *Journal of Hydraulic Engineering*, 126(11):818–826. 34

Parker, G., Shimizu, Y., Wilkerson, G., Eke, E. C., Abad, J. D., Lauer, J., Paola, C., Dietrich, W. E., and Voller, V. (2011). A new framework for modeling the migration of meandering rivers. *Earth Surface Processes and Landforms*, 36(1):70–86. xi, 2

Parker, G. and Wilcock, P. R. (1993). Sediment feed and recirculating flumes: Fundamental difference. *Journal of Hydraulic Engineering*, 119(11):1192–1204. 45

Pierson, T. C., Pringle, P. T., and Cameron, K. A. (2011). Magnitude and timing of downstream channel aggradation and degradation in response to a dome-building eruption at Mount Hood, Oregon. *Geological Society of America Bulletin*, 123(1-2):3–20. 9

Podolak, C. J. P. and Wilcock, P. R. (2013). Experimental study of the response of a gravel streambed to increased sediment supply. *Earth Surface Processes and Landforms*, 38(14):1748–1764. 9, 10

Powell, D. M. (1998). Patterns and processes of sediment sorting in gravel-bed rivers. *Progress in Physical Geography*, 22(1):1–32. 11, 12, 84

Powell, D. M., Ockelford, A., Rice, S. P., Hillier, J. K., Nguyen, T., Reid, I., Tate, N. J., and Ackerley, D. (2016). Structural properties of mobile armors formed at different flow strengths in gravel-bed rivers. *Journal of Geophysical Research: Earth Surface*, 121(8):1494–1515. 2015JF003794. 29, 87

Proffitt, G. and Sutherland, A. (1983). Transport of non-uniform sediments. *Journal of Hydraulic Research*, 21(1):33–43. 29, 87

Qian, H., Cao, Z., Liu, H., and Pender, G. (2016). Numerical modelling of alternate bar formation, development and sediment sorting in straight channels. *Earth Surface Processes and Landforms*, 607:613–622. ESP-15-0409.R2. 12, 16, 56, 60, 84, 90

Recking, A. (2010). A comparison between flume and field bed load transport data and consequences for surface-based bed load transport prediction. *Water Resources Research*, 46(3):1–16. W03518. 28

Recking, A., Piton, G., Vazquez-Tarrio, D., and Parker, G. (2015). Quantifying the Morphological Print of Bedload Transport. *Earth Surface Processes and Landforms*, 41(6):809–822. 29, 30, 87, 88, 135

Reisenbüchler, M., Bui, M. D., and Rutschmann, P. (2016). Implementation of a new Layer-Subroutine for fractional sediment transport in SISYPHE. In *XXIIIrd TELEMAC-MASCARET User Conference 2016 Proceedings Book*. 35, 36

Repetto, R., Tubino, M., and Paola, C. (2002). Planimetric instability of channels with variable width. *Journal of Fluid Mechanics*, 457:79–109. 7, 8, 131

Robins, P. E., Lewis, M. J., Freer, J., Cooper, D. M., Skinner, C. J., and Coulthard, T. J. (2018). Improving estuary models by reducing uncertainties associated with river flows. *Estuarine, Coastal and Shelf Science*, 207:63 – 73. 175

Rodrigues, S., Bréhéret, J.-G., Macaire, J.-J., Moatar, F., Nistoran, D., and Jugé, P. (2006). Flow and sediment dynamics in the vegetated secondary channels of an anabranching river: the loire river (france). *Sedimentary Geology*, 186(1-2):89–109. 132

Rodrigues, S., Claude, N., Juge, P., and Breheret, J.-G. (2012). An opportunity to connect the morphodynamics of alternate bars with their sedimentary products. *Earth Surface Processes and Landforms*, 37(2):240–248. 12, 110, 153, 155

Rodrigues, S., Le Hir, P., Moatar, F., and Claude, N. (2016). Transferts de particules dans le continuum fluvio-estuarien. *La loire fluviale et estuarienne : un milieu en evolution*, 1:85–111. 132

Rodrigues, S., Mosselman, E., Claude, N., Wintenberger, C. L., and Juge, P. (2015). Alternate bars in a sandy gravel bed river: generation, migration and interactions with superimposed dunes. *Earth Surface Processes and Landforms*, 40(5):610–628. 5, 8, 84, 110, 129, 130, 131, 153, 155

Schielen, R. M. J. (1995). *Nonlinear stability analysis and pattern formation in morphological models*. Rijksuniversiteit te Utrecht. 9

Schumm, S. A. (1981). Evolution and response of the fluvial system, sedimentologic implications. *Recent and Ancient Nonmarine Depositional Environments: Models for Exploration*, 31:19–29. xi, 4

Schuurman, F. and Kleinhans, M. (2011). Self-formed braid bars in a numerical model. In *AGU Fall Meeting Abstracts*. 56, 61

Scorpio, V., Zen, S., Bertoldi, W., Surian, N., Mastronunzio, M., Dai Prá, E., Zolezzi, G., and Comiti, F. (2018). Channelization of a large Alpine river: what is left of its original morphodynamics? *Earth Surface Processes and Landforms*, 43(5):1044–1062. 5, 15

Seal, R., Paola, C., Parker, G., Southard, J. B., and Wilcock, P. R. (1997). Experiments on downstream fining of gravel: I. Narrow-channel runs. *Journal of Hydraulic Engineering*, 123(10):874–884. 12, 45, 84, 108

Seminara, G. (1998). Stability and morphodynamics. *Meccanica*, 33(1):59–99. 84, 130

Serlet, A. J., Gurnell, A. M., Zolezzi, G., Wharton, G., Belleudy, P., and Jourdain, C. (2018). Biomorphodynamics of alternate bars in a channelized, regulated river: An integrated historical and modelling analysis. *Earth Surface Processes and Landforms*, 43(9):1739–1756. 15

Shaw, J. B., Mohrig, D., and Whitman, S. K. (2013). The morphology and evolution of channels on the Wax Lake Delta, Louisiana, USA. *Journal of Geophysical Research: Earth Surface*, 118(3):1562–1584. 11

Shields, A. (1936). *Anwendung der Aehnlichkeitsmechanik und der Turbulenzforschung auf die Geschiebebewegung*. PhD thesis, Technical University Berlin. 26

Singh, U., Crosato, A., Giri, S., and Hicks, M. (2017). Sediment heterogeneity and mobility in the morphodynamic modelling of gravel-bed braided rivers. *Advances in Water Resources*, 104:127–144. 11, 12, 13, 28, 56, 84, 130, 155, 158, 174

Siviglia, A. and Crosato, A. (2016). Numerical modelling of river morphodynamics: latest developments and remaining challenges. *Advances in Water Resources*, 90:1–9. 15, 28, 56, 84

Siviglia, A., Stecca, G., and Blom, A. (2017). *Modelling of Mixed-Sediment Morphodynamics in Gravel-Bed Rivers Using the Active-Layer Approach*, chapter 26, pages 703–728. Wiley-Blackwell. 34, 173, 174

Siviglia, A., Stecca, G., Vanzo, D., Zolezzi, G., Toro, E. F., and Tubino, M. (2013). Numerical modelling of two-dimensional morphodynamics with applications to river bars and bifurcations. *Advances in Water Resources*, 52:243–260. 4, 15, 56, 110

Sloff, C., Bernabè, M., and Baur, T. (2003). On the stability of the Pannerdense Kop river bifurcation. In *Proc. 3rd IAHR Symposium on River, Coastal and Estuarine Morphodynamics: Proceedings RCEM 2003*. 16

Soulsby, R. (1997). *Dynamics of marine sands: a manual for practical applications*. Thomas Telford. 26, 88

Southard, J. (2006). 12.090 Introduction to Fluid Motions, Sediment Transport, and Current-Generated Sedimentary Structures, Fall 2006. Online, Massachusetts Institute of Technology: MIT OpenCourseWare. http://ocw.mit.edu (Accessed). License: Creative Commons BY-NC-SA. 45

Stecca, G., Siviglia, A., and Blom, A. (2014). Mathematical analysis of the Saint-Venant-Hirano model for mixed-sediment morphodynamics. *Water Resources Research*, 50(10):7563–7589. 71, 158, 173

Stecca, G., Siviglia, A., and Blom, A. (2016). An accurate numerical solution to the Saint-Venant-Hirano model for mixed-sediment morphodynamics in rivers. *Advances in Water Resources*, 93:39–61. 34, 35, 71, 86, 158, 173

Struiksma, N. and Crosato, A. (1989). *Analysis of a 2-D Bed Topography Model for Rivers*. Wiley Online Library. 56, 106

Struiksma, N., Olesen, K., Flokstra, C., and De Vriend, H. (1985). Bed deformation in curved alluvial channels. *Journal of Hydraulic Research*, 23(1):57–79. 4, 7, 8, 130, 131

Sun, J., Lin, B., and Yang, H. (2015). Development and application of a braided river model with non-uniform sediment transport. *Advances in water resources*, 81:62–74. 130

Sun, Z. and Donahue, J. (2000). Statistically derived bedload formula for any fraction of nonuniform sediment. *Journal of Hydraulic Engineering*, 126(2):105–111. 28

Sutherland, A. (1987). Static armour layers by selective erosion. *Sediment Transfer in Gravel-Bed Rivers. John Wiley & Sons New York*, n/a:243 – 260. 11

Sutherland, D. G., Ball, M. H., Hilton, S. J., and Lisle, T. E. (2002). Evolution of a landslide-induced sediment wave in the Navarro River, California. *Geological Society of America Bulletin*, 114(8):1036–1048. 9

Sutherland, J., Peet, A., and Soulsby, R. (2004). Evaluating the performance of morphological models. *Coastal engineering*, 51(8-9):917–939. 138

Takebayashi, H. and Egashira, S. (2001). Dynamic state of sand bar formed on non-uniform sediment bed. *Proceedings of Hydraulic Engineering*, 45:727–732. 12, 13, 84

Tal, M. and Paola, C. (2010). Effects of vegetation on channel morphodynamics: results and insights from laboratory experiments. *Earth Surface Processes and Landforms*, 35(9):1014–1028. 3, 13

Talmon, A., Struiksma, N., and Van Mierlo, M. (1995). Laboratory measurements of the direction of sediment transport on transverse alluvial-bed slopes. *Journal of Hydraulic Research*, 33(4):495–517. 26, 27, 58, 88, 92, 135, 138, 139

Tassi, P., Bokhove, O., and Vionnet, C. (2007). Space discontinuous Galerkin method for shallow water flows kinetic and HLLC flux, and potential vorticity generation. *Advances in water resources*, 30(4):998–1015. 71

Tassi, P., El-Kadi Abderrezzak, K., Claude, N., Hervouet, J.-M., Ata, R., Mattia, F., Wang, D., Magnier, B., and Zhang, Q. (2013). Simulation numérique des structures morphodynamiques (barres) dans un milieu fluvial. Technical report, EDF R&D, LNHE. Note-H-P74-2013-04062-FR. 15, 16

Tassi, P., Villaret, C., Van, L., and van Bang, D. (2015). *Reference manual Sisyphe 7.1*. EDF R&D, LNHE-LHSV, 6 Quai Watier, 78401 Chatou cedex. 16

Temmerman, S., Bouma, T., Govers, G., Wang, Z., De Vries, M., and Herman, P. (2005). Impact of vegetation on flow routing and sedimentation patterns: Three-dimensional modeling for a tidal marsh. *Journal of Geophysical Research: Earth Surface*, 110(F4):n/a – n/a. 13

Tockner, K., Uehlinger, U., and Robinson, C. T. (2008). *Rivers of Europe*, volume 1. Elsevier. 132

Tonina, D. and Buffington, J. M. (2007). Hyporheic exchange in gravel bed rivers with pool-riffle morphology: Laboratory experiments and three-dimensional modeling. *Water Resources Research*, 43(1):1–16. 84

Toro-Escobar, C. M., Paola, C., Parker, G., Wilcock, P. R., and Southard, J. B. (2000). Experiments on downstream fining of gravel. II: Wide and sandy runs. *Journal of Hydraulic Engineering*, 126(3):198–208. 12, 45, 84, 108

Tritthart, M., Liedermann, M., Schober, B., and Habersack, H. (2011a). Non-uniformity and layering in sediment transport modelling 2: river application. *Journal of Hydraulic Research*, 49(3):335–344. 12, 84

Tritthart, M., Schober, B., and Habersack, H. (2011b). Non-uniformity and layering in sediment transport modelling 1: flume simulations. *Journal of Hydraulic research*, 49(3):325–334. 12, 84

Tubino, M. (1991). Growth of alternate bars in unsteady flow. *Water Resources Research*, 27(1):37–52. 9

Tubino, M., Repetto, R., and Zolezzi, G. (1999). Free bars in rivers. *Journal of Hydraulic Research*, 37(6):759–775. 4, 7, 111

Tubino, M. and Seminara, G. (1990). Free-forced interactions in developing meanders and suppression of free bars. *Journal of Fluid Mechanics*, 214:131–159. 4, 5, 13, 84

Van der Mark, C. and Blom, A. (2007). A new and widely applicable tool for determining the geometric properties of bedforms. *Enschede, The Netherlands. University of Twente*, n/a:1–48. 34

Van der Meer, C., Mosselman, E., Sloff, C., Jagers, B., Zolezzi, G., and Tubino, M. (2011). Numerical simulations of upstream and downstream overdeepening. In *RCEM 2011: Proceedings of the 7th IAHR Symposium of River, Coastal and Estuarine Morphodynamics, Beijing, China, 6-8 September 2011*. Citeseer. 26, 58, 88, 135

van Maren, D. S. and Cronin, K. (2016). Uncertainty in complex three-dimensional sediment transport models: equifinality in a model application of the Ems Estuary, the Netherlands. *Ocean Dynamics*, 66(12):1665–1679. 175

Van Rijn, L. C. (1984). Sediment transport, part III: bed forms and alluvial roughness. *Journal of hydraulic engineering*, 110(12):1733–1754. 134, 158, 175

Vanzo, D., Siviglia, A., Zolezzi, G., Stecca, G., and Tubino, M. (2011). Interaction between steady and migrating bars in straight channels. In *RCEM 2011*. 15, 110

Venditti, J., Dietrich, W., Nelson, P., Wydzga, M., Fadde, J., and Sklar, L. (2010). Effect of sediment pulse grain size on sediment transport rates and bed mobility in gravel bed rivers. *Journal of Geophysical Research: Earth Surface*, 115(F3):1–11. 9

Venditti, J., Nelson, P., Minear, J., Wooster, J., and Dietrich, W. (2012). Alternate bar response to sediment supply termination. *Journal of Geophysical Research: Earth Surface*, 117(F2):1–12. 10

Vionnet, C. A., Tassi, P. A., and Martin Vide, J. P. (2004). Estimates of flow resistance and eddy viscosity coefficients for 2D modelling on vegetated floodplains. *Hydrological Processes*, 18(15):2907–2926. 137

Viparelli, E., Blom, A., and Moreira, R. R. H. (2017). *Modeling Stratigraphy-Based Gravel-Bed River Morphodynamics*, chapter Modeling Stratigraphy-Based Gravel-Bed River Morphodynamics, pages 609–637. John Wiley & Sons, Ltd. 34, 35, 56, 86, 97, 174

Viparelli, E., Sequeiros, O. E., Cantelli, A., Wilcock, P. R., and Parker, G. (2010). River morphodynamics with creation/consumption of grain size stratigraphy 2: numerical model. *Journal of Hydraulic Research*, 48(6):727–741. xii, 36, 288

Vreugdenhil, C. B. (2013). *Numerical methods for shallow-water flow*, volume 13. Springer Science & Business Media. 18, 25, 57, 85, 134

Wang, D., Tassi, P., El Kadi Abderrezzak, K., Mendoza, A., Abad, J., and Langendoen, E. J. (2014). 2D and 3D numerical simulations of morphodynamics structures in large-amplitude meanders. *River Flow 2014*, 1:1105–1111. 16

Weiyan, T. (1992). *Shallow Water Hydrodynamics: Mathematical Theory and Numerical Solution for a Two-dimensional System of Shallow Water Equations*. Number vol. 55 in Elsevier oceanography series. Water & Power Press. 18, 25, 57, 85, 134

Whiting, P. J. and Dietrich, W. E. (1993). Experimental constraints on bar migration through bends: Implications for meander wavelength selection. *Water Resources Research*, 29(4):1091–1102. 8, 131

Whiting, P. J., Dietrich, W. E., Leopold, L. B., Drake, T. G., and Shreve, R. L. (1988). Bedload sheets in heterogeneous sediment. *Geology*, 16(2):105–108. 11

Wilcock, P. R. and Crowe, J. C. (2003). Surface-based transport model for mixed-size sediment. *Journal of Hydraulic Engineering*, 129(2):120–128. vii, 11, 24, 26, 28, 29, 31, 32, 45, 49, 58, 87, 103, 135, 158, 167, 173

Wilcock, P. R. and McArdell, B. W. (1993). Surface-based fractional transport rates: Mobilization thresholds and partial transport of a sand-gravel sediment. *Water Resources Research*, 29(4):1297–1312. 45

Wintenberger, C. L., Rodrigues, S., Bréhéret, J.-G., and Villar, M. (2015). Fluvial islands: First stage of development from nonmigrating (forced) bars and woody-vegetation interactions. *Geomorphology*, 246:305–320. 9, 13, 84, 129, 131

Wintenberger, C. L., Rodrigues, S., Jugé, P., and Villar, M. (2017). Survie des semis de ligneux pionniers dans les lits fluviaux: approche in et ex situ des facteurs de contrôle abiotiques et biologiques des espèces Populus nigra et Salix alba. *Géomorphologie: relief, processus, environnement*, 23(3):233–252. 13

Wu, F.-C., Shao, Y.-C., and Chen, Y.-C. (2011). Quantifying the forcing effect of channel width variations on free bars: Morphodynamic modeling based on characteristic dissipative Galerkin scheme. *Journal of Geophysical Research: Earth Surface*, 116(F3):5717–5734. xi, 8, 131

Wu, F.-C. and Yang, K.-H. (2004). A stochastic partial transport model for mixed-size sediment: Application to assessment of fractional mobility. *Water Resources Research*, 40(4):1–12. 28

Wu, F.-C. and Yeh, T.-H. (2005). Forced bars induced by variations of channel width: Implications for incipient bifurcation. *Journal of Geophysical Research: Earth Surface*, 110(F2):1–22. 8, 129, 131

Wu, W. (2004). Depth-averaged two-dimensional numerical modeling of unsteady flow and nonuniform sediment transport in open channels. *Journal of hydraulic engineering*, 130(10):1013–1024. 12, 84

Yalin, M. S. (2017). *Fluvial processes*. CRC Press. 5

Zen, S., Zolezzi, G., and Tubino, M. (2014). A theoretical analysis of river bars stability under changing channel width. *Advances in Geosciences*, 39(39):27–35. 7, 131

Zolezzi, G. and Seminara, G. (2001). Downstream and upstream influence in river meandering. Part 1. General theory and application to overdeepening. *Journal of Fluid Mechanics*, 438:183–211. 26, 56, 58, 88, 135

Appendices

APPENDIX A

NUMERICAL MODELLING OF THE SECONDARY CURRENT AND THE INFLUENCE OF HYDROLOGY ON MORPHODYNAMICS OF BARS IN A CHANNEL EXPANSION/CONTRACTION, LOIRE RIVER, FRANCE

Numerical modelling of the secondary current and the influence of hydrology on morphodynamics of bars in a channel expansion/contraction, Loire River, France

Jiaze Li, Florian Cordier, Nicolas Claude, Pablo Tassi

September 24, 2018

Abstract

In this study, two dimensional and three dimensional hydrodynamic models are used to simulate to better understand the secondary flow structures and a series of different water discharges are applied with the 2d morphodynamic model to investigate the morphological evolution of bars presented in a reach of the Loire river corresponding in a zone of contraction/expansion. Comparisons of hydrodynamic models are performed on several hydraulic variables including the primary and secondary currents, the magnitude and direction of flow velocity vectors, the bed shear stresses. The results of comparison show a good consistence between 3d model, 2d model with and without secondary current corrections. Secondary currents have therefore no significant effect in this study site. The results of morphodynamic model show that it tends to form the forced bars and the morphological evolution reaches more quickly the quasi-stationary station under high flow discharge. Inversely, the free migrating bars are formed under low flow discharge due to the highly instability of flow structure.

1 Introduction

Alluvial bars are present in the majority of sandy and gravel bed rivers (Claude et al. [12]). The height and width of these river bed forms are respectively of the same order of magnitude as the water depth and the river width (Jackson [26]). Bars interact with the flows and sediment transport, and they influence strongly the morphological evolution of rivers, with consequences for navigation, water intakes and infrastructure (Bridge [6], Claude [11], Claude et al. [12], Jaballah et al. [25]).

Two different type of bars can be classified: free bars and forced bars (Seminara and Tubino [39]). Free bars are induced by the instability of turbulent flows over an erodible bed (Callander [8], Colombini et al. [14], Seminara and Tubino [39], Tubino [44], Claude et al. [12]). Forced bars are developed under the influence of planimetric constraints such as curvature and width variations of a channel, and are quasi-stationary (Claude et al. [12]). The bars modify the flow structure imposed by the channel width variations and promote the nonuniformity of the flow at the channel's scale (Claude et al. [12]). Hybrid bars form on morphodynamically unstable river beds, likes free bars, but the presence of a permanent flow deformation, induced by an external factor (forcing), such as a change in channel geometry, fixes their location. For this reason, hybrid bars do not migrate and their wavelength corresponds to the one of zero-celerity free bars, which is generally 2 to 3 times longer than wavelength of migrating bars. (Crosato et al. [15], Duró et al. [16], Rodrigues et al. [37])

In fluvial reaches, flow directions are rarely distributed uniformly along a given cross section, due to the presence of bars or riverbank geometrical changes, such as in areas of confluence, bifurcation, or sudden change of the channel width (Claude et al. [12]). In a curved channel, the flow experiences a radial acceleration and the centrifugal forces acts in proportion to the mean velocity (Wang and Tassi [47]). The flow on the surface is directed to the outer bank and it is contrary at shallower depths. This imbalance creates a cross-stream component of flow, further inducing the secondary (or helical, spiral) flow pattern. Two-dimensional models have been widely used for shallow water. Nevertheless, these models fare hardly

in channels with significant curvature, due to that the vertical velocity distribution is nonuniform and the 2d model can not account for the effects of helical secondary flow. For that the lateral component of flow can be an important influence on morphological evolution, it is often necessary to correct velocity vectors to represent the primary (parallel to the mean direction vectors) and secondary (perpendicular to the mean direction vector) velocities (McLelland et al. [30]). Therefore, secondary flow corrections for depth-averaged models have been well documented in the literature by Bernard and Schneider [3], Finnie et al. [19], Wang and Tassi [47]. In the Telemac-Mascaret modelling system, the approach proposed by Bernard and Schneider [3] have been implemented. It is based on the solution of an empirical transport equation for streamwise vorticity that mimics the depth-averaged influence of secondary flows (Wang and Tassi [47]). Several numerical simulations have been performed with and without accounting secondary currents corrections, which are in agreement with experimental results (Bernard and Schneider [3], Finnie et al. [19], Wang and Tassi [47]).

Besides, many studies have been investigated on the relationship between hydrology and the morphological evolution of rivers braided river (Mosley [34], Mosley [33], Marti and Bezzola [29], Milan et al. [32], Surian et al. [42], Welber et al. [49]) and multi-channels rivers (Coleman [13], Wathen and Hoey [48], Ham and Church [21], Eaton and Lapointe [17], Chappell et al. [9]). Nevertheless, few studies have focused on the morphological evolution in a channel expansion/contraction by distinguishing the effect of floods and periods of low water within the expansion/contraction zone. There is no many information on the relationships between hydrological variations (floods, periods of low water), the morphological configuration of the bars (alternate, transverse) and the erosion / deposit sediment processes (quantification and spatialization).

The objective of the present work is divided in two parts. 1) is to evaluate the importance of three dimensional effects leading to the formation of secondary flows in a reach of the Loire river corresponding to a zone of channel contraction/expansion with presence of bars (Figure 1). To this goal, 2d hydrodynamic models with and without secondary currents formulations are calibrated on the site of Brehemont on the Loire River from field observation. The validated friction coefficient is then used to build a Telemac-3d model which is compared with 2d models in order to further identify the existence of secondary currents in the study site. Several hydraulic variables including the primary and secondary currents, the magnitude and direction of flow velocity vectors, and the bed shear stresses are performed and compared in the 2d and 3d models. 2) is to investigate influence of different hydrological conditions on morphodynamics of bars. a series of water discharges are chosen according to the hydrogramme observed over the past 25 years. The altitudinal evolution of riverbed, the solid discharge and the total volume of eroded/deposited sediment are calculated

A description of the materials and methods used for this study is given in Section 2, which includes the filed measurements, the formulation of the mathematical and numerical model, the calculation of primary, secondary velocity, bed shear stress estimation and characterization of the different hydrological conditions. In section 3.1, the numerical results of 2d and 3d hydrodynamic models, the comparison of hydraulic variables near the river bottom are detailed. Then, on the basis of these results, a discussion is held on the importance of secondary current effects in this study site, uncertainty of field measurements and study limitation. In section 3.2, the numerical results of topography of riverbed are shown and the discussion on morphological evolution are given. The general conclusions of this work are given in Section 4.

2 Materials and methods

2.1 Presentation of the Loire River

The 1012 km long Loire river is the largest river in France, draining a catchment area of 117,500 km^2. The study site (Figure 1) is located in the middle reach of the Loire river at 790 km downstream from the source, in the vicinity of the village of Bréhémont (47°17′43.31″N, 0°20′33.80″E). In this region, the Loire river presents a succession of single to multiple-channel patterns, depicted by the occurence of alternate, transverse, middle and higher mode bars in the main channel. The riverbed also presents secondary channels which are connected and islands (i.e. vegetated central or higher mode bars) which are partially

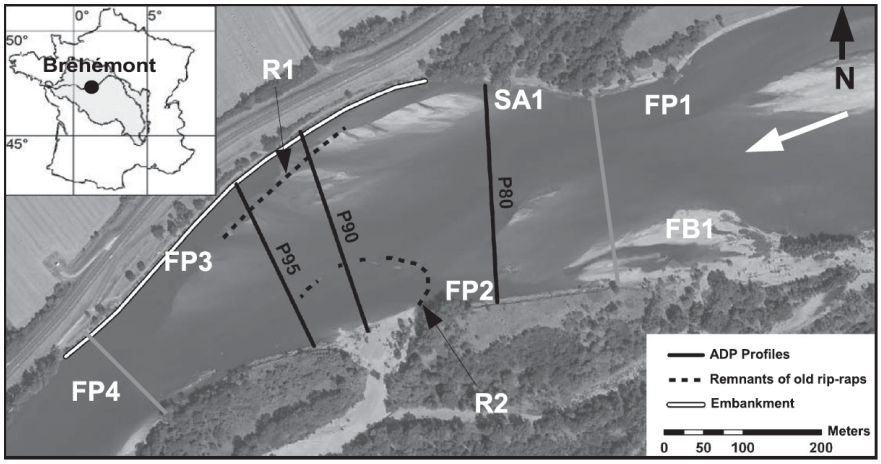


Figure 1: Location of the ADP profiles, old rip-raps and embankment, and forced bar-pool topography, where the gray lines delimit the area of interest (adapted from Claude et al. [12]). The white arrow denotes the flow direction. FB = Forced Bar, FP = Forced Pool, R = Rip-rap, SA = Sedimentation Area.

submerged during flooding events.

The study reach corresponds to a channel widening followed by a contraction area. The presence of embankements on the right riverbank sustaining the main channel curvature, the submerged stretches of rip-rap corresponding to vestiges of ancient bank protection, the longitudinal channel widths variations (from 175 to 300 m) and the connexion with a secondary channel (activated for discharges upper than 700 m^3/s) generate a permanent geometrical forcing.

The bed material is mainly composed of a mixture of siliceous sand and gravel and is highly mobile, with a Shields number of approx. 0.10 when the flowrate is equal to 386 m^3/s, with respect to the mean flowrate which is around 430 m^3/s. The sediment diameters d_{50} and d_{90} (corresponding to the 50^{th} and 90^{th} centile of the grain size distribution [m]) are equal to 1.33 and 5.18 mm, respectively.

2.2 Field measurements

Daily riverbed topography records of 0.5 m resolution using multibeam echosoundings are available, as well as longitudinal water free surface profiles. The spatial distribution of velocities has been monitored on three cross-sections (namely P80, P90 and P95, Figure 1) using an ADP (Acoustic Doppler Profiler). Upstream and downstream of the area of interest, the riverbed and secondary channels topography are obtained by linear interpolation of cross-sections measured in 2009 which are regularly spaced of 60 m along a distance of 2km. Lidar data of 25 cm resolution from 2004 is used to reconstruct the floodplain and riverbanks.

Three field measurements corresponding to the daily monitoring on 19 June 2010 (386 m^3/s), on 22 June 2010 (1030 m^3/s) and on 11 December 2010 (1950 m^3/s) are used for this study (Figure 2). More details are given in Claude et al. [12].

2.3 Mathematical and numerical model

The morphodynamic model presents two components: a hydrodynamic module and and a morphodynamic module.

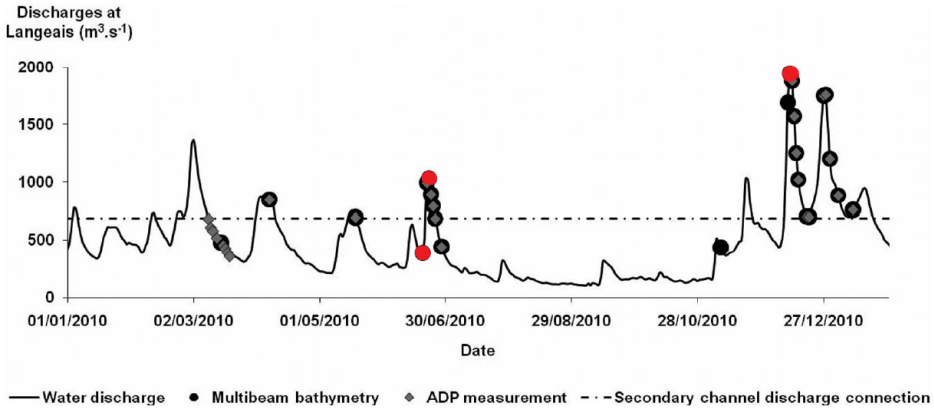


Figure 2: Distribution of the measurements on the hydrograph of the Langeais gauging station (4.5 km upstream from the study site) Claude et al. [12]. The red points denote three field measurements used in this study.

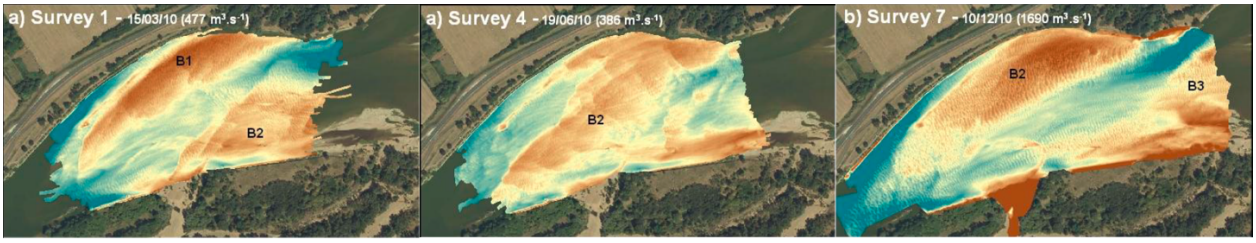


Figure 3: Bar configurations: alternate bars, transverse bar and lateral bar.

2.3.1 Hydrodynamic module

For better understand the importance of secondary currents and choose a suitable hydrodynamic model, three different hydrodynamic models are set-up for this study: (1) a two-dimensional hydrodynamic model without secondary current corrections, (2) a two-dimensional hydrodynamic model with secondary current corrections, and a (3) three-dimensional hydrodynamic model.

2d hydrodynamic model without secondary current corrections The two-dimensional hydrodynamic model is based on the solution of the shallow-water equations (SWE):

$$\begin{cases} \partial_t h + \vec{u}\cdot\nabla(h) + h\nabla\cdot(\vec{u}) = 0 \\ \partial_t u + \vec{u}\cdot\nabla(u) = -g\partial_x z_f - gS_{f,x} + h^{-1}\nabla\cdot(h\nu_t\nabla u) \\ \partial_t v + \vec{u}\cdot\nabla(v) = -g\partial_y z_f - gS_{f,y} + h^{-1}\nabla\cdot(h\nu_t\nabla v) \end{cases} , \tag{1}$$

where t (s) is the time, $\partial_t = \partial/\partial_t$, $\nabla = (\partial_x, \partial_y)$ is the gradient vector field, g= 9.81 m.s^{-2} is the acceleration of gravity, h (m) is the water depth, $z_f = z_b + h$ (m) is the free surface elevation, z_b (m) the elevation of the bed topography, $\vec{u} = (u, v)$ (m/s) is the depth-averaged flow velocity vector with u (resp. v) (m/s) the component along the Cartesian x-axis (resp. y-axis) direction respectively, with $|\vec{u}|$ (m/s) the module of $\vec{u}$, $S_{f,x}$ (resp. $S_{f,y}$) corresponds to the components of the friction law $\vec{S_f}$ [-] along the Cartesian $x-$axis (resp. $y-$axis), and ν_t (m^2/s) is the turbulent eddy viscosity term that models the so-called Reynold stresses and the differential dispersion terms originated from the lack of vertical uniformity of the horizontal velocity field. The friction law $\vec{S_f}$ [-] of Chézy is given as follow:

$$\vec{S_f} = (S_{f,x}, S_{f,y}) = \frac{\vec{u}|\vec{u}|}{C^2 h} , \tag{2}$$

where $S_{f,x}$ and $S_{f,y}$ correspond to the components of the friction law $\vec{S_f}$ [-] along the longitudinal $x-$axis and transversal $y-$axis direction respectively and C [m$^{1/2}$/s] corresponds to the Chézy friction coefficient. The formula 3 is used to calculate the equivalent friction coefficient of Chézy denoted $C_f = g/C^2$ [-] as a function of the equivalent roughness height of the bed denoted with k_s [m]:

$$C = 2\Big[\log\Big(\frac{30h}{ek_s}\Big)/\kappa\Big]^{-2} , \tag{3}$$

where κ is the von Kármán coefficient (= 0.40 for clear waters) and e is the base of the natural logarithm.

2d hydrodynamic model with secondary current corrections The secondary currents processes in the Telemac-Mascaret Modelling system are based on the formulation of Bernard and Schneider [3]. The correction for secondary flow effects on the depth-averaged hydrodynamics field can be accounted by first solving the shallow water equations for velocity and depth without the secondary flow correction (Equation 1), then solving transport equation of vorticity:

$$\frac{\partial\Omega}{\partial t} + u\frac{\partial\Omega}{\partial x} + v\frac{\partial\Omega}{\partial y} = \frac{A_s\sqrt{C_f}|\vec{u}|^2}{Rh(1+9h^2/R^2)} - D_s\sqrt{C_f}\Omega\frac{|\vec{u}|}{h} + \frac{1}{h}\nabla\cdot(\nu_t h\nabla\Omega) \tag{4}$$

where Ω is the streamwise vorticity, ρ is the water density, A_s, D_s are empirical coefficients that determine the rate of vorticity production and dissipation, respectively. h is the water depth and $\vec{u}$ is the depth-averaged velocity vector ($\bar{u} + \bar{v}$). R is the local radius of curvature:

$$R = \frac{|\vec{u}|^3}{uv(v_y - u_x) + u^2 v_x - v^2 u_y} \tag{5}$$

where u_i is i-component of velocity u and v_i is i-component of velocity v. The solution of equation 4 allows the calculation of the streamwise stresses that result from the deviation of velocity from the depth-averaged velocity:

$$\tau_s = \rho h|\vec{u}|\Omega\sqrt{C_f} \tag{6}$$

With above equations, the accelerations induced by secondary currents are computed as follows in a Cartesian coordinate system:

$$S = (S_x, S_y) \approx \rho^{-1} \frac{\vec{u}}{|\vec{u}|} \left[\vec{n} \cdot \nabla(h\tau_s) + \frac{2h\tau_s}{r} \right] \tag{7}$$

The normal derivative of the depth-averaged secondary shear stress is calculated as:

$$\vec{n} \cdot \nabla(h\tau_s) = \frac{v(h\tau_s)_x - u(h\tau_s)_y}{|\vec{u}|} \tag{8}$$

where $\vec{n}$ is a unit vector normal to the depth-averaged velocity vector $\vec{u}$. The subscripts x and y = derivatives.

Finally by replacing the results from equation 7 into the shallow water equations, the shallow water equation with secondary flow correction can be solved. More details are given in Wang and Tassi [47]. After a sensibility test of the empirical coefficients (Appendix A), A_s is set equal to 7.071 and D_s is set equal to 0.5.

3d hydrodynamic model Telemac-3d solves the 3D Navier-Stokes equations with a finite element discretization under a non-hydrostatic approximation:

$$\begin{cases} \frac{\partial U}{\partial x} + \frac{\partial V}{\partial y} + \frac{\partial W}{\partial z} = 0 \\ \frac{\partial U}{\partial t} + U\frac{\partial U}{\partial x} + V\frac{\partial U}{\partial y} + W\frac{\partial U}{\partial z} = -\frac{1}{\rho}\frac{\partial p}{\partial x} + \nu\nabla^2(U) + F_x \\ \frac{\partial V}{\partial t} + U\frac{\partial V}{\partial x} + V\frac{\partial V}{\partial y} + W\frac{\partial V}{\partial z} = -\frac{1}{\rho}\frac{\partial p}{\partial y} + \nu\nabla^2(V) + F_y \\ \frac{\partial W}{\partial t} + U\frac{\partial W}{\partial x} + V\frac{\partial W}{\partial y} + W\frac{\partial W}{\partial z} = -\frac{1}{\rho}\frac{\partial p}{\partial z} - g + \nu\nabla^2(W) + F_z \end{cases} , \tag{9}$$

where U, V, W (m/s) are three-dimensional components of velocity along the Cartesian $x-$axis (resp. $y-$axis, $z-$axis) , p (pa) is pressure, ν (m^2/s) is kinematic viscosity and F_x, F_y, F_z are source terms.

The non-hydrostatic approximation is based on the pressure decomposition into hydrostatic and hydrodynamic parts, allowing an accurate computation of the vertical velocity (Magnier et al. [28]). Turbulent stresses and turbulent fluxes are modeled by using turbulent viscosity and turbulent gradient diffusion hypothesis, which respectively introduce eddy viscosity and eddy diffusivity. The standard $k-\epsilon$ turbulence model is used. The 3D finite element mesh is obtained by first diving a 2d domain with non-overlapping linear triangles and then by extruding each triangle along the vertical direction into linear prismatic columns that exactly fit the bottom and the free-surface. 5, 8 and 15 horizontal layers are used in this study. A homogeneous distribution of levels is performed in the vertical direction (classical sigma transformation). The height of levels varies depending on the water depth.

2.3.2 Morphodynamic module

The morphodynamic module is based on the Exner equation (Exner [18], Garcia [20]). In case of non-uniform sediment, the Exner equation is applied to every size fraction of sediment in which the mixture is subdivided. The following procedure is adopted: *i*) the sediment mixture is discretized into sediment fractions, and for each fraction the representative sediment diameter is given, *ii*) the bedload transport capacity equation and the mass conservation formula are applied for each separate fraction of sediment.

The solution for sediment mass conservation is based on the mathematical concept proposed by Hirano [24], who developed a continuity model for the vertical sorting of sediment. The method is based on the decomposition of the bed into a homogeneous top layer, called *active layer*, and an unchanging homogeneous *substrate* (Church and Haschenburger [10]). The active layer is a fully mixed layer, defined as the layer where all the bed fluctuations are concentrated (Blanpain [4], Stecca et al. [41]). Following Hirano [24]'s concept, the bed is discretized in the vertical direction as follows:

$$z_b = \eta_{a:1} + L_a \quad , \tag{10}$$

where $\eta_{a:1}$ [m] denotes the absolute elevation of the interface between the active layer and the substrate, and L_a [m] corresponds to the active layer thickness. The sediment mass continuity equation is given as follows Parker et al. [35]:

$$L_a \partial_t F_{a,i} + \left[F_{a,i} - \mathcal{F}_{a:1,i}\right] \underbrace{\partial_t L_a}_{=0} = \frac{1}{\epsilon_0}\left[\mathcal{F}_{a:1,i} \nabla \cdot \vec{q_b} - \nabla \cdot \vec{q_{b,i}}\right] \quad , \tag{11}$$

where $\partial_t L_a = 0$ because the active layer thickness is assumed to be constant during the whole simulation, $F_{a,i}$ is the volume fraction content of the i^{th} size fraction in the active layer and $\mathcal{F}_{a:1,i}$ is the volume fraction content of the i^{th} size fraction in the interface separating the active layer and the substrate, $\vec{q_b} = (q_{b,x}, q_{b,y}) = q_b(\cos\alpha, \sin\alpha)$ [m^2/s] corresponds to the total volumetric bedload solid discharge per unit of width without pores, with components $q_{b,x}$ and $q_{b,y}$ along the $x-$ and $y-$ axis directions respectively, $\vec{q_{b,i}} = (q_{b,i,x}, q_{b,i,y}) = q_{b,i}(\cos\alpha_i, \sin\alpha_i)$ [m^2/s] corresponds to the fractional volumetric bedload solid discharge per unit of width without pores of the i^{th} size fraction, $\epsilon_0 = (1 - P_0)$ with P_0 the bed porosity, α is the angle between the bedload and the x-axis direction and α_i the angle between the transport rate of the i^{th} size fraction and the x-axis direction. In the current model, the vertical sorting of sediment is made possible by discretizing the substrate into several sublayers (Blom [5]), where the fraction volume content of i^{th} size fraction of sediment in the k^{th} sublayer is denoted $F_{k,i}$. The implementation of the above equation requires the specification of the active layer and the sublayer thicknesses, the interfacial exchange fractions and the number of sublayers (Viparelli et al. [46]). Vertical fluxes of sediment are computed following the formulation of Hirano [24]:

$$\mathcal{F}_{a:1,i} = \begin{cases} F_{a,i} & \text{if } \partial_t z_b > 0 \\ F_{1,i} & \text{if } \partial_t z_b < 0 \end{cases} \tag{12}$$

where $F_{1,i}$ corresponds to the fraction volume content of i^{th} size fraction of sediment in the first sublayer.

It is of key interest to accurately estimate the sediment transport in natural rivers, since bar evolution (*i.e.* armor formation and *break-up*) depends on fractional transport rates estimation. Therefore, the authors proposed to use the model of Wilcock and Crowe [51](WC-2003), which is interesting in the way that *i*) it is based on surface investigations and is particularly adapted for the prediction of transient conditions of bed armoring and scenarios of bed aggradation/degradation, *ii*) it considers the full size distribution of the bed surface (from finest sands to coarsest gravels), *iii*) it was calibrated under a wide range of water discharges and sediment mixtures, *iv*) the hiding function has been designed to resolve discrepancies observed from previous experiments including the hiding-exposure effect of sand content on gravel transport for weak to high values of sand contents in the bulk, and *v*) it has already showed efficiency when applied for morphodynamics modelling An et al. [1]. For each i^{th} size fraction, the magnitude of the fractional transport rate without gravitational effects $q_{b0,i} = |\vec{q_{b0,i}}|$ [m^2/s] is estimated using the bedload capacity formula of Wilcock and Crowe [51]:

$$W_i^* = f(\tau_b/\tau_{r,i}) = \frac{\Delta_s g q_{b0,i}}{F_{a,i} u_*^3} \quad , \tag{13}$$

where W_i^* [-] corresponds to the dimensionless transport rate for the i^{th} size fraction of sediment, $\Delta_s = \frac{\rho_s}{\rho} - 1$ [-] is the relative submerged sediment density, with ρ [kg/m^3] the water density and ρ_s the sediment density [kg/m^3], τ_b [Pa] is the bed shear stress, $\tau_{r,i}$ [Pa] the reference shear stress of the i^{th} size fraction defined as the value of τ_b at which $W_i^* = 0.002$ and $u_* = \sqrt{\tau_b/\rho}$ [m/s] the shear velocity (also called friction velocity). The transport function of WC-2003 is defined as follows:

$$W_i^* = \begin{cases} 0.002{\Phi_i}^{7.5} & \text{for } \Phi_i < 1.35 \\ 14\left(1 - \frac{0.894}{{\Phi_i}^{0.5}}\right)^{4.5} & \text{for } \Phi_i \geq 1.35 \end{cases} \quad , \tag{14}$$

where the ratio $\Phi_i = \tau_b/\tau_{r,i}$ is incorrectly referred to as Φ in the literature Wilcock and Crowe [51], Recking et al. [36].

A hiding-exposure function is defined to estimate $\tau_{r,i}$ so that the sediment transport rates are lowered for finer fractions (i.e. increase of $\tau_{r,i}$) and increased for coarser material (i.e. decrease of $\tau_{r,i}$). This is accounted in the model as follows:

$$\frac{\tau_{r,i}}{\tau_{r,m}} = \left(\frac{d_i}{d_{s,m}}\right)^{b_i} \quad \text{with} \quad b_i = \frac{0.67}{1 + \exp\left(1.5 - \frac{d_i}{d_{s,m}}\right)} \quad , \tag{15}$$

where d_i [m] corresponds to the sediment diameter of the i^{th} size fraction, $d_{s,m}$ [m] is the mean sediment diameter of surface, $\tau_{r,m}$ [Pa] is the reference shear stress of the mean sediment diameter of surface and b_i is the power-coefficient of the hiding-exposure function which is incorrectly referred to as b in the literature. $\tau_{r,m}$ is computed as a function of the dimensionless median reference shear stress of bed surface ${\tau^*}_{r,m}$ such that ${\tau^*}_{r,m} = \frac{\tau_{r,m}}{\Delta_s \rho g d_{s,m}}$ where ${\tau^*}_{r,m} = 0.021 + 0.015\exp[-20F_s]$, with F_s the fraction volume content of sand at the bed surface [-].

By using independent sediment transport measurements, several authors Recking et al. [e.g. 36], An et al. [e.g. 1] have showed that the performance of the formula of WC-2003 could be improved by modifying one or several parameters. In this work, the authors proposed to calibrate the sediment transport formula by estimating the fractional transport rates of sediment with multiplying ${W_i}^*$ by a dimensionless coefficient called α_b.

Sediment transport capacity formulas are generally fitted against experimental data under the assumption of a flat bed (neglecting the gravitational effects). Natural riverbeds may show milder or steeper slopes due to the presence of dunes, ripples, steps, or pools in the longitudinal direction and curves in the transverse direction. As a result, gravity effects increase the bedload transport in downslope sections and lessen the movement of particles in upslope directions. Several formulas have been proposed to take into account the bed slope effect on *i*) the magnitude Koch [27], Soulsby [40] and *ii*) the direction of bedload transport Koch [27], Talmon et al. [43]. The correction of bedload magnitude is modelled with the formula proposed by Koch [27], where the fractional transport rate $q_{b0,i}$ is modified as a function of the bed slope degree with respect to the current direction:

$$q_{b,i} = q_{b0,i}\Big(1 - \beta_1 \partial_s z_b\Big) = q_{b0,i}\Big[1 - \beta_1\big(\partial_x z_b \cos\delta + \partial_y z_b \sin\delta\big)\Big] \quad , \tag{16}$$

where β_1 is an empirical coefficient accounting for the streamwise bed slope effect, δ is the angle between the current and the x-axis direction, and s the coordinate along the current direction. The bedslope effect is similar to a diffusion term in the bed evolution equation Van der Meer et al. [45] and may smooth the bed topography and prevent from numerical instabilities Zolezzi and Seminara [52], Cabrit [7]. The correction of bedload direction is given by the relation of Bendegom [2]:

$$\tan\alpha_i = \frac{q_{b,i,n}}{q_{b,i,s}} = \frac{\sin\delta - T_i \partial_y z_b}{\cos\delta - T_i \partial_x z_b} \quad , \tag{17}$$

where α_i is the angle between the sediment transport vector of the i^{th} size fraction of sediment and x-axis direction which will deviate from the bed shear stress vector due to gravity effects, $q_{b,i,n}$ and $q_{b,i,s}$ correspond to the bedload magnitudes along the normal to the current direction and the streamwise direction, respectively, and where the coefficient T_i is calculated as follows Talmon et al. [43]:

$$T_i = \frac{1}{\beta_2 \sqrt{\tau^*_{b,i}}} \quad , \tag{18}$$

where $\tau^*_{b,i}$ is the bed shear stress adimensionnalized by the i^{th} size fraction of sediment also known as Shields parameter and scales the gravity effects as a function of the grain diameter of the i^{th} size fraction, and β_2 is an empirical coefficient used as a calibration parameter.

The total shear stress τ [Pa] is calculated from the depth averaged flow velocity field, where $\tau = 0.5\rho C_f(u^2 + v^2)$ and C_f is equal to the sum of skin friction and bedform drag. In this study, the bed shear stress is determined as a function of the total shear stress:

$$\tau_b = \mu\tau \quad , \tag{19}$$

where $\mu = C'_f/C_f$ is the friction factor and C'_f [-] is the equivalent Chézy coefficient only due to skin friction and is the only component acting on bedload Mendoza et al. [31]. C'_f is calculated assuming a flat bed by using the Nikuradse's formula (Equation 3), where the roughness height k'_s [m] is a function of the mean sediment diameter at the bed surface with:

$$k'_s = \alpha_{ks} \times d_{s,m} \quad , \tag{20}$$

with α_{ks} a calibration parameter. Garcia [20] summarized different values of α_{ks} measured in the field and in the laboratory ranging from 1 to 6.6.

The numerical solution of Equations 1 is based on the finite element method P_1, where the advective terms are computed with the method of the characteristics. The numerical solution of the sediment transport continuity equation (Equation 11) is performed by a procedure that combines an implicit finite element scheme and an edge-based explicit upwind advection scheme. This procedure assures mass-conservation at machine accuracy, monotonicity of tracers, copes with dry zones and is easily applicable to domain decomposition Hervouet et al. [22].

2.4 Calculation of primary and secondary components of flow velocities

The directions of the primary u_p (m/s) and secondary u_s (m/s) components of flow velocity at any point of the domain are obtained from the difference between the depth-averaged direction of the velocity and the direction of the vector at the point concerned. The components u_p and u_s are calculated as follows:

$$u_p = u\cos(\phi - \psi) \tag{21}$$

$$u_s = u\sin(\phi - \psi) \tag{22}$$

where u is the flow velocity at each vertical cell, ϕ is the orientation of the vector u with respect to y direction, and ψ is the orientation of the mean vector velocity on the vertical with respect to y direction. (Claude et al. [12], Rozovskii [38])

2.5 Bed shear stress estimation

For two-dimensional model, the total bed shear stress τ_b (pa) is calculated from the depth averaged flow velocity:

$$\tau_b = \rho C_f \frac{\sqrt{u^2 + v^2}}{2} \tag{23}$$

where τ_b is total bed shear stress (pa)

Using above method (23) is only valid for formulae relying on a depth-integrated velocity, which is not applicable in the 3d model. Due to the fact that the velocity on the solid boundaries is not zero in 3d model, the velocity is taken at a small distance Δz from the boundary, which allow us to evaluate friction velocity U_* and bed shear stress τ_b (Hervouet [23]):

$$U_* = \frac{\kappa U_{plane1}}{ln(\frac{33\Delta z}{k_s})} \tag{24}$$

$$\tau_b = \rho {U_*}^2 \tag{25}$$

where k_s (m) is Nikurade's roughness-length value, U_{plane1} (m/s) is velocity at the first point above the bottom and Δz (m/s) is altitude of this point above the bottom.

Finally, τ_b for measurements can be estimated by the law of the wall (Claude et al. [12]):

$$\tau_b = \rho \left[\frac{\kappa u}{\ln\left(\frac{z}{(z_0)_{SF}}\right)} \right]^2 \tag{26}$$

where u (m/s) is velocity measured at the first point above the bottom, z (m) is altitude measured at the first point above the bottom and $(z_0)_{ZF}$ (m) is height at which $u = 0$, taken equal to 0.095 D_{90} (Claude et al. [12], Wilcock [50]).

Period	1986 - 2011	March 2010 - January 2011	Spring	Low flows	Winter
		Survey 1 - 11	Survey 1 - 6	Survey 6 - 7	Survey 7 - 11
Q_{10}	104	123	253	110	700
Q_{50}	320	295	389	164	890
Q_{90}	924	844	780	494	1750
BFI	0.76	0.7	0.68	0.76	0.65

Figure 4:

2.6 Characterization of the different hydrological conditions

The morphological evolution of the channel in the expansion/contraction zone is mainly conditioned by the configuration and morphodynamics of the bars, and by hydrology (Claude [11]). For better investigate the influence of hydrology on the morphological evolution of bars, a series of different water discharges are applied to the numerical morphodynamic model with a duration of one year.

Figure 4 presents the values of the various hydrological parameters calculated for the last 25 years, for the whole follow-up time period monitored by Claude [11] and for each of its subdivisions periods. In order to be more representative, a series of water discharges of 150 m^3/s, 350 m^3/s, 500 m^3/s, 750 m^3/s, 1000 m^3/s, 1500 m^3/s and 2000 m^3/s are used in this study. The initial topography is chosen from the bathymetric survey realized on 15/03/2010 by Claude [11].

3 Results and discussion

The results and discussion are presented in logical sequence. The first part presents the influence and importance of secondary current by comparing the different hydrodynamic models, which is a fundamental component for the whole morphodynamic model. The second part is for the purpose of studying the influence of hydrology on the morphological evolution of bars.

3.1 Hydrodynamic - Influence and importance of secondary current

3.1.1 Model calibration and numerical results

Two-Dimensional model The 2d hydrodynamic model calibration is performed by using the values of Mean Absolute Error and Root Mean Squared Error computed along the longitudinal profiles of free surface and cross-sectional profiles of flow velocity. More details on the calibration step are given in Appendix B. Figure 5 presents a comparison of velocity profiles between field measurements and 2d hydrodynamic numerical results for different values of k_s ranging in [0.05; 0.5]m. This parameter is showed to strongly influence flow velocity (Magnier et al. [28]). Decreased roughness heights induce larger flow velocity. Furthermore, any variation of the k_s has more influence on the velocity in the midchannel than near the riverbanks.

The red solid lines (Figure 5) represent the 2d hydrodynamic model results computed with calibrated k_s (0.072 m, 0.148 m and 0.198 m for 19 June 2010, 22 June 2010 and 11 December 2010) respectively considering secondary currents effects. The numerical results are in agreement with measurements on P80. Except on 19 June 2010 near the right riverbank (Figure 5), velocities computed by numerical model are found to be smaller than measurements near the right riverbank. For all bar configurations on P90 and P95 near the right riverbank, 2d numerical model do not represent well the field measurements.

Three-Dimensional model Figure 6, 7, 8 are used to compare flow velocity profiles between field measurements and 3d hydrodynamic numerical results obtained with using 5, 8 and 15 horizontal layers. In

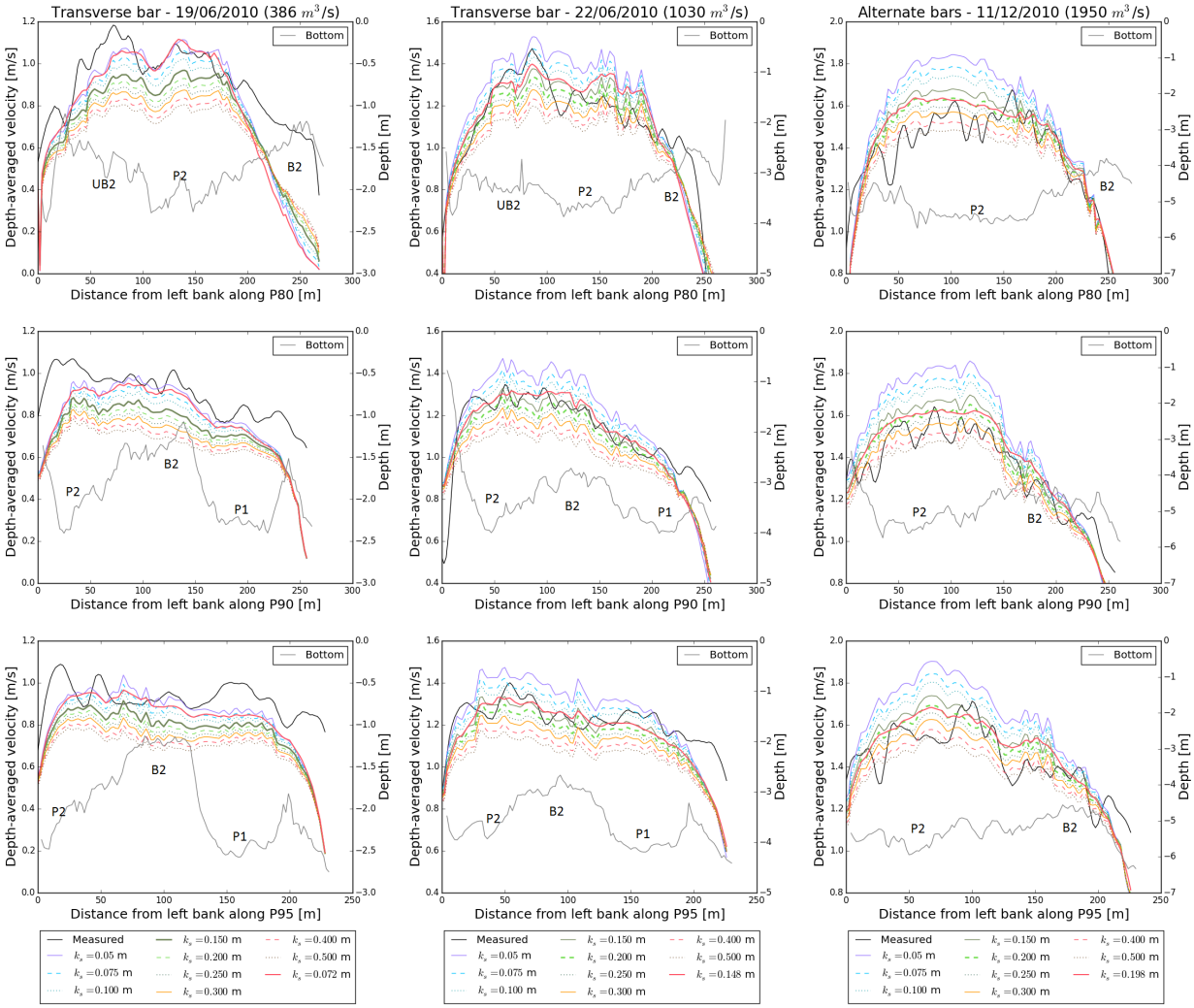


Figure 5: Cross-sectional profiles of flow velocity computed numerically with $k_s \in [0.05; 0.5]$ m and measured by Claude et al. [12]. The red solid lines correspond to the hydrodynamic model results (2d with secondary currents effect) computed with the calibrated k_s.

general, the spatial distribution of primary velocities is well represented by the 3d numerical model. The primary velocity is slightly smaller (-0.2 m/s) than filed measurement and the differences of velocity magnitude are more significant for a lower water discharge (Figure 6). For secondary velocities, the numerical results are generally twice larger than measurements but the numerical results of the vertical velocities are twice smaller than measurements. (Appendix C)

According to the general observation of field measurements of Claude et al. [12], with regard to the pattern of the secondary vectors, the vertical vectors and secondary currents, the analysis only exhibits two small structures.

Firstly, considering the alternate bars configuration on P80 (Figure 8), close to the Bar 2 located near the right bank, the velocity vectors are directed toward the right bank near the surface and dive toward the riverbed on the edge of Bar 2. For this first flow structure, due to the underestimation of vertical flow velocities, the downdraft current and the recirculation observed in situ can not be well represented accurately by the 3d hydrodynamic model.

Secondly, for all P90 and P95, between the bar and the right bank, two layers composed of large secondary velocities and small vertical velocities can fairly well be distinguished in nature. The vectors are directed toward the right bank near the surface and those near the bottom are directed toward the left bank. Unlike the field observation, the velocity vectors computed numerically are highly homogeneous along the vertical direction. They are equally composed of large secondary velocities and small vertical velocities (Figure 6, 7), whereas, with a constant direction towards the left bank, which is consistent with the vectors of field measurement near the bottom.

Outcomes from sensibility test to the horizontal discretization in 5, 8 and 15 layers show that a higher number of horizontal levels reduces the velocity magnitudes, which is reflected on the decrease of primary velocity. According to Magnier et al. [28], the refinement and re-interpolation of the meshes do not improve significantly the estimation of the velocities and the vertical velocities. In our study, using 5 horizontal levels is found to be an optimal compromise in terms of computational efficiency and results accuracy.

3.1.2 Comparison of hydraulic variables

To better understand the flow structures, differences between 2d and 3d models, several hydraulic variables including the magnitude and direction of flow velocity, the bed shear stresses are compared. The Nikuradse coefficient k_s equal to 0.072 m, 0.148 m and 0.198 m for 19 June 2010, 22 June 2010 and 11 December 2010 according to the calibration test in 2d model, and a distribution of 5 vertical planes is used for 3d model.

Flow velocities Figure 9 presents the transversal distribution of depth-averaged flow velocity magnitudes for the field measurements and numerical results. Figure 10 presents the transversal distribution of flow velocity magnitudes near the riverbed for the field measurements and 3d numerical results. In general, the numerical results are in good agreement with field measurements.

The results of 2d and 3d model are more consistent over Bar2 near the right bank on 80. Nevertheless, for P80 on 19 June 2010 (Figure 9a), the numerical results are smaller (-0.4 m/s) than field measurements over the Bar 2 near the right bank. For the same cross sectional profile on 22 June 2010 and on 11 December 2010, the numerical results are higher than field measurements near the left edge of Bar 2 and near the left bank, respectively.

Flow directions As highlighted by Claude et al. [12], the depth-averaged direction of the flow shows that the streamlines mainly follow a streamwise direction for all water stages and bar configurations. Nevertheless, the bank location and the channel width variations can influence locally the flow direction. In this study reach, a small flow divergence induced by the upstream channel expansion on P80 shows that water flow toward the right bank on the right side of the section. Similarly, the channel contraction causes a small flow convergence downstream on P95, with the outer streamlines slightly directed toward the center of the channel (Claude et al. [12]).

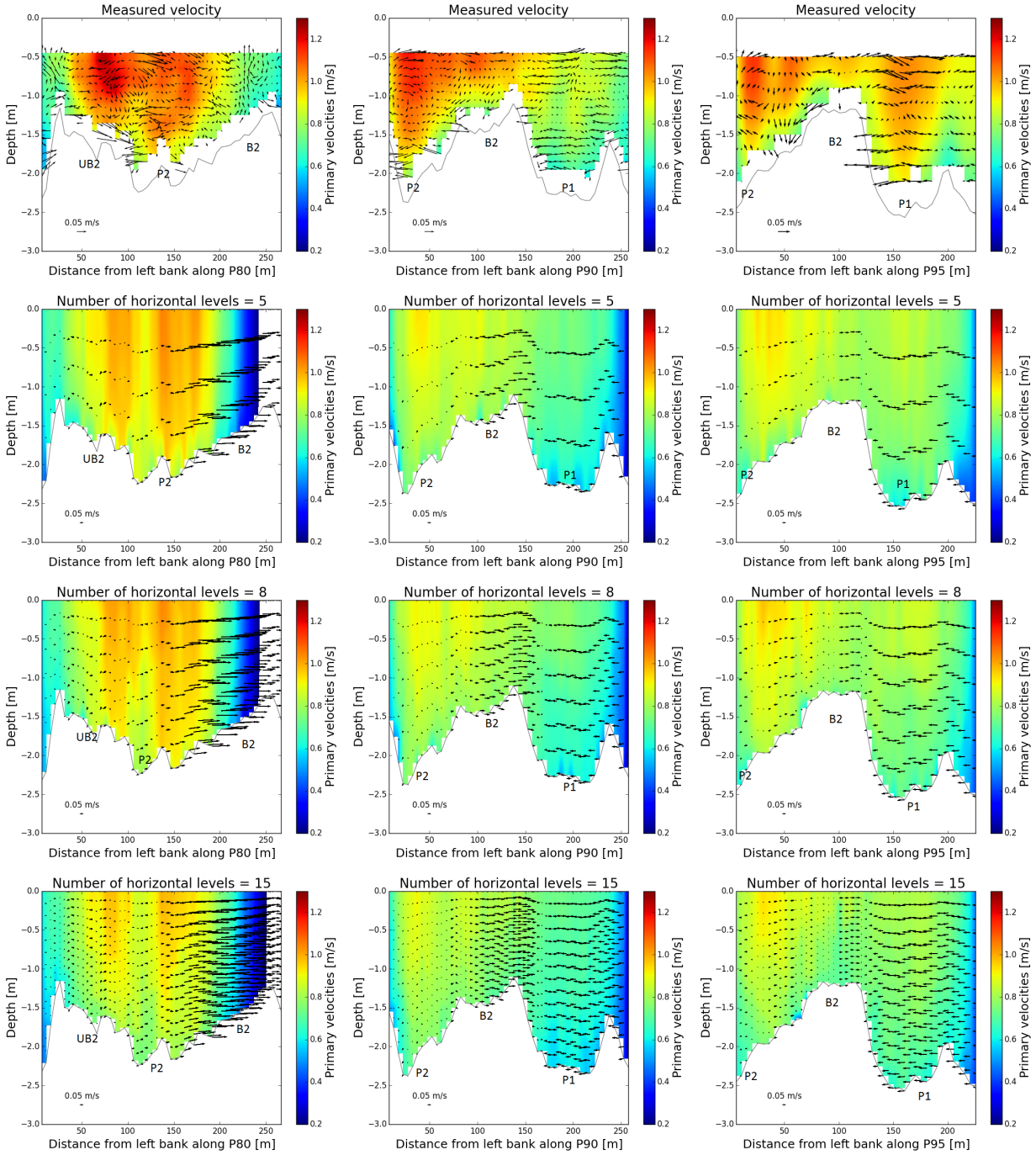


Figure 6: Cross-sectional profiles of primary, secondary and vertical flow velocities measured by Claude et al. [12] and computed with the 3d hydrodynamic model on 19 June 2010 (386 m^3/s) with the transverse bar configuration. Arrows correspond to the secondary and vertical velocity components. The colorbar is used for primary velocity.

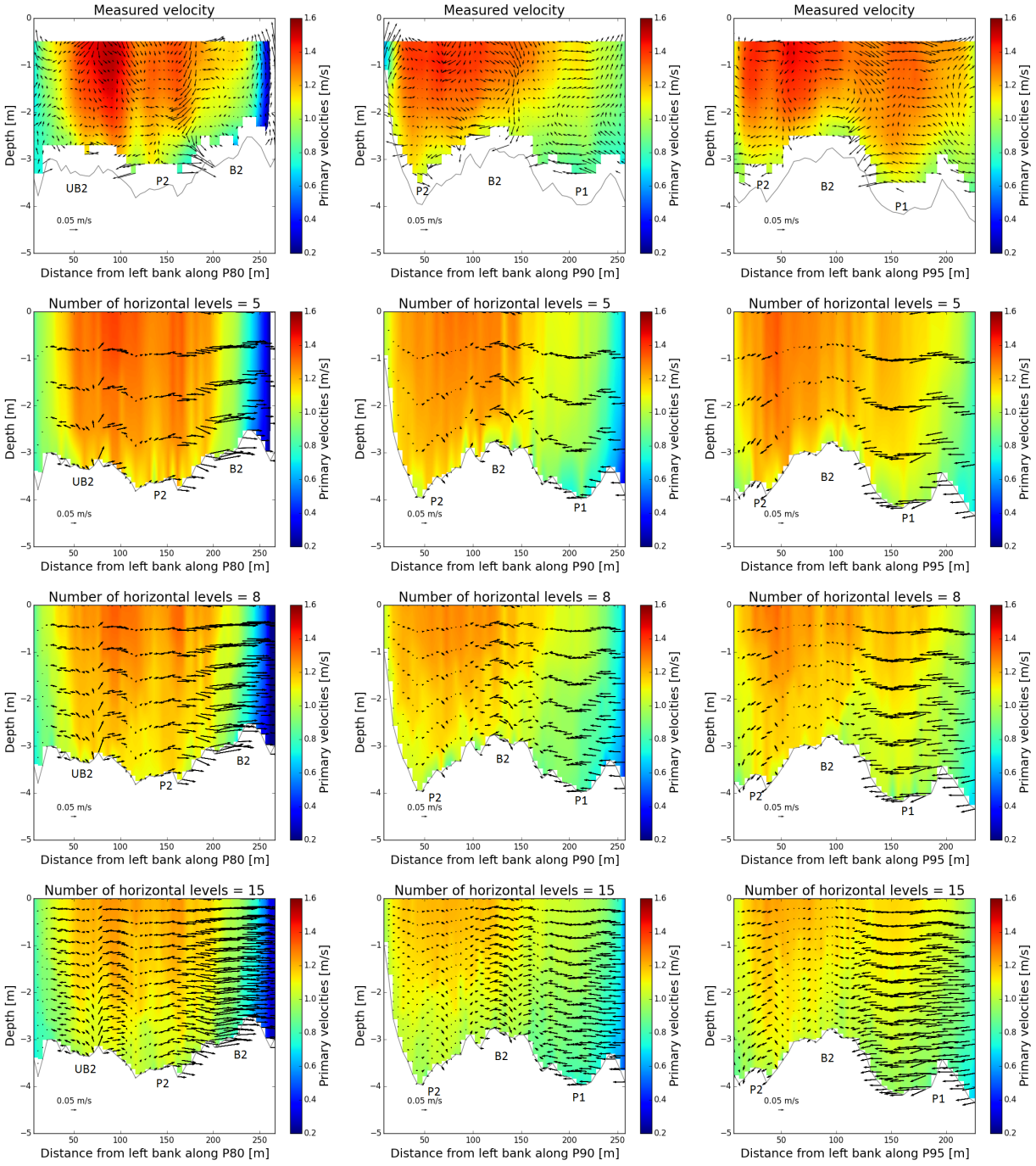


Figure 7: Cross-sectional profiles of primary, secondary and vertical flow velocities measured by Claude et al. [12] and computed with the 3d hydrodynamic model on 22 June 2010 (1030 m^3/s) with the transverse bar configuration. Arrows correspond to the secondary and vertical velocity components. The colorbar is used for primary velocity.

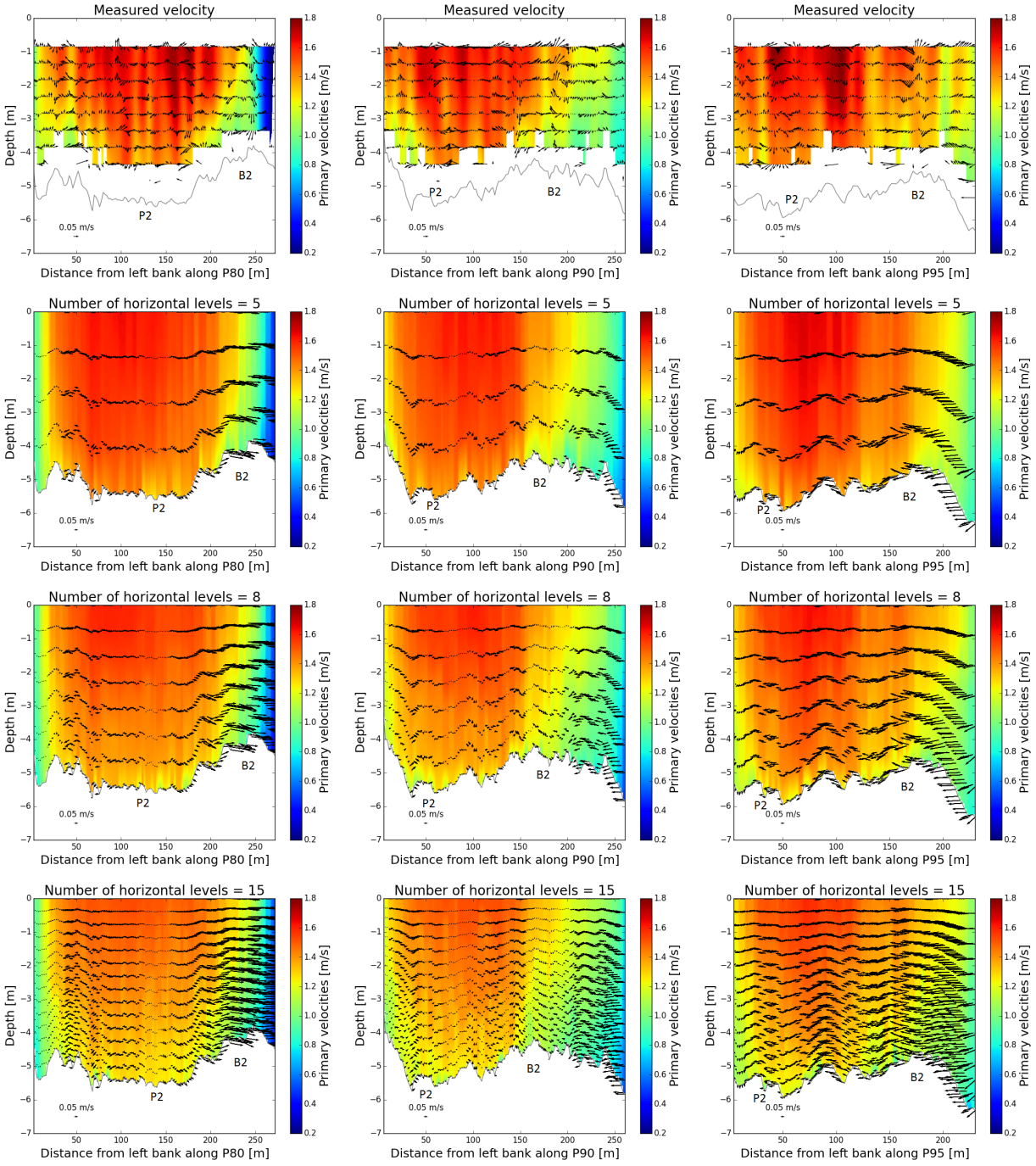


Figure 8: Cross-sectional profiles of primary, secondary and vertical flow velocities measured by Claude et al. [12] and computed with the 3d hydrodynamic model on 11 December 2010 (1950 m^3/s) with the alternate bar configuration. Arrows correspond to the secondary and vertical velocity components. The colorbar is used for primary velocity.

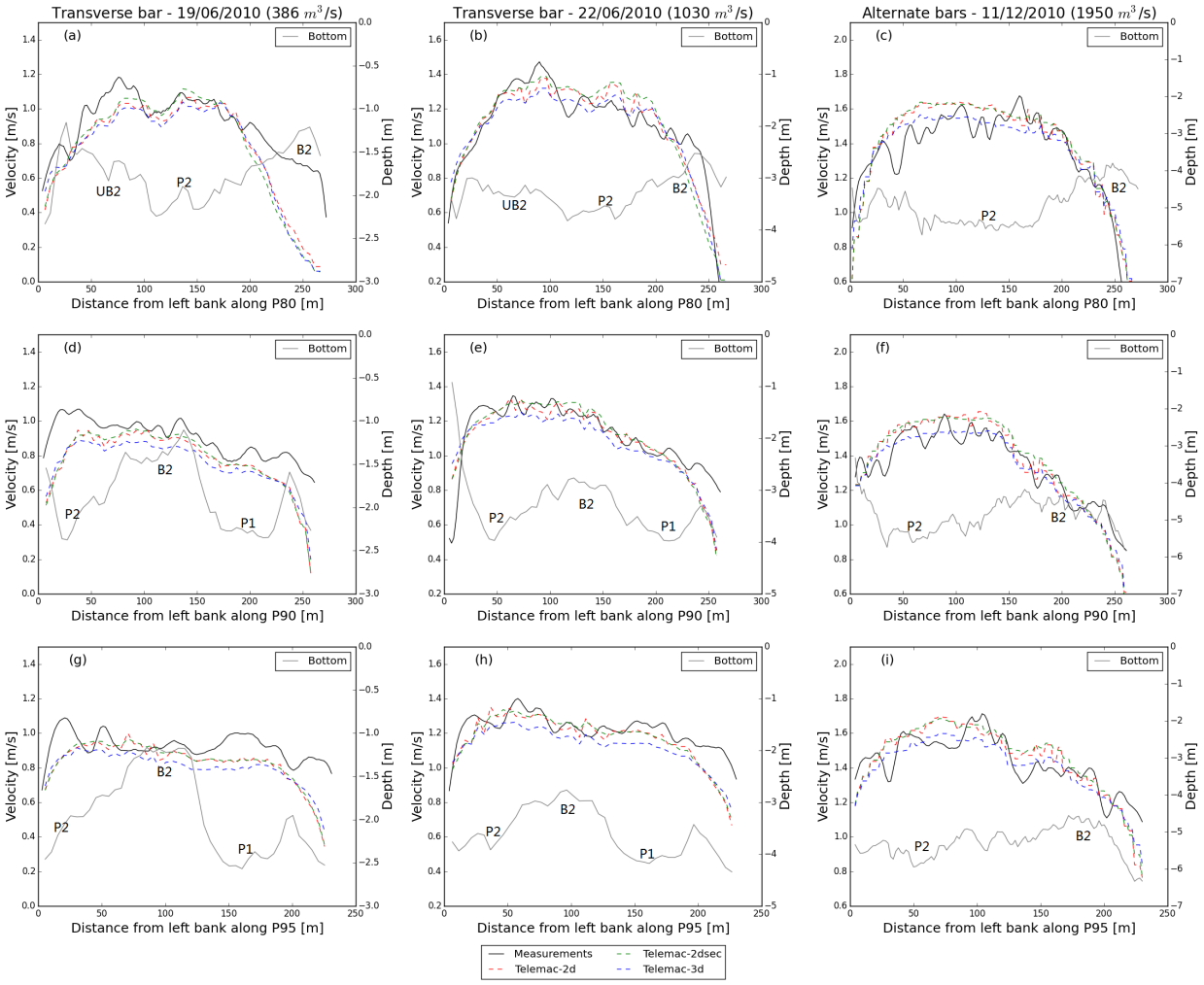


Figure 9: Comparison of flow velocities between the field measurement and hydrodynamic model results on cross-sectional profiles. All velocities correspond to the depth-averaged velocities.

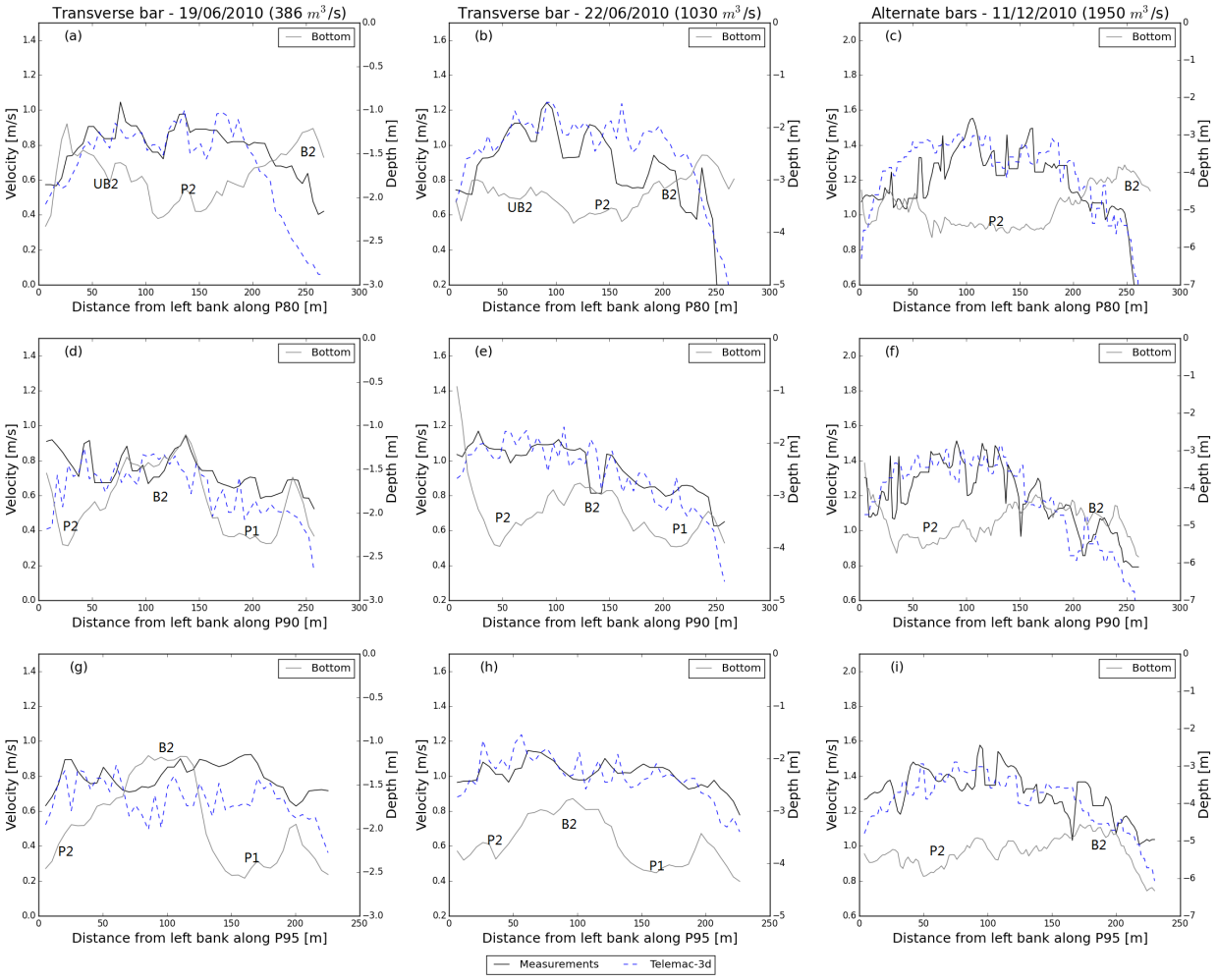


Figure 10: Comparison of flow velocities between the field measurement and 3d hydrodynamic model results on cross-sectional profiles. All velocities correspond to the flow velocities near the riverbed.

Figure 11 show that the computed flow directions and field measurements are consistent, except that the directions observed from the field measurements show more variability. On P80 on 22 June 2010 (Figure 11b), the water flow tends to be directed toward the left bank over the Unit bar 2 and Pool 2, whereas, this behavior is more important according to field observation.

Bed shear stresses As an essential element for the morphodynamic numerical model, a distribution of total bed shear stresses τ_b is presented on Figure 12. They are calculated by using equation 23 in 2d model, equation 25 in 3d model and estimated by equation 26 for field measurements. According to Claude et al. [12], the critical bed shear stress τ_c calculated reaches 0.78 Pa and the sediments are highly mobile in the study reach.

Considering the same bar configuration (Figure 12a, 12b, 12d, 12e, 12g, 12h), the 2d and 3d numerical models tend to compute larger bed shear stresses τ_b in high water discharges. Overall, bed shear stresses estimated from measurements vary between 2 and 6 Pa but the simulated bed shear stresses can reach around 14 Pa for a discharge of 1950 m^3/s (Figure 12c, 12f, 12i) on 11 December 2010. The differences of τ_b between numerical results and measurements are more important on Pool 2 and less important on Bar 2 near the right riverbank. In general, differences are not significant on bed shear stresses computed by the 2d and 3d model (Figure 12).

3.1.3 Discussion

Numerical results are generally in agreement with field measurements in regard to the magnitude and direction of velocity vectors, except that there are differences (+5.8 Pa) in term of bed shear stresses for high water discharge on 11 December 2010 (Figure 12). Furthermore, for different hydrodynamic models, the results of comparison show a good consistence between 2d model, 2d model in consideration of secondary currents and 3d model.

In general, flow velocities are well represented by the 2d and 3d models for the different flow discharges and bar configurations. Except for P80 on 19 June 2010, flow velocities are much smaller than measurements above Bar 2 near the right bank. This can be explained by the presence of a recirculation structure in the numerical models located upstream of P80 for low water discharge (Figure 13). The head of Bar 2 located near the right section of P80 can be considered as a geometrical forcing, with low water depths (around 1 m) above Bar 2 on 19 June 2010. The presence of horizontal water recirculation (around surface of 160m×50m with flow velocity varying between 0.02 m/s to 0.24 m/s) tends to rebalance the distribution of water discharge along section P80, which decrease on right side of P80. For same transverse bar configuration, the scale of water recirculation becomes much smaller (50m×25m) with a higher water discharge of 1030 m^3/s on 22 June 2010.

Secondary currents effects For results of secondary currents, 2d models with and without secondary currents corrections do not present significant differences. In addition, 3d results of secondary velocities on cross sectional profiles neither show obvious pattern of recirculation. According to Claude et al. [12] in field measurements, the lateral and vertical velocities have low values varying around 0.05 m/s and 0.1 m/s, respectively. Therefore, it is possible that secondary currents are less important and their effects are negligible in this study reach, in comparison to the primary velocity magnitude varying between 0.34 m/s and 1.72 m/s.

Influence of remnants of rip-raps Figure 5 shows cross-sectional profiles of flow velocity computed numerically with 2d model and measured by Claude et al. [12]. The results show that the 2d model has difficult to represent the field measurements on P90 and P95 near the riverbank. It could be explained by no representation in the model of remnants of old rip-raps (Figure 1). The mesh size (mean size 5 m) of 2d numerical model is not small enough to represent the scale of rocks (20-30 cm) used for rip-raps. Compared with transverse bar configuration, the difference of numerical results and measurements decreases with the presence of alternate bars, due to that the rip-raps are mostly covered by sediments during this period.

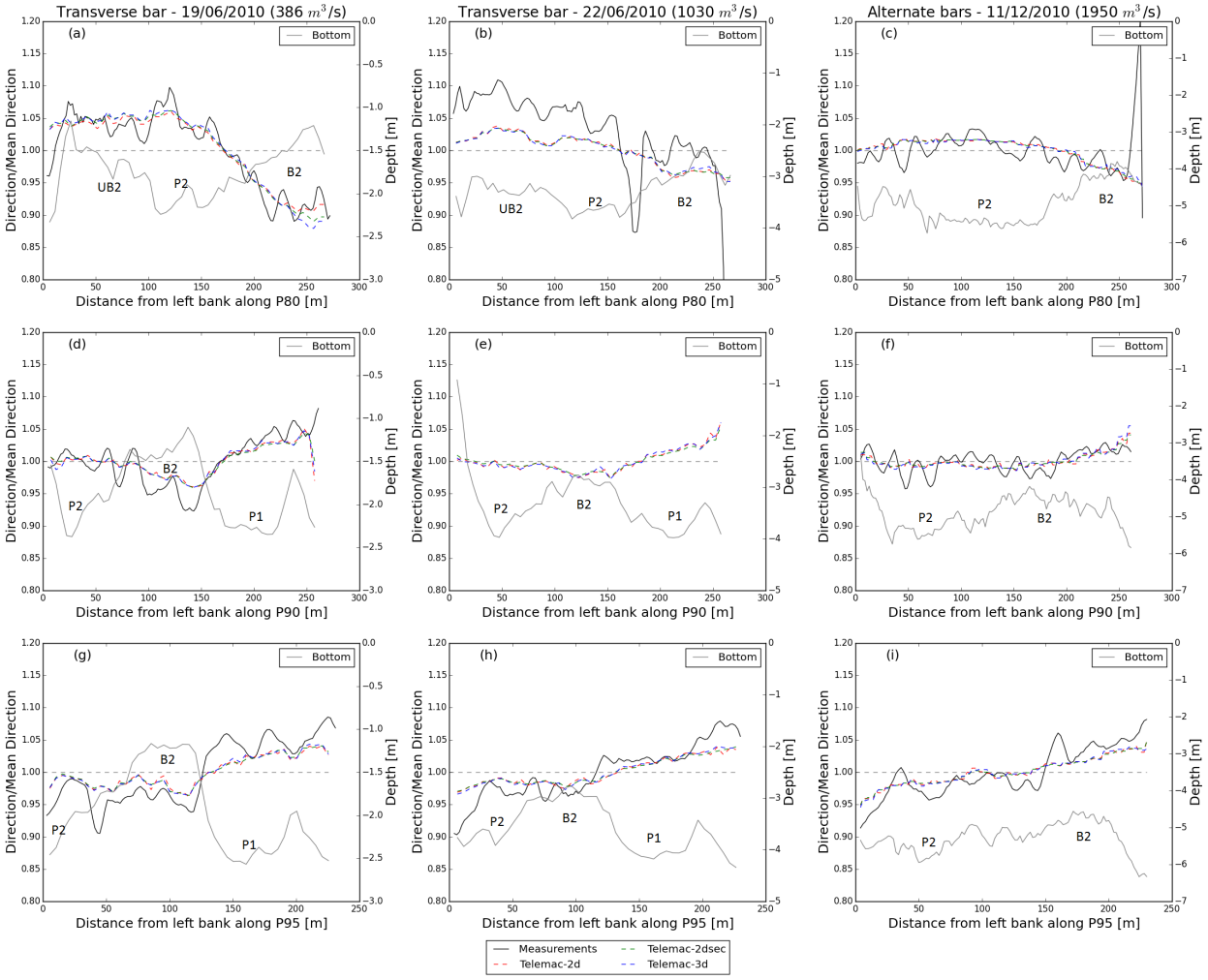


Figure 11: Comparison of flow directions between the field measurement and hydrodynamic model results on cross-sectional profiles. The directions in 2d model are represented by the ratio between the flow direction in each vertical line and the cross-sectional averaged direction. The directions in 3d model and field measurement are represented by the ratio between the flow direction near the riverbed and cross-sectional averaged direction. When the ratio of directions is greater than 1 (horizontal gray line), the flows tend to be directed toward the left bank and vice versa. No available measurements on P90 on 22/06/2010.

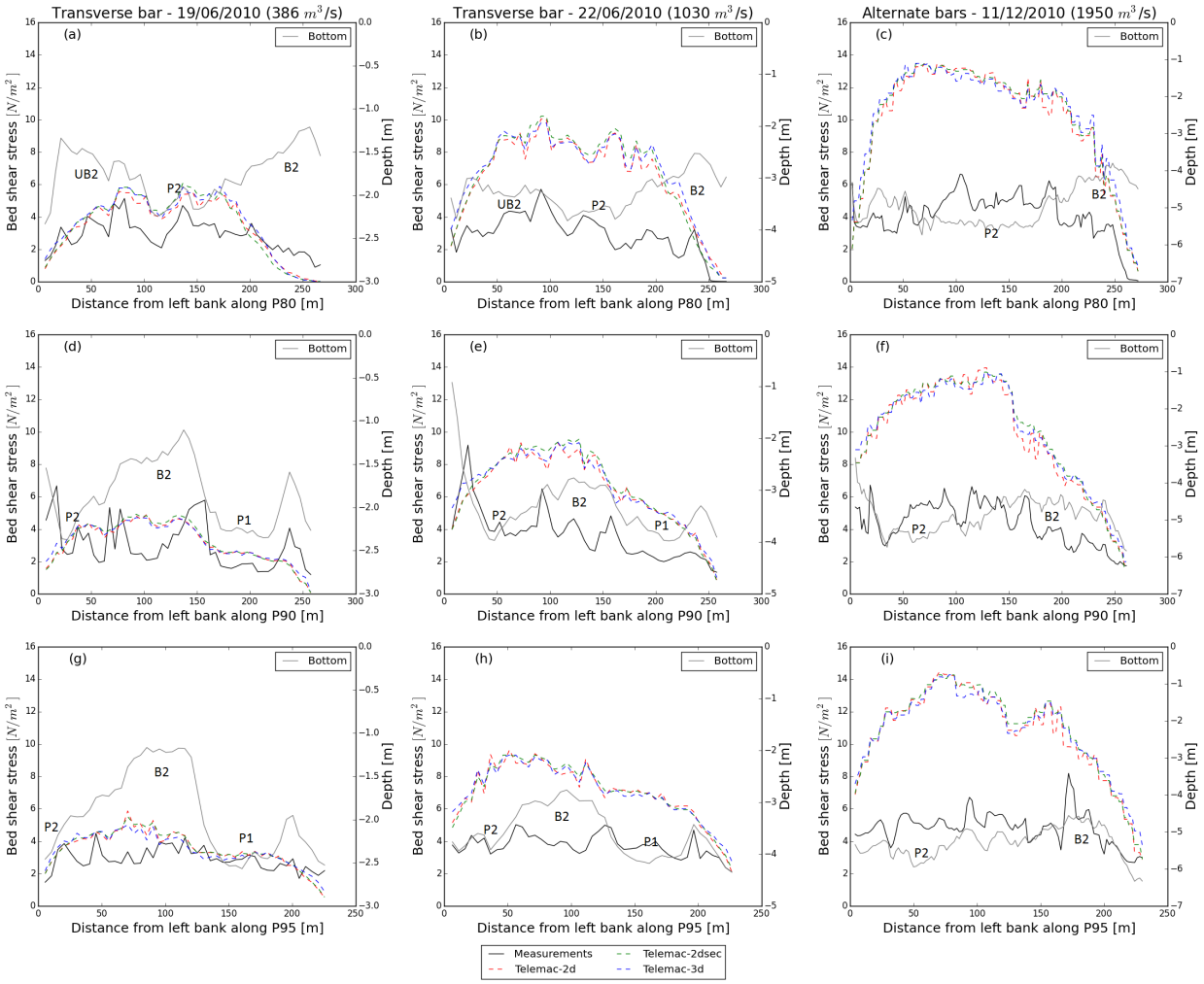


Figure 12: Transversal distribution of bed shear stresses

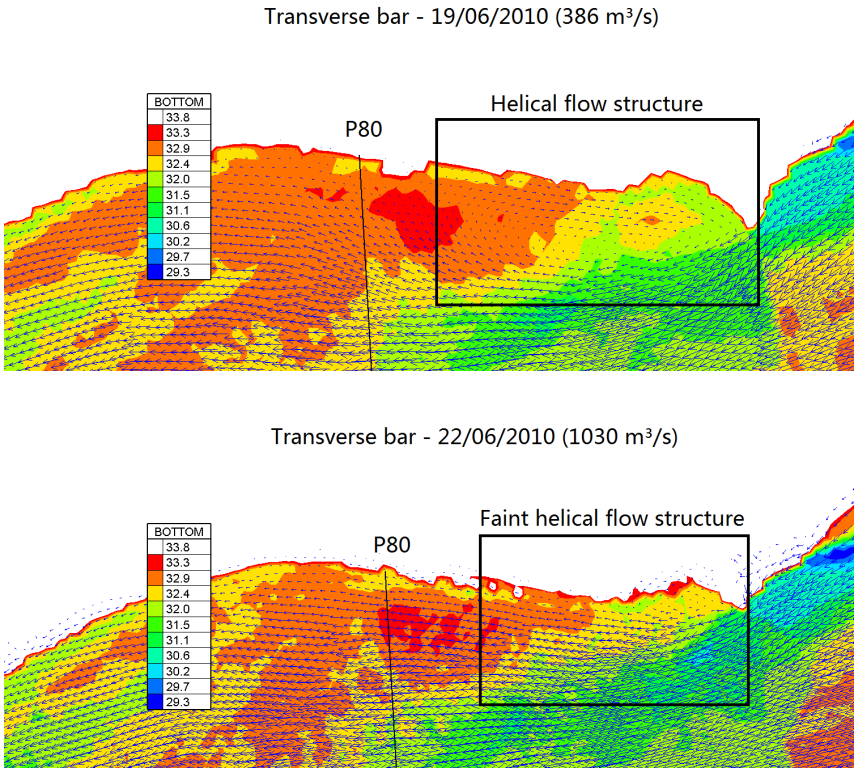


Figure 13: Plan view of flow velocity distribution showing the formation of an helical flow structure located upstream of P80 a) low flow on 16 June 2010 and b) high flow on 22 June 2010.

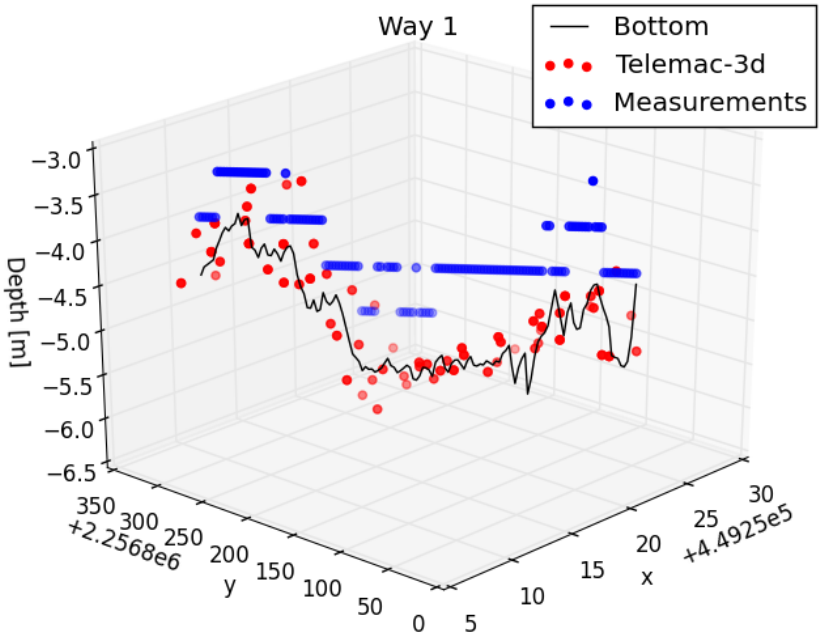


Figure 14: Comparison of the locations of point between the field measurements and extraction from 3d model results on cross-sectional profiles (P80 on 11/12/2010).

Uncertainty of field measurements Furthermore, regarding the accuracy and uncertainty of field measurement data mentioned by Claude et al. [12], the mean standard error for each individual flow velocity measurement was 0.094 m/s. The biases with respect to current meter measurements were maximum for low flow velocity at a value of -0.08 m/s, for an average flow velocity less than 0.87 m/s. Therefore, low flow velocities obtained by ADP should be regarded with care. Besides, Figure 14 shows the actual location of points measured and extracted from model results. All the points measured near the river bottom are higher (maximum 1.62 m on Figure 14) than the ones extracted from Telemac-3d.

Estimation of bed shear stresses As an important element discussed in this study, the bed shear stresses τ_b computed from 2d and 3d simulation results present a highly consistency. However, there are still large differences between the τ_b calculated from the numerical results and estimated from the field measurement. What is noteworthy is that friction on the bottom is a major unknown in environmental studies, and the friction laws themselves are mostly empirical (Hervouet [23]). The friction coefficients C_f and k_s (Equation 24, 25) used in 2d and 3d models are empirical, so does the grain roughness $(z_0)_{ZF}$ in equation 26 for calculation from field measurements. Therefore, the comparison of bed shear stresses estimated for different methods should be regarded with rigorous attitude.

In this case that 2d and 3d models do not have a large difference, considering of the computation time will help to improve the efficiency. Table 1 shows generally the computation time for different models. The simulation time configuration are all the same with the time step of 0.5 s and the duration of 40000 s.

Model	Computation time	Number of processing cores
3d hydrodynamic model (15 levels)	7h 27m 29s	56
3d hydrodynamic model (8 levels)	2h 30m 42s	56
3d hydrodynamic model (5 levels)	1h 20m 2s	56
2d hydrodynamic model (with seccur)	8m 9s	16
2d hydrodynamic model	8m	16

Table 1: Computation time for different models.

3.2 Morphodynamic - Influence of hydrology on the morphological evolution of bars

According to the results of hydrodynamic models, the secondary currents has no significant importance in this study site. 2D model is accurate enough to be used in the morphodynamic module.

3.2.1 Morphological evolution of the riverbed

Figure 18, 19, 20, 21, 22, 23 and 24 present the numerical results of topography for water discharges of 150 m^3/s, 350 m^3/s, 500 m^3/s, 750 m^3/s, 1000 m^3/s, 1500 m^3/s and 2000 m^3/s respectively. Each figure shows 15 daily topographical maps captured around every 25 days for the whole simulation (from day 0 to day 366).

For a discharge of 150 m^3/s (Figure 18), the morphological evolution is generally in an inactive status. At the early stage of process, Bar 1 is almost non-submerged and Bar 2 migrates extremely slowly in the downstream and lateral directions. Sediment coming from upstream is deposited and accumulates near Bar 2, which becomes also non-submerged due to the increased bar height (Figure 15).

For discharges of 350 m^3/s and 500 m^3/s (Figure 19 and 20), the system is highly mobile and bar dynamics is intense. Main part of Bar 1 has been washed away after around 120 days, except the bar head which remains in the stagnation zone. Due to the accumulation of height contributed by the upstream sediment supply, some part of the bars are non-submerged (day 300, day 325, day 366 in Figure 16 and day 366 in Figure 17). For discharges of 350 m^3/s and 500 m^3/s, bars evolve in order of alternate bars configuration, transverse bar configuration and lateral bar configuration (day 0, day 125, day 175 in Figure 19 and day 0, day 150, day 225 in Figure 20).

For discharges of 750 m^3/s and 1000 m^3/s (Figure 21 and 22), bars located near the left bank migrate preferentially downstream than laterally, according to the comparison of morphological evolution from day 59 to day 85 for the discharge of 500 m^3/s (appendix D.3 Figure 43) and from day 64 to day 86 for the discharge of 1000 m^3/s (appendix D.5 Figure 48). The tail of Bar 1 is eroded during the first 100 days of simulation. A new lateral bar is forming later, which results from a combination of the head of Bar 1 and the deposited sediment coming from upstream. Morphological evolution become slow at the late stage of simulation.

For discharges of 1500 m^3/s and 2000 m^3/s (Figure 23 and 24), the morphodynamics reaches an equilibrium state in the study area at the late stages of the simulation, staring from approximately $t = 275$ days. Bar 1 and Bar 2 are located in the stagnation zone and the entrance of secondary channel respectively (Figure 25). No clear transverse bar configuration has been observed in these two scenarios.

For low flow discharges, the flow is sinuous with multiple channels pattern observed. Inversely, the flow is rectilinear and constrained in the thalweg for high water discharges, which becomes less sinuous with respect to the one forming at low flow rate. More details of the morphological evolution and sediment transport are given in Appendix D.

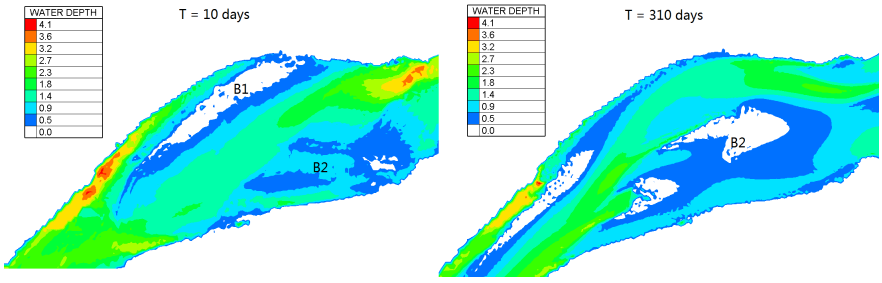


Figure 15: Planform distribution of the water depth in the channel expansion/contraction area showing the non-submerged parts of the bars for water discharge of 150 m^3/s.

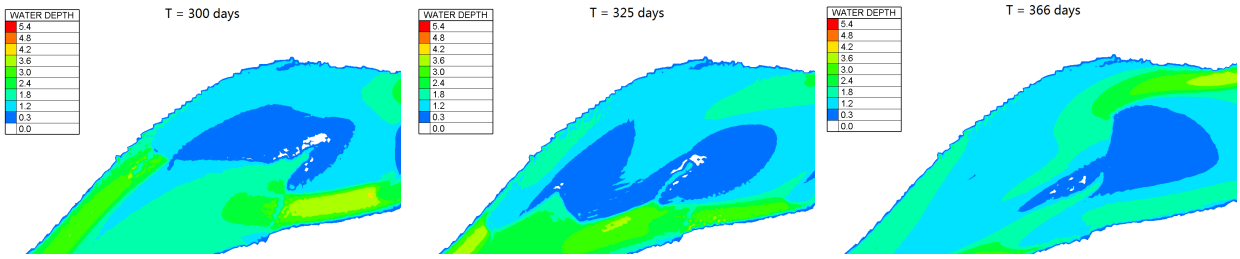


Figure 16: Planform distribution of the water depth in the channel expansion/contraction area showing the non-submerged parts of the bars for water discharge of 350 m^3/s.

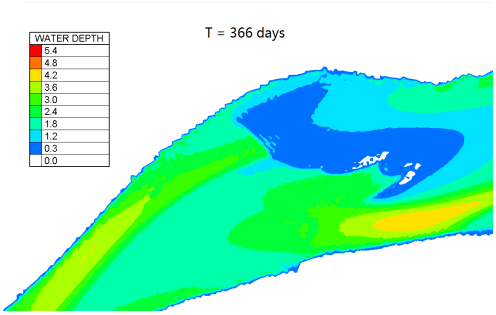


Figure 17: Planform distribution of the water depth in the channel expansion/contraction area showing the non-submerged parts of the bars for water discharge of 500 m^3/s.

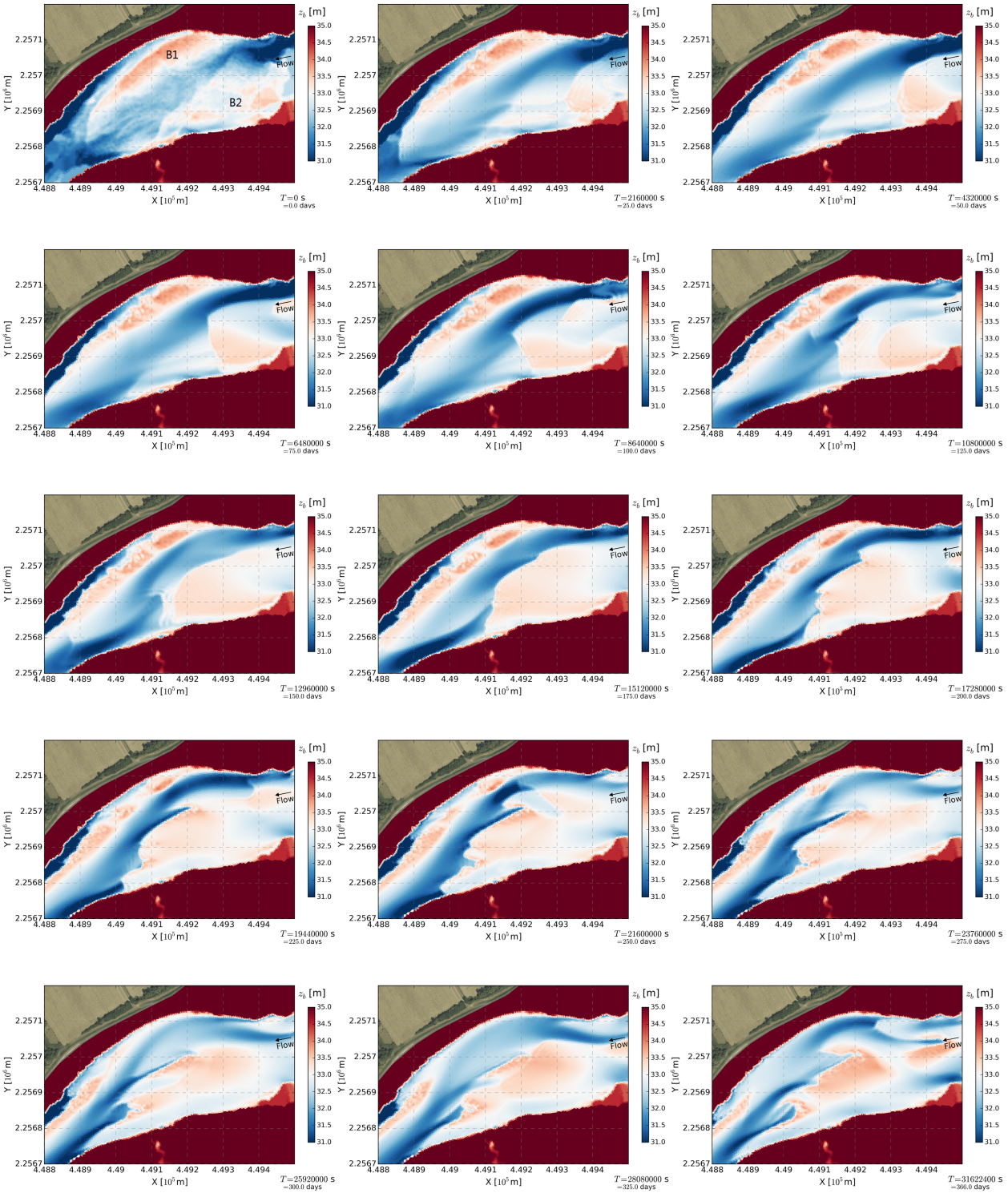


Figure 18: Planform bed topography computed numerically with a constant water discharge of 150 m^3/s on the study area, captured every 25 days during 1 year of simulation.

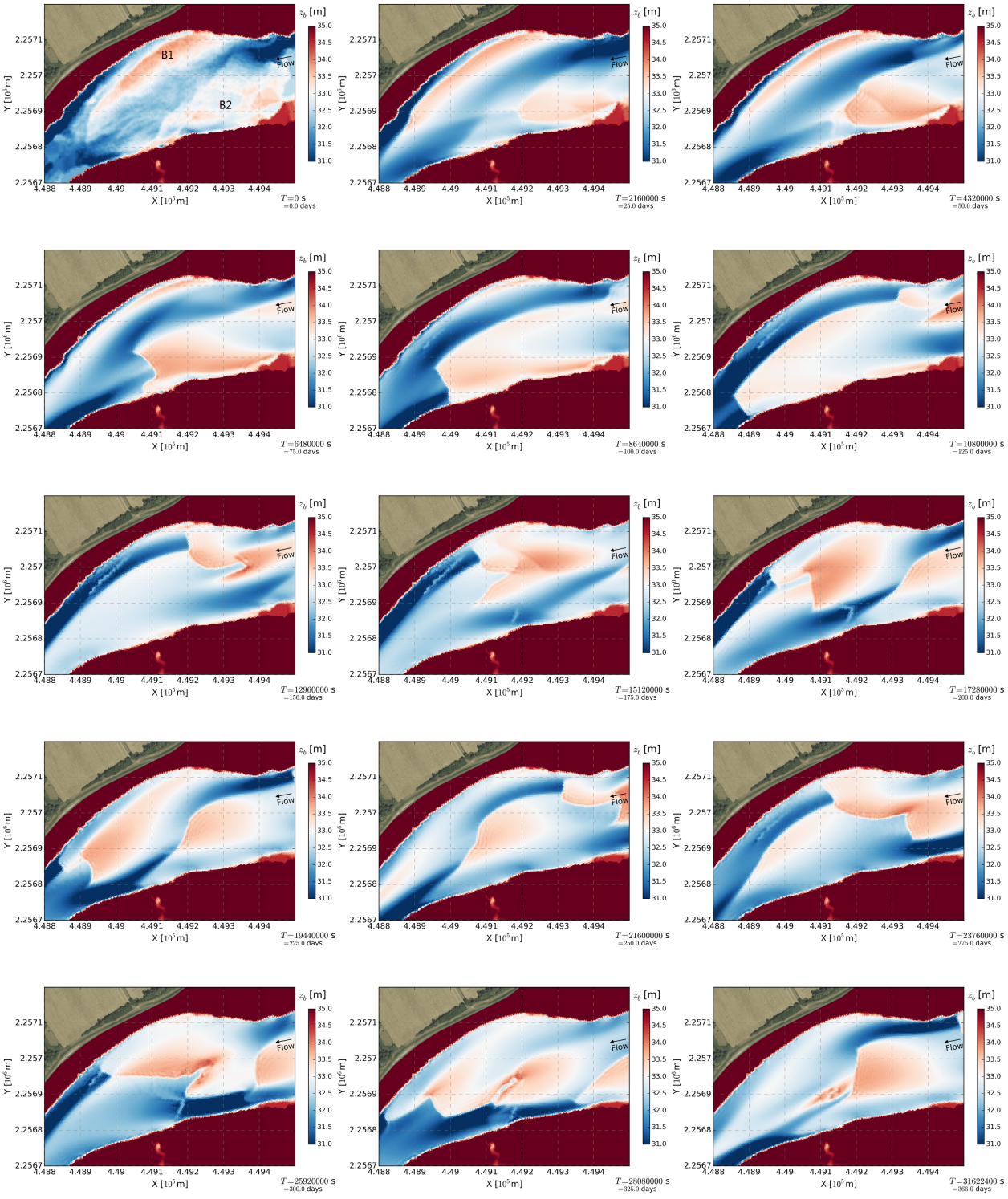


Figure 19: Planform bed topography computed numerically with a constant water discharge of 350 m^3/s on the study area, captured every 25 days during 1 year of simulation.

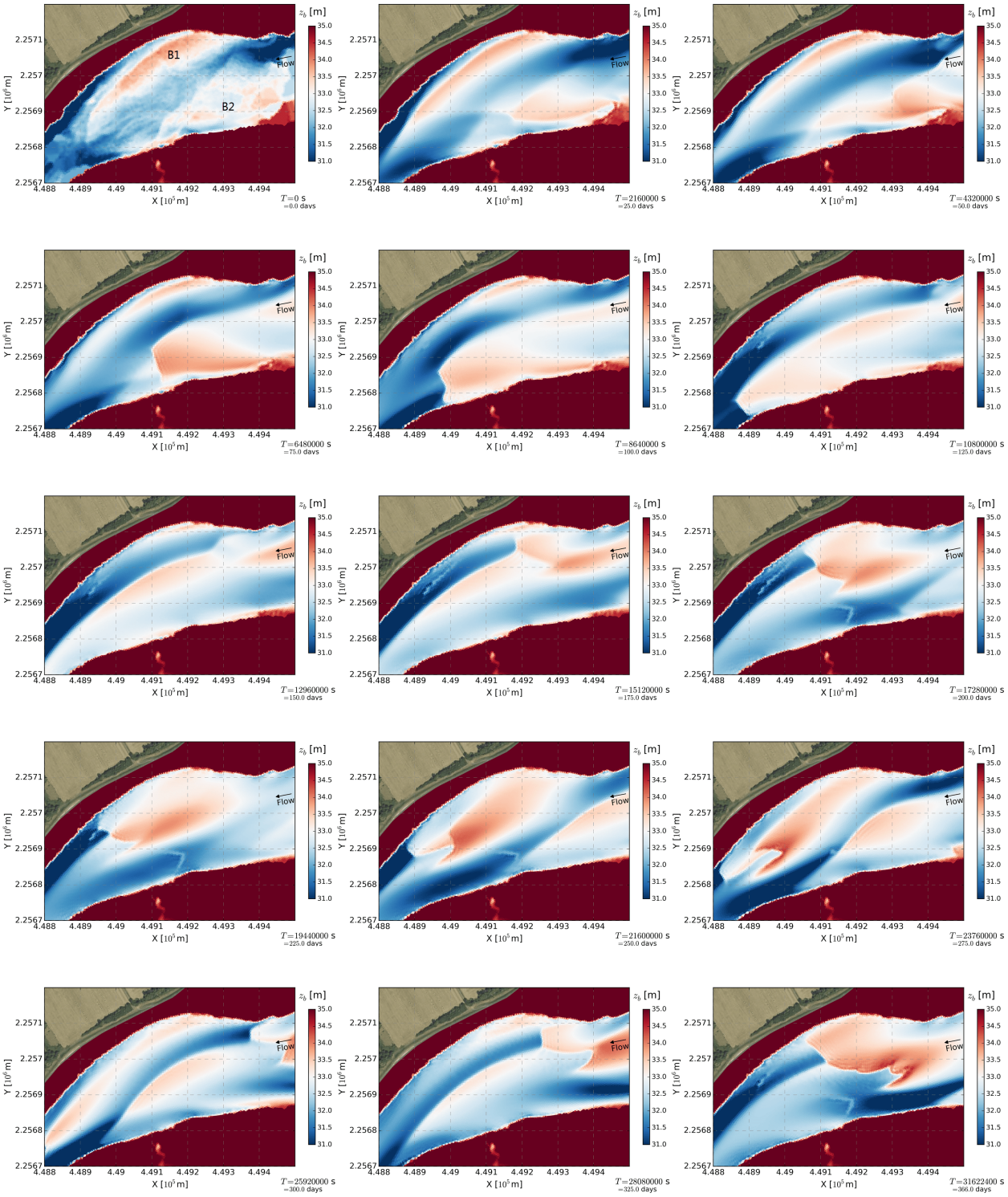


Figure 20: Planform bed topography computed numerically with a constant water discharge of 500 m^3/s on the study area, captured every 25 days during 1 year of simulation.

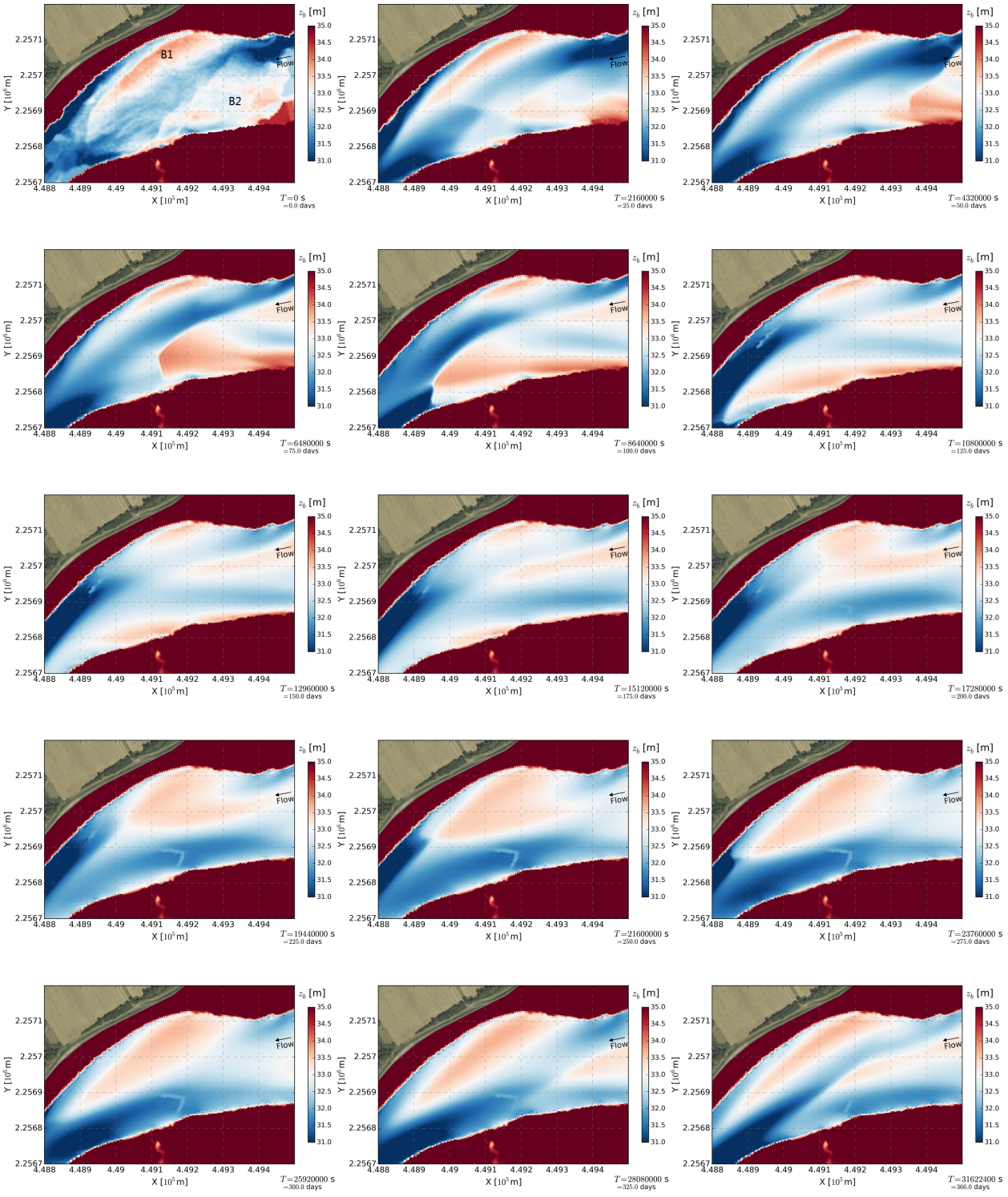


Figure 21: Planform bed topography computed numerically with a constant water discharge of 750 m^3/s on the study area, captured every 25 days during 1 year of simulation.

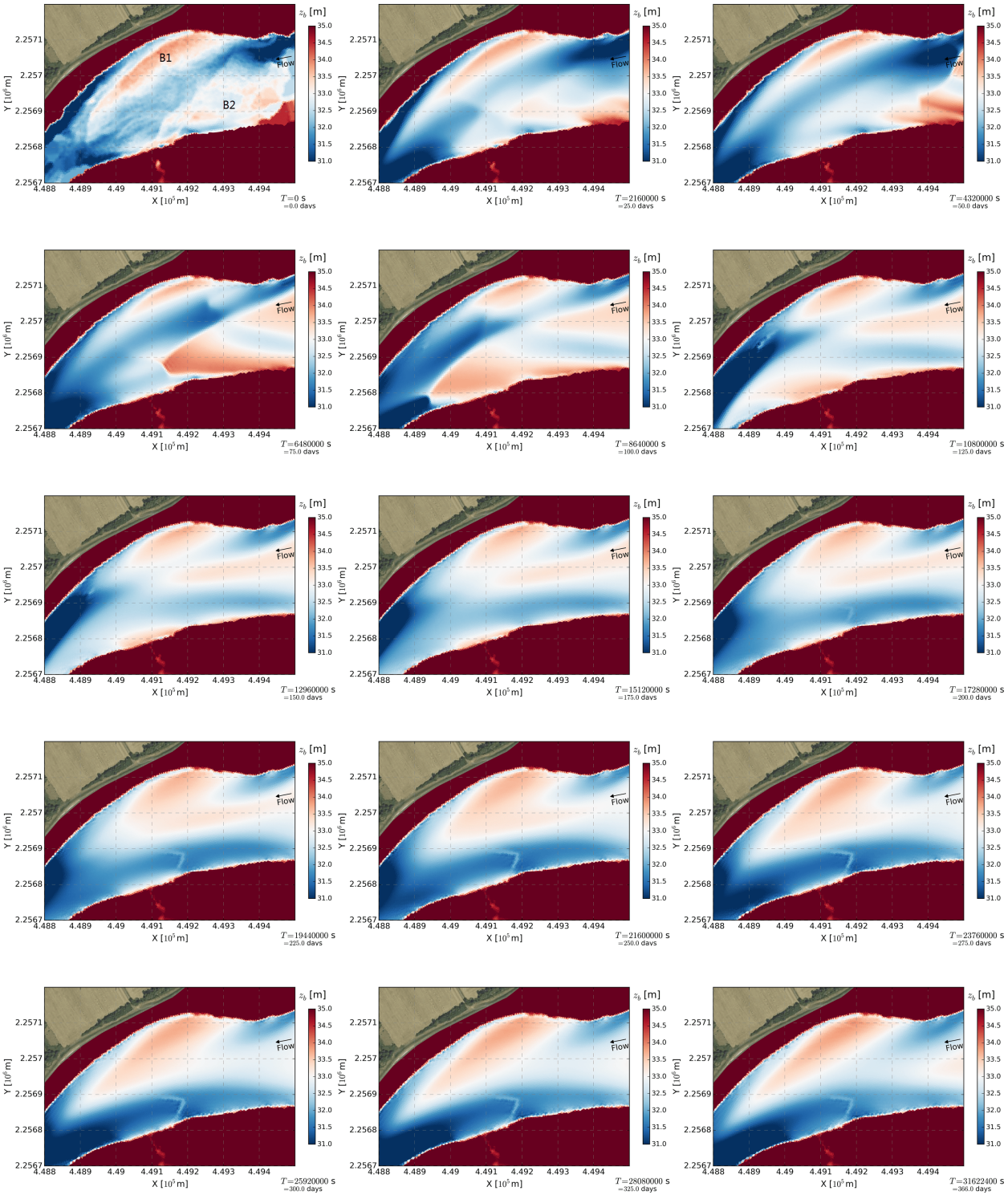


Figure 22: Planform bed topography computed numerically with a constant water discharge of 1000 m^3/s on the study area, captured every 25 days during 1 year of simulation.

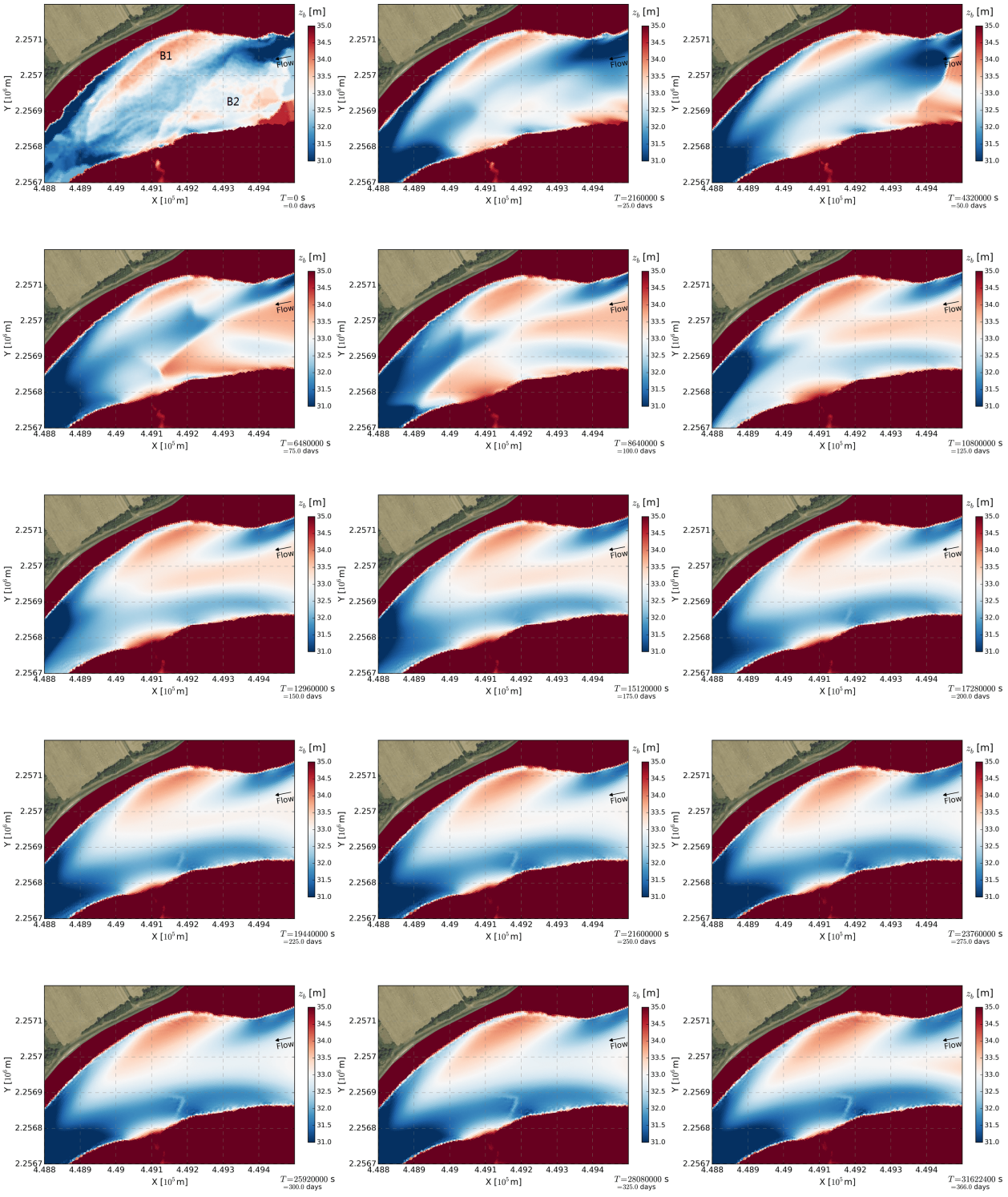


Figure 23: Planform bed topography computed numerically with a constant water discharge of 1500 m^3/s on the study area, captured every 25 days during 1 year of simulation.

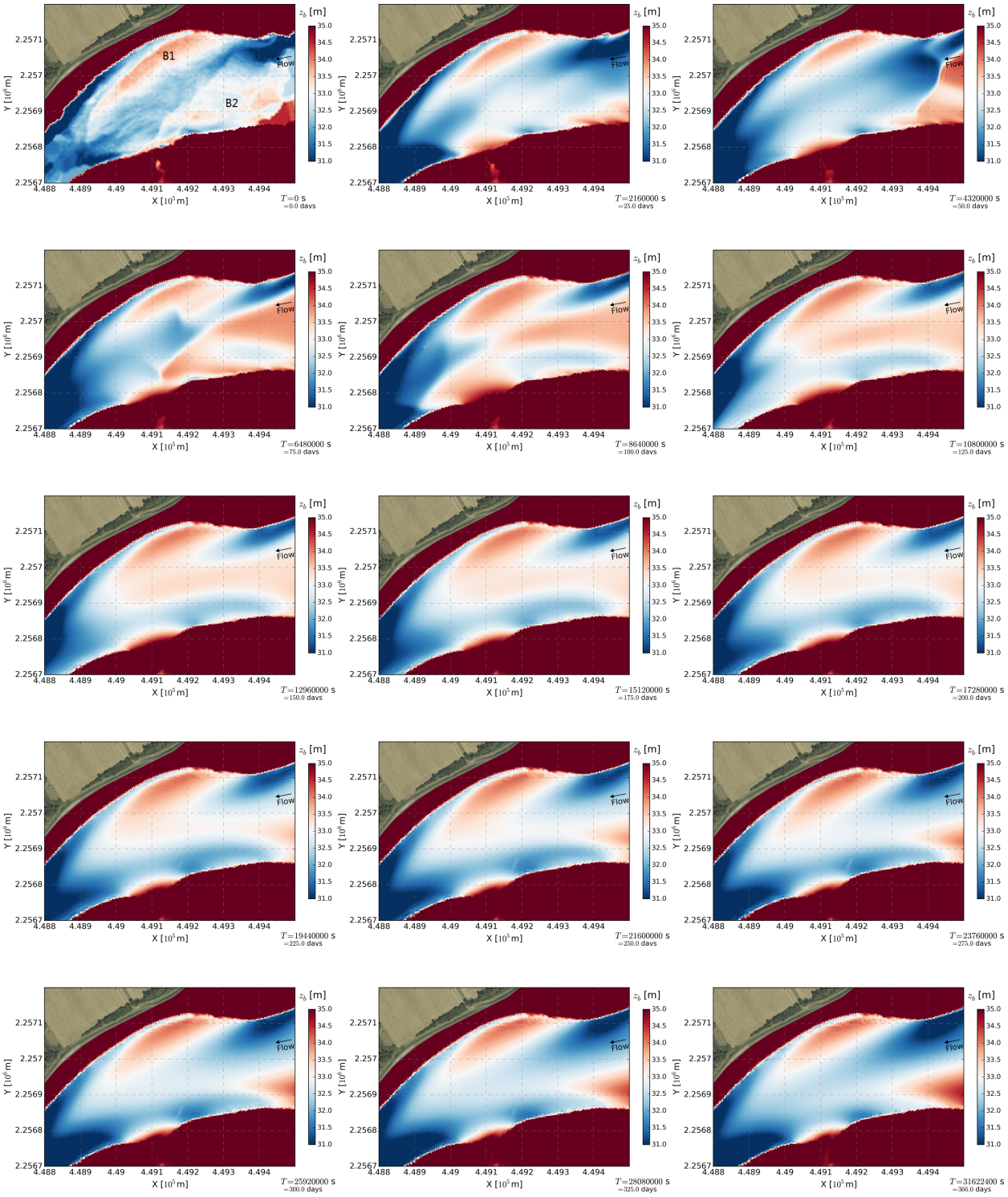


Figure 24: Planform bed topography computed numerically with a constant water discharge of 2000 m^3/s on the study area, captured every 25 days during 1 year of simulation.

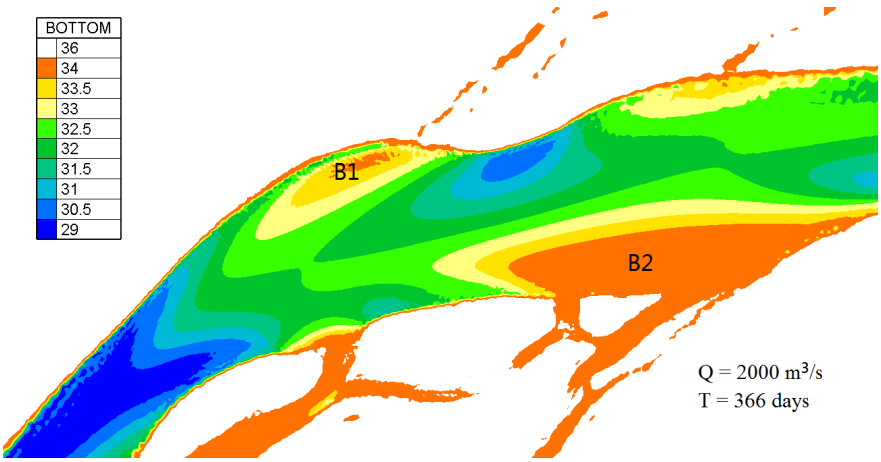


Figure 25: Topographical maps of numerical result at the end of the simulation (366 days) with a water discharge of 2000 m^3/s

3.2.2 Evolution of sedimentary storage

Figure 26 shows the average volumes of eroded sediment and deposited sediment per day in the study area. The expansion/contraction zone is generally under deposit. In consistence with the morphological analysis results, morphological evolution processes are highly active for water discharges of 350 m^3/s and 500 m^3/s. Morphodynamics evolution achieves finally the quasi-stationary condition for water discharges of 1500 m^3/s and 2000 m^3/s.

3.2.3 Discussion

In general, the morphological evolution considering high water discharges reaches quasi-stationary but not with low flow discharges. A periodic phenomenon of bars configuration is observed during the simulation, which is in order of alternate bars - transverse bar -– lateral bar -– alternate bars. This periodic phenomenon is more obvious under low flow discharge such as 350 m^3/s and 500 m^3/s (day 0, day 125, day 175 in Figure 19 and day 0, day 150, day 225 in Figure 20). Besides, the field observation by Claude [11] shows as well the similar phenomenon (Alternate bars on 15/03/10 - transverse bar on 19/06/10 - lateral bar on 10/12/10 - alternate bars on 10/01/11). Nevertheless, this phenomenon is not universal. For high water discharge, the transverse bar configuration becomes less obvious, due to the increase of its own instability under high flow velocity. Besides, the bars located near the left bank move preferentially downstream than laterally, which has no sufficient opportunity to make it reach and be integrated into the rest part of Bar 1 at the stagnation zone to form the transverse bar configuration.

Influence of the stagnation zone Figure 27 presents the morphological evolution under different hydrological conditions after 60 days. The duration of 60 days is chosen to minimize the influence of upstream sediment supply and to better present the morphological evolution of initial Bar 1. According to Claude [11], a stagnation zone is located near the right bank of expansion section (Figure 1). By comparing the surface of rest part of Bar 1 and altitudinal evolution of riverbed, it is easy to find that the influence of stagnation zone increases with the increase of water discharges. It could be explained by that the flow velocity is much higher and the flow direction is less deflected towards the right part of river channel for high water discharges.

Interaction between flow structure and bar morphodynamics According to Claude et al. [12], the interactions between flow structure and morphodynamics of bars in a channel expansion/contraction is essential to better understand the morphological evolution process. Bars induce a topographic forcing which modify the flow structure already imposed by the right bank curvature, the channel width variations, and the forced units (bars and pools). Figure 28 shows the variation of flow directions along P83 profile over

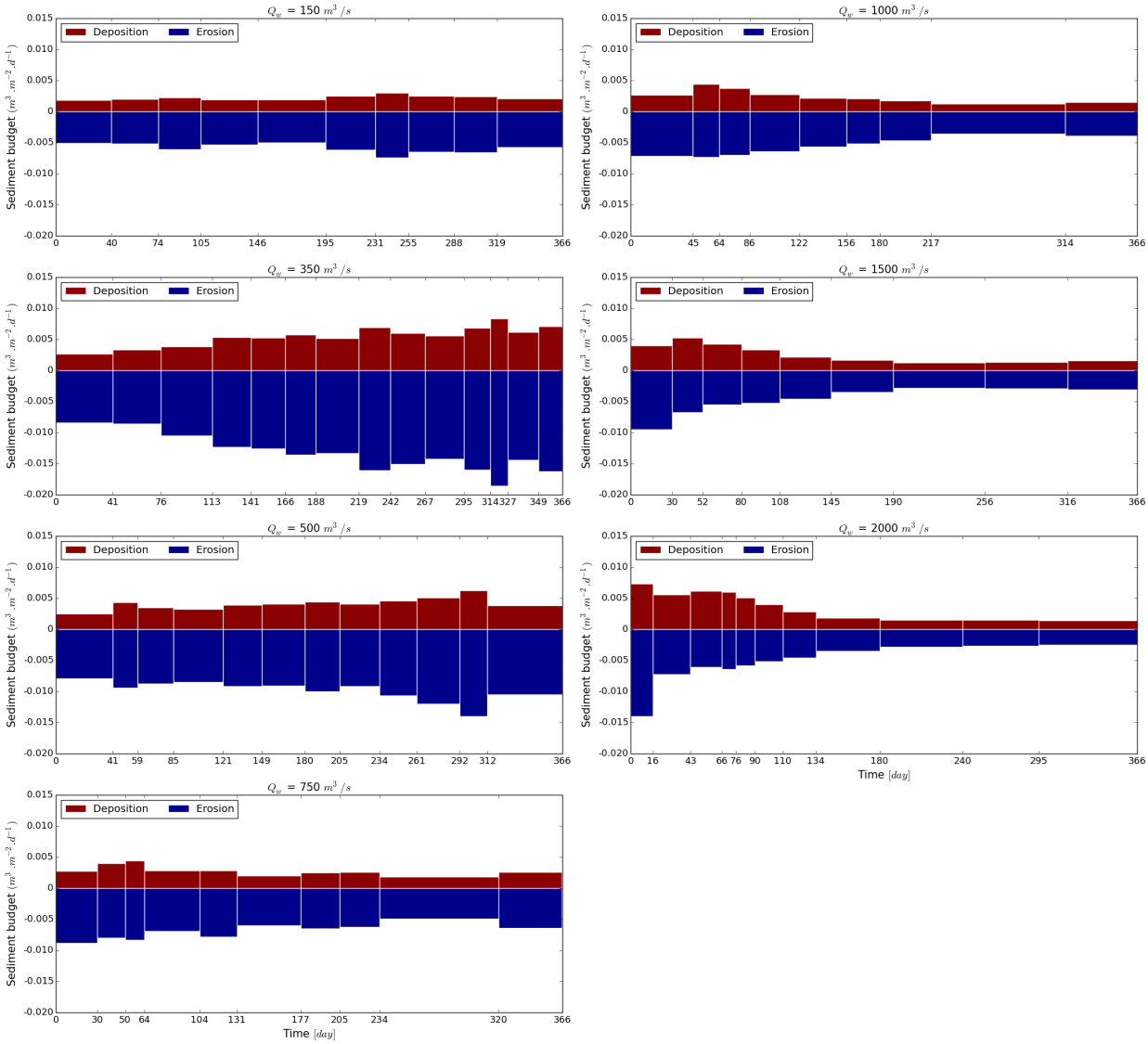


Figure 26: Average volumes of eroded sediment and deposited sediment per square meter per day in the channel expansion/contraction area.

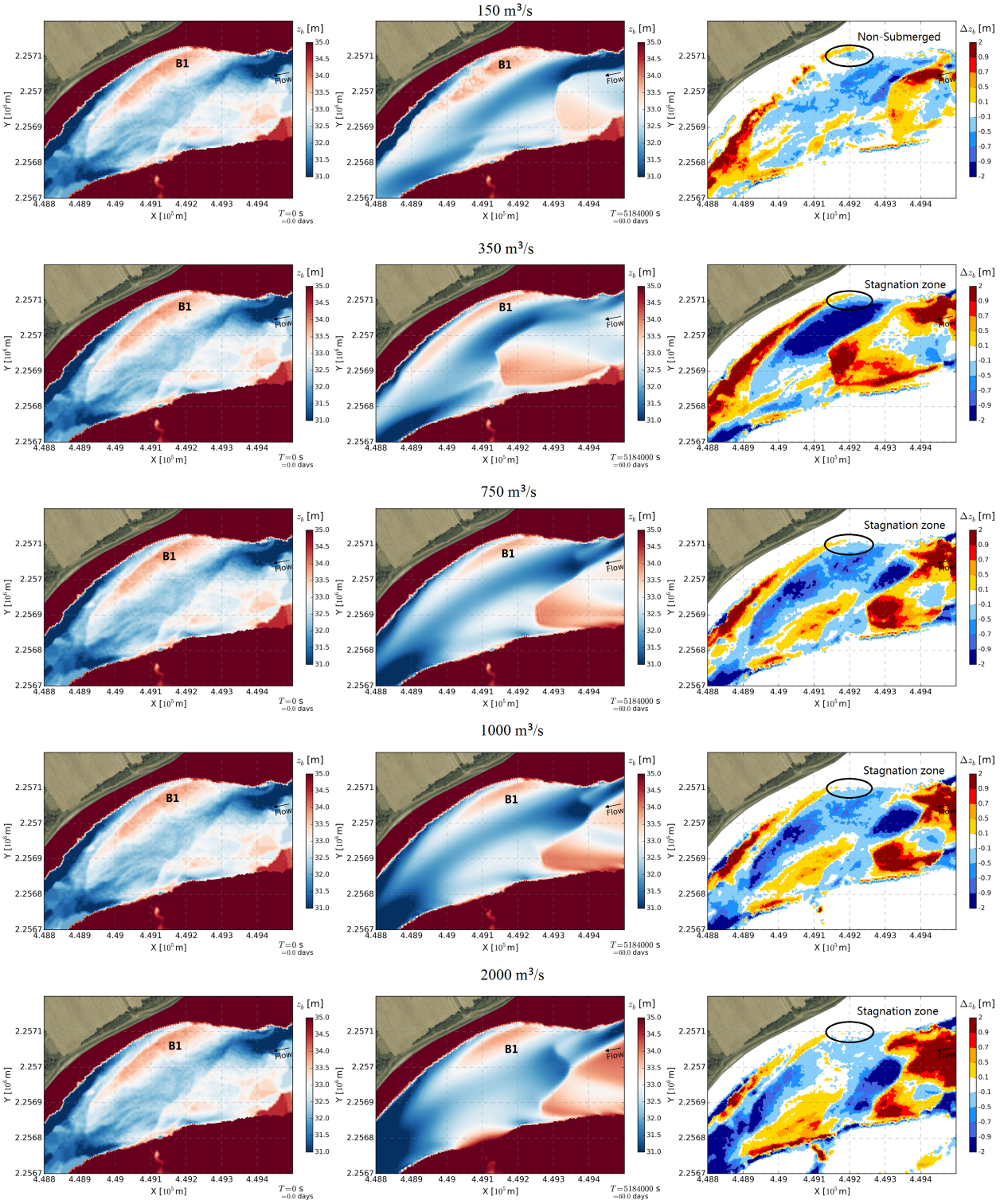


Figure 27: Stagnation zone

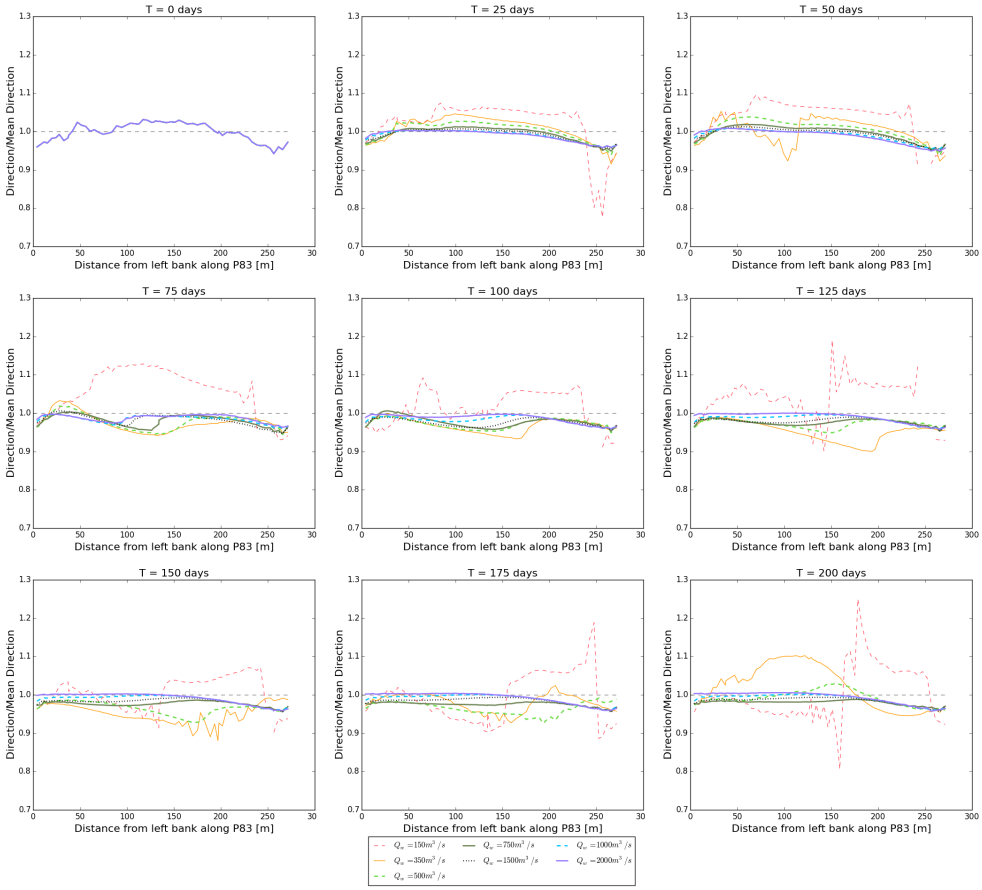


Figure 28: Variation of flow direction along cross-section P83 over time. When the ratio of directions is greater than 1 (horizontal gray line), the flow direction tends to be directed toward the left bank and vice versa.

time. For water discharges above 1500 m^3/s, the flow directions are more uniform towards the main flow direction and they are less variable over the time, which means the configuration and morphology of the bars barely influence the flow structure due to the decrease of relative height of bars, and decreased bar morphological evolution over time.

4 Conclusion

The current objectives of this study were two fold. Part 1 allowed the comparison of 2d hydrodynamic model with and without secondary currents corrections, and 3d model to identify the existence and importance of secondary currents in a channel expansion/contraction with presence of bars. Part 2 evaluated the influence of different hydrological conditions on the morphodynamic of bars to better understand the morphological evolution process.

In the first part, all the models are calibrated with field measurements and the numerical results show that there is no significant importance of secondary currents. Furthermore, several hydraulic variable including the primary and secondary currents, the magnitude and direction of flow velocity vectors, the bed shear stresses are compared between the different models. In general, all the numerical results are in agreement with field measurements, except the bed shear stresses due to different estimation methods. Nevertheless, it is not possible to compute accurately the same flow structure as in situ. The influence of remnants of rip-raps

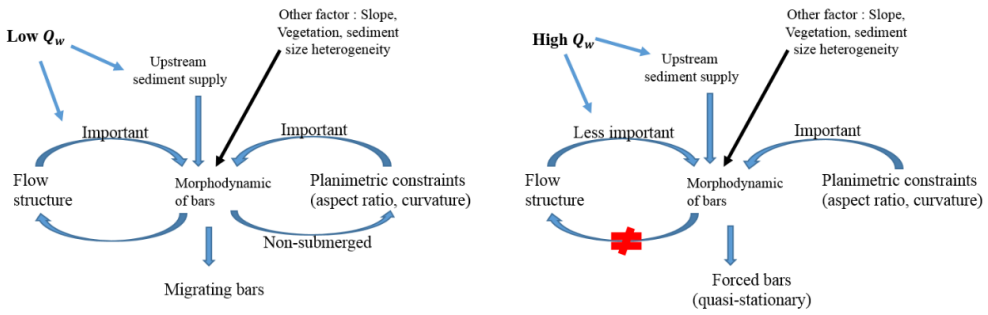


Figure 29: Conceptual scheme summing-up bar morphodynamics under different hydrological conditions

should be considered into the model and the uncertainty of field measurements needs to be verified. Future works implying on the morphodynamic model should be carried for a better understanding of formation and evolution of bars in natural systems.

On the basis of a calibrated two-dimensional morphodynamic model, a multitude of simple hydrological scenarios with constant water discharges ranging from low to high flows are considered. The results show that the morphological evolution reaches the quasi-stationary condition at the end of simulation under high flow discharges but not low flow discharges and the transverse bar configuration is clearly missing under high flow discharges. Besides, due to the strong deflection of water flow induced by topographic forcing, the effect of stagnation zone is less obvious under low flow discharge. Figure 29 shows a brief summary of morphodynamics of bars under different hydrological conditions.

For low flow discharges, the interactions between the flow structure and bar morphodynamics are evident. Bars promote a non-uniform flow in the channel and the non-uniformity of the flow encourages the lateral migration of the macroforms which completes the periodic phenomenon of alternate bars - transverse bar - lateral bar (Claude et al. [12]). In the case of non-submerged bars, bars become a new temporary planimetric constraints which could condition the morphodynamic of bars in turn. For low flow discharges, it is tend to form the free migrating bars due to the highly instability of flow and the flow is generally sinuous with multiple channels pattern.

For high flow discharges, the configuration and morphology of the bars barely influence the flow structure due to the decrease of relative height of bars. The bars located near the left bank generally move rapidly more towards downstream than lateral, which cause the obvious missing of transverse bar configuration. The planimetric constraints play the main role in bars development, which explains that the morphological evolution tends to form forced bars (quasi-stationary structures) in this case. The flow is rectilinear and constrained in the thalweg, which becomes less sinuous with respect to the one forming at low discharges.

In general, the morphological evolution of alluvial rivers is conditioned by many factors such as the river slope, the vegetation, the sediment size heterogeneity and other factors such as boundary conditions. In this study, the influence of hydrology has been partly investigated. Besides, the different hydrological conditions affect as well as the upstream sediment supply. Future works should be carried out to better understand how upstream bars form and how they modify the bar morphodynamics in the channel expansion/contraction area.

References

[1] C. An, Y. Cui, X. Fu, and G. Parker. Gravel-bed river evolution in earthquake-prone regions subject to cycled hydrographs and repeated sediment pulses. *Earth Surface Processes and Landforms*, 42(14): 2426–2438, 2017.

[2] L. V. Bendegom. Some considerations on river morphology and river improvement, de ingenieur vol. 59–4, pp. b1–11. *Dutch. English translation: Nat. Res. Council of Canada, Tech. Transi*, 1054:1963, 1947.

[3] R. S. Bernard and M. L. Schneider. Depth-averaged numerical modeling for curved channels. Technical report, ARMY ENGINEER WATERWAYS EXPERIMENT STATION VICKSBURG MS HYDRAULICS LAB, 1992.

[4] O. Blanpain. *Dynamique sédimentaire multiclasse: de l'étude des processus à la modélisation en Manche*. PhD thesis, Université de Rouen, 2009.

[5] A. Blom. Different approaches to handling vertical and streamwise sorting in modeling river morphodynamics. *Water resources research*, 44(3), 2008.

[6] J. S. Bridge. *Rivers and floodplains: forms, processes, and sedimentary record*. John Wiley & Sons, 2009.

[7] O. Cabrit. *Modélisation des flux pariétaux sur les tuyères des moteurs à propergol solide*. PhD thesis, Montpellier 2, 2009.

[8] R. Callander. Instability and river channels. *Journal of Fluid Mechanics*, 36(3):465–480, 1969.

[9] A. Chappell, G. L. Heritage, I. C. Fuller, A. R. Large, and D. J. Milan. Geostatistical analysis of ground-survey elevation data to elucidate spatial and temporal river channel change. *Earth Surface Processes and Landforms: The Journal of the British Geomorphological Research Group*, 28(4):349–370, 2003.

[10] M. Church and J. Haschenburger. What is the "active layer"? *Water Resources Research*, 53(1):5–10, 2017.

[11] N. Claude. *Processus et flux hydro-sédimentaires en rivière sablo-graveleuse: influence de la largeur de section et des bifurcations en Loire moyenne (France)*. PhD thesis, Tours, 2012.

[12] N. Claude, S. Rodrigues, V. Bustillo, J.-G. Bréhéret, P. Tassi, and P. Jugé. Interactions between flow structure and morphodynamic of bars in a channel expansion/contraction, loire river, france. *Water Resources Research*, 50(4):2850–2873, 2014.

[13] J. M. Coleman. Brahmaputra river: channel processes and sedimentation. *Sedimentary Geology*, 3(2-3): 129–239, 1969.

[14] M. Colombini, G. Seminara, and M. Tubino. Finite-amplitude alternate bars. *Journal of Fluid Mechanics*, 181:213–232, 1987.

[15] A. Crosato, E. Mosselman, F. Beidmariam Desta, and W. S. Uijttewaal. Experimental and numerical evidence for intrinsic nonmigrating bars in alluvial channels. *Water Resources Research*, 47(3), 2011.

[16] G. Duró, A. Crosato, and P. Tassi. Numerical study on river bar response to spatial variations of channel width. *Advances in Water Resources*, 93:21–38, 2016.

[17] B. Eaton and M. Lapointe. Effects of large floods on sediment transport and reach morphology in the cobble-bed sainte marguerite river. *Geomorphology*, 40(3-4):291–309, 2001.

[18] F. M. Exner. *Zur physik der dünen*. Hölder, 1920.

[19] J. Finnie, B. Donnell, J. Letter, and R. S. Bernard. Secondary flow correction for depth-averaged flow calculations. *Journal of Engineering Mechanics*, 125(7):848–863, 1999.

[20] M. H. Garcia. Sediment transport and morphodynamics. In *Sedimentation engineering: Processes, measurements, modeling, and practice*, pages 21–163. 2008.

[21] D. G. Ham and M. Church. Bed-material transport estimated from channel morphodynamics: Chilliwack river, british columbia. *Earth Surface Processes and Landforms: The Journal of the British Geomorphological Research Group*, 25(10):1123–1142, 2000.

[22] J. Hervouet, E. Razafindrakoto, C. Villaret, et al. Dealing with dry zones in free surface flows: a new class of advection schemes. In *Proceedings of the 34th World Congress of the International Association for Hydro-Environment Research and Engineering: 33rd Hydrology and Water Resources Symposium and 10th Conference on Hydraulics in Water Engineering*, page 4103. Engineers Australia, 2011.

[23] J.-M. Hervouet. *Hydrodynamics of free surface flows: modelling with the finite element method*. John Wiley & Sons, 2007.

[24] M. Hirano. River-bed degradation with armoring. In *Proceedings of the Japan Society of Civil Engineers*, volume 1971, pages 55–65. Japan Society of Civil Engineers, 1971.

[25] M. Jaballah, B. Camenen, L. Pénard, and A. Paquier. Alternate bar development in an alpine river following engineering works. *Advances in water resources*, 81:103–113, 2015.

[26] R. G. Jackson. Hierarchical attributes and a unifying model of bed forms composed of cohesionless material and produced by shearing flow. *Geological Society of America Bulletin*, 86(11):1523–1533, 1975.

[27] F. Koch. *Bed level computations for curved alluvial channels*. Delft Hydraulics Laboratory, 1980.

[28] B. Magnier, N. Claude, C. Villaret, S. Rodrigues, and P. Tassi. Numerical simulation of flow structures in the presence of alternate and transverse bars: application to the loire river (france). In *XXth TELEMAC-MASCARET. User Conference 2013*, pages 31–36, 2013.

[29] C. Marti and G. R. Bezzola. Bed load transport in braided gravel-bed rivers. *Braided rivers: process, deposits, ecology and management*, 36:199–215, 2006.

[30] S. McLelland, P. Ashworth, and J. Best. Velocity correction methods in open channels: Description, critique and recommendations. *Consult. Rep. FAP24*, 1994.

[31] A. Mendoza, J. D. Abad, E. J. Langendoen, D. Wang, P. Tassi, and K. E. K. Abderrezzak. Effect of sediment transport boundary conditions on the numerical modeling of bed morphodynamics. *Journal of Hydraulic Engineering*, 143(4):04016099, 2016.

[32] D. J. Milan, G. L. Heritage, and D. Hetherington. Application of a 3d laser scanner in the assessment of erosion and deposition volumes and channel change in a proglacial river. *Earth Surface Processes and Landforms: The Journal of the British Geomorphological Research Group*, 32(11):1657–1674, 2007.

[33] M. Mosley. Response of braided rivers to changing discharge. *Journal of Hydrology (New Zealand)*, pages 18–67, 1983.

[34] M. P. Mosley. Analysis of the effect of changing discharge on channel morphology and instream uses in a braided river, ohau river, new zealand. *Water resources research*, 18(4):800–812, 1982.

[35] G. Parker, M. Hassan, and P. Wilcock. 10 adjustment of the bed surface size distribution of gravel-bed rivers in response to cycled hydrographs. *Developments in Earth Surface Processes*, 11:241–285, 2007.

[36] A. Recking, G. Piton, D. Vazquez-Tarrio, and G. Parker. Quantifying the morphological print of bedload transport. *Earth Surface Processes and Landforms*, 41(6):809–822, 2016.

[37] S. Rodrigues, E. Mosselman, N. Claude, C. L. Wintenberger, and P. Juge. Alternate bars in a sandy gravel bed river: generation, migration and interactions with superimposed dunes. *Earth Surface Processes and Landforms*, 40(5):610–628, 2015.

[38] I. Rozovskii. Concerning the question of velocity distribution in stream bends. *DAN URSR Report of the Academy of Sciences of the Ukraine SSR*, 1, 1954.

[39] G. Seminara and M. Tubino. Alternate bars and meandering: free, forced and mixed interactions. *River meandering*, 12:267–320, 1989.

[40] R. Soulsby. *Dynamics of marine sands: a manual for practical applications*. Thomas Telford, 1997.

[41] G. Stecca, A. Siviglia, and A. Blom. An accurate numerical solution to the saint-venant-hirano model for mixed-sediment morphodynamics in rivers. *Advances in Water Resources*, 93:39–61, 2016.

[42] N. Surian, L. Mao, M. Giacomin, and L. Ziliani. Morphological effects of different channel-forming discharges in a gravel-bed river. *Earth Surface Processes and Landforms*, 34(8):1093–1107, 2009.

[43] A. Talmon, N. Struiksma, and M. Van Mierlo. Laboratory measurements of the direction of sediment transport on transverse alluvial-bed slopes. *Journal of hydraulic research*, 33(4):495–517, 1995.

[44] M. Tubino. Growth of alternate bars in unsteady flow. *Water Resources Research*, 27(1):37–52, 1991.

[45] C. Van der Meer, E. Mosselman, C. Sloff, B. Jagers, G. Zolezzi, and M. Tubino. Numerical simulations of upstream and downstream overdeepening. In *RCEM 2011: Proceedings of the 7th IAHR Symposium of River, Coastal and Estuarine Morphodynamics, Beijing, China, 6-8 September 2011*. Citeseer, 2011.

[46] E. Viparelli, A. Blom, and R. R. H. Moreira. Modeling stratigraphy-based gravel-bed river morphodynamics. *Gravel-Bed Rivers: Processes and Disasters*, pages 609–637, 2017.

[47] D. Wang and P. Tassi. Secondary flow corrections into the telemac-mascaret modelling system. In *21st TELEMAC-MASCARET User Conference 2014*, pages 239–247, 2014.

[48] S. Wathen and T. Hoey. Morphological controls on the downstream passage of a sediment wave in a gravel-bed stream. *Earth Surface Processes and Landforms: The Journal of the British Geomorphological Group*, 23(8):715–730, 1998.

[49] M. Welber, W. Bertoldi, and M. Tubino. The response of braided planform configuration to flow variations, bed reworking and vegetation: the case of the tagliamento river, italy. *Earth Surface Processes and Landforms*, 37(5):572–582, 2012.

[50] P. R. Wilcock. Estimating local bed shear stress from velocity observations. *Water Resources Research*, 32(11):3361–3366, 1996.

[51] P. R. Wilcock and J. C. Crowe. Surface-based transport model for mixed-size sediment. *Journal of Hydraulic Engineering*, 129(2):120–128, 2003.

[52] G. Zolezzi and G. Seminara. Downstream and upstream influence in river meandering. part 2. planimetric development. *Journal of Fluid Mechanics*, 438:183–211, 2001.

Appendices

A Sensibility test of A_s and D_s

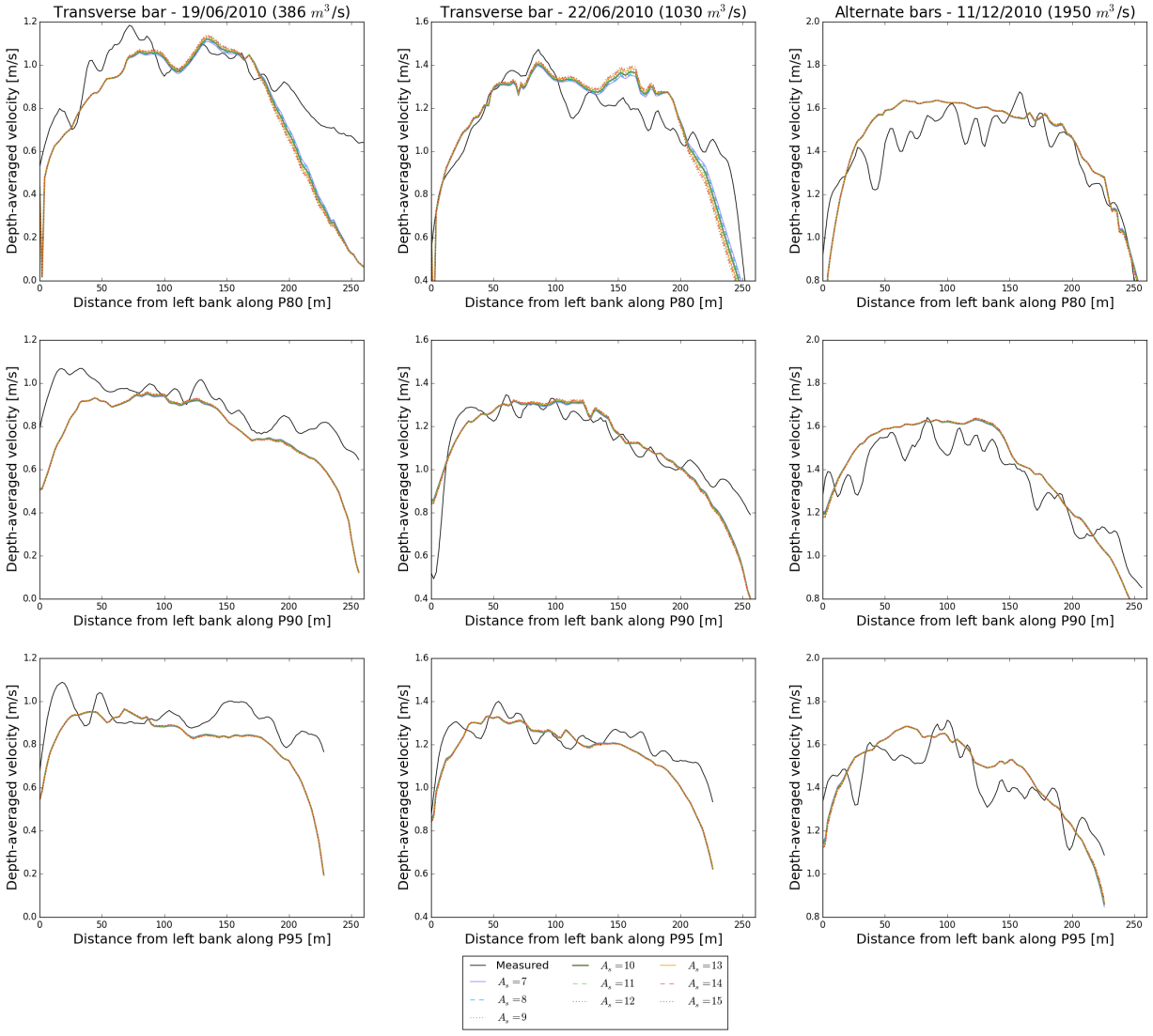


Figure 30: Sensibility test of coefficient A_s that determine the rate of vorticity production in transport equation for streamwise vorticity.

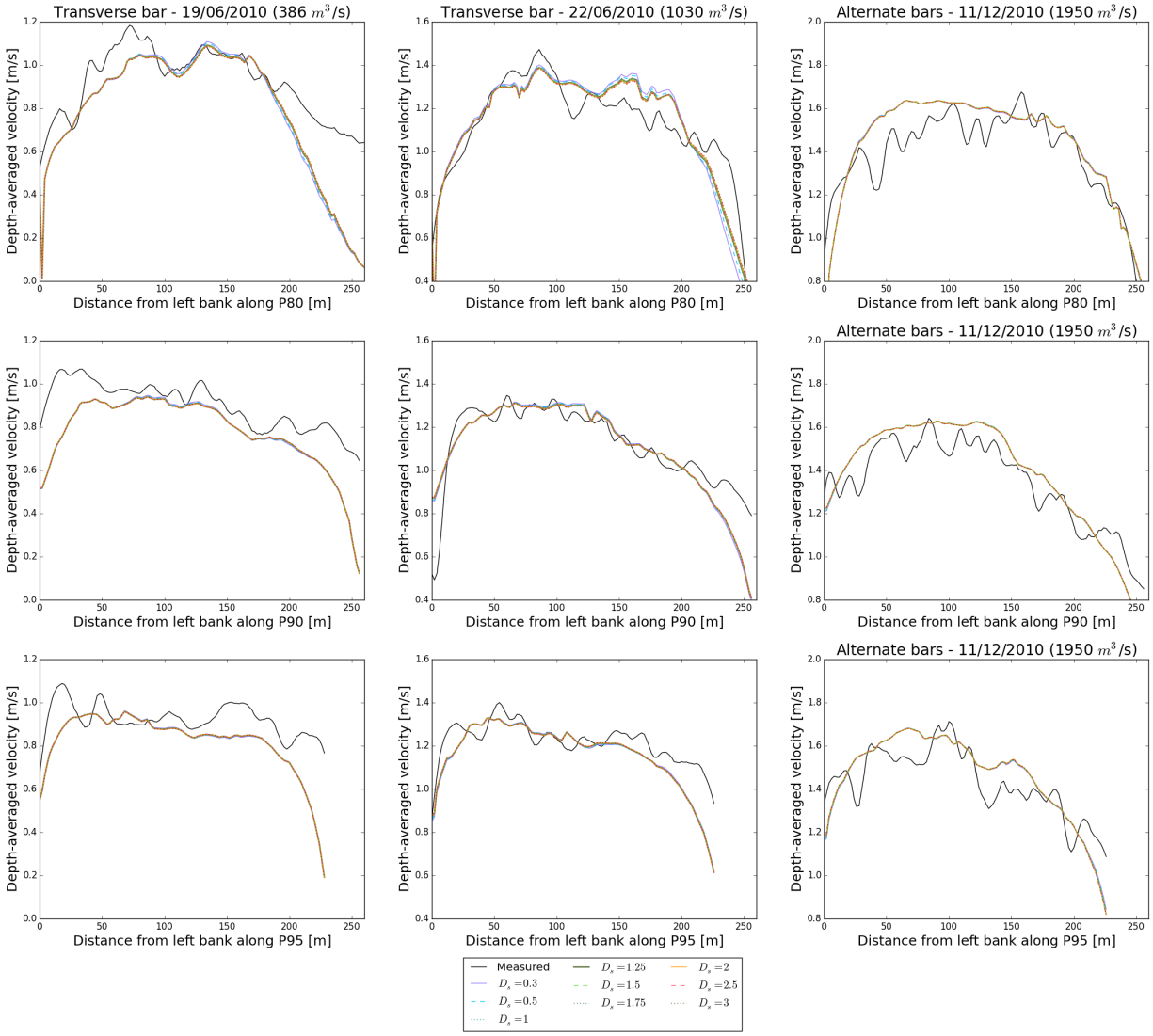


Figure 31: Sensibility test of coefficient D_s that determine the rate of vorticity dissipation in transport equation for streamwise vorticity.

B 2d hydrodynamic model calibration of k_s

June 19, 2010		Ks [m]								
		0,05	0,075	0,1	0,15	0,2	0,25	0,3	0,4	0,5
L1	MAE [m]	0,1	0,05	0,01	0,06	0,12	0,16	0,2	0,27	0,33
	RMSE [m]	0,11	0,05	0,02	0,07	0,12	0,16	0,2	0,27	0,33
L2	MAE [m]	0,04	0,02	0,06	0,13	0,18	0,23	0,27	0,34	0,39
	RMSE [m]	0,04	0,03	0,07	0,13	0,18	0,23	0,27	0,34	0,39
L3	MAE [m]	0,06	0,01	0,04	0,1	0,16	0,2	0,24	0,31	0,37
	RMSE [m]	0,07	0,02	0,04	0,1	0,16	0,2	0,24	0,31	0,37
P80	MAE [m]	0,15	0,15	0,16	0,18	0,2	0,22	0,23	0,25	0,27
	RMSE [m]	0,22	0,21	0,21	0,22	0,23	0,23	0,24	0,26	0,27
P90	MAE [m]	0,11	0,13	0,15	0,18	0,19	0,21	0,22	0,24	0,26
	RMSE [m]	0,16	0,17	0,18	0,2	0,21	0,23	0,24	0,26	0,27
P95	MAE [m]	0,11	0,12	0,13	0,15	0,17	0,19	0,2	0,22	0,24
	RMSE [m]	0,15	0,16	0,17	0,18	0,2	0,21	0,22	0,24	0,25
Total		4,00	5,5	2,5	0	0	0	0	0	0
Ks,cal [m]		0,072								

Figure 32: Values of MAE and RMSE computed along the longitudinal profiles of free surface and cross-sectional profiles of flow velocity obtained with $k_s \in [0.05; 0.5]$ m on 19 June 2010.

June 22, 2010		Ks [m]								
		0,05	0,075	0,1	0,15	0,2	0,25	0,3	0,4	0,5
L1	MAE [m]	0,21	0,14	0,08	0,03	0,09	0,15	0,21	0,3	0,37
	RMSE [m]	0,22	0,14	0,08	0,04	0,1	0,16	0,21	0,3	0,37
L2	MAE [m]	0,24	0,16	0,1	0,02	0,06	0,13	0,18	0,27	0,34
	RMSE [m]	0,24	0,17	0,11	0,03	0,07	0,13	0,18	0,27	0,35
L3	MAE [m]	0,21	0,13	0,07	0,03	0,1	0,16	0,21	0,3	0,38
	RMSE [m]	0,21	0,13	0,08	0,03	0,1	0,16	0,22	0,31	0,38
P80	MAE [m]	0,14	0,1	0,09	0,08	0,08	0,09	0,1	0,11	0,13
	RMSE [m]	0,16	0,13	0,12	0,11	0,11	0,11	0,12	0,14	0,16
P90	MAE [m]	0,13	0,1	0,08	0,07	0,08	0,1	0,11	0,14	0,16
	RMSE [m]	0,16	0,13	0,12	0,11	0,12	0,13	0,13	0,15	0,17
P95	MAE [m]	0,1	0,08	0,07	0,08	0,09	0,11	0,13	0,16	0,18
	RMSE [m]	0,13	0,11	0,11	0,11	0,12	0,13	0,14	0,17	0,19
Total			0,3333333	1,3333333	9,1666667	0,8333333	0,3333333			
Ks,cal [m]		0,148								

Figure 33: Values of MAE and RMSE computed along the longitudinal profiles of free surface and cross-sectional profiles of flow velocity obtained with $k_s \in [0.05; 0.5]$ m on 22 June 2010.

December 11, 2010		Ks [m]								
		0,05	0,075	0,1	0,15	0,2	0,25	0,3	0,4	0,5
L1	MAE [m]	0,16	0,08	0,03	0,08	0,15	0,22	0,27	0,37	0,45
	RMSE [m]	0,16	0,09	0,03	0,08	0,16	0,22	0,27	0,37	0,45
L2	MAE [m]	0,2	0,12	0,06	0,04	0,12	0,18	0,24	0,33	0,41
	RMSE [m]	0,21	0,13	0,06	0,05	0,12	0,18	0,24	0,33	0,41
L3	MAE [m]	0,18	0,1	0,04	0,06	0,14	0,2	0,26	0,35	0,43
	RMSE [m]	0,19	0,11	0,05	0,06	0,14	0,2	0,26	0,35	0,43
P80	MAE [m]	0,19	0,17	0,15	0,12	0,1	0,09	0,09	0,09	0,1
	RMSE [m]	0,23	0,2	0,18	0,16	0,14	0,13	0,13	0,13	0,14
P90	MAE [m]	0,19	0,16	0,13	0,1	0,08	0,07	0,06	0,07	0,09
	RMSE [m]	0,21	0,18	0,15	0,12	0,1	0,08	0,08	0,09	0,1
P95	MAE [m]	0,19	0,16	0,13	0,1	0,09	0,09	0,09	0,09	0,1
	RMSE [m]	0,22	0,18	0,16	0,13	0,11	0,1	0,1	0,11	0,13
Total				4	2	0	2,5	3,5	0	
Ks,cal [m]		0,198								

Figure 34: Values of MAE and RMSE computed along the longitudinal profiles of free surface and cross-sectional profiles of flow velocity obtained with $k_s \in [0.05; 0.5]$ m on 11 December 2010.

C Primary, secondary and vertical components of flow velocity computed with the hydrodynamic model

PRIMARY VELOCITIES

	Measured		N_5		N_8		N_15	
	Max (m/s)	Mean (m/s)	Max (m/s)	Mean (m/s)	Max (m/s)	Mean (m/s)	Max (m/s)	Mean (m/s)
P80	1,250	0.915	1.048	0.756	1,043	0.752	0,992	0.728
P90	1,183	0.883	0,939	0.733	0,917	0.734	0,920	0.713
P95	1,146	0.914	0,949	0.783	0,979	0.786	0,938	0.760

SECONDARY VELOCITIES

	Measured		N_5		N_8		N_15	
	Max (m/s)	Mean (m/s)	Max (m/s)	Mean (m/s)	Max (m/s)	Mean (m/s)	Max (m/s)	Mean (m/s)
P80	0.114	0.0200	0,310	0.094	0,311	0,095	0,279	0.086
P90	0,112	0,023	0.118	0,051	0,121	0,052	0,111	0,049
P95	0,116	0,024	0,132	0,057	0,133	0,057	0,131	0,055

VERTICAL VELOCITIES

	Measured		N_5		N_8		N_15	
	Max (m/s)	Mean (m/s)	Max (m/s)	Mean (m/s)	Max (m/s)	Mean (m/s)	Max (m/s)	Mean (m/s)
P80	0,061	0,015	0,041	0,007	0,039	0,007	0,033	0,006
P90	0,072	0,009	0,029	0,005	0,026	0,005	0,023	0,004
P95	0,052	0,013	0,021	0.005	0.020	0,005	0,019	0,004

Figure 35: Primary, secondary and vertical flow velocity on 19 June 2010.

PRIMARY VELOCITIES

	Measured		N_5		N_8		N_15	
	Max (m/s)	Mean (m/s)	Max (m/s)	Mean (m/s)	Max (m/s)	Mean (m/s)	Max (m/s)	Mean (m/s)
P80	1,533	1,085	1,380	1,083	1.337	1.050	1,253	1,016
P90	1,442	1,267	1,310	1,073	1,287	1,047	1,219	1,008
P95	1,467	1,207	1,348	1,121	1,326	1,091	1,246	1,054

SECONDARY VELOCITIES

	Measured		N_5		N_8		N_15	
	Max (m/s)	Mean (m/s)	Max (m/s)	Mean (m/s)	Max (m/s)	Mean (m/s)	Max (m/s)	Mean (m/s)
P80	0,143	0,017	0,234	0,077	0.235	0.080	0,222	0,078
P90	0,111	0,022	0,117	0,048	0,117	0,046	0,115	0,045
P95	0,111	0,024	0,160	0,067	0,156	0,067	0,157	0,068

VERTICAL VELOCITIES

	Measured		N_5		N_8		N_15	
	Max (m/s)	Mean (m/s)	Max (m/s)	Mean (m/s)	Max (m/s)	Mean (m/s)	Max (m/s)	Mean (m/s)
P80	0,114	0,021	0.105	0.011	0.116	0.010	0,089	0,009
P90	0,129	0,020	0,062	0,010	0,056	0,009	0,054	0,008
P95	0,075	0,017	0,067	0,012	0,055	0,010	0,056	0,009

Figure 36: Primary, secondary and vertical flow velocity on 22 June 2010.

PRIMARY VELOCITIES

	Measured		N_5		N_8		N_15	
	Max (m/s)	Mean (m/s)	Max (m/s)	Mean (m/s)	Max (m/s)	Mean (m/s)	Max (m/s)	Mean (m/s)
P80	1,777	1,314	1,644	1,363	1,602	1,319	1,529	1,269
P90	1,737	1,347	1,630	1,332	1,615	1,289	1,535	1,242
P95	1,803	1,428	1,677	1,398	1,639	1,352	1,590	1.302

SECONDARY VELOCITIES

	Measured		N_5		N_8		N_15	
	Max (m/s)	Mean (m/s)	Max (m/s)	Mean (m/s)	Max (m/s)	Mean (m/s)	Max (m/s)	Mean (m/s)
P80	0,114	0,024	0,203	0,061	0,213	0,062	0,202	0,060
P90	0,103	0,029	0,124	0,034	0,132	0,034	0,135	0,034
P95	0,162	0,033	0,184	0,101	0,188	0,099	0,179	0.099

VERTICAL VELOCITIES

	Measured		N_5		N_8		N_15	
	Max (m/s)	Mean (m/s)	Max (m/s)	Mean (m/s)	Max (m/s)	Mean (m/s)	Max (m/s)	Mean (m/s)
P80	0,106	0,026	0,063	0,012	0,067	0,011	0,065	0,010
P90	0,110	0,023	0,046	0,012	0,047	0,011	0,046	0,010
P95	0,087	0,026	0,101	0,018	0,098	0,017	0,111	0,015

Figure 37: Primary, secondary and vertical flow velocity on 11 December 2010.

D Morphological evolution for distinct constant water discharges

D.1 Discharge of 150 m^3/s

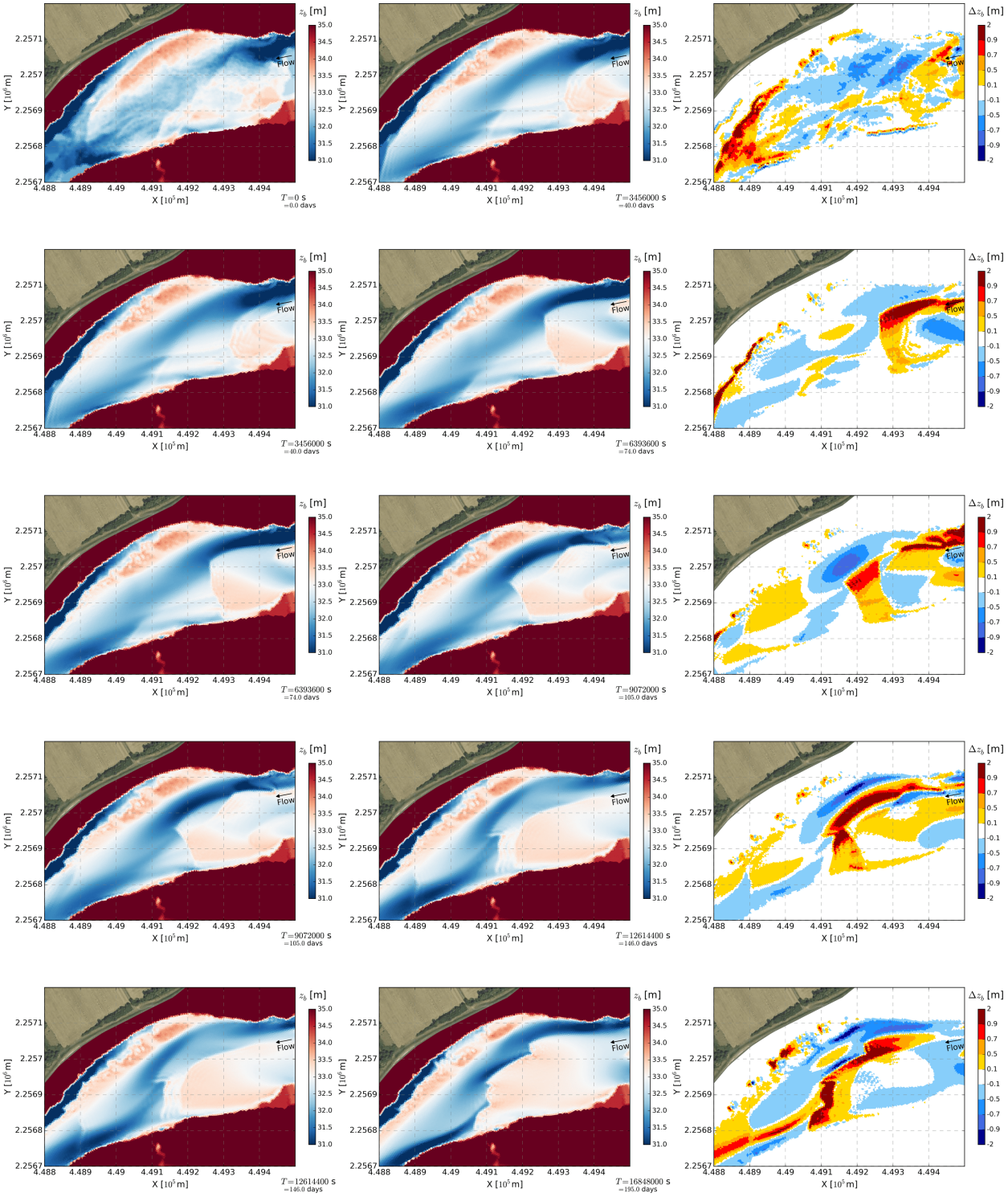


Figure 38: Morphological evolution of riverbed for water discharge of 150 m^3/s

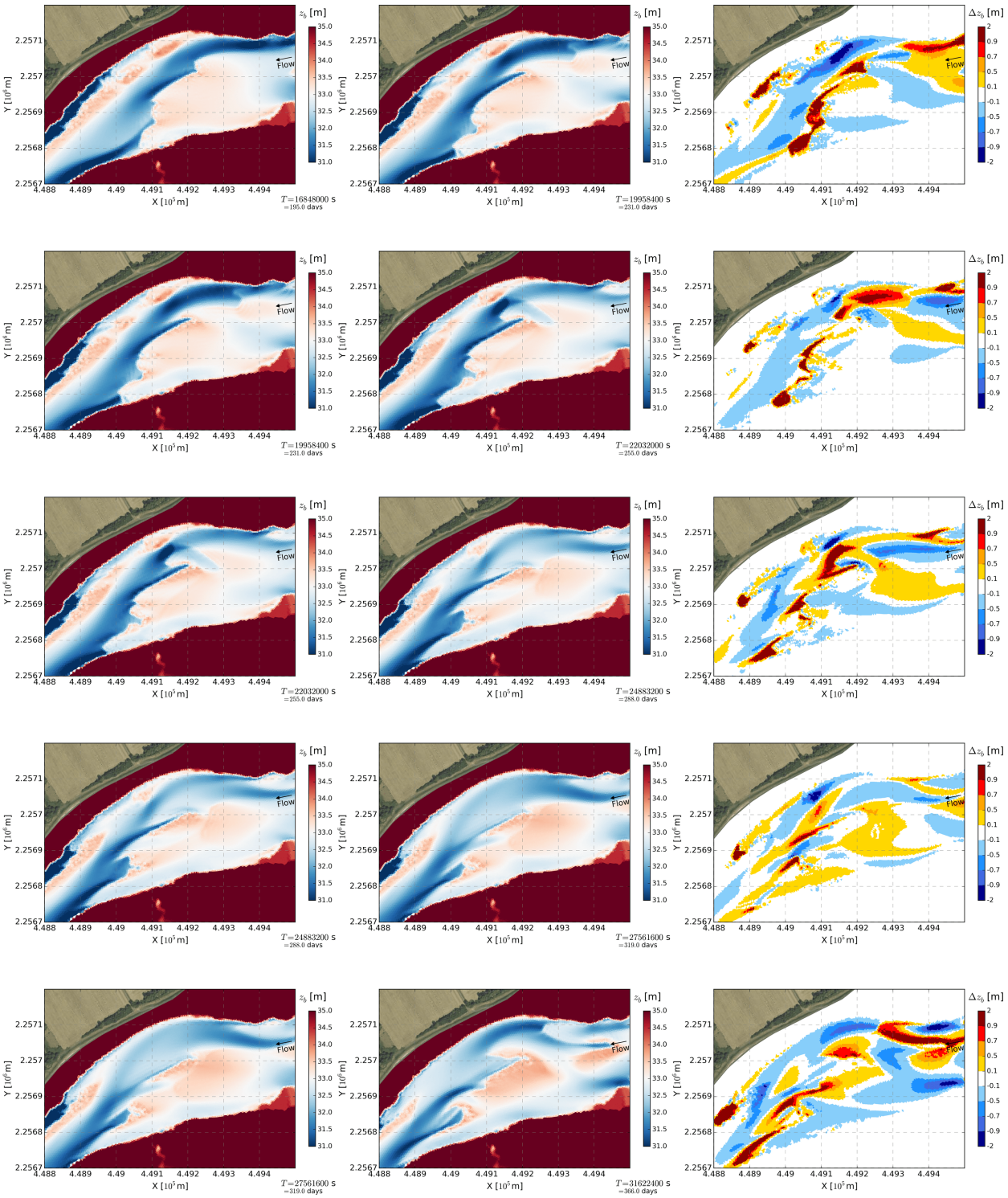


Figure 39: Morphological evolution of riverbed for water discharge of 150 m^3/s

D.2 Discharge of 350 m^3/s

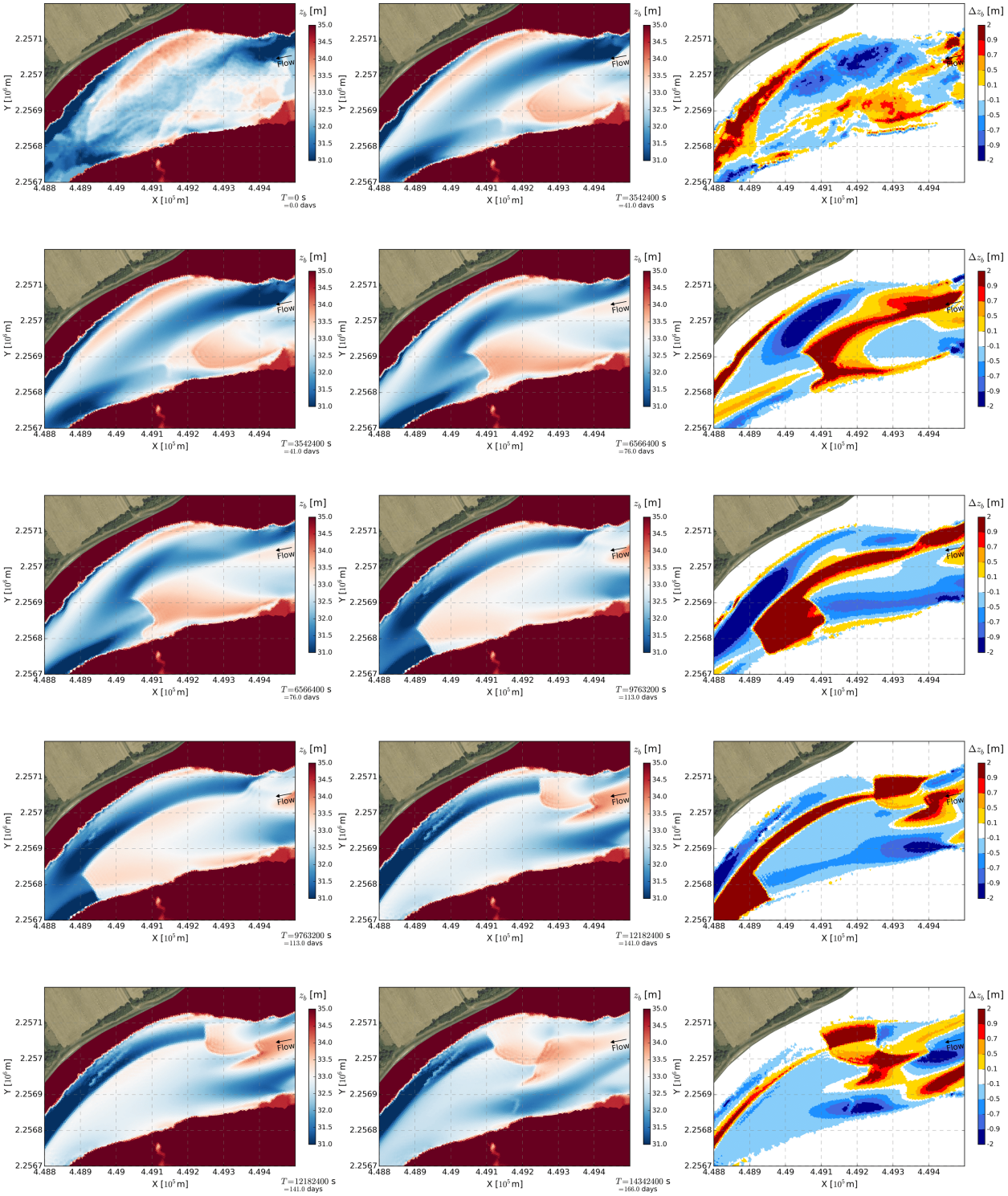


Figure 40: Morphological evolution of riverbed for water discharge of 350 m^3/s

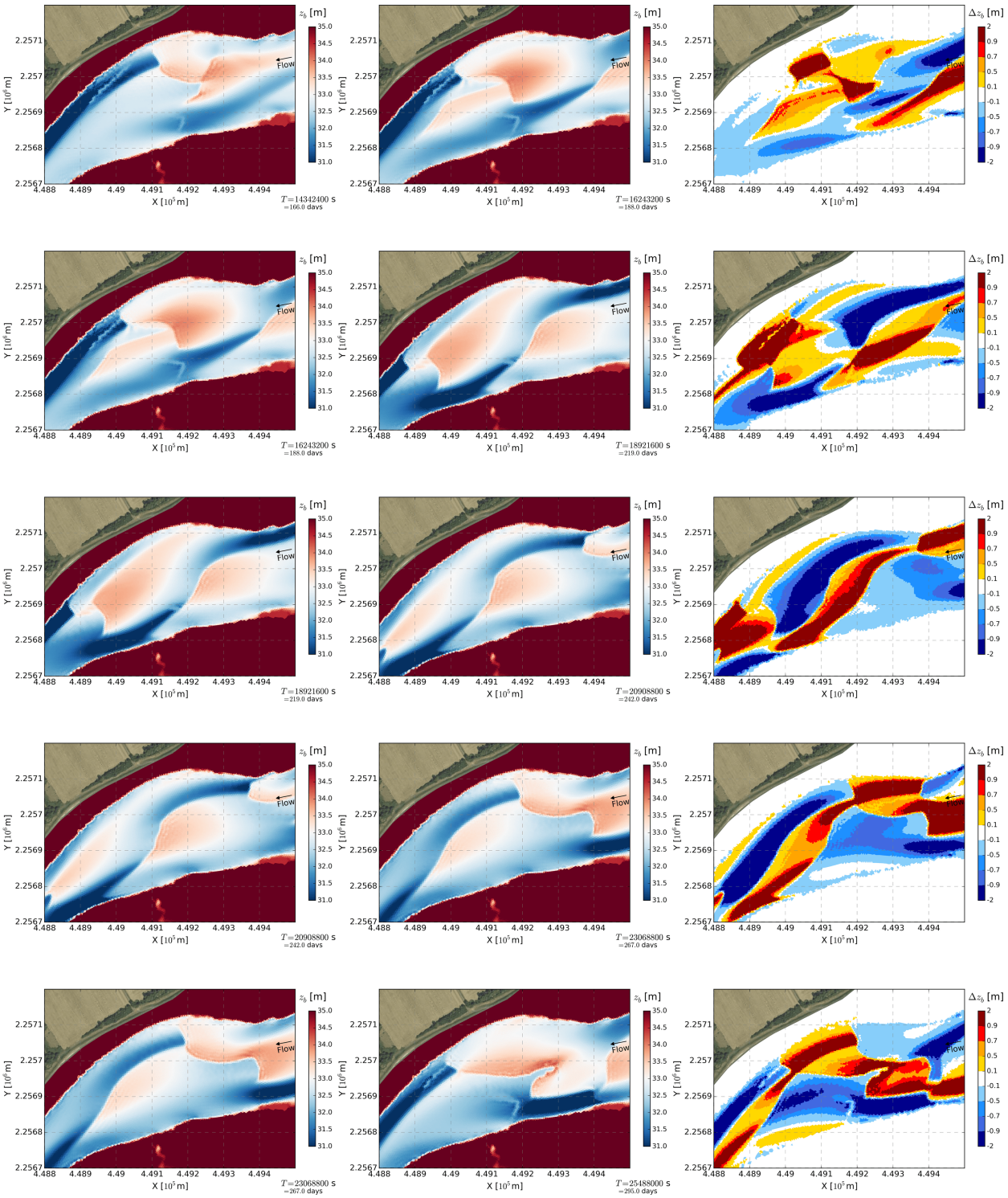


Figure 41: Morphological evolution of riverbed for water discharge of 350 m^3/s

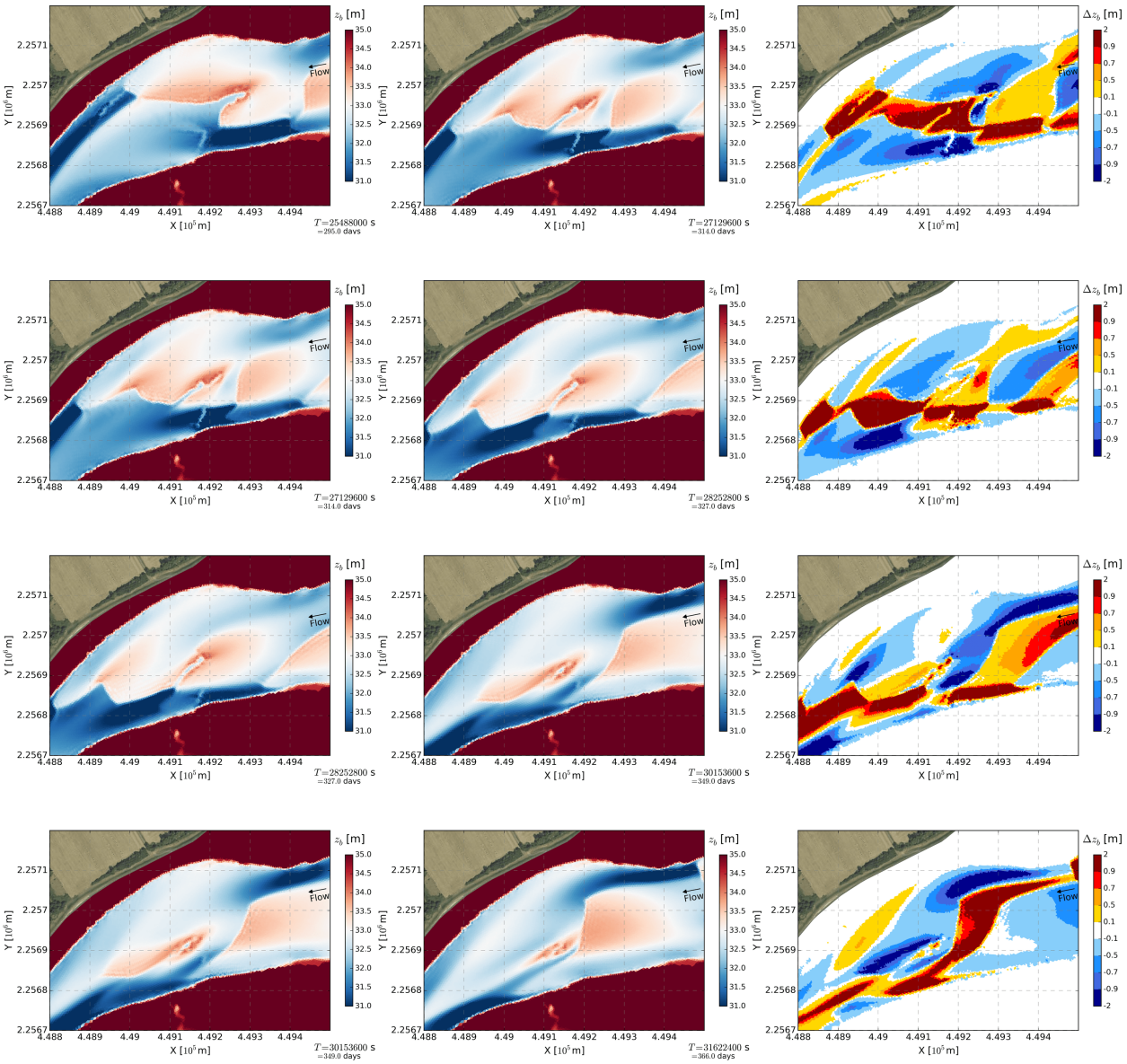


Figure 42: Morphological evolution of riverbed for water discharge of 350 m^3/s

D.3 Discharge of 500 m^3/s

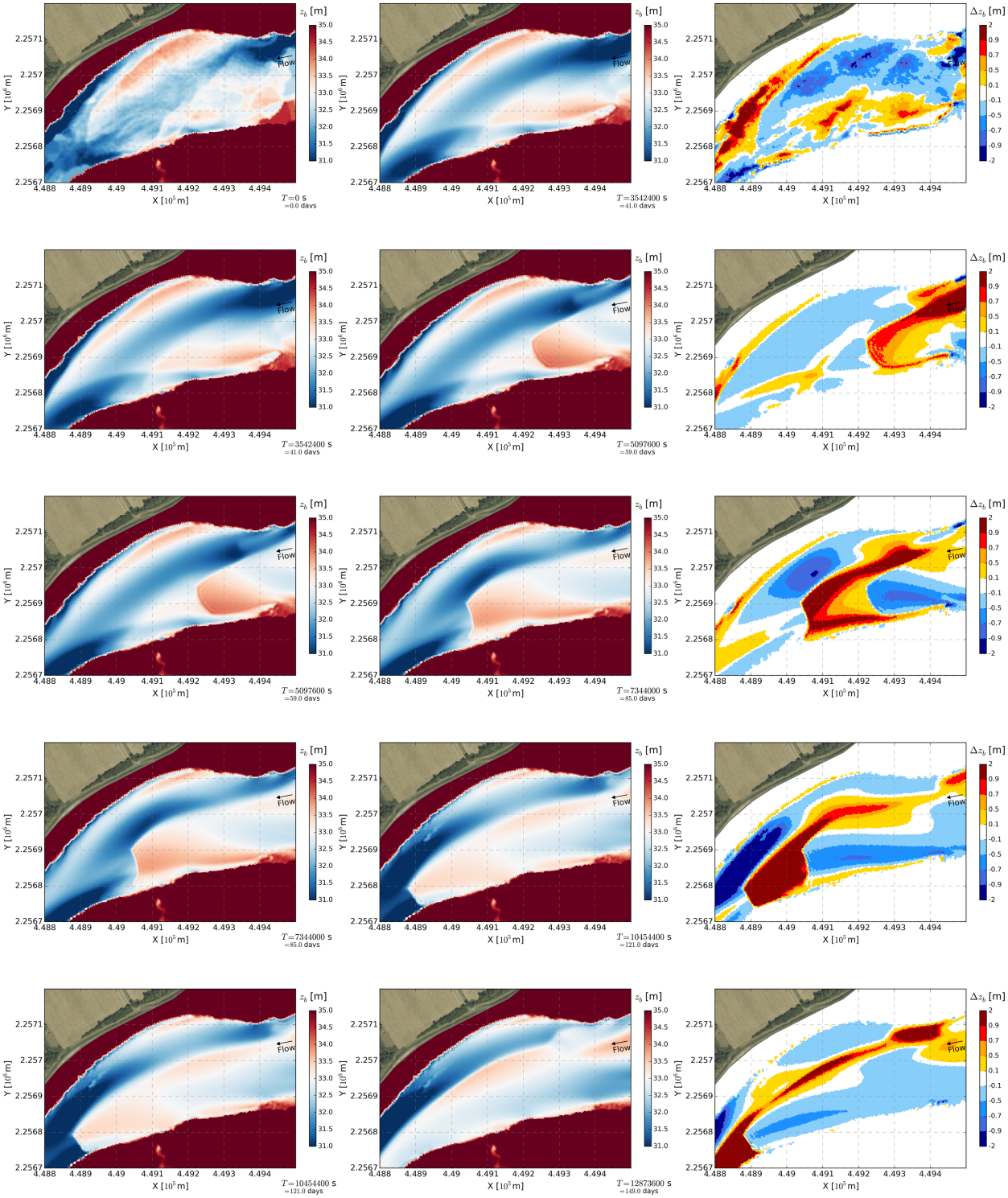


Figure 43: Morphological evolution of riverbed for water discharge of 500 m^3/s

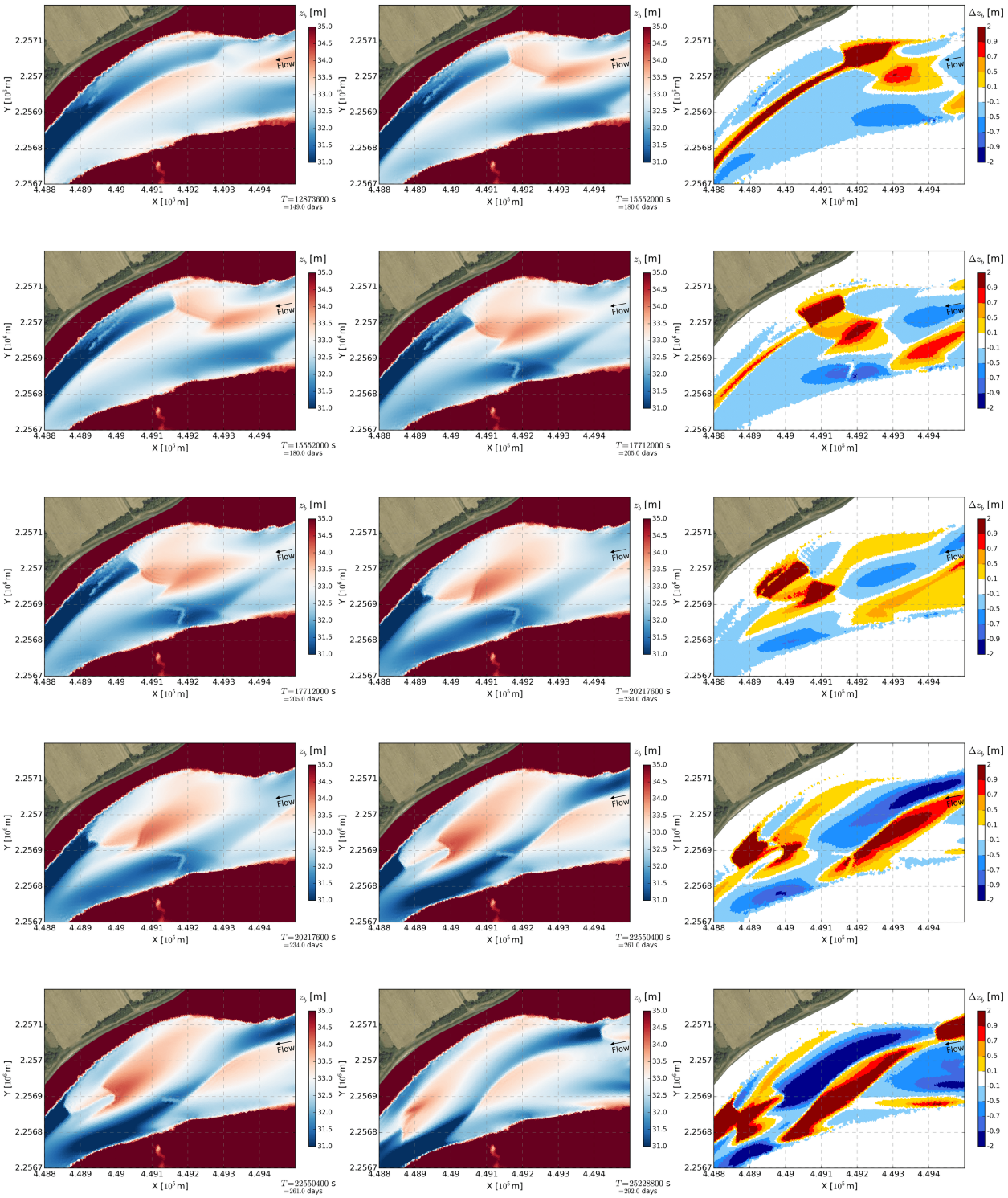


Figure 44: Morphological evolution of riverbed for water discharge of 500 m^3/s

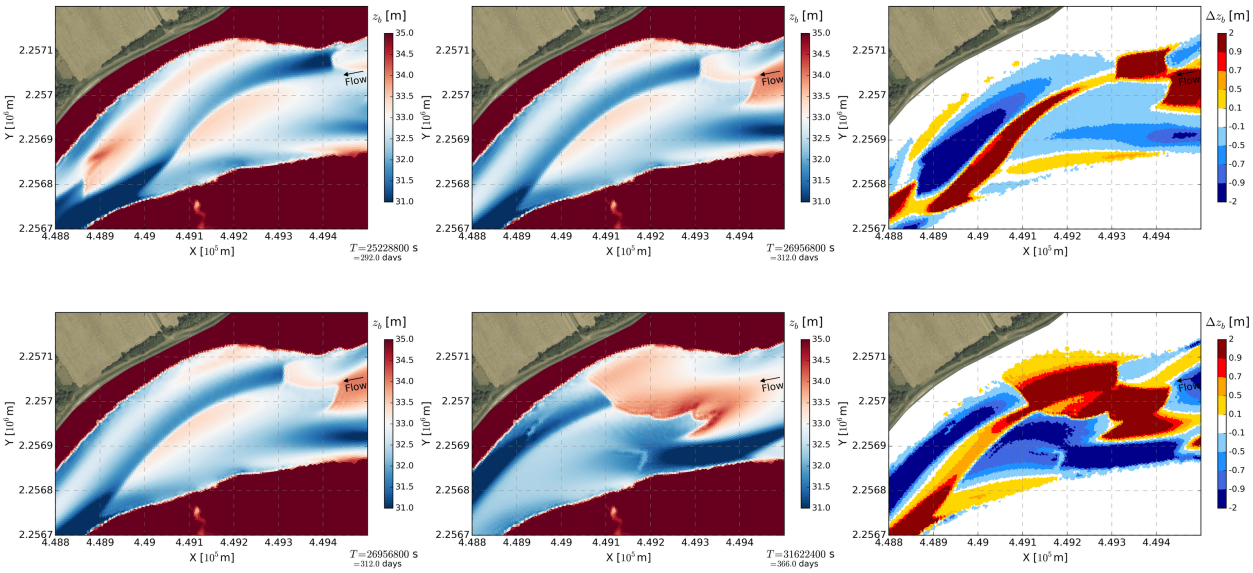


Figure 45: Morphological evolution of riverbed for water discharge of 500 m^3/s

D.4 Discharge of 750 m^3/s

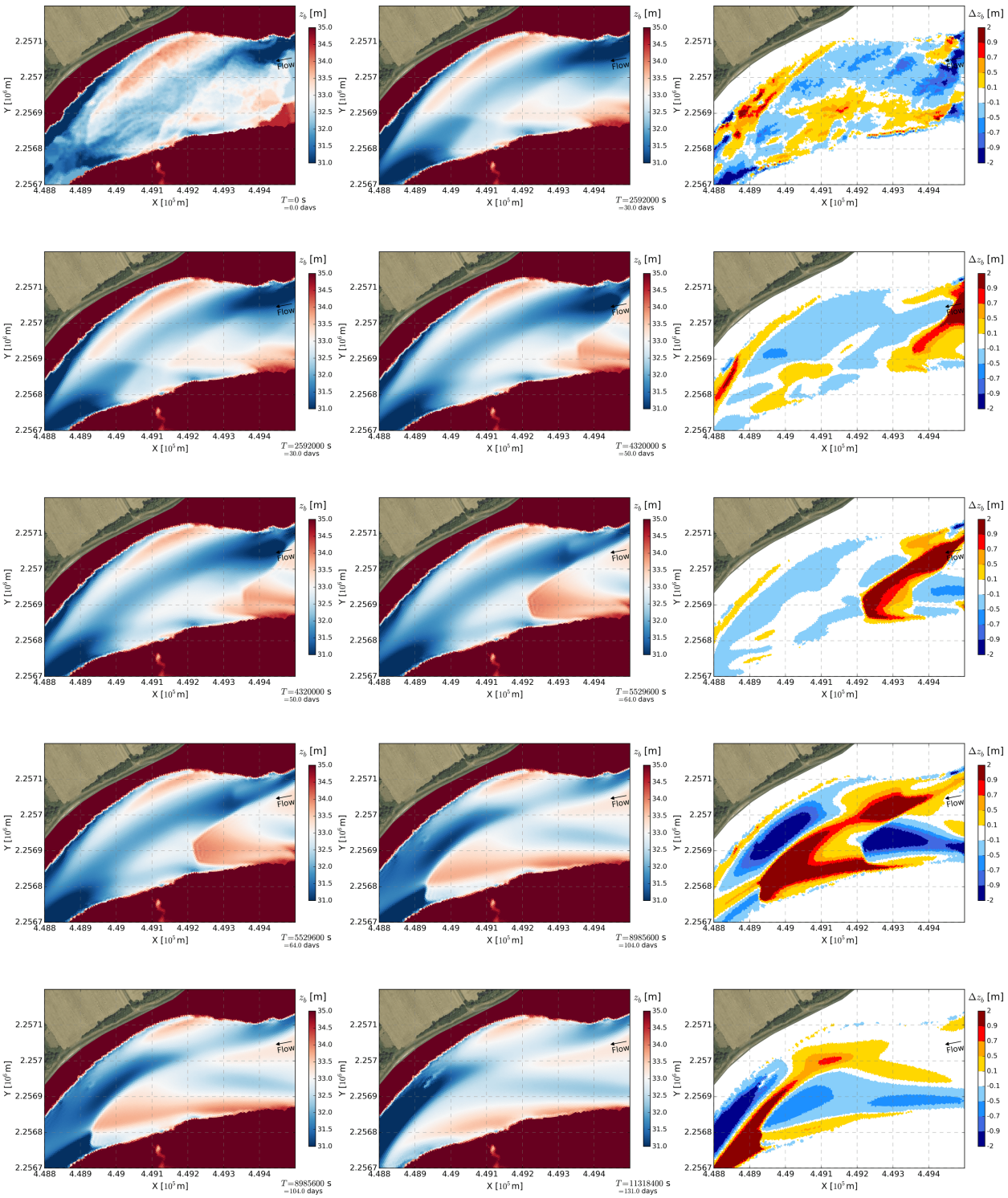


Figure 46: Morphological evolution of riverbed for water discharge of 750 m^3/s

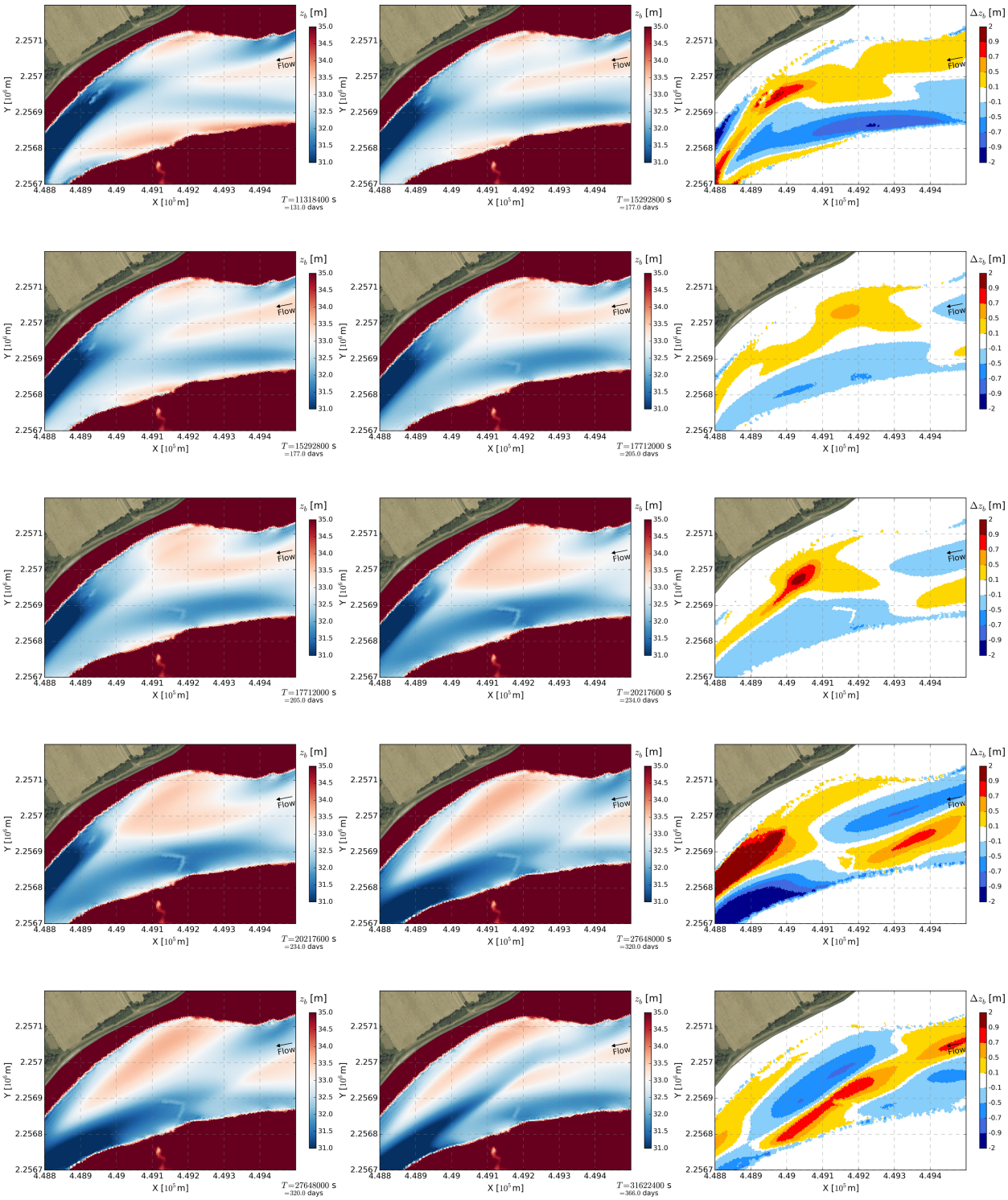


Figure 47: Morphological evolution of riverbed for water discharge of 750 m^3/s

D.5 Discharge of 1000 m^3/s

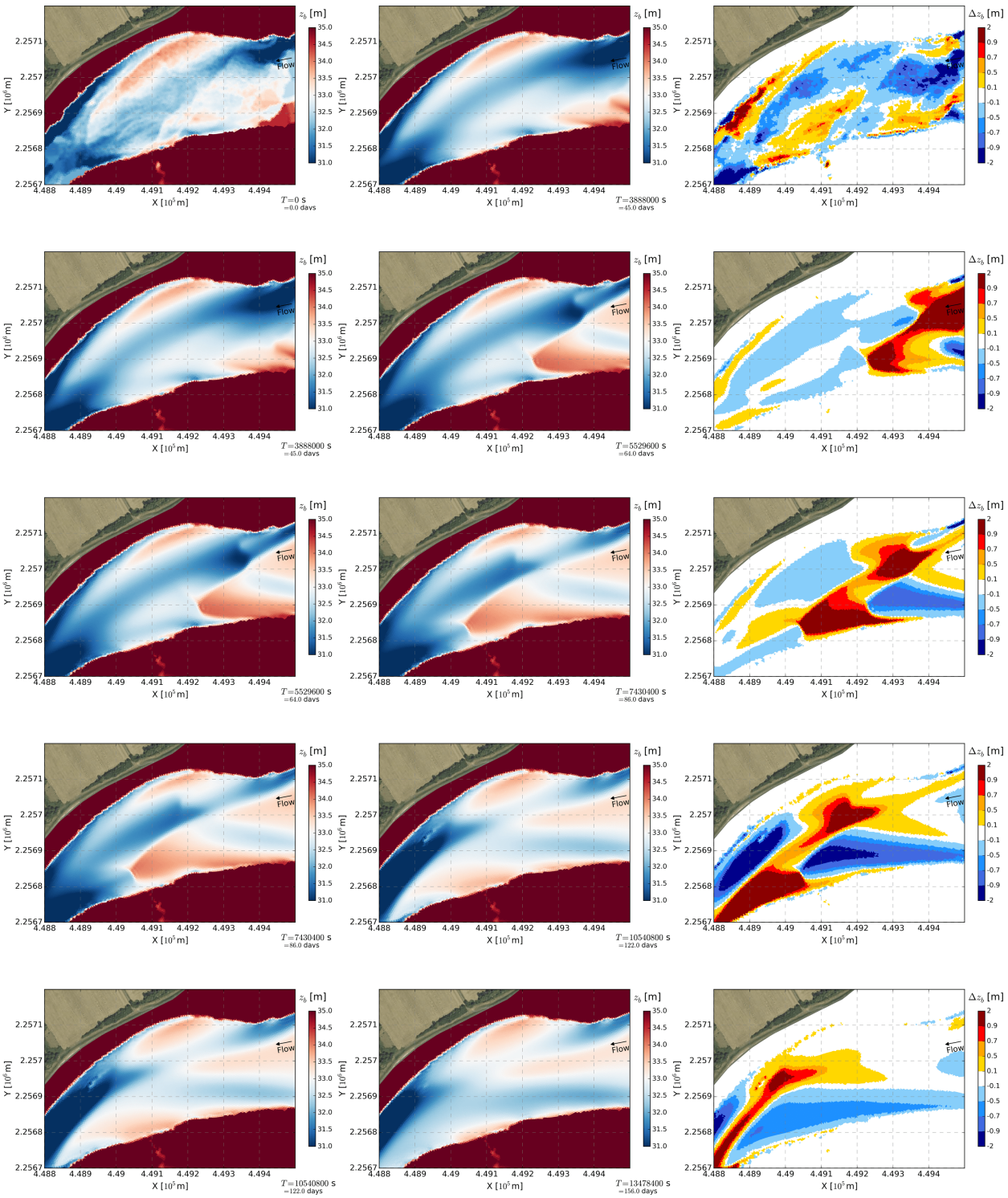


Figure 48: Morphological evolution of riverbed for water discharge of 1000 m^3/s

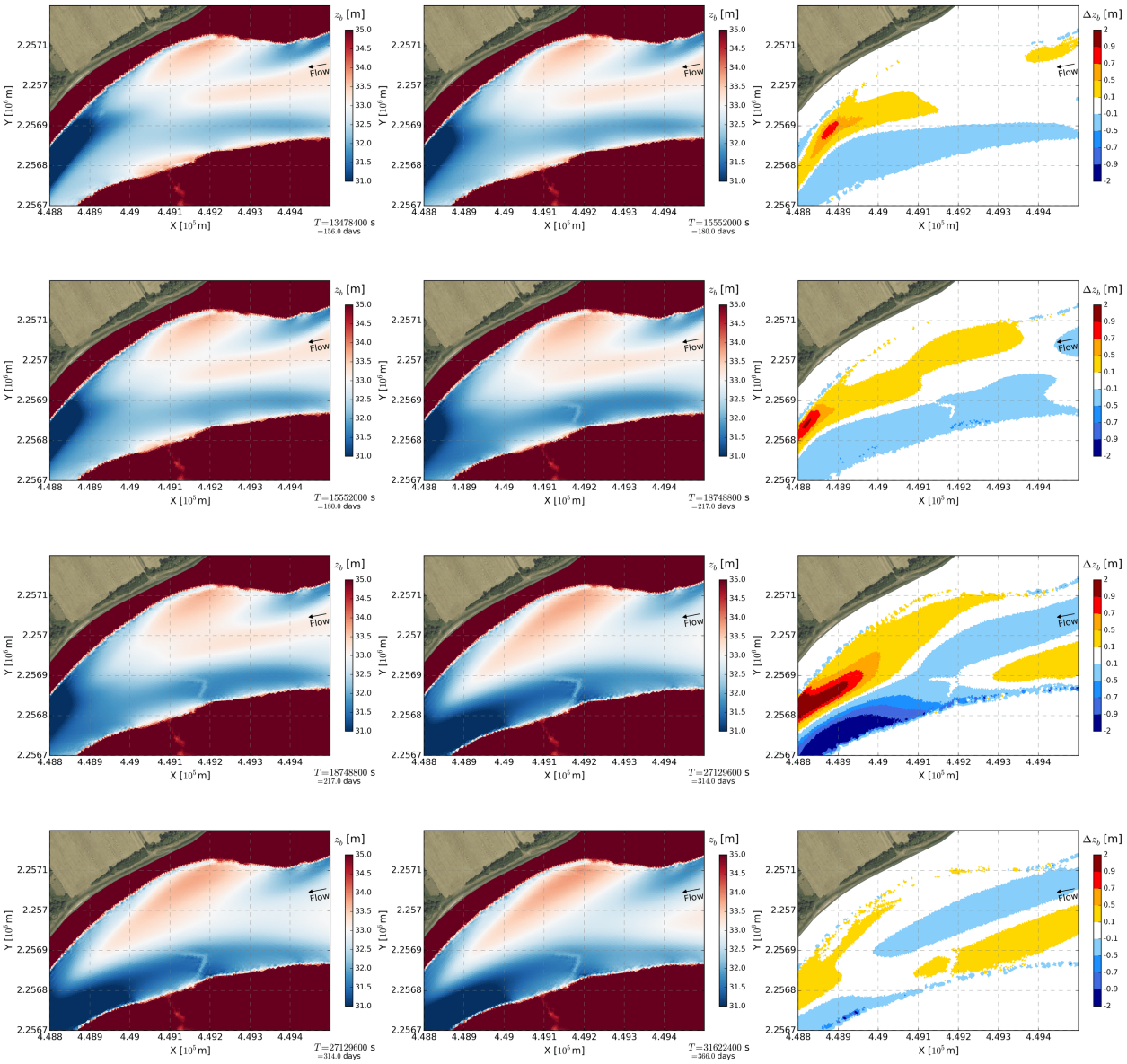


Figure 49: Morphological evolution of riverbed for water discharge of 1000 m^3/s

D.6 Discharge of 1500 m^3/s

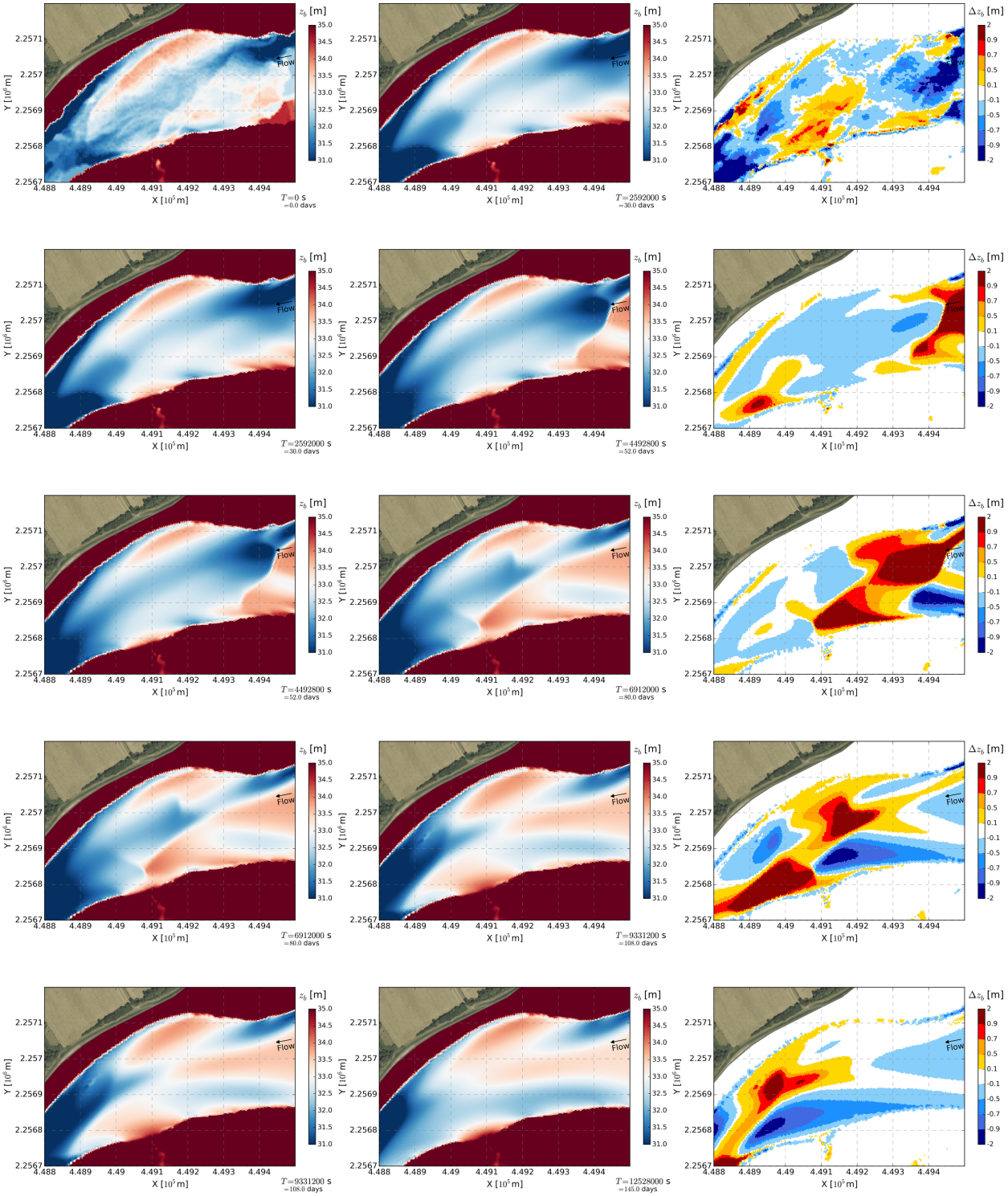


Figure 50: Morphological evolution of riverbed for water discharge of 1500 m^3/s

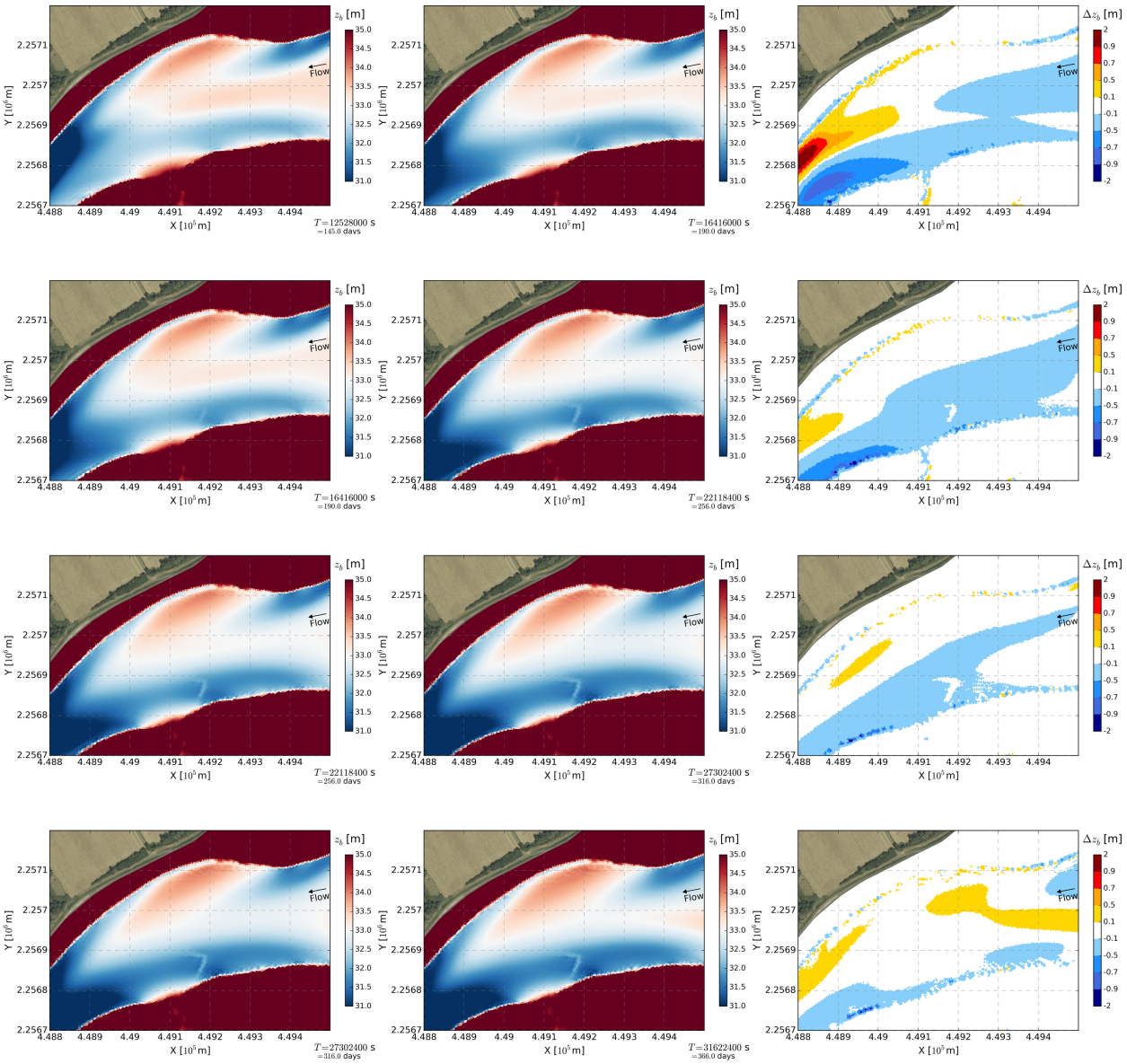


Figure 51: Morphological evolution of riverbed for water discharge of 1500 m^3/s

D.7 Discharge of 2000 m^3/s

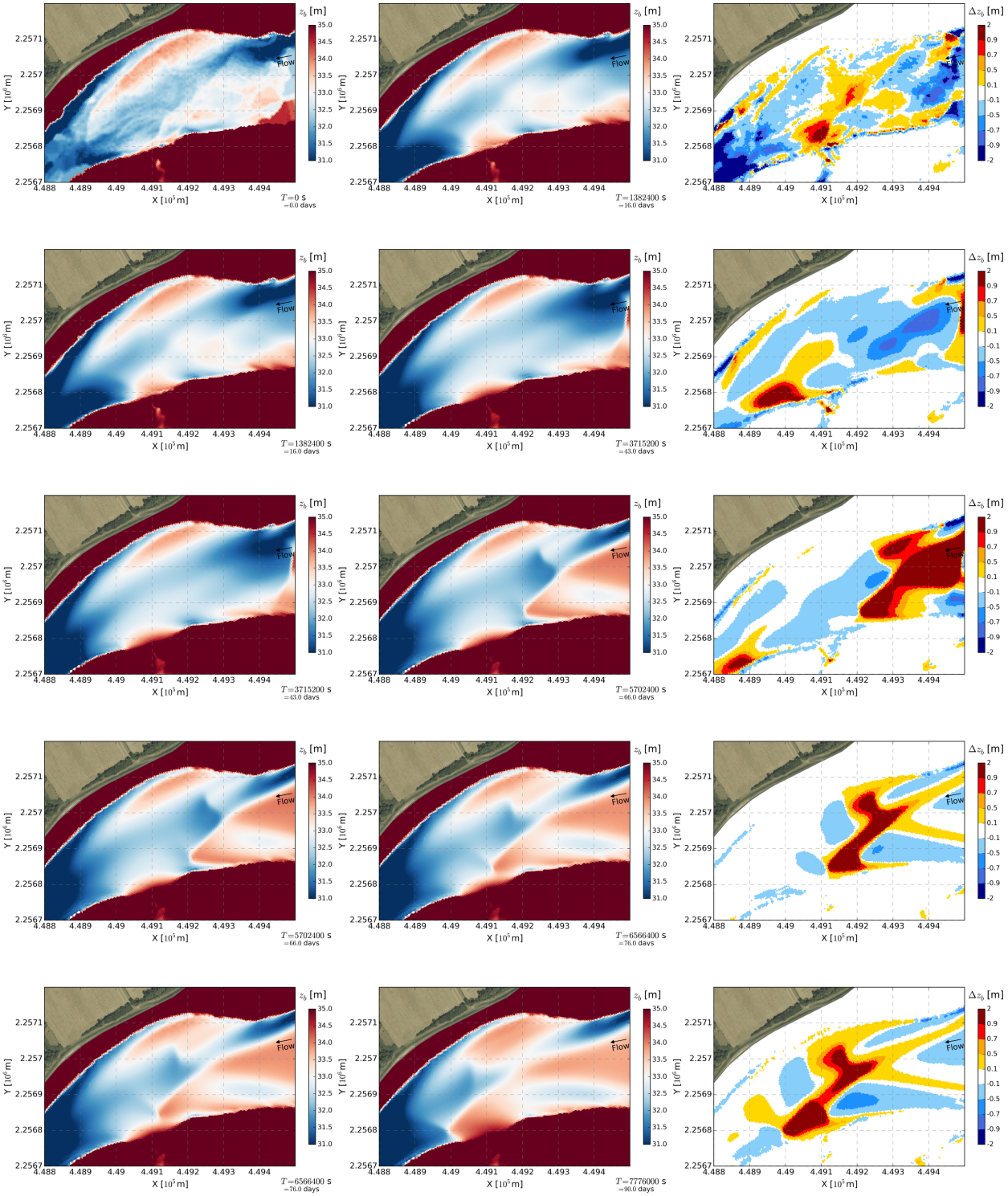


Figure 52: Morphological evolution of riverbed for water discharge of 2000 m^3/s

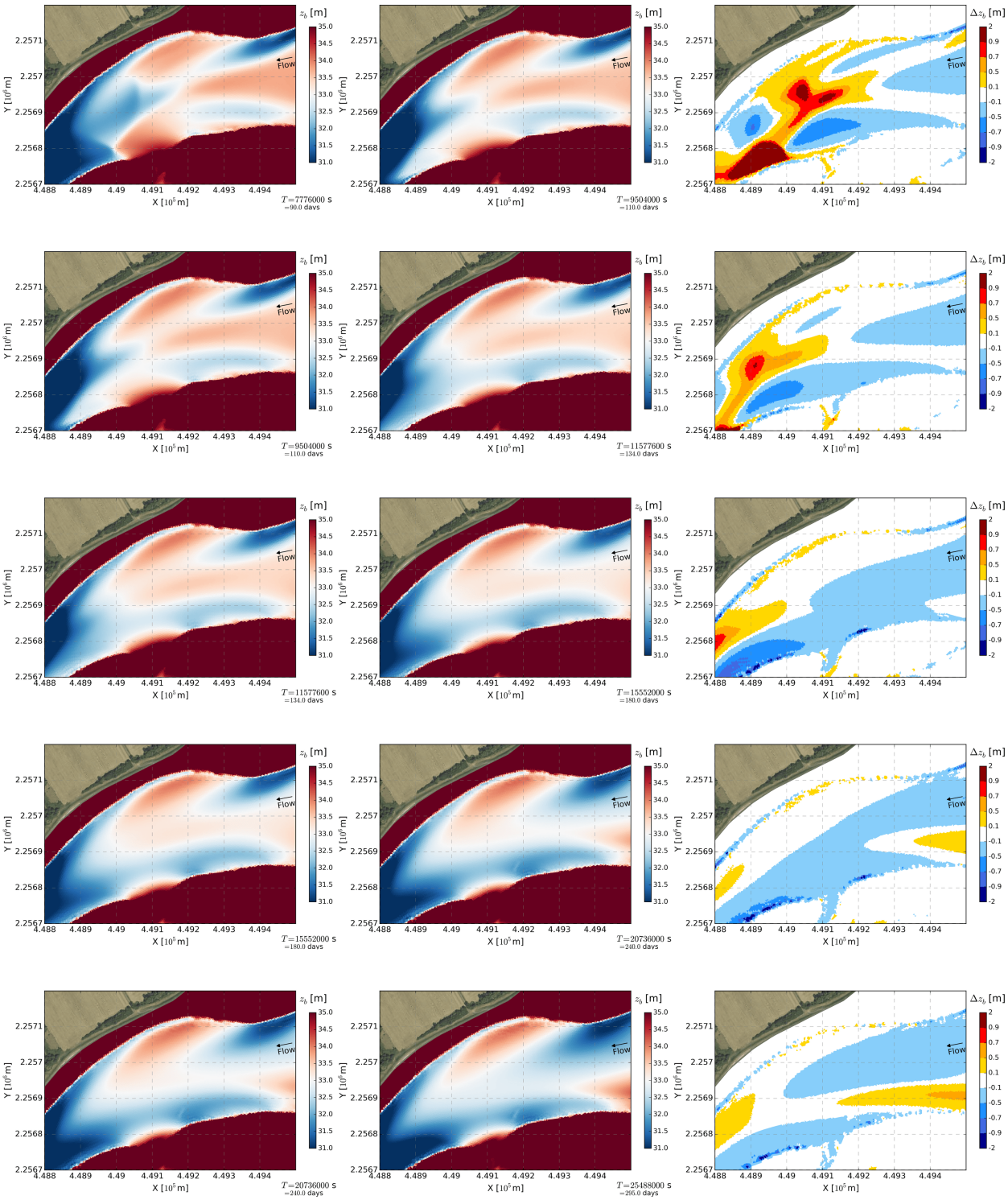


Figure 53: Morphological evolution of riverbed for water discharge of 2000 m^3/s

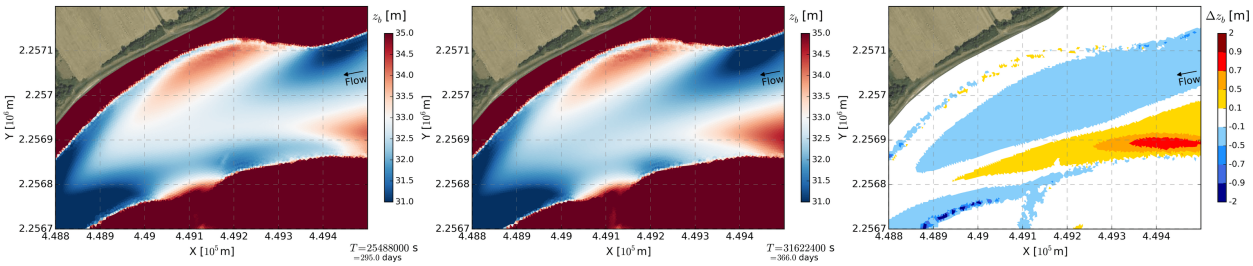


Figure 54: Morphological evolution of riverbed for water discharge of 2000 m^3/s

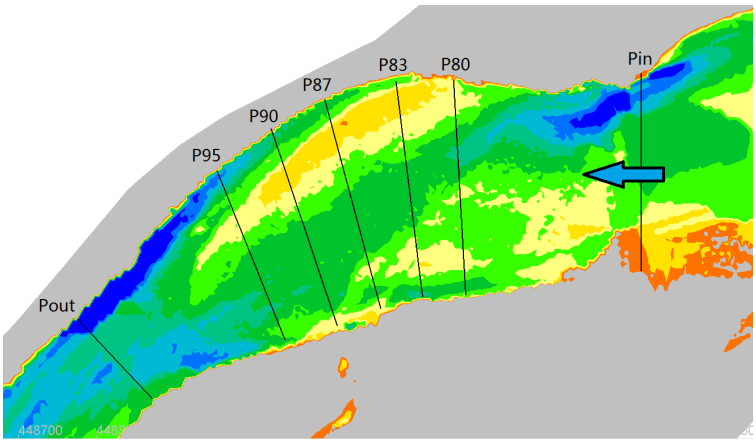


Figure 55: Seven cross-sectional profiles for extract the solid discharge. Two cross sections are located at the entrance and at the end of expansion/contraction zone. Other five intermediary cross-sections are distributed across the expansion/contraction zone.

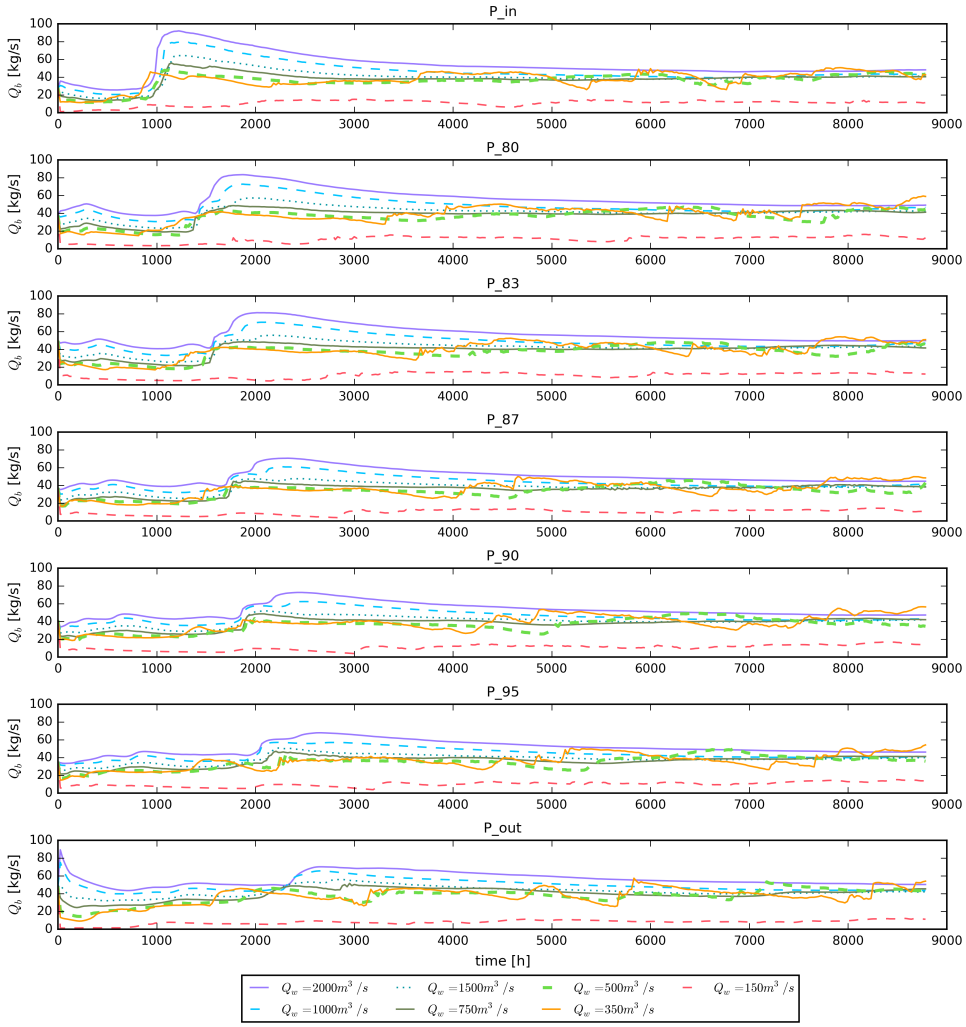


Figure 56: The average solid discharge along each cross-sectional profiles over time for distinct constant water discharges

APPENDIX B

MATHEMATICAL ANALYSIS OF THE FORMULA OF WILCOCK AND CROWE (2003)

The work presented here is part of the Msc. internship thesis of Chenyu Liu, entitled *Numerical modelling of bedload non-uniform sediment transport*

by
Chenyu Liu[1], Florian Cordier[2,3], Pablo Tassi[2,3], Nicolas Claude[3] and Damien Pham Van Bang[4]
[1]Ecole Polytechnique Universitaire de Nice-Sophia Antipolis (France)
[2]Laboratoire d'Hydraulique Saint-Venant (Chatou, France)
[3]EDF R&D LNHE - Laboratoire National d'Hydraulique et Environnement (Chatou, France)
[4]INRS-ETE, LHE & Lab. CT-Scan (Québec, Canada)

Corresponding author: florian.cordier@edf.fr

III Mathematical analysis of bedload transport formulas

Since Du Boys [6], a large number of theoretical and empirical equations have been developed to predict bedload transport rates for a large range of particle grain sizes and hydraulic conditions [1]. Two common types of sediment transport models were presented in the literature [22]. The first type of models are based on the water discharge. This discharge-type of model is developed to find a direct relation between the flow discharge Q and the sediment transport rate q_b, generally referred to the sediment rating curve. The second type of models are based on bed shear stress which indicates the force caused by the flow and applied on the bed surface, for example, the Meyer-Peter and M$\ddot{u}$ller formula (MPM) [15].

Models based on the flow discharge are limited as the flow discharge is not the only element that affects the transport rate. It is quite obvious that a relatively small channel with an important discharge will not produce the same solid discharge as in a relatively big river with the same discharge [25]. Other key elements such as the river width, slope, density of sediment, roughness of river-bed and bed material composition would also affect significantly the sediment transport.

Models based on bed shear stress have been wildly used [25]. These models are relevant as they are physical-based. They are formulated on the force that works directly on the sediment that leads to the particle movement. The critical shear stress is the threshold beyond which the particles would begin to move [22].

Sediment transport can be classified as uniform sediment and graded sediment. Graded sediment situation is in which coarser sediment and finer sediment are mixed. Hiding/exposure effect occurs as sediment with different grain size interact with each other.

The comparisons between different formulas are presented herein. Mathematical analysis is also performed in order to verify the applicable scope and conditions of each formula, and to find out the ranges of key parameters and variables used for different sediment transport formulas.

In this study, the graded sediment transport is computed with formulas that are derived from the one proposed by Meyer-Peter and M$\ddot{u}$ller [15], originally developed in the framework of uniform sediment, and a formula derived from the transport of wide graded sediment, proposed by Wilcock and Crowe [19].

The current analysis aims at analysing the next formulas:

1. The Meyer-Peter and M$\ddot{u}$ller formula [MPM] [15];
2. The MPM formula modified by Egizaroff [MPME] [8];
3. The Wilcock and Crowe formula [WC-2003] [19].

III.1 MPM formula [1948]

Meyer-Peter and M$\ddot{u}$ller formula is an excess shear stress type of equation. It is based on the relation between the solid discharge q_b [g/m/s] and the difference between effective shear stress τ_b [Pa] and the critical shear stress τ_c [Pa]. Critical shear stress is defined as the shear stress required for the initiation of grain mobility [15].

According to MPM formula, the bedload transport rate q_b is calculated as a power function of the exceeding shear stress (amount of shear stress exceeding the threshold) :

$$q_b \propto (\tau_b - \tau_c)^{\gamma}, \tag{4}$$

which it is only valid when $\tau_b \in [\tau_c, +\infty]$.

The Meyer-Peter and M$\ddot{u}$ller formula is given as:

$$\frac{q_b}{\sqrt{g(S-1)d^3}} = \alpha(\tau_b^* - \tau_c^*)^{\gamma}, \tag{5}$$

where $\alpha = 8$, $\gamma = \frac{3}{2}$, S the ratio between the density of sediment and the density of water which yields: ρ_s/ρ, d [m] the geometric size of the sediment, ρ_s [kg/m^3] the density of sediment and ρ [kg/m^3] the density of water. τ_c^* denotes the dimensionless critical shear stress, τ_b^* denotes the dimensionless shear stress, which is also called Shields number [15].

The Shields number is calculated as:

$$\tau_b^* = \frac{\tau_b}{(S-1)\rho g d}, \tag{6}$$

where d the grain size, g the acceleration of gravity.

The transport rate q_b is a strictly increasing function of the dimensionless shear stress (Figure 1), which tends to 0 near τ_c and to infinity when τ_b tends to infinity.

$$\lim_{\tau^* \to \tau_c^*} q_b = 0 \qquad \lim_{\tau^* \to +\infty} q_b = +\infty \tag{7}$$

where as measured that the threshold of shear stress $\tau_c^* \approx 0.047$.

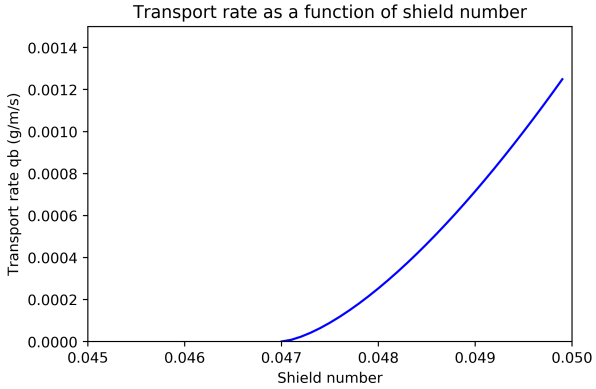


Figure 1: Solid discharge q_b as a function of Shield number τ_b^* for MPM formula.

By replacing Eq.(3) into Eq.(2) yields:

$$q_b = \frac{\alpha g (S-1)^{(0.5-\gamma)} d^{(1.5-\gamma)}}{\rho^\gamma} (\tau_b - (S-1)\rho g d \tau_c^*)^\gamma \tag{8}$$

The above equation shows that:

$$q_b \propto \tau_b^\gamma \tag{9}$$

For graded sediment, Eq.(5) can be rewritten as:

$$\frac{q_{b,i}}{\sqrt{g(S-1){d_i}^3}} = F_i \alpha (\tau_{b,i}^* - \tau_{c,i}^*)^\gamma, \tag{10}$$

$$q_{b,i} = F_i \frac{\alpha g (S-1)^{(0.5-\gamma)} {d_i}^{(1.5-\gamma)}}{\rho^\gamma} (\tau_b - (S-1)\rho g d_i \tau_{c,i}^*)^\gamma \tag{11}$$

where F_i is the fraction volume content of the i^{th} size fraction of sediment and :

$$q_{b,i} \propto (\tau_b^\gamma, F_i) \tag{12}$$

As a power function, the formula of MPM is continuous in its range of validity, where the solid transport tends to increase with the shear stress.

Therefore, the shear stress must satisfy the condition:

$$\tau_b - ((S-1)\rho g d \tau_{c,i}^*) \geq 0 \tag{13}$$

Which indicates also as the form of dimensionless shear stress:

$$\tau_b^* - \tau_{c,i}^* \geq 0 \tag{14}$$

As a conclusion, the formula of Meyer-Peter and M$\ddot{u}$ller is only valid when the dimensionless shear stress is greater or equals to the critical shear stress;

If the effective shear stress is smaller than the critical shear stress, the solid transport rate is 0 in the model:

$$q_b = \begin{cases} \dfrac{\alpha}{\sqrt{(S-1)gd^3}}[\tau_b - (S-1)\rho g d\tau_c^*]^\gamma & \text{if} \quad \tau_b > (S-1)\rho g d\tau_c^* \\ 0 & \text{otherwise} \end{cases} \tag{15}$$

III.2 Formula of MPM modified by Egiazaroff [1965]

The formula of MPM modified by Egiazaroff [1965] includes the coefficient ξ_i accounting for the hiding/exposure effect, Eq.(2) becomes:

$$\frac{q_{b,i}}{\sqrt{g(S-1){d_i}^3}} = F_i\alpha(\tau_{b,i}^* - \xi_i\tau_{c,i}^*)^\gamma \qquad \text{with} \quad \gamma = 3/2 \tag{16}$$

The hiding/exposure coefficient of Egiazaroff ξ_i is computed as follows:

$$\xi_i = \left[\frac{\log(19)}{\log(19d_i/d_m)}\right]^2 \tag{17}$$

where d_m [m] corresponds to the mean grain diameter of sediment.

With the increase of ξ_i, the transport rate q_b tends to decrease and vice versa.

Figure 2 shows the variation of the hiding-exposure coefficient of the i^{th} class of sediment as the function of d_i/d_m :

$$\lim_{d_i/d_m \to (1/19)} \xi_i = +\infty \qquad \lim_{d_i/d_m \to +\infty} \xi_i = 0 \tag{18}$$

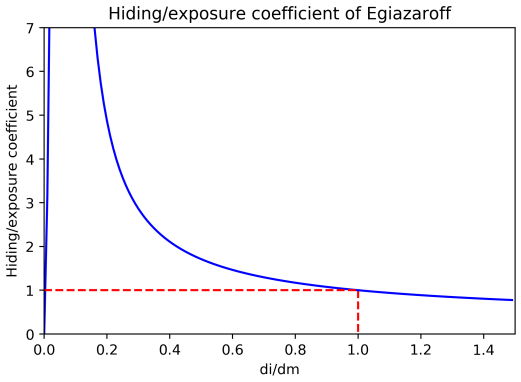


Figure 2: Hiding-exposure coefficient ξ_i as the function of d_i/d_m.

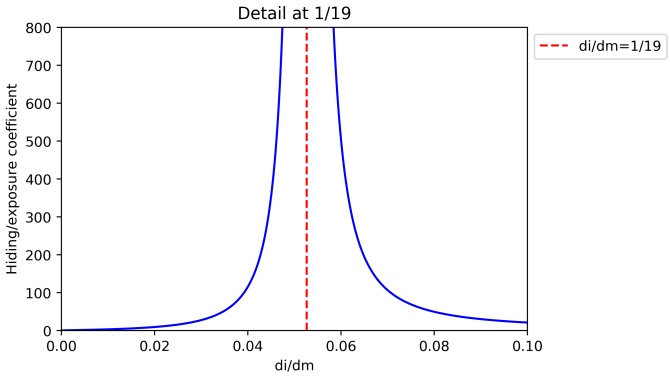


Figure 3: Detail at $d_i/d_m \approx 1/19$

It is showed that the hiding/exposure coefficient proposed by Egiazaroff gives an expecting representation of the hiding/exposure effect for coarser material as it tends to increase the transport rate ($\xi_i < 1$). However, for the sediments that are way smaller than mean grain size sediment (finer material), the coefficient seems to predict physically irrelevant values of hiding/exposure effect.

To be precise (Figure 3), when the ratio of the i^{th} diameter and the median grain size is close or less than the value 1/19, the hiding/exposure coefficient of Egiazaroff provides unrealistic values:

1. When $d_i < \frac{1}{19} d_m$, the evolution of ξ_i does not correspond to the hiding/exposure effect, meaning that when the diameter increases, the hiding/exposure coefficient which should be decreasing is increasing. Therefore the equation is not valid in this range.
2. When $d_i = \frac{1}{19} d_m$, the coefficient ξ_i tends to ∞ and is invalid ($\xi_i = \infty$), meaning that the estimation of the transport rate of particles whose diameter is equal to $\frac{1}{19} d_m$ equals to zero.
3. When $d_i \geq \frac{1}{19} d_m$, the coefficient ξ_i becomes significantly high and becomes invalid.

III.3 WC-2003 formula

Wilcock and Crowe [19] proposed a bedload formula for graded sediment composed of a mixture of sand and gravel. This formula is also a function of the shear stress, and it includes the hiding/exposure function.

The sediment transport rate is calculated as follows:

- The dimensionless reference shear stress, defined as the dimensionless shear stress for the sand component $\tau^*_{r,m}$, is calculated as a function of the volume fraction content of sand at the bed-surface F_s:

$$\tau^*_{r,m} = 0.021 + 0.015 \exp[-20 F_s], \tag{19}$$

  where F_s takes a value in the range $[0, 1]$.

As showed in Figure 4, $\tau^*_{r,m}$ is a continuous, strictly decreasing function of F_s.

$$\tau^*_{r,m}(F_s = 0) = 0.036 \quad \tau^*_{r,m}(F_s = 1) = 0.021 \tag{20}$$

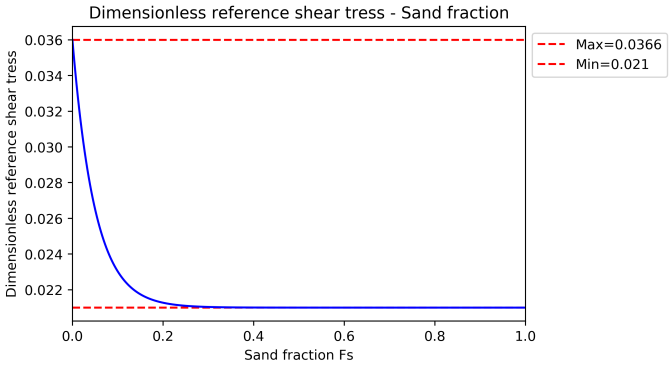


Figure 4: Dimensionless shear stress $\tau^*_{r,m}$ as a function of the fraction of sand F_s.

It is reasonable that when the sand fraction on the bed-surface increases, the dimensionless reference shear stress decreases respectively with the mean surface diameter of sediment.

The reference shear stress that indicates the shear stress of the mean size sediment on the bed surface is calculated:

$$\tau_{r,m} = \tau^*_{r,m}(S - 1)\rho g d_{s,m} \tag{21}$$

It is straight forward that $\tau_{r,m}$ varies in the same way as $\tau^*_{r,m}$, that is to say $\tau^*_{r,m}$ increases with the same tendency as $\tau_{r,m}$.

- Incorporate the hiding/exposure function into the calculation of the reference shear stress of each size class on the surface.

  The hiding/exposure function of WC-2003 yields:

$$\tau_{r,i} = \tau_{r,m}\left(\frac{d_i}{d_{s,m}}\right)^{b_i}, \tag{22}$$

  where:

$$b_i = \frac{0.67}{1 + \exp\left(1.5 - \frac{d_i}{d_{s,m}}\right)}, \tag{23}$$

  where the power function of this hiding/exposure function b_i is strictly continuous, increasing as a function of $d_i/d_{s,m}$ [Fig 5], where:

$$\lim_{d_i/d_{s,m}\to 0} b_i = 0.122225 \quad \text{and} \quad \lim_{d_i/d_{s,m}\to +\infty} b_i = 0.67. \tag{24}$$

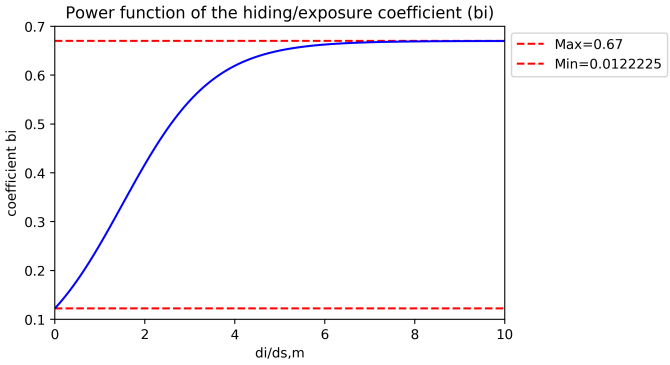


Figure 5: Variation of the power function of hiding/exposure coefficient b_i.

According to Wilcock and Crowe (2003), for uniform sediment, the reference shear stress is estimated approximately to 1:1 as the function of $d_i/d_{s,m}$[19]. Figure 6 presents the hiding/exposure coefficient $(d_i/d_{s,m})^{b_i}$ as the function of $d_i/d_{s,m}$:

$$\lim_{d_i/d_{s,m}\to 0}\left(\frac{d_i}{d_{s,m}}\right)^{b_i} = 0 \qquad \lim_{d_i/d_{s,m}\to \infty}\left(\frac{d_i}{d_{s,m}}\right)^{b_i} = +\infty \tag{25}$$

For finer sediment ($d_i/d_{s,m} < 1$), the hiding/exposure coefficient decreases the mobility by increasing the reference shear stress $\tau_{r,i}$. For coarser sediment ($d_i/d_{s,m} > 1$), the hiding/exposure coefficient decreases the mobility by increasing the reference shear stress $\tau_{r,i}$.

This proves that this equation successfully represents the hiding/exposure phenomenon, as it tends to lower the transport rate of finer material and larger the transport rate for coarser material.

- Calculate the dimensionless transport rate for each class of sediment as a function of ϕ_i, with $\phi_i = \tau_b/\tau_{r,i}$.

  The dimensionless transport rate is determinated by the following function:

$$W_i^* = \begin{cases} 0.002\phi_i^{7.5} & \text{for} \quad \phi_i < 1.35 \\ 14\left(1 - \frac{0.894}{\phi_i^{0.5}}\right)^{4.5} & \text{otherwise} \end{cases} \tag{26}$$

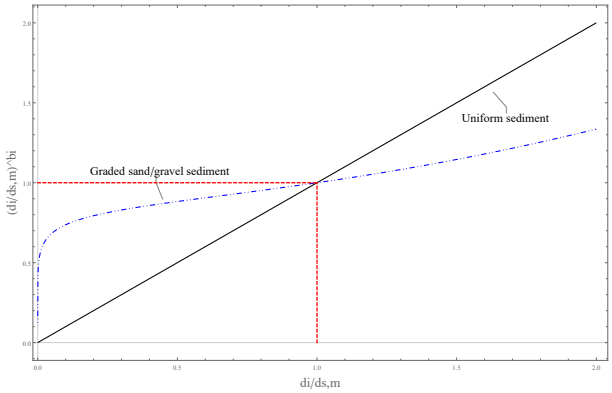


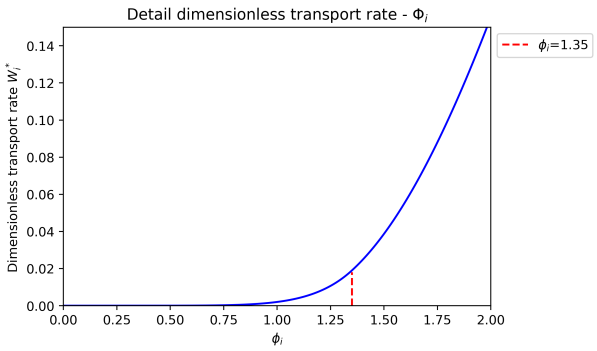
Figure 6: Hiding/exposure coefficient $(d_i/d_{s,m})^{b_i}$ as a function of $d_i/d_{s,m}$.

where:

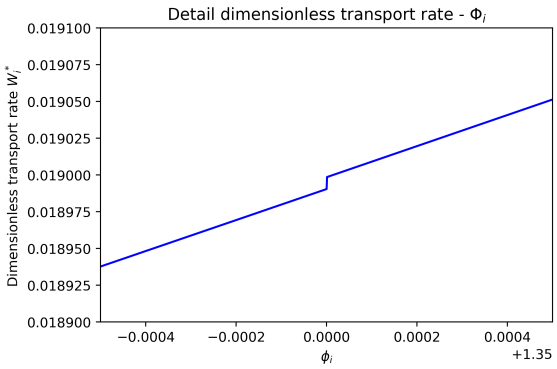
$$W_i^* = \frac{(\rho_s/\rho - 1)gq_{b,i}}{F_i u_*^3}, \tag{27}$$

where u_* the friction velocity.

The function of dimensionless transport rate W_i^* with ϕ_i is given in Figure 7.



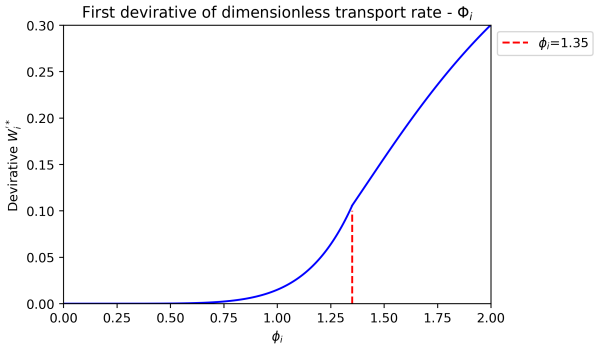
(a) Dimensionless transport rate W_i^* as a function of ϕ_i.



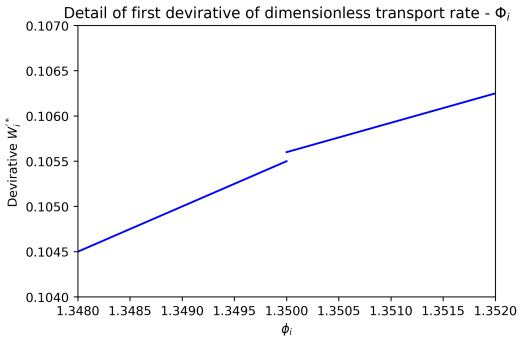
(b) Detail of Figure 8a at the point ϕ_i=1.35

Figure 7: Dimensionless transport rate as a function of ϕ_i

It's showed that W_i^* as a function of ϕ_i is discontinuous at the point $\phi_i = 1.35$ (Figure 7b) and that the derivative $W_i'^*$ is also discontinuous at the point $\phi_i = 1.35$ (Figure 8):



(a) First derivative of the dimensionless transport rate as function of ϕ_i.



(b) Detail of Figure 10 at the point ϕ_i=1.35

Figure 8: First derivative of the dimensionless transport rate as a function of ϕ_i

The limit values are presented below:

$$\begin{aligned} \lim_{\phi \to 0} W^* &= 0 & \lim_{\phi \to 0} W^{'*} &= 0 \\ \lim_{\phi \to 1.35^+} W^* &= 0.189984 & \lim_{\phi \to 1.35^-} W^* &= 0.189904 \\ \lim_{\phi \to 1.35^+} W^{'*} &= 0.105667 & \lim_{\phi \to 1.35^-} W^{'*} &= 0.105502 \\ \lim_{\phi \to +\infty} W^* &= 14 & \lim_{\phi \to +\infty} W^{'*} &= 0 \end{aligned} \tag{28}$$

These values show that the dimensionless transport rate formula and its first derivation are not continuous. These discontinuities could lead to problems of discontinuity of the transport rates computed by the numerical model.

III.4 Additional limitations of WC-2003 formula

Besides the discontinuity inside the dimensionless transport rate equation, the formula of WC-2003 displays also two other limitations which are presented below.

III.4.1 Estimation of the reference shear stress

The first limitation was discussed by de Linares et al [14]: in the article of Wilcock and Kenworthy [27], the behaviour of bimodal sand-gravel mixtures was divided into 2 cases:

- The first case is the gravel-dominant mixture, which means that the proportion of gravel is relatively large, while the sand is sparse and have negligible influence on gravel. The gravel behaves as an uni-modal gravel mixture with the same critical shear stress as the sediment mixture.
- The second case is the sand-dominant mixture, sand barely receives no interactions from the sparse gravel and have the same critical shear stress, since proportion of gravel is relatively small so almost every gravel is isolated and surrounded by the sand. Gravels with different grain sizes would not interact each other as in uni-modal mixture, so for gravels, transport is size selective.

This behaviour has also been observed experimently by Kuhnle [12] in 1993 and in river by Wathen et al [23] in 1995.

In these two cases, the sand fraction always has the same critical shear stress and that is why in WC-2003 formula, sand fraction can be used as the variable to calculate the median reference shear stress $\tau_{r,m}$.

The schematic behaviour of different cases is showed in Figure 9.

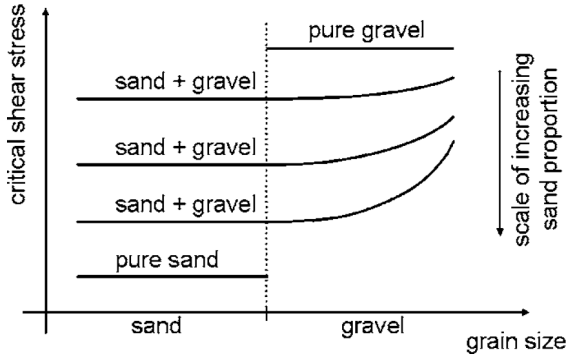


Figure 9: Critical shear stress as a function of the grain size

But in WC-2003 formula, the reference shear stress is calculated with the interpolation of the hiding/exposure function. Reference shear stresses of the sand with different grain sizes are different, which means that the transport of sand is also size-selective, which is inconsistent with the hypotheses.

III.4.2 Discretization of the grain size distribution

As showed in Figure 4, the dimensionless reference shear stress is a function of the sand fraction, and when the sand fraction is relatively small (i.e. varying from 0% to 20%), with slights variation of the sand fraction, dimensionless reference shear stress varies intensively.

In the classic way of the discretization of the grain size distribution, choosing the number of classes and choosing the method of discretization will influence the calculation of sand fraction, which would lead to errors in the calculation of the reference shear stress.

For example, assuming that the sand fraction is equal to 10%, by applying the equation (19), the dimensionless shear stress equals to 0.02302.

- With using a single size fraction to discretize the GSD, the sand fraction will be calculated as 0. The dimensionless reference shear stress will be calculated as 0.036 with 56% of relative error.
- With using two size fractions, the sand fraction will be calculated also as 0. The dimensionless would be 0.036 with 56% error.
- With using five size fractions, the sand fraction is right at 0.1 which corresponds to the real case, at this time, the dimensionless shear stress is calculated correctly.
- With using ten size fractions, the sand fraction will be calculated as 5% which will have about 13% relatove error.

The discretization not only influences the values of the grain sizes used in the formula, but also affects the sand fraction which is one of the key parameters inside the WC-2003 formula.

This limitation proves that, even with a high-number of classes of discretization (e.g. 10 classes), if a good discretization method has not been chosen and the sand fraction can not be calculated properly, the estimation of the dimensionless reference shear stress will lead to strong errors and later compute incorrectly the transport rate of sediment.

III.4.3 Solutions of these two limitations

In order to avoid these limitations and to reduce the error, a new discretization method can be proposed:

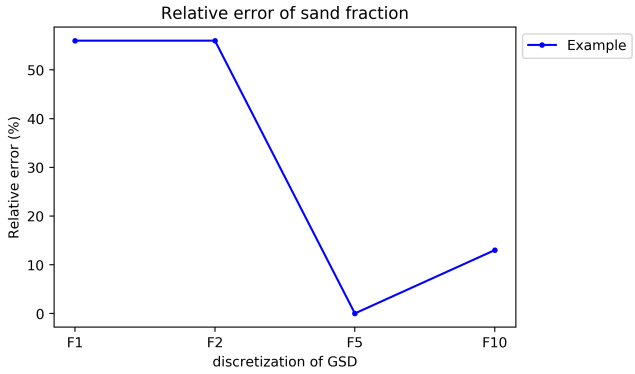


Figure 10: Example of relative errors between real sand fraction and calculated sand fraction

The part of sand and the part of gravel can be considered separately, setting just one class of sand and several classes of gravel. Doing so can ensure that the sand fraction always has the same critical shear stress, at the same time, using directly the real sand fraction or just ensure that the first class of sediment is composed of sand. Doing so can ensure the accuracy of the dimensionless reference shear stress.

III.5 Comparison between two hiding/exposure functions

As mentioned by Wilcock and Crowe [19], the hiding/exposure coefficient of WC-2003 takes a different forms in comparison with the one inclued in the MPM-E formula. The reference shear stress τ_r is proposed to replace the critical shear stress τ_c as it is hard to estimate [26], the process of $(d_i/d_{s,m})^{b_i}/(d_i/d_{s,m})$ can transform the hiding/exposure coefficient of WC-2003 [2003] into the same form as the one of Egiazarof [1965].

The magnitude that indicates the effect of the hiding/exposure function of WC-2003 by $(d_i/d_{s,m})^{b_i}/(d_i/d_{s,m})$ as a function of $d_i/d_{s,m}$:

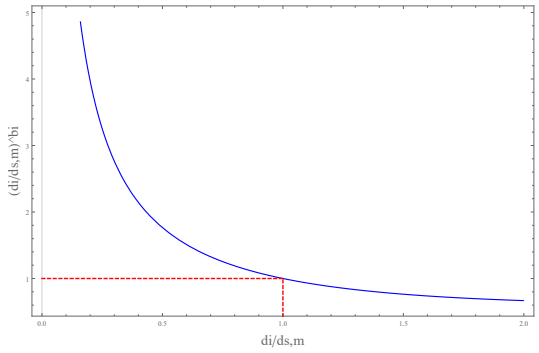


Figure 11: New term of hiding/exposure coefficient $(d_i/d_{s,m})^{b_i}/(d_i/d_{s,m})$ as a function of $d_i/d_{s,m}$.

In the same way as ξ_i denotes the hiding/exposure function of Egiazaroff, the value $(d_i/d_{s,m})^{b_i}/(d_i/d_{s,m})$ denotes the one of WC-2003. These two coefficients are compared as the function of $d_i/d_{s,m}$ in Figure 12 and Figure 13.

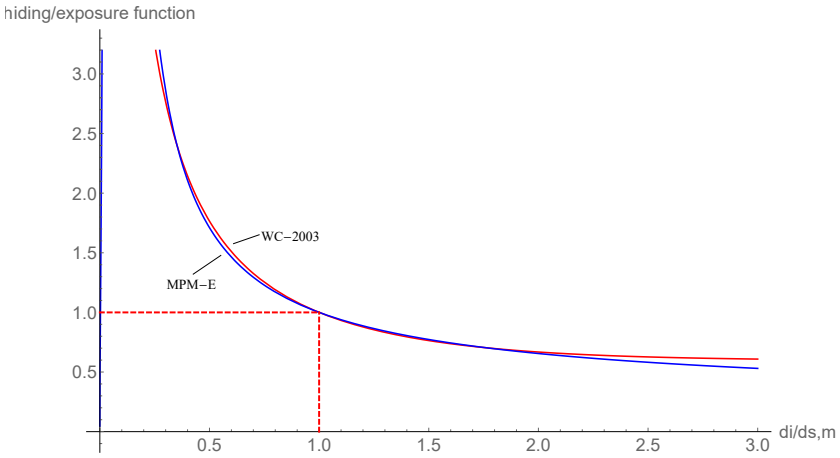
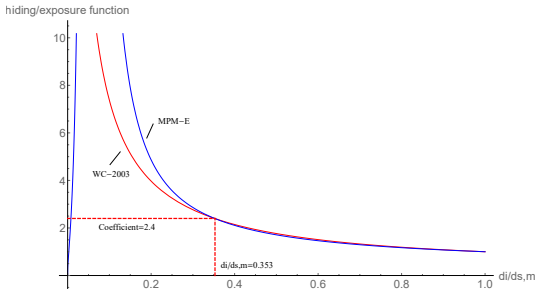
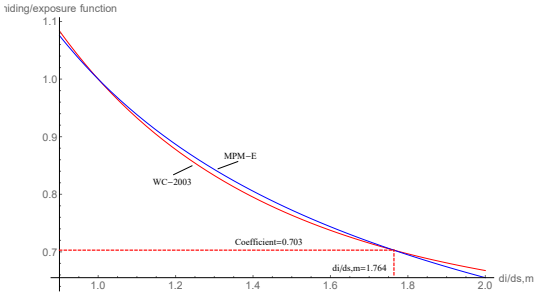


Figure 12: Comparaison of hiding/exposure coefficient ξ_i and $(d_i/d_{s,m})^{b_i}/(d_i/d_{s,m})$ as a function of $d_i/d_{s,m}$.



(a) Comparison when $d_i/d_{s,m}$ varies in [0, 1]



(b) Comparison when $d_i/d_{s,m}$ varies in [0.9, 2]

Figure 13: Comparison of two hiding/exposure functions in detail

When $d_i/d_{s,m}$ = 0.353, 1.000 and 1.764, the coefficients calculated by the hiding/exposure function of MPM modified by Egiazaroff and that of WC-2003 formula are identical.

It is also observed that when $d_i/d_{s,m}$ is smaller than 1/19, the hiding/exposure coefficient of WC-2003 is still relevant as it is greater than 1 and decreases when the sediment diameter increases, while the one of Egizaroff becomes irrelevant (CF. III.2 & III.3).

The difference between the hiding/exposure coefficient is given in Figure 14:

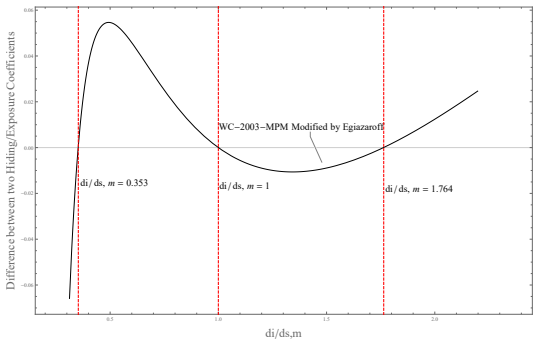


Figure 14: $(d_i/d_{s,m})^{b_i}/(d_i/d_{s,m}) - \xi_i$ as a function of $d_i/d_{s,m}$.

For $0.3 \leq d_i/d_{s,m} < 3$, the difference between both hiding/exposure functions is relatively small.

As showed in Figure 15, two hiding/exposure functions (calculated as $((d_i/d_{s,m})^{b_i}/(d_i/d_{s,m}) - \xi_i)/\xi_i$) have only 10% relative errors as a function of $d_i/d_{s,m}$ in the range of [0.245,2.67].

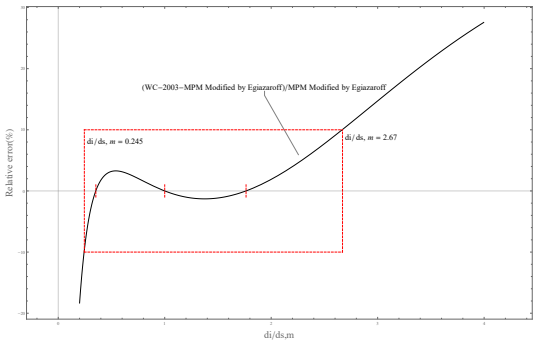


Figure 15: Relative error between two hiding/exposure function.

To conclude, hiding/exposure functions proposed by WC-2003 and MPM-E are both physically represent the hiding/exposure phenomenon, while MPM-E formula is invalid for a range of finer sediment ($d_i/d_{s,m} \approx 1/19$ or $d_i/d_{s,m} < 1/19$).

At $d_i/d_{s,m} = 0.353, 1$ and 1.764, identical hiding/exposure effect is obtained by both formulas and as $d_i/d_{s,m}$ in the range of [0.245,2.67], these two formulas give similar results with only 10% of difference.

Furthermore, it is found that when $d_i/d_{s,m}$ is out of the range of $[0.245, 2.67]$, the hiding coefficient of WC-2003 estimates less hiding effect than the method of MPM modified by Egiazaroff. In other word, the coarser sediment estimates to be harder to move and the transport rate is less important (less exposure effect), the fine sediment estimates to be easier to move and the transport rate is more important (less hiding effect) by using the WC-2003 formula.

III.6 Conclusion of the mathematical analysis

This section mainly focus on the description of three bedload transport formulas and the mathematical analysis of these formulas. The results are showed as below:

For the MPM formula, it is relatively simple as it is proposed for uniform sediment. The application of this formula for graded sediment is not accurate as it does not consider the hiding/exposure effect.

For the MPM-E formula, it is proposed based on the MPM formula by including a hiding/exposure coefficient. This formula is suitable for both uniform and graded sediment, but the hiding/exposure function of MPM-E formula is not perfect as it cannot be applied for all range of sediment. For a range of fin sediment (smaller than, equal to or slightly larger than 1/19 of the mean diameter of sediments on the bed-surface), it would cause wrong estimation of partial transport rate.

Three limitations are found for WC-2003 formula: (i) the discontinuity of the dimensionless transport rate formula, (ii) When a unsuitable GSD discretization method is chose, the critical shear stress calculated for sand component would be different. This is inconsistent with the hypotheses, (iii) When a unsuitable GSD discretization method is chose, the sand fraction would be wrongly calculated may cause a huge different estimation of the transport rate.

To fix the limitations (ii) and (iii) of WC-2003 formula, a proper GSD discretization method can be proposed: consider the sand and the gravel separately, setting just one class of sand to ensure the same critical shear stress and the right sand fraction, then setting several class of gravel.

The hiding/exposure function of MPM-E and WC-2003 formulas are compared, they are both effective, in the range of $d_i/d_{s,m}$ = [0.353, 1.764], hiding/exposure function of WC-2003 has a stronger effect .

In other words, with identical condition, the transport rate of finer sediments calculated by WC-2003 formula should be smaller (compare to the result of MPM modified by Egiazaroff), and the transport rates of coarser sediments calculated by WC-2003 should be greater (compared to the result of MPM modified by Egiazaroff).

While the function in WC-2003 gives a weaker effect on hiding/exposure function out of the range of [0.353, 1.764] which indicates that by using the method of WC-2003 to simulate the sediment transport, coarser sediments are harder to move and fine sediments are easier to move compare to the method of MPM modified by Egiazaroff.

In other words, with identical condition, the transport rate for finer sediments calculated by WC-2003 should be greater (compared to the result of MPM modified by Egiazaroff), and the transport rate for coarser sediments calculated by WC-2003 should be smaller(compare to the result of MPM modified by Egiazaroff).

References

[1] Batalla, R. (1997). Evaluating bed material transport equations using field measurements in a sandy gravel bed stream, arbúcies river, ne spain. *Earth Surface Processes and Landforms*, 22(2):121–130.

[2] Batalla, R. (2004). The importance of sediment and sediment processes for river basin management. European Sediment Research Network.

[3] Benjamin Magnier, Nicolas Claude, C. V. S. R. P. T. (2013). Numerical simulation of flow structures in the presence of alternate and transverse bars: application to the loire river (france).

[4] Claude, N. (2012). *Processus et flux hydro-sédimentaires en rivière sablo-graveleuse : influence de la largeur de section et des bifurcations en Loire moyenne (France).* Theses, University of Tours.

[5] Claude. N, S. Rodrigues, V. B. J. G. B. P. T. and Juge, P. (2014). Interactions between flow structure and morphodynamic of bars in a channel expansion/contraction, loire river, france. *Water Resources Research*, 50.

[6] Du Boys, M. (1879). Etudes du régime du rhône et de l'action exercée par les eaux sur un lit afond de graviers indéfiniment affouillable. *Ann. Ponts Chaussées 5*, page 141–195.

[7] Eaton, B. C., L. M. F. (2001). Effects of large floods on sediment transport and reach morphology in the cobble-bed sainte marguerite river. *Geomorphology.*, 40:291–309.

[8] Egiazaroff, I. V. (1965). Calculation of nonuniform sediment concentrations. *J. Hydraul. Div., Am. Soc. Civ. Eng.*, 91:225.

[9] Florian Cordier, Pablo Tassi, N. c. S. R. A. C. (2017). Numerical modelling of the graded sediment transport based on the experiments of wilcock and crowe (2003).

[10] Garcia, M. H. (2008). "sedimentation engineering," processes, measurements, modelling. and practice. *ASCE Mannuals and Reports on Engineer Practice*, 110, pp.1-1132.

[11] Gomez, B., C. M. (1989). An assessment of bed load sediment transport formulae for gravel bed rivers. *Water Resources Research*, 25 (6):1161.

[12] Kuhnle, R. A. (1993). Incipient motion of sand-gravel sediment mixtures. *J. Hydraul. Eng*, 119(12), 1400–1415.

[13] Marwan A. Hassan, Michael Church, J. X. Y. Y. (2008). Sapatial and temporal variation of sediment yield in the landscape: Example of huanghe (yelliw river). *Geophysical Research Letter*, 35(6).

[14] Matthieu, D.L., B. P. (2007). Critical shear stress of bimodal sediment in sand-gravel rivers. *J. Hydraul. Eng. 133, 555–559.*

[15] Meyer-Peter, E. and Müller, R. (1948). Formulas for bed-load transport. *Hydraulic Engineering Reports*.

[16] Miguel Wong, G. P. (2006). Reanalysis and correction of bed-load relation of meyer-peter and müller using their own database. *Journal of Hydraulic Engineering*, 132(11):1159–1168.

[17] Mosley, M. P. (1982). Analysis of the effect of changing discharge on channel morphology and instream uses in a braided river, ohau river, new zealand. *Water Resour. Res*, 18:800–812.

[18] Parker, Gary, D. S. S. H. (1982). Model experiments on mobile, paved gravel bed streams. *Water Resources Research*, 18(5):1395–1408.

[19] Peter R Wilcock, J. C. C. (2003). Surface-based transport model for mixed-size sediment. *Journal of Hydraulic Engineering*, 129(2):120–128.

[20] Pinto Martins, D., B. J. S. J. (2009). Dynamics of water flow and sediments in the upper paraná river between porto primavera and itaipu dams, brazil. *Latin American Journal of Sedimentology and Basin Analysis*, 16:111–118.

[21] S. Dhamotharan, A. Wood, G. P. H. S. (1980). Bedload transport in a model gravel stream. Project Report EPA/R 806632-01-0, St. Anthony Falls Hydraulic Laboratory,University of Minnesota, Corvallis Environmental Research Laboratory Corvallis, Oregon 97330.

[22] Sensing, W. M. K. R. and Planetary Sciences Lab, U. o. W. (2006). Full lecture. sediment transport.

[23] Wathen, S. J., F. R. I. H. T. B. W. A. (1995). Unequal mobility of sand and gravel in weakly bimodal river sediments. *Water Resour. Res*, 31(8):2087–2096.

[24] Welber, M., B. W. T. M. (2012). The response of braided planform configuration to flow variations, bed reworking and vegetation: the case of the tagliamento river, italy. *Earth Surface Processes and Landforms.*, 37:572–582.

[25] Wilcock, P. R. (2004a). Lecture note 1 - sediment transport. Available from geo.berkeley.edu.

[26] Wilcock, P. R. (2004b). Lecture note 3. Sediment Transport – The Sediment Problem.

[27] Wilcock, P. R. e. S. T. K. (2002). A two-fraction model for the transport of sand/gravel mixtures. *Water Resour. Res*, Res. 38(10): 1194-1205.

APPENDIX



IMPLEMENTATION OF WC-2003 IN SISYPHE V7P3

The work presented here has been conducted during the Ph.D. thesis of Florian Cordier, entitled *Implementation of WC-2003 in Sisyphe V7P3*

The following subroutines have been edited in order to implement the formula of WC-2003:

- recall of the module INTERFACE_SISYPHE in interface_sisyphe.f
- modification of the module INTERFACE_SISYPHE_BEDLOAD in interface_sisyphe_bedload.f
- modification of the subroutine BEDLOAD_FORMULA in bedload_formula.f
- modification of the subroutine BEDLOAD_MAIN in bedload_main.f
- modification of the subroutine BEDLOAD_SOLIDISCHARGE in bedload_solidischarge.f
- creation of the subroutine BEDLOAD_WILCOCK_CROWE in the user Fortran file.

A new interface BEDLOAD_WILCOCK_CROWE is defined in the interface INTERFACE_SISYPHE_BEDLOAD. Changes are re-compiled with recalling the interface INTERFACE_SISYPHE, which calls the interface
INTERFACE_SISYPHE_BEDLOAD. A table of double precision type called SANFRA is defined in BEDLOAD_MAIN. This variable is computed one time at each computational node and at each time-step of the computation, and is used to compute F_s. This variable is transmitted successively to the subroutines
BEDLOAD_SOLIDISCHARGE, BEDLOAD_FORMULA and BEDLOAD_WILCOCK_CROWE.

A threshold is defined so that sediment transport is strictly equal to 0 if the computed transport rates are very close to 0 (*i.e.* $q_{b0,i} < 1 \times 10^{-12}$). This numerical treatment is defined to prevent from numerical issues due to values close to the 0 machine.

```
!                     **********************************
                      MODULE INTERFACE_SISYPHE_BEDLOAD !
!                     **********************************
      [...]
!
      !============================!
        SUBROUTINE BEDLOAD_FORMULA !
      !--------------------------------------------------------------------!
!
     &  (U2D, V2D,UCMOY, HN, CF, MU,TOB, TOBW, UW, TW, THETAW, FW,
     &   ACLADM, UNLADM,KSP,KSR, AVA,  NPOIN, ICF, HIDFAC, XMVS, XMVE,
     &   DM, GRAV, VCE,  HMIN, XWC, D90, KARMAN, ZERO,
     &   PI, SUSP, AC, HIDING, T1, T2, T3, T4, T5, T6, T7, T8, T9, T10,
     &   T11,CFP, QSC, QSS,IELMT,SECCURRENT,SLOPEFF,
! FC
     &   COEFPN, CALFA, SALFA,BIJK,HOULE, SANFRA)
! ENDFC
!
      [...]
      DOUBLE PRECISION, INTENT(IN)    :: BIJK,AVA(NPOIN)
! FC
      DOUBLE PRECISION, INTENT(IN)    :: SANFRA(NPOIN)
! ENDFC
      !--------------------------------------------------------------------!
      END SUBROUTINE BEDLOAD_FORMULA
      !====================================================================!
!
      [...]
```

```
      !=====================================================================!
30      SUBROUTINE BEDLOAD_MAIN !
      !---------------------------------------------------------------------!
!
      [...]
      CHARACTER(LEN=24), INTENT(IN)    :: CODE
35 ! FC
!      DOUBLE PRECISION, INTENT(OUT)    :: SANFRA(NPOIN)
! ENDFC
!
      !---------------------------------------------------------------------!
40    END SUBROUTINE BEDLOAD_MAIN
      !=====================================================================!
!
      [...]
      !=====================================================================!
45      SUBROUTINE BEDLOAD_SOLIDISCHARGE !
      !---------------------------------------------------------------------!
!
     &  (MESH, U2D, V2D, UNORM, HN,  TW, UW, MU,TOB, CF, TOBW, FW,
     &   THETAW, AVA,  MASKPT, MASKEL, ACLADM, UNLADM,KSP, KSR,LIQBOR,
50   &   QBOR, DEBUG, NPOIN, NPTFR, IELMT, ICF, KENT, OPTBAN,
     &   HIDFAC, GRAV, DM, D90, XWC, XMVE, XMVS, VCE, HMIN,
     &   HIDI,KARMAN, ZERO, PI, KARIM_HOLLY_YANG,
     &   SUSP, MSK,T1, T2, T3, T4, T5, T6, T7, T8, T9, T10,
     &   T11,T12, AC,HIDING, QSC, QSS,
55   &   SLOPEFF, COEFPN, PHISED, CALFA, SALFA, BETA, ZF_C, S,
     &   DEVIA, BETA2, SECCURRENT,BIJK,HOULE,UNSV2D,
! FC
     &   U3D,V3D,CODE,SANFRA)
! ENDFC
60    [...]
      CHARACTER(LEN=24), INTENT(IN)    :: CODE
! FC
      DOUBLE PRECISION, INTENT(IN)    :: SANFRA(NPOIN)
!      DOUBLE PRECISION SANFRA(NPOIN)
65 ! ENDFC
      !---------------------------------------------------------------------!
      END SUBROUTINE BEDLOAD_SOLIDISCHARGE
      !=====================================================================!
!
70    [...]
!
! FC
      !=====================================================================!
        SUBROUTINE BEDLOAD_WILCOCK_CROWE !
75    !---------------------------------------------------------------------!
     &(TOB, MU, ACLADM, DM, AVA, GRAV, XMVE, XMVS, SANFRA, QSC, AC, ACP,
     & SLOPEFF, COEFPN)
!
      USE BIEF_DEF
80    USE DECLARATIONS_SPECIAL
      IMPLICIT NONE
      INTEGER,           INTENT(IN)    :: SLOPEFF
      TYPE(BIEF_OBJ),    INTENT(INOUT) :: QSC, COEFPN
      DOUBLE PRECISION, INTENT(IN)    :: XMVE, XMVS, GRAV, DM, AC,
85   &                                    AVA(QSC%DIM1), SANFRA(QSC%DIM1)
      TYPE(BIEF_OBJ),    INTENT(INOUT) :: ACP ! WORK ARRAY T1
```

```
      TYPE(BIEF_OBJ),   INTENT(IN)    :: TOB, MU
      TYPE(BIEF_OBJ),   INTENT(IN)    :: ACLADM
      !--------------------------------------------------------------------!
      END SUBROUTINE BEDLOAD_WILCOCK_CROWE
      !====================================================================!
! ENDFC
!======================================================================!
!======================================================================!
!
      END INTERFACE
      END MODULE INTERFACE_SISYPHE_BEDLOAD
```

Listing C.1: Update of interface_sisyphe_bedload.f.

```
!                     *************************
                      SUBROUTINE BEDLOAD_FORMULA
!                     *************************
!
     &(U2D,V2D,UCMOY,HN,CF,MU,TOB,TOBW,UW,TW,THETAW,FW,
     & ACLADM, UNLADM,KSP,KSR,AVA,NPOIN,ICF,HIDFAC,XMVS,XMVE,
     & DM,GRAV,VCE,HMIN,XWC,D90,KARMAN,ZERO,
     & PI,SUSP, AC, HIDING, T1, T2, T3, T4, T5, T6, T7, T8, T9, T10,
     & T11,TETAP, QSC, QSS,IELMT,SECCURRENT,SLOPEFF,
     & COEFPN,CALFA,SALFA,BIJK,HOULE, SANFRA)
!
      [...]
! FC
      DOUBLE PRECISION SANFRA(NPOIN)
! ENDFC
!======================================================================!
!======================================================================!
!                                 PROGRAM                              !
!======================================================================!
!======================================================================!
      [...]
      ! ======================================= !
      ! IV(10) - WILCOCK AND CROWE 2003 FORMULATION!
      !         NON-UNIFORM TRANSPORT           !
      ! ======================================= !
      ELSEIF(ICF == 10) THEN
!
        CALL BEDLOAD_WILCOCK_CROWE
     & (TOB, MU, ACLADM, DM, AVA, GRAV, XMVE, XMVS, SANFRA, QSC, AC, T1,
     & SLOPEFF, COEFPN)
!
      [...]
      RETURN
      END
```

Listing C.2: Update of bedload_formula.f.

```
!                     **********************
                      SUBROUTINE BEDLOAD_MAIN
!                     **********************
```

```
!
      [...]
!+-+-+-
```

```
          IF(DEBUG > 0) WRITE(LU,*) 'END_BEDLOAD_SOLIDISCHARGE'
      [...]
!=====================================================================!
!=====================================================================!
!
      RETURN
      END
```

Listing C.3: Update of bedload_main.f.

```
!                     *******************************
                      SUBROUTINE BEDLOAD_SOLIDISCHARGE
!                     *******************************
!
     &(MESH,U2D,V2D,UNORM,HN,TW,UW,MU,TOB,CF,TOBW,FW,THETAW,
     & AVA,MASKPT,MASKEL,ACLADM,UNLADM,KSP,KSR,LIQBOR,
     & QBOR,DEBUG,NPOIN,NPTFR,IELMT,ICF,KENT,OPTBAN,
     & HIDFAC,GRAV,DM,D90,XWC,XMVE,XMVS,VCE,HMIN,
     & HIDI,KARMAN,ZERO,PI,KARIM_HOLLY_YANG,
     & SUSP,MSK,T1,T2,T3,T4,T5,T6,T7,T8,T9,T10,
     & T11,T12,AC,HIDING,QSC,QSS,
     & SLOPEFF,COEFPN,PHISED,CALFA,SALFA,BETA,ZF_C,S,
     & DEVIA,BETA2,SECCURRENT,
     & BIJK,HOULE,UNSV2D,U3D,V3D,CODE,SANFRA)
!
      [...]
      CHARACTER(LEN=24), INTENT(IN)     :: CODE
!
! FC
      DOUBLE PRECISION, INTENT(IN)     :: SANFRA(NPOIN)
! ENDFC
      [...]
      CALL BEDLOAD_FORMULA
     &  (U2D,V2D, UNORM,HN, CF, MU,TOB, TOBW, UW, TW, THETAW, FW,
     &   ACLADM, UNLADM, KSP,KSR,AVA, NPOIN, ICF, HIDFAC, XMVS, XMVE,
     &   DM, GRAV, VCE, HMIN, XWC, D90, KARMAN, ZERO,
     &   PI, SUSP, AC, HIDING, T1, T2, T3, T4, T5, T6, T7, T8, T9,
     &   T10, T11, T12, QSC, QSS, IELMT,SECCURRENT,
     &   SLOPEFF, COEFPN, CALFA, SALFA, BIJK, HOULE, SANFRA)
      IF (DEBUG > 0) WRITE(LU,*) 'END_BEDLOAD_FORMULA'
!
      [...]
!---------------------------------------------------------------------
!
      RETURN
      END
```

Listing C.4: Update of bedload_solidischarge.f.

```
!                     ************************
                      SUBROUTINE BEDLOAD_WILCOCK_CROWE
!                     ************************
!
     &(TOB, MU, ACLADM, DM, AVA, GRAV, XMVE, XMVS, SANFRA, QSC, AC, ACP,
```

```
     & SLOPEFF,COEFPN)
!
!*********************************************************************
! SISYPHE   V7P3                                     15/12/2017
!*********************************************************************
!
!brief    WILCOCK AND CROWE NON-UNIFORM TRANSPORT FORMULATION.
!
!history  F.CORDIER (EDF-LNHE)
!+        15/12/2017
!+        V7P3
!~~~~~~~~~~~~~~~~~~~~~~~~~~~~~~~~~~~~~~~~~~~~~~~~~~~~~~~~~~~~~~~~~~~~~~~
!| AC              |<->| CRITICAL SHIELDS PARAMETER
!| ACP             |<->| MODIFIED SHIELDS PARAMETER
!| COEB            |-->| POWER COEFF OF THE HIDING-EXPOSURE FUNCTION
!| COEFPN          |<->| CORRECTION OF TRANSORT FOR SLOPING BED EFFECT
!| DENS            |-->| RELATIVE DENSITY
!| DM              |-->| SEDIMENT GRAIN DIAMETER
!| GRAV            |-->| ACCELERATION OF GRAVITY
!| QSC             |<->| BED LOAD TRANSPORT
!| SANFRA          |-->| SAND FRACTION
!| SLOPEFF         |-->| LOGICAL, SLOPING BED EFFECT OR NOT
!| TETAP           |-->| ADIMENSIONAL SKIN FRICTION
!| TORATIO         |-->| RATIO BETWEEN BED SHEAR STRESS AND TORI
!| TORI            |-->| REFERENCE SHEAR STRESS OF THE I-TH SIZE SEDIMENT
!| TORM            |-->| REFERENCE SHEAR STRESS OF THE MEDIAN SEDIMENT
!| WI              |-->| DIMENSIONLESS TRANSPORT RATE OF WC-2003
!| WCC             |-->| COEFFICIENT OF CALIBRATION
!~~~~~~~~~~~~~~~~~~~~~~~~~~~~~~~~~~~~~~~~~~~~~~~~~~~~~~~~~~~~~~~~~~~~~~~
!
      USE BIEF
      USE INTERFACE_SISYPHE,
     &      EX_BEDLOAD_WILCOCK_CROWE => BEDLOAD_WILCOCK_CROWE
      USE DECLARATIONS_SISYPHE, ONLY : MPM_ARAY
      USE DECLARATIONS_SPECIAL
      IMPLICIT NONE
!
!+-+-+-+-+-+-+-+-+-+-+-+-+-+-+-+-+-+-+-+-+-+-+-+-+-+-+-+-+-+-+-+-+-+-+-+
!
      INTEGER,           INTENT(IN)    :: SLOPEFF
      TYPE(BIEF_OBJ),    INTENT(INOUT) :: QSC, COEFPN
      DOUBLE PRECISION,  INTENT(IN)    :: XMVE, XMVS, GRAV, DM, AC,
     &                                    AVA(QSC%DIM1)
      DOUBLE PRECISION,  INTENT(IN)    :: SANFRA(QSC%DIM1)
      TYPE(BIEF_OBJ),    INTENT(INOUT) :: ACP ! WORK ARRAY T1
      TYPE(BIEF_OBJ),    INTENT(IN)    :: ACLADM
      TYPE(BIEF_OBJ),    INTENT(IN)    :: TOB, MU
!
!+-+-+-+-+-+-+-+-+-+-+-+-+-+-+-+-+-+-+-+-+-+-+-+-+-+-+-+-+-+-+-+-+-+-+-+
!
      INTEGER I
      DOUBLE PRECISION TORM, TORI, TORATIO, WI, COEFB, WCC
!      DOUBLE PRECISION SANFRA(QSC%DIM1)
!
!=====================================================================!
!                               PROGRAM                               !
!=====================================================================
!
```

```
      CALL CPSTVC(QSC,ACP)
      CALL OS('X=C     ', X=ACP, C=AC)
!
!     SLOPE EFFECT: SOULBY FORMULATION
!
      IF(SLOPEFF.EQ.2) THEN
        CALL OS('X=XY    ', X=ACP, Y=COEFPN)
      ENDIF
!
!    COEFFICIENT TO CALIBRATE THE FORMULA
      WCC = 1.0D0
!
      DO I=1,QSC%DIM1
       TORM = (0.021D0 + 0.015D0*EXP(-20.D0*SANFRA(I)))*(XMVS/XMVE-1.D0)
     &      *XMVE*GRAV*ACLADM%R(I)
       COEFB = 0.67D0/(1.0D0+EXP(1.5D0-DM/ACLADM%R(I)))
       TORI = TORM*((DM/ACLADM%R(I))**COEFB)
       TORATIO = TOB%R(I)*MU%R(I)/TORI
       IF (TORATIO.LT.1.35D0) THEN
          WI = 2.D-3*(TORATIO**7.5D0)
       ELSE
          WI = 14.D0*((1.D0-0.894D0/SQRT(TORATIO))**4.5D0)
       ENDIF
       QSC%R(I)=WCC*WI*AVA(I)*((TOB%R(I)*MU%R(I)
     & /XMVE)**1.5D0)/((XMVS/XMVE-1.D0)*GRAV)

! IF VERY LOW TRANSPORT WE IMPOSE QB = 0 (TO AVOID NUMERICAL ARTEFACTS)
       IF (QSC%R(I).LT.1.D-12)THEN
         QSC%R(I)=0.0D0
       ENDIF
      ENDDO
!
!=======================================================================
!
      RETURN
      END
!
```

Listing C.5: Update of bedload_wilcock_crowe.f.

APPENDIX D

REVIEW OF THE ACTIVE LAYER MODEL IMPLEMENTED IN THE TELEMAC-MASCARET SYSTEM BY DE LINARES (SISYPHE V7P2)

The work presented here has been conducted during the Ph.D. thesis of Florian Cordier, entitled *Review of the active layer model implemented in the Telemac-Mascaret System by De Linares (Sisyphe V7P2)*

Vertical sorting of sediment is managed until Sisyphe V7P2 with a *bookkeeping layer model* [Blom, 2008; Viparelli et al., 2010] based on the definition of the *active layer concept* [Hirano, 1971]. The function of bookkeeping allows the storage of sediments fractions in a substrate subdivided in several layers. In principle, the active layer is defined as the unique layer subject to instataneous elevation changes (*i.e.* transport, erosion or deposition) and layers below correspond to the substrate which doesn't change immediatly in response to sediment transport [Blanpain, 2009] and references therein. The active layer thickness is a sensible parameter in numerical modelling and its formulation varies in function of the phenomenon to model Church and Haschenburger [2017]. While the one-dimensional bookkeeping model of Viparelli et al. [2010] is based on the definitions of layers above a given (and fixed in time) reference datum, in Sisyphe the initial layers elevation is defined as function of the elevation of the riverbed. This difference may result in a sharp decrease of RAM use for the study of systems which present a high difference in riverbed elevation from the upstream to the downstream.

Numerical procedure

The numerical treatment of vertical sediment sorting is performed as follows until Sisyphe V7P2:

1. The fractional evolution of the riverbed is computed trhough a parameter $\partial z_{b,i}$,
2. The active layer thickness $L_{a,t+\Delta t}$ it either defined as a constant during all the simulation or can be calculated as a function of the sediment size (here as a function of $d_{s,m}$, see. line 7),
3. Several scenarios are proposed in function of the number of layers filled with sediment at the time t:
   (a) If only one layer exists (*i.e.* the active layer and the number of layers $N_{lay,t}$ is equal to 1 and the second layer thickness $L_{2,t}$ is equal to 0) or if the riverbed is non-erodible (*i.e* the riverbed elevation is equal to the non-erodible elevation, $z_b = z_r$), an episode of aggradation is followed by the addition of sediment in the active layer and the creation of a second layer if the thickness of the active layer becomes higher than L_a, while erosion is followed by a decrease or a complete suppression of the active layer. When the active layer thickness computed after a time step of Δt is thin enough (*i.e.* $L_{a,t+\Delta t} < 1.10^{-5}$ m), truncation errors may affect the fractional volumes of sediment and an appropriate treatment is performed (line 96 $\rightarrow$ 115).
   (b) If two or more layer exists (*i.e.* $N_{lay,t} > 1$ and $L_{2,t} > 0$), the numerical process is more complex than in the case with a single layer. In case of aggradation (*i.e* deposition), the computation of fractional volume content of sediments for the active and the second layers is made differently from the case with a single layer (see. D) and is not straightforward. In case of degradation (*i.e.* erosion, several scenarios can be proposed:
      i. if the erosion is larger than the thickness of the active layer L_a, computations are stopped with an error message (line 76),
      ii. if the erosion is higher than the thickness of the second layer, the second layer disappears and is mixed between the active and the third layer if $N_{lay} \geq 3$ (line 32 $\rightarrow$ 48), or is destroyed if $N_{lay} = 2$ (line 50 $\rightarrow$ 64),
      iii. if the erosion is lower than the second layer thickness (*i.e.* $-\partial z_b > L_2$), no layer is destroyed, the fraction of sediment in the active layer is computed as a

weighted average of eroded sediment and sediment from the second layer, while the fraction of sediment in the second layer remains identical (line 65 → 73).

(c) A number of verifications are made in the code to ensure the mass continuity (*i.e.* the relevant estimation of fractional volumes of sediment) and to avoid errors due to truncation. Errors are raised with the keyword `PLANTE`.

In the current model, the initial thickness of each layer which represent the initial stratigraphy can be specified in the Fortran file `init_avai.f`.

Variables used in the model

$d_{s,m}$	▷ Median (mean) grain diameter (also referred to as d_{50}) at time $t + \Delta t$ [m]
Δt	▷ Time step duration [s]
$F_{a,i,t}$	▷ Fraction volume content of i-*th* sediment class in the active layer
$F_{k,i,t}$	▷ Fraction volume content of i-*th* sediment class in the k-*th* layer
L_a	▷ Active layer maximal thickness at time $t + \Delta t$ [m]
$L_{a,t}$	▷ Active layer thickness at previous time step [m]
$L_{a,t+\Delta t}$	▷ New active layer thickness [m]
$L_{k,t}$	▷ k-*th* substrate layer thickness at previous time step [m]
$L_{k,t+\Delta t}$	▷ New k-*th* substrate layer thickness [m]
L_T	▷ Erodible thickness of sediments equal to $z_b - z_r$ [m]
$N_{lay,t}$	▷ Number of layers at time t
$N_{lay,t+\Delta t}$	▷ Number of layers at time $t + \Delta t$
∂z_b	▷ Evolution of the riverbed during Δt [m]
$\partial z_{b,i}$	▷ Evolution of the riverbed during Δt for i-*th* size class of sediment [m]
z_b	▷ Absolute elevation of the riverbed topography at time $t + \Delta t$ [m]
z_r	▷ Absolute elevation of the non-erodible layer at time $t + \Delta t$ [m]
`AUX`	▷ Auxiliary variable to compute fractional evolution
`CONST_ALAYER`	▷ Boolean for active layer thickness definition
`NSICLA`	▷ Number of size classes of sediment
`NPOIN`	▷ Number of computational nodes
`PLANTE`	▷ Bad termination of computation
`TEST`	▷ Variable used to test truncation errors
`TEST2`	▷ Variable used to test truncation errors
`ZERO`	▷ Definition of a numerical zero

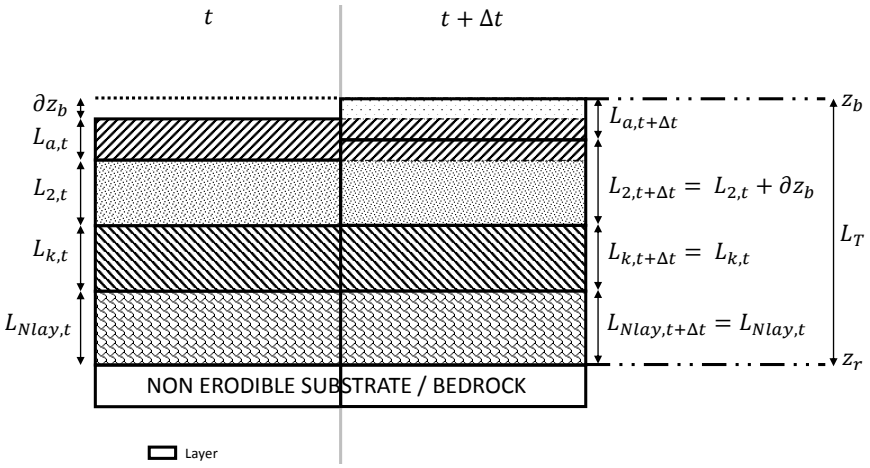


Figure D.1: Illustrations of variables used in the model of De Linares *et al.* [2007] in the case of bed aggradation.

Pseudo-code of the algorithm in Sisyphe V7P2

1: ZERO = E^{-7}

2: **for** J=1,NPOIN **do** ▷ Note: All variables below are dependent of the node j

3: **if** $L_{a,t} < 0$ **then** ▷ Previous active layer thickness is negative

4: PLANTE

5: **end if**

6: **if** NOT CONST_ALAYER **then**

7: $L_a = 3 * d_{s,m}$ ▷ Active layer thickness definition

8: **end if**

9: $N_{lay,t+\Delta t} = N_{lay,t}$

10: $L_T = z_b - z_r$

11: **if** $L_T < 0$ **then** ▷ Previous topography below the non-erodible layer

12: PLANTE

13: **end if**

14: $\partial z_b = 0$

15: **for** I=1,NSICLA **do** ▷ Total bed evolution during Δt

16: $\partial z_b = \partial z_b + \partial z_{b,i}$

17: **end for**

18: **if** $N_{lay,t} > 1$ **then** ▷ **If 2 or more layers**

19: **if** $\partial z_b \geq 0$ **then** ▷ **Aggradation**

20: $L_{2,t+\Delta t} = L_{2,t} + \partial z_b$ ▷ Aggradation of L_2 to keep L_a constant

21: **for** I=1,NSICLA **do**

22: AUX=$\dfrac{F_{a,i,t} L_a + \partial z_{b,i}}{L_a + \partial z_b}$

23: $F_{2,i,t+\Delta t} = \dfrac{\text{AUX}\partial z_b + F_{2,i,t} L_{2,t}}{L_{2,t+\Delta t} + \partial z_b}$

24: $F_{a,i,t+\Delta t} = \dfrac{F_{a,i,t} L_a - \text{AUX}\partial z_b + \partial z_{b,i}}{L_a}$

25: **end for**

26: **if** $F_{a,i,t+\Delta t} > 1$ or $F_{a,i,t+\Delta t} < 0$ **then** ▷ Error case 1

27: PLANTE

28: **end if**

29: $L_{a,t+\Delta t} = L_a$

30: **else if** $\boxed{-L_a < \partial z_b < 0}$ **then** ▷ **Degradation**

31: **if** $\boxed{-L_{2,t} < \partial z_b}$ **then** ▷ Degradation greater than L_2 thickness

32: **if** $\boxed{N_{lay,t} > 2}$ **then** ▷ If 3 layers or more

33: **for** `I=1,NSICLA` **do**

34: $F_{a,i,t+\Delta t} = \dfrac{F_{a,i,t}L_a + \partial z_{b,i} + F_{2,i}L_{2,t} - F_{3,i}(\partial z_b + L_{2,t})}{L_a}$

35: **if** $\boxed{F_{a,i,t+\Delta t} > 1 \text{ or } F_{a,i,t+\Delta t} < 0}$ **then** ▷ Error case 2

36: `PLANTE`

37: **end if**

38: $F_{2,i,t+\Delta t} = F_{3,i,t}$

39: **for** `k=3:`$N_{lay,t}$ **do**

40: $F_{k,i,t+\Delta t} = F_{k+1,i}$

41: **end for**

42: **end for**

43: $L_{a,t} = L_a$

44: $N_{lay,t+\Delta t} = N_{lay,t} - 1$

45: $L_{2,t+\Delta t} = L_{2,t} + \partial z_b + L_3$

46: **for** `k=3:`$N_{lay,t}$ **do**

47: $L_{k,t+\Delta t} = L_{k+1,t+\Delta t}$

48: **end for**

49: **else** ▷ If only 2 layers

50: **for** `I=1,NSICLA` **do**

51: **if** $\boxed{z_b > z_r}$ **then** ▷ Active layer still exists

52: $F_{a,i,t+\Delta t} = \dfrac{F_{a,i,t}L_a + \partial z_{b,i} + L_{2,t}F_{2,i,t}}{L_a + \partial z_b + L_{2,t}}$

53: **if** $\boxed{F_{a,i,t+\Delta t} > 1 \text{ or } F_{a,i,t+\Delta t} < 0}$ **then** ▷ Error case 3

54: `PLANTE`

55: **end if**

56: **else** ▷ Active layer destroyed

57: $F_{a,i,t+\Delta t} = 0$

58: **end if**

59: $F_{2,i,t+\Delta t} = 0$ ▷ Second layer destroyed

60: **end for**

61: $N_{lay,t+\Delta t} = N_{lay,t} - 1$ ▷ Second layer is destroyed resulting in -1 layer

62: $L_{a,t+\Delta t} = L_T$

63: $L_{2,t+\Delta t} = 0$

64: **end if**

65: **else** ▷ Degradation less than L_2 thickness
66: **for** I=1,NSICLA **do**
67: $F_{a,i,t+\Delta t} = \frac{F_{a,i,t}L_a + \partial z_{b,i} - \partial z_b F_{2,i,t}}{L_a}$
68: **if** $\boxed{F_{a,i,t+\Delta t} > 1 \text{ or } F_{a,i,t+\Delta t} < 0}$ **then** ▷ Error case 4
69: PLANTE
70: **end if**
71: **end for**
72: $L_{a,t+\Delta t} = L_a$
73: $L_{2,t+\Delta t} = L_{2,t} + \partial z_b$
74: **end if**

75: **else** ▷ Erosion greater than active layer thickness (*i.e.* $-\partial z_b > L_a$)
76: PLANTE
77: **end if**

78: **else** ▷ **0 or 1 layer**
79: **if** $\boxed{L_T > L_a}$ **then** ▷ **New sediment height upper than L_a - layer 2 created**
80: $N_{lay,t+\Delta t} = 2$
81: $L_{2,t+\Delta t} = z_b - z_r - L_a$
82: $L_{a,t+\Delta t} = L_a$
83: **for** I=1,NSICLA **do**
84: $F_{2,i,t+\Delta t} = F_{a,i,t}$
85: $F_{a,i,t+\Delta t} = \frac{F_{a,i,t}(L_a - \partial z_b) + \partial z_{b,i}}{L_a}$
86: **if** $\boxed{F_{a,i,t+\Delta t} > 1 \text{ or } F_{a,i,t+\Delta t} < 0}$ **then** ▷ Error case 5
87: PLANTE
88: **end if**
89: **end for**
90: **else** ▷ **Only one layer remaining**
91: **if** $\boxed{L_{a,t} + \partial z_b > 1.10^{-15}}$ **then** ▷ If new active layer thickness larger than 1.10^{-15}
92: **for** I=1,NSICLA **do**
93: $F_{a,i,t+\Delta t} = \frac{F_{a,i,t}L_{a,t} + \partial z_{b,i}}{L_{a,t} + \partial z_b}$
94: $F_{2,i,t+\Delta t} = 0$
95: **end for**
96: **if** $\boxed{L_{a,t} + \partial z_b < 1.10^{-5}}$ **then** ▷ If thickness smaller than 1.10^{-5}, normalisation
97: TEST1=0
98: **for** I=1,NSICLA **do**
99: $F_{a,i,t+\Delta t} = max(0, min(1, F_{a,i,t}))$
100: TEST1 = TEST1 + $F_{a,i,t+\Delta t}$
101: **end for**

102: **if** $\boxed{(\texttt{TEST1-1})^2 > 0}$ **then** ▷ Normalisation
103: **for** I=1,NSICLA **do**
104: $F_{a,i,t+\Delta t} = \dfrac{F_{a,i,t+\Delta t}}{max(\texttt{TEST1}, 1.10^{-21})}$
105: **end for**
106: **end if**
107: **end if**
108: **else** ▷ If new thickness of active layer less than 1.10^{-15}
109: $F_{a,1,t+\Delta t} = 1$
110: $F_{2,1,t+\Delta t} = 1$
111: **for** I=2,NSICLA **do**
112: $F_{a,i,t+\Delta t} = 0$
113: $F_{2,i,t+\Delta t} = 0$
114: **end for**
115: **end if**
116: **end if**
117: $L_{a,t+\Delta t} = L_T$ ▷ Only active layer remaining
118: $L_{2,t+\Delta t} = 0$
119: $N_{lay,t+\Delta t} = 1$
120: **end if**

121: TEST1$= 0$ ▷ **Truncation errors on final fractions**
122: TEST2$= 0$
123: **for** I=1,NSICLA **do**
124: **for** K= 1(=a),NLAYER **do**
125: **if** $\boxed{F_{k,i,t+\Delta t} > 1 \text{ or } F_{k,i,t+\Delta t} < 0}$ **then** ▷ Error
126: PLANTE
127: **else** ▷ Clipping
128: $F_{a,i,t+\Delta t} = max(F_{a,i,t+\Delta t}, 0)$
129: $F_{a,i,t+\Delta t} = min(F_{a,i,t+\Delta t}, 1)$
130: **end if**
131: **end for**
132: TEST1 = TEST1 + $F_{a,i,t+\Delta t}$
133: TEST2 = TEST2 + $F_{2,i,t+\Delta t}$
134: **end for**
135: **if** $\boxed{\texttt{TEST1} > 0 \text{ and } (\texttt{TEST1} - 1)^2 > 0}$ **then** ▷ Error on sum of fractions in active layer
136: PLANTE
137: **end if**
138: **if** $\boxed{\texttt{TEST2} > 0 \text{ and } (\texttt{TEST2} - 1)^2 > 0}$ **then** ▷ Error on sum of fractions in layer 2
139: PLANTE
140: **end if**

141: **end for** ▷ End of loop on nodes

142: Other operations ▷ Computation of the total volume of sediment in the domain and clean stop for all processors if problem

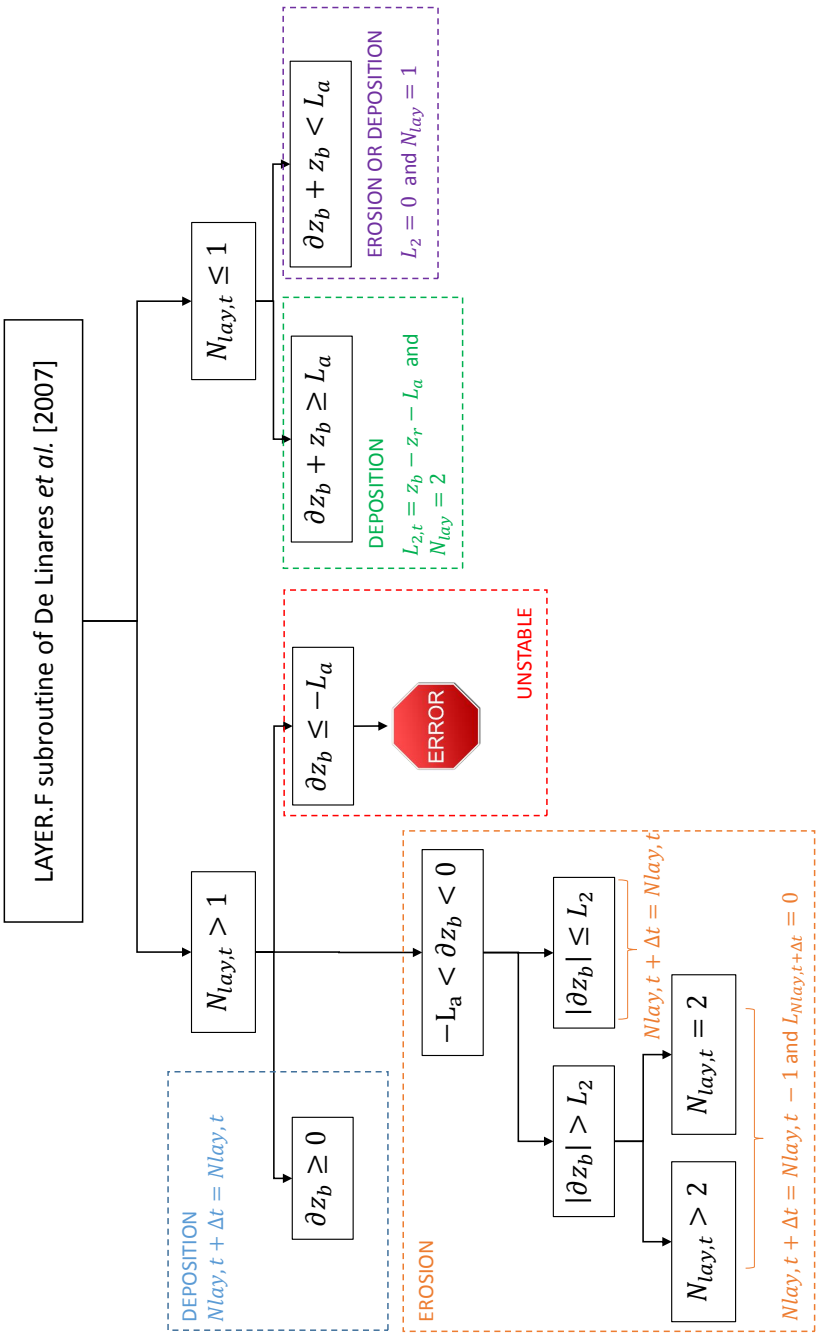


Figure D.2: Schematization of the algorithm of De Linares *et al.* [2007].

Limitations and inconveniences of the model

Computation of volume content fractions during bed aggradation

It is not always clear why an auxiliary variable named `AUX` is used to estimate fractions of sediment in the active layer and the second layer during aggradation scenarios (line 23 $\rightarrow$ 25, see comments and discussions in the original Fortran file), while another definition is used if we refer to the scenario of aggradation in the case where the second layer is created (line 83 $\rightarrow$ 85).

Addition of new layers during aggradation

Numerical treatment of aggradation processes is limited in this version of Sisyphe because no stratigraphy reconstruction (*i.e.* no new underlying layer creation) is made possible during scenarios of aggradation (line 19 $\rightarrow$ 29). This results in a loss of information on the GSD of deposits, which tends to be averaged the more L_2 increases during scenarios of aggradation.

Code robustness

According to user's feedbacks, this code often stops after several time steps with raising an error message of the type " error in layer". This error is due to a ill-posed treatment of the layers thicknesses at transitions between erodible and rigid bed and erroneous computations of fractional volume contents of sediment. The algorithm is tested on a scenario derived from Lanzoni's P2009 experiment (see Chapter 4), where we impose an initial sediment column of 1 cm everywhere in the channel. The last numerical simulation stops at $t = 6730$ s with the error message showed in Figure D.3 (in this example 2 processors are used with the gfortran compiler).

Complexity/understanding of the numerical model

The algorithm implemented in the current model is too complex because the treatment of the stratigraphy is based on the number of layers that is present at a given time step of the computation. A more relevant way to model bed stratigraphy is presented in the next section.

```
================================================================================
 ITERATION   336500    TIME:  1 H 52 MIN  10.0000 S     (   6730.0000 S)

 BEDLOAD EQUATION SOLVED IN    10 ITERATIONS
 BEDLOAD EQUATION SOLVED IN    10 ITERATIONS
--------------------------------------------------------------------------------
                           SEDIMENT SLIDE

 MASS-BALANCE (IN VOLUME, INCLUDING VOID):
 SUM OF THE EVOLUTIONS :   -0.4927212E-07 M3
 BOUNDARY   1 BEDLOAD FLUX =   -0.1123899E-03  ( M3/S  >0 = ENTERING )
 BOUNDARY   2 BEDLOAD FLUX =    0.1099263E-03  ( M3/S  >0 = ENTERING )
 TOTAL        BEDLOAD FLUX =   -0.2463606E-05  ( M3/S  >0 = ENTERING )
 LOST VOLUME                     :   -0.5187084E-18 M3  ( IF <0 EXIT )

 MASS BALANCE FOR SEDIMENT CLASS :           1
 TOTAL VOLUME:   1.2051627223805883
 SUM OF THE EVOLUTIONS FOR THIS CLASS:   -0.1561624E-06
 VOLUME THAT ENTERED THE DOMAIN FOR THIS CLASS:   -0.1561624E-06 M3
 LOST VOLUME                     :   -0.2620508E-18 M3  ( IF <0 EXIT )

 MASS BALANCE FOR SEDIMENT CLASS :           2
 TOTAL VOLUME:  0.59358811023736147
 SUM OF THE EVOLUTIONS FOR THIS CLASS:    0.1068903E-06
 VOLUME THAT ENTERED THE DOMAIN FOR THIS CLASS:    0.1068903E-06 M3
 LOST VOLUME                     :   -0.2576701E-18 M3  ( IF <0 EXIT )

 MAXIMAL EVOLUTION        :    0.9764204E-05 NODE  :  14258
 MINIMAL EVOLUTION        :   -0.1460282E-04 NODE  :  19515
 TOTAL MAXIMAL EVOLUTION  :    0.1755148E-01 NODE  :  14033
 TOTAL MINIMAL EVOLUTION  :   -0.1499080E-01 NODE  :   9339
 PROBLEM IN LAYER: J,TEST1        4379   6.4623731875678572E-006
 IN LAYER 1 SUM OF FRACTIONS NOT 1
STOP AFTER AN ERROR IN LAYER

PLANTE: PROGRAM STOPPED AFTER AN ERROR
RETURNING EXIT CODE:           2
-------------------------------------------------------------------------------
MPI_ABORT was invoked on rank 0 in communicator MPI_COMM_WORLD
with errorcode 2.
```

Figure D.3: Listing output in the command-line interface of the simulation showing the typical error encountered with the algorithm developed by De Linares *et al.* de Linares and Belleudy [2007] at transitions between an erodible bed and a rigid bed.

APPENDIX E

ACTIVE LAYER MODEL IMPLEMENTED IN THE TELEMAC-MASCARET SYSTEM IN THIS WORK (SISYPHE V7P3)

The work presented here has been conducted during the Ph.D. thesis of Florian Cordier, entitled *Active layer model implemented in the Telemac-Mascaret System in this work (Sisyphe V7P3)*

The following subroutine has been edited in order to implement the bookkeeping active layer of Hirano [1971]:

- modification of the subroutine LAYER in layer.f

The pseudo-code can be found in Section 2.2.2. The Fortran code is presented below:

```
!                    ***************
!                    SUBROUTINE LAYER
!                    ***************
!
     &(ZFCL_W,NLAYER,ZR,ZF,ESTRAT,ELAY,MASBAS,ACLADM,NSICLA,NPOIN,
     & ELAYO,VOLTOT,ES,AVAIL,CONST_ALAYER,DTS,ESTRATNEW,NLAYNEW)
!
!======================================================================
!  SISYPHE   VXXX                                        MARCH 2017
!  REVIEWED, CORRECTED AND IMPROVED BY Florian CORDIER et al. 2017
!  EDF R&D Chatou Lab., LNHE, FRANCE
!+
!brief    UPDATE SEDIMENT FRACTION AND NUMBER OF SEDIMENT LAYERS
!+
!+           ACTIVE LAYER IS LAYER 1 WITH THICKNESS ELAY
!+
!history  Florian CORDIER et al.
!+        2017
!+        The original subroutine has been reviewed and tested for ...
    different numbers of layers under
!+        several scenarios of riverbed evolution. The mathematical ...
    model of the original version
!+        was ill-posed for the determination of volumes fractions of ...
    sediment and lead to sediment
!+        mass discontinuities. The determination of fractions is fully ...
    reviewed byCordier et al. and some
!+        parts of the code are re-adapted (thickness determined before ...
    the fractions, etc.)
!+
!
!~~~~~~~~~~~~~~~~~~~~~~~~~~~~~~~~~~~~~~~~~~~~~~~~~~~~~~~~~~~~~~~~~~~~~~~~
!| ACLADM          |-->| MEAN DIAMETER OF SEDIMENT
!| AVAIL           |<->| SEDIMENT FRACTION FOR EACH LAYER, CLASS, POINT
!| CONST_ALAYER    |-->| CONSTANT ACTIVE LAYER THICKNESS OR NOT
!| ELAY            |<->| ACTIVE LAYER THICKNESS FOR EACH POINT
!| ELAYO           |<->| ACTIVE LAYER THICKNESS
!| ES              |<->| LAYER THICKNESSES
!| ESTRAT          |<->| ACTIVE STRATUM THICKNESS FOR EACH POINT          ...
    FC : NOT USED !!
!| ESTRATNEW       |<->| ACTIVE STRATUM THICKNESS AT TIME T+DT            ...
    FC : NOT USED !!
!| MASBAS          |-->| INTEGRAL OF TEST FUNCTIONS
!| NLAYER          |<->| NUMBER OF LAYER FOR EACH POINT                   ...
    FC : NOT USED !!
!| NLAYNEW         |<->| NUMBER OF LAYER AT TIME T+DT      FC : NOT USED ...
    !!
!| NPOIN           |-->| NUMBER OF POINTS
```

```
!| NSICLA          |-->| NUMBER OF SIZE CLASSES FOR BED MATERIALS
!| VOLTOT          |<->| TOTAL VOLUME OF SEDIMENT IN THE BED
!| ZF              |-->| ELEVATION OF BOTTOM
!| ZFCL_W          |-->| BED EVOLUTION FOR EACH SEDIMENT CLASS
!| ZR              |-->| NON ERODABLE BED
!~~~~~~~~~~~~~~~~~~~~~~~~~~~~~~~~~~~~~~~~~~~~~~~~~~~~~~~~~~~~~~~~~~~~~~~~~~~~
!
      USE BIEF
      USE DECLARATIONS_SISYPHE , ONLY : NOMBLAY
      USE DECLARATIONS_SPECIAL
      USE DECLARATIONS_TELEMAC2D , ONLY : LT
      IMPLICIT NONE
!
!+-+-+-+-+-+-+-+-+-+-+-+-+-+-+-+-+-+-+-+-+-+-+-+-+-+-+-+-+-+-+-+-+-+-+-+-+
!
      TYPE (BIEF_OBJ),  INTENT(IN)    :: ZFCL_W,ZR,ZF
      TYPE (BIEF_OBJ),  INTENT(IN)    :: MASBAS,ACLADM
      INTEGER,          INTENT(IN)    :: NSICLA,NPOIN
      DOUBLE PRECISION, INTENT(IN)    :: DTS
      LOGICAL,          INTENT(IN)    :: CONST_ALAYER
      TYPE (BIEF_OBJ),  INTENT(INOUT) :: NLAYER,ESTRAT,ELAY
      DOUBLE PRECISION, INTENT(INOUT) :: ELAY0
      DOUBLE PRECISION, INTENT(INOUT) :: ES(NPOIN,NOMBLAY)
      DOUBLE PRECISION, INTENT(INOUT) :: AVAIL(NPOIN,NOMBLAY,NSICLA)
      DOUBLE PRECISION, INTENT(INOUT) :: VOLTOT(NSICLA),ESTRATNEW(NPOIN)
      INTEGER         , INTENT(INOUT) :: NLAYNEW(NPOIN)
!
!+-+-+-+-+-+-+-+-+-+-+-+-+-+-+-+-+-+-+-+-+-+-+-+-+-+-+-+-+-+-+-+-+-+-+-+-+
!
      DOUBLE PRECISION P_DSUM
      EXTERNAL         P_DSUM
      INTEGER  P_ISUM
      EXTERNAL P_ISUM
!
!-----------------------------------------------------------------------
!
      INTEGER I,J,K
      DOUBLE PRECISION EVOL,LTH,TEST2,REST,FRACT,THICK
      DOUBLE PRECISION ZERO
!
!     Table containing the maximal thicknesses that can be attained by ...
    the layers
      DOUBLE PRECISION ESM(NOMBLAY)
!     Table containing layers thicknesses at time t
      DOUBLE PRECISION ES_OLD(NOMBLAY)
!     Number of layers filled with sediment at time t+dt
      INTEGER NFILL
!     Integer that takes value 0 if no layer creater, 1 if a layer is ...
    created, -1 if a layer is destroyed
      INTEGER LAY_CREATED
!
!!-----------------------------------------------------------------------
!-----------------------------------------------------------------------
!         I. INITIALIZATION OF VARIABLES AND USER PARAMETERIZATION
!!-----------------------------------------------------------------------
!-----------------------------------------------------------------------
!                       I.1 DATA INITIALIZATION
!-----------------------------------------------------------------------
```

```
      DATA ZERO/0.D0/
      NFILL = 0
      LAY_CREATED = 0
!
      DO J=1,NPOIN
       ! Re-initialization of the variables for each node loop
       NFILL = 0
       LAY_CREATED = 0
!-----------------------------------------------------------------------
!                I.2 STORAGE OF PREVIOUS LAYER THICKNESSES
!-----------------------------------------------------------------------
!  Maximal thickness that can be reached by the substrate layers ... excepted
!  from the deepest layer filled with sediment at time t+dt.
!
       DO K = 1, NOMBLAY
         ES_OLD(K) = ES(J,K)
         IF (ES_OLD(K).GT.ZERO) LAY_CREATED = LAY_CREATED - 1
       ENDDO
!
!-----------------------------------------------------------------------
!          I.3 USER DEFINED MAXIMAL THICKNESSES OF SEDIMENT LAYERS
!-----------------------------------------------------------------------
!  Maximal thickness that can be reached by the substrate layers ... excepted
!  from the deepest layer filled with sediment at time t+dt.
       ESM(1) = ELAY0
       DO K = 2, NOMBLAY
         ESM(K) = 1.0D0*ELAY0
       ENDDO
!
!!-----------------------------------------------------------------------
!-----------------------------------------------------------------------
!           II. UPDATE THE NUMBER AND THE THICKNESS OF SEDIMENT LAYERS
!-----------------------------------------------------------------------
!!-----------------------------------------------------------------------
!  The computation of the new layers thicknesses is performed before the
!  computation of fractional volumes contents of sediment
!
! LTH = Thickness of the sediment column between the rigid bed and the ... riverbed surface
       LTH = ZF%R(J)-ZR%R(J)
!
       IF(NOMBLAY.EQ.1)THEN
         ES(J,1)=MAX(0.D0,ZF%R(J)-ZR%R(J))
!
       ELSE
         ES(J,1)=MIN(ELAY0,MAX(0.D0,ZF%R(J)-ZR%R(J)))
         REST=ZF%R(J)-ZR%R(J)-ES(J,1)
         DO K=2,NOMBLAY-1
           ES(J,K)=min(ESM(K),max(0.D0,REST))
           REST=max(0.D0,REST-ES(J,K))
         ENDDO
         ES(J,NOMBLAY)=max(0.D0,REST)
       ENDIF
!
       ELAY%R(J)= ES(J,1)
       ESTRAT%R(J)=ES(J,2)
```

```
!
       DO K = 1, NOMBLAY
         IF (ES(J,K).GT.ZERO) THEN
            LAY_CREATED = LAY_CREATED + 1
            NFILL = NFILL + 1
         ENDIF
       ENDDO
!
!-----------------------------------------------------------------------
!                III.    UPDATE OF SEDIMENT FRACTIONS
!-----------------------------------------------------------------------
!-----------------------------------------------------------------------
!     III.1 TEMPORAL BED ELEVATION CHANGE
!-----------------------------------------------------------------------
        EVOL  = 0.D0
        DO I=1,NSICLA
          EVOL = EVOL + ZFCL_W%ADR(I)%P%R(J)
        ENDDO
!
!      THE BED LEVEL CHANGE MUST BE LESS THAN THE ACTIVE LAYER THICKNESS
!      TO AVOID INSTABILITIES
        IF(ABS(EVOL).GT.ELAY0)THEN
          WRITE(LU,*) '*********** WARNING ******************'
          WRITE(LU,*) 'TOO MUCH BED CHANGE AT POINT J=',J
          WRITE(LU,*) 'DECREASE DT OR INCREASE ELAY0'
          WRITE(LU,*) 'EVOL=', EVOL, '    ELAY0=',ELAY0
          WRITE(LU,*) '************************************'
          CALL PLANTE(1)
          STOP
        ENDIF
!
!-----------------------------------------------------------------------
!            III.2  UPDATE OF FRACTIONS FOR DEPOSITION
!-----------------------------------------------------------------------
!      AVOID TO COMPUTE WEIRD FRACTIONS WHEN SIMULATIONS ARE RESTARTED ...
   USING
!      THE SEDIMENTOLOGICAL FILE (SKIPS THE FIRST TIME-STEP)
       IF(LT.GT.1.0D0)THEN
!      (fractions are calculated from the deepest layer until the top ...
   one)
        IF(EVOL.GT.0.D0) THEN
!
          DO I=1,NSICLA
!
!       1)   DEEPEST FILLED LAYER
!           If the deepest layer at time t+1 is the active layer
            IF(NFILL.LE.1)THEN
               FRACT = ZFCL_W%ADR(I)%P%R(J)
!           If the deepest layer at time t+1 is not the active layer
            ELSE
               FRACT = AVAIL(J,NFILL-1,I)*EVOL
            ENDIF
!
              IF(LAY_CREATED.EQ.0)THEN
            AVAIL(J,NFILL,I) = (ES_OLD(NFILL)*AVAIL(J,NFILL,I)
     &                         + FRACT)
     &                         / ES(J,NFILL)
```

```
              ELSE
            AVAIL(J,NFILL,I) = FRACT/EVOL
              ENDIF

!
!         2)   LAYERS ABOVE THE DEEPEST FILLED LAYER
            IF(NFILL.GT.1)THEN
              IF(LAY_CREATED.EQ.0)THEN
                 THICK = ES_OLD(NFILL-1)-EVOL
              ELSE
                 THICK = ES_OLD(NFILL-1)-ES(J,NFILL)
              ENDIF
              DO K=NFILL-1,1,-1
                IF(K.EQ.1)THEN
                   FRACT = ZFCL_W%ADR(I)%P%R(J)
                ELSE
                   FRACT = AVAIL(J,K-1,I)*EVOL
                ENDIF
                AVAIL(J,K,I) = (THICK*AVAIL(J,K,I)
     &                          + FRACT)
     &                          / ES(J,K)
              ENDDO
            ENDIF
            DO K=1,NOMBLAY
              AVAIL(J,K,I) = MAX(AVAIL(J,K,I),ZERO)
              AVAIL(J,K,I) = MIN(AVAIL(J,K,I),1.D0-ZERO)
            ENDDO
          ENDDO
!
!-----------------------------------------------------------------------
!               III.3    UPDATE OF FRACTIONS FOR EROSION
!-----------------------------------------------------------------------
!      (fractions are calculated from the top layer until the deepest ...
    one)
!
        ELSEIF(EVOL.LT.0.D0)THEN
!
          DO I=1,NSICLA
!
!          1) IF THE NODE CONTAINS SEDIMENT AT TIME t+1
           IF (NFILL.GT.0)THEN
!
!            1A) FRACTIONS IN THE TOPPEST LAYER
!            1Ai) If only the active layer is filled with sediment at ...
    time t+1
            IF ((NFILL.EQ.1))THEN
              IF(LAY_CREATED.EQ.0)THEN
!                PRINT *, 'NOLAY CREATED'
!                CALL PLANTE(1)
!                STOP
                AVAIL(J,1,I)= ( AVAIL(J,1,I)*ES_OLD(1)
     &                        + ZFCL_W%ADR(I)%P%R(J) )
     &                        / ES(J,1)
              ELSE
                AVAIL(J,1,I)= ( AVAIL(J,1,I)*ES_OLD(1)
     &                        + AVAIL(J,2,I)*ES_OLD(2)
     &                        + ZFCL_W%ADR(I)%P%R(J) )
     &                        / ES(J,1)
```

```
                ENDIF
!            1Aii) If two or more layers are filled with sediment at ...
    time t+1
             ELSE
                AVAIL(J,1,I)= ( AVAIL(J,1,I)*ES_OLD(1)
     &                        - AVAIL(J,2,I)*EVOL
     &                        + ZFCL_W%ADR(I)%P%R(J) )
     &                        / ES(J,1)
             ENDIF ! END 1A)

!            1B) FRACTIONS IN THE LAYERS BETWEEN THE ACTIVE AND THE ...
    DEEPEST (only if NFILL>2 at time t+1)
             IF (NFILL.GT.2)THEN
!               1Bi)  For all the layers sandwiched by the active (1) ...
    and the deepest filled layer (NFILL)
                DO K = 2, NFILL-1
                  AVAIL(J,K,I)= ( AVAIL(J,K,I)*(ES_OLD(K)+EVOL)
     &                          - AVAIL(J,K+1,I)*EVOL    )
     &                          / ES(J,K)
                ENDDO
             ENDIF !  ENDIF 1B)

!            1C) FRACTION IN THE DEEPEST FILLED LAYER (NFILL)
             AVAIL(J,NFILL,I)= AVAIL(J,NFILL,I)
!
           ENDIF     ! ENDIF 1)

           DO K=1,NOMBLAY
             AVAIL(J,K,I) = MAX(AVAIL(J,K,I),ZERO)
             AVAIL(J,K,I) = MIN(AVAIL(J,K,I),1.D0-ZERO)
           ENDDO
!
         ENDDO      ! ENDLOOP NSICLA
!
!-----------------------------------------------------------------------
!           III.4   NO UPDATE OF FRACTIONS IF NO EVOLUTION
!-----------------------------------------------------------------------
        ELSE
!         No fractions update is performed
        ENDIF        ! END DEPOSITION/EROSION/NO-CHANGE
       ENDIF ! SKIP TS1
!
!-----------------------------------------------------------------------
!  III.5 FRACTIONS OF PHYSICAL SEDIMENT SET TO 0 IF NO SEDIMENT IN THE ...
    LAYERS at time t+1
!-----------------------------------------------------------------------
       IF(ES(J,NOMBLAY).LE.ZERO)THEN
          DO K=NFILL+1, NOMBLAY
             DO I=1, NSICLA
                 AVAIL(J,K,I) = 0.0D0
             ENDDO
!             AVAIL(J,K,NSICLA) = 1.0D0
          ENDDO
       ENDIF
!-----------------------------------------------------------------------
      ENDDO ! EndLoop J nodes
!
!-----------------------------------------------------------------------
```

```
!       IV. COMPUTATION OF THE TOTAL VOLUME OF SEDIMENTS IN THE DOMAIN
!-----------------------------------------------------------------------
      DO I = 1, NSICLA
        VOLTOT(I) = 0.D0
      ENDDO
      DO I=1,NSICLA
        DO J=1,NPOIN
          DO K=1,NOMBLAY
            VOLTOT(I) = VOLTOT(I) + ES(J,K)*AVAIL(J,K,I)*MASBAS%R(J)
          ENDDO
        ENDDO
      ENDDO
!
      IF(NCSIZE.GT.1) THEN
        DO I=1,NSICLA
          VOLTOT(I) = P_DSUM(VOLTOT(I))
        ENDDO
      ENDIF
!-----------------------------------------------------------------------
!
      RETURN
      END
```

Listing E.1: Update of layer.f.

APPENDIX F

IMPLEMENTATION OF THE SEDIMENT RECIRCULATION IN SISYPHE V7P3

The work presented here has been conducted during the Ph.D. thesis of Florian Cordier, entitled *Implementation of the sediment recirculation in Sisyphe V7P3*

The following subroutines have been edited in order to implement the sediment recirculation:

- modification of the subroutine `CONLIT` in conlit.f

The implementation of sediment recirculation is performed with modifying the subroutine `conlit.f`. The procedure consists on computing the solid transport rates exiting the downstream boundary at the previous time step of computation for each size fraction (here `NSICLA`=2) of sediment (lines 40→41 and 61→62), and redistributing the same volume of sediment at each upstream computational node (lines 108→110). This last step requires to specify manually the number of upstream nodes at line 109. In the case where $t = 0$ s (*i.e.* first time-step), the prescribed fractional transport rates are set equal to 0. In the case where the transport rate is close to the zero machine, we impose a transport rate equal to 0. The Fortran code is given below.

```
!                     *****************
                      SUBROUTINE CONLIT
!                     *****************
!
     &(NBOR,AT)
      [...]
!
!history  F.CORDIER (EDF-LNHE)
!+        15/12/2017
!+        V7P2
!+        Recirculation of sediment from downstream at t to upstream a t...
   +1
!~~~~~~~~~~~~~~~~~~~~~~~~~~~~~~~~~~~~~~~~~~~~~~~~~~~~~~~~~~~~~~~~~~~~~~~~~~~~
      [...]
! FC
      USE INTERFACE_PARALLEL, ONLY : P_IMAX, P_ISUM, P_DSUM
! ENDFC
      IMPLICIT NONE
      [...]
      DOUBLE PRECISION, EXTERNAL :: QGL
!
! FC
!     INITIALISATION OF QOUT AND RECIRCULATE (1 MEANS YES, 0 MEANS NO)
      DOUBLE PRECISION QOUT(NSICLA)
      INTEGER RECIRCULATE, J
!-----------------------------------------------------------------------
      RECIRCULATE = 1
! ENDFC
!
!     INITIALISATION OF YADEB
!
      IF(NFRLIQ.GE.1) THEN
        DO I=1,NFRLIQ
          YADEB(I)=0
        ENDDO
      ENDIF
!
! FC
!     WE COMPUTE QSOUT FOR EACH CLASS OF SEDIMENT
      IF(NSICLA.GT.1) THEN
          CALL OS('X=Y     ',X=T2,Y=FLBCLA%ADR(1)%P)
```

```
          CALL OS('X=Y     ',X=T3,Y=FLBCLA%ADR(2)%P)
      ENDIF
!
      DO I=1, NSICLA
        QOUT(I)=0.D0
      ENDDO
! END FC
       [...]
        IF(LIEBOR%I(K).EQ.KADH) THEN
          LIEBOR%I(K)= KLOG
! FC - We comment these lines
!        ELSEIF(LIEBOR%I(K).EQ.KENT) THEN
!         WARNING !!!!!!!!!!!!!!    DYNAMITE !!!!!!!!!
!         FOR COMPATIBILITY OF OLD STUDIES, LIEBOR=KENT SUPERSEDES ...
   LIQBOR=KENT
!         IF BOTH ARE GIVEN AS KENT
!          LIQBOR%I(K)= KSORT
! ENDFC
        ENDIF
! FC - SUM OF THE EXITING VOLUMES OF SEDIMENT AT EACH NODE FOR EACH SIZE...
     FRACTION
        IF(LIQBOR%I(K).EQ.KSORT) THEN
             QOUT(1)=QOUT(1) +T2%R(K)
             QOUT(2)=QOUT(2) +T3%R(K)
! ENDFC
        ENDIF
!       CASES WHERE WE HAVE A PRESCRIBED DISCHARGE
      [...]
!     DEALING WITH PRESCRIBED SOLID DISCHARGES
! FC
!     COMMUNICATE J AND QOUT FROM ALL PROCESSORS
!
      DO I=1, NSICLA
        IF(NCSIZE.GT.1) THEN
          QOUT(I)=P_DSUM(QOUT(I))
        ENDIF
      ENDDO
      IF(NCSIZE.GT.1) J=P_ISUM(J)
! ENDFC
!
      IF(NFRLIQ.GT.0) THEN
        DO IFRLIQ=1,NFRLIQ
          IF(NCSIZE.GT.1) YADEB(IFRLIQ)=P_IMAX(YADEB(IFRLIQ))
          IF(YADEB(IFRLIQ).EQ.1) THEN
!
!         READING BOUNDARY CONDITION FILE WITH SOLID DISCHARGE
!
! FC - comment these lines
!       IF(CHARR) THEN
!     AVOID OVERRIDING WITH SUSPENDED SEDIMENT TRANSPORT
!          IF(SIS_FILES(SISLIQ)%NAME(1:1).NE.' ') THEN
!               SOLDIS(IFRLIQ)=QGL(IFRLIQ,AT)
!          ENDIF
!       ENDIF
!
!            CALL DISIMP(SOLDIS(IFRLIQ),Q2BOR,NUMLIQ%I,IFRLIQ,NSOLDIS,
!     &                  T5,T1,
!                           MASK OF LIQUID BOUNDARIES DONE IN SISYPHE
```

```
!     &                   NPTFR,MASK%R,MESH)
! ENDFC
!
            IF(NSICLA.GT.1) THEN
              DO I=1,NSICLA
                DO K=1,NPTFR
                  IF(NUMLIQ%I(K).EQ.IFRLIQ.AND.
    &                LIQBOR%I(K).EQ.KENT) THEN
! FC - comment this line
!                   QBOR%ADR(I)%P%R(K)=AVAIL(NBOR(K),1,I)*T1%R(K)
! ENDFC
                    IF (RECIRCULATE.EQ.1.AND.LT.NE.1) THEN
                        QBOR%ADR(I)%P%R(K)=QOUT(I)/16.0D0
                    ELSE
                        QBOR%ADR(I)%P%R(K)=0.0D0
                    ENDIF
                    IF (QBOR%ADR(I)%P%R(K).LT.1.0D-12) THEN
                       QBOR%ADR(I)%P%R(K)=0.0D0
                    ENDIF
                  ENDIF
                ENDDO
              ENDDO
! FC - comment this line
!             ELSE
!               DO K=1,NPTFR
!                 IF(NUMLIQ%I(K).EQ.IFRLIQ.AND.
!     &              LIQBOR%I(K).EQ.KENT) THEN
!                   QBOR%ADR(1)%P%R(K)=T1%R(K)
!                 ENDIF
!               ENDDO
! ENDFC
            ENDIF
          ENDIF
        ENDDO
      ENDIF
      [...]
!-----------------------------------------------------------------------
!
      RETURN
      END
```

Listing F.1: Update of conlit.f.

APPENDIX G

ARCHITECTURE AND MAIN CHARACTERISTICS OF THE HPC USED IN THIS WORK

This page is available on-line at
https://si-scientifique.edf.fr/index.php/Architecture_EOLE_Clusters

De si-scientifique

Frontales d'accès

Adresses IP

- eole → eole.hpc.edf.fr (10.123.3.246)

5 frontales d'accès sont derrière cette IP virtuelle Eole :

- eole1 → eole1.hpc.edf.fr (10.123.3.241)
- eole2 → eole2.hpc.edf.fr (10.123.3.242)
- eole3 → eole3.hpc.edf.fr (10.123.3.243)
- eole4 → eole4.hpc.edf.fr (10.123.3.244)
- eole5 → eole5.hpc.edf.fr (10.123.3.245)

N.B : Après l'authentification, les noms des frontales apparaîtront sous la forme eofront[1-5] (et non eole[1-5]).

Sommaire

- 1 Frontales d'accès
  - 1.1 Adresses IP
  - 1.2 Configuration matérielle
- 2 Noeuds de calculs
  - 2.1 Noeuds de calculs standards
  - 2.2 Noeuds de calculs grande mémoire
  - 2.3 Noeuds graphiques
  - 2.4 Système de fichiers distribué GPFS
  - 2.5 Systèmes de fichiers NFS
- 3 Gestionnaires de jobs
  - 3.1 Les partitions
  - 3.2 QOS

Configuration matérielle

Frontales		Processeurs				RAM	Réseau		Disque dur	
Nom	Qté	Modèle	CPU	Cores/CPU	Cores		Ethernet	Rapide	Capacité	Point de montage
eole[1-5]	5	Intel® Xeon® CPU E5-2680 v4 @ 2.40GHz (Broadwell) (https://ark.intel.com/products/91754/Intel-Xeon-Processor-E5-2680-v4-35M-Cache-2_40-GHz)	2	14	28	256Gio	1 x Intel 82576 Gigabit Ethernet dual port	1 x Intel OPA Omni-Path Gen1	1To (SATA)	/tmp

Noeuds de calculs

Noeuds de calculs standards

Compute node		Processeurs				RAM	Réseau		Disque dur	
Nom	Qté	Modèle	CPU	Cores/CPU	Cores		Ethernet	Rapide	Capacité	Point de montage
eocn[0001-1164]	1164	Intel® Xeon® CPU E5-2680 v4 @ 2.40GHz (Broadwell) (https://ark.intel.com/products/91754/Intel-Xeon-Processor-E5-2680-v4-35M-Cache-2_40-GHz)	2	14	28	128Gio	1 x Intel 82576 Gigabit Ethernet dual port	1 x Intel Omni-Path Gen1 100Gb/s PCIe3.0	1To (SATA)	/tmp

Noeuds de calculs grande mémoire

Compute node		Processeurs				RAM	Réseau		Disque dur	
Nom	Qté	Modèle	CPU	Cores/CPU	Cores		Ethernet	Rapide	Capacité	Point de montage
eobm[0001-0096]	96	Intel® Xeon® CPU E5-2680 v4 @ 2.40GHz (Broadwell) (https://ark.intel.com/products/91754/Intel-Xeon-Processor-E5-2680-v4-35M-Cache-2_40-GHz)	2	14	28	256Gio	1 x Intel 82576 Gigabit Ethernet dual port	1 x Intel Omni-Path Gen1 100Gb/s PCIe3.0	1To (SATA)	/tmp
eobm[0097-0144]	48	Intel® Xeon® CPU E5-2680 v4 @ 2.40GHz (Broadwell) (https://ark.intel.com/products/91754/Intel-Xeon-Processor-E5-2680-v4-35M-Cache-2_40-GHz)	2	14	28	512Gio	1 x Intel 82576 Gigabit Ethernet dual port	1 x Intel Omni-Path Gen1 100Gb/s PCIe3.0	1To (SATA)	/tmp
eobm[0145-0160]	16	Intel® Xeon® CPU E5-2637 v4 @ 3.50GHz (Broadwell) (https://ark.intel.com/products/92983/Intel-Xeon-Processor-E5-2637-v4-15M-Cache-3_50-GHz)	2	4	8	256Gio	1 x Intel 82576 Gigabit Ethernet dual port	1 x Intel Omni-Path Gen1 100Gb/s PCIe3.0	1To (SATA)	/tmp
eobm[0161-0162]	2	Intel® Xeon® CPU E7-8867 v3 @ 2.50GHz (Haswell) (https://ark.intel.com/products/84681/Intel-Xeon-Processor-E7-8867-v3-45M-Cache-2_50-GHz)	4	16	64	2Tio	1 x Intel 82576 Gigabit Ethernet dual port	1 x Intel Omni-Path Gen1 100Gb/s PCIe3.0	1.2To (SAS)	/tmp

Noeuds graphiques

Graphical node		Processeurs				RAM	Réseau		GPU	Disque dur	
Nom	Qté	Modèle	CPU	Cores/CPU	Cores		Ethernet	Rapide		Capacité	Point de montage
eogn[0001-0032]	32	Intel® Xeon® CPU E5-2637 v4 @ 3.50GHz (Broadwell) (https://ark.intel.com/products/92983/Intel-Xeon-Processor-E5-2637-v4-15M-Cache-3_50-GHz)	2	4	8	256 Gio	1 x Intel 82576 Gigabit Ethernet dual port	1 x Intel Omni-Path Gen1 100Gb/s PCIe3.0	NVIDIA Corporation K80 (http://www.nvidia.fr/object/tesla-k80-fr.html)	1To (SATA)	/tmp
eogn[0033-0064]	32	Intel® Xeon® CPU E5-2637 v4 @ 3.50GHz (Broadwell) (https://ark.intel.com/products/92983/Intel-Xeon-Processor-E5-2637-v4-15M-Cache-3_50-GHz)	2	4	8	128 Gio	1 x Intel 82576 Gigabit Ethernet dual port	1 x Intel Omni-Path Gen1 100Gb/s PCIe3.0	NVIDIA Corporation K80 (http://www.nvidia.fr/object/tesla-k80-fr.html)	1To (SATA)	/tmp

Système de fichiers distribué GPFS

Le cluster EOLE dispose d'un ensemble de serveurs GPFS proposant un système de fichiers distribué monté sur tous les nœuds de calculs et les frontales :
Ce système de fichier est accessible dans /home/$USER, /scratch/$USER & /projets.

Point de montage	Niveaux redondance	Quota Utilisateur	Sauvegardes	Fréquence des sauvegardes	Durée de rétention
/home	Raid 6	250Go	OUI	Journalière	15 versions de fichiers maximum pendant 60 jours
/projets	Raid 6	500Go (*)	OUI	Journalière	15 versions de fichiers maximum pendant 60 jours
/scratch	Raid 6	2To	NON	N/A	N/A

(*) Pour chaque espace projet stocké dans /projets, le quota est appliqué au groupe administrateur de cet espace, c'est à dire `cl-pj-<projet>-admin`.

Systèmes de fichiers NFS

Les volumes offerts par les clusters de données TGVD (R&D) et SSSv2 (DIPNN) sont disponibles sur les frontaux de connexion et sur les

nœuds graphiques.

Point de montage	Device NFS	Direction
/data/projets/echanges.004	/mnt/.tgvd/co-retd-tgvd/echanges.004	R&D
/data/projets/mutualise_collaboratif.005	/mnt/.tgvd/co-retd-tgvd/mutualise_collaboratif.005	R&D
/data/projets/patrimoine_collaboratif.006	/mnt/.tgvd/co-retd-tgvd/patrimoine_collaboratif.006	R&D
/data/projets/patrimoine_reference.007	/mnt/.tgvd/co-retd-tgvd/patrimoine_reference.007	R&D
/data/projets/patrimoine_probant.008	/mnt/.tgvd/co-retd-tgvd/patrimoine_probant.008	R&D
/data/projets/patrimoine_projets.003	/mnt/.tgvd/co-retd-tgvd/patrimoine_projets.003	R&D
/data/projets/projets.001	/mnt/.tgvd/co-retd-tgvd/projets.001	R&D
/data/projets/projets.002	/mnt/.tgvd/co-retd-tgvd/projets.002	R&D
/data/rd/netdata	/mnt/.tgvd/netdata	R&D
/data/septen	/mnt/.sss/septen	Ingénierie Nucléaire
/data/unie	/mnt/.sss/unie	Ingénierie Nucléaire
/data/commun/nucleaire	/mnt/.sss/commun/nucleaire	Ingénierie Nucléaire

Gestionnaires de jobs

Le gestionnaire de jobs utilisé sur le cluster de calcul Eole est Slurm version 16.05.6.

Les partitions

Les partitions existantes à ce jour :

PartitionName	Nodes	Default	MaxTime	State	QoS
cn	eocn[0001-1164]	YES	INFINITE	UP	cnpartlimit
bm	eobm[0001-0162]	NO	INFINITE	UP	
gn	eogn[0001-0064]	NO	INFINITE	UP	

QOS

Les QoS existantes à ce jour :

Name	Priority	GraceTime	PreemptMode	UsageFactor	GrpTRES	MaxWall
test	2500	00:00:00	cluster	1.000000	node=10	00:30:00
cnpartlimit	0	-	cluster	1.000000	cpu=2610	-
cn_all_short	100	00:00:00	cluster	1.000000	-	08:00:00
bm_all_short	100	00:00:00	cluster	1.000000	-	08:00:00
gn_all_short	100	00:00:00	cluster	1.000000	-	08:00:00
cn_all_long_rd	10	00:00:00	cluster	1.000000	cpu=16701	8-00:00:00
bm_all_long_rd	10	00:00:00	cluster	1.000000	cpu=2744	8-00:00:00
gn_all_long_rd	10	00:00:00	cluster	1.000000	cpu=328	8-00:00:00
cn_all_long_ingenuc	10	00:00:00	cluster	1.000000	cpu=9372	8-00:00:00
bm_all_long_ingenuc	10	00:00:00	cluster	1.000000	cpu=686	8-00:00:00
gn_all_long_ingenuc	10	00:00:00	cluster	1.000000	cpu=82	8-00:00:00

Récupérée de « https://si-scientifique.edf.fr/index.php?title=Architecture_EOLE_Clusters&oldid=4591 »

- Dernière modification de cette page le 29 août 2018 à 14:19.
- Cette page a été consultée 503 fois.

Florian Cordier

Laboratoire d'Hydraulique Saint-Venant et EDF R&D LNHE Chatou Lab.

Bars morphodynamics in trained rivers with heterogeneous sediment

ABSTRACT:

Rivers often present a wavy bed topography due to the presence of bars, corresponding to large sediment deposits alternating with deeper areas (pools). Intense and continual river engineering works altering the river geometry, flow regime and sediment supply can impact bar morphodynamics at the reach scale. A deep knowledge of bar processes is important for river managers, because bars actively control the river bed topography and influence bank erosion, with consequences for navigation, water intakes, infrastructure and the quality of their habitats. Although the origin of bar formation and propagation is well understood, the understanding of bar morphodynamics in rivers remains limited due to the non-linearity of a complex combination of variables of control. Sediment non-uniformity is an inherent characteristic of rivers, but its impact on bar properties, even considering simple configurations, is still unclear. This Ph.D. thesis aims at investigating the impact of sediment size heterogeneity on bars in rivers with non-erodible banks, using a two-dimensional morphodynamic model implemented in the Telemac-Mascaret system. Several key improvements of the model (new sediment transport formula dedicated to non-uniform material, vertical sediment sorting) have been proposed to reach the state of the art in modelling the influence of heterogeneous sediment on river bar morphodynamics. Firstly, the numerical model is applied to reproduce periodic bar morphodynamics with uniform and non-uniform sediment distribution in an idealized channel geometry and well controlled boundary conditions. Secondly, the morphodynamic model is applied to a sandy-gravel reach of the middle Loire river, presenting a combination of multiple internal and external forcing parameters, such as longitudinal variations of the channel width and variable hydrology. Numerical results show that periodic bars of different types (free/hybrid) and patterns (low/high bar mode) exhibit distinct sediment sorting patterns. Spatial sediment sorting is showed to not affect the averaged migrating bars characteristics, while it impacts significantly steady bar characteristics such as elongation and damping, which in turn increases further downstream bars mobility. Furthermore, a larger sediment size heterogeneity is showed to increase the degree of sediment sorting, with consequences on the dimensions and mobility of bars as explained previously. General outcomes of this thesis show the validity of the modelling approach, demonstrate its applicability for other study cases, and propose diverse recommendations for river engineers to model and predict bar morphodynamics processes before designing effective river management solutions.

Key words: Fluvial morphodynamics, sediment transport, alluvial bar, heterogeneous sediment, numerical modelling, fluvial engineering.